ELECTRIC MULTIROTOR DESIGN AND OPTIMIZATION

A Dissertation
Presented to
The Academic Faculty

by

Dmitry Bershadsky

In Partial Fulfillment
of the Requirements for the Degree
Doctor of Philosophy in the
School of Aerospace Engineering

Georgia Institute of Technology
August 2017

ELECTRIC MULTIROTOR DESIGN AND OPTIMIZATION

Approved by:

Professor Eric N. Johnson, Advisor
School of Aerospace Engineering
Georgia Institute of Technology

Professor Daniel Schrage
School of Aerospace Engineering
Georgia Institute of Technology

Professor Eric Feron
School of Aerospace Engineering
Georgia Institute of Technology

Professor Brian German
School of Aerospace Engineering
Georgia Institute of Technology

Dr. Phillip Jones
Founder
Scion UAS

Date Approved: 17 July 2017

ACKNOWLEDGEMENTS

I would like to thank my parents, grandparents, friends, my advisor Dr. Eric Johnson, the members of his UAVRF, namely Nimrod Rooz, Claus Christmann, Jack Mooney, Pierre Valdez, Steve Haviland, Lee Whitcher, Joshua Carnes, Eric Avari, Marc-Henri Bleu-Laine, Nick Willard, and Mitchell Sanders for their help with the work described in this document and the occasional pushes I needed to write about it. I would also like to thank Dr. Brian German, Dr. Daniel Schrage, Dr. Phillip Jones, Dr. Mark Costello, and Dr. Eric Feron for their time and insightful comments during both the proposal and defense.

TABLE OF CONTENTS

LIST OF TABLES

LIST OF FIGURES

SUMMARY

Multirotors are being deployed for an ever increasing variety of tasks and missions. As these vehicles become more ubiquitous and used for different types of work, the need to design them efficiently for specific missions and tasks becomes more critical. One of the more involved tasks of designing a multirotor unmanned aerial vehicle (UAV) is the selection of a propulsion system that will provide desired performance. Rigorous methods for selecting these drive components, that is, the motors, propellers, and batteries for electric UAVs are not readily available. Currently, many UAV designs are based on legacy selections or limited and at times largely incorrect manufacturer data. The existing design methods are either simplistic or lacking in analysis and validation of component selection. Proper propulsion system design should address the mission requirements for which the vehicle is being designed. A mission might be comprised of a combination of airspeeds, durations, ranges, altitudes, temperatures, payloads and the like. A proper design methodology is the best chance that the designer has to create a new vehicle that will be mission-capable. In addition to being mission-capable, the vehicle should be task-capable. Tasks such as object manipulation or otherwise interacting with the UAV's environment require that vehicles be capable of, among other things, the ability to produce forces and moments. At times, these requirements will drive designs away from "standard" existing designs where rotors are co-planar to provide capability and degrees of freedom (DOFs) that the standard designs do not have.

This work satisfies the need for more thorough method of propulsion component selection for electric VTOL (eVTOL) propulsion system design by bridging traditional

aircraft sizing and electric multirotor design. Presented here is a framework for both analysis of an existing propulsion system, and also optimization of a propulsion system given a set of mission requirements for generic multirotor vehicles. The system of both the analyzer and optimizer is termed multirotor sizing tool (MST). The analyzer is capable of taking in and/or estimating a multitude of propulsion system parameters to predict the performance profile of the system including range, endurance, speed, power, sensitivities. The optimizer designs a propulsion system to satisfy goals such as desired endurance, range, maneuverability, and so forth. It designs the lightest possible vehicle within in a range of design variables set by the user. The modeling of electrical propulsion system components is described. MST is then used to design several vehicles which are built and flown, and predicted vs. measured data are presented. In addition to describing the MST, the study addresses the optimization of orientation of selected rotors in order to achieve rates in multiple axes. A study of configurations and effects on rate authority is also presented, including combinations of co-axial and pusher/tractor configurations, standard, non-standard coplanar and non-coplanar rotor layouts and different frames. Thrust stand, wind tunnel, and flight test results are included. Two novel configuration designs are presented, both an upgrade of existing configurations.

0.1 List of Symbols and Abbreviations

Abbreviations

3D	three dimensional
A2D	analog to digital
AC	alternating current
AOA	angle of attack, also α
BEMT	blade element momentum theory
BLDC	brushless DC (motor)
CCW	counter-clockwise
CG	center of gravity, center of mass
CW	clockwise
COTS	commercial, off-the-shelf
DOF	degree(s) of freedom
eVTOL	electric VTOL, referring to the propulsion system's energy source
EXPT	experiment to answer RQ
DC	direct current
DFC	direct force control
ESC	electronic speed controller
FPA	flight path angle, also γ
FW	firmware
GA	genetic algorithm
GTOW	gross takeoff weight
GUST	Georgia Tech UAV Simulation Tool
LUT	look up table
MDO	multidisciplinary design optimization
MR	multirotor
MST	multirotor sizing tool, or validator and optimizer

PWM	pulse-width modulation or modulated
ROC	rate of climb
RQ	research question
RPM	rotations per minute
RTF	ready to fly
UAS	unmanned aircraft system
UAV	unmanned or uninhabited aerial vehicle
UAVRF	UAV Research Facility
VTOL	vertical takeoff and landing

Vehicle configurations

+4	four rotors, four arms, front arm aligned with $+x_B$
X4	four rotors, four arms, front two arms bisected by $+x_B$
+6	six rotors, six arms, front arm aligned with $+x_B$
X6	six rotors, six arms, front two arms bisected by $+x_B$
Y6C	six coaxial rotors, three arms, front two arms bisected by $+x_B$
Y6sC	six semi-coaxial rotors, three arms, front two arms bisected by $+x_B$
+8	eight rotors, eight arms, front arm aligned with $+x_B$
X8	eight rotors, eight arms, front two arms bisected by $+x_B$
X8C	eight coaxial rotors, four arms, front two arms bisected by $+x_B$
+12	twelve rotors, twelve arms, front arm aligned with $+x_B$
X12	twelve rotors, twelve arms, front two arms bisected by $+x_B$
X12C	twelve coaxial rotors, six arms, front two arms bisected by $+x_B$
	these vehicle configurations are shown in Figures 1 and 2

Symbols

α	angle of attack, also AOA
A	swept rotor disc area

A_f	flat plate area
β	blade physical twist, or sideslip
B	number of blades per propeller
c	wing chord
c_R	c/R
C_D	drag coefficient
C_L	lift coefficient
C_P	power coefficient
C_Q	torque coefficient
C_T	thrust coefficient
c_b	battery discharge rating
C	battery energy capacity
C_{td}	capacity degradation due to temperature
d_b	discharge fraction, or depth of discharge
dr	differential blade radial section
d_t	throttle command
dt	change in time
dL	incremental lift
dQ	incremental torque
D	drag force
η_E	ESC efficiency
η_M	motor efficiency
η_G	gearing efficiency
η_T	electrical thrust efficiency
ϵ	arm dihedral angle
f	function, objective function
F	force vector

g	gravity, scalar or vector
G	gear ratio
I	inertia
I_0	no load current drawn by one motor
I_a	current drawn by avionics
I_d	current drawn by all motors
I_m	current drawn by 1 motor
I_p	current drawn by payload
I_t	current drawn total
J	advance ratio
κ	dummy variable
K_v	motor speed constant
λ	arm azimuth
Λ	wheelbase or characteristic length
l	arm length
L	total blade lift
m_{avn}	avionics mass
m_b	battery mass
m_e	ESC mass
m_m	motor mass
m_p	propeller mass
m_{pay}	payload mass
m_t	total vehicle mass, GTOW
m_w	motor mass
M_{tip}	blade tip Mach number
M	moment vector
N_g	GA number of generations

N_m	number of motors
N_p	number of propellers
ω	angular velocity
Ω	rotations per minute, also RPM
ϕ	vehicle roll
Φ_B	battery weight fraction
ψ	vehicle yaw
p_p	propeller pitch
p_{mat}	propeller composition
P	Cartesian position vector
P_e	electrical power
P_i	induced power
P_m	mechanical power
P_{pro}	profile power
P_{par}	parasite power
Q	total propeller torque
Q_r	radial segment propeller torque
r	blade radial section location
r_R	r/R
r_{b_B}	position vector of battery in body frame
r_{ri_B}	position vector of ith rotor in body frame
R	rotor radius
R_b	battery internal resistance
R_e	ESC internal resistance, also R_{DSON}
R_m	motor internal resistance
R_w	wiring harness internal resistance
Re	Reynolds number

s	battery serial cells
s_D	separation non-dimensionalized by diameter
S	wing span or serial cell count
S_w	wing area
θ	vehicle pitch
τ	equivalent thrust vector tilt
T	thrust force
T_r	thrust force required or BEMT thrust at radial section r
T_C	temperature, C
u	control vector
v_i	induced velocity at the propeller disc
v_v	induced velocity at the vena contracta
V_c	operational voltage per cell
$V_{c50\%}$	operational voltage per cell at 50% depth of discharge
V_{td}	voltage degradation with temperature
V_s	voltage seen by motor coils
w	rotational speed rad/s
W	GA weight array
x_B	vertical body axis, positive forward
ξ	thrust overhead
X	design variable array
y_B	lateral body axis, positive right
ζ	motor tilt angle around arm
z_B	lateral body axis, positive down

CHAPTER I

INTRODUCTION

1.1 Motivation

Electric multirotors have received an explosive amount of attention in the last decade. These aerial robots are used in an increasing number of industries for an ever widening variety of applications. These robots are becoming more capable at a rapid rate, both in terms of their avionics, which help them to carry out difficult tasks, and their propulsion systems, which provide the thrust and endurance necessary to complete them. There are many areas being studied which support this growth rate including algorithm development, avionics miniaturization and processing power enhancement, sensor work, and many others. This thesis focuses on the propulsion system's design in particular to help facilitate this rapid growth. The design includes the geometry and configuration of the propulsion system components, i.e., their layout on the vehicle. Studies into design and propulsive efficiency enhancement for these vehicles are critical to enable them to carry more payload to where it is needed, whether that be sensors, computers, manipulators, batteries, supplies, or whatever is required by the mission. These relatively small vehicles need to find efficiency wherever possible to overcome the generally high inefficiencies in energy requirements to keep them operating. This thesis aims to investigate some of these inefficiencies in an attempt to provide suggestions to lessen their detriment to propulsion and hence the overall system.

1.2 Thesis organization

This thesis begins by mentioning some of the works in the literature regarding design of aircraft, focusing on unmanned electric vehicles. These are organized into two categories: sizing and configuration. "Sizing" deals with selection of specific or a class of components which will allow a vehicle to accomplish a mission. "Configuration" deals with the positioning and orientation of these components on the vehicle in order to enable a capability on a more tactical level; that is, optimization of force and moment capability in certain axes. The ideas of sizing and configuration together encompass the high-level design of propulsion systems described in this thesis. To investigate both of areas, electric propulsion components are identified and modeled, with emphasis placed on the rotor. A framework herein called multirotor sizing tool (MST) is proposed and described with example use cases. Using components of this, a configuration optimizer is proposed and described and used to study the effects of rotor layout on vehicle performance and is used to optimize configurations of several vehicles. Multirotor aerodynamics are briefly studied to increase the accuracy of these models. Wind tunnel data is provided for multirotor aerodynamic data. A multi-degree of freedom thrust stand is designed and built to study inter-rotor aerodynamic effects.

1.2.1 Contributions

Primary contributions of this thesis:

1. Framework and tool to validate electric multirotor performance that is validated on a set of multirotors in hover
    - input is a set of propulsion system parameters
    - output is a mission that's possible with the propulsion system

    The tool is capable of handling:

- generic vehicle configurations including but not limited to multirotors, fixed wing, helicopter, hybrid vehicles, N_m heterogenous rotors
- battery dynamics, including effects of discharge rate, temperature
- environmental effects including altitude, temperature, wind

2. First framework and tool to optimize generic electric multirotor propulsion system for a particular mission using rubber components using classical approach to aircraft design
    - input is a set of mission parameters
    - output is a set of rubber propulsion system parameters capable of the required mission
3. Parametrization (rubberization) of propulsion components: motors, batteries, propellers, ESCs
4. Multirotor wind tunnel data and findings
    - multiple configurations for small multirotors: 122 to 450 mm, canopies, RTF configurations
    - C_{L_α}, C_{D_α}
5. Adjustable thrust stand design which can record thrust, independent P_e, and P_m with data for several configurations:
    - first review of semi-coaxial configuration
    - first review of co- vs. counter- rotating coaxial configuration
    - first review of puller vs. pusher configuration
    - first review of wake-wake interaction
    - coaxial

6. Framework to optimize generic rotor configurations which can handle:
    - N_m heterogenous rotors
    - positions and orientations may be generic, symmetric
7. Acceleration authority design space of multiple standard and non-coplanar configurations for ζ, ϵ for multiple vehicle types
    - quad to dodecarotors
    - co- and counter- rotating
    - pure to absolute maximum impure envelope
    - effect of configurations on rates
8. Novel multirotor design: *Y6sC* Figure 1 (j)
    - first description of semi-coaxial which is more efficient than coaxial configuration
    - rate advantages over *Y6C* in all axes
    - gains in two DOFs with no change in propulsion system: now $\ddot{x}, \ddot{y}$ are possible
9. For the "standard DFC" *X6* Figures 1 (i), 5
    - design optimization of rates using 1-24 DOF with different axis weights, dynamics coupling constrained and relaxed
    - design optimization for unknown single fault tolerance
    - mapping between ζ, ϵ and equivalent thrust vector tilt
    - hover trim attitude envelope

- second novel design: efficiency enhancement if rotors are pointed at eachother to mimic configuration described in section 4.1.10.4 and shown in Figure 52

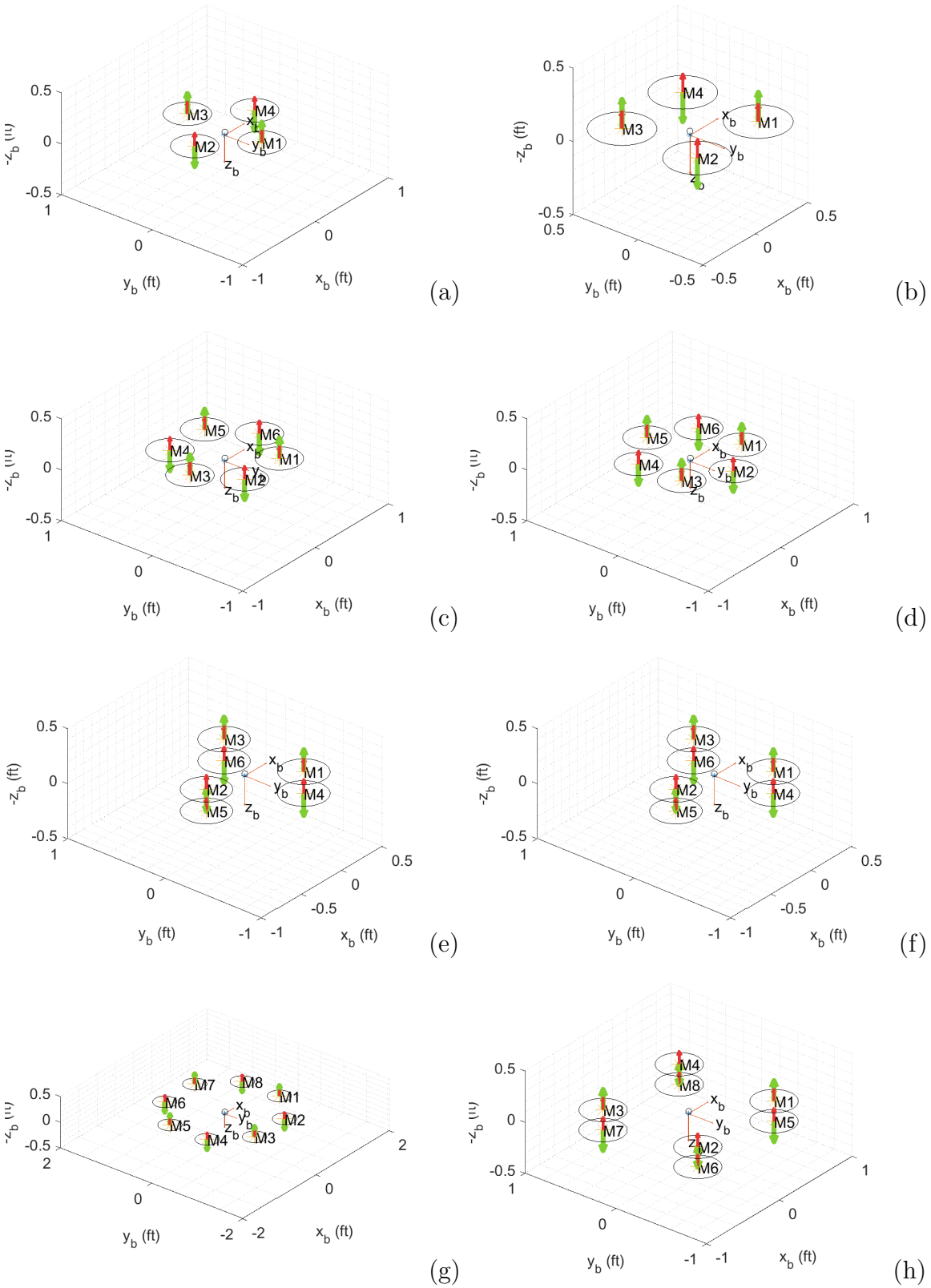

Figure 1: Multirotor configurations: a) *+4*, b) *X4*, c) *+6*, d) *X6*, e) *Y6C*, f) *Y6C* counter-rotating, g) *X8*, h) *X8C*. Red short arrows are thrust vector, green long arrows are right-handed rotation vector.

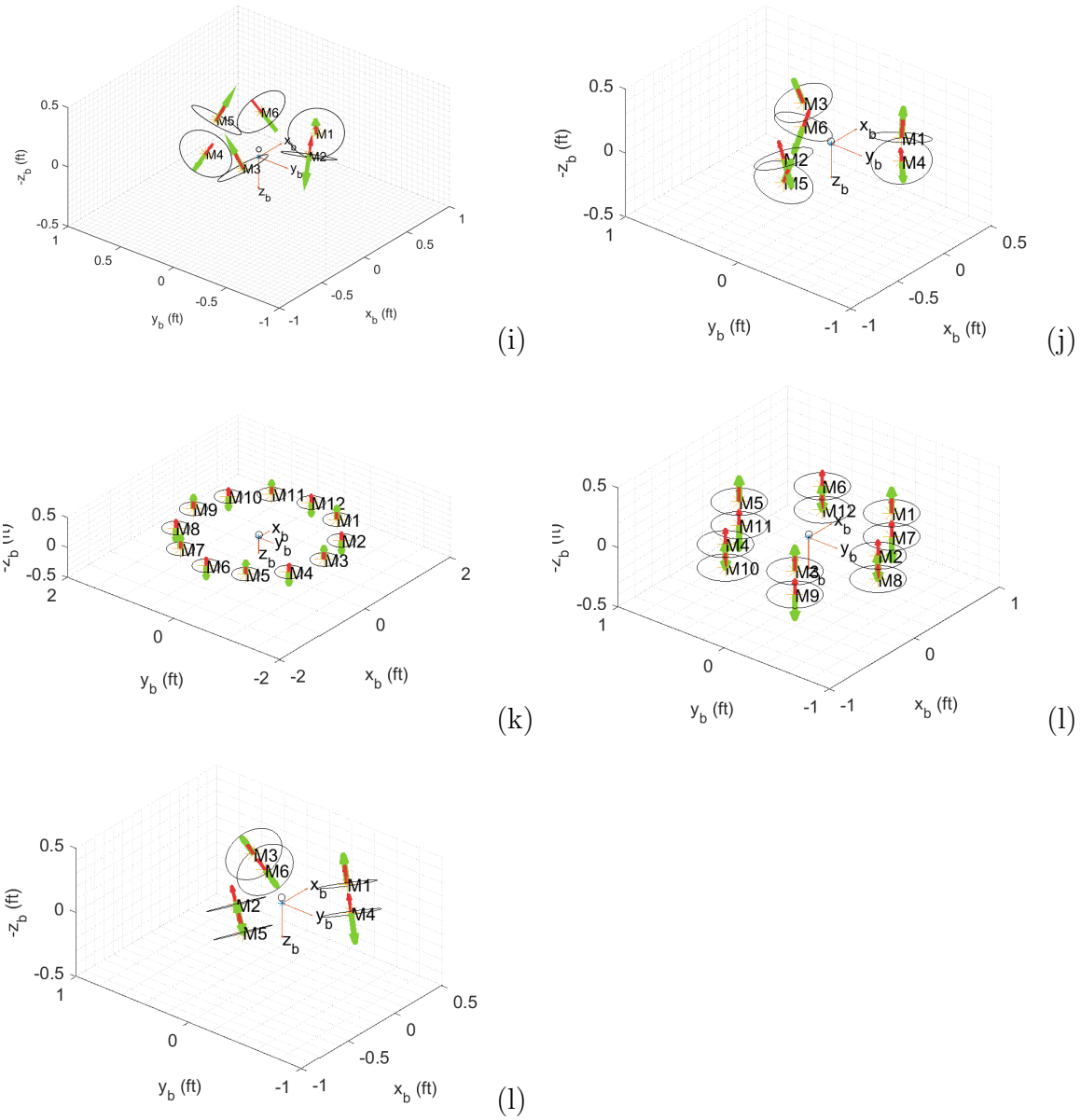

Figure 2: Multirotor configurations: i) *X6* DFC $\zeta = 30°, \epsilon = 15°$, j) *Y6sC*, k) *+12*, l) *X12C*, m) *Y6C* $\zeta = 30°, \epsilon = 15°$. Red short arrows are thrust vector, green long arrows are right-handed rotation vector.

CHAPTER II

MULTIROTOR DESIGN CONSIDERATIONS, METHODS, AND ANALYSES

2.1 Background: multirotor electric propulsion system design considerations

There are multiple considerations that must be addressed when designing a multirotor UAV propulsion system. Design questions and requirements might range from designing a vehicle specific to a required mission, to designing a mission given a vehicle or set of components. The scope of the design space may encompass some or all of the variables described in this study, be they mission level, task level, or component level parameters. The designer should be able to create a vehicle to accomplish a set of tasks, and likewise estimate what tasks an existing vehicle design can accomplish. They should be able to do so with few or multiple constraints on the design. Constraints might come in the form of economical, physical, or time-based conditions which must be met and all differently effect the design and analysis of the capability of a UAS. There may for example be a constraint on the type of rotors to be used, whereas the other components may be freely selected. Or, all components but a rotor are already selected, perhaps due to legacy or stock availability. There may be other considerations but the ones discussed in this document are considered as primary design variables in that they greatly affect flight performance such as range, payload capacity, endurance, and maximum accelerations. Understanding the complex interplay between propulsion system components and their environment is key in successful mission or task based design of a multirotor vehicle.

This section briefly identifies the naming convention for common multirotor layouts, as well as some less common ones. Then, the four main propulsion system components are described in terms of propulsion system design, as well as available methods for multirotor design. Afterwards, questions are posed that will form the direction for the rest of the document, the answers to which will begin to fill some of the holes which remain in the literature.

2.1.1 Multirotor layout and naming convention

The layout of propulsion components will clearly have an effect on the multirotor, with layout types having pros and cons over others. Many so-called "standard" designs have emerged and gained traction in the multirotor community due to their simplicity. Other less "standard" designs have been attempted and are not commonly produced, trirotors with one actuated rotor for example.

There are several loose conventions for naming multirotor vehicles. The naming convention proposed for this study is as follows. The first letter denotes the arm layout for "standard" configurations; that is, $X/V/Y/+$ denote the positions of the arms starting with the front two arms. X, V, and Y, a special case of X, all mean that the front-axis bisects the two front arms. The V frame is a special case that is not considered in this study but is described by Achtelik [1]. $+$ indicates that the front-axis is parallel to the front arm. Y is a special case of the X frame and is used for tri- and hexarotors. The number indicates the number of independent rotors. That is, the number of motor/propeller pairs. A motor with coaxial propellers will not be considered here but would be labeled as one rotor. The letter C denotes a configuration with coaxial rotors; a motor and propeller stacked on top of another pair of the same. The vehicles considered here are shown in Figures 1 and 2, where propeller discs are plotted as circles. The green arrow indicates the spin direction of each rotor using the "right hand rule." Each rotor is labeled with a number starting

from the x_B axis and increasing clockwise looking from the top toward $+z_B$. The red arrow indicates each rotor's thrust vector. The "o" indicates the CG of the vehicle.

Take the *X4*, *X8*, *X8C* as examples. The *X4* would denote an *X* frame with 4 motors, where forward is between the two front arms, seen in Figure 1 (b). The *X8*'s front-axis would also bisect the front two of 8 arms, each with a rotor, shown in Figure 1 (g). The *X8C* would be be 8 coaxial rotors with the front two of four arms once again bisected with the forward-axis, as in Figure 1 (h). As mentioned *Y* is a special case of an *X* frame to match existing terminology where a *Y6C*'s front splits the forward two of 3 arms, each with a coaxial pair of rotors, in Figure 1 (e). *Y6C* also disambiguates the configuration with *X6C*, which would have 4 arms with two of the four arms having two coaxial rotors. *Y3* or trirotors will not be considered in this study. The *X6* DFC vehicle in the second figure (i) is the subject of many of the later sections of this study.

2.1.2 Motor

Brushless DC (BLDC) motors are used for all of the vehicles described by this study. These are commonly preferred over older, brushed designs for their greater efficiency in converting electrical to mechanical energy. BLDC motor designs have two configurations, outrunner (OR) and inrunner (IR), which define the component of the motor that rotates and is attached to the output or actuation axle. IR motors spin an axle with magnets inside of array of windings arranged circularly around it. OR BLDC motors invert the IR design and wrap a bell of magnets around the winding array. Although IR motors allow for some tighter installations due to the body of the motor being static, the OR configuration allows those motors to produce more torque than their IR counterparts. This makes IR BLDC motors a common choice for many small (< 100 g) multirotor builds, and OR a good choice for anything larger. It is possible to use gearing (Parrot AR drone is a popular design) as well but due to the inherent

complexity, many designs use direct drive BLDC OR motors. In a direct drive design, the propeller is directly attached to the motor axle. One benefit however of a geared design is the potential to hide a motor's axle mostly inside the motor body, making it more durable in the event of a crash. Of course, the gearing is now accepting the brunt of the crash energy, but this may be easier to replace than a motor axle.

Along with the maximum power production capability, the most important parameter of motor selection is the speed constant, or K_v, measured in RPM/V. It is the manufacturer's indication of roughly how fast the motor will spin when unloaded per applied volt across its wrapping wires. Once the motor is loaded, i.e. a torque load from a propeller, the RPM/V response of the motor will change. K_v must thus be properly matched to the selection of the propeller, ESC, and battery, as well as chosen for resulting efficiency and lift capability. With respect to the propeller, the motor should be able to handle the mechanical and torque electrical power loads applied by turning the propeller. Too high of a K_v or voltage, and the motor may be unable to handle the torque loads at high throttle, or may spin in a lower efficiency regime with too low of an RPM at low throttle. Too low of a K_v and the throttle command may be too high to generate sufficient thrust to fly. Generally a lower K_v motor that spins a larger and/or low-pitched propeller will be more energy-efficient (at hover) than a high K_v motor with a smaller and/or high-pitched propeller due to a lower induced velocity to produce the same thrust. Of course, for forward flight, this may not be the case and needs to be considered. One advantage of the latter however is higher performance for acrobatic flying. A smaller diameter propeller will react to motor torque quicker than a larger one for quicker changes in thrust required in this style of flying. The hardware and firmware of the ESC should also be able to handle not only the electrical power required, but also the timing of the motor which is related to the physical configuration of the motor, as well as the loads and commands applied to it. The latter is out of scope for this work.

2.1.3 Propeller

Propeller composition, radius, pitch, and number of blades must also be chosen to work properly with the chosen motor. The material from which the propeller is made might affect the efficiency of the propeller at different RPMs. This may occur for softer propellers due to flexure of the blades changing effective angle of attack at radial sections away from designed angles. This effect is described by Harrington[2]. At the same RPM, assuming the blade is not stalled, increasing the propeller pitch and number of blades generally generates more thrust. This however comes at a cost of lower efficiency and increased electrical and mechanical power requirements on the motor. Increasing the propeller's radius is generally more efficient, assuming the rest of the drive system is capable of handling the load. This is because the larger propeller, with all else being equal, may spin slower to generate the same thrust. This allows the induced velocity to drop, thereby increasing propulsive efficiency, at least in hover, by lowering the power required to generate the same thrust. To see this effect, consider two rotors, one with radius R_1 and the other with radius $R_2 > R_1$. Assume that all else is equal, including the required thrust T_r in both situations. Recall that thrust is (via momentum theory) estimated by

$$T_r = \dot{m} v_v \tag{1}$$

where v_v is the air flow speed at the vena contracta (assuming $V_\infty = 0$), which is equivalent to $2v_i$ when ignoring viscous effects. T_r may be rewritten as

$$T_r = 2\dot{m} v_i \tag{2}$$

Mechanical power P_m required to generate this thrust is

$$
\begin{aligned}
P_m &= T_r v_i \\
&= 2(\dot{m} v_i) v_i \\
&= 2(\rho A v_i v_i) v_i \\
&= 2\rho\pi R^2 v_i^3
\end{aligned}
\tag{3}
$$

It is clear from this relation that once rotor disc area A_1 increases to A_2, in order to generate the same T_r, v_{i2} must be lower than v_{i1}. As P_m is proportional to v_i^3, the rotor in case two with $v_{i2} < v_{i1}$ requires less power to generate the same thrust T_r. Doubling the disc area A (i.e., $R_2/R_1 = \sqrt{2}$) drops P_m by reducing v_{i2} to $\sqrt{A_1/A_2}$. This yields $P_{m2}/P_{m1} = \sqrt{A_1/A_2} = 0.71$. Doubling the disc radius halves P_m required. When viscosity effects are considered, v_v is lower than $2v_i$. This slightly drops the power requirement P_m as seen in physical tests[3]. Achtelik [1] provides a similar analysis for power and dynamics.

2.1.4 Battery

Although technologies with higher specific energy densities, such as gas engines, fuel cells, and others are available, they will be considered out of scope for this study. This study considers common, current, hobby-grade batteries. Newer hobby-grade battery lithium polymer (LiPo) compositions are capable of specific energy of up to around 250 Wh/kg [4], about an order of magnitude lower than gunpowder, and two orders of magnitude lower than kerosene. The rapid development in this area has spurred projections of technologies capable of 400 Wh/kg by 2020[5]. Many commercial off the shelf (COTS) batteries are easily capable of discharging at currents greater than 100 A, some for extended periods of time. These batteries have all but replaced the previous NiCd and NiMH batteries which were used for hobby-grade vehicles in the past. Another composition known as lithium ion (LiIon), commonly used in consumer electronics such as laptops, has a specific energy 50% better than LiPo compositions,

although maximum discharge rates are lower, which makes them better choices for more efficient vehicles.

Other compositions include lithium iron phosphate (LiFe, LiFe PO_4, or LFP), which have a specific energy of around 100 Wh/kg. While they are heavier than other lithium compositions, they are considered to be more stable under discharge and when subjected to damage. Unlike LiPo batteries, they will not explode when punctured and their cells exposed to the air. These batteries are also reported to be able to withstand a greater number of discharges (2,000-10,000 [6] until degrading to 80% of their original capacity than other types mentioned above (up to 2,000 for LiPo[7]). This of course is a function of discharge rate, depth of discharge, temperature, and other factors. See 3.3.4 for LiIon data.

Aside from chemical composition, other main parameters must be considered when selecting a battery or batteries for the vehicle, although they are not necessarily independent. The battery's cell configuration and capacity must be considered. The battery must be chosen such that sufficient but not excessive voltage exists to power the propulsion system and avionics. LiFe cells have a maximum charged voltage of around 3.65 V/cell, whereas LiPo and LiIon cells are charged to 4.2 V/cell. Batteries are built by stacking cells in series (S) and parallel (P) to achieve endurance, payload, and discharge rate goals. Stacking cells in series increases the pack's voltage, while adding more cells in parallel increases its capacity. Higher voltage generally means more top speed for the rotors, which may increase payload. Parallel cells also increase the amount of energy stored, partially dictating the endurance of the vehicle and discharge rate of the battery. For example, a 4S1P LiPo battery has four cells in series and one in parallel, giving a fully charged voltage of 16.8 V, while the same configuration LiFe battery will be fully charged at 14.6 V. This value must correspond with the selection of motor K_v and propeller to achieve proper RPM and thrust values to lift the vehicle, along with any regulators that power other onboard electrical

systems.

The capacity, normally measured in mAh, determines the energy storage of the battery. A 1,500 mAh battery can provide 1.5 A of current for 1 hour if discharged to 100%. Batteries which are discharged to around 80% of their capacity per usage also tend to last longer than those which are discharged to a greater extent. The discharge rate, related to the so-called "C-rating" of a battery, is a manufacturer's indication of the discharge capability of the battery. A 40 C 1,500 mAh battery in an operational condition is capable of sustaining 60 A discharge for some amount of time. The power requirements of the drive system must be taken into account when selecting the battery.

2.1.5 Electronic Speed Controller

At a high level, the electronic speed controller (ESC) takes a pulse-width modulated (PWM) control signal, generally 1 ms (off) to 2 ms (full), and converts it to direct current (DC) through the wrapping wires on the BLDC motor's stator. The frequency of the switching, done by onboard field-effect transistors (FETs), partially determines the rotation of the rotor on the motor. The main parameter when selecting ESCs to consider is the maximum rated amperage. This must be sufficiently higher than the required drive current per motor such that the FETs do not overheat and fail. A secondary decision is whether or not to use ESCs with a battery eleminator circuit (BEC) onboard. These are often switching regulators (SBECs). These regulate main battery voltage down to usually 5 V to power other avionics. If this is not necessary, it is sometimes better to use optically isolated (OPTO) ESCs to save energy and heat, as the BECs tend to be inefficient and may cause unnecessary heating and energy loss. Often times standalone BECs are used (uBECs), which are power regulators that are not built into the ESC. Another operationally critical design choice is the software on the ESC, as this greatly changes the dynamic behavior of the rotor. In fact,

poor choices in ESC firmware (FW), for example a wrong timing setting, may even damage the rotor, potentially causing rotational FET-pole timing desynchronization, overheating, and/or even fire. Although it is important, ESC FW is out of scope for this sizing and dynamics study.

2.2 Selected propeller aerodynamic analysis methods

There are many studies which detail the modeling of lifting surfaces. Of interest to this thesis are the methods to analyze and predict performance of rotary lifting surfaces as are used on propellers. These propellers of course are instrumental to the function of the multirotor, producing both thrust for translation and torque for attitude control. As such, it is important to understand some of the major methods for predicting their performance. These methods range in complexity from low-fidelity rapid ones to higher-fidelity computational methods. An example of the latter is commonly referrred to as computational fluid dynamics (CFD) simulation. These methods solve a complex set of equations to model the flow of fluid around some body, such as a propeller in a particular configuration. As this thesis is concerned with the early design phase of multirotors, such methods are excessive for the purposes discussed here. Lower-fidelity methods such as momentum theory are more appropriate at this level and are described here.

2.2.1 Momentum theory

Momentum (or actuator disc) theory has been studied for over 120 years. It is a well-known propeller analysis technique studied extensively by [8] and [9]. This method models the airflow passing through a rotor disc as a streamtube, which is radially compressed as the air accelerates through the disc. Incompressible flow is assumed and Bernoulli's equation is used to derive pressure distributions and hence thrust estimates for the rotor. McCormick [10] provides a good overview of the method. The method states that the thrust produced by the rotor is

$$T = \dot{m}\Delta V \tag{4}$$

where ΔV is the change in velocity from far upstream V_∞ to far downstream $V_\infty + 2v_i$ of the rotor disc. In a hover state, $V_\infty = 0$. The velocity v_i is the induced velocity at the rotor disc. This result is helpful when conceptualizing the high-level tradeoffs of different rotors. The techniques are relatively simple and yet may be used to quickly yield some interesting results (i.e., 2.1.3). The method also provides intuition into the power required to produce the thrust of equation 4, given by

$$P_m = T(V_\infty + v_i) \tag{5}$$

Again, this provides intuition into the performance of rotors, but this method does not consider rotational flow or many other complicating factors of accurately modeling rotors such as profile drag or vortices. As such, the power estimated here will be lower than what will be seen in practice. However, the techniques are valid as a first order approximation for high-level design where the propeller geometry is not of interest. An extension of this method is described next.

2.2.2 Blade element momentum theory

Today there are many manufacturers and propeller designs available to the multirotor designer, all of which affect the performance or the rotor, and hence the multirotor. If blade design is of interest, momentum theory alone is not sufficient to predict the performance of the rotor. Drzewiecki [11] did much of the work developing blade element momentum theory (BEMT) in which a blade is divided into radial cross sections of radial length dr. In each cross section or blade element, and hence the name, the airfoil may be specified for calculation of each element's forces (decomposed into lift and drag), namely by using the airfoil's C_L and C_D, along with the flow velocity at each radial segment r. This is seen in Figure 3.

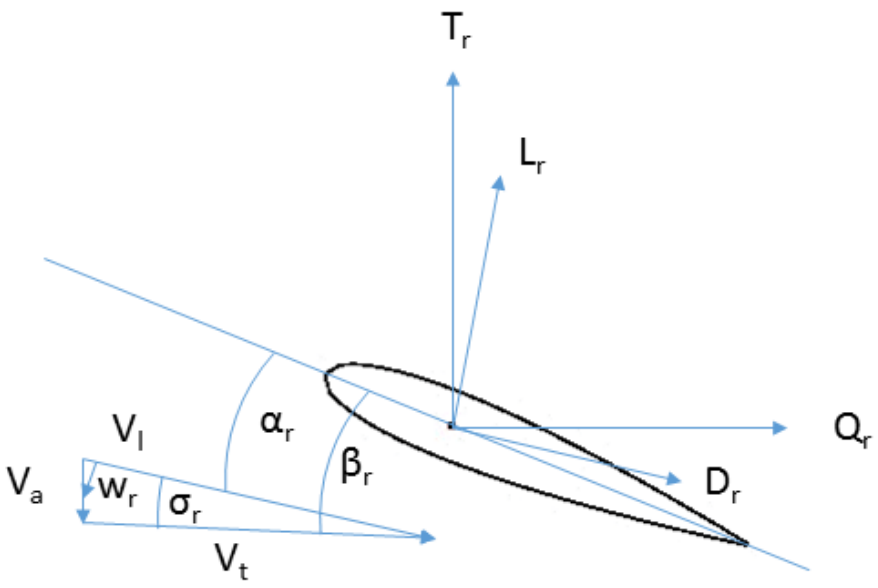

Figure 3: NACA 0015 blade cross section at radial section r with local velocity V_l decomposed into axial and tangential directions

The radial flow velocity V_t is created by rotation of the radial segment at ωr along the axial direction, along with the wake produced by the rotor w_r. The axial speed of the air entering the rotor plane V_∞ caused by wind or translation of the rotor through the air and w_r sum to produceV_a. The segment lifts L_r and drags D_r may then be integrated along the radial segments and summed from equation 6.

$$\begin{aligned} T_r &= c\frac{1}{2}\rho V_l^2(C_L cos(\sigma) - C_D sin(\sigma))dr \\ Q_r &= rc\frac{1}{2}\rho V_l^2(C_L sin(\sigma) + C_D cos(\sigma))dr \end{aligned} \tag{6}$$

The geometry of the blade is included thus as the aero data C_L and C_D, blade chord c, and twist of the blade β. The integrated radial segment lifts become thrust and integrated drag becomes torque, both acting along the rotation axis for simple cases (non-oblique flow) rotated by σ. Each of these will be multiplied by N_B, the number of blades per rotor. During the calculation, the local velocity at each blade element must be estimated. The induced velocity v_i, a function of the geometry and

rotational speed of the rotor, must be calculated in order to determine the overall flow velocity V_l at each element [12]. Often momentum theory is used to calculate this value, but other methods exist. Extensions of this method allow another advantage over momentum theory. Because of the drag experienced by the rotor, the air mass in turn experiences torque, which causes swirling in the fluid downstream of the rotor disc. This indicates that the propeller will produce a tangential velocity component of w_r. One common technique to deal with part of this effect is to calculate the tangential and axial induction factors a^t and a^a, respectively given by equation 7,

$$\begin{aligned} a^t &= \frac{\omega_a}{2\omega} \\ a^a &= \frac{v_i}{V_\infty} \end{aligned} \tag{7}$$

where ω_a is the local angular velocity aft of the rotor. This allows us to calculate the axial and tangential components of local velocity given by equation 8,

$$\begin{aligned} V_t &= \omega r(1 - a^t) \\ V_a &= V_\infty(1 + a^a) \end{aligned} \tag{8}$$

It is now possible to iterate to find w_r for this radial section. Imagine the propeller disc is now divided into annular rings with thickness dr. The thrust and torque of each annular ring may be calculated as described by momentum theory. The section thrust is calculated by equation 4 as the mass flow rate times the change in velocity in the axial direction, and the torque at this section is the mass flow rate times the change in velocity in the tangential direction times the radius from the hub of the radial section.

$$\begin{aligned} T_r &= 4\pi r\rho V_\infty^2(1 + a^a)dr \\ Q_r &= 4\pi r^3\rho V_\infty^2\omega(1 + a^a)a^t dr \end{aligned} \tag{9}$$

Equating equations 9 and 6 and solving iteratively for a^a and a^t allows calculation of w_r, V_l, and thus the thrust and torque of the condition may be calculated. The

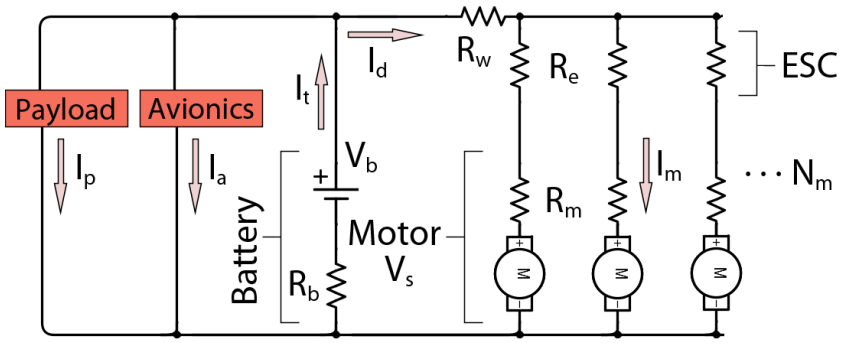

Figure 4: MST propulsion system electrical model.

treatement up to this point is likely sufficient for the purposes of this dissertation, although Prouty [13] and Leishman [3] discuss other extensions such as corrections for tip losses, wake contraction, and others.

The above is developed considering fixed wing configurations, where V_∞ is largely axial due to the standard flight condition of this type of aircraft. In this dissertation, as multirotors are considered, oblique flow is more standard, where V_∞ is generally rotated at large angles, usually close to 90° away from the axial direction . Theys [14] describes experiments comparing BEMT calculations and observations made in a wind tunnel for a low Reynolds number rotor, such as the ones considered here. In that study, it is stated that BEMT fails to predict performance at these angles. Theys proposes a correction factor factor for these less-axial inflow conditions.

2.2.3 Electrical modeling

This section is used to calculate power required for hover and cruise. This is needed by the analyzer and optimizer described in section 3.1.3. It does so by summing the torque components on all of the propeller blades on the vehicle. Standard equations of power are applied to all components shown in Figure 4.

Assuming a steady hover, the mean voltage seen by the motor coils V_s of one motor is

$$V_s = d_t s V_c - I_d(R_b + R_w + R_e + R_m) \tag{10}$$

Drive current I_d is the sum of current for all motors, and I_m includes the no load current I_0 for each motor. This approximation is an acceptable way to model the motor, although there are others. This approximation is deemed acceptable for the purposes here due to the results of section 3.3.6. It is also important to account for the change in internal battery resistance R_b as current demand changes. Current pulled through this resistor will generate heat and this power must be accounted for in the analysis. The effect is described by Stepaniak[15]. For all analyses, ESC efficiency η_E is assumed to be 97% [16]. Wiring resistance R_w is taken from standard copper wire, assumed to be of a particular gauge and length, scaled with the current requirement I_d. Internal resistance of the battery R_b is scaled with the qualitative condition of the battery specified by the user and as described by Ampatis[17]. ESC resistance R_e may be estimated from manufacturer datasheets. Motor resistance R_m may be estimated as a function of K_v[18], or as well from datasheets.

Motor RPM is calculated based on the voltage seen by the motor coils. This is sent to the BEMT for the torque calculation.

$$RPM \approx K_v V_s / G \tag{11}$$

This no-load RPM is for directly driven or geared drive trains. It is important to note that the actual RPM will be lower as load is applied to the motor. The reduction in RPM depends on amount of torque applied, and generally for the hobby class of propellers discussed here, RPM has been found to decay at a rate of approximately 15-20% per blade added to the propeller (specifically for the 1900 K_v Multistar 1804 motor and Gemfan 5030 propeller). In reality, this clearly will depend on the torque of the motor at the required RPM, and inertia of the load, as well as other factors, but this approximation is deemed acceptable for the purposes here due to the results of section 3.3.6, and Figure 39. Voltage V_s increases by a linear amount related to d_t. Gear efficiency η_G is also considered at this point, i.e. about 3-6% increase in power required for a spur gear, as is commonly used in engineering calculations. Helicopter

governed head speeds may also be specified as applicable. The motor current I_m is calculated using the aerodynamic torque required by the rotor:

$$I_d = N_m(Qw/(\eta_M V_s) + I_0)/\eta_E \tag{12}$$

where w is the angular speed of propeller.

Drive, payload, and avionics currents are summed to arrive at the total current requirement in the given condition.

$$I_t = I_d + I_p + I_a \tag{13}$$

This should include other power sinks such as tail rotors for helicopters (around 5%[3]) and coaxial propeller losses (around 15%[3] depending on separation). To calculate the flight time, the algorithm compares the requirement I_t and the battery capacity. A discharge percentage less than 100% is generally used and may be specified by the user to elongate the life of the battery.

2.3 Propulsion system sizing and design methods

Few general, rigorous, and comprehensive design and sizing methods for electric propulsion systems are currently available. Many of the existing methods are either too specific to be applicable to general electric vehicles with either standard or non-standard geometries. For larger and full-sized vehicles such as turbine-powered, manned helicopters, the required fuel fraction (RF) method [19],[20],[21] has been used for many years. However, as mentioned, this method is currently geared toward large, gas/jet fueled aircraft. The spirit of the method is similar to that proposed here - given a mission, the RF method provides a minimum required engine size, in addition to attempting to size components such as rotor blades, transmissions, and GTOW. A similar method to size electric vehicle drive components has not yet been found in available literature. Many other design methodologies[22], [23], [24],

[25], [26], [27], [28], [29] focus on full-sized and/or fixed wing aircraft. The NASA Design and Analysis of Rotorcraft (NDARC)[30] tool is developed to size full-sized rotorcraft to particular missions. Nam[31] considers probabilistic effects on sizing in the conceptual design phase. Nam[32] also considers sizing for full-sized electric fixed-wing aircraft. Pate [33] describes using an optimizer to design vehicles for multiple missions out of a database of modular components. Aguilar [34] describes a database-based method for estimating UAV performance. Quan [35] provides a good high level overview of hobby multirotor design including in depth looks into various aspects such as flight controllers, rotors, batteries, and others.

Several rigorous propulsion system design studies have been presented in literature. Latorre[36] documents a design process using blade element and momentum theory (BEMT) to select the motors, propellers, and batteries in an iterative fashion. Gur[18] describes a multi-disciplinary optimization (MDO) method in designing a propulsion system. The method attempts to meet goals (i.e., loiter time, rate of climb (ROC)) and presents a modeling analysis of motors and batteries. A sensitivity analysis to certain propeller design elements is also presented. Daskilewicz [37] describes the effects of uncertainty on the Pareto region for design variables in such an approach. Achtelik [1] details balance of efficiency and redundancy on multirotors, including tradeoffs of several frame types and handling the fault on a hexarotor. Lundström[38] describes an approach to designing the propulsion system and the chassis for small fixed-wing UAVs in a semi-automated fashion. To study the effects of varying payload on design characteristics, Ampatis[17] shows a design method using parameterized data from motors, batteries, and ESCs. They consider the vehicle diameter, energy, motor length, and battery weight. The authors also consider the effects on the design of varying the total number of motors. The modeling of electrical propulsion systems is also described. Bouabdallah[39] details a method for iteratively designing

a multirotor vehicle with a maximum mass and length to achieve a desired thrust-to-weight ratio. The method is specific and requires a database of actuator, battery, and airframe components to calculate the masses inside each loop iteration. Another database optimizer is proposed by Magnussen [40] who also provides some modeling and identification of several rotors, including dynamics. The methodology presented in this thesis, in contrast, attempts to parameterize drive components to eliminate the requirement to use a database for propulsion system design and optimization. Cinar[41] describes a sizing system based on the SysArc design environment, which relies on a database of propulsion components. A baseline aircraft is required when sizing a new vehicle, and the mission must be similar to that which baseline aircraft is designed. Chakraborty[42] also describes a design methodology based on SysArc which is aimed at full-scale aircraft by building up subsystems and considering their effects on the overall system in the design phase. Winslow [43] describes a similar architecture for the one proposed here, adding onto the parametrization of equipment by considering small scale brushed DC (BDC) motors. The author provides data for maximum torque and power based on motor mass, which data could expand the applicability of the framework described here.

Traub [44] and Avanzini [45] calculate optimal battery weight fraction for endurance and range of fixed wing and provides detailed Li Ion modelling [46]. It is of interest to calculate the optimal battery weight fraction for multirotors. Gatti[47] provides such a calculation. Avanzini [48] also details discharge dynamics modeling for batteries. Wang [49] details the optimization of a tail sitter aircraft with respect to endurance by considering wing loading and battery ratio. Abdilla [50] demonstrates modeling power required for rotorcraft and investigates transient power requirements for vehicle manuevering. Riboldi [51] details sizing of an electric fixed wing aircraft. Donateo [52] studies performance losses for multiple lithium-based battery chemistries compared to fuel cells. McCrink [53] modifies BEMT modeling of rotors based on a

Reynolds number-based power available model.

Other ideas for optimizing a design and increasing endurance have been proposed. Abdilla [54] and Chang [55] suggest using a rucksack optimization to optimize a vehicle's battery, which is comprised of small units that are discharged and dropped from the vehicle. While this lowers the total mass of the vehicle during flight, akin to using up solid/liquid fuel, this idea has numerous issues to be overcome. For example environmental impacts, complexity of the battery and release mechanism, and ensuring that each unit is capable of handling the power requirements to operate the vehicle as it is being discharged. Still, this approach gives comparison of multiple batteries to the ideal infinitely divisible battery. Other attempts have been made at increasing endurance and range by using autonomous charging stations [56] or battery swapping stations [57]. These of course require infrastructure and might be useful when that can be afforded by the mission. Indoor concepts using shore power are also described in literature (e.g. [58]). Beamed power in multiple forms has been described as well, for instance Nugent's laser power system [59]. Others [60] describe heterogeneous rotors for increases in efficiency over standard design.

Less rigorous methods in terms of optimality of electric propulsion system design also exist. One method uses online software; Benito[61] describes a process of designing a multirotor using eCalc. eCalc [62] has become one of the go-to tools for some UAV designers, primarily in the hobbyist market. The software allows users to input specific lists of components and will provide a calculated flight time and other useful data. Similar to the online validation algorithm [63] described by Bershadsky[64], it allows designers to check flight endurance and other characteristics of some types of common vehicles: heli/multirotors, planes, and ducted fans. This method allows for a form of validation once a specific list of components is chosen as eCalc requires that the specific drive components are provided to the tool.

The methodology proposed here is built in order to address some of the gaps existing in literature. It is meant to assist in the early phases of UAV design, focusing on multirotors. The methodology is broken down into two components: an analyzer and an optimizer. The analyzer is built to accept propulsion component parameters to predict performance and is described in section 3.3.6. The drive optimizer algorithm proposed in this work is essentially the analyzer in reverse with optimization, which the authors believe is at this point a unique capability. This is described in section 3.1.1. It takes in mission parameters for a generic multirotor UAV and outputs the propulsion system parameters that will accomplish the mission requirements. The algorithms presented here may be used in conjunction with or in lieu of existing tools such as this one either to validate each other, or at least provide a starting point for design of an electric UAV's propulsion system. In order to perform optimization without a database, the ability to rubberize propulsion components is required. In contrast to some of the above studies, the methodology described by this work abstracts propulsion system characteristics by parametrizing them. This allows users to input only relevant drive system parameters instead of selecting specific components from a database, described in section 3.2. Note that although this alleviates the need for a component database, it does not preclude the use of one. Selected studies are also introduced, such as wind tunnel measurement of multirotor aerodynamics described in section 3.3.1. These data, presented for 122-450 mm (diagonal rotor to rotor) multirotors, are a complement to the study presented by [65], which feature multirotors sized 350-1120 mm [1].

2.4 Propulsion system configuration design methods

Mulirotors are quickly being tasked with more intricate tasks including object manipulation, perching, and data harvesting. Some of these tasks are complicated, such as

[1]The NASA study referenced here was not available at the time that the experiment presented here was run.

autonomous object assembly, grasping, and interaction with the environment. To expand the capabilities of these vehicles, more dexterous control of multirotors is desired. One area that has received attention is over-actuation or direct force control (DFC), where the vehicle is able to actuate in 6 DOFs directly. That is, it does not need to change attitude to reject disturbances or translate for small speeds. These vehicles are generally flown with the detriment of sacrificing hover efficiency for DFC. Several studies have been written with regard to the feasibility and optimization of this concept for multirotors, developing several non-standard or novel designs. Augugliaro [66] describes building tensile structures in difficult to access places. Mellinger [67] describes aerial grasping control, estimation, and relevant mechanical design. Fumagalli [68] develops a model for interaction with the environment of a multirotor using a compliant manipulator. Gioioso [69] performs a stability analysis of different interaction tasks. Yuksel [70] provides a force observer for these tasks as well. A company is also investigating using DFC to perform the tedious task of cleaning windows and solar panels for large buildings and arrays [71].

Jiang [72] claims another benefit for DFC: faster disturbance rejection than a standard vehicle. Because the vehicle has direct access to produce small forces in the direction of the disturbance, it is shown that the vehicle is capable of quicker responses to these, without having to reorient itself to do so. Jiang [73] also describes a vehicle utilizing DFC to swab an exhaust shaft at a power facility. The same authors also performs an optimization study for the orientation of rotors from 0-35° of motor roll about the arm (referred to as ζ in this thesis). There is no treatment of negative ζ or any dihedral, or any other vehicle types.

More extreme DFC designs have also been investigated. Crowther [74], Jiang [75], Kaufman[76], Rajappa[77], and Nikou [78] also describe non-coplanar multirotor designs which can actuate in 6 DOFs. Brescianini [79] describes the design and modeling of a vehicle capable of a true 6 DOF actuation configuration. In the study,

the author optimizes the orientations of 6 and 8 rotor vehicle, with positions pinned to particular polyhedra. They built and flew a cube vehicle providing flight results for a vehicle with 8 reversible rotors. They use a simplified force, torque model and are not able to fully decouple translational and rotational dynamics. The vehicle described here can fly in arbitrary orientations due to its symmetry, but is on the more inefficient side of hover power in these attitudes due to the rotors facing in multiple, more independent directions. That is, if rotors aren't used for hover in a particular attitude, they merely become payload. The author also shows the vehicle catching a ball thrown inside a controlled environment. Nikou [78] designs a heptarotor using an optimizer. The structure and rotor positioning and orientation is arbitrary, so this is likely a more extreme example of DFC optimization leading to hover inefficiency. Park [80] describes the design, modeling and control of yet another omni-directional vehicle with nearly arbitrary positioning and orientations on a pole. This study also proposes a reversible rotor by stacking two of the same propeller on the shaft and using reversible ESCs. This, the author claims, allows for a gain of actuator authority for a marginal loss of efficiency. Kiso [81] considers optimization of a constant inertia vehicle with no rotor dynamics. Only counter-rotating coaxial rotors with no wake-wake interference or arm dihedral are considered and the metric of "manipulability" is introduced. The section of work in this thesis that deals with dynamics and optimization is partially an extension of the work described by Mehmood [82], where only one vehicle type and no negative motor tilt or dihedral angles were considered.

Another method to gain DOFs is by using mechanisms to tilt rotors while in air, thereby increasing the directional volume in which force and torque can be applied. Ryll [83] shows an over-actuated vehicle built around a ring featuring tilting rotors and a force volume, in addition to design, control, and modeling of it. Ryll [84] and Papachristos [85] write about tilt-rotor multirotor vehicles. This in-flight method for overactuation allows the vehicle to access certain DOFs and is potentially more

efficient in terms of using rotors more to hover instead of as payload. The tilt of the rotors allows for some level of DFC with limited authority, as DOFs must be traded, often coupling motion dynamics in different directions. In addition to these limitations, although they have an increased volume of actuation angles, the added weight and complexity of tilting mechanisms detracts from the allure of these vehicles. Langkamp [86] describes another method of actuation control by using variable pitch rotors in a DFC configuration. This method complicates the rotor but adds yet another set of DOFs accessible to the vehicle.

Others have studied separation of lift and DFC actuators. Long [87] describes a configuration with multiple adjustable rotors which allow for limited DFC while two larger rotors generate the thrust required to overcome gravity force. Much like a blimp deicing, this is a good attempt at reducing the potential inefficiency of having multiple rotors responsible for both DFC and lift. That is, the inefficiency of large rotors oriented in directions during hover which do not contribute to countering the force of gravity.

There is a great deal of work in the area of control and also fault tolerant control of these vehicles. Mellinger [88] describes trajectory generation and control for aggressive manuevers on multirotors. Franchi [89] describes an independent estimator for position and attitude for control of fully actuated vehicles. Mueller describes maintaining control of a quadrotor vehicle with the loss of up to three rotors. Giribet [90] describes how tilting rotors by a small amount toward the center of the vehicle allows for rejecting disturbance torques in all directions, even with a fault. Michieletto [91] considers rotor failure on DFC vehicles and develops a controller to keep a hexarotor in hover with a fault. Falconi [92] creates a position tracking fault tolerant controller which abandons attitude control when a rotor fails. Lee [93] takes the failure scenario a step further for the hexarotor and applies constant pitch and roll commands, again abandoning yaw, to keep altitude of the vehicle. Rajappa discusses optimization of

the rotor tilt angle for minimum control effort to achieve a trajectory. A different hover description is given by Mueller [94], who relaxes the definition of hover to include a non-zero angular velocity position hold. This is useful when rotor failures allow trading full attitude control for position control.

Aerodynamics of these small vehicles at low Reynolds numbers (on the orders of 10,000 - 100,000) are becoming of interest as modeling becomes more detailed and optimization becomes more important. Markusic [95] describes a thrust stand for electric rotor evaluation. Many designs exist but this design is of interest to the study described by this thesis. Rand [96] describes an optimization technique for stacking coaxial rotors and use of BEMT modeling techniques in hover and axial flight. Leishman [97] describes the same with further detail and introduces the optimum coaxial rotor system. For oblique flow, Theys [14] describes experiments comparing BEMT calculations and observations made in a wind tunnel for a low Reynolds number rotor, such as the ones considered in this thesis. In that study, it is stated that BEMT fails to predict performance at these angles. Theys proposes a correction factor factor for these less-axial inflow conditions. Otsuka [98] studies some of the aspects of multirotor aerodynamics of interest in this study. In it, they propose a design with partially overlapping blades, much like existing designs such as the CH-47. This design's main advantage over a standard X8 is to save lateral size by partially overlapping the rotors. There is a reduction in hover efficiency of course due to wake-rotor interaction, which is studied for this configuration. Tip to tip distance is also studied and found to not be a factor affecting efficiency (although this is contradicted by Alexandrov [99], who claims that there is an optimal gap distance for multirotors). Counter-rotating rotors only are described in that study, and no wake effects at oblique angles are considered, nor is mechanical power or efficiency.

2.5 The need for a new framework, research questions

While there is a great body of ever emerging research literature regarding multirotor aircraft design, there are still plenty of areas that beg for closer investigation. The research questions (RQs) and associated experiments (EXPTs) in this section attempt to address some of these areas, and the rest of the thesis is motivated by this section. Research questions are first posed and expanded. Then, experiments are described to address some of the gaps in the literature described in 2.3 and 2.4. The former is considered as mission-level design, and the latter is design for the tactical or the task level. Mission-level design should allow a UAV to perform a particular set of tasks. Of interest here are missions that will require specific velocities, altitudes, payloads, endurances, ranges, and/or similar requirements. A task may then be defined as a goal on a shorter time scale than a mission; namely of interest here are tasks which require linear and/or angular acceleration. A vehicle designed to a particular task should be capable of accelerating in certain directions with a particular authority. These acceleration capabilities might enable different types of precise manipulation or information harvesting missions and tasks which may require endurance and/or specific types of dexterity, such as the types described in 2.4.

2.5.1 Mission-level questions

RQ 1. How do we design the lightest vehicle system for mission-level requirements?

Of interest here is to design the lightest and/or most efficient vehicle system which is capable of accomplishing a particular mission. In the absence of more specific requirements (i.e., extreme crash-worthiness) which might drive a robust system to the heavier end, the driver to design a light vehicle is, in general, to reduce power requirements. This has the added benefits of reducing structural complexity, materials cost, physical size, as well as others. Which factors must be considered, and which

components require modeling, and how do we optimize them? Which components are the most relevant ones to model?

RQ 1a. How do we perform sizing optimization?

Most of the sizing methods for eVTOL vehicles rely on a database of COTS propulsion components. The components are selected based on criteria such as generated power, weights, and voltages. While the approach is certainly valid, it leads to a quantized design space which might bias a chosen design toward an undesired direction. It also does not create room for custom made components, which may have benefits to the designer. To create an "ideal", non-quantized design requires another method, involving parametrization of COTS components into generic ones. These components are known as rubber components described by Schrage [20], as they may be sized or molded to fit their specific, respective requirements. For example, manufacturers might produce batteries in capacity denominations of 200 mAh. While this might be sufficient for most designs, it may drive the design of a very small vehicle to be potentially overweight on one side, or to suffer endurance losses on the other. This rubber approach opens the ability to custom build components tailored to a specific mission. To be able to optimize a propulsion system, it is necessary to first be able to model predict performance of each of the relevant components.

RQ 1b. How do we model components to predict performance?

One question to answer is that, in order to correctly model performance of a multirotor vehicle, what is the set of the most important propulsion-related parameters needed? Knowledge of this will be necessary for the effective sizing of multirotor systems. In addition to the set of propulsion system and other parameters, where

should most effort be concentrated when attempting to size a vehicle? That is, since resources are limited, where is a high level of detail needed to model the multirotor's propulsion system and where is a lighter approach acceptable? It is desirable to know when to call an analysis "good enough" to proceed with a design, and to have an approach that is generic enough to apply to as many potential vehicle configurations as possible while maintaining validity in analysis results.

The propulsion system is identified as batteries, electronic speed controllers (ESCs), motors, propellers, and associated wiring. Of these, by far the most complicated part of the multirotor propulsion system in terms of modeling is the interaction between the propeller and the air through which it turns. Propeller modeling has received attention in literature for over 120 years (see section 2.1.3). Modeling this system is difficult due to the complex interaction of the propeller and the atmosphere, as well as the propeller with it's own dynamics, including rotor blade flapping. Which of these parameters are sufficient to perform a sizing of an electric vehicle? Since mission-level requirements are several orders of magnitude longer term than the dynamics of rotors, perhaps it may be acceptable to ignore some of these dynamics effects. More modern methods of predicting performance include computational fluid dynamics (CFD) approaches. These methods may be an accurate (see section 2.1.3), but only when used properly, and at best it is slow. Less complex methods may be investigated such as Blade Element and Momentum Theory (BEMT) as a quicker, simpler method that may be sufficient for performance prediction and sizing. Other methods include classical, closed-form solutions from momentum theory, although like the other approaches, this one has a tradeoff of pros and cons associated with it as well, briefly documented in section 2.1.3.

Many studies have investigated the modeling of electric motors which provide propulsion to the vehicles discussed here. McDonald [100] provides a parametric motor model for this scale of vehicle. What of these models is necessary to consider?

How far may these models be abstracted and still retain a level of accuracy needed for mission-level propulsion system design? Batteries, especially the hobby-grade batteries of interest here due to their ubiquity, have been modeled in the literature and have well documented discharge dynamics. Their discharge is dependent on several factors which should be identified and considered for mission-level sizing, as they are the energy source for the UAVs considered here. ESCs which drive the rotor, may affect performance of the rotor on a short time scale but will not likely affect mission-level analyses of multirotors. Other than perhaps changing the efficiency of the propulsion system, the rest of the effects might be negligible for the purposes of $RQ1$.

RQ 1c. How much power does it take for cruise and what does the power bucket look like for multirotors? What about aerodynamic lift and drag data of multirotors? What is the ideal battery weight fraction for endurance?

The so-called "power-bucket" [3] for helicopters is found by summing the powers (i.e., profile, induced, parasite, tail rotor, ancillary) required to hover and cruise at 0° flight path angle (FPA). The summation of these powers shows a dip, and hence "bucket" at a particular airspeed. This airspeed is important, as it informs the designer of the most optimal airspeed for endurance. The same data may be used to find the optimal airspeed for range as well. At the moment, no data is published for multirotors in this regard. Unlike helicopters, which generally have an articulated joint or set of joints at the rotor hub, multirotors generally have rigid rotors. This forces the dynamics for the multirotor to behave differently than those of a helicopter in many ways. Most notably, a multirotor, unlike a helicopter, generally must pitch or roll with greater angle in the direction of desired travel by reorienting its thrust vector in that direction. Because of this, the parasitic component of the required power curve will likely begin to dominate at a lower ratio of the speed to the maximum speed for

a multirotor. This should change the shape of the total power required for forward flight. For helicopters, the power bucket is well documented, showing the cruise speed for best endurance and one for best range. It is useful to generate such a figure for multirotors in order to optimize missions for these vehicles.

To study the effects of cruise on multirotors, aerodynamic effects will need to be investigated. While there are many studies on aerodynamics of large-scale vehicles, no experimental flight test or wind tunnel data were available for multirotor aerodynamics data, namely drag polars. These data are necessary to correctly predict cruise performance of multirotor vehicles, especially as cruise velocity increases thereby increasing adverse lift, where applicable, and drag of the vehicle. Multirotors often are designed as flat plates, so once they pitch into the direction of travel, this negative angle of attack (AOA) causes lift in the down direction, and the lift is termed adverse, as it now must be compensated for with higher thrust. These aerodynamics coefficients may be estimated as with simple calculations of simple shapes, but there is a desire to treat this with a more accurate approach.

Another question often asked is related to the sizing of the battery. While a larger battery generally has more energy capacity and hence a greater ability to keep a vehicle in the air for a longer time, it will be heavier, which must be compensated for by the rotors, and thereby the battery itself. Is there an optimal battery weight fraction for multirotors?

EXPT 1a, b. Performance prediction, components modeling

To attempt to answer the first part of *RQ* 1, a modeling effort was aimed at identifying and characterizing a reasonable set of propulsion system components and parameters. Propulsion system components were identified as rotors (i.e., generally one propeller and a motor, although other configurations are considered as well), the

electronic speed controller (ESC) which drives the rotor, the battery, which provides the energy needed by the rotor/ESC assembly. Modeling the rotor to a sufficient level yields the best results when attempting to predict the performance of multirotors. Modeling this correctly is vital since this is by far the single greatest sink of power on the vehicle. In terms of sizing, the most important aspects of a motor are maximum continuous power, the motor's speed constant K_v, resistance R_m, and no load current I_0. These are used to create a motor model to interact with the other propulsion system components.

Due to the difficulty of properly designing propellers, it is likely that many hobby-grade propellers are either copies of eachother, or are derived off of copies. Some companies like Tmotor apparently scale rotors of the same family such that a linear difference corresponds to a specific difference in thrust at the same RPM. Therefore, for a large subset of COTS propellers that "appear" similar, it is hypothesized that a scalable, geometrical model may be a valid one to use for sizing. That is, having the geometry of a 3x5 (3 in diameter, 5 in pitch) propeller of a certain type, it may be possible to estimate the geometry of a 10x4 (10 in diameter, 4 in pitch) propeller of the same family or manufacturer. Propeller pitch p_p, radius R, and material all play important parts in the rotor's performance. Propellers are abstracted using these parameters to create a generic propeller model for the validator and optimizer.

The battery's chemistry, weight, capacity, and cell configuration are all critical components, and hence all tend to be manufacturers' selling points. These should be considered when sizing a vehicle. Discharge dynamics of different types of batteries may also greatly affect a vehicle's sizing.

The electronic speed controller (ESC) has a vital role in the dynamic response of a vehicle, with each one featuring hardware of differing capabilities, and of course different control software or firmware (FW). However, in terms of sizing, the effects of these are likely fairly benign, as the most important factor to consider, other than

weight, is the ability of the ESC to handle the power requirements of the rotor.

To investigate the question, first a framework is developed to attempt to estimate the performance of multirotor vehicles. This was used to test the subset of propulsion system parameters and compared to actual data (i.e., data from thrust stands and flight tests) to ensure it is sufficient to predict performance and/or size a vehicle. Models were developed for propulsion system components, parametrizing them to allow for rubberization of these components. Once this was deemed successful by comparing component predictions (i.e., power, weight) and run against actual vehicle systems to predict their performance to an acceptable accuracy, an optimizer was added to the framework. This optimizer allows the framework to run in two directions. The first direction is as just described: inputting the vehicle's propulsion system yields an estimate of performance characteristics such as endurance, range, and power required. The parameterized or rubberized components allow executing the reverse direction as well: inputting a set of mission parameters yields the required propulsion system parameters to accomplish it. An extension of this experiment was to put the analyzer portion of this work on an online website to allow users to run their own designs and provide feedback. This crowd-sourced feedback would in turn be used to validate the models and/or improve them and hopefully uncover any issues in using this system for sizing. The results of work related to this are described in 3.3.6 and 3.4.1.

Some areas of this modeling received additional attention, as they are deemed important and found as holes in current literature. For instance, no data is published regarding lift and drag coefficients of multirotor UAVs. These C_L/C_D data are required to accurately estimate required power in cruise, climb, and/or descent of any aerial vehicle. Estimates were used for these data using simple shapes in EXPT 1a. As drag and adverse lift increases at higher UAV speeds, the accuracy of these data becomes more important proportional to air velocity squared. While estimates might

be acceptable, better data was desired. As such, a wind tunnel was used to carry out the experiment to measure aerodynamic data for several different COTS quadrotors. The low speed aerocontrols wind tunnel at GA Institute of Technology [101] was used. Many frames of various sizes were used with different equipment configurations to calculate C_{L_α} and C_{D_α}. In total, nine different frames and a total of 25 different configurations were tested in the wind tunnel. The frames ranged in size from 122 mm wheelbase (maximum or diagonal motor to motor distance) up to 450 mm. All frames were run without propellers, and some were run bare while others were loaded to the otherwise "ready to fly" configuration. The aim of this study is to provide baseline C_L/C_D data to be used in addition to the H-force of the rotors described by Stevens [102]. The results of this experiment are described in 3.3.1.

EXPT 1c. Power required for cruise

Two experiments were attempted to study the power bucket for multirotor vehicles. In the first experiment, several vehicles which are outfitted with electrical power monitoring are flown level at various airspeeds. The data recorded should give evidence to the electrical power required at each of these airspeeds in response to the mechanical power requirement of steady state flight. The electrical power required of course differs from the mechanical power required but should still reflect the power bucket in the data, and gives the worst case power requirement as opposed to the pure mechanical power. In total, four quadrotors are flown equipped with a current and voltage sensor to attempt to measure required power for cruise at multiple airspeeds.

The second experiment was conducted in software. The Georgia Tech UAV Simulation Tool (GUST) developed and described by Johnson[103] is a high-fidelity dynamics simulator which allows for modeling multirotor vehicles, in addition to others. The first experiment is repeated in software for two of the multirotors. These data

are compared to the predictions of the algorithms developed here. Results of these experiments are described in 3.3 for a quadrotor, and in 4.1.6.3 for two types of hexarotor.

To answer the ideal battery weight fraction question, two methods are attempted. First, the MST optimizer just described is used to size a high-endurance multirotor. Second, a momentum theory approach is taken to calculate the theoretical value.

2.5.2 Task-level questions

RQ 2. For a multirotor, what linear and angular rates are possible in different coplanar and non-coplanar configurations?

Today, the vast majority of multirotors share their propulsion system orientation design with other "standard" multirotors. These vehicles have their rotors oriented in a coplanar fashion with all rotor thrust vectors parallel and in the same direction. Generally, all thrust vectors are pointing straight up along the $-z_B$ direction. With a few exceptions, this dictates that for these standard vehicles, only four degrees of freedom are directly accessible to the vehicle's controller and actuators, i.e., θ, ϕ, ψ, and $-z_B$. By tilting the rotor planes such that rotors are not coplanar, it is possible to directly achieve rates in directions other than those possible in these standard multirotor designs. This might be done dynamically in flight, but this study will consider only fixed orientations of propulsion components. In literature, this technique may be called over-actuation or direct force control (DFC) if the controller is able to capitalize on the rotor geometry, as described in 2.4. DFC adds the ability to control force in up to two additional DOFs: those in the x_B and y_B axes, generally defined in the lateral plane of an aerial vehicle as shown in Figure 1.

Some multirotors have dihedral ϵ on their arms with the claim of slight position

stability gains. Others use dihedral for DFC purposes, such as the CyPhy LVL 1 vehicle [104]. Others including the LVL 1 have motor tilt ζ applied to the rotor about the arm's axis. A design with DFC has several benefits over traditional, coplanar designs. First, force may be applied in these directions without the delay of the vehicle's attitude dynamics in order to reorient the thrust vectors into the desired direction. This might be useful if quick, slight adjustments are needed in the lateral axes, and is potentially faster than coplanar designs [72]. Second, depending on the number and orientation of actuators, because the vehicle does not have to reorient itself to apply force in these directions, the DOFs may begin to decouple. This means that a vehicle capable of DFC in a certain axis does not have to change attitude to accelerate in that direction. This fact has the added benefit of allowing the UAV to hover at non-zero pitch and roll trim angles. The CyPhy vehicle forms what will be referred to as the "standard DFC" UAV for the discussions in this document. Vehicles with such a configuration design do not have access to the full 6 DOF, but come close. This is of course because none of the rotors in this design point "down", and if no diehdral is applied, two of the rotors are coplanar (M2 and M5, seen in 2 (i)). None of the rotors axes point in the $+z_B$ direction so this vehicle is capable of a true 5.5 DOF, with the other 0.5 DOF accessible indirectly via throttling down near hover or otherwise having gravity to some extent aligned with $+z_B$. To directly control that axis would require orienting some rotor such that component of the thrust vector is along the $+z_B$ direction.

RQ 2a. What is the actuation authority of a DFC UAV?

It is desired to estimate the actuation authority of a vehicle's propulsion system before physically building should the vehicle need to meet some acceleration requirements or goals, or to give the designer/operator an idea of the vehicle's handling

Figure 5: The "standard *X6* DFC" configuration referred to in this thesis.

qualities. There are several ways that studies have calculated and visualized this authority, generally showing the capability to produce force and torque in each DOF (see [105]. Doing so provides a relativistic comparison between designs with different rotor orientations which allows for the potential of configuration optimization.

If the designer is interested in control in the two lateral axes (i.e., x_B and y_B), tilting the motors or applying dihedral to the arms is one way to achieve this. If we take the motor tilt and arm dihedral on a DFC hexarotor to be design variables ζ and ϵ, respectively, what are the tradeoffs in different axes for varying these variables? DFC hexarotors have been proposed in literature described in 2.4 and even monetized, such as the CyPhy LVL 1 mentioned above. There are documented studies that investigate optimal configurations and effects of number and orientations of rotors. However, there are no studies in the literature that look into the following:

- pure vs. impure motion

  It is important to distinguish between pure and impure motion. During pure motion, force or torque is maximized in one DOF at a time; i.e., forces and torques in all other DOFs are theoretically zero. This is probably the more interesting variant to consider for most designs, as designs with highly-coupled dynamics might be undesirable. On the other hand, investigating the force and

torque authority during potentially impure motion (i.e., forces and torques are maximized in one DOF, but not necessarily constrained to zero in all other axes) gives the absolute theoretical maximum authority in a specific direction. This might be useful for emergency or interaction maneuvers where it might be possible to produce larger forces and/or torques. Studying both pure and impure motion provides insight into the entire envelope of a vehicle's true actuation authority.

- multiple vehicle types

  DFC hexarotors have been studied in terms of actuation authority. This study considers the hexarotor in addition to other vehicle types including quad-dodecarotors, shown in 1 and 2.

- co-rotating vs. counter-rotating

  Many coaxial vehicle designs exist including 3DR's X8 [106] and others. Many of these use counter-rotating coaxial rotors, while others such as Altus [107] uses a heterogeneous co-rotating configuration, probably to help increase the control bandwidth of the slower top rotors. There are no studies that investigate the effects of using co- vs. counter-rotating coaxial rotors. Some of the vehicle types considered in this study have coaxial rotors and it is interesting to investigate the effect on efficiency or authority, if any, of the rotation configuration.

- faults

  Many studies such as those described in 2.4 investigate the effects of rotor faults on multirotors. However, it is interesting to investigate the effects of faults on DFC UAVs specifically and use this data to design more robust vehicles.

In this study, it is necessary to elaborate on the definition of trimmability, fault tolerance, and degree of actuation. Degree of actuation refers to the level of authority of a vehicle in terms of how many DOFs are directly accessible. Some of the literature

referenced in the review calculate shapes of possible force and torque. A fully actuated vehicle has direct access to all six DOFs (i.e., three linear and three angular, both in positive and negative directions). Note: this is a misnomer for man referenced vehicles as they do not have direct access to $+z_B$. An example of a fully actuated vehicle might be a DFC vehicle with 3D rotors, or a vehicle where rotors can actuate in all six DOFs directly, both in positive and negative directions, an example of which is described by [79].

A trimmed state will be defined as one in which the vehicle "hovers." That is, for fully trimmed hover, there is essentially no acceleration in any of the six DOFs. For a multirotor, this would imply that it is capable of hovering while holding some position. Of course, strictly speaking in reality, there will be small, non-zero accelerations as the vehicle hovers in a trimmed state, as it responds to both internal and external purturbations. Fighting purturbations would be acceptable, but the mean integrated value of these over some time should be zero. Trim must then be defined on a long enough time span where the average of these centers around zero.

If it is not fully actuated, the vehicle must trade off control in DOFs to be considered trimmed. That is, it must surrender control in certain axes to gain control in others. In these partially trimmed states, vehicles make attitude corrections to hold position such as the ones described by Mueller [94]. Mueller describes a vehicle that surrenders control in the yaw axis to maintain hover. Partial trim is then the state when a vehicle maintains control over some minimal set of DOFs. For multirotors of this study, this will be defined as follows:

To be maximally trimmed, the vehicle should be able to hover, and produce positive and negative rates in every direction. Only then is the vehicle fully actuated. To be considered partially trimmed, the vehicle should be able to produce rates $\dot{p}$ or $\dot{q}$ and $\dot{r}$ and $-\ddot{z}$ where $\dot{p}$ or $\dot{q}$ are traded to indirectly control $\ddot{x}_I$ and $\ddot{y}_I$. For minimally trimmed hover, the vehicle should be able to produce $\dot{r}$ and $-\ddot{z}$, as $\dot{p}$ and $\dot{q}$ are traded

to indirectly control $\ddot{x}_I$ and $\ddot{y}_I$. A similar hover description is given by Mueller [94], who relaxes the definition of hover to include a non-zero angular velocity position hold.

Fault tolerance will be defined as maintaining some level of trimmability in the event of a failed rotor. At a high level, fail safe will be defined as the ability to land safely after a fault has occurred. For the purposes of this study, fail safe will be defined as the ability to maintain minimal trim, with the assumption that a vehicle is theoretically capable of doing so until landing.

Fail operational will be defined as the ability to carry on with normal flight operations following a flight. This generally applies for over-actuated vehicles, or those that have the ability to control five or more DOFs (since four is sufficient to operate, i.e., pitch, roll, yaw, throttle) given that the one that fails does not fully disable one of the four independent DOFs.

RQ 2b. What are the effects of standard configurations x vs. +?

There are groups of standard multirotor configurations that differ only in the placement of "forward" and "right" in the vehicle axes x_B and y_B. One notable example is the quadrotor in the X and $+$ configurations, shown in Figure 1 (a, *+4*) and (b, *X4*), as well as (c, *+6*) and (d, *X6*). Many early multirotors [108] were designed in the $+$ configuration, which had forward/backward/left/right aligned with each one of the arms. This however is argued to be an inferior design in terms of angular rate capability to the X configuration, where these directions are aligned between the arms. There are other practical benefits as well to the X configuration, including unobstructed forward views for cameras mounted inboard. In the $+$ case, one motor is throttled up to perform a roll or a pitch manuever, whereas in the X case there are two. The moment arms for both pure pitch and roll are decreased in the X case to

cos(45°) = 71% that of the + configuration. However, since there are now two rotors contributing thrust to the maneuver, there should be 41% more torque available for pure maneuvers in the X case. For a simple inertia model where the contribution of rotors is via point masses, the roll and pitch inertia is halved in the X case. So, with double the torque and around half the inertia X should be capable of higher rates in pitch and roll. A more careful look at these configurations for multiple vehicle types is desired.

RQ 2c. Is counter-rotating or co-rotating more efficient for coaxial setups? Pusher or puller? Tip to tip distance? Wake-wake interactions?

To allow for more options in design, rotors may be arranged in pusher or puller configurations. Many "standard" designs use a puller configuration wherein the propeller is located above the motor, pulling the motor (hence, "puller" or "tractor") when generating thrust. In a pusher configuration, the propeller is under the motor, instead pushing it when generating thrust. For fixed wing installations, several have studied the relative efficiencies of these two configurations including Godston [109], and it is generally believed that the pusher configuration is less efficient on these aircraft. However, in hover, both due to unobstructed wash air and more ground effect (since the pusher is closer to the ground) as applicable if the rotor is in range, it is possible that the pusher configuration is more efficient. For some multirotor designs it is beneficial or necessary to have rotor discs overlapping. This might be from a number of factors, for example partially overlapping discs might be needed to compress the frame size, or fully overlapping/coaxial rotors to reduce the number of arms required for mounting more rotors, with the additional benefit of perhaps increasing angular rates as compared to the case which has a higher inertia (an effect of requiring more arms, mounts). The coaxial rotor configuration is another common one that has

been studied for many years. This comes in several flavors; coaxial rotors and coaxial propellers. In the former, both the propeller and the motor are stacked on top of another pair of the same assembly. In the latter, one motor drives two or more propellers. Both have been studied in depth but no data has been found to compare the difference in propulsive efficiency when the propellers are spinning counter-rotating vs. co-rotating. In both cases, the upstream or top propeller pushes air into the downstream or bottom propeller. The airflow seen at the bottom propeller has two general components: flow in the in-rotor plane (or vertical) and perpendicular (or horizontal) directions. The vertical component acts in several ways upon the lower rotor, one of which is to reduce the angle of attack of the bottom blade as it increases the relative airspeed of the blade in the axial direction (see section 2.1.3). The swirl created by the upper blade should alleviate this effect when the blades are counter-rotating since the swirling air's velocity drives it faster into the bottom blade. This effect is reversed for co-rotating blades, and should reduce the thrust on the bottom blade when compared to the counter-rotating case for the same bottom blade RPM.

The distance between blade tips or motor axles is another design choice. There are studies that look into the efficiency changes with varying this effect (see section 2.4). However, there are none that look into co-rotating rotors while varying tip-tip separation. There are also no studies that report on wake interaction with varying angles of wake-wake incidence. Data here might be useful for enhancing the accuracy of rate calculations (and thereby also the data used by the optimizer described by this study) when rotor orientation geometries produce wake-wake interactions. This situation is easily seen in the case where arm-lengths are similar and rotors are tilted into or away from eachother, as the rotors in the DFC hexarotor in 5 and 2 (i).

RQ 2d. What are other ways to aerodynamically increase actuation authority?

For low speed flight, what are some ways to increase the rates of these UAVs? Since the rest of the study ($RQ\ 2through\ 3$ assumes a near-hover condition, lifting bodies such as wings are out of scope for the discussion, although they are considered for RQ 1. This leaves several options for authority increase. Of course, increasing the maximum thrust or response time of the rotor is one obvious option. This may be done by any to all of the following: lowering the GTOW and/or inertia, increasing K_v, P_p, N_m, battery voltage, and the like.

For the first two methods (lowering GTOW and inertia), ideas have been documented in literature. Postulated by [110], shortening the characteristic length of the vehicle increases its ability to produce angular rates. Shortening the arms has the effect of decreasing the mass and inertia of the vehicle while also decreasing the maximum possible torque generated by the rotors. The former appears to have a greater effect on the achievable rates, even with lower achievable torque. It is interesting to investigate whether other degrees of freedom might be used, e.g., asymmetric arm azimuths and the like. As for the rest of the methods (e.g., K_v, P_p), the sizing optimizer in RQ 1 or the designer could select more powerful rotors for these axes.

Another way to increase rates has been postulated in literature, as described in 2.4. In general, for a given maneuver, some rotors will be low or idle compared to the ones contributing to the maneuver. It is possible to use these in "non-standard" ways to increase rates of that maneuver. For example, many acrobatic hobby fliers use so-called "3D" rotors, or rotors that are capable of producing thrust in both directions along the rotor's axis. This is in opposition to standard rotors which produce thrust in only one direction. This might come in several common forms including collective pitch propellers and symmetric or stacked propellers with ESCs capable of reversing motor direction. Collective pitch propellers, as commonly used in helicopters, have many advantages over fixed pitch rotors. For instance, the ability to reverse their

thrust magnitude and direction without reversing their spin direction or angular velocity is one of these advantages. They may also be used to more efficiently match the flight condition (e.g., lower pitch for hover, increase pitch for cruise) and change thrust levels without changing motor/engine RPM (ref helicopters, MR with collective) enabling the implementation of slower-response gas engines. They do however increase both the mechanical and potentially the controller complexity of the vehicle by adding another DOF. Fixed-pitch symmetric propellers take away the complexity of links and hinges in the rotor but may be optimized for a narrower set of flight conditions than those rotors with variable pitch, usually featuring a flat airfoil. Another idea posited by Otsuka [98] provides the designer with more options since symmetric propellers are less prevalent than those designed for spinning in one direction. Two propellers designed to spin in the same direction are stacked on the same motor axle with one propeller rotated 180 degrees along it's longitudinal axis. If the ESC is capable of reversing the motor direction in either of these situations, each rotor doubles it's effective control range. This might be used by a "standard" multirotor to hover upside down, produce higher angular rates, or a DFC multirotor to potentially hover at a more extreme attitude. 3D rotors will not be considered in this version of the study.

EXPT 2a, b. Actuation authority: achievable linear and angular rates

A framework was developed using components of the one developed to answer *RQ* 1 which adds dynamics components to analyze motion during the shorter-term tasks in *RQ* 2. These components are needed to analyze dynamic behaviors of vehicles. The new dynamics framework is capable of simulating generic vehicles, which are composed of the propulsion system components described above. These may be generically positioned, heterogeneous, and independently controlled. The framework is modular and several controllers are implemented to command the rotors in order

to optimize for maximum rates in all six physical degrees of freedom. The framework is executed for UAVs of multiple configurations to study the effects of these configurations on the actuation authority of the vehicle. This work is described in 4.1. Standard configuration ($+$ vs X) effects and others are described in 4.2. This section also details fault cases, counter- and co-rotating and semi-coaxial and coaxial setups for quad- to dodecarotor vehicles.

In an attempt to validate the dynamics estimator, predicted results are compared to data recorded by actual flown vehicles. Many vehicles are designed using carbon fiber tubular arms and central clamps, as well as motor-mount clamps, which make for easy-to-assemble and resilient frames. Another advantage of these frames is the ability to change the motor tilt angle ζ with a couple of bolts without the need to design tilting mounts. This design provides a good mechanism to quickly change and test different motor tilt angles. Dihedral ϵ is not as straight forward but can be controlled by manufacturing clamps with a built in angle for each tube, or putting an angle on the motor mount itself. Because of this, ζ and ϵ will form part of the scope of the design variables used in experiments to answer most of these research questions. The other two design variables are armlength l (half of wheelbase), and arm azimuth λ. Of course, as a practical matter, ζ and l generally tend to be easier to physically realize than the other two, at least with tubular arms. Arm length and azimuth are more or less only considered for a special case of $RQ3$. More general motor placement will not be addressed, although the algorithms and methodology developed here certainly are capable of analyzing this situation. Results of this portion of the experiment are found in 4.1.6.3.

EXPT 2c, d. Multirotor aerodynamics

Because multirotors on this scale are relatively new in the field, there are only a

number of studies into the aerodynamics of the rotors used to operate them. The results of this experiment are used to augment the dynamics in the rest of the document where wake-wake and wake-rotor interactions cannot be ignored. As such, a thrust stand has been designed, built, and used to investigate the effects these several configurations' effects on efficiency, namely those of co- vs. counter-rotating coaxial and semi-coaxial setups, pusher/puller mounted rotors, tip-tip clearance, wake interaction, and ground/ceiling effect. The thrust stand test also includes a look at ground effect, which is well studied in literature as well as ceiling effect, which is less often studied (Powers [111], Rossow [112]). With the advent of smaller vehicles and indoor navigation systems becoming possible, such effects may be used to perhaps lengthen flight times for small vehicles operating near flat ceilings or floors. Data were averaged for about two minutes for all results presented in 4.1.10.

RQ 3. What is the best configuration for the X6 DFC vehicle?

What does the best configuration look like for this vehicle type? What exactly does "best" mean in this context? Knowing what the design space looks like in terms of vehicle configuration and it's resulting performance is not enough when it comes time to design the vehicle, so there should be a way to select the final configuration based on the available data.

RQ 3a. What is the best X6 to be single unknown fault tolerant?

What is best hexarotor (Y6, *X6*) configuration to be single unknown fault tolerant? That is, when the controller knows about a fault, what is the best design in terms of post-fault rate authority? The study will include coplanar and non-coplanar rotors.

RQ 3b. Motor roll, arm dihedral for standard DFC X6 is equivalent tilting entire thrust vector $x°$?

Clearly, acquiring control in new DOFs or increasing control in those DOFs is not generally without consequence. Moving thrust vectors away from the "standard," co-planar configuration (via motor tilt and arm dihedral) may have effects such as reducing authority in other axes, i.e., pitch, roll, and z-body. Some axes may benefit however, i.e., the x-body, y-body, and yaw axes. This is purely a geometric effect of the resulting thrust configuration, manifesting two ways; first, the thrust vectors tilt away from being perpendicular or parallel to those axes (thereby reducing torque/force potential in that direction), and into others. Second, should the angles be extreme enough, actuator saturation no longer enables the controller to find a suitable set of commands to satisfy acceleration requests. For instance, if the arm dihedral is 85°, the vehicle may not be able to hover due to insufficient authority existing to fight gravity. However, for the feasible design space, one metric for this might be something like: what is the mapping between the motor tilt and/or dihedral angle and the equivalent tilt of the entire thrust vector of the vehicle for lateral acceleration? Mehmood [82] claims that an x degree motor tilt ζ in thrust vector is equivalent to tilting the entire thrust vector in hover by $\frac{x}{2}°$. It is interesting to compare results to this finding and to add the dihedral variable as well. Also, the dynamics used by Mehmood do not include several nonlinear terms, which may play a significant role in the results for vehicles with motors capable of large angular accelerations.

RQ 3c. What is the maximum hover pitch and roll trim angle for an X6 DFC UAV?

In some situations, it may be desirable to hover at an attitude where the z_B axis

is not perpendicular with z_I in the local frame. For example, this may be useful while landing on a slanted surface, or interacting with an object that requires such a non-zero attitude. With DFC, it is possible to hover with a non-zero pitch and/or roll, even at arbitrary angles for some vehicles [79]. This study however will focus on the "standard" design, such as the Cyphy LVL 1. At some angle, depending of course on propulsion system parameters and orientations, it becomes impossible to either 1) produce sufficient thrust to hover in that attitude, or to 2) produce enough force in the proper directions to hover in place.

It is easy to misinterpret the LUTs in C in a way as to believe that a DFC vehicle, capable of producing more than 1 g of acceleration in the x_B and/or y_B direction, is able to hover when that direction is aligned with the gravity vector. That is, if the LUT shows that the vehicle is capable of 2 g in -x_B, can the vehicle hover when pitch is -90°? While it should be able to not lose altitude, hovering in place may not be possible because no rotors are producing force in a direction to stop lateral drift. In the -90° example, the resulting thrust vector is pointing up and forward (in body) so no force keeps it from holding position. To investigate the ability of the vehicle to hover at these attitudes, new LUT tables would need to be generated. The LUT plots would have to be regenerated with the specific attitude of interest to get the steady state force balance with the gravity vector in the correct direction. The only change is that the gravity vector must be rotated in body (or equivalently the motor thrust vectors and locations are rotated). Given this, it is may be useful to find out the maximum trim angle for hover that such a DFC vehicle can maintain.

RQ 3d. What are the rotor orientation configurations to provide the best linear and angular rates for a non-coplanar X6?

For a hexarotor, what is the best rotor configuration to achieve the highest rates in

all linear and angular axes? This question has been investigated at least to some extent by Mehmood [82] for the example case of *RQ* 2 above, describing the hexarotor with motor tilt and dihedral oriented in a "symmetric" method and showing optimized designs using a multiobjective optimization (MDO) approach. However, this allows for only two degrees of freedom in one quadrant and only one type of vehicle. While other vehicle types described by 2.4 have been flown, departing further from the standard, coplanar designs generally reduces efficiency, as some rotors are not used for hover and are flown as dead weight/payload. Of course, this is not to say that those designs are necessarily less efficient in hover than those in *RQ* 2. Given this, it is interesting to investigate whether or not more optimal designs might be found by increasing the DOFs available to the optimizer for a vehicle similar to the DFC hexarotor described by *RQ* 2. This might be done by relaxing some constraints defined there; some examples being the symmetry condition and allowing some combination of free armlength(s), azimuth(s), arm dihedral(s), motor tilt(s), and perhaps others. There are many ways to allow the design space to grow which can quickly get infeasible in terms of computational analysis. For example, allowing the rotors to be oriented in any direction already introduces at least two DOFs (two rotations to get to any orientation), and this is for a symmetric vehicle like the one studied by Mehmood [82] and earlier by Jiang [105]. Allowing each rotor to have an independent orientation costs at least 12 DOFs. Introducing motor location adds more DOFs and could be done several ways. The most general being of course the 3 cartesian coordinates. Per motor, this gives 18 DOFs. Another way to do the same is with arm length and azimuth in a polar fashion. This produces another six DOFs for azimuth and one or six DOFs for arm length, depending on whether or not symmetry is applied or each armlength is allowed to vary independently. Because of this quick growth in analysis complexity with the DOFs, the study presented here will scope the DOFs to a manageable set for more tractable discussion.

EXPT 3, a. Orientation configuration optimization

To investigate *RQ* 3, an optimizer is used to select the configuration of the vehicle shown in Figure 5. The optimizer has ζ and ϵ as DOFs to design the vehicle, and an array of weights is used to indicate goals to the optimizer as to in which directions to optimize rates. Asymmetric (about the xz plane) vehicles are not considered except in *EXPT* 3*d*. Heterogenous rotors are not considered, although the framework is capable of handling them. Results of this section are described in section 4.3.

The same optimization technique is run on the standard *X6* with a failed rotor. In this case, rotors M1-M3 are failed, as the vehicle is symmetric. Once this is done, the optimizer is run on the dataset to find the vehicle with the highest rates, weighing angular rates higher than linear ones. This is done to maintain the ability to have at least a partially trimmed hover.

EXPT 3b, c. Equivalence of thrust vector tilt and ζ and/or ϵ and extreme hover trim

One metric to describe the authority of an *X6* DFC vehicle is the equivalence of reorienting the rotors with tilting the entire thrust vector of the vehicle. This provides some insight into the effectiveness of the added DFC authority. This is described specifically for the *X6* vehicle in 4.1.8.

The *X6* DFC UAV is then subjected to a set of test conditions to find the maximum roll and pitch values for hover as a function of ζ. The results of this are seen in 4.1.9.

EXPT 3d. Relaxed constraint optimization of the X6 DFC UAV

The experiment for this relaxes constraints on the DOFs for the optimizer, allowing between 2-24 DOFs to try to find a more optimal vehicle than the standard, xz-symmetric design. The experiment setup is described in detail by section 4.1.5 and results are discussed in section 4.3.

CHAPTER III

A FRAMEWORK FOR MISSION-LEVEL ELECTRIC PROPULSION SYSTEM SIZING AND OPTIMIZATION

This section is motivated by RQ 1, 1a: "How do we design the lightest vehicle system for mission-level requirements?" and "How do we perform sizing optimization?" from 2.5.1.

The presented methodology is composed of two main components or paths, shown in Figure 6. Throughout this document, the framework may be referred to as the multirotor sizing tool (MST), composed of the "drive analyzer" and the "drive optimizer". If the vehicle is already designed, i.e., the propulsion system parameters are already selected) it is possible to estimate performance characteristics using knowledge of propulsion system parameters (e.g. K_v, P_p, C, etc). This may help confirm that a vehicle is capable of performing a certain mission. The outputs include power to hover, endurance, maximum range, tip speeds, and many other outputs. This is the analyzer, or the first path.

The drive analysis tool is used when vehicle parameters are the inputs, and one is interested in determining capabilities of the vehicle. This might be used to analyze the selection of component parameters. If both the mission and vehicle design parameters are specified, the analyzer also allows for a sensitivity analysis of design parameters, as well as a best range and endurance analysis around the specifications. This is shown in the bottom part of Figure 6. The analyzer is used to validate the performance of the parametrization, electrical, and BEMT model used by the optimizer, described in section 3.3.6.

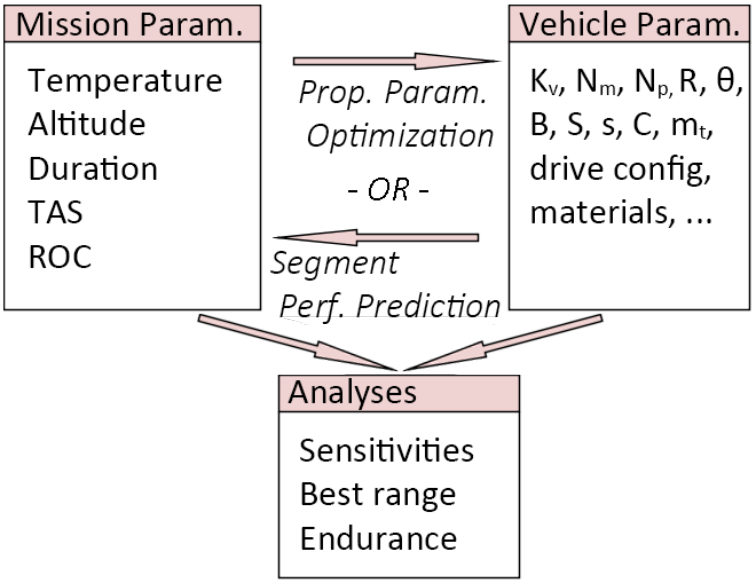

Figure 6: MST overview and workflow. When referring to MST, the "Prop. param. optimization" direction in the figure is referred to as the "optimzer," and "segment perf. prediction" in the figure is referred to as the "analyzer"

The second path is in the reverse sense, known as the drive optimizer. If only mission parameters are known (e.g. true air speed (TAS), payload, segment endurance, temperatures, etc.), the optimizer will attempt to design the propulsion system parameters to complete that mission. There are several modes for the optimizer, described below, which the goals that it seeks to achieve (e.g., a certain hover endurance, range, speed, etc.). The output, by default, is the lightest mass vehicle that is capable of completing a mission. Other options include but are not limited to smallest rotors, most efficient hover, cruise, etc.

The drive optimizer algorithm is so called as it assists in mapping desired mission parameters to the needed vehicle design parameters. That is, given a desired mission capability, such as a cruise for a certain duration, the drive optimizer will attempt to design a vehicle's propulsion system (as well as others; chassis parameters, wingspan, chord, and others if desired) such that the vehicle's performance will be adequate to accomplish the mission.

Both the analysis and optimization algorithms consider aspects of the following

drive components: motors, electronic speed controllers (ESCs), propellers, batteries, and wiring. Non-drive components considered include payload, structure, and avionics, which are used for weight budget and power draw calculations.

3.1 Propulsion system sizing and performance prediction

3.1.1 Optimizer flow

The output of proposed optimizer allows a designer to select propulsion parameters for motors, ESCs, propellers, batteries, and power wiring harness. In arriving at these outputs, vehicle performance and physical data are also predicted. To do so, the method attempts to select the parameters, and in effect, size the propulsion system to accomplish a specific user-defined mission. It does so within a set of user defined parameter limits. Figure 7 shows the overview of the method. Starting with the user's inputs for a mission, limits, and objectives, the method splits the mission into mission blocks or segments for which power required calculations are made, described by section 3.1.3. The user may also set optimization objectives to guide the optimizer such as minimum mass, highest thrust to weight, most efficient cruise, etc. When the power required per segment has been calculated, the method may select the set of interim parameters to define the required propulsion system. These interim parameters are used to design the propulsion system's rotors for the worst-case requirements (e.g., fastest cruise, etc.) and the total energy required drives the battery size. The high-level, propulsion parameter output of the tool are required motor constant K_v, current I_t (and thereby ESC, capacity, drive wiring gauge, and battery discharge rating C_b), propeller radius R and pitch p_p, battery capacity C, and serial and parallel battery cell counts S and P, respectively. Other outputs include or may include number of motors N_m, wing chord c, or other user-specified optimizer goals. The entire set of mission segments thus generates a set of interim propulsion system parameters and this set is used by the optimizer to select a final parameter

list. The overall optimizer flow, expanded and seen in Figure 8, is run for each mission segment. Mission parameters are used to find the aircraft pitch θ and thrust required T_R (block D), which is gained by an overhead parameter ξ. The overhead parameter is added so that the vehicle can produce T_R at less than 100% throttle. T_R is then used to find required RPM to select the rotor seen in Figure 11. With the rotor selected, the algorithm calculates the power required and masses of all components shown in Figure 12. Instead of using power required to size the propulsion system like in classical methods, power is not used to size the rubber motor. It is only used to size the battery, ESC, wiring, and may be used to ensure that the rubber motor is capable enough before proceeding with the design. Once power is calculated, masses of all components can be predicted, and thus the total required mass. This includes the mass of the battery m_b, wiring m_w, motors m_m, chassis m_c, propellers m_p, and avionics m_{avn}. The calculation of these rubber component masses occurs in Figure 12, using the parametrization functions described in 3.2. The total required mass m_r is checked against an allowable maximum mass m_a of each loop step; the outer loop begins at some low m_a and continues to increment m_a until m_r is equal or less than m_a.

3.1.2 Mission definition

In the proposed method, a mission is specified which will drive the requirements of the propulsion system design. A mission is composed of building block segments. Each segment is defined by: the time duration t_i, airspeed V_{TAS} and flight path angle (FPA or γ) or rate of climb (ROC), and total mass m_T (i.e., total vehicle mass to account for potential changes in payload). Figure 9 shows a hypothetical mission for a 2.3 kg winged quadrotor which has eight segments. The vehicle carries a 0.6 kg payload which it must drop at some location in segment five after a one minute hover. Assume for discussion each segment takes one minute and (i.e., the x scale

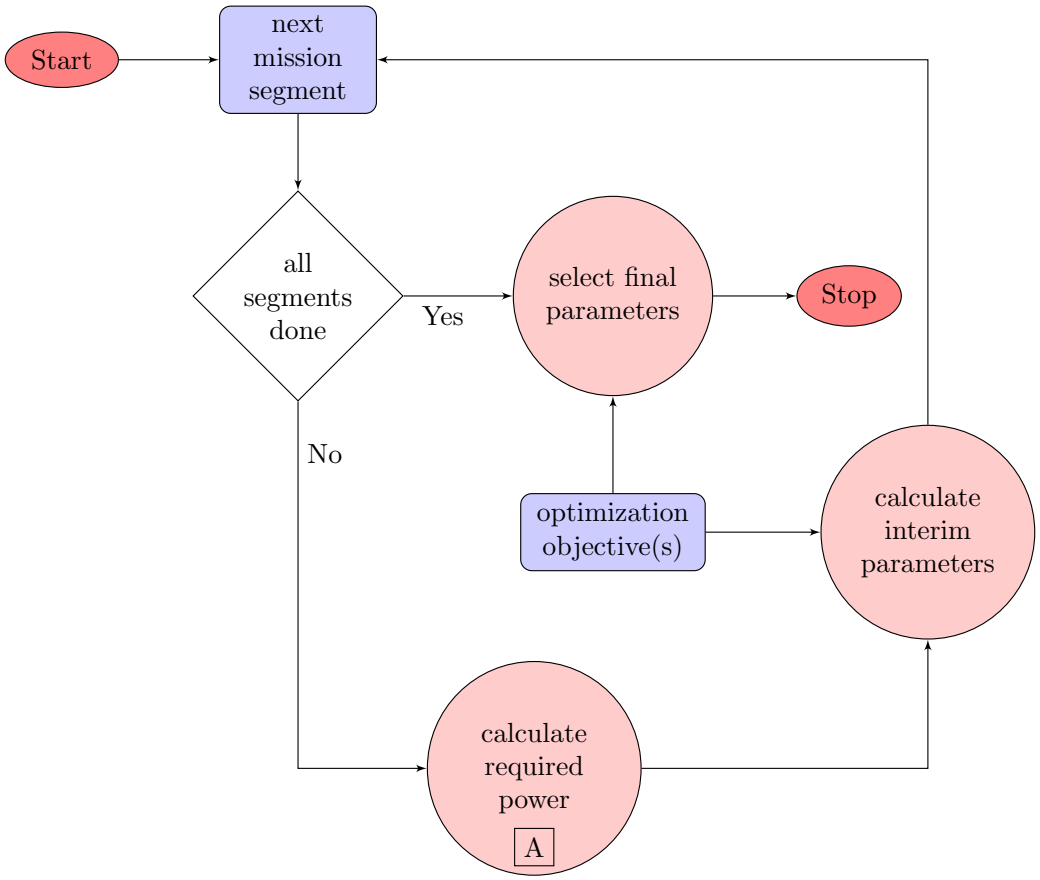

Figure 7: Propulsion system parameter optimizer overview. Figure 8 shows the expanded version of this figure when the optimization objective is to minimize mass. Block A is described by section 3.1.3. The mission segments are like those shown in 9

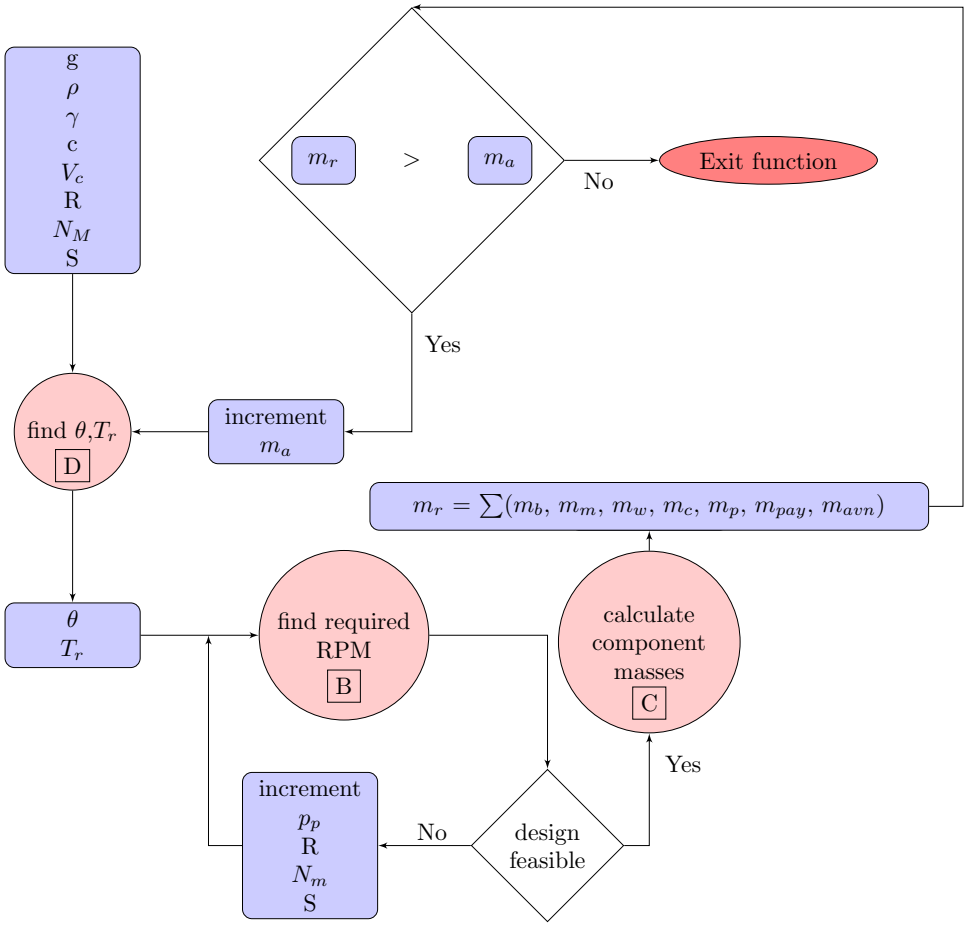

Figure 8: Optimizer per-mission segment overall flowchart. This particular optimizer is set to find the lightest possible vehicle to accomplish the specified mission segment. See Figure 11 for more information on block B. Block C is found in Figure 12. Block D is described in Figure 10

.

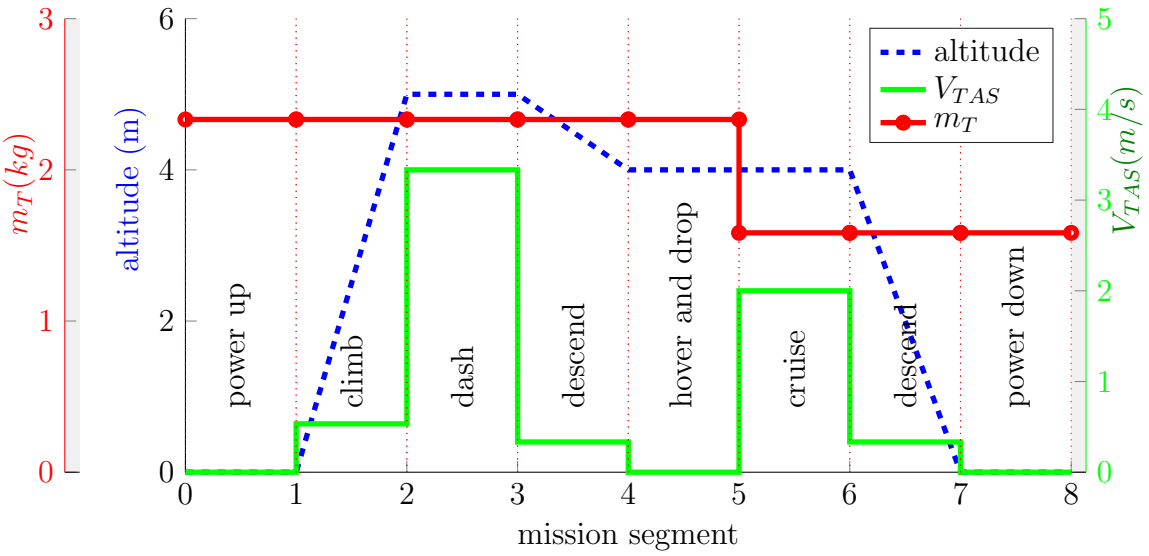

Figure 9: Schematic mission profile for a remote delivery vehicle

is in minutes). In this mission, the vehicle spends a minute on the ground booting and otherwise initializing. The vehicle then spends a minute climbing to its cruising altitude, spends a minute in cruise to the target, descends, hovers and drops the payload, and then cruises back to the helipad, descends, lands, and spends a minute powering down.

3.1.3 Power required calculation

Looping through each mission segment, as seen in Figure 7, the power required needs to be calculated. Each mission segment is used to size a propulsion system, that is, to select propulsion system parameters and by default, provide a minimum mass vehicle required to accomplish that segment. For ground segments, where the vehicle is only powering avionics will only function to increase the size of the battery. The vehicle parameters will be sized for each segment except for those where the vehicle does not leave the ground. Ground segments may be important to consider to adequately size the battery capacity, especially when these segments are lengthy and/or avionics current I_a is a large percentage of the current budget I_t[113]. The power required for all of the other segments (climbs, cruises, hovers) may be calculated in many ways.

The proposed way is as follows.

To get power required, in this implementation, thrust required T_R and vehicle pitch θ are needed. This is done by considering Figure 10. All aerodynamic forces are calculated relative to the local freestream velocity. Lift, drag, and buoyancy (to keep the method generic for lighter than air vehicles) for each component are found: overall L, D, and B are summed and a loop attempts to find T_R, α_R, and vehicle pitch θ_R to maintain a steady state, seen in Figure 10, in the condition desired by the segment. The required thrust T_R is multiplied by a ratio ξ which determines the available overhead authority of the rubber rotors. That is, if T_R is calculated as 5 lbf, T_R is set to 5ξ lbf. When ξ is set to two, the vehicle will hover at 50% throttle which is used for all optimization described by this thesis. Buoyancy is considered to allow for sizing of airships and/or calculations in dense environments such as water. Multiple solutions may exist for finding the above parameters to maintain a steady state. In such a case, the solution with the smallest T_R is chosen.

The power required depends on several sets of factors: environmental, mission segment, and vehicle characteristics. Environmental data that are required include gravitational acceleration g, fluid density ρ, and ambient temperature. These may change depending on many conditions (e.g., whether the vehicle is underwater or on Mars) and must be considered when calculating the power budget. Each will directly affect the required power to accomplish any mission. Relevant segment parameters include desired flight path angle γ, ROC or V_{TAS}, and time spent in each segment t_i. Vehicle data generally include lift and drag parameters ($C_L(\alpha)$ and $C_D(\alpha)$ described in section 3.3.1, areas S_w and A_f) for all relevant bodies (e.g., fuselages or wings) and respective incidence angles/controller schemes (for free or tilt wings/rotors), motor dihedral or incidence angles, total mass m_T, number of motors N_M, etc.

With T_R known, we wish to find the power required. T_R and other relevant data are used in a BEMT function for further calculation, seen in Figure 11. To do

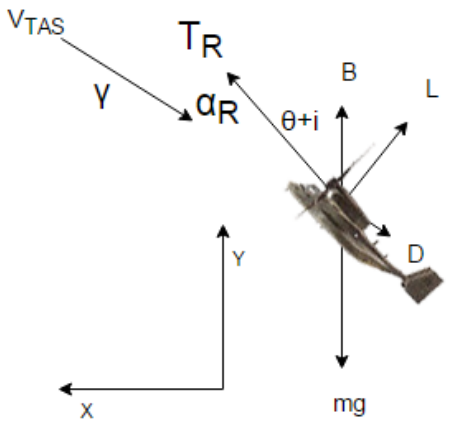

Figure 10: Determining required thrust in steady state maneuver, used for block D in Figure 8

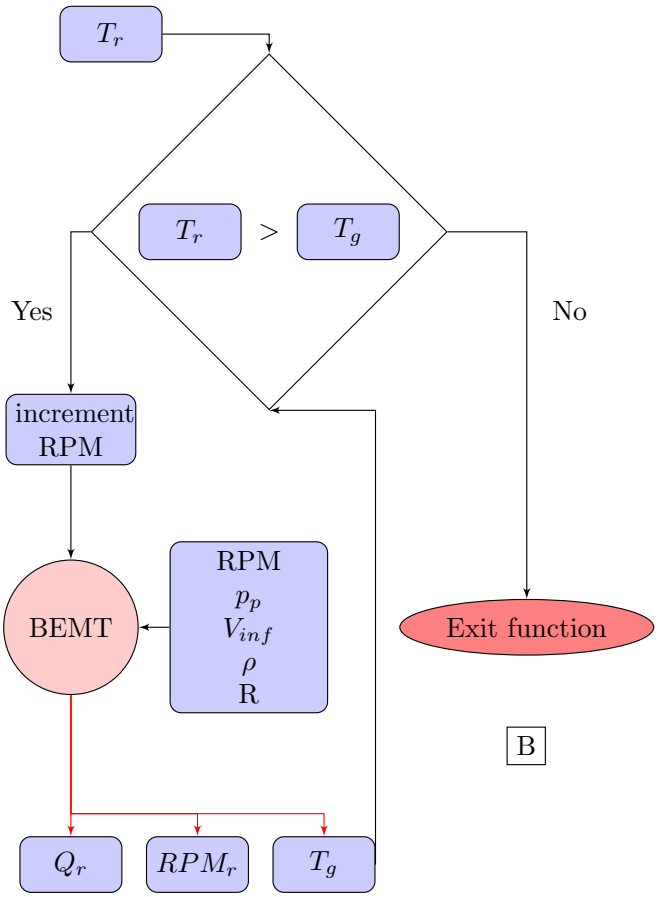

Figure 11: Find required RPM and torque to complete a mission segment for the set of propulsion system parameters, block B of Figure 8. These are used to calculate power required.

this, the generated thrust T_g for a set of iterated rotors is calculated by the BEMT. By iterating propeller radius R and pitch p_p, the function finds the required RPM (RPM_r) to produce the required thrust T_R. These parameters are used to build a generalized propeller for use in BEMT's T and Q calculations in equation 6. In order to do this, a parameterized propeller model is required. The proposed propeller parametrization for β and c as a function of its radial section and p_p, which are described further in section 3.2.4. For this study, the $C_L(\alpha)$ and $C_D(\alpha)$ are taken from the NACA 0015 profile [114]. Otherwise, specific blade geometries may be used. In addition to RPM_r, the BEMT function outputs the required aerodynamic torque Q_r. Using Q_r, the required drive current I_d may then be calculated, seen in Figure 12. This is done as explained in section 2.2.3. The function makes the strong assumption that the motor efficiency η_M is a constant 75-85% and uses eq. (12) to find I_d. To find the required K_V, RPM_R is used in conjunction with the operating voltage of the battery V_s.

With required drive current I_d known, almost every parameter needed to estimate the size of the vehicle is now in known. Figure 12 may be used to find the masses of all components. There are two options for doing this: with a database of components or with parametrization. To eliminate the labor-intensive process of generating, maintaining, and relying on a database, parametrization is chosen. This is done using functions of component parametrization described in section 3.2. The parametrizations are used to construct rubber components for the optimizer to size the vehicle. Rubber components may have parameters that may or may not be readily available on the market. For instance, the optimizer may select motors with a K_v of 732.4. The designer may be limited by available hardware and be forced to choose to use something close to that value.

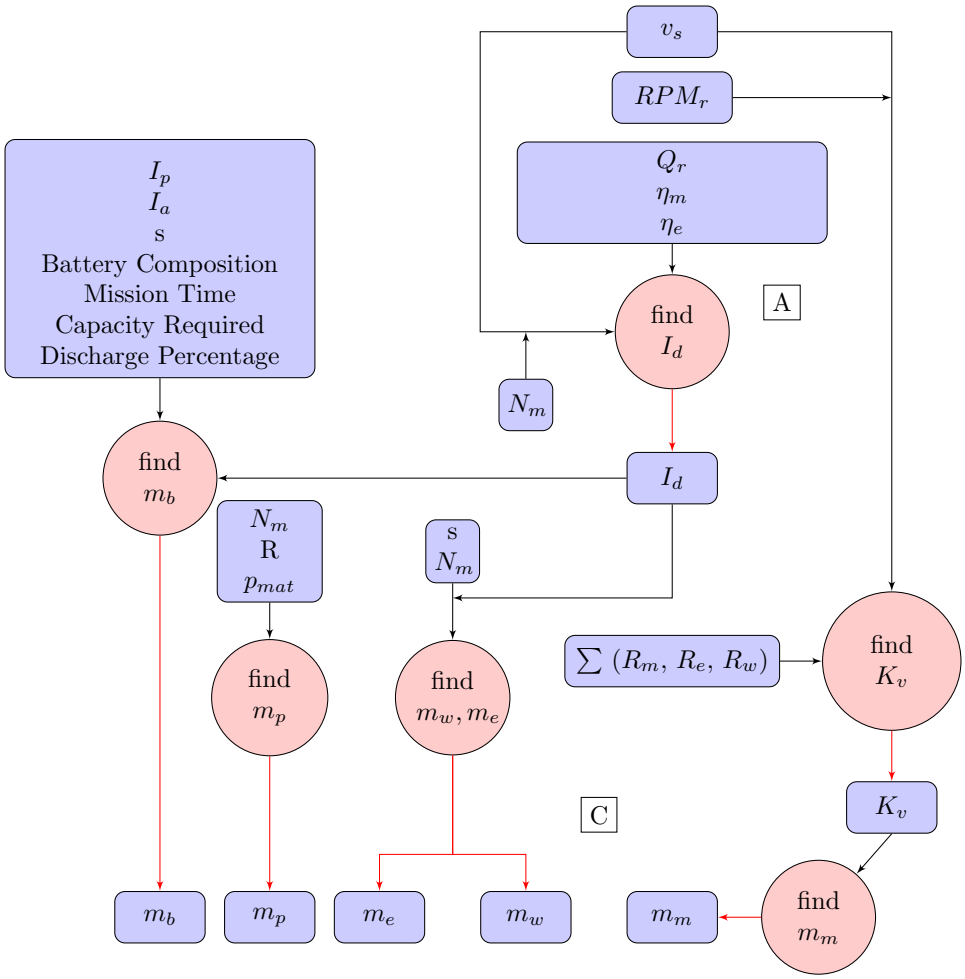

Figure 12: Find the propulsion system component masses given the electrical and mechanical requirements. Expansions of block A of Figure 7 and C of Figure 8

3.1.3.1 Feasibility of optimizer solutions

Recall that the proposed method works by abstracting the drive components into appropriate parameters. This removes the need to the have a model or data of specific motors, propellers, ESCs, and batteries, and instead relies on their parameters. That is, a database of parts is not required, although is not precluded. To illustrate the abstraction, consider a motor. The methodology does not require knowledge of a specific motor and its respective performance data. Instead, it uses standard motor parameters (ie, K_v, winding resistance R_m, no-load current I_0, etc) for predicting the motor's performance capabilities. One important side effect to note, because of this abstraction, the resulting optimizer propulsion system parameter set (i.e., motor, propeller, ESC, and battery) is what is required. When selecting a physical propulsion system based on the optimizer's output, the user must confirm that all equipment to be used is capable of the electrical and mechanical performance requirements reported by the optimizer prior to implementation. For instance, assume a 1100 K_v motor is selected as optimal for a particular mission. As far as the optimizer is concerned, that motor (or, really class of motors) will be able to handle the required current for some specified flight condition in that mission segment. This is not to say that every 1100 K_v motor is capable of completing the mission. Motors in this, and every class, all have different maximum currents I_{max}, I_0, and R_m. These may shift the validity of the optimizer output one way or another. Most importantly, the user must confirm that the motor to be used is capable of the power throughput required. These are generally listed as maximum continuous power (MCP) and maximum burst power (MBP) which is valid for short time periods. For example, the manufacturer's specifications of maximum motor power should be confirmed to be higher than the power required reported by the optimizer for the mission segment. In a similar fashion, all propulsion system components must be checked. Propellers, hubs, chassis, and other structural components should be able to handle dynamic and static forces that

will be experienced when in flight, all out scope for this study.

3.2 Propulsion system component parameterization

This section is motivated by RQ 1b: "How do we model components to predict performance?" from 2.5.2.

In order to run the optimizer and create rubber components for it, some parameterization needs to be performed for all relevant propulsion system components. If specific components are not specified, these rubberized components are needed as they will be stretched to find an optimal system by the optimizer. A relationship was found between the masses and several key characteristics of all drive components considered by both the validation and optimization algorithms. These are necessary to abstract actual components into just the key characteristics to enable the algorithms to guess the masses of the components required to lift the vehicle. They are used in both validation and optimization algorithms, proposed in later sections. In addition, the propeller's geometry needs to be parameterized as described in 3.1.3.

3.2.1 Motor

The data shown here consider both IR and OR motors, the latter being a more popular choice for many multirotor configurations for their generally higher torque (per mass) and ease of installation. Figure 13 shows the trend of high K_v motors having low mass and vice versa, also studied by Gur[18], although with less motors, and with a broader focus on motor types, including heavy duty/high voltage motors. Both IR and OR motors are plotted in the figure.

Figure 13 shows that in general, IR motors tend to be heavier per unit K_v than OR motors.

The trend in Figure 13 generates eq. (14), providing a mapping between K_v and

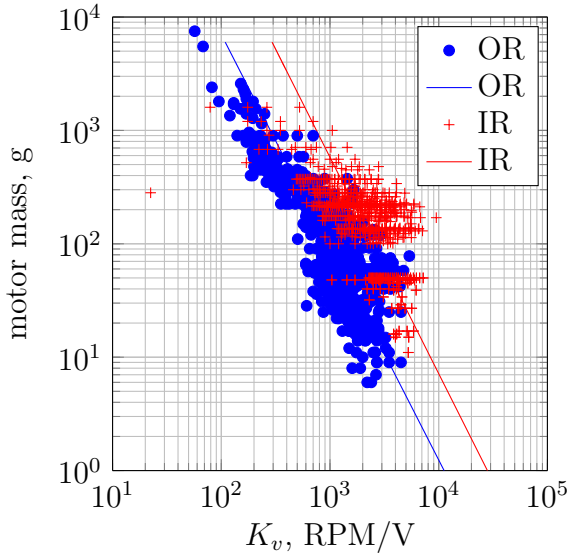

Figure 13: OR and IR K_v to mass relationship.

predicted motor mass m_m for both OR and IR motors.

$$m_m = 10^{p_1} K_v^{p_2},\ g \tag{14}$$

where p_1 is 4.0499 and p_2 is -0.5329. For IR, p_1 is 4.4482 and p_2 is -0.5242. Of particular interest for this study are motors in the range of K_v and mass shown in Figure 14, as they are popular choices for the hobby-sized vehicles considered below.

Eq. (14) is modified to match some of the lower K_v motors available on the market, as the original fit does not match market survey data well in this region between 0 and around 500 K_v for hobby-grade motors. The modified equation for OR motors is seen in Figure 14 as OR H. Around 991 OR and 696 IR BLDC motors [115] were used with incomplete entries removed.

In addition to parameterizing the mass as a function of K_v, we are interested in the resistance of the motor, as generally, larger motors have larger electrical resistances. Gur[18] shows that the internal resistance of the motor R_m is a function of K_v or mass.

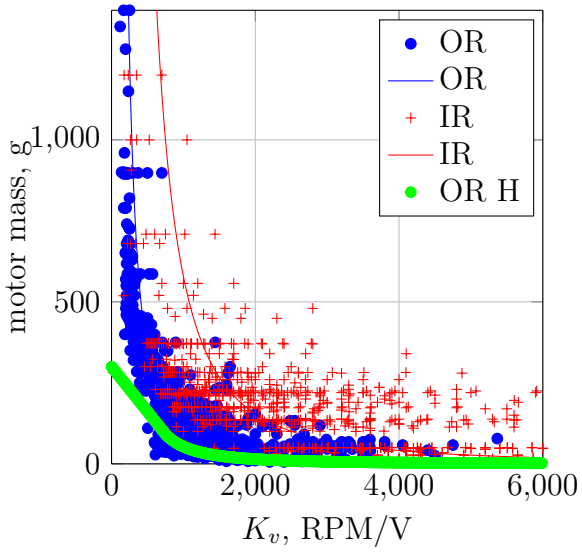

Figure 14: OR and IR K_v to mass relationship. OR H is the modified curve used for the analyzer and optimizer tools.

3.2.2 ESC

Data from around 20 ESCs rated for up to 100 A are taken to study the relationship between ESC mass and current throughput capacity. These data are shown in Figure 15. Eq. (15) is the function found that provides a mapping between an ESC's maximum rated amperage and its mass:

$$m_e = p_1 A_{max},\ g \tag{15}$$

where p_1 is found to be 0.8421. In addition to ESC mass, it is useful to know the resistance of an ESC when it is operating. Ampatis[17] shows that the resistance of an ESC R_e is between 9 and 45 $m\Omega$. This value is $3R_{DSON}$, where R_{DSON} is the resistance of one path from the input to the output of the ESC when the path is shorted.

Wiring, including all signal and power lines, has been found to weigh around 5% of the GTOW of all UAVRF multirotor vehicles. This fraction is used for all calculations

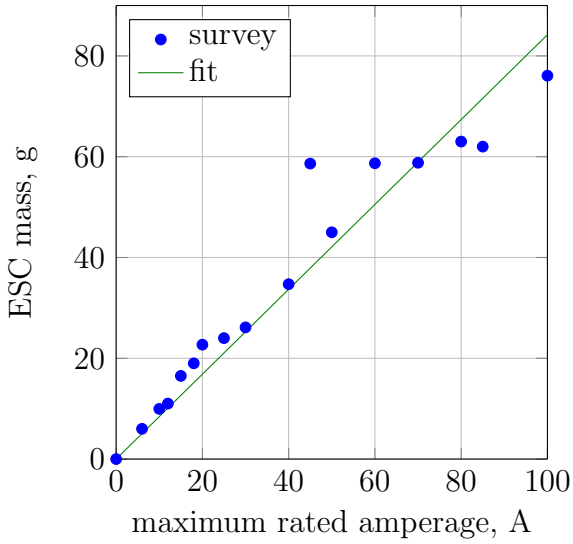

Figure 15: Masses of ESCs and their respective maximum amperage rating.

by the tool.

$$m_w = 0.05 m_t \tag{16}$$

Wiring resistance R_w is small and is scaled with the amperage required I_d.

3.2.3 Battery

A parameterization of battery mass and related capacity is also required for the algorithm to function. Data found are shown in Figure 16.

Eq. (17) is the map between battery capacity and mass, assuming 1P configuration, calculated by considering approximately 30 common LiPo batteries [116]. For the same chemistry, the mass of the battery is more or less linear with number of cells contained within it:

$$m_b = (p_1 s + p_2) C,\ g \tag{17}$$

where p_1 is 0.026373 and p_2 is 2.0499e-05. Gur[18] also studies the relationship between battery capacity C in mAh and mass.

As with the other electrical components, the battery's total internal resistance must be estimated. Ampatis[17] shows the calculation of resistance of the battery R_b.

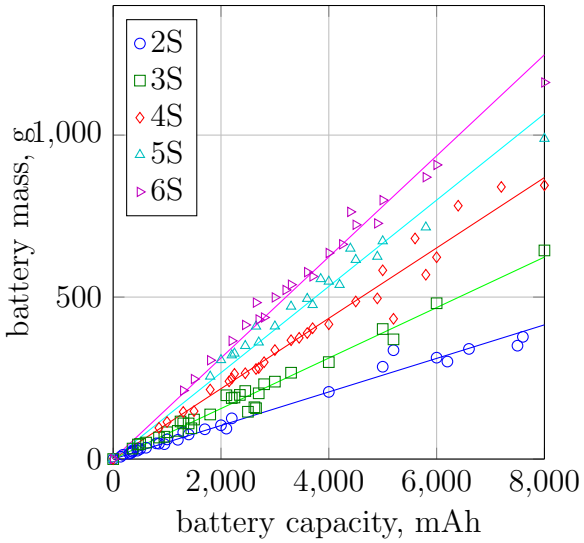

Figure 16: Battery masses for configurations between 2S and 6S. All batteries surveyed have 1P configuration.

This will also be used in the electrical model described in this paper.

3.2.4 Propeller

The propeller needs to be parameterized for the BEMT as described in section 3.1.3. Propellers of varying compositions including nylon-plastic, carbon fiber, wood, and other plastic have also been characterized, providing a mapping between material, radius, and mass. Data from about 30 propellers are shown in Figure 17. As with many of the parameterized values, these will depend on the manufacturer and model of the propeller. There are other factors which influence the propeller's mass that have been ignored for simplicity. These may include and are not limited to: hub geometry, thickness profiles in every dimension, and material compositions.

The mass of the propeller is found by

$$m_p = p_1(2R)^2 + p_2 2R + p_3,\ g \tag{18}$$

where p_1 is 0.08884 and p_2 is 0 for wooden propellers, 0.05555 and 0.2216 for plastic, 0.1178 and -0.3887 for nylon reinforced plastic, and 0.1207 and -0.5122 for carbon fiber. R is radius in inches.

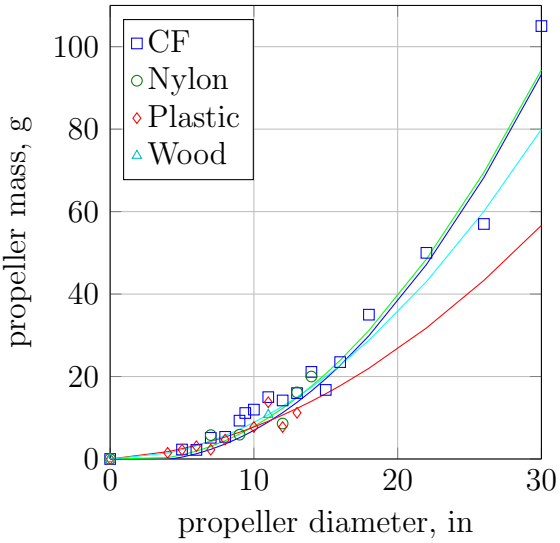

Figure 17: Masses of propellers of various diameters composed of four materials.

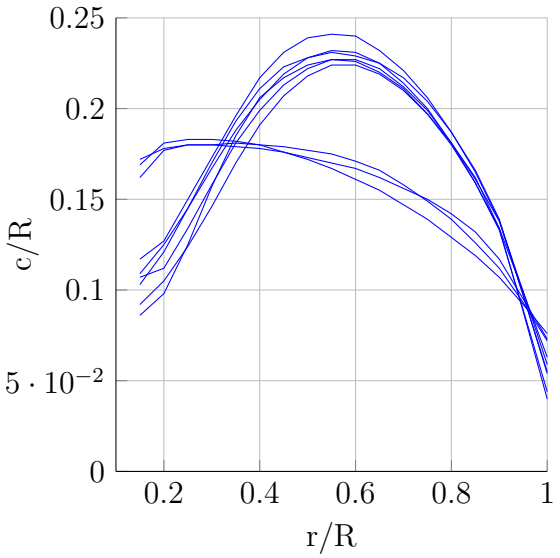

Figure 18: Non-dimensionalized propeller blade chord at radial section r/R. Data shown from GWS Slowfly and DirectDrive propellers, extracted from [117]

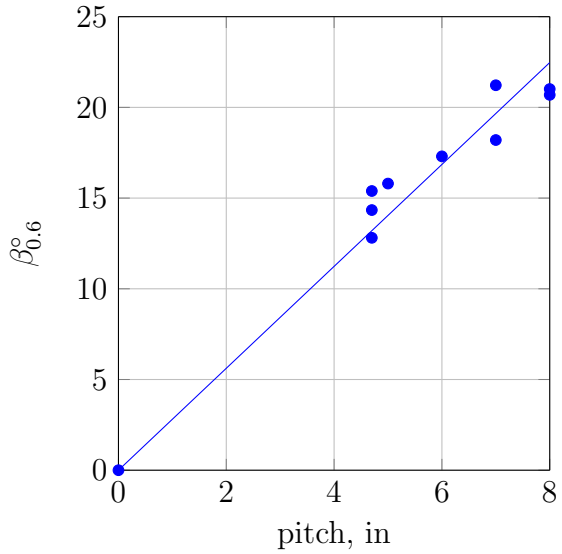

Figure 19: Twist of GWS blades at $r/R = 0.6$ compared to indicated blade pitch, extracted from [117]

In addition to mass information, geometrical data are parameterized for propellers. This allows the use of a generic, averaged propeller if a specific geometry is not available or selected. Geometrical propeller data are taken from Brandt[117]. Specifically for this paper, we will consider GWS Slowfly and DirectDrive propellers, although other available data are also compiled and stored in separate, user selectable functions in the algorithm. This is necessary to feed the thrust calculation loop of equation 6, as the lift per radial segment of the propeller is calculated based on these data.

Eq. 19 provides the physical twist angle β at the radial segment $r_R = r/R$ for an existing set of GWS propellers and data from the above propellers are shown in Figure 20.

$$\beta = p_1 r_R^3 + p_2 r_R^2 + p_3 r_R + p_4, \ ^{\circ} \tag{19}$$

where, for this subset of propellers, p_1 is 30.322 p_2 is -64.731, p_3 is 23.008, p_4 is 20.558.

These data are averaged to provide a basis function for $\beta(r_R)$. This function

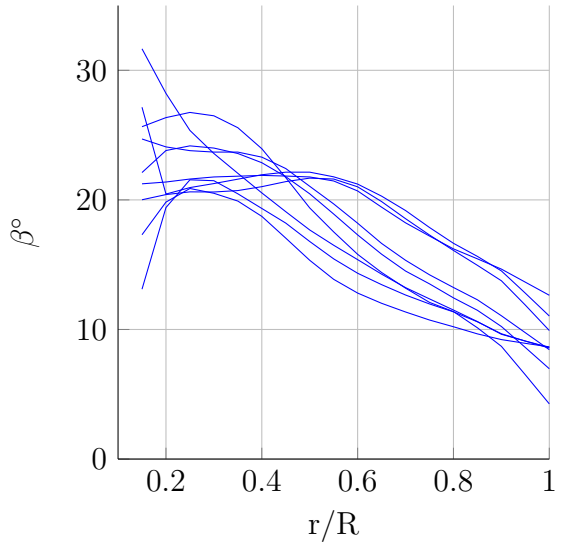

Figure 20: Blade twist at radial sections r/R for nine GWS Slowfly and DirectDrive propellers, extracted from [117]

is scaled by a function considering the pitch of the blade. The scaling is found by investigating the effect of pitch rating on the actual twist $\beta(r_R)$ of the blade at r/R = 0.6. Pitch may be qualitatively defined as the linear, axial distance traveled by the propeller (at $r_R = 0.6$) should it be rotated by one revolution. This relationship between a pitch label and the physical twist β of a propeller may be seen in Figure 19 for the GWS propellers.

p_p, β, and inflow velocity are calculated by the BEMT algorithm and form the angle of attack of the blade section at r_R. If the flight condition includes a non-zero airspeed, the vertical component is added to V_0 to achieve the final angle of attack of the blade segment. Lastly, eq. 20 provides the chord at r/R for all nine GWS propellers described, also needed by the BEMT loop to calculate thrust. The distinction between the Slowfly and DirectDrive propellers is evident in the figure. For this subset of GWS propellers,

$$c_R = p_1 r_R^3 + p_2 r_R^2 + p_3 r_R + p_4 \tag{20}$$

where p_1 is -0.2872 p_2 is -0.1637, p_3 is 0.4551, p_4 is 0.05648.

3.2.5 Structural

A survey of a few UAVRF vehicles was completed to parameterize the proportion of structural to GTOW. The algorithm assumes a very light-weight vehicle to have a structure of 8% of GTOW (GTQ Mini[113]), and a heavy-weight vehicle to have a ratio of 40% (GTQ2[118]). The ratio used for the discussion below is 20% . In order to estimate chassis weights, this value is more or less arbitrarily chosen, but obviously may be changed for specific optimizations. It is difficult to estimate this correctly because there are multiple ways to design a chassis, so an arbitrary value must be used.

$$m_c = 0.2 m_t \tag{21}$$

3.2.6 System Analysis

The analyzer may be used to substantiate the selection of components for a UAV design. This includes validation of the outputs of the optimizer algorithm described below. Given a propulsion system design, the algorithm allows a user to confirm that the vehicle will be capable of the mission for which it is designed. This is done in two ways. First, the electrical power requirements that the drive components will be subjected to in the mission flight condition are calculated so that relevant data of the selected components may be compared to manufacturer specified limits. This attempts to ensure that the selected components are capable of handling loads such as current and torque. Second, the time endurance of the vehicle will also be calculated so that the user may confirm that the vehicle will be capable of completing the mission should the drive components handle the other requirements calculated.

The calculation method also provides a maximum range analysis. The analysis will provide the best airspeed for maximum range, and since the method is geared toward VTOL vehicles, the pitch angle from vertical required to attain it. In addition to this, the method provides a sensitivity analysis to design parameters, including motor K_v,

propeller diameter and pitch, GTOW, battery capacity, altitude, number of motors, and wingspan. This helps identify key design parameters around the desired flight condition.

The analyzer algorithm performs all calculations based on the input of given or estimated characteristics of drive system components and their masses. Outputs of the method are described below and include hover time, design space sensitivities, drive system loading requirements in terms of RPM, torque, mechanical and electrical power. Other data are also available as outputs of the analyzer. These are shown for an example vehicle below in Table 4.

3.2.7 Analyzer hover time calculation

The analyzer algorithm first uses a loop to arrive at the linear throttle input d_t required to allow the vehicle to hover, climb, or dash as specified by the mission scenario inputs. The hover case is described first and cases with airspeed are described below. The throttle required to hover must be sufficient such that the total thrust calculated based on this throttle balances the weight force of the vehicle. The throttle required, along with the inputs described below, are passed to a BEMT calculator to calculate thrust generated by each propeller. The BEMT algorithm is also fed propeller characteristics, all of which are derived from models described in the parameterization and mission inputs. Throttle d_t is incremented until it is sufficient to accomplish the mission segment.

The vehicle's total mass must either be provided or estimated. The estimation of component weights is described in detail in the parameterization section. Eqns. 14, 15, 17, 18, and 21 for estimating m_m, m_e, m_w, m_b, m_p, respectively are used to find the GTOW m_t. The m_t, number of motors N_m, motor K_v, number of propellers N_p, number of blades per propeller B, propeller radius R, propeller pitch p_p, and current analyzer loop throttle command d_t are passed to the BEMT

algorithm to calculate the thrust generated by all propellers. Other inputs include results of eqns. 19, 20, the no-load current of the motor I_0, current draw of other power sinks I_a and I_p, propeller material, battery configuration, composition, and qualitative quality, flight altitude and associated air density, calculated using the ISA standard atmosphere.

Together with the data above, a section lift and torque are calculated using the BEMT equations. For this study, the $C_L(\alpha)$ and $C_D(\alpha)$ are taken from the NACA 0015 profile [114]. The entire blade section is integrated and which provides the total lift and torque applied by each propeller blade. This lift and torque is then scaled by the number of blades per propeller and the number of propellers on the vehicle.

The algorithm also allows for pitch-controlled propeller hubs. When the user selects such a hub, all hubs on the vehicle are assumed to be pitch-controlled. The throttle required sent to the BEMT by the outer loop is turned into a blade pitch command, subject to the maximum allowable pitch specified by the hub geometry. The blade planform is also selectable to be of a more traditional helicopter blade style, where $\beta(r_R)$ and $c(r_R)$ are assumed constant. Also in such a case, a governor may be enabled which controls the PWM command to the motor, thereby ensuring that the RPM at the head does not exceed a specified value. Otherwise, a headspeed may be specified for the BEMT calculations.

The algorithm has limited capacity for lifting bodies. Three types of lifting bodies are considered. First, the body of the vehicle has a selectable $C_L(\alpha)$ and $C_D(\alpha)$. If data or an estimate are available, this may be adjusted or ignored for the purposes of all calculations. The second and third types are wings. For these, the algorithm accepts $C_L(\alpha)$ and $C_D(\alpha)$. Wings may be either fixed to the body via an incidence angle, or free/actuated and controlled to a specified α.

3.3 Range calculation, power required for cruise

This section is partly motivated by RQ 1c: "How much power does it take for cruise and what does the power bucket look like for multirotors? What about aerodynamic lift and drag data of multirotors?" from 2.5.1.

Since missions may be composed of segments requiring states other than hover (i.e., steady state cruise, climb, or descent), the components of forces must be estimated, shown in Figure 10. Starting at a vertical thrust axis aligned with gravity, the algorithm uses an iterative loop to calculate the angle required to achieve a desired airspeed and/or FPA. Constraints are set so that the vehicle does not lose altitude during the cruise if FPA = 0°. A climb rate may also be specified. The method considers lifting bodies and control, their incidence angles, as well as controlled wings that keep a constant angle of attack with the free stream. For each α, the vehicle's total L and D is calculated using data described in section 3.3.1. The loop quits when the total lift is nearly equal to the weight force of the vehicle and all other forces cancel, producing a steady state condition.

In the outer, throttle required loop, the angle calculated by the above loop is used to add axial flow into the propellers. V_∞, the axial component of the TAS, is added to the V_0 component in the BEMT calculator. As in the hover case, the BEMT implementation assumes a uniform inflow. As mentioned, the BEMT implementation may or may not handle these cases well. To determine the validity of results, several experiments are attempted as described in $EXPT$ 1c.

The first attempt at this experiment is to use MST to find the power bucket for multirotors. The analyzer algorithm attempts to calculate the vehicle's time endurance for a range of airspeeds. Using these with the angular iteration above, a maximum range is available for each condition, providing roughly "optimal" airspeeds for maximum range and maximum endurance. Of course, this is range in the wind

reference frame, so any wind would have to be taken into account for planning purposes. These data predicted are compared to data recorded in $EXPT$ 1c described in 2.5.1.

GUST is used to simulate flight of *Eagle*, the vehicle described in section 3.4.2. The math used by GUST to calculate thrust, power, and other relevant parameters is described by Prouty [13]. The vehicle is also simulated in MST. The results are seen in 21. Both GUST and MST results are shown along with classical equations from Prouty. The data point labeled P_{eFT} is the electrical power to hover recorded in an actual 120 minute hover flight test. Both the classical equations and GUST predict a larger power bucket than does MST. This makes MST more conservative when predicting cruise power.

MST and GUST are in reasonable agreement with other predicted data. For example, MST has the cruise speed for maximum range at about 37 ft/s. This occurs where the slope of V_{TAS}/P is highest while intersecting the origin. This matches closely with what is seen in 21 showing GUST ideal cruise speed for range of around 31 ft/s. The cruise speed for maximum endurance for MST is around 12 ft/s while GUST predicts 25 ft/s. Maximum endurance occurs where P is lowest. As the models are quite different from eachother, there may be a number of factors that are responsible for the differences. The GUST model uses performance equations described by Prouty [13] to predict thrust and power. The BEMT implementation used by MST uses a digitized version of the geometry of the blades to try to predict thrust. Induced velocity calculations also differ, as does the drag aerodynamic vehicle modeling. This might explain the differences seen in the models.

Despite the differences noted above, GUST and MST share a close result for cruise. The pitch angle θ of the vehicle required to maintain steady state cruise is shown in 22. Note the very close agreement between MST and GUST. To calculate θ, MST uses the force balance described around and shown in 10.

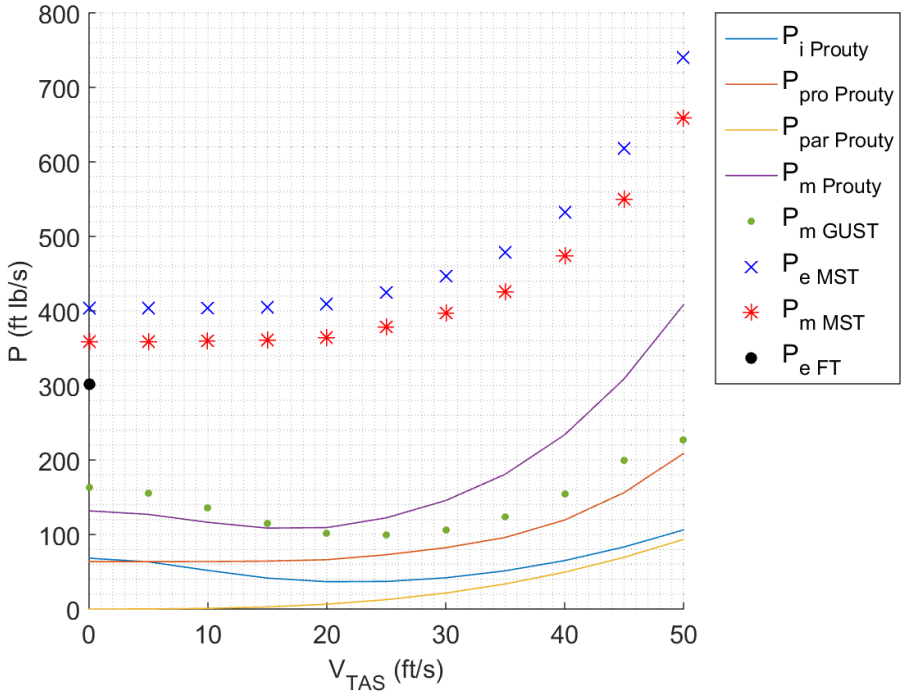

Figure 21: Simulated power required for cruise, *Eagle*

A vehicle was equipped with a Pixhawk and power module, which measured current and voltage. The vehicle was flown between two waypoints on a calm day. However, the data was not conclusive, as the voltage sensor sagged heavily compared to an independent FRSKY telemetry voltage sensor. In an attempt to remedy this, a DJI M100 vehicle was tested next with a custom written Android phone application to pull record data while in flight. However, the data was again not conclusive as any behavior was masked by a large noise amplitude and a slow, variable data rate.

For the power bucket of the X6 DFC vehicle, refer to section 4.1.6.3.

3.3.1 MR chassis wind tunnel testing

This section is motivated by RQ 1: What about aerodynamic data of chassis? from 2.5.1.

To measure C_L/C_D data for multirotors, several configurations were tested in a low-speed wind tunnel at Georgia Institute of Technology [101]. The full list of results

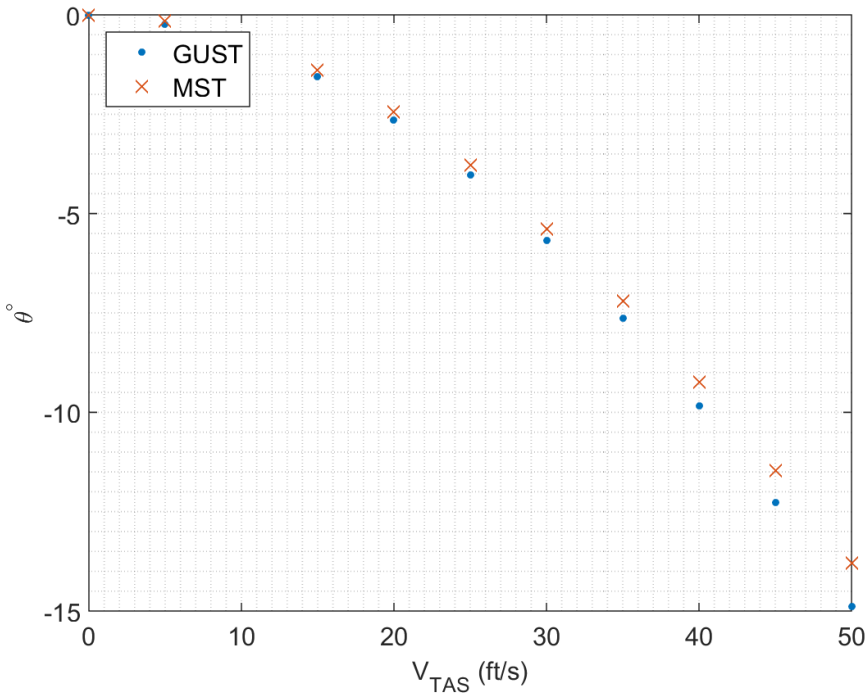

Figure 22: Simulated pitch angle required for cruise compared to classical calculations, Eagle

and data may be seen in the Appendix B.2. Noteable results will be included in this section. Some of the configurations that were tested were:

- 122 mm to 450 mm ready to fly frames
- Frames using flat top plates vs. canopy, Figure 23 (a)
- Bare frames vs. ready to fly frames, Figure 23 (b)
- Small racing X frame vs. larger H frame, Figure 23 (c)
- HD camera on board vs. no camera on board, Figure 23 (d)
- Cased vs. bare 5.8 GHz clover video transmitter antenna, Figure 23 (e)

These configurations were chosen based on several criteria. A representative set of multirotors used commonly for hobby racing were chosen. These are generally

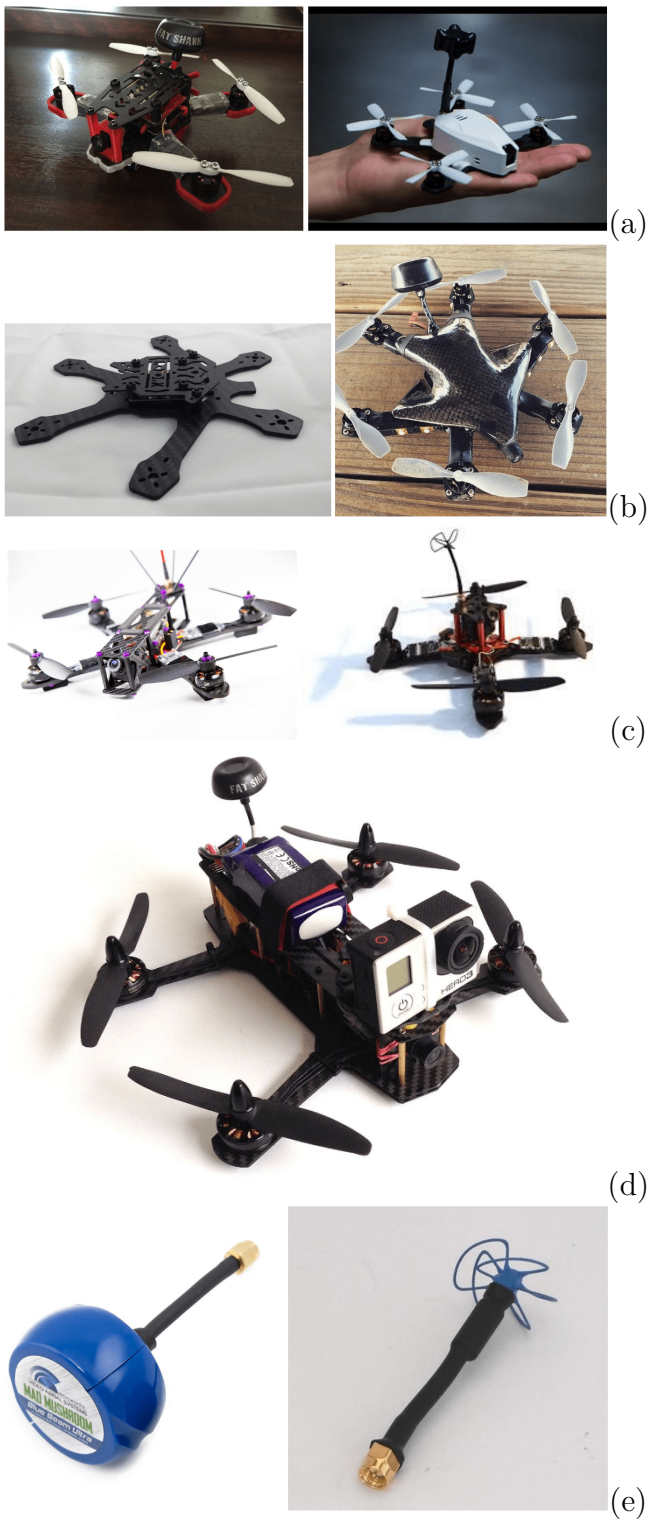

Figure 23: Configurations studied in wind tunnel, hobby multirotors made for acrobatics and racing: (a, left) 122 mm multirotor with flat vs (a, right) canopy, (b, left) 155 mm *Atom* chassis, (b, right) RTF 155 mm *Raiju* hexarotor, (c, left) 250 mm *H* frame *ZMR* vs (c, right) *X* frame *Shrike*, (d) 250 mm *ZMR* quadrotor with GoPro HD camera, (e, left) cased vs (e, right) uncased 5.8 GHz antenna. Thanks to Nick Willard for the photos.

flown at high speeds where aerodynamic effects will be important to consider. Some of these vehicles can fly up to a claimed 150 mph [163] and even 180 mph [164] with their propellers in advance ratios of around 0.35. There is currently a surge of interest and development in the area of multirotor racing with speculation and unsubstantiated claims by companies sometimes being the basis for design decisions. For instance, several companies have claimed that adding "aerodynamic" canopies (Figure 23 (a) and (b)) would increase aerodynamic performance by reducing drag and adverse lift. To test this claim, the frames were run and compared against the frames with canopies. If there is a benefit, it must be weighed against the increased mass of the vehicle. Another claim common in the multirotor racing community is that adding an HD camera such as a GoPro (Figure 23 (d)) or Xaoimi Yi will be a detriment to the aerodynamic performance of the racing drone by adding drag in high-speed situations. Although it is true that the weight added is often detrimental, adding around 10-30% to the GTOW, it is interesting to test whether or not the effects on aerodynamics are as profound. Many of these small UAVs are flown using a first person view (FPV) video downlink, especially during high-speed racing and acrobatics. The most popular video transmitter antennae for the 5.8 GHz video link, known as cloverleaves, have been encased inside plastic covers for crash resilience. These are tested against an uncased clover antenna an otherwise identical frame to determine the effect of casing these on aerodynamic coefficients.

The frames were swept through AOAs of 0 to -90° at 15.8 m/s wind speed. This AOA range corresponds the general flight range between hover or slow drift where α = 0° to 90°, which might be a climb or an unsustainable dash. Angles in between those two might be seen during a cruise condition. To measure the aerodynamic coefficients of each multirotor frame and configuration, a 3D-printed adapter was created to mount the vehicles to the load cell. The wind tunnel's load cell assembly (sting) has limits of +30 to 30° in pitch and +45 to 45° in yaw. The adapter was

designed such that the sting would be capable of supporting the vehicle from 0 to -90° in AOA. The 3-DOF sting measures side, axial, and normal forces in its frame. A coordinate rotation is used to then produce forces in the wind frame. The sting and the vehicle are also offset by 45°, so the measured angle of attack by the sting had to be shifted by 45° to give the true angle of attack of the vehicle. The sting's force measurements, rotated into the the wind frame of reference, were then normalized by the dynamic pressure, the diagonal motor to motor distance (wheel base) squared to calculate lift and drag coefficients.

Figure 23 shows all vehicles tested in stock, ready to fly (RTF) configurations, sans propellers. The entire dataset may be found in the Appendix Figures 64 through 75. This includes all vehicles between 122 and 450 mm wheelbases that were tested. Before these data were collected, the assumed values for C_{L_α} were estimated using a linear function symmetric about where $C_{L_{min}}$ occurred at -45° = -0.1, and $C_{L_{max}}$ = 0 occurred at 0 and -90°. This $C_{L_{min}}$ was estimated using a guess at 10% of the efficiency of a generic flat plate, due to multiple parts protruding from the plane of the plate [161]. This turns out to be close to what was observed in the wind tunnel data, seen in Figure 24. Note that C_{L_α} is negative in value, as it is adverse lift; the multirotor pitching in the negative direction (nose-down) to cruise causes this unwanted lift in the $+z_B$ direction. As for drag, C_{D_α} was assumed to be a linear function between a $C_{D_{max}}$ of 0.85 occurring at -90° to a $C_{D_{min}}$ of 0.35 occurring at 0° AOA. This was chosen such that the frame exhibits drag somewhere between a rounded rectangle and a rounded cube [160]. Again, the behavior matches closely to what is seen in Figure 24, although the values were different; measured values were closer to $C_{D_{min}} \approx 0.05$ and $C_{D_{max}} \approx 0.32$.

The data collected showed several unexpected trends. For example, flying with a front-mounted HD camera improves aerodynamics of the vehicle (at the cost of added weight, of course). This may be due to the fact that this provides flow shielding to

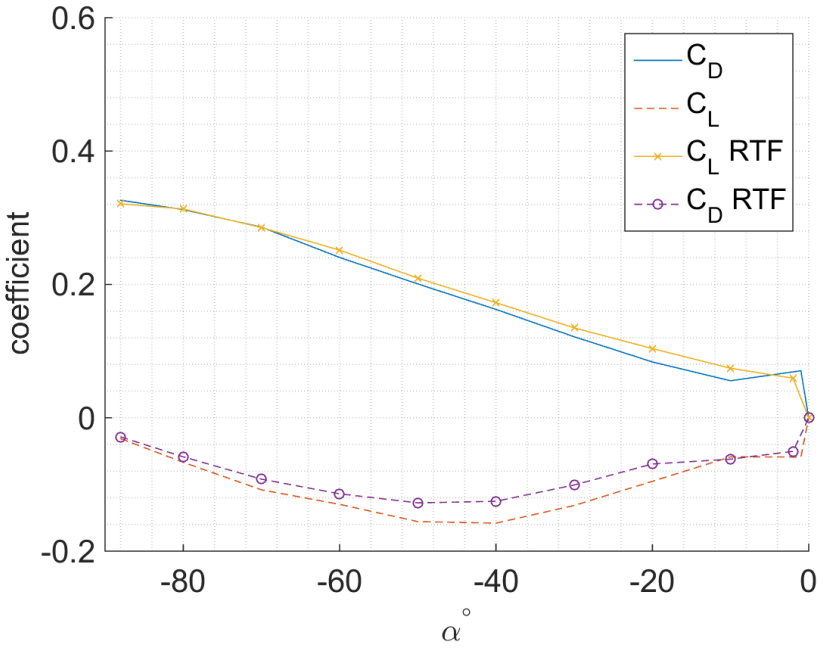

Figure 24: TBS Vendetta 250 mm *H* frame aerodynamic data, with and without motors (no propellers)

the rest of the frame behind the camera, as the camera becomes the leading edge of the vehicle, seen in Figure 23 (d). Adverse lift coefficient C_{L_α} was found to be about 30% lower on average through the α range, while C_{L_α} increased by a negligible amount, about an average of 3%. This is seen in Figure 25.

Adding an aerodynamic canopy on the 122 mm *Atom* quadrotor increased drag by an average of 10% but reduced adverse lift by an average of 24% over the AOA range. It appears that for this vehicle, the benefit isn't seen until above an AOA of -20°, below which adverse lift is increased without a canopy. After this inflection point, lift is decreased. On the 155 mm *Raiju* the benefit is less obvious; the canopy adds adverse lift at low α, although an inflection is seen at $\alpha \approx$ -35° where a small benefit is seen. C_{D_α} appears to increase at high α for this vehicle when a canopy is added. Figure 23 (b) shows the canopy for illustrative purposes; the antenna, rotors, and a camera were not added while taking these data. More data may be found in the Appendix B.2.

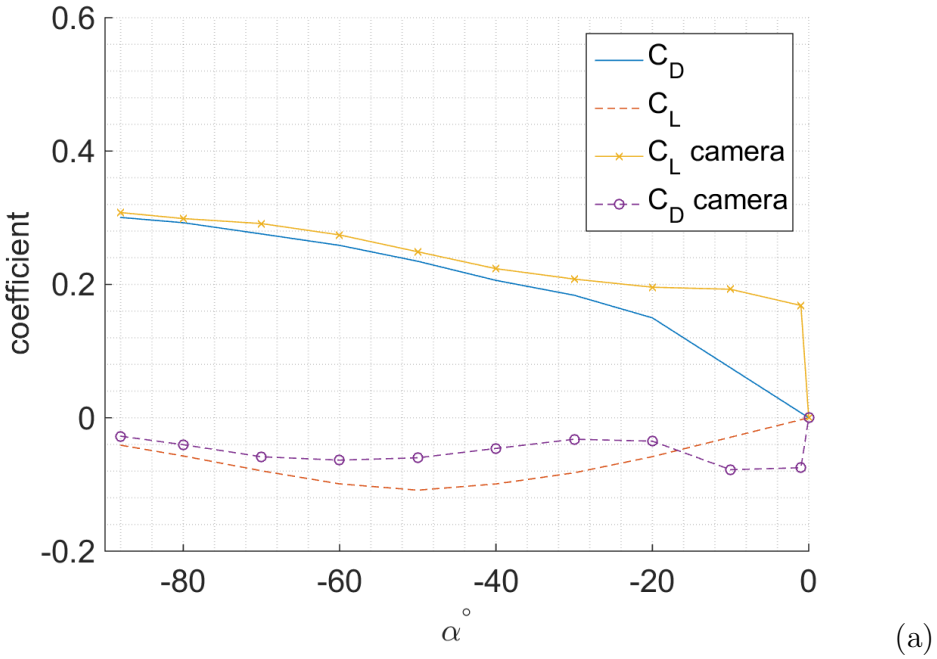

Figure 25: Hoku 230 mm X frame aerodynamic data, RTF with and without an HD camera (no propellers)

3.3.2 Sensitivity analyses

The analyzer algorithm calculates hover time sensitivities to design parameters. The sensitivities allow a user to incrementally move around the design space and evaluate the effect of the parameter shift in question on the hover time capability of the vehicle. These parameters include commonly changed ones such as motor K_v, propeller pitch and radius, GTOW, battery capacity, and hover altitude. Hover altitudes use both MSL and AGL, the latter for hover in ground effect (HIGE).

For each sensitivity, a linearisation of values, for example, dt/dK_v, are derived around the set point, where dt is the change in hover time and dK_v is the desired K_v increment. The analyzer is rerun changing K_v +/- dK_v. The two resultant values are then used to calculate a linear dt/dK_v at the set point. Of course, as the increment becomes larger, the linear assumption deteriorates, but should be sufficient for most

Table 1: Effects of temperature on Panasonic NCR18650B 3.4 Ah lithium ion cell voltage and capacity at 1C discharge

T_C (°C)	C_{max} (mAh)	$V_{c50\%}$ (V)
40	3450	3.45
25	3390	3.41
0	2950	3.30
-10	2800	3.15
-20	2190	2.95

conditions with small increments. For battery capacity and propeller radius, the algorithm will calculate additional masses resulting from adding/subtracting increments of both parameters. Sensitivity analyses for several parameters are shown below for two vehicles at the UAVRF.

3.3.3 Effects of temperature on battery performance

Battery performance is affected by the temperature in which the battery is operating. Operation in cold or hot environments drastically affect [4],[152] the performance of LiPo and LiIon batteries. Some manufacturers claim that the optimal temperature for LiPo operation is above 68-70 °F [153]. LiIon data from Panasonic describing the NCR18650B cell [134], the manufacturer of quality LiIon cells, suggests 104 °F is most ideal.

Both the capacity and voltage of the battery are reduced exponentially at different rates far away from this optimal temperature. These trends may be observed in the LiIon data sheet. The operating voltage of the battery drops according to the data seen in Table 1, derived from manufacturer data. The data show the effects of temperature on maximum capacity and voltage sag at half depth of discharge. Using simple performance degradation factor for capacity and mean voltage at half depth of discharge valid between -4 and 104 °F is created as a crude way to account for extreme temperatures. The factor used is calculated by equation 22

$$C_{max} = p_1 T_C^3 + p_2 T_C^2 + p_3 + p_4, \tag{22}$$

where temperature is measured in C. The coefficients are p_1 = 0.0071374, p_2 = -0.63861, $p_3 = 24.865$, $p_4 = 3029.2$. The factor C_{td} is then simply $C_{max}(T_C)/C_{max}(40)$.

For voltage per cell at half depth of discharge, equation 23 is used,

$$V_{c50\%} = p_1 T_C^3 + p_2 T_C^2 + p_3 + p_4, \tag{23}$$

where the coefficients are p_1 = 3.582e-06, p_2 = -2.934e-04, p_3 = 9.939e-03, p_4 = 3.292. Like capacity, the voltage degredation factor V_{td} is $V_{c50\%}(T_C)/V_{c50\%}(40)$. In addition to these effects, below around 10% discharge, the voltage sag is quite nonlinear, unlike the region between 10% and 95% at optimal temperature. The cell failure near 100% discharge is much more linear at colder temperatures. See [134].

3.3.4 Other effects

The maximum capacity of a battery diminishes with the number of charge/discharge cycles that it has undergone. For the NCR18650B LiIon cells, the effect is approximately linear for a 1C full discharge/charge cycle. After 500 cycles, C_{max} drops to about 2,200 mAh from 3,400. The corresponds to -2.4 mAh per cycle.

A ground effect correction [3], 4.1.10 is applied to all flight calculations. The power required to hover is scaled by the HIGE correction described, which is a function of the AGL altitude of the vehicle, which is assumed to be the same as separation of the propeller disc and the ground.

The BEMT model runs in two modes; one considering inflow and one without. Inflow velocity is calculated by iterative means. For general, hobby-sized vehicles in the range of 0-2 kg in hover, the flight times only vary about 1-2% between the two BEMT solutions whereas the computation time may vary up to +20% for each loop. As it is not readily clear which is more accurate considering other sources of error, it

is recommended that the inflow model not be considered for most calculations unless forward flight is required.

3.3.5 Areas for improvement

One of the greater sources of error for this methodology implementation is the propeller airfoil assumption used for cases when a specific propeller's geometry is not used. The best case is of course using the geometry of the propeller to be flown. For example, in all analyses described in this paper, the NACA 0015 airfoil is for all BEMT calculations. This airfoil, of course, is generally a poor assumption, especially for propellers with higher pitch values. This is due to the zero camber of the symmetric NACA 0015 as compared to the non-zero cambers of most propellers available in the hobby market. Bohorquez[154] shows that C_p/C_t of a propeller can vary greatly when a non-zero camber is used as opposed to when the airfoil is symmetric. This may greatly change the thrust and power calculations produced by the BEMT.

Along with the standard BEMT assumptions (e.g., independence of radial segments, steady flow, no wake expansion) which normally over predict the efficiency of propellers, other errors creep into the solution from simplifications made to the involved calculations. Blade flex is also not well modeled at this time, in any axis. Tip losses are ignored, as are flow impingement and wake interactions between rotors.

A simple electric propulsion system model has been presented. One area for improvement is in the motor model. More work needs to be done to model the RPM performance of a loaded motor, especially when B is greater than 2. Also, current limitations of motors should be parameterized to throw away impossible configurations when optimizing the drive system. Another such area is the battery model which does not include V_c sag dynamics. When a LiPo battery is stressed, the cell voltage may drop abruptly, especially under 3.5 V for the various (3S Thunderpower, Zippy, and Turnigy Nano batteries between 20-90 C) batteries used by the UAVRF.

The aerodynamics model of the propellers would benefit from knowledge of a more accurate airfoil of the propellers modeled instead of the NACA 0015 used, which is symmetric. The ground effect correction applied is only valid in a hover case and needs to be updated to include downwash from wings and forward flight effects. Tip losses are also currently not modeled.

3.3.6 Validation of analyzer algorithm

A survey was done in an attempt to validate the modules (BEMT, component parameterization functions) that are used in both the analyzer and optimizer. The survey compares reported maximum hover or flight times and those calculated by the analyzer. Table 2 shows results from vehicles that were tested. For each vehicle to be tested, the vehicle's parts characteristics must be available. All vehicles in the table have corresponding characteristics including, at a minimum, motor K_v and number of motors, propeller diameter and pitch, battery configuration and capacity, and GTOW, all available from each respective source. Of course, the nature of the survey brings with its data a certain anecdotal aspect, although with a large enough sample size, results should be valuable. Several of the vehicles surveyed are part of the UAVRF fleet and the authors have averaged endurance data from hundreds of flights. Of the vehicles surveyed, the mean absolute error between reported and analyzer-calculated flight times is 5.7%, as seen in table 2.

3.3.6.1 Deployment

As mentioned in $EXPT$ 1, the vehicle analyzer was launched in February 2015 [63]. This was in order to reach out to the multirotor user community to expand the number and types of vehicles compared in section 3.3.6. Since then to date, it has performed over 17,000 calculations from over 10,000 unique users. Unfortunately (or fortunately), only around 10 have sent feedback, and two of those have led to useful upgrades.

Table 2: Flight time calculation validation survey, multiple vehicle types and respective reported and analyzer-predicted hover endurance

Type	Vehicle	Endurance reported min	Calculated min	Δ %
QR	GTQ Mini[119]	5.5	5.8	-5.5
QR	Quadshot (hover)[120]	7	9.2	-31.4
QR	HS 250[119]	7.5	6.9	8.0
COAX	Helibaby[121]	8	7.8	2.5
QR	BlckBd QR[119]	8.5	8.4	1.2
QR	Blade Nano QX[122]	10	9.5	5.0
QR	KMEL500[123]	11	11.6	-5.5
QR	DIYD QR 1 (Gstv)[124]	12	12.1	-0.8
SMR	T-REX 600e[125]	13	12.8	1.5
OR	3DR X8[106]	15	14.9	0.7
BWB	Quadshot (cruise)[120]	15	14.9	0.7
QR	DJI Inspire[126]	15	14.8	1.3
HR	MB Hexa[119]	15.5	16.7	-7.7
QR	Hummingbird[127]	18.3	18.9	-3.3
QR	3DR Iris+[128]	19	18.2	4.2
QR	DJI Phantom 1[129]	25	25.5	-2.0
QR	DJI M600[130]	35	35.0	0.0
QR	QR 4[131]	73.5	72.3	1.6
QR	QR 3[132]	87	73.5	15.5
QR	QR 1[132]	97.1	101.7	-4.7
QR	QR 5[132]	109.7	107.5	2.0
QR	QR 2[132]	129.2	102.5	20.7
			mean err, %:	0.4
			mean abs err, %:	5.4

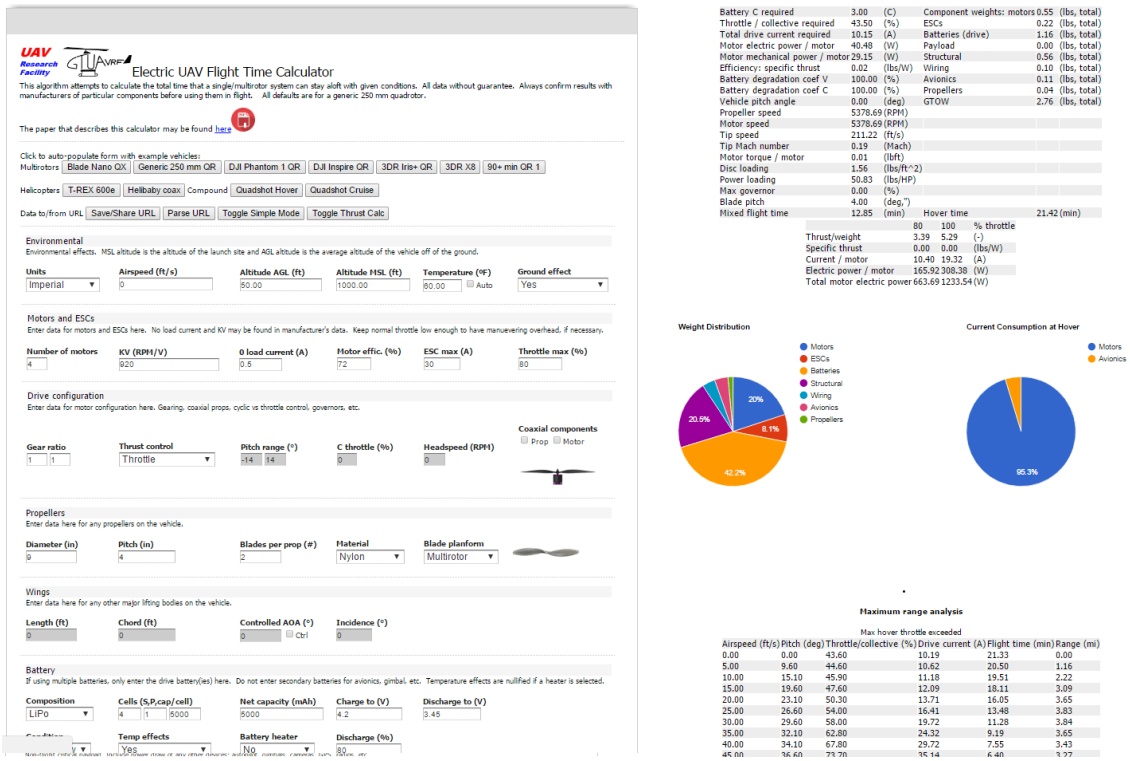

Figure 26: MST analyzer deployed on public webpage [63]

3.4 Application of the analysis and optimization algorithms

3.4.1 Case study for propulsion system optimzation: *GTQ Mini*

The optimizer and analyzer tools were used in the design of several vehicles for the UAVRF. Later sections will describe propulsion system design of a long endurance vehicle ("Eagle", section 3.4.2) and a fleet of vehicles for the MBZIRC competition in 2017. This section will focus on one vehicle in particular. The *GTQ-Mini*[113] *Frobenius* is the winner of the 2015 AHS MAV Challenge held in Virginia and is seen in Figure 27. *GTQ Mini* was built specifically for the competition by the Georgia Tech Aerial Robotics (GTAR) team. The vehicle was to maneuver in a GPS-denied environment with no external navigation aides and was to comply with a 500 g maximum GTOW. GTAR decided to employ a vision algorithm which required a heavy, i7 processor to deploy successfully. The computer used requires an average 3 A draw at around 16 V (4S). To select the drive system, the drive optimizer was used. The

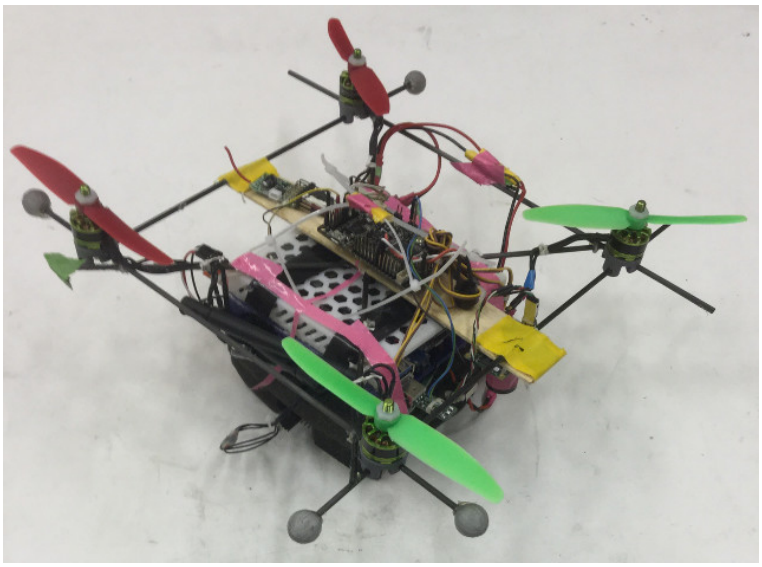

Figure 27: *GTQ Mini Frobenius* 500 g autonomous multirotor

results of the optimizer are seen in Table 3. R was constrained to 2.5 inches due to physical size limitations imposed by the competition and design. The other inputs of relevance are a 10 minute desired hover endurance and a maximum weight of 500 g.

The Multistar 1704, 1900 K_v motors fit the weight and power budget and although they do not match closely with the optimizer output, they at least come the closest of the motors which were available to GTAR at the time. In addition, the 1383 K_v motors were chosen based on a ξ of 1.3, which was deemed to be too low anyway in terms of manuevering power overhead. Note the increase in I_d when switching from 1383 to 1900 K_v. These motors were tested to ensure that they are an appropriate choice. Because the MST tool was largely untested at the time of design of this vehicle, combinations of 3S and 4S battery, 5030 (shorthand for 5 in diameter, 3 in pitch), 5030x3 (3-bladed), and 6030 propeller configurations were tested. The combination with the best balance of thrust, flight time, and motor temperature was 4S 5030 for this motor. In contrast to what is shown by Mulgaonkar[133], this vehicle draws about 65% of the total power for propulsion in hover due to the power-hungry i7 computer and small motors.

Table 3: Drive optimizer outputs for *GTQ Mini* design.

Parameter	Value
s	4
K_v, RPM/V	1383
C, mAh	936
R, in	2.5
p_p, in	3.0
Ω_{hover}, RPM	11600
I_d, A	3.52
m_t, g	496.3
m_b, g	104.7
m_m, g	116.1
m_e, g	37.9
m_p, g	11.6
m_{pay}, g	165
m_{avn}, g	20
m_w, g	13.5

Table 4 shows the analyzer outputs for the vehicle. The 850 mAh batteries keep the vehicle in the air for about 6.5 minutes and in weight for the competition, although the 1300 mAh battery used for testing keeps it in the air for about 9-10 minutes, depending on allowed level of battery discharge.

A maximum range analysis is also performed for the vehicle assuming perfect 850 mAh batteries and HOGE (hover out of ground effect), shown in Table 8. These data have not been validated in flight test. Table 4 also predicts the propeller RPM during hover to within the resolution of the tachometer used to measure the RPM during an actual flight.

As seen in Table 4, the analyzer method predicts an I_d of 4.49 A for hover. When added to the i7 I_p of about 3 A during processor-heavy calculations, the total current required to hover I_t becomes about 7.5 A. This matches well to what is observed when a current meter was used during a hover flight. Table 5 shows other compared values from the actual vehicle.

Note the algorithm's estimates for all components but payload. In this case, the

Table 4: Analyzer general system outputs for *GTQ Mini* at hover

Vehicle parameters			*Components*		
c_b	6	C	Motors	64	g
d_t at t_0	41.25	%	ESCs	62.29	g
I_d	4.49	A	Drive batteries	95.39	g
P_e / motor	17.93	W	Payload	0	g
P_m / motor	12.91	W	Structural	95.41	g
specific thrust / motor	7.01	g/W	Wiring	24.95	g
Bat temperature coef. V	100	%	Avionics	50	g
Bat temperature coef. C	100	%	Propellers	4.68	g
θ	0	$\circ$	GTOW	499	g
Propeller speed	11600	RPM		80%, 100% d_t	
Motor speed	11600	RPM	Thrust/weight	3.79, 5.92	-
Tip speed	77.13	m/s	Specific thrust	2.64, 2.83	g/W
M_{tip}	0.23	Mach	I_m	2.80, 4.09	A
Motor torque / motor	0.0035	Nm	P_m	44.73, 65.26	W
Disc loading	9.85	kg/m^2			
Power loading	28.07	kg/kW			
Max governor	0	%			
p_p	3	$\circ$,in			
Mixed flight time	4.08	min	Hover time	6.81	min

payload is the i7 computer and related avionics, which has an installed weight of about 175 g including a RAM module, USB serial devices, and WiFi module with antennae. Table 5 shows the estimates as compared to actual measured weights used on the competition vehicle. Other than that and the structural component, the predictions match closely to what is observed. The structural component is off because eq. 21 assumes that the structure will be less efficient in terms of weight than what was produced in order to be in weight for the competition.

A sensitivity analysis is also performed at the design point. These parameters are varied with all other parameters held constant. It is possible to run this with an MDO wrapper to provide an indication of where design efforts should be concentrated. Table 6 presents the inputs taken by the algorithm, whose outputs are shown in Table 7.

Table 5: Analyzer predictions from Table 4 compared to flight measurements for *GTQ Mini* in HOGE.

Parameter	Predicted	Measured
RPM	11600	11560 mean
I_t, A	7.49	7.8 mean
Motors, g	64	68
ESC, g	62.29	38
Battery, g	95.39	96
Structural, g	95.41	41
Wiring, g	24.95	20
Avionics, g	50	47
Propellers, g	4.68	6.8
Payload, g	-	175

Table 6: Calculated sensitivity analysis inputs for *GTQ Mini* at hover.

Parameter	$+/-\Delta$
K_v, RPM/V	100
Prop diameter, in	0.5
Prop pitch, in	0.5
GTOW, g	50
Capacity, mAh	100
Altitude, m	3000
TAS range, m/s	0-15.24

According to the algorithm, the vehicle, around the setpoint described, would benefit most in terms of flight endurance by increasing the battery capacity. Increasing any other value would reduce the flight time and vice versa. Although this has not been rigorously validated and is, of course, a linearization, the change of battery from 850 to 1300 mAh increases flight time by about four minutes, roughly equivalent to the algorithm's prediction of 0.84 min/100 mAh. That is,

$$(0.84\,min/100\,mAh)(1300 - 850\,mAh) = +3.78\,min\,predicted \tag{24}$$

which is approximately correlates to what is observed: approximately a four minute increase in endurance. Physically changing the other parameters has not yet been tested. Flights are terminated when any battery cell reaches 3.6 V (loaded)

Table 7: Sensitivity analysis outputs for *GTQ Mini* at hover

Sensitivity parameter	Specific sensitivity			
dt/dK_v	-0.0018	min/K_v	-0.18	min/100 K_v
dt/dD	-0.66	min/in	-0.33	min/0.5 in
dt/dP	-1.29	min/in	-0.64	min/0.5 in
dt/dm	-0.01	min/g	-0.33	min/50 g
dt/dC	0.01	min/mAh	0.84	min/100 mAh
dt/dAlt	-0.000393	min/m	-1.18	min/3000 m

to extend battery MTBF.

Table 8: Calculated maximum range analysis outputs for *GTQ Mini* at various TAS.

TAS m/s	Pitch °	d_t %	I_d A	Endurance min	Range km
0	0	39	4.24	7.18	0
1.52	9.1	40	4.37	6.99	0.64
3.05	14.6	41.3	4.58	6.7	1.22
4.57	18.6	43.4	4.97	6.22	1.7
6.1	22.1	46.2	5.54	5.63	2.06
7.62	25.6	49.7	6.28	5.01	2.29
9.14	28.1	53.4	7.12	4.46	2.45
10.67	30.6	57.7	8.13	3.94	2.52
12.19	33.1	62.7	9.22	3.5	2.56
13.72	35.1	68	10.33	3.14	2.58
15.24	37.1	73.7	11.21	2.9	2.65

3.4.2 Battery sizing case study: Eagle

The system is also used to optimize the battery configuration of a long endurance multirotor seen in Figure 28. The goal of the project is to achieve a flight time as close as possible to two and a half hours on a single charge using commercially available battery cells. The optimizer is run with several constraints. Due to cost, availability, and size considerations, power systems up to 6S, propellers up to 30 inches in diameter and 15 inch p_p, and motors 80 K_v and up were considered. These limits are placed keeping in mind that generally a larger propeller at a lower RPM will be more efficient. Battery chemistry is selected to be lithium ion for the excellent energy

Figure 28: *Eagle* long endurance multirotor with 30x10.5" propellers

density of this configuration. More advanced energy sources, such as fuel cells, are not considered due to expense and complexity, although they will allow for a greater flight endurance.

3.4.3 Optimization with MST

Given the above constraints, the optimizer methodology output is seen in tables 3.4.3 and 3.4.3. The first shows the rubber propulsion system required to accomplish the mission. It also compares the rubber optimizer data to the parameters of the built vehicle, described later. The latter shows the estimated size of each of the components and the total vehicle, and the battery mass fraction (ϕ_b, discussed below) of the configuration. Note that a higher series-cell count may yield a more efficient power system in terms of current required, however, when the system is considered as a whole with added weight of serial cells not contributing to battery capacity, may not be more efficient in terms of hover endurance. Also, to extend flight time as much as possible, or to simulate what may be ideally possible, discharge percentage d_b is set

to 100%. This practice is not generally acceptable for actual flight, as battery and/or vehicle damage will occur. Also note the even values on RPM, pitch, and diameter. These are due to the step sizes for each parameter. Decreasing the step sizes has a small effect on these values but increases computation time, so it is left as is.

Table 9: Optimizer output for rubber propulsion system requirements for 140 minute hover, $d_b = 1$.

Parameter	Value (rubber)	Value (built)
Battery configuration	6S	6S
Battery capacity	44378 mAh	40800 mAh
Propeller diameter	30”	30”
Propeller pitch	10.5”	10.5”
RPM_{hover}	1400 RPM	1390 RPM
K_v	112 RPM/V	100 RPM/V
P_{hover}	417 W @ 22.2 V	409 W @ 22.5 V

Table 10: Optimizer sizing prediction for long endurance vehicle. Rubber outputs compared to built vehicle.

Component	mass (rubber)	mass (built)
Battery	3722 g	3358 g
Motors	1076 g	1064 g
ESCs	63 g	100 g
Propellers	633 g	532 g
Wiring	262 g	54 g
Chassis	257 g	448 g
Avionics	20 g	91 g
Misc	-	44g
Total	6034 g	5691 g
Φ_b	0.62	0.61

3.4.3.1 Including Battery Dynamics

The optimizer in the method above assumes simplified battery electrodynamics; that is, that the battery is capable of holding a constant voltage (3.7 V/cell for LiPo and 3.45 for LiIon is used here, the values near half depth of discharge) throughout the flight, and can handle the discharge rate required. LiPo batteries begin to lose voltage nonlinearly below about 3.4 V/cell, where LiIon cells may be discharged to

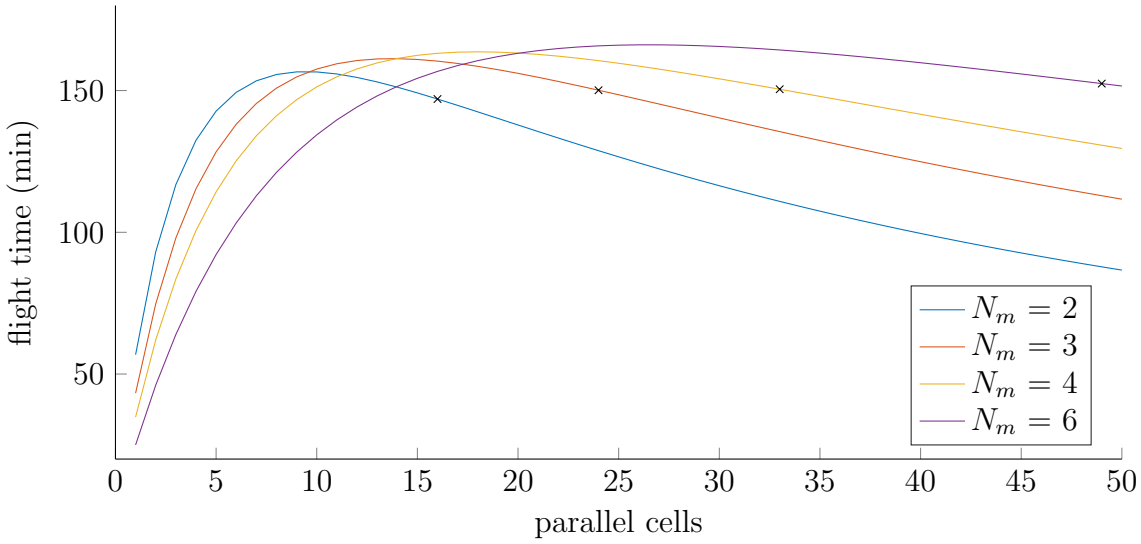

Figure 29: Battery parallel cell configuration selection at 6S with U8-16 100 K_v motor and 30x10.5 propellers. Simulated data.

around 2.7 V/cell before damage begins to set in. However, real LiPo and LiIon batteries experience voltage sag when discharged. The magnitude of sag depends on many factors including battery temperature, discharge rate, discharged amount, and discharge cycles [134]. Further modeling is described by Traub [46]. Battery data taken from Panasonic, the manufacturer of the NCR18650B cells selected to power the vehicle described here, are digitized and used to simulate the entirety of the flight. As the voltage drops throughout the flight, current increases to provide a constant power to the propulsion system. Note the sharp decline in voltage in Figure 30 near the capacity of the cells, below around 2.7 V, which for the equipment used, is 3.4 Ah at 100° F. Below this temperature, the battery dynamics change and reduce both the capacity and the ability of the battery to provide power. Also, the discharge dynamics in the area of below about 10% depth of discharge for these batteries becomes nonlinear. See section 3.3.3. Including battery dynamics has about a 5% effect on estimated flight time as opposed to the prediction when using a constant value of voltage of 3.7 V/cell for LiPo and 3.45 for the LiIon.

Looking at the various cell configurations, it is possible to optimize the parallel cell

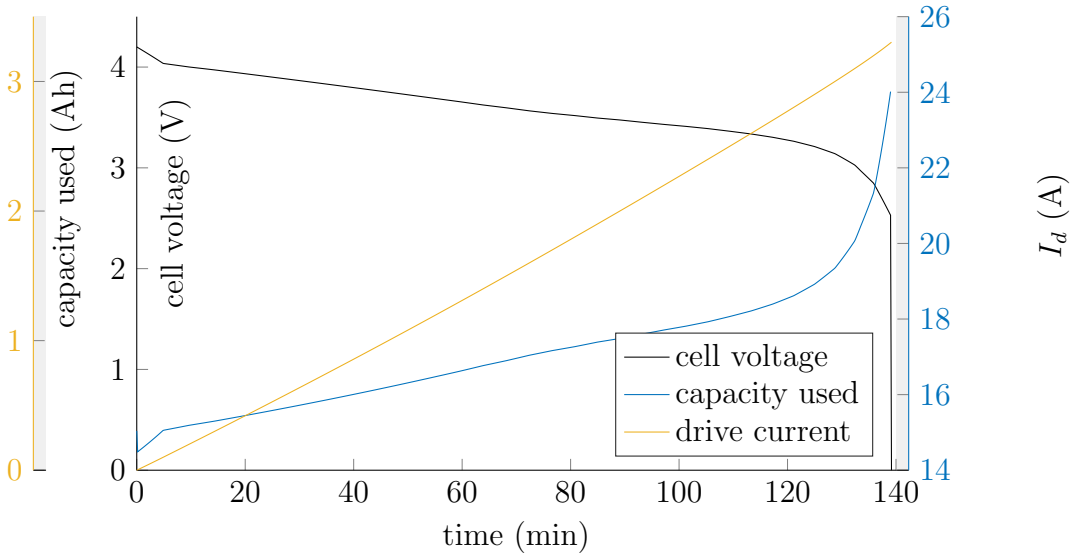

Figure 30: Simulated lithium ion discharge dynamics for a flight lasting over two hours using 6S12P Panasonic 18650B cells.

count of the battery pack. Figure 29 shows the response in simulated hover endurance to a change in number of motors N_m and the battery parallel cell configuration. Black "x" marks denote the point at which the weight of the vehicle equals or exceeds the maximum thrust available. Flight endurance estimates past those points are not feasible due to motor power constraints. Even though a birotor is more efficient, the hexarotor has the greatest flight time because it can carry more batteries. A quadrotor is chosen due to its simplicity and relatively lower cost. Note the diminishing returns when adding additional packs in parallel beyond around 12 with N_m four, seen in the figure. The configuration's number of cells in parallel is also limited by the rotor power available near the end of the flight, when the voltage sags, driving the required throttle command d_t near 100%.

Figure 30 shows simulation results of the 6S12P pack that was settled upon. The motors chosen were Tiger Motor U8-16 100 K_v with a 30x10.5 propeller from the same manufacturer. Although these motors are not, according to the manufacturer, capable of turning these large propellers, simulation and subsequent thrust stand data confirms that they are more than capable. This rotor is easily able to provide the

power required to hover. Twelve parallel 6S packs easily provide the current required to hover at a 40.8 Ah capacity, with hover power never requiring more than 0.5 C, equivalent to about 20 A. The batteries are tested up to 2 C and are found to be usable below 1.5 C. The actual built vehicle weighs around 5.7 kg. The difference is mainly from the size of the battery pack, as the optimizer wants a 6S13P configuration; other details may be seen in Table 3.4.3. The vehicle has been flown at around 5.7 kg at 920 ft AGL at 77 °F ambient temperature and power data logging shows good tracking with simulated data. Because of the performance increase of the battery pack, a warm day is ideal, even with the drop in air density.

3.4.4 Classical momentum theory method

To judge the results of the optimizer, the rubber battery mass fraction Φ_b obtained above is compared to a theoretical ideal value. It can be shown that the "optimal" Φ_b for hover is 2/3 of the GTOW of the vehicle. From momentum theory, the power required to hover can be estimated as

$$P_{R,hover} = \kappa_1 (mg)^{3/2}, \tag{25}$$

where κ_1 is $1/\sqrt{2\rho A}$, although this will not be relevant for the purposes here and hence is replaced with a constant for simplicity. The usable energy storage capacity of a battery is generally linear with mass m_b[64]

$$E_b = \kappa_2 m_b, \tag{26}$$

where κ_2 is $d_b k$; k is the battery's gravimetric energy density, and d_b is the capacity discharge fraction or depth of discharge. The latter is important when considering practical battery management, although it will not affect the ideal Φ_b. Ideal hover time may then be estimated as

$$t_{hover} = E_b / P_{R,hover} = \kappa_2 \kappa_1^{-1} g^{-3/2} m_b (m_b + m_v)^{-3/2}, \tag{27}$$

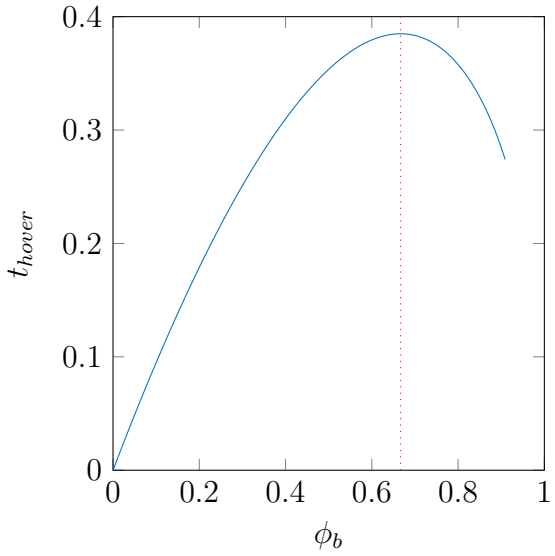

Figure 31: Battery mass fraction and effect on ideal, relative hover time. Ideal Φ_b occurs at 2/3 GTOW. This matches that for an electric fixed wing as described by [44] and eVTOL by [47]

where m_v is the GTOW sans m_b. Simplifying further and setting ψ to $\kappa_2\kappa_1^{-1}g^{-3/2}$ and differentiating, we find

$$\frac{d}{dm_b}[t_{hover}] = -\psi/2(m_b - 2m_v)(m_b + m_v)^{-5/2}, \tag{28}$$

which shows that with a maximum t_{hover} occurs when $m_b = 2m_v$, or, when m_b is 2/3 of the GTOW.

Figure 31 graphically shows the effect varying Φ_b on the relative, ideal hover time. This value obviously has several caveats, but is a good area to aim for when optimizing the hover time of a vehicle. Many times in reality, multirotor propulsion components cannot handle the elctrical and/or mechanical loads required to achieve this ideal Φ_b. For instance, if the motor is pushed to its maximum throttle (when a high thrust for a heavy vehicle or high rates is required) efficiencies may drop, or the motor may not even be able to handle the required load.

This analysis is done assuming hover conditions. A similar analysis could be performed for forward flight/climb/descent if the vehicle is to be optimized for such

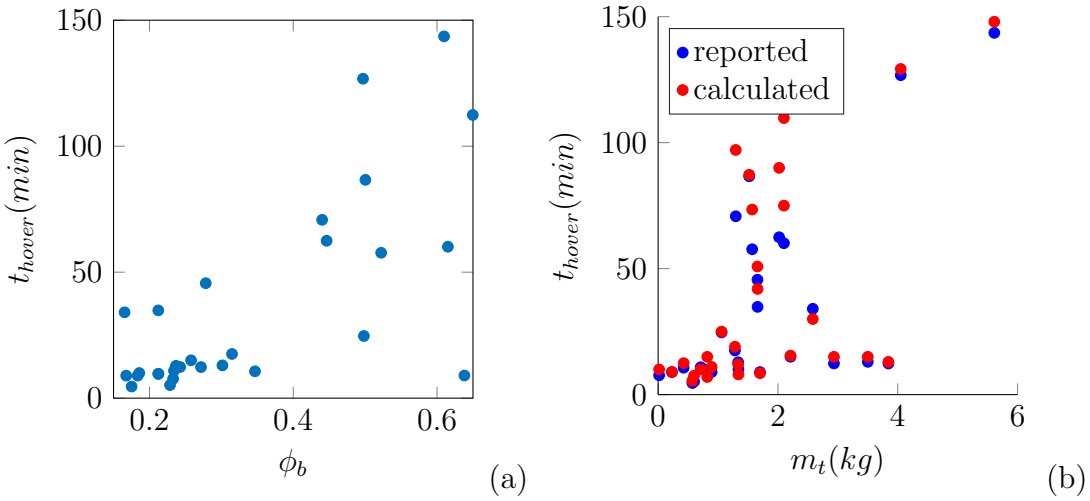

Figure 32: Approximate hover or flight endurance with battery fraction Φ_b for two dozen mainly hobby-grade, VTOL vehicles (a), (b) reported and calculated hover or flight endurance with battery fraction GTOW for two dozen mainly hobby-grade, VTOL vehicles.

a condition. Other factors that keep actual vehicles from complying to the ideal Φ_b include physical constraints, such as resolution, cost, and availability of COTS components. These factors may further drive design decisions away from the two-thirds optimum. Note that this result matches the one described by Traub [44] for electric fixed wings and is independent of battery type.

Figure 32 (a) shows the set of vehicles used for a form of validation of the algorithms described here. Again, generally vehicles with Φ_b approaching 2/3 have a longer flight endurance, but this depends on what is discussed above, i.e., the capabilities of the propulsion system and desired rates. Figure 32 (b) shows the endurance of the same set of vehicles with their GTOW, with heavier vehicles generally allowing for a higher flight endurance [135]. This effect may also be seen in Figure 29.

CHAPTER IV

SYSTEM PHYSICAL CONFIGURATION

4.1 Achievable rates with coplanar and non-coplanar rotors

This section is motivated by RQ 2, 2a: "For a multirotor, what linear and angular rates are possible in different coplanar and non-coplanar configurations?"
"What is the actuation authority of a DFC UAV?" from 2.5.2.

There are multiple vehicles designs in literature that depart from the more standard, coplanar designs as described in 2.4. These designs have multiple advantages over standard vehicles. Some allow for direct force control in > 4 DOF, sometimes in all 6 DOF. However, for the case of hover, as designs depart from the standard, coplanar configuration (where all rotors may be used fully to fight gravity), hover efficiency tends to drop as rotors are rotated away from the gravity force direction. Another advantage stems from this however: the ability to hover at non-zero ϕ and θ angles using DFC (this is discussed in greater detail in 4.1.9). While these vehicles are interesting, for the purposes of this section, more symmetric or standard designs will be studied. The ten vehicles included here are listed below, following the naming convention described in section 2.1.1.

- Quadrotors: *+4, X4*
- Hexarotors: *Y6C, Y6sC, +6, X6*
- Octarotors: *X8, X8C*
- Dodecarotors: *X12, X12C*

  These vehicles may be seen in Figures 1 and 2

The different configurations of these vehicles are commonly chosen types, as described in the naming convention section, namely $+$ and X configurations. While an *X4* and a *+4* may have similar rate capabilities, the axes in which the rates are possible are different in the two cases. For instance, a *+4* may be capable of the same roll rate that an *X4* can generate, but not in the roll axis; instead, the same rate on the *+4* may be possible around an axis between x_B and y_B, but not around x_B (like on the *X4*). These configurations are thus varied to investigate the differences in vehicle-axes aligned authority.

The other configuration variable is co-rotating vs. counter-rotating rotors when applicable. This applies to vehicles with stacked rotors, e.g., *Y6C*, *X12C*. Many coaxial vehicle designs exist. 3DR and many others use counter-rotating coaxial rotors [106]. Altus [107] a co-rotating configuration, turning to a heterogeneous coaxial configuration probably to help increase the bandwidth of the slower top rotors. There are no studies that investigate the dynamics effects (aerodynamics effects are discussed in 4.1.10) of using co- vs. counter-rotating coaxial rotors. Some of the vehicle types considered in this study have coaxial rotors and it is interesting to investigate the effect on efficiency or authority, if any, of the rotation configuration.

Many studies investigate the effects of rotor faults on multirotors, some of which are referenced in sections 2.4 and 2.3. However, it is interesting to investigate the effects of faults on actuation authority of DFC UAVs. These studies are run assuming the controller knows about the fault using a fixed control allocation. The assumption that the controller is aware of the fault is valid for several reasons. First, modern ESCs are capable of bidirectional communication with the FC. One simple method to detect a rotor fault might then be to compare the command to the measured RPM on the ESC. Some filter might be used to determine a fault based on these data. Second, estimation strategies might be used (perhaps in conjunction with the previous method) to estimate which rotors may have failed as described by Falconi

[136].

4.1.1 Authority analysis framework

To investigate the authority of these vehicles, a framework must be developed. It must be capable of predicting dynamics in response to motor commands. The dynamics developed are described below, in 4.1.2. To use these, simulation of a controller is needed to provide motor commands for generating the authority envelopes. Many studies detail various controllers for a multitude of vehicles, some of which are referenced in sections 2.4 and 2.3. This section details the controllers used for the study. The dynamics derivation is detailed in 4.1.2 and the optimization framework is described by 4.1.5.

Before considering controllers, it is important to distinguish between the ability to produce rates in pure and impure motion. In pure motion, force or torque is maximized in one direction. During this manuever (i.e., a pure roll or a pure y_B acceleration) forces and torques in all other DOFs are constrained to zero. Studying pure motion gives insight into the authority of the vehicle in more steady, non-coupled motions which may be desirable in normal operating conditions. However, highly-coupled dynamics might be desirable in specific situations, i.e., emergency manuevers which require the absolute maximum rates in a certain direction. For instance, if a critical obstacle is detected, the controller may wish to ignore coupling and apply the maximum acceleration possible in a direction as to avoid the obstacle. Investigating the force and torque authority during potentially impure or coupled motion (i.e., forces and torques are maximized in one DOF, but not necessarily constrained to zero in all other axes) gives the absolute theoretical maximum authority in a specific direction. A look at both pure and impure motion provides insight into a more entire envelope of directional authority of the UAV.

To scope this study, an in-depth investigation of controllers is not considered. Five

simple control strategies are used instead and are briefly described here. The first controller attempted (controller 1) is a simple minimization process. This controller is not capable of pure motion, and also does not provide any guarantee of optimality. First, a poor assumption is made (to control the size of the minimization search space and thereby decrease processing time) that the rotors are capable of only bang-bang control; 0 or 100% throttle. Every possible combination of unique motor commands is pre-calculated and builds an array of size $6x2^{N_m}$. The six columns are possible force and moment unit vectors. When a maneuver is requested, the manuever is converted to a unit vector, and a simple minimization is performed against the force and moment array to find the closest match. This control array is passed to the motors and then to the dynamics section to predict motion. However rapid, this controller is only used to provide part of the solution and is used to test the framework, as using this provides no guarantee of optimality or purity of motion.

The second controller uses a genetic algorithm (GA) in an effort to select all motor commands to maximize acceleration in desired direction and zero the others. While this works for quadrotors, the size of the search space grows with the number of rotors. The benefit of this controller over controller 1 is closer to a guarantee of a maximization of acceleration. However, the quick growth of the search space greatly slows the controller down, creating the need for a more rapid approach.

The third controller attempts to us a dynamics inversion approach to find motor commands. The dynamics described in section 4.1.2 are inverted to calculate motor commands based on large requested rates. This approach however is underdetermined in vehicles with more than six rotors and it is difficult to constrain rotor commands for these vehicles. Also, since this study desires to consider faults, this may change the ability of this controller to find suitable (and again, constrained) commands. A more generic controller is needed as the vehicles described here have a generic number of rotors N_m. A different controller is needed to address these

Table 11: Optimization problem for fixed-allocation controllers enforcing pure motion (a) and allowing impure motion (b) to maximize rates in 6 DOF

maximize δt	**subject to** (a)	**subject to** (b)
$\ddot{x}_I$	$\ddot{y}_I, \ddot{z}_I, \dot{\omega} = 0$	-
$\ddot{y}_I$	$\ddot{x}_I, \ddot{z}_I, \dot{\omega} = 0$	-
$\ddot{z}_I$	$\ddot{x}_I, \ddot{y}_I, \dot{\omega} = 0$	-
$\dot{p}$	$\ddot{P}_I, \dot{q}, \dot{r} = 0$	-
$\dot{q}$	$\ddot{P}_I, \dot{p}, \dot{r} = 0$	-
$\dot{r}$	$\ddot{P}_I, \dot{p}, \dot{q} = 0$	-

shortcomings.

The fourth and fifth controllers used are based on a sequential quadratic programming (SQP) approach. The MATLAB *fmincon* (from the Mathworks documentation) "function solves a quadratic programming (QP) subproblem at each iteration. *fmincon* updates an estimate of the Hessian of the Lagrangian at each iteration using the BFGS formula (see *fminunc* and references [137] and [138]). *fmincon* performs a line search using a merit function similar to that proposed by [139], [137], and [138]. The QP subproblem is solved using an active set strategy similar to that described in [140]." The ability to assert pure motion constraint is the main draw of this method, and is the difference between controllers four and five. Due to the configuration and the types of vehicles chosen, the options desired (i.e., faults and motion purity), optimization capability, and the ability for offline analysis (i.e., non-requirement of real-time processing) the SQP optimizer is finally chosen to produce motor commands for this study. Controller 5, henceforth known as "the controller", will be referred to by the remainder of this section.

The controller is run in two modes, as described above: pure and impure motion modes. The optimization formulation is seen in Table 11. When pure mode is desired, column *a* in the table applies, and column *b* applies should impure motion be desired. The controller attempts to maximize rates in all six directions, depending on the

Table 12: Array for k optimizer target maneuvers in Figure 33 to ensure positive and negative directions as well as hover are considered

x_B	y_B	z_B	ϕ	θ	ψ
1	0	0	0	0	0
0	1	0	0	0	0
0	0	0	1	0	0
0	0	0	0	1	0
0	0	0	0	0	1
-1	0	0	0	0	0
0	-1	0	0	0	0
0	0	-1	0	0	0
0	0	0	-1	0	0
0	0	0	0	-1	0
0	0	0	0	0	-1
0	0	0	0	0	0

desired maneuver.

The optimizer accepts manuevers in terms of directions to maximize. Twelve maneuvers are run, seen in Table 12. Note that maneuvers in $+z_B$ are not considered, as for the purposes of the discussion here, no rotors are pointed in that direction. In hover of course gravity provides $\ddot{z}_B$. There are studies which consider a true 6 DOF optimization some of which are described in 2.4. The final row in the Table corresponds to a hover condition. These form the k maneuvers in figure 33.

For the purposes of this investigation, the vehicles all share the same propulsion components, unless otherwise noted. The EMAX 2205 2300 K_v motor is used, powered by a 4S battery. Gemfan 5x3 propellers are simulated for all vehicles unless otherwise noted, as the propulsion calculator used here (described by 2.2 and 3.1) provides a usable match in calculated performance to what is observed in actual static tests, described in 4.1.6.1.

The size of the vehicles is chosen to be around 250-290 mm of wheelbase. This size is a commonly manufactured one and is easier to test than larger vehicles in terms of space - the smaller vehicles may be easily flown indoors with no wind. Verification flights are then easier, especially since the UAVRF has constructed several vehicles

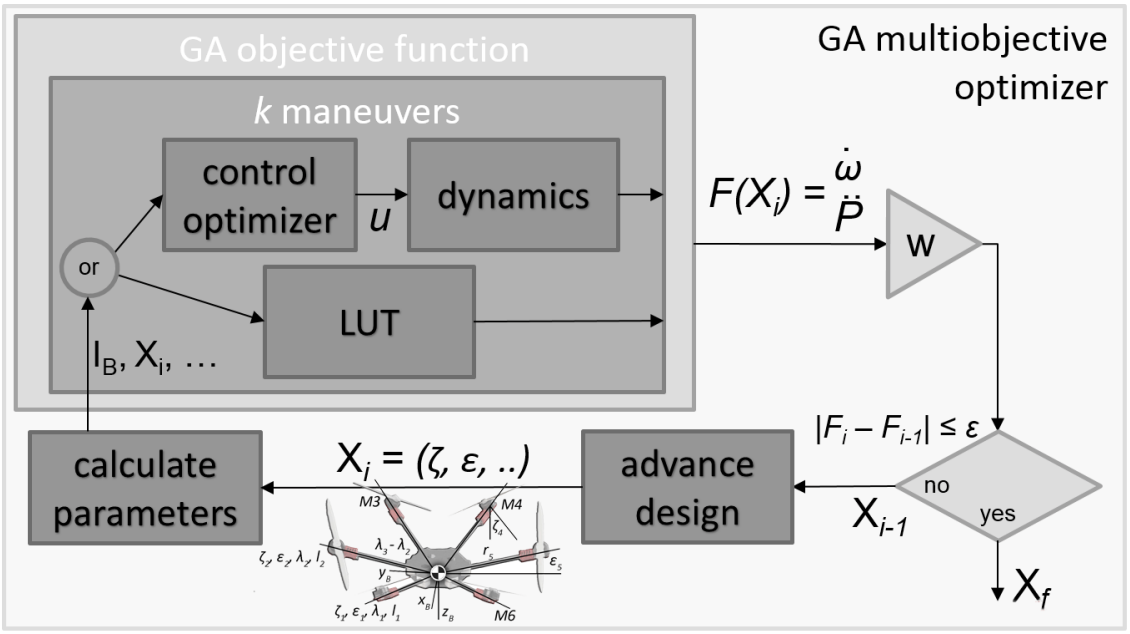

Figure 33: Optimizer overview for selecting ζ, ϵ, λ, l

of this size. For the vehicles with more rotors, the chassis grows by a linear amount to support the rotors and other equipment, described by equation 21.

4.1.2 Kinematics and dynamics modeling

Most of the simulated vehicles used in the study of this section are modeled using "hobby-grade racing" propulsion equipment. This loose category applies to relatively high-K_v motors, high-pitch propellers, light-weight frames leading to high thrust to weight ratios, at times exceeding 12:1 (see "Cobra" vehicle in section 4.1.6.3). This allows the feasible propulsion configuration design space to be pushed to a larger range than those for less capable vehicles. Unless otherwise stated, rotors are modeled using the Emax 2205 2300 K_V motor spinning a Gemfan 5x3 propeller on a 4S battery and a 290 mm wheelbase. Physical properties such as inertia and GTOW are scaled such that they are realistic - each component has it's own mass and inertia, which is used to calculate the overall vehicle properties.

4.1.3 Kinematics

The reference frames used in this study are described here. The inertial reference frame is used when denoted by a subscript I. Since most studies considered here are analyzed at steady state, the rotation of the Earth is ignored, leaving the local-level frame (NED) to be considered as inertial. The body frame is denoted by a subscript B and is fixed to the vehicle body, originating at the center of gravity (CG). A standard Cartesian reference system is used, with x_B denoting direction of the "front" of the vehicle, y_B pointing right, and z_B aligned with the down direction. See Figure 1. Each rotor has it's own reference frame as well, denoted by subscript R. Rotors are stuck to arms of variable length oriented by two angles (azimuth and dihedral), described below. To move between the reference frames, the following mappings are developed using standard direct cosine matrices (DCMs). To map between the body and inertial frames, map L_{IB} is used, following the 3,2,1 rotation sequence [155]:

$$\begin{aligned} L_{IB} &= L_z(\psi)L_y(\theta)L_x(\phi) \\ &= \begin{bmatrix} c(\psi) & -s(\psi) & 0 \\ s(\psi) & c(\psi) & 0 \\ 0 & 0 & 1 \end{bmatrix} \begin{bmatrix} c(\theta) & 0 & s(\theta) \\ 0 & 1 & 0 \\ -s(\theta) & 0 & c(\theta) \end{bmatrix} \begin{bmatrix} 1 & 0 & 0 \\ 0 & c(\phi) & -s(\phi) \\ 0 & s(\phi) & c(\phi) \end{bmatrix} \end{aligned} \tag{29}$$

where ψ is the yaw angle of the vehicle, 0 for the purposes of this study, but defined as positive nose-right around z_B. θ is the vehicle's pitch angle about the y_B axis, with positive being nose up. The roll angle ϕ is measured around x_B with positive being right side down. The terms inside are abbreviated (i.e., c$(\cdot)$ and s$(\cdot)$ are a cosine and sine operator, respectively).

The mapping between each rotor and the body frame is defined as

$$
\begin{aligned}
L_{BR_i} &= L_z(\lambda_i)L_y(\epsilon)L_x(\zeta_i) \\
&= \begin{bmatrix} c(\lambda_i) & -s(\lambda_i) & 0 \\ s(\lambda_i) & c(\lambda_i) & 0 \\ 0 & 0 & 1 \end{bmatrix} \begin{bmatrix} c(\epsilon_i) & 0 & s(\epsilon_i) \\ 0 & 1 & 0 \\ -s(\epsilon_i) & 0 & c(\epsilon_i) \end{bmatrix} \begin{bmatrix} 1 & 0 & 0 \\ 0 & c(\zeta_i) & -s(\zeta_i) \\ 0 & s(\zeta_i) & c(\zeta_i) \end{bmatrix}
\end{aligned} \tag{30}
$$

where λ_i is the azimuth angle of the arm supporting motor i, defined as positive clockwise (looking from the top toward $+z_B$. The dihedral angle of the arm is ϵ_i where positive is up (i.e., along $-z_B$). The motor tilt angle ζ_i defines the angle around the arm's axis that the motor's axle makes with the $-z_B$ axis before dihedral is applied to the arm. Thus, to rotate from the rotor frame to the inertial frame, a rotation sequence is performed as

$$
L_{IR_i} = L_{IB}L_{BR_i} \tag{31}
$$

The arms are numbered $1, 2, ...N$ starting from the x_B axis clockwise looking from the top. Rotors are labeled in the same fashion, starting with top rotors and wrapping around to bottom rotors for coaxial systems. The baseline vehicle considered by this study is a symmetric hexarotor, with 0 dihedral and 0 motor tilt, and an azimuth difference of 60 ^{o} between each arm. This is termed here as a "standard" hexarotor. For symmetric hexarotors with a one-DOF tilt (i.e., all rotors have the same tilt angle value), M1 is rotated such that it's wake points toward that of rotor six. Each rotor's tilt angle is given by equation 32.

$$
-(-1)^i\zeta \tag{32}
$$

The CG of the vehicle is found by mass-averaging the positions of each component; the motor, propeller, arm, ESC and associated wiring, as well as a battery and a center plate for mounting the arms, seen in Eq. 33.

$$[\sum_{i=1}^{N_r} r_{ri_B}(m_{mi}+m_p)+\frac{1}{2}\sum_{i=1}^{N_{arms}}(r_{ri_B}m_{ai})+m_b r_{b_B}]/m_T \tag{33}$$

Masses are calculated as described in 3.2. The ESC is mounted in the middle of the arm and the rotor is at the end of the arm. The total mass is calculated in the same fashion.

Vehicle inertia is calculated as the sum of inertias of all relevant components (i.e., propulsion components with arms and plate) are all considered in Eq. 34.

$$I_{tpi_B} = m_{pi}\begin{bmatrix} (r_{r2i_B}+r_{r3i_B})^2 & 0 & 0 \\ 0 & (r_{r1i_B}+r_{r3i_B})^2 & 0 \\ 0 & 0 & (r_{r1i_B}+r_{r2i_B})^2 \end{bmatrix} \tag{34}$$

I_{tpi_R} is the translational component of propeller i in the rotor frame.

$$I_{tmi_B} = m_{mi}\begin{bmatrix} (r_{r2i_B}+r_{r3i_B})^2 & 0 & 0 \\ 0 & (r_{r1i_B}+r_{r3i_B})^2 & 0 \\ 0 & 0 & (r_{r1i_B}+r_{r2i_B})^2 \end{bmatrix} \tag{35}$$

I_{tmi_R} is the translational component of motor i in the rotor frame.

The center section is estimated as a sphere with the mass of the battery, chassis, avionics, payload, and part of the wiring. It is centered at the origin of the coordinate system for the vehicle. With the translational component:

$$I_{c_B} = \\ 2/5 m_c \begin{bmatrix} |r_r|^2/16+(r_{2c_B}+r_{3c_B})^2 & 0 & 0 \\ 0 & |r_r|^2/16+(r_{1c_B}+r_{3c_B})^2 & 0 \\ 0 & 0 & |r_r|^2/16+(r_{1c_B}+r_{2c_B})^2 \end{bmatrix}$$

$$m_c = (m_b + f(m_s) + m_{avi} + m_p + f(m_w)) \tag{36}$$

where m_c is the mass of the central component.

The propeller is modeled as a slender plate in terms of inertia.

$$I_{p_R} = \quad m_{pi} \begin{bmatrix} 1/120 d_{pi}^2 & 0 & 0 \\ 0 & 1/120 d_{pi}^2 & 0 \\ 0 & 0 & 1/12 d_{pi}^2 \end{bmatrix} \tag{37}$$

The motor is modeled as a cylinder with a radius a fraction of r_r.

$$I_{m_R} = \quad m_{mi} \begin{bmatrix} 1/12 f(r_r)^2 & 0 & 0 \\ 0 & 1/12 f(r_r)^2 & 0 \\ 0 & 0 & 1/2 f(r_r)^2 \end{bmatrix} \tag{38}$$

The rotor inertia tensor is then a rotated sum of the applicable parts: the motor, propeller, and translational components.

$$I_{ri_B} = L_{BR_i}[I_{pi_R} + I_{mi_R}]L_{BR_i}^T + I_{tpi_B} + I_{tmi_B} \tag{39}$$

The arm inertia tensors are shown in Eq. 40, modeled as thin plates.

$$I_{ai_B} = L_{BR_i} m_{ai} \begin{bmatrix} 1/30 f(r_r)^2 & 0 & 0 \\ 0 & 1/30 f(r_r)^2 & 0 \\ 0 & 0 & 1/30 f(r_r)^2 \end{bmatrix} + I_{tmi_B} \tag{40}$$

The inertia of each rotor is defined in Eq. 41.

$$I_{i_B}^* = I_{ri_B} \tag{41}$$

Lastly, the total body inertia tensor is found in Eq. 42.

$$I_{b_B} = \quad \sum_{i=1}^{N_{arms}} I_{ai_B} + \sum_{i=1}^{N_r} I_{ri_B} + I_{cB} \tag{42}$$

4.1.4 Dynamics

The vehicles modeled here are assumed to be rigid bodies with the exception of the rotors, which are treated as rotating subsystems, denoted by a superscript $*$. Higher

order rotor dynamics (e.g., flapping) are not considered. A traditional Newton-Euler equations [155] are developed to describe the dynamic response of each vehicle in this study.

$$
\begin{aligned}
G_I &= \dot{h}_I \\
G_B &= L_{BI}\dot{h}_I \\
&= \{h_B = I_B\omega_B + h_B^*\} \\
&= \dot{h}_B + \widetilde{\omega}_B h_B + \dot{h}_B^* + \widetilde{\omega}_B h_B^* \\
&= \dot{h}_B + \widetilde{\omega}_B h_B + \sum_{i=1}^{N_r}(\dot{h}_{i_B}^* + \widetilde{\omega}_B h_{i_B}^*) \\
&= \cancelto{0}{\dot{I}_B}\omega_B + I_B\dot{\omega}_B + \widetilde{\omega}_B I_B\omega_B + \sum_{i=1}^{N_r}(\cancelto{0}{\dot{I}_{i_B}^*}\omega_{i_B}^* + I_{i_B}^*\dot{\omega}_{i_B}^* + \widetilde{\omega}_B I_{i_B}^*\omega_{i_B}^*) \\
&= M_B^t
\end{aligned}
\tag{43}
$$

In Eq. 43, $\omega_{i_B}^*$ is the angular acceleration of the rotor in response to a motor command given by the flight controller. Because this study is interested in maximum rates, the simulated flight controller may regularly command sudden 50 to 100% increases in throttle. Coupling this with high-K_V motors and light propellers, this term cannot be neglected as it may be on the order of 10,000 rad/s^2 [142].

Inertial rates $\dot{I}_B^*$ in Eq. 43 of the body are assumed to be equivalent to 0 as the vehicle is modeled as a rigid body. The same holds for the $\dot{I}_{i_B}^*$, the inertial rate of the rotor.

The total external moments M_B^t are sums of the thrust and aerodynamic moments.

$$
\begin{aligned}
M_B^t &= M_B^r + M_B^a \\
M_B^r &= \sum_{i=1}^{N_r}(L_{BR_i}[\widetilde{r}_{i_R}T_{i_R}^r + Q_{i_R}^r])
\end{aligned}
\tag{44}
$$

where M_B^r is thrust moment, which is produced by rotor thrusts acting around the vehicle's CG, M_B^a is the drag moment caused by drag forces of the vehicle rotating

through the air. The latter of these is generally 0 for the purposes of this study. The profile drag of the rotor spinning applies a counter torque $Q^r_{i_R}$ to the vehicle.

For linear equations, Eq. 45 shows the relation between mass m, inertial accelerations $\ddot{P}_I$, and external forces F^t_I.

$$\begin{aligned} F^t_I &= m\ddot{P}_I, \\ \ddot{P}_I &= F^t_I / m \end{aligned} \tag{45}$$

The sum of external forces in Eq. 46 is composed of gravity force F^g_I, aerodynamic drag F^a_I, and the sum of rotor forces F^r_I. The latter is composed of the rotated rotor thrusts of every rotor $T^r_{i_R}$.

$$\begin{aligned} F^t_I &= F^g_I + F^a_I + F^r_I \\ F^r_I &= L_{IB} \sum_{i=1}^{N_r} (L_{BR_i} T^r_{i_R}) \end{aligned} \tag{46}$$

The aerodynamic drag F^a_I is equivalent to 0 for the purposes of this section of the study as most of the simulations are run at or near hover conditions.

Rearranging and combining Eqs. 43 and 45 yields Eq. 47 for the linear and angular rates of the multirotor vehicle, i.e., $\ddot{P}_I$ and $\dot{\omega}_B$, respectively.

$$\begin{bmatrix} \dot{\omega}_B \\ \ddot{P}_I \end{bmatrix} = \begin{bmatrix} -I_B^{-1}[I_B\omega_B + \widetilde{\omega}_B I_B \omega_B + \sum_{i=1}^{N_r}(I^*_{i_B}\dot{\omega}^*_{i_B} + \widetilde{\omega}_B I^*_{i_B}\omega^*_{i_B})] \\ F_I / m \end{bmatrix} +$$

$$\begin{bmatrix} -I_B^{-1}[\widetilde{r}_{1R} L_{BR_1} K_{T_1} \hat{u_1}_R - L_{BR_1} K_{Q_1} \hat{u}_1 \ \cdots \ \widetilde{r}_{N_r R} L_{BR_{N_r}} K_{T_{N_r}} \hat{u}_{N_r R} - L_{BR_{N_r}} K_{Q_{N_r}} \hat{u}_{N_r R}] \\ m^{-1}[L_{BR_1} K_{T_1} \hat{u_1}_R \ \cdots \ L_{BR_{N_r}} K_{T_{N_r}} \hat{u_{N_r}} R] \end{bmatrix}$$

$$\cdot \begin{bmatrix} \Omega_1^2 \\ \vdots \\ \Omega^2_{N_r} \end{bmatrix} \tag{47}$$

The rotor thrust vector $\hat{u}_{iR}$ is $[0 \ 0 \ -1]'_R$ is rotated into the inertial frame. The rotor's thrust and torque coefficients K_T and K_Q are calculated by fitting the RPM

thrust curve calculated for each rotor using the techniques described by sections 2.2 and 3.1. The counter torque applied using the K_Q term is in the opposite direction of ω_i since the aerodynamically-induced rotor torque is in the opposite direction of ω_i. The simulated rotor is spun from 0 to 100% throttle, and the resulting thrust and torque are recorded used to calculate this fit. See section 4.1.6.1 for more details. This formulation allows for thrust to be calculated more quickly for repetitive function calls as compared to running the more intensive thrust calculation on every iteration. This quadratic method is common in relating rotor RPM to thrust ([77], [156], [157]). For counter-rotating coaxial rotors, K_T of all rotors on the downstream side is scaled by 0.78 and by 0.71 for co-rotating rotors. Similarly, K_Q is scaled by 1.17 for downstream co-rotating rotors and 0.89 for co-rotating rotors. These effects of course are a function of rotor-rotor separation, wake-wake interaction angle, the relative RPM of each rotor. The corrections are based on the findings described in 4.1.10. Being mindful of the large number of function calls needed in later sections, these corrections are applied in lieu of recalculating thrusts and torques based on inflow induced by the upstream rotors, which would also be a valid approach, but would increase calculation time. Note that $\dot{\omega}_{iB}^{*}$ is assumed constant in the range of 1,000 to 10,000 rad/s^2. This assumption is made as the dynamics of the rotor are several orders of magnitude faster than the dynamics of the entire vehicle; thus, the assumption is assumed valid.

4.1.5 Propulsion orientation configuration optimizer

This section describes optimization of the *X6* DFC MR's propulsion configuration. An optimizer is used for this purpose and is described here. The optimizer will design the hexarotor based on some user-defined goals. The optimization of this vehicle has multiple goals, i.e., six linear and six angular accelerations. There are six (instead of three) linear and angular accelerations because optimizing a design for positive and negative directions in the same axis will yield different solutions, unless perhaps 3D

rotors or stacked rotors as suggested by [80] are utilized. Because of the multiple optimization goals, the designer must supply some way for the optimizer to prioritize the axes. The weights W are chosen based on which rates are more desirable to the designer. One way to choose weights is to leave them all identical. This is not ideal however in this application because of the different units of the six DOFs; it is nonsensical to compare their rates directly. That is, the three linear accelerations are not directly comparable to the three angular accelerations. This will lead to the optimizer designing a vehicle that is more agile in whatever axes the scalar acceleration values are generally higher. For the small vehicles investigated here, the angular rates ($^\circ/s^2$ or rad/s^2) would generally win over the linear rates (m/s^2 or ft/s^2). It is possible to also choose weights such that, for example, the linear rates are weighted much heavier than the angular ones, or vice versa. This allows the optimizer to design a vehicle that is either very fast in linear or angular acceleration. Another way to choose weights is to normalize the rates to some limits such that the limits are the same, for example 0 to 1 non-dimensional. Yet another way is to scale the linear rates such that they are of the same order of magnitude as the angular ones. This might still be nonsensical and leads into a heuristics discussion that will be avoided here.

The optimizer is constrained to only find feasible designs. Feasibility in this context is broken down into two criteria. First, blades must not intersect when they are spinning. A 3D circle-circle intersection algorithm is used A.1. This checks for propeller strikes against other propellers only. Chassis and other components are ignored. The second feasibility check is whether or not the design may be trimmed in static hover. The vehicle should be able to hover against gravity and small disturbances, being able to produce some forces and moments in other axes. Hover and trim are defined in *RQ* $2a$ of section 2.5.2.

The overall flow of the propulsion component orientation configuration optimizer is seen in Figure 33. The SQP controller described by 4.1.1 resides in the *control*

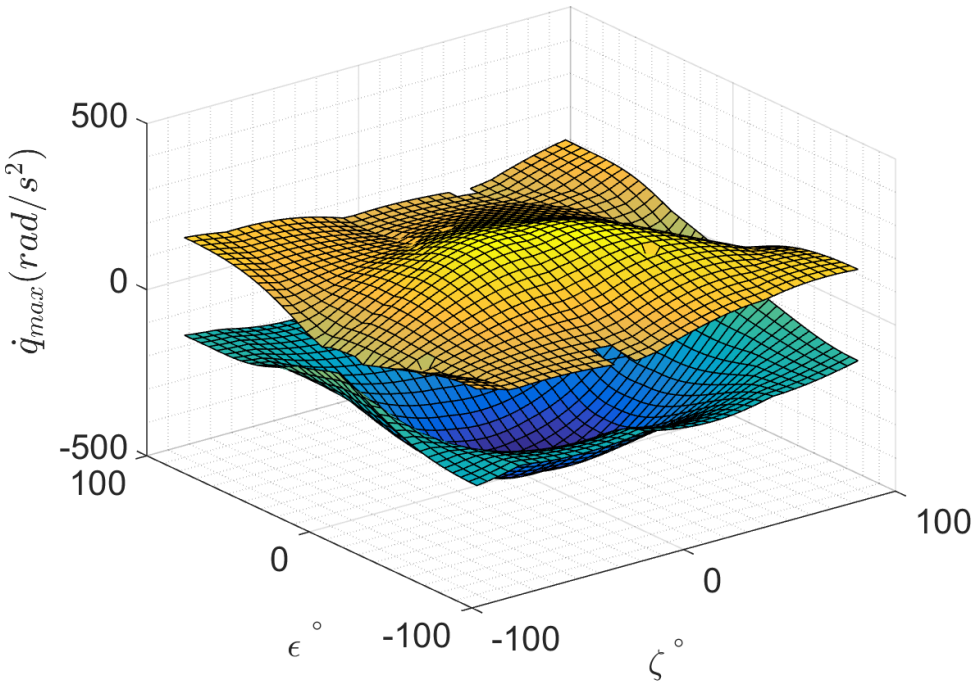

Figure 34: *X6* $\dot{q}$ design space, pure motion not enforced, M1 faulted

optimizer block. The output of the controller is a control vector $u_{1\times N_m}$, with a zero for any faulted motors. The elements for functional rotors n are Ω_n^2. These may be directly used in 47 to calculate linear and angular rates. This section alone is used to generate the LUTs referenced in the Figure. These LUTs are generated by sweeping through ζ and ϵ and constructing the standard *X6* DFC vehicle. The design variables are both swept through -90 to +90° to generate the grid of data. This vehicle design utilizes one value of ζ and ϵ as described in 2.5.2. An example LUT is seen in Figure 34, and a few others are reproduced below from the appendix.

This shows the results of the SQP controller run with the pure motion constraint for q_{max} in both positive and negative directions. Figure 35 shows the same but for the pure motion constraint relaxed. Figure 36 shows with *M1* faulted (front right).

These LUTs may be used to optimize the ζ and ϵ angles depending on what capabilities are desired. They are shown for all combinations of vehicles and parameters including results of the thrust stand data in section 4.1.10 in the appendix section C.

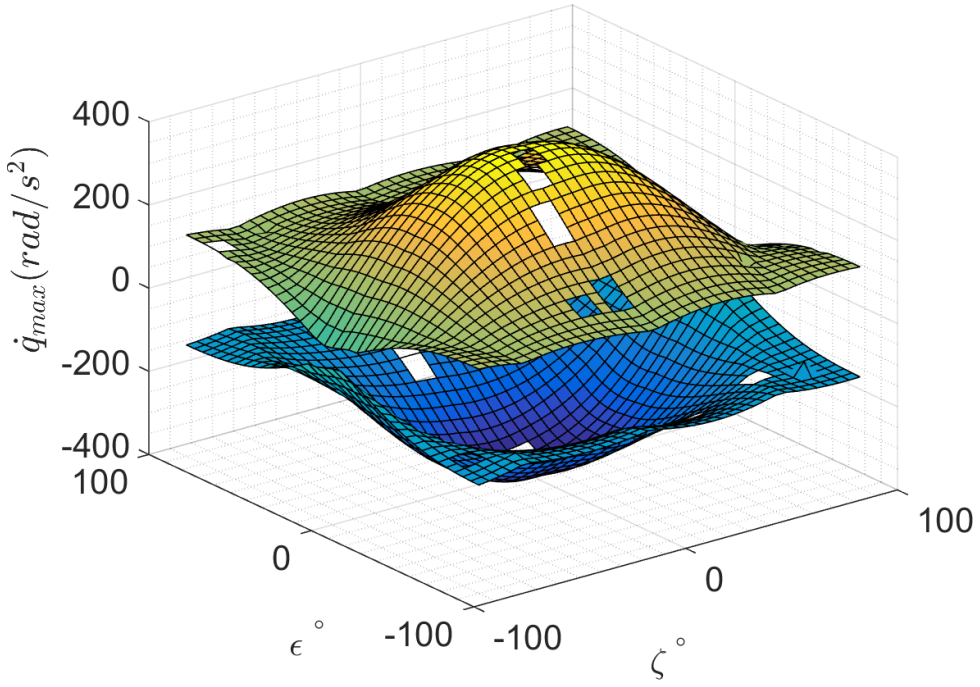

Figure 35: *X6* $\dot{q}$ design space, pure motion not enforced, no rotor faults

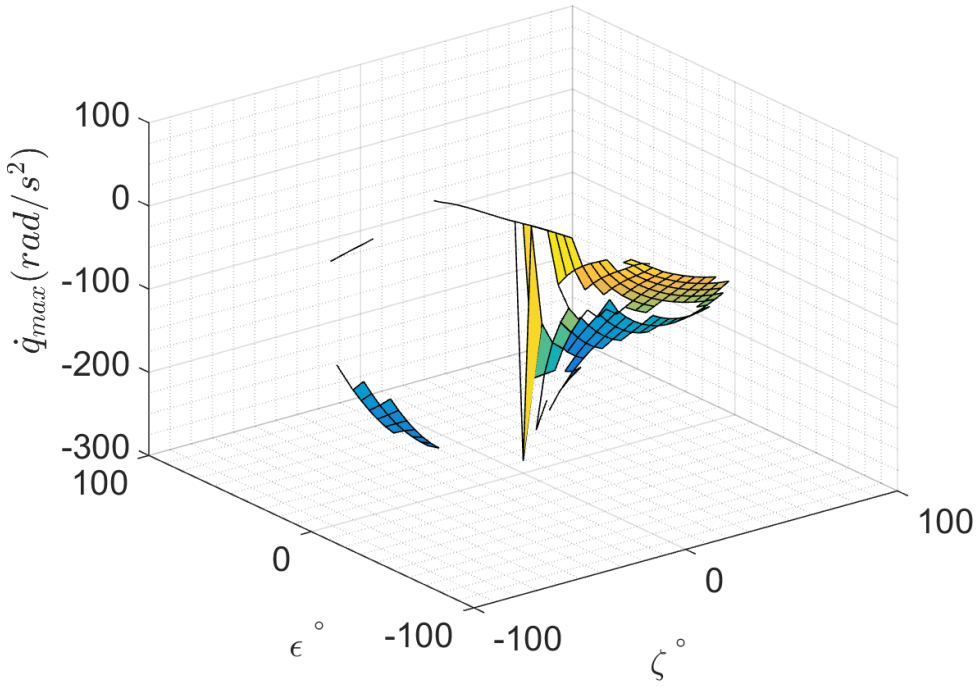

Figure 36: *X6* $\dot{q}$ design space, pure motion enforced, rotor faults: *M1*. Note loss of authority in $+\dot{q}$ direction

Table 13: Optimization *type* schedule for 1-24 DOF optimization of vehicle configuration. Each *type* has a different subset of free and number of design variables

Type	ζ (DOF)	ϵ (DOF)	λ (DOF)	l (DOF)	Σ DOF	Use LUT
1	fixed	free (1)	fixed	fixed	1	Yes
2	free (1)	fixed	fixed	fixed	1	Yes
3	fixed	fixed	fixed	free (1)	1	-
4	free (1)	free (1)	fixed	fixed	2	Yes
5	fixed	fixed	free (6)	fixed	6	-
6	fixed	free (6)	fixed	fixed	6	-
7	free (6)	fixed	fixed	fixed	6	-
8	free (6)	free (6)	fixed	fixed	12	-
9	free (6)	free (6)	fixed	free (6)	18	-
10	free (6)	free (6)	free (6)	free (6)	24	-

A higher level optimizer is then applied on top of this to further develop the framework. MATLAB's genetic algorithm (GA) based on [137] and [138] is chosen. This algorithm is chosen for several factors. First, the nature of the problem is suitable for multiobjective solver, as there are 12 rates we wish to maximize. Second, since some of the problems have a large number of DOFs and the behavior is nonlinear, a genetic algorithm is a natural choice. Matlab is chosen due to legacy, as the rest of the framework has been developed in MATLAB. This allows for easier integration of the optimizer. The GA algorithm is used because it is a multiobjective approach. Unlike single objective optimization, the GA is capable of handling multiple objectives simultaneously using Pareto optimization. In this case, the multiple objectives are the accelerations in the 6 dynamic DOF, totaling 12 since there are two directions in each of the 6 dynamics DOF.

The optimizer is run according to the schedule established in 13. The *type* indicates the index of the run class, which is defined by the DOFs allowed. The four design variables ζ (motor tilt), ϵ (arm dihedral), λ (arm azimuth), and l (arm length) as seen in Figure 37 are either fixed or free. For free variables, these are either all independent, denoted by a (6), or all dependent, denoted by a (1). For the latter, all arms/rotors have the same value of that variable. For the former, the optimizer

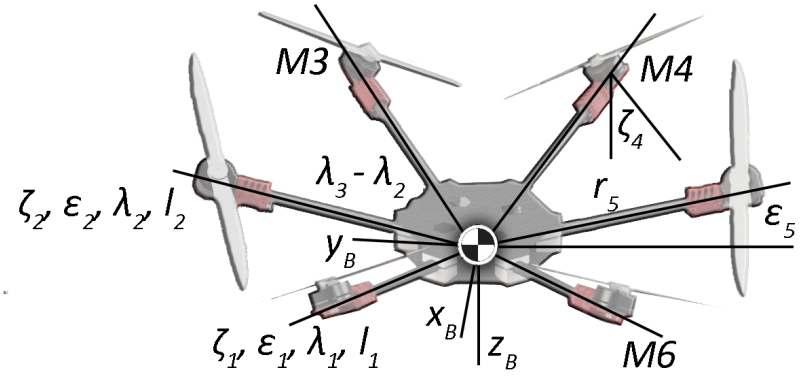

Figure 37: Design variables ζ, ϵ, λ, l shown on a DFC *X6*

Table 14: Optimization options for vehicle configuration for each *type*: each *sub-type* has axis weights and dynamics purity constraints.

sub-type	dynamics	W					
1	pure	-[1	1	1	1	1	1]
2	pure	-[100	100	100	1	1	1]
3	pure	-[1	1	1	100	100	1]
4	impure	-[1	1	1	1	1	1]
5	impure	-[100	100	100	1	1	1]
6	impure	-[1	1	1	100	100	1]
7	impure	-[100	100	1	1	1	1]
8	pure	-[100	100	1	1	1	1]
9	impure	-[30	30	1	1	1	1]

is free to choose six independent values, one for each arm/rotor. Runs 1, 2, and 4 are capable of using the LUTs generated by varying only ζ and ϵ. This dramatically speeds up the optimization process for these *types*.

In Figure 33, the overall structure of the framework is seen. With the exception of the final row for hover (which is instead used for a feasibility check), the maneuvers in 12 form the k *maneuvers* feeding the fitness or objective functions of the GA optimizer. Depending on the specific run type, either a LUT or the control optimizer and dynamics are rerun to generate the maximum rates $\dot{\omega}_{B_k}$ and $\ddot{P}_{I_k}$. Once all 11 maneuvers are run and are found to be feasible (i.e., all 12 maneuvers are possible

according to the controller and no interpropeller strikes are found), the GA advances the design using a weight array. The weight array W is applied to the rate matrix element wise as in 48.

$$f(X_i) = [W_1\dot{p}_{max}\ W_2\dot{q}_{max}\ W_3\dot{r}_{max}\ W_4\ddot{x}_{I_{max}}\ W_5\ddot{y}_{I_{max}}\ W_6\ddot{z}_{I_{max}}] \tag{48}$$

The array is negative in value as the GA is running a minimization problem. The X_i array of design variables contains the i-th iteration of some set of ζ (motor tilt), ϵ (arm dihedral), λ (arm azimuth), and l (arm length), specified by the DOFs of the optimization problem. The iteration denotes each time the design is advanced by the optimizer. When the optimizer selects a new iteration, essentially all of the parameters of the vehicle must be recalculated. These include all relevant values including inertia, and thrust and torque vectors. The feasibility checks described are run again to ensure the design is physically feasible and is capable of being trimmed.

Each *type* has an associated *sub-type*, seen in 14 which specifies the type of dynamics and W. Other options are fault(s), if any, and co- or counter rotation where applicable. These options only apply to the LUTs generated for the vehicles described in 4.1. For the portion of the study where the GA is free to design the X6 DFC vehicle, all options are employed and described in 4.3. With 10 *types* and 9 *sub-types*, 90 different runs are executed. A high performance cluster [1] is used because of the large number of options and the potentially lengthy execution time of each. The cluster is also used to generate all 60 LUT types considered here. This includes four options for 10 vehicle types described above. Interesting LUT observations are described in 4.3 and the entire set of LUTs may be found in the appendix C.

[1]The H. Milton Stewart School of Industrial & Systems Engineering Condor [141] cluster is used for all LUT generation and optimization runs.

4.1.6 Results and Validation

4.1.6.1 Rotor performance

Table 2 implies the acceptable performance of the thrust calculator used for this study. However, since only one rotor type is used for this dynamics section of the study, a more in-depth look at the performance of the calculator is feasible. This should allow for an idea of the applicability of conclusions derived here to an actual vehicle similar to the one studied. The simulated rotor used in the simulated vehicles presented here is analyzed on a thrust stand to compare thrust, RPM, and power data to what is predicted. The propeller is first compared to the study by Brandt [117] which shows static and dynamic thrust stand data for multiple propellers. One type of propeller studied there is similar to the one used in this study. Although the propeller used in their study is not identical, it is similar in geometry to the simulated one used here. The simulated propeller is run at 7000 RPM and at various advance ratios J and compared to the data measured by Brandt.

Figure 38 shows the predicted thrust, torque, and efficiency coefficients for this propeller with acceptable agreement with the predicted one, considering that the propeller is not exactly identical in geometry or composition. For a more fair comparison, and one that is more applicable to the near-zero J condition in this study, the rotor is tested on a static thrust stand. Figure 39 shows much closer agreement to the predicted data so the output of the rotor calculations are more than adequate for the purposes of this work.

The rotors used in the dynamics portion of this study employ the 5x3 propeller described above and Emax 2205 2300 K_v motors. Dynamics data have been published on these rotors [142]. From these data, the maximum rates of angular acceleration for this configuration is found to be on the order of 1,000 to 10,000 rad/s^2. The conservative former value is used for analyses described in this study. Rotor data for larger rotors, the ones used in the vehicle described in section 3.4.2, are seen in the

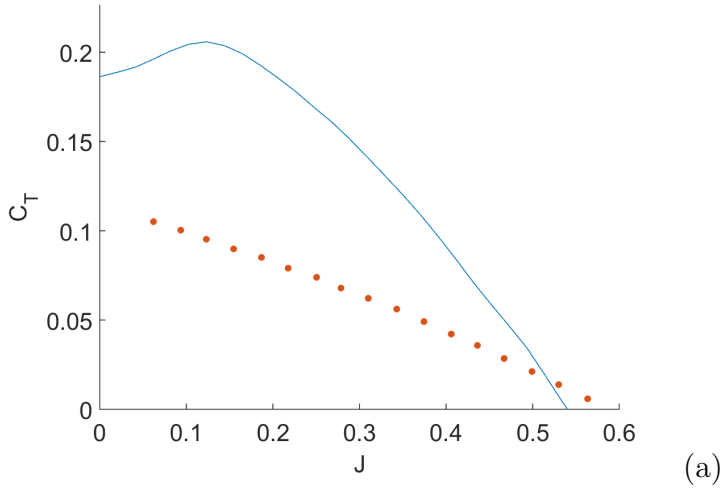

(a)

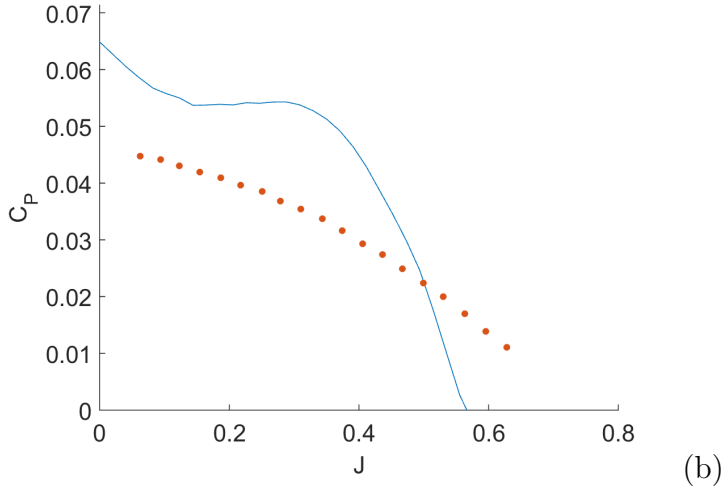

(b)

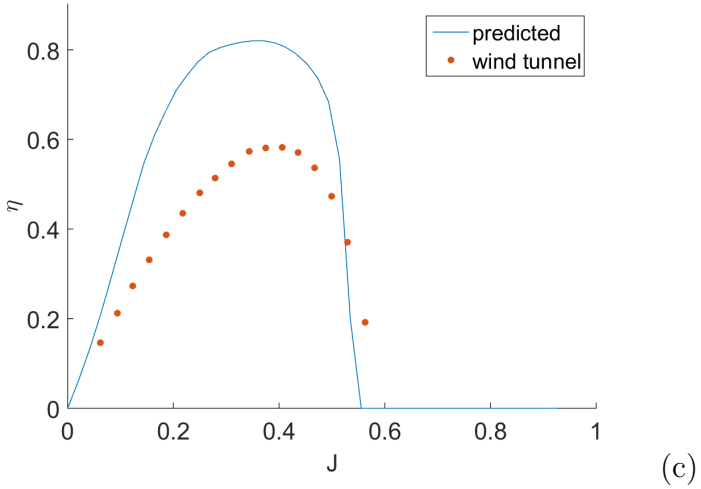

(c)

Figure 38: Simulated vs. measured static and dynamic thrust data for GWS 5x3 propeller, a) C_T, b) C_P, c) η. Differences mostly due to blade geometry. Measured data is extracted from [117]. These sized vehicles generally fly at advance ratio J of between 0 to 0.15, up to 0.34 for high performance racing multirotors using propellers of this size

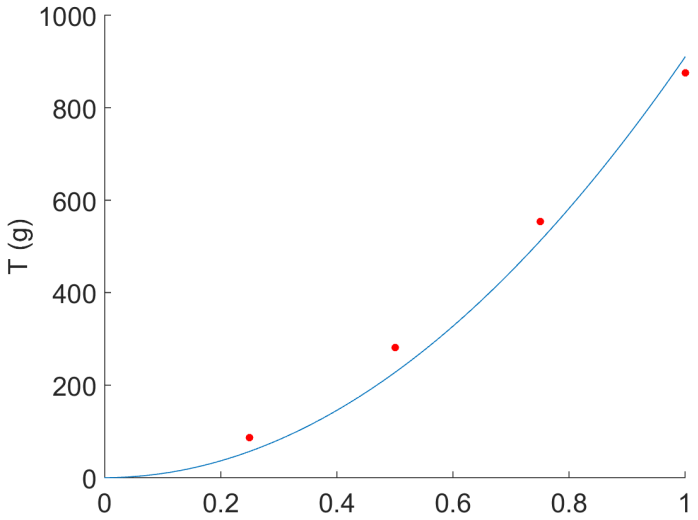

(a)

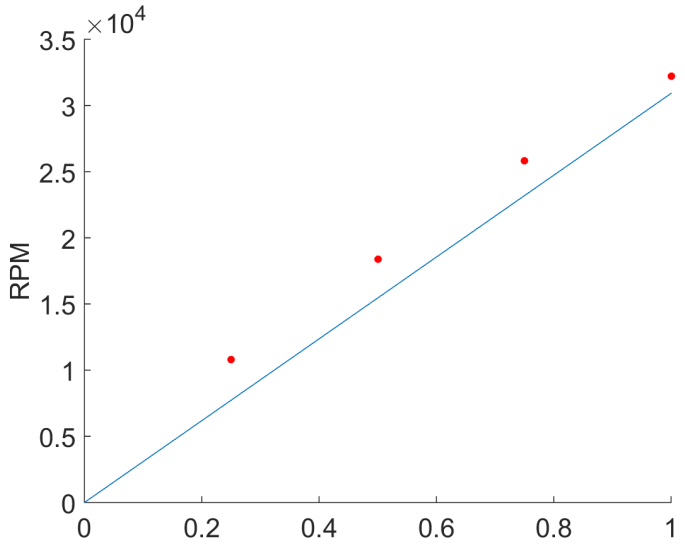

(b)

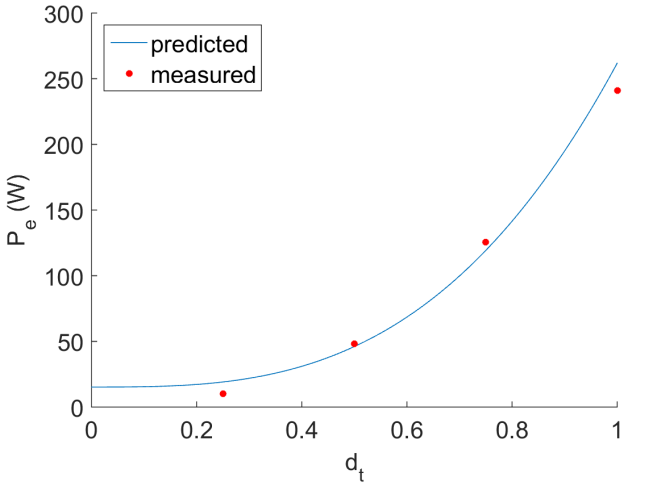

(c)

Figure 39: Predicted vs. measured static thrust data for GWS 5x3 propeller, a) T, b) RPM, c) P_e. This rotor is used for all vehicles described in this section unless otherwise noted.

Table 15: Predicted and measured inertia components of two vehicles

Frame	I_{zz} predicted (kg m^2)	I_{zz} measured (kg m^2)	Δ (%)
X4	0.0038	0.0030	26.7
X6	0.0077	0.0062	24.2

appendix section B.1.

4.1.6.2 Inertia estimation

An inertial measurement rig similar to [143] was constructed [2] to measure a single axis of the inertia tensor. This test is performed to validate the inertia calculations. As in section 4.1.6.1, because the study here is mainly interested in relative effects of propulsion configurations, the exact data is not required. However, again, it is desirable to understand the applicability of the conclusions made from the results of these calculations. Two vehicles are run through the calculator to estimate their inertia around the z_B axes. Because mounting is difficult in the other axes and only a ballpark confirmation is desired, only this axis is investigated. A 250 mm wheelbase quadrotor and a 290 mm hexarotor are both measured on the rig and compared to the predicted values, showin in 15.

Both vehicles have the same hardware and the same frame style, with the only difference being the number of arms, rotors, and chassis size. Both vehicle predictions use the process described in sec. 4.1.3 are consistently 20% higher than the measured values, but are acceptable for the purposes of this study. The simplifications made when modeling the components are likely the main cause of this discrepancy, although of course, it is possible that measurement error plays a small role in this as well.

4.1.6.3 Prediction comparisons to actual X6 DFC UAV

The predicted rates are compared to the data in the logs of two *X6* DFC vehicles. The first vehicle called "Cobra" is an X6 seen in Figure 40, and is flown to test the

[2] Thanks to Lee Whitcher for allowing me to utilize his inertia measurement rig.

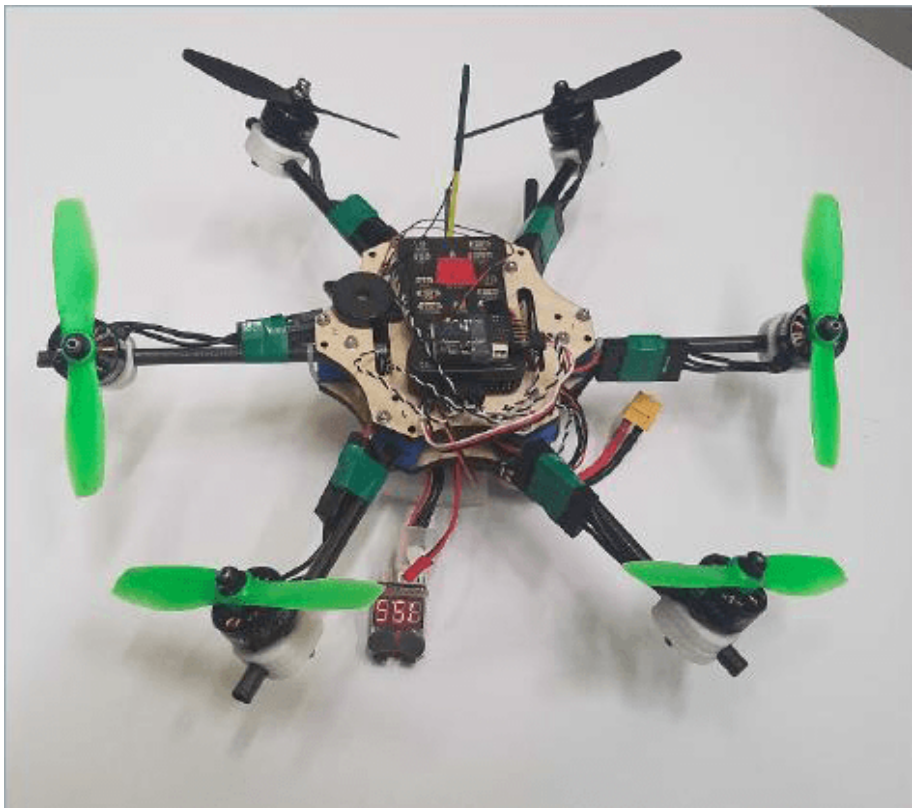

Figure 40: *Cobra* DFC *X6* multirotor, $(\zeta, \epsilon) = (30°, 0°)$

maximum attainable rates in under a custom-written DFC controller. The controller pulses the vehicle in the six desired directions, and the data are recorded in an onboard log. Both the simulated and flown vehicle are powered by six Tmotor F80 1900 K_v motors with Gemnfan 5x4.5 BN propellers. A 4S battery power the rotors angled at $\zeta = 30°$ and $\epsilon = 0°$. The predicted and logged rates are shown in 16. The $+\ddot{z_B}$ data are omitted because the value is approximately g as expected when throttle is cut.

From the logged data, it appears that the vehicle is capable of achieving just about the predicted pure rates in the linear axes, -z_B being predicted within 4%, and $+x_B$ having the largest error of about 8%. This discrepancy is due to a number of factors of varying importance. The main difference is the controller used on the flown vehicle vs. that in the optimizer described here. The motor commands are limited by the Pixhawk controller used on the flown vehicle; that is, the motor commands

Table 16: "Cobra" predicted and flight test rates. Italicized (angular) rates are not directly comparable as the controllers used are not identical. The flown controller asked for 10-20% of the available authority for the angular data: 10% in pitch, 15% in roll, 10% in yaw. Note that this roughly corresponds to the respective percentage of maximum pure rate in each direction, although this effect should not quite be linear

axis	predicted pure	impure	observed	units
$+\dot{p}$	142.2	324.5	*16.7*	rad/s^2
$+\dot{q}$	117.4	241.4	*16.3*	rad/s^2
$+\dot{r}$	86.4	174.7	*9.5*	rad/s^2
$+\ddot{x}_B$	16.1	22.6	14.8	ft/s^2
$+\ddot{y}_B$	10.2	19.5	9.9	ft/s^2
$-\dot{p}$	-142.2	-324.5	*-16.2*	rad/s^2
$-\dot{q}$	-117.4	-241.4	*-16.4*	rad/s^2
$-\dot{r}$	-86.4	-174.7	*-9.6*	rad/s^2
$-\ddot{x}_B$	-9.3	-22.6	-7.9	ft/s^2
$-\ddot{y}_B$	-10.2	-19.5	-8.5	ft/s^2
$-\ddot{z}_B$	-85.1	-85.1	-82.0	ft/s^2

Table 17: Cobra predicted and flight test motor commands

axis	SQP predicted						FC observed					
	d_{t_1}	d_{t_2}	d_{t_3}	d_{t_4}	d_{t_5}	d_{t_6}	d_{t_1}	d_{t_2}	d_{t_3}	d_{t_4}	d_{t_5}	d_{t_6}
hover	27	27	27	27	27	27	45	44	45	46	46	45
$+\dot{p}$	10	0	11	45	55	43	57	33	53	54	42	58
$+\dot{q}$	54	29	0	0	26	55	55	36	58	56	39	53
$+\dot{r}$	49	6	55	6	49	0	43	43	43	45	45	46
$+\ddot{x}_B$	0	75	7	7	75	0	14	82	15	24	84	24
$+\ddot{y}_B$	54	24	0	55	31	01	62	41	14	62	46	16
$-\dot{p}$	45	55	43	10	0	11	57	35	54	54	41	57
$-\dot{q}$	0	26	55	54	29	0	49	30	56	55	35	49
$-\dot{r}$	6	49	0	49	06	55	43	43	43	45	45	46
$-\ddot{x}_B$	43	0	39	39	0	43	53	35	60	59	41	52
$-\ddot{y}_B$	1	31	54	0	24	54	18	42	61	14	41	63
$-\ddot{z}_B$	100	100	100	100	100	100	93	77	89	89	65	93

in Table 17 aren't the same as are found by the SQP controller described in section 4.1.1. However, many of them exhibit the same behavior. The linear axes are in close agreement at least qualitatively.

In the log, the roll and pitch rates commanded are 10-20% of the maximum: 10% in pitch, 15% in roll, 10% in yaw. Note that this does not linearly scale with the actual rate achieved, but should be close. Another possibility to explain the difference is related to the logging system used. Due to the relatively slow rate of the log recording (25 Hz), the maximum accelerations are likely not recorded, as the dynamics may happen quite quickly relative to this rate. This manifests in larger errors in the angular acceleration calculations, as only raw gyro (angular velocity) data are recorded, requiring a rate calculation. Linear accelerations are recorded directly. In addition to these, since the tests are flown manually where the pilot must input commands to the vehicle, the time it takes until the command reaches 100% is non-zero. During this time, the controller may chase the command up to 100%, reducing the vehicle rate. Also, while chasing the command, a rate damper is applied to the pilot command which may further attenuate the rate. The differences in the calculated to actual inertia probably have a large role in these discrepancies as well; these would manifest in the angular discrepancies of course, causing errors on the order of 20% if the linear error holds described in 4.1.6.2. Vibrations and inaccuracies when attempting to hold hover also compound the differences between predicted and recorded values. The battery is mounted via a velcro strap. This could also move the CG closer to one side, favoring that one direction for angular rates, and worsening the other.

Secondary effects to explain differences also exist. One of these is the fact that there is a non-zero settling time to establish the flow for each rotor and it's RPM. Although this is likely a second order effect, during this time, the vehicle's body rates may effect the maximum thrust generation as now V_∞ increases for each propeller

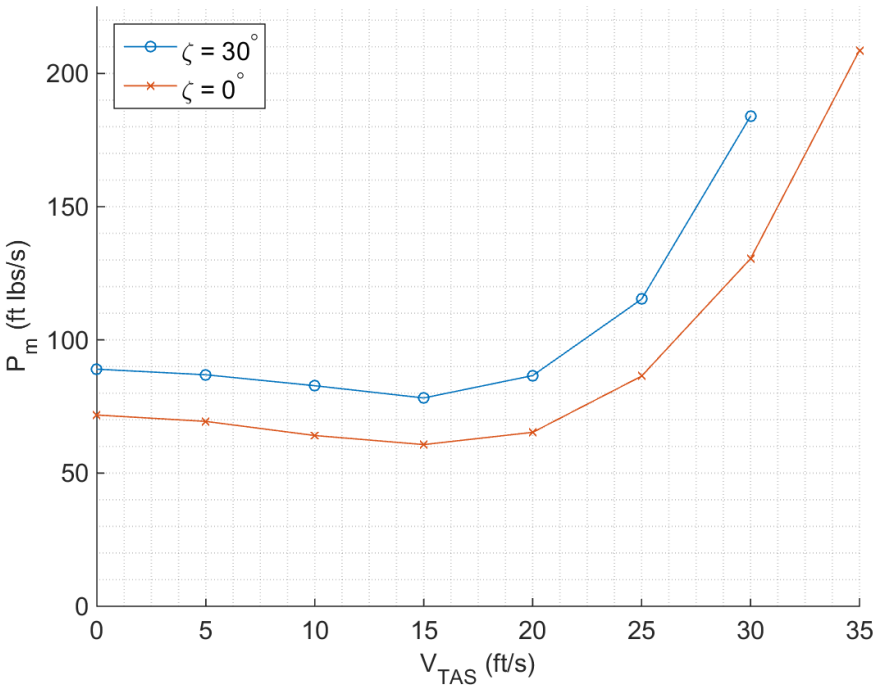

Figure 41: Simulated power required for cruise, Vulture

responsible for generating the rate. A lower actual achievable thrust will decrease the rate authority, explaining a small part of the difference seen. In the simulated data, motor saturation limits the controller in the $+x_B$ direction for pure motion, but in -x_B the highest motor command is around 75%. For $\pm y_B$, the highest motor command is about 54%.

4.1.7 Power required for DFC cruise

To study the effect of ζ on the power required to cruise of these vehicles, GUST is again used as in 3.3 to compare a flat hexarotor to one with $\zeta = 30°$. The math used by GUST is described by [13]. The simulated effect on power required is shown in Figure 41. The corresponding pitch angles are shown in Figure 42.

It is seen from Figure 41 that the simulated power required to hover is 24% higher for the $\zeta = 0°$ case than the coaxial vehicle. This difference grows to 41% at 30 ft/s. Note from Figure 42 that around 10 ft/s, the $\zeta = 30°$ vehicle must pitch in

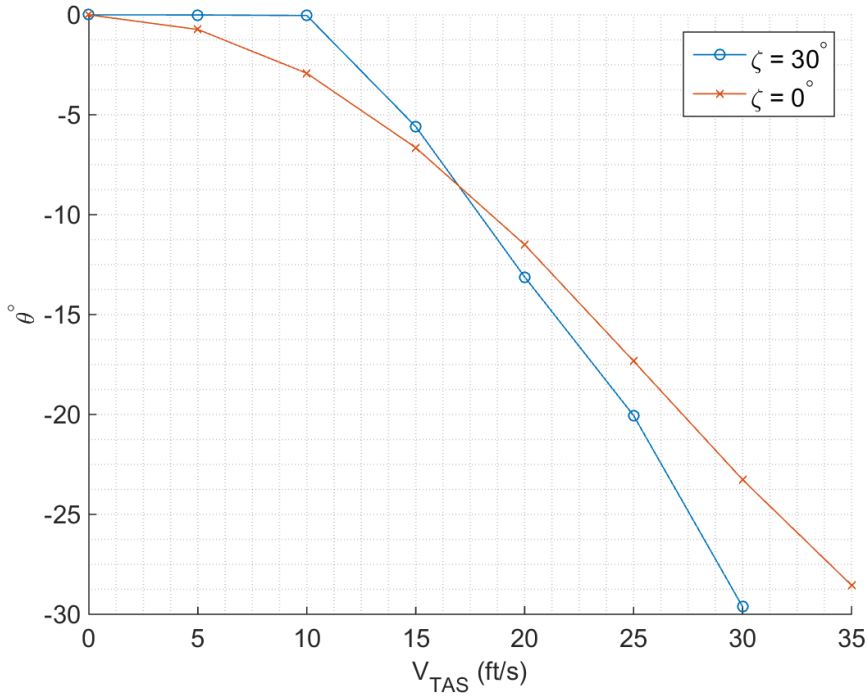

Figure 42: Simulated pitch angle required for cruise, Vulture

the direction of travel to accelerate as it runs out of DFC authority. This daisychain process is discussed further in [144].

4.1.8 Equivalent tilt of thrust vector for X6 DFC UAV

This section is motivated by RQ 3c: "Motor roll, arm dihedral for standard DFC X6 is equivalent tilting entire thrust vector X°?" from 2.5.2.

For the standard *X6* DFC UAV only one motor tilt ζ angle and one arm dihedral ϵ angle are design variables, applying these angles is equivalent to tilting the entire hover thrust vector in terms of lateral accelerations. The ratio of τ/ζ and τ/ϵ provides insight into this equivalency. The equivalent thrust tilt angles τ_x and τ_y are calculated by 49 for the two lateral directions.

$$\begin{aligned} \tau_x &= sin^{-1}(\ddot{x}_{max}/g) \\ \tau_y &= sin^{-1}(\ddot{y}_{max}/g) \end{aligned} \tag{49}$$

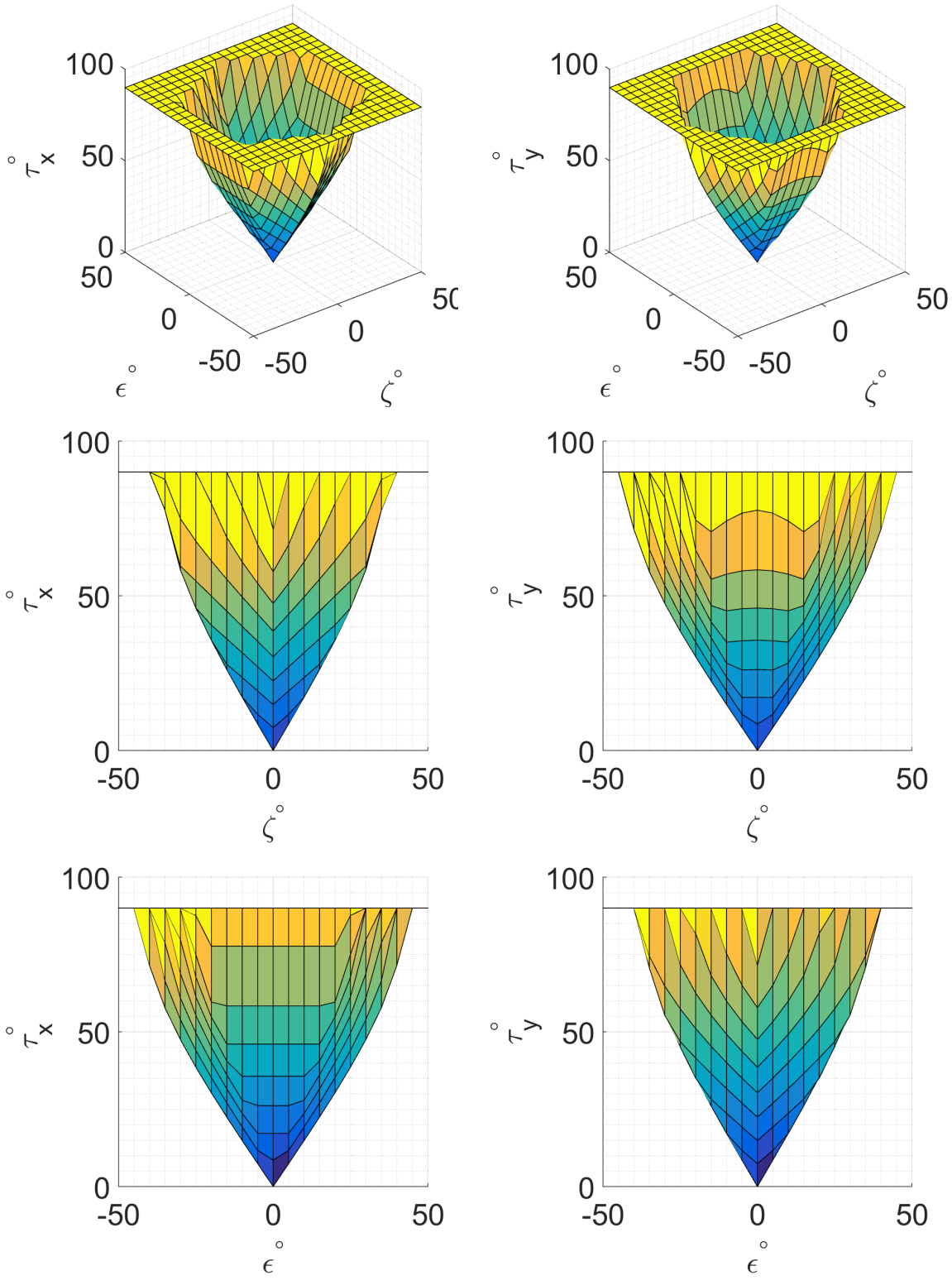

Figure 43: Actuation authority in x_B and y_B as a function of ζ and ϵ, and mapping to equivalent thrust vector tilt, at hover

It may be seen from the simulated *X6* data in Figure 43 that τ_x/ζ is around 1.7 for low angles, increasing to 2.2 near the limit. That is, the equivalent tilt of the thrust vector is nearly 2:1 for tilt in ζ. For dihedral, the ratio is smaller, with τ_x/ϵ is 1.5 for small angles, increasing to 1.8 near the limit around 45°. Thus, for a 1° change in dihedral, the acceleration achievable in the x_B axis is equivalent to having rotated the entire hover-thrust vector by about 1.5°.

Similarly, in the other axis, τ_y/ζ is about 1.7 at low angles, and increases to 2.2 near the limit. For dihedral, τ_y/ϵ is near 1.5 at small angles and grows to 1.7 near the limit at around 45°.

4.1.9 Maximum trimmed-hover attitudes

This section is motivated by RQ 3d. "What is the maximum hover pitch and roll trim angle for an X6 DFC UAV?" from 2.5.2.

To investigate the maximum trimmed-hover pitch and roll angles θ_{max} and ϕ_{max}, the system is run for X6 DFC vehicles at ζ angles between 0 and 70°. The controller attempts to trim the vehicle at each ϕ and θ angle from 0 to 90° and the maximum angle where the vehicle may be trimmed is recorded. Each vehicle's mass is also scaled corresponding to a hover fraction $m_i g/T_{max}$ from 0.1 to 1. This is done since θ_{max} and ϕ_{max} are found to be a function of the capability of the propulsion system, the mass is scaled to reveal the trends observed in Figures 44 and 45.

As expected, higher ζ angles generally allow for trimmed-hover angles further from 0°. This is of course dependent on the headroom available for the propulsion system, defined by the hover fraction $m_i g/T_{max}$. Also as expected, the higher the hover fraction (i.e., lower headroom), the less the propulsion system is capable of doing at extreme angles, lowering both θ_{max} and ϕ_{max} .

Note that positive and negative values of θ_{max} are different for the same respective

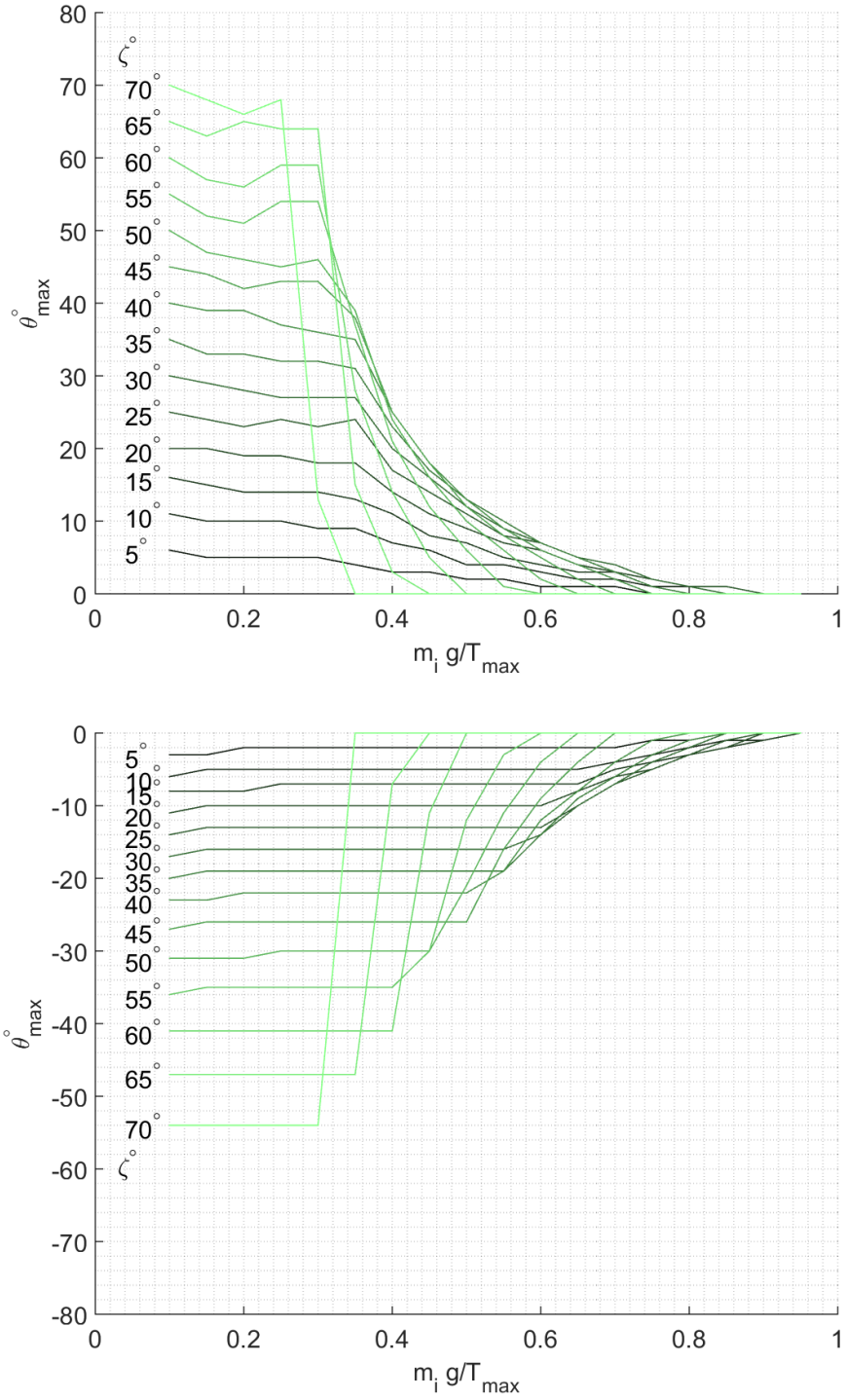

Figure 44: ζ and weight to maximum-thrust ratio effects on maximum trimmed-hover pitch angle for DFC *X6*

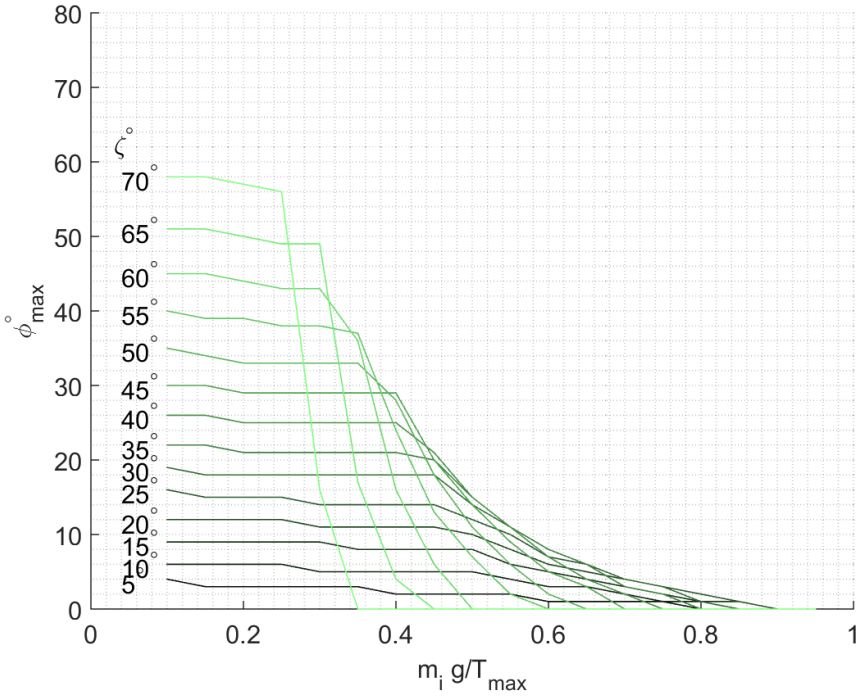

Figure 45: ζ and weight to maximum-thrust ratio effects on maximum trimmed-hover roll angle for DFC *X6*

values of ζ. This is due to the purity of motion constraint required here (for hover) and the asymmetric nature of the x_B-direction authority. The asymmetric capability is seen in Figure 203. This effect is due to the geometrical asymmetry of the vehicle about the $y_B - z_B$ plane, i.e., the configuration of rotors, and the controller used. Of course, since the figure is generated in a hover condition, the shape of these will change, but it provides an illustrative example of the asymmetry of the design. Note that if pure motion is not considered, the maximum authority in both directions of $\ddot{x}_B$ becomes identical, at least in hover, seen in Figure 199. However, this will preclude a pure hover, as producing these higher values of $\ddot{x}_B$ will produce accelerations in some or all of the other 5 DOFs. Because the vehicle is symmetric about the $x_B z_B$ plane, ϕ_{max} is identical in both the positive and negative senses.

If greater trimmed-hover in negative θ (nose-down) is desired, it may be tempting to rotate the rotors in the $-\zeta$ instead. While this is possible, this will reduce the yaw

authority of the vehicle as the rotors used for yaw will now produce counter torque in the wrong way due to their spin directions. This adverse yaw is discussed in 4.2, the effects of which are visible in Figure 203 on left side of plot at -ζ.

4.1.10 Thrust stand results

This section is motivated by RQ 2c and 2d: "Is counter-rotating or co-rotating more efficient for coaxial setups? Pusher or puller? Tip to tip distance? Wake-wake interactions?" and "What are other ways to aerodynamically increase actuation authority?" from 2.5.2.

This section details some brief results based on a thrust stand study of rotor aerodynamics. Several motor and stand orientation cases were used to analyze the relative thrust performance and efficiency these configurations: fully coaxial, semi-coaxial, co- and counter-rotating cases with differing separation distances (measured relative to the center of each propeller's hub), ground and ceiling effects on a single rotor at different clearances, and coplanar angled cases with both co- and counter-rotation at a fixed separation distance. Each trial consisted of changing the motor positioning along the bracket, starting the data acquisition, and adjusting the RPM of each rotor to 3000 after calibration. This ensured repeatability of the results and an accurate measure of thrust that would be comparable between orientations.

4.1.10.1 Thrust stand implementation

A thrust stand is designed and constructed to assist the investigation of the questions motivating this section. The thrust stand is capable of measuring thrust, independent torque, current, voltage measurements from two rotors in customizable configurations. The stand is seen in Figure 46.

Many studies [95] use an inverted pendulum thrust stand design set up for measuring, among other types, electric propulsion data for high-power applications. For lower power systems, and namely this set of experiments, an L-arm stand with mounted

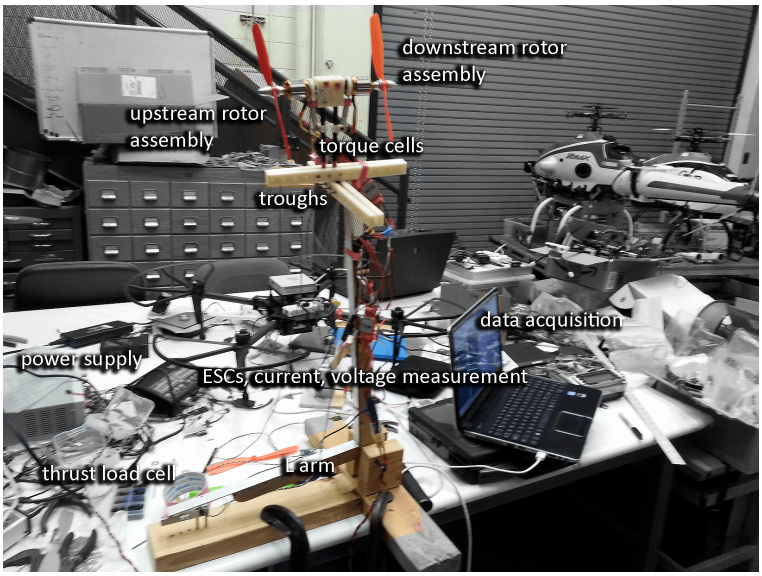

Figure 46: Adjustable thrust stand to measure thrust, independent torque, current, voltage

load cells is a sufficient design. A thrust stand such as this is useful in measuring static performance of motors in different configurations. Its size also makes the stand modifiable to run dynamic performance trials in a wind tunnel (see section 5.2). This set up is unique in its ability to read the moment, or reaction torque, applied from the motor onto the theoretical drone or UAV vehicle in response to aerodynamic blade drag torque, as well as the overall thrust. This research was aimed to quantitatively test the effect of motor orientations/conditions on overall thrust forces, torques, and resulting electrical and mechanical powers.

This system minimizes undesired ground/ceiling effects associated with more simple, low-clearance, vertically mounted stands, and allows for multiple motors in multiple coaxial, semi-coaxial, and coplanar configuration. The pivot point in the bottom of the stand largely eliminates non-axial moments, passing essentially only the moment created by thrust to the Uxcell 5 kg load cell, which measures overall thrust. Two independent load cells are mounted against two more independent motor mounts, which are free to rotate on bearings around each rotor's rotation axis. These mechanisms allow for aerodynamic torque measurement of each motor independently. Turnigy

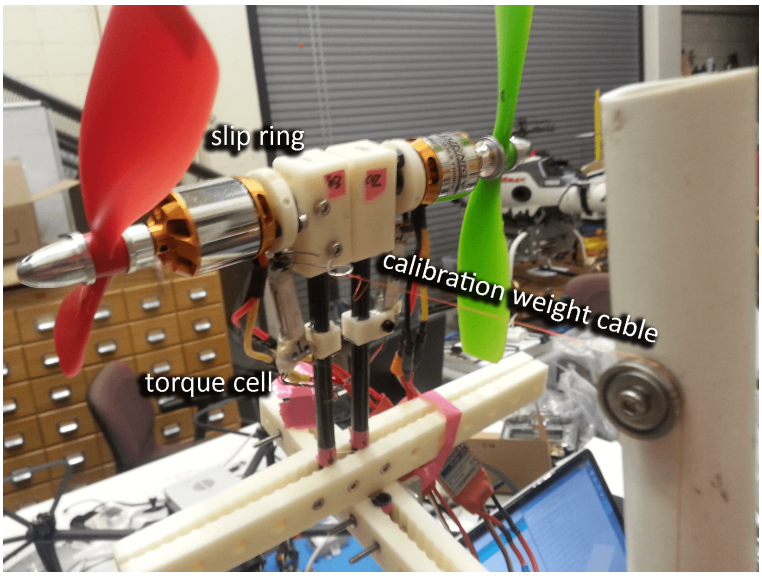

Figure 47: Thrust stand torque load cell calibration

2836\8 1100 K_v brushless motors were mounted on bearings inside a sleeve, which had protruding screws, mounted 45° from each other. For torque measurement for each motor, a Uxcell 0.1 kg load cell was centered without contact between the two screws on the rotating disc to measure torque once the motor started spinning. This allows the cell to measure torque in both directions so that the stand does not have to be physically modified once the rotor direction is inverted. Of course, the three wires hanging from the motor add a non-negligible restoring moment, so torque measurements would need to be calibrated for more accurate values of torque. However, since the motor bearing sleave is only free rotate less than 15°, this undesirable restoring moment should be small compared to the aerodynamic torque. Also, this study is more focused on relativistic effect of configuration changes. Data are compared to the database released by Brandt [117] to ensure readings are of the correct order. The rotor, arm coupler, bearing/sleeve, and carbon arm form the arm/rotor assembly.

Long, 3D-printed brackets with motor assembly troughs (seen in Figures 46 and 47) and screw holes were mounted on top of the L-arm. The whole arm/rotor assembly was then mounted through a rectangular, pressed fit bracket to a rod that could be

independently moved along the cutouts at the top of the L. Two of these assemblies were made so that coaxial and coplanar motor orientation cases could be tested. HX711AD modules were used to read the load cell voltages. Using this set up in tandem with variable brackets, each motors orientation, spin direction and attached propeller (8x4.5 GWS) could be altered independently. This was particularly useful to discern noticeable changes in performance between co-rotating and counter-rotating coaxial rotor cases in several different orientations. A 600 W bench power supply set to 12 V was connected to a parallel voltage sensor, then through two Turnigy 30 A Plush electronic speed controllers (ESCs) and a receiver. The ESCs were then each connected in series to separate in-line ACS712 current sensors, and connected to the motors. The voltage sensor, the two current sensors for motor 1 (upstream, when applicable) and motor 2 (downstream, when applicable), the torque load cells and thrust load cell were each connected to separate analog input pins in an Arduino Pro Mini board. This board was connected through the serial port to the computer, which could then calibrate and record the values for each sensor. The Parallax Data Acquisition tool (PLX-DAQ), an Microsoft Excel-based serial monitor client, was then used to open the Arduino serial stream to record sensor data.

Before testing, a known mass was affixed to a thin wire and run through a simple, smooth pulley to each load cell, seen in Figure 47. This created a moment of one of the screw pins in the rotating sleeves onto the load cell. This known mass set a baseline for the A2D gains set to calculate forces and torques. Biases were then set in the Arduino software to account for inaccuracies in the raw data from the load cells. For the thrust cell, the mass was simply placed on top of it to simulate pressure from the L-arm. These values were calibrated for any differences in moment arms in all three cells. The load cell values are tared before each run with any configuration changes.

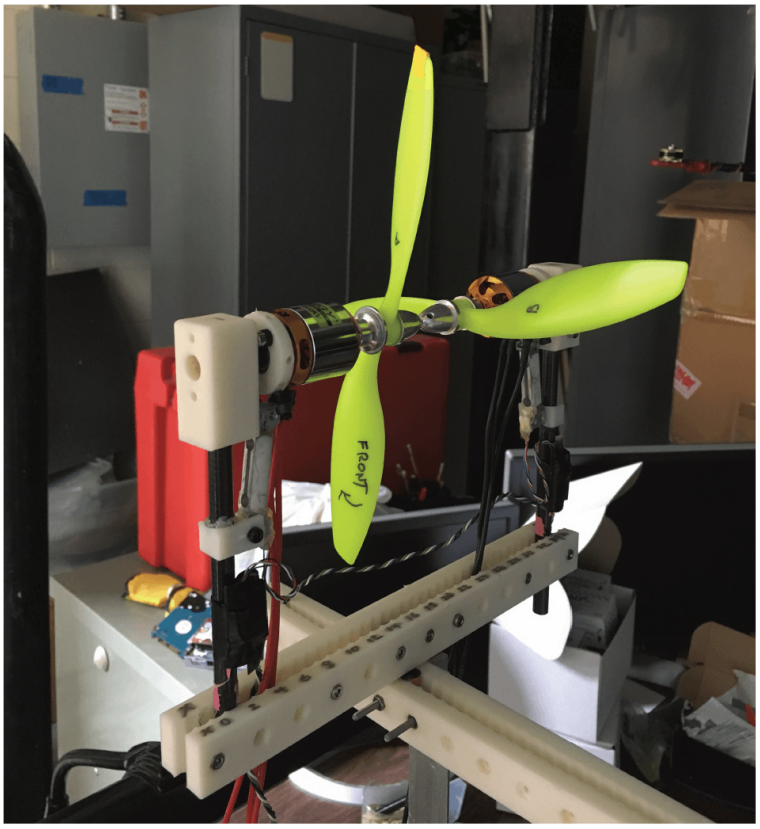

Figure 48: Thrust stand configuration for coaxial rotors

4.1.10.2 Coaxial and semi-coaxial rotors

As described in many parts of the document, the coaxial configuration is commonly used in multirotor design. This has inspired a closer investigation into coaxial rotors at this scale. Two rotors are mounted on an adjustable bracket as seen in fig 48.

While coaxial, the motors had varying separation distances from 1.8 inches to 13.6" hub to hub, corresponding to diameter-nondimensionalized values s_D of 0.23 to 1.7. The data recorded are seen in Figure 49.

Since the wake of the upstream rotor contracts, as described by momentum theory, it effects less area of the downstream rotor. This might reduce the interference power loss. However, the freestream velocity ingested by the downstream rotor also increases, which also has the effect of increasing torque on the downstream rotor.

An average thrust of 76.4 g (co-rotating) and 81.7 g (counter-rotating) was found

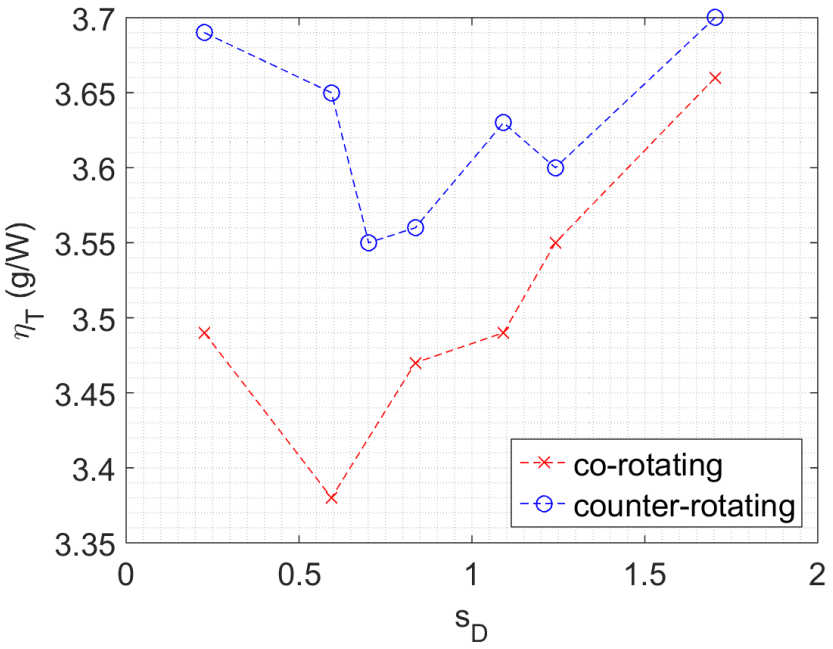

Figure 49: Co- vs. counter-rotating coaxial rotors at different hub-hub separations

for these test conditions (i.e., 12 V and 3000 RPM for both motors 1 and 2), indicating the counter-rotating configuration suffers less thrust loss than the co-rotating configuration when coaxially mounted (as compared to two independently mounted rotors). The counter-rotating configuration appears to be more efficient for essentially all values of s_D; this counter-rotating coaxial configuration was found to be from about 1 to 6% more efficient. When stacking rotors in this configuration, almost no difference was seen in the upstream rotor's mechanical or electrical power, confirming the results found in [98]. A side benefit of the counter-rotating coaxial case is the reduction of high-speed retreating blade stall as compared to the co-rotating case due to the increase in tangential velocity seen by the downstream propeller. In the co-rotating case, aerodynamic steady state torque of the downstream rotor increased by up to 25%. A noticeable amount of additional vibration was observed in the co-rotating case, indicating high levels of turbulence.

The configuration where rotors are mounted in a semi-coaxially as is inspired by

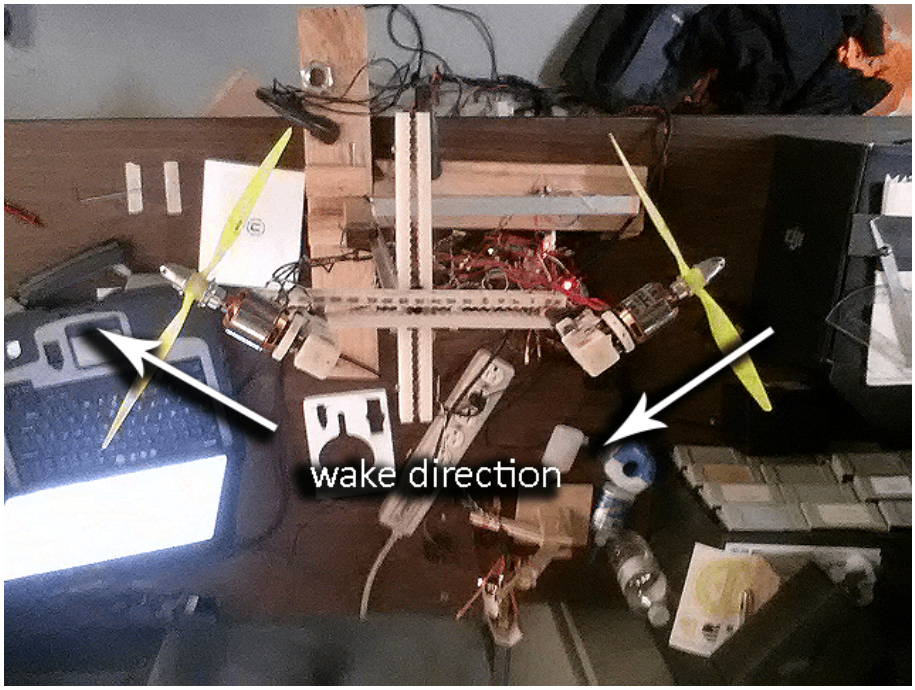

Figure 50: Semi-coaxial configuration on thrust stand. Both rotors spin such that the wake airflow is aimed generally to the left, producing thrust generally to the right.

the *Y6sC* described in 4.2.2. The thrust stand setup configuration is showin in 50.

It is seen from Figure 51 that near $\zeta = 30°$, thrust achieved is nearly that which is expected at that rotor geometry. The geometric, expected thrust is the thrust that would be expected in the $-z_B$ axis (as if these are mounted on a multirotor arm) ignoring aerodynamics interactions between the two rotors. That is, The base value of the geometric thrust at $\zeta = 0°$ is the sum of the upstream rotor's thrust when the downstream rotor is off, and vise versa.

This geometric expected thrust in the equivalent of $-z_B$ ignoring wake effects is equivalent to what is observed near $\zeta = 30°$ and beyond on the thrust stand. This is indicates that the wake of the upstream rotor is no longer affecting the downstream rotor. Note from the figure that as ζ increases (i.e., the rotors become less coaxial), efficiency in thrust in $-z_B$ increases. This must be a function of the specific rotors and their RPM but these data serve to illustrate the point that semi-coaxial rotors *still* outperform coaxial ones in thrust in $-z_B$, even though they are rotated away

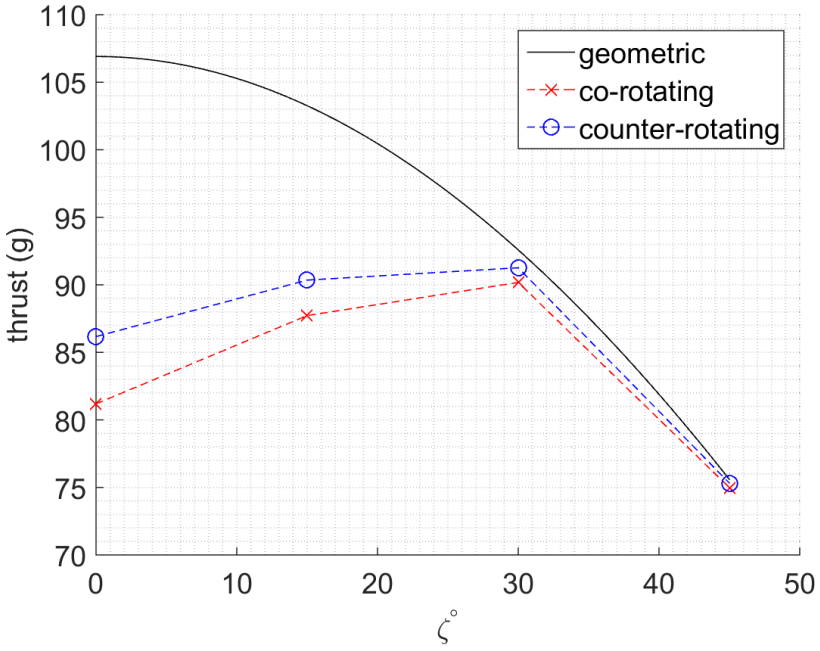

Figure 51: Semi-coaxial configuration (see Figure 2(j)) expected thrust in response to geometric angle compared to measured thrust including inter-rotor aerodynamics. Semi-coaxial configuration at 30° produces more thrust than the coaxial configuration at 0°

from the $-z_B$ axis, which serves to geometrically decrease thrust in that direction. As in the coaxial trials, the counter-rotating configuration appears to be more efficient. This is also seen in the figure at $\zeta = 0°$.

Note the 19% loss in thrust at $\zeta = 0°$ (coaxial) configuration for counter-rotating rotors and the 24% loss for co-rotating rotors. The difference between the two disappears as the upstream wake rotates away from the downstream rotor.

4.1.10.3 Tractor vs. pusher

There are studies [165], [158] for fixed wing vehicles regarding efficiency of the tractor vs. pusher rotor configuration. It is found by these studies that the tractor configuration is more efficient for the vehicles studied. However, these results may not directly apply to multirotors since wing and body downwash on fixed wings in forward flight will affect these results. While multirotors may experience similar effects in cruise,

Table 18: Static tractor vs. pusher rotor configuration efficiency

tractor, (g/W)	pusher, (g/W)
4.12	4.42

hover studies for these effects on these vehicles are lacking. The tractor (or puller) vs. pusher effect trials are an attempt to give evidence to whether motor positioning on the top or bottom of a multirotor's arm is more efficient.

The results are shown in Table 18 for the same rotor described above (3000 RPM 8x4.5 GWS propeller) mounted as shown in Figure 47. The 7% increase in efficiency in the pusher configuration suggests that it may be preferable to mount rotors under the arm, should the design spend a large percentage of its time in hover. This may change of course should the multirotor enter cruise, as the arm upstream of the rotor may cause turbulence or shadow the downstream rotor from the flow. This should be investigated in a wind tunnel. One downside to the pusher configuration on multirotors is the increased need to ensure rotor clearance from the ground and other obstacles. This is sometimes done with taller landing gear.

4.1.10.4 Wake-wake interaction

The thrust stand in this scenario is configured to with two rotors angled by ζ away from each other to simulate the configurations described in other sections, seen in Figure 52. From [98] it is claimed that coplanar separation distances has little effect on thrust values. It is apparent that counter-rotating rotors may be moved as close together as possible without diminishing the amount of thrust, in order to conserve physical space. Therefore, in the angled trials, it was decided that separation between the rotors was of lower priority than angle change or rotational direction. As in the coaxial case, counter-rotation appears to remain more efficient than the co-rotating case in each angled run.

An interesting effect was observed when analysing the data produced by this

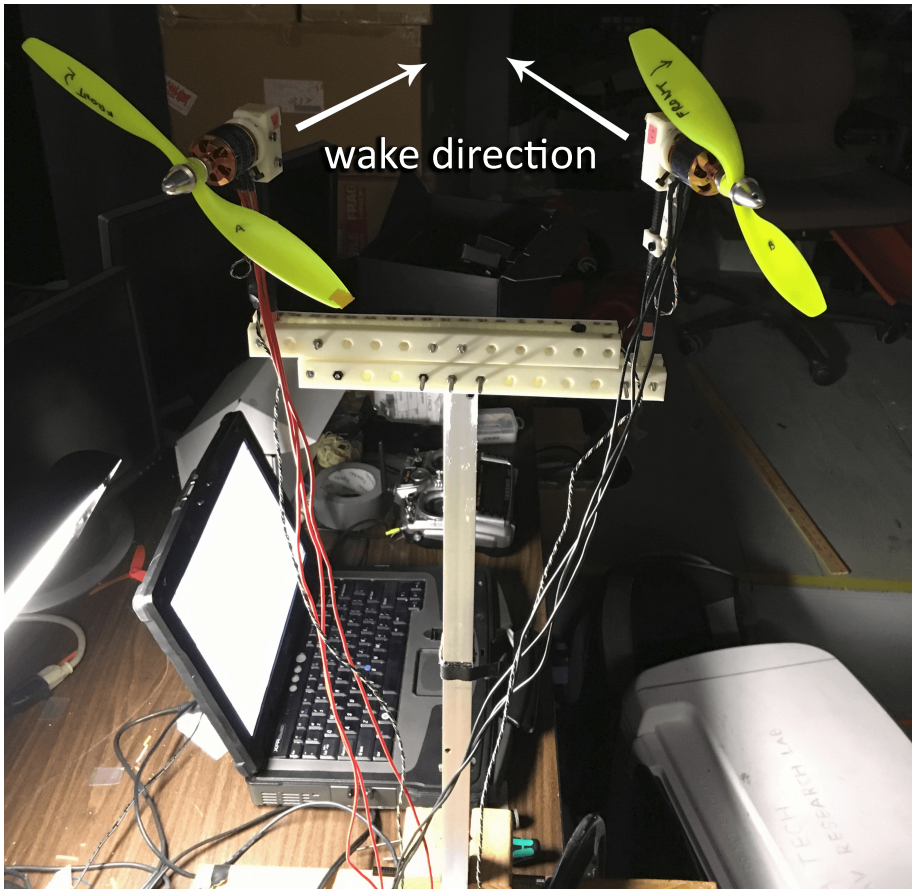

Figure 52: Thrust stand configuration to measure wake-wake interaction at 30° with co-rotating rotors

Table 19: Wake-wake interaction configuration; predicted geometric thrust ignoring aerodynamics compared to measured thrust

Configuration	ζ°	$T_{expected}$ (g)	$T_{measured}$ (g)	Δ (%)
Co-rotating	0	103.5	103.5	0.0
	15	100.0	98.7	-1.3
	30	89.6	88.4	-1.4
	45	73.2	73.0	-0.2
	60	51.8	49.8	-3.8
Counter-rotating	0	98.6	98.6	0.0
	15	95.2	98.2	3.0
	30	85.4	88.4	3.5
	45	69.7	74.0	6.2
	60	49.3	56.3	14.2

experiment, seen in Table 19. The measured decrease of thrust in the equivalent -z_B direction (the bisector of the two rotor axes pointing along the thrust vector) is compared to what is expected ignoring any aerodynamics effects. The baseline values of co- and counter-rotating thrust at $\zeta = 0^\circ$ are found and used to calculate the expected thrust column by simply considering the thrust in the z_B direction in response to the thrust vectoring.

As expected, thrust loss increases with ζ at a predictable rate for the co-rotating configuration. The predictions are within about 4% of the observations. Interestingly, thrust does not fall off in the same way in the counter-rotating case. This indicates that one of the main drawbacks of applying ζ, the geometric loss of thrust, is less than expected, with a 14% advantage over the predicted value at $\zeta = 60^\circ$.

4.1.10.5 Ground and ceiling effects

Figure 53 shows the effect of both ground and ceiling effect on a pusher and tractor, respectively.

In ground effect tests, no discernible electrical thrust efficiency differences were observed from the control value of a single rotor unaffected, to a ground separation of about 8 ” from the rotor hub. Here from the 6 ” separation to 1.5 ”, the thrust values

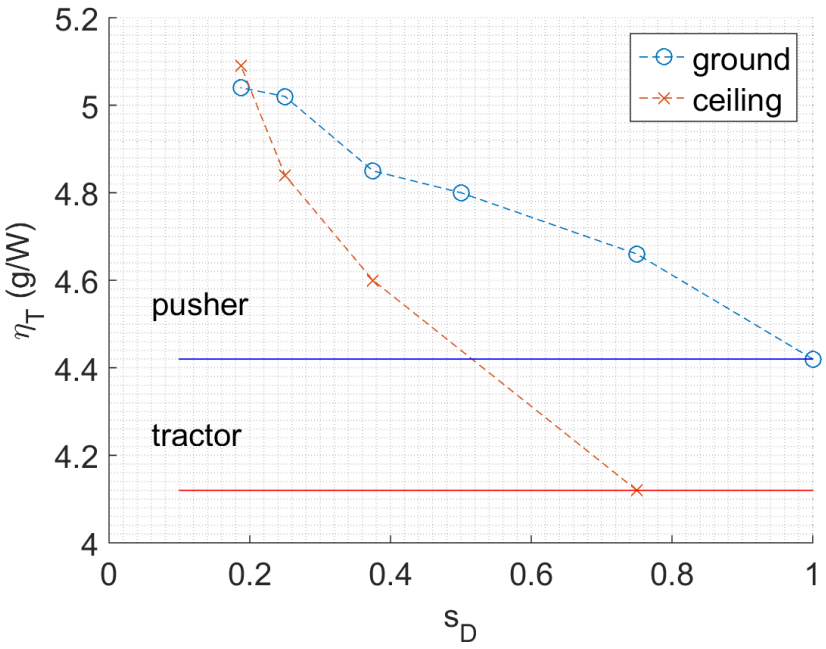

Figure 53: Tractor vs. pusher configuration rotor efficiency in ground and ceiling effect

Table 20: Comparative ground vs. ceiling effects on thrust at hub to ground/ceiling separation normalized by rotor diameter

Separation (in)	s_D	T_{ground}	$T_{ceiling}$ (g)	Δ (%)
6	0.75	50.4	54.1	7.4
3	0.38	56.7	59.1	4.4
2	0.25	57.2	62.4	9.2
1.5	0.19	52.9	65.4	23.6

increased by 4.8%. Ceiling effect also affected data in the trials in the same way expected from previous studies. From the trials, the ceiling configuration maintained a thrust advantage over "ground" one when both were the same distance away. For instance, at the same 3000-RPM level, for separations of 6 inches and below, the thrust in each ceiling trial was about 4-24% greater than the thrust for the ground effect trials, seen in Table 20. Note that the ground effect trial is run as a pusher and the ceiling effect trial is run as a tractor.

Table 21: Efficiency of Gemfan 6x4 propellers co-mounted, stacked on the same axle, CW + CW and CW + CCW

	RPM	T (g)	g/W
CW	5332	41.65	3.28
CW	6026	54.53	3.08
CW + CCW	5250	7.57	0.31
CW + CW	6020	67.07	2.59

4.1.10.6 Other configurations

Park [80] suggests the use of two propellers co-mounted with opposing spin directions on the same motor, so that when the motor direction is CW, for example, the rotor is a pusher. In such a configuration, when the motor direction is reversed, the thrust direction reverses and the rotor becomes a tractor. This may have practical applications such as inverted flight, and interesting to this study, increased ability to produce rates. There are clearly aerodynamic drawbacks of having two propellers of opposing directions on the same motor, but if the loss in efficiency is acceptable, and 3D ESCs are available, this may be an interesting option. To study the loss of efficiency of such a configuration, one propeller Gemfan 6x4 is used to establish a control data set. Then two of the same propellers (CW + CW) and two oppositely twisted propellers (CW + CCW) are used to record data to discern any noticeable changes in efficiency to justify this design option.

The results are seen in Table 21. For this pair of propellers compared to the control data, there was observed a 90% drop in thrust for the CW + CCW combination. This is as expected, because with the rotors rotated, the propeller facing the opposite direction would still generate almost the same amount of thrust in the opposite direction. However, with the two identical CW propellers stacked and one inverted as suggested by [80], there is a 24% increase in thrust with at 84% the efficiency of the control rotor. The same trend will likely hold true if the ESC were to reverse the rotor direction, with the only difference being described by 4.1.10.3, as now the rotor

reverses from tractor to a pusher. The author that suggests this configuration uses a larger, more efficient propeller and RPM which seems to take a less detrimental degradation in efficiency.

4.2 Configuration effects on rates

This section is motivated by RQ 2b: "What are the effects of standard configurations x vs. +?" from 2.5.2.

Selected conclusions based on the LUTs generated by the process described in 4.1.5 are considered by this section. The full set of these may be seen in the Appendix Figures 77 through 345. Most of the attention in this section is concentrated on hexarotors, which are of greatest interest to this thesis, although quadrotors, octorotors, and dodecarotors are also discussed. Configurations such as $+$ and X frames, counter- and co-rotating coaxial setups are described, with pure and impure motion constraints. These LUTs are mappings between ζ and ϵ pairs and the resulting vehicle maximum rates in all 12 DOFs: $+\ddot{z}_B$ is equivalent to g in hover, as in the generation of the LUTs, no rotors have the ability to apply force along the $+z_B$ direction.

LUTs are generated with the full dynamics described in the 4.1.2 section, with vehicle parameters recalculated at each point in the ζ, ϵ design space. This must be done for the following reasons. First, all rotor geometry (i.e., rotor unit vectors, rotation matrices, etc) must be recalculated. Second, inertia and CG must be recalculated. If each arm of the MR is defined as passing through the CG in a simple calculation, arm dihedral angle alone will not affect pitch or roll rates. This is because the maximum moments before and after dihedral rotation are both parallel to eachother. However, the inertia of the vehicle will change, as will the CG - this is why the vehicle parameters must be recalculated on every change in ζ or ϵ. Because of this, a non-zero effect of dihedral on roll and pitch rates is visible in all generated LUT data. Inter-rotor wake interaction effects are also included in all LUT data,

including co and counter rotating coaxial aerodynamic effects as described in 4.1.10. Rotors used to generate these are unidirectional; they are not 3D rotors, which would be able to generate thrust and torque in two directions by reversing spin direction.

4.2.1 Quadrotors

Some expected results are seen in the LUTs. It is easily seen in Figures 79 and 83 that a *+4* is only capable of pure pitch and roll if the rotors are coplanar when ζ and ϵ are both 0°. These results help to partially conceptually validate the framework, as this is what is expected. The same is seen for the *X4* of course in Figures 156 and 159. This is of course because with any non-zero ζ or ϵ pitch and roll maneuvers become coupled with linear accelerations. For instance, to roll left, *M1* and *M2* will spin up faster than *M3* and *M4*, which will also cause a non-zero -$\ddot{y}$. Of course, this does not mean the design is not feasible, it merely indicates that pure motion in these directions is not possible. The impure plots for the same vehicles give an idea of the maximum rates when this coupling is ignored.

Also, as expected, with the failure of any one rotor, pure motion is largely lost, with the exception of some specific cases. Figure 155 shows the complete loss of direct authority of attitude around the -x_B axis with the loss of *M1*. Of note here are the few feasible solutions when $\zeta = \epsilon$ up to 30°, 30°. In general for all of these LUTs, some of these "outliers" may be valid or they may be artifacts of the numerical precision or tolerance of the optimizer. With the same failure, half of the authority in pure pitch is lost with only positive q now possible. Interestingly, as in the roll axis, a few feasible solutions exist when $\zeta = -\epsilon$ between -15° to +30° ζ, seen in Figure 158. Figure 161 shows the loss of one direction of yaw at 0°, 0°. This type of hover has been demonstrated on paper and in flight by [145] where yaw is surrendered in order to achieve altitude control with the failure of two diagonally opposing (i.e., *M1* and *M3*) rotors.

The *+4* loses pure roll and pitch capability immediately with the failure of one rotor. One direction of yaw is possible however; see Figures 78, 82, and 86.

Interestingly, a few (but probably practically infeasible) pure motion solutions - $\ddot{z}_B$ exist even with a fault when $\zeta < 20°$, although this is dependent on which rotor fails, seen in Figure 98. The controller is able to find some solutions for pure yaw at extreme rotor angles that beat the rates of the *X4*, but this is only feasible in this axis; the other axes are not capable of pure motion. This is seen in Figures 87 and 162.

The *X4* has higher p and q rates at $\zeta, \epsilon = (0°, 0°)$ through over $(55°, 50°)$. General trends are also a expected in these Figures. Impure pitch and roll authority are highest at $\zeta, \epsilon = (0°,0°)$ and fall off with the increase of either design variable. This is because the moments in the axes of interest that the rotors can generate are now smaller as compared with those when they are co-planar. See Figures 81 and 157. Yaw authority also scales with ζ by orienting thrust vectors in the directions to be able to generate yaw moment by using rotor thrust. Notice in Figure 160 that adverse yaw occurs with -ζ, reducing yaw authority advantage as opposed to the $+\zeta$ configuration.

Another item to note here is that an *X4* with positive ϵ should be faster at rejecting lateral disturbances than a coplanar *X4*, for the same reasons given by [72] for the *X6*; that is, consider a disturbance forcing the vehicle in $+y_B$. To hold position, the coplanar vehicle would normally roll left. To do so requires spinning up *M1* and *M2*. If the vehicle has dihedral, spinning these two up immediately applies force in $-y_B$, causing a quicker rejection of the disturbance.

4.2.2 Hexarotors

4.2.2.1 +6 vs. X6, pure rates

From Figures 102 and 179 it is clear that the *+6* achieves higher pure rates in most of the design space in the p axis. At the origin where $\zeta, \epsilon = (0°, 0°)$, both vehicle configurations are able to produce the same pure roll rate. As with the quadrotor,

departing from $\zeta, \epsilon = (0°, 0°)$ in the design space reduces the maximum rates in the roll axis. However, unlike the quadrotor, many more combinations in the design space yield feasible pure motion due to the over actuation of this vehicle.

The *X6* wins out on pure rates in the roll axis, again being identical to the *+6* at 0°, 0°, seen in Figures 105 and 187.

For absolute maximum rates, when the pure motion constraint is relaxed, the *X6* outperforms the *+6* from $\zeta, \epsilon = (0°, 0°)$ to about (30°, 30°) in the roll axis, shown in Figures 101 and 175. The opposite is true for the q axis, seen in Figures 104 and 183. As expected, rates in r are identical, shown in Figures 107 and 191.

In the linear axes, several differences between the *+6* and *X6* are also seen. The *X6* is capable of higher rates in the x_B axis in the standard design discussed throughout this document. Until about $\zeta = 60°$, the *X6* slightly edges out the *+6* for $+\ddot{x}_{B_{max}}$. At 70°, the rate increases another 10% although by this point the design becomes largely impractical due to the required power to hover. These effects are seen in Figures 111 and 203.

Pure rates in the y_B axis are generally higher again on the *+6*, although differences are slight, similar to those in the x_B axis. Note that at -ζ appears appealing, although adverse yaw limits the yaw authority in this when $\zeta < 0°$. Rates in this axis are shown in Figure 114 and 211.

The performance of these two configurations in the z_B axis should be identical since the only difference in configuration is is λ_i in the $x_B y_B$ plane. This is indeed seen in Figures 117 and 219.

When impure motion is considered looking at absolute maximum linear rates, the two designs are more or less identical, with small tradeoffs. Depending on the location in the design space, especially at small angles, switching between the X and $+$ configuration is nearly identical to switching the values of ζ and ϵ in the same configuration. Note this effect in Figures 110 and 199 for $\ddot{x}_B$ and 113 and 207 for $\ddot{y}_B$

for both vehicles.

Again, as expected since the motor commands are identical to the pure version, absolute maximum z_B linear rates are identical for these two designs, seen in Figures 116 and 215.

4.2.2.2 Rotor failure on the X6

When a rotor fails on the *X6*, the ability to achieve pure motion is largely destroyed with respect to the volume over the design space seen in the LUTs. If *M1* fails, there is a complete loss of pure control over $-p$, $+q$, and large loss over control of $+r$ over the ζ, ϵ design space. With the fault of a rotor, linear rates are affected as well. With the fault of *M1*, either the ability to produce + or -$\ddot{x}_B$ and + or -$\ddot{y}_B$ are lost. Unless -ζ is used, with the added detriment of adverse yaw, no pure -$\ddot{x}_B$, +$\ddot{y}_B$, or -$\ddot{z}_B$ is possible with a fault on *M1*. The latter effect is likely the only argument for using -ζ in a design, working both in the *X6* and *+6* frames, although this is specific to the case when *M1* fails. Failures in *M2* or *M3* have similar effects which may be mitigated with -ζ, at least in the case of pure control over -$\ddot{z}_B$, the effects of which are seen in Figures 357.

Failure of *M2* has an effect similar to failure or *M1* in $\ddot{y}_B$, and the effect of a *M3* failure on the same is seen in Figures 208,209, and 210 for rotor *M1*, *M2*, *M3* failure, respectively. In the x_B axis, rotor failures affect the design space as seen in Figures 200,201, and 202 for rotor *M1*, *M2*, *M3* failure, respectively

Failure of rotor 2 does not affect pure roll rates, seen in Figure 177, as this rotor is does not necessarily need to be used to roll. Other effects of failing rotors are seen in the appendix. Failures of rotors *M4*, *M5*, or *M6* should behave in a similar fashion as the above due to the symmetry of the vehicle about the $x_B z_B$ plane.

In opposition to these findings, Mehmood [82] claims that if any non-zero ζ is used, all pure motion is lost for the *X6* as compared to standard vehicle in response

to a rotor fault, although that study did not the investigate the three quadrants of the design space where $(\zeta, \epsilon) < (0°, 0°)$. Another difference between the results found here and Mehmood's is the asymmetry between $\ddot{x}_{max}$ and $\ddot{y}_{max}$ as described in 4.1.8. The difference may stem from a different controller being used in that study, or the different dynamics considered here. This subset of the data presented here also agree in behavior with the data presented by Jiang [105]. In that study, a multiroror with the same design as the *X6* discussed here with $\zeta = 0$ to 35° is presented. That study finds the same asymmetry found here with a factor of about 1.6-1.7 between rates generated in the x_B and y_B axes, with the $\ddot{x_B}$ being constantly higher (note in that study the rotated axes when comparing results). That is, the *X6* with only non-zero ζ can produce more (pure) acceleration in the x_B direction than in y_B by about 60%. For impure motion, the difference is closer to 15%.

Giribet [90] finds that if a small ϵ is applied, the vehicle becomes fault tolerant with the loss of one rotor. However, rotor dynamics and aerodynamics are not considered in that study, which may reflect in the difference in results. In this study, with $\epsilon = 0°$, the hexarotor is already single fault tolerant in terms of impure motion. The controller used in this study even finds command solutions corresponding to pure motion for the standard *X6* with no dihedral (although pure rates in several directions are quite small). The same controller is not able to find pure solutions at $\epsilon = 15°$. The answer here appears to depend on what controller is used and what type of motion is allowed; that is, how much drift is acceptable in each of the axes of an actual vehicle.

There are no remarkable differences between the *+6* and *X6* under same failure condition. There is a slightly larger volume over ζ, ϵ that is purely controllable for q and r on the *X6* seen in the appendix. Essentially all of these comparisons between the two configuration types also holds when the pure motion constraint is relaxed, also seen in the appendix.

4.2.2.3 Y6C vs. the novel Y6sC

Another type of standard hexarotor is the *Y6C* is shown in Figure 1 (e, f). Although the *Y6C* has the advantage of lower inertia and potentially lower physical complexity than the *X6*, it is not directly capable of DFC in the x_B and y_B axes, a gain of two DOF for the same propulsion system. One suggested modification to this design made here is termed the *Y6sC*, where the "s" indicates "semi-coaxial." The design is shown in Figure 2 (j), where the downstream (lower) rotors are mounted at the negative of the ζ of the upstream (top) rotors. Another advantage of this design is the airflow from the upstream to the downstream rotor is not perpendicular to the downstream rotor's plane. This is advantageous in that the downstream rotor does not ingest the full wash of the upstream rotor, which should act to decrease the loss of efficiency of this stacked configuration. This is described further in section 4.1.10. This is in opposition to the *Y6C* when ζ is applied, seen in Figure 2 (m), where the same angle is applied such that the rotors stay coaxial. The $Y6sC$ design has not been described or flown in literature.

One downside to the design is the height of the mount (the distance from the seat of the motor to the arm) scales with ζ to avoid propeller strikes between the top and bottom rotors. However, this design gains some of the advantages seen by the *X6*, and at a generally lower inertia cost if the motor mounts are light. The main advantage of the *Y6sC* over the *Y6C* is the gained ability to generate acceleration in the x_B and y_B axes. The *Y6C* requires dihedral to gain authority in the x_B and y_B axes and no solution is found for this using ζ, as seen in the LUTs. Even so, both positive and negative rates are possible either the x_B or in the y_B axes, but not both simultaneously. However, even in this case, from Figure 328 it should be clear that acquiring y_B authority by using ζ requires relinquishing capability in x_B.

When compared to an *X6*, the *Y6cS* has nearly double the roll rate capability due to the the inertia differences. The rate is not doubled because the inertia isn't actually

halved and the moment is slightly smaller in the *Y6sC* case due to the semi-coaxial rotors. In the yaw direction, the *Y6sC* wins again with about 50% more authority. This difference drops by about 15% when aerodynamic effects are considered, using data acquired in section 4.1.10.

Any rotor faults on the *Y6C* are detrimental to the pure motion design space. When *M1* is faulted on the *Y6sC*, half of the design space for pure roll is taken out, seen in Figure 302. However, the *Y6sC* with a faulted rotor does better for pure motion in p, q than *Y6C* with no faults at most any values of ζ, ϵ although many solutions are not found, especially in r as seen in the Figures in the appendix.

4.2.3 Octorotors, dodecadrotors

Compared to the *X8*, the *X8C* is capable of more than 1.5 times the rates in the p, q, and r axes. These results are consistent with those of the *X6* vs. *Y6C* case. These results, and others are seen in the appendix for each vehicle and each axis.

Rate data for *X12* and *X12C* configurations are also seen in the appendix. Pure runs never converged for most angles so their data are omitted. This is must be due to the larger number of degrees of freedom available to the controller for these vehicles.

4.3 Optimization of X6 DFC UAV rotor configuration

This section is motivated by RQ 3e, 3a: "What are the rotor orientation configurations to provide the best linear and angular rates for a non-coplanar multirotor?" and "What is the best configuration for the X6 DFC vehicle?"
from 2.5.2.

To investigate the question motivating this section, the optimizer described in 4.1.1 is used to select vehicle configurations to maximize performance in axes of interest. The optimizer is run in different configurations, or *types*, for the *X6* vehicle using 13. These *types* specify the degrees of freedom available to the optimizer. Types one, two,

Table 22: Design variables and corresponding GA optimizer design space for the *X6* DFC UAV

Variable	minimum	maximum
ζ	-90°	90°
ϵ	-90°	90°
λ	-180°	180°
l	0.35 ft (106 mm)	1.5 ft (457 mm)

and four have the advantage of speed, as they are set up to use the LUTs provided in the appendix and described in 4.2. The other seven *types* must recalculate control commands and dynamics on every iteration, as described by 4.1.1. The optimizer is run with the weights specified in Table 14, such that 90 runs are executed in total (10 *types* x 9 *sub-types*). These are run on a Condor [141] HPC due to the number of calculations required with the design variables (see Figure 37) and corresponding design space shown in Table 22. The results are displayed following analysis of data of over 800 runs yielding 3,531,924 GA generations, with a mean of 392,436 per *type*.

The arm lengths l of all vehicles in all *types* (with the exception of 3, 5, 9, and 10) are set to 290 mm. *Type* 5 has l set to 2 m. This is done in an effort to accelerate the optimizer's run time by running into less propeller strikes during execution, as this commonly happens when the only variables are λ of each arm and all are free.

The weights determine the goal of the optimizer. The optimizer can either tend toward angular rates, linear rates, or some combination of both. The structure of the $sub-type$ array shown in 14 is an attempt to run a multitude of combinations of these to investigate the different designs chosen by the optimizer. Note that the weights are negative since the optimizer is running a minimizer. Linear rates for these vehicles are generally on the order of 50 ft/s^2 while angular rates are in the range of 50-500 rad/s^2 [3] for the vehicles considered here. As such, weights for *sub-types* 1, 3,

[3]The weights used for optimization were chosen for a vehicle that erroneously had higher rates in the linear axis than angular, unlike what is seen here; the error was fixed and LUTs updated but the GA optimizer was run on these data. The weights are left for discussion and results will not change as they are still qualitatively correct.

4, and 6 should favor linear rates, while 2, 5, 7, 8 should favor angular rates. *Sub-type* 9 should scale the angular rates such they are relatively close in value to the linear rates, which makes for a more even comparison of apples and oranges.

In addition to these weights, the dynamics constraint is relaxed for some of the runs to accelerate some of the runs. Although the designs that the impure optimizer might come up with may not be capable of pure motion, they may be, and still may add an interesting aspect to the investigation.

To evaluate the optimizer's designs, the rates are non-dimensionalized by the maximum rates of two control vehicles with the weights removed. The control vehicles are both *X6* DFC vehicles with $\zeta = \epsilon = 0°$, and $l_{control} = 290$ mm for every *type* other than *type* 5, where $l_{control} = 4$ m. Purity of motion is considered as well when non-dimensionalizing, i.e., for $sub - types$ 4-7 and 9. The rates for the control vehicles in the linear axes x_B and y_B are zero. For comparison, these rates are set to unity so that the rates gained in the linear axes may be compared instead of being lost as $X/0$ in division by zero.

4.3.1 Optimization: types 8, 9, 10 for 12-24-DOF optimization

Type 8 begins the high-DOF sets of optimzation runs, allowing the optimizer to choose six independent values for ζ_i and ϵ_i. These runs begin to become largely infeasible quickly as the problem complexity grows quickly with the design space size. With 12 DOFs, it the Condor server is now tasked to run for months and likely will not settle on an optimal design within a reasonable timeframe. However, the *RQs* posed by this thesis were answered without the need for results from these optimizations.

Type 9 takes *type* 8 and frees up l as well, bringing the number DOFs to 18. *Type* 10 frees up all 24 DOFs; 6 per each of the 4 design variables. This optimization will likely not finish within the forseeable future, but with Condor's ability to process multiple runs of this might lead to an interesting direction. Should any of these runs

Table 23: Best design for *type* 1, *sub-type* 6 optimization: $\Delta\%$ comparison to control vehicle in positive and negative directions of all 6 axes along with fitness score, average number of generations

$\Delta\%$ +						$\Delta\%$ -						GA data	
p	q	r	x	y	z	p	q	r	x	y	z	$\Delta\%f$	N_g
-45	-34	25	3487	4042	0	-59	-34	26	3487	4042	-39	3.5	39032

(*types* 5-10) find a design with better rates than the symmetric vehicles in run *types* 1-4, this might make a case for a non-symmetric vehicle. Several hundred thousand feasible designs have been produced, with varying axis-authority tradeoffs, although none have a clear advantage over the ones described below.

For the less symmetric configurations found by *types*, it is likely to have trimmed hover and maximum rates at non-zero values of pitch and roll. These factors are not considered, as they would add either two more DOFs to the optimizer, or another grid search inside the optimization. The grid of course would be over ϕ and θ, the resolution of which will determine the extra calculation load. Both of these would dramatically slow down optimizer execution and as such these are not considered.

4.3.2 Optimization: types 1, 2, and 4 for dihedral and motor tilt

Optimization *types* 1, 2, and 4 are run to confirm that, in general, designs with angles close to $\epsilon = \zeta = 0°$ are best for angular rates $\dot{p}$ and $\dot{q}$ and linear rate $\ddot{z}$, and designs with higher angles for those variables will be better for linear rates $\ddot{x}$ and $\ddot{y}$ and angular rate $\dot{r}$. These runs have one DOF such that all rotors are rotated by the same angle once the optimizer chooses it. Of course, consecutive ζ angles alternate sign as the vehicle is constructed.

For *type* 1, where ϵ is free, some selected results are shown in Table 23.

Optimization *sub-type* 6 found this configuration after 2316 generations on one of ten independent design runs. Note that this optimization type attempts to maximize mainly linear rates, as they are weighted heavily by this *sub-type*. The design is shown in Figure 54. Note the anhedral chosen by the optimizer. All *sub-types* optimization

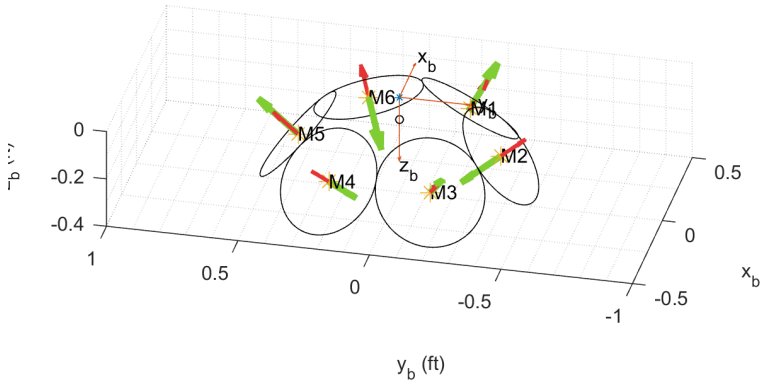

Figure 54: 1-DOF *X6* configuration optimization for rates, free $\epsilon(1)$

runs selected $\epsilon < 0$ as their best designs with ϵ of the design described here of -49.1 °. This design gives up between 45 and 59 % of authority in the angular axes to gain DFC control of x_B and y_B. Note the values in the table are in those axes are compared to unity, as the baseline vehicle has no authority in these axes. The fitness function compared to the control vehicle is gains 3.5 % (due to the linear-heavy weighting selected for this optimization).

For *type* 2, where ζ is free, two of the best designs in terms of improvement of the fitness function is shown in Table 24 and Figure 55. Sub-types 3, 6, and 8 both converged to ζ of about -65°. The first row of data corresponding to *sub-type* 3 which weighs linear rates heavily shows a -65° ζ vehicle. Note the effect of adverse yaw here compared to the vehicle which is shown in the second row which is built with $\zeta = 22.1°$. The effect on yaw is seen in the percentage improvement in the r axis: even with 3 times the angle in the top design, the bottom design achieves double the improvement (350%) in yaw authority. The top design (Figure 55 (a)) is found after 5201 generations, and the bottom design (Figure 55 (b))is found after 6101.

Type 4 is 2-DOF to investigate whether or not combining the ζ and ϵ angles is

Table 24: Best design for *type* 2, *sub-type* 3 (row 1) and 5 (row 2) optimization: $\Delta\%$ comparison to control vehicle in positive and negative directions of all 6 axes along with fitness score, average number of generations

$\Delta\%$ +						$\Delta\%$ -						GA data	
p	q	r	x	y	z	p	q	r	x	y	z	$\Delta\%f$	N_g
-64	-56	168	3205	3459	0	-64	-56	168	4320	3459	-81	5929	20824
-42	-37	350	5194	4484	0	-42	-37	350	5194	4484	-92	2512	24424

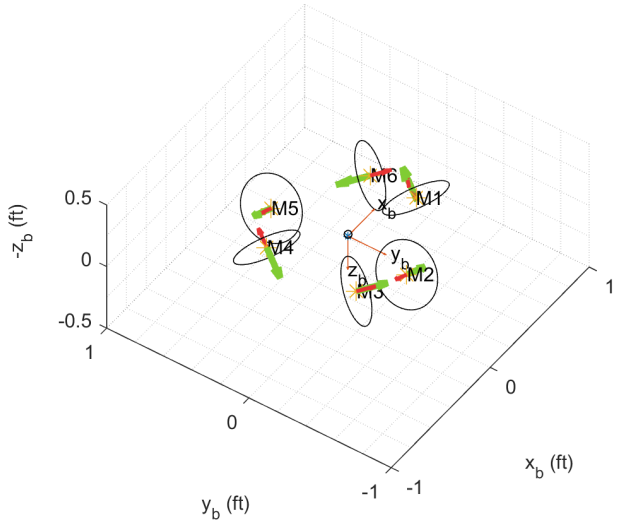

(a)

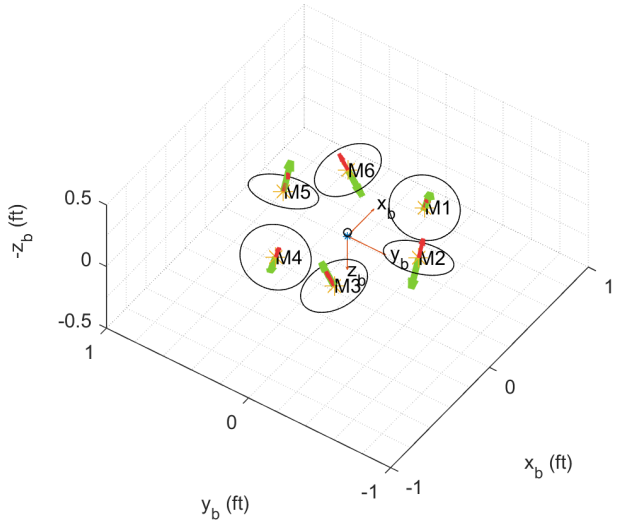

(b)

Figure 55: 1-DOF *X6* configuration optimization for rates, free $\zeta(1)$ for *sub-types* 3 (a) and 5 (b)

useful for maximizing rates. There are no noteworthy designs found by this optimizer, although sub-types 1 and 3 both converged on (ζ, ϵ) = (-65°, 10.1°) and sub-type 2 converged on (ζ, ϵ) = (65°, 19.9°). The results of this *type* are also used as a basis to determine whether or not *types* 8-10 find a better vehicle.

This optimization is also used to investigate *RQ 3a. What is the best X6 to be single unknown fault tolerant?*. To determine this, rotors *M1* through *M3* are faulted and a LUT is generated for each case. The LUTs are seen in the Appendix (for $\dot{p}$, see Figures 176, 177, 202, and so forth.) Since the goal is to be single unknown fault tolerant, these are put together using a *union* operator, and then the optimizer is run on them to determine the best configuration. The resulting LUTs are seen in Figure 56 for q and r, the worst and best looking axes respectively after the composite is created using a pure motion constraint. When the constraint is relaxed, the same axes are seen in Figure 57. The rest of the Figures are seen in the Appendix Figure 357 for purity of motion constrained and relaxed. Angular rates have priority such that at least partial trim can be maintained. The resulting design of the optimizer is (ζ, ϵ) = (0.0°, 0.0°), indicating that the best design for single fault tolerance is the standard design if pure motion is to be enforced. Changing the GA weighs does not affect this solution. Of course, pure motion may not be practical when a fault actually occurs. When the optimizer's purity of motion constraint is relaxed, the best design becomes (ζ, ϵ) = (75.2°, 44.5°). The weights used here are of *sub-type* 6 which weigh linear axes heavily. If angular axes are weighted more heavily with *sub-type* 7 or 8 weights, the solution becomes (ζ, ϵ) = (9.5°, -9.0°). This design is more feasible for most vehicles as the ζ is much less extreme than in the previous case.

4.3.3 Optimization: type 3 for wheelbase

Type 3 is a 1-DOF run to compare against the results of [110], which state that a vehicle with lower characteristic length will have higher rates. That is, balance

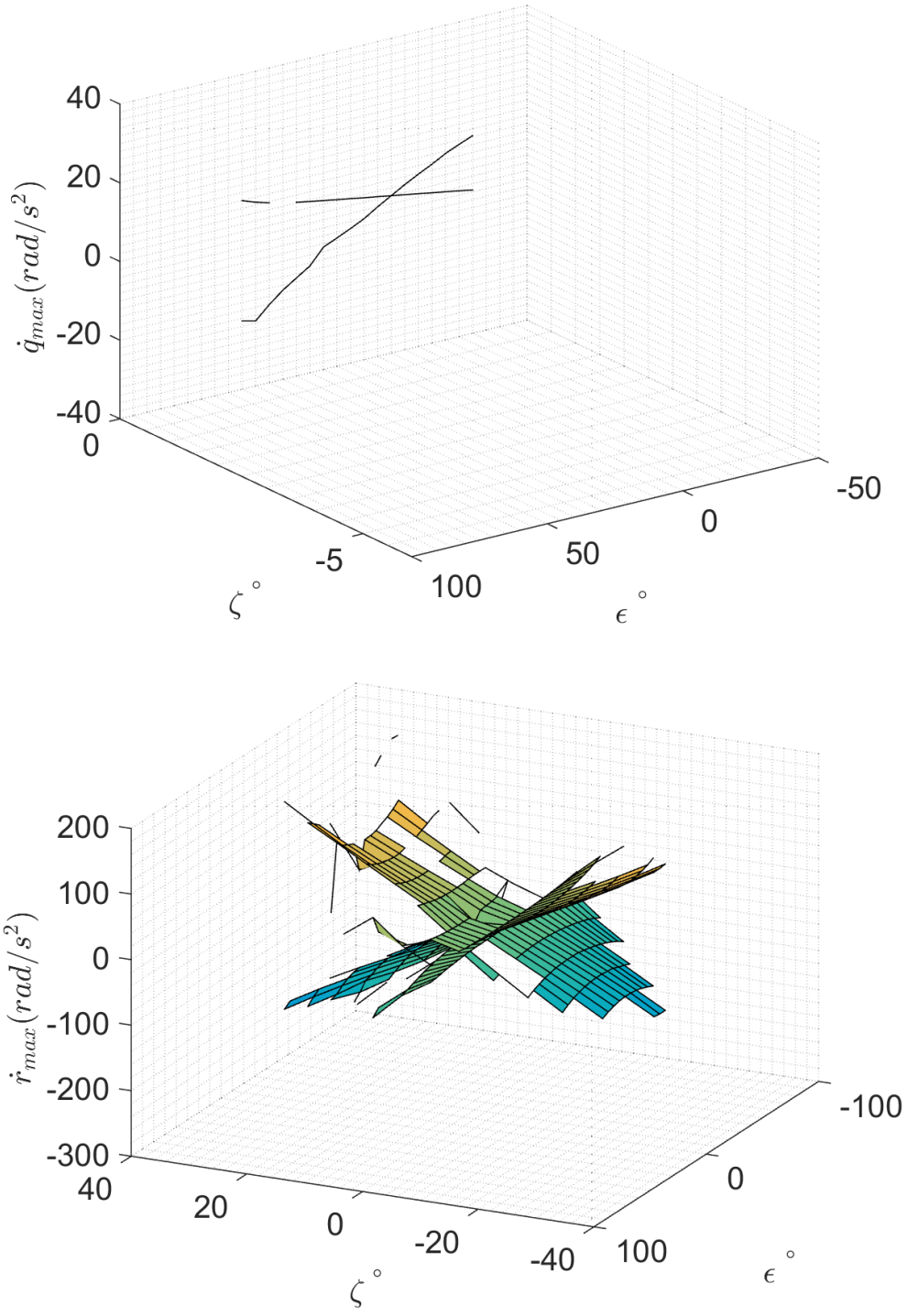

Figure 56: Composite LUT for *X6* failures of rotors *M1* through *M3*, pure motion enforced

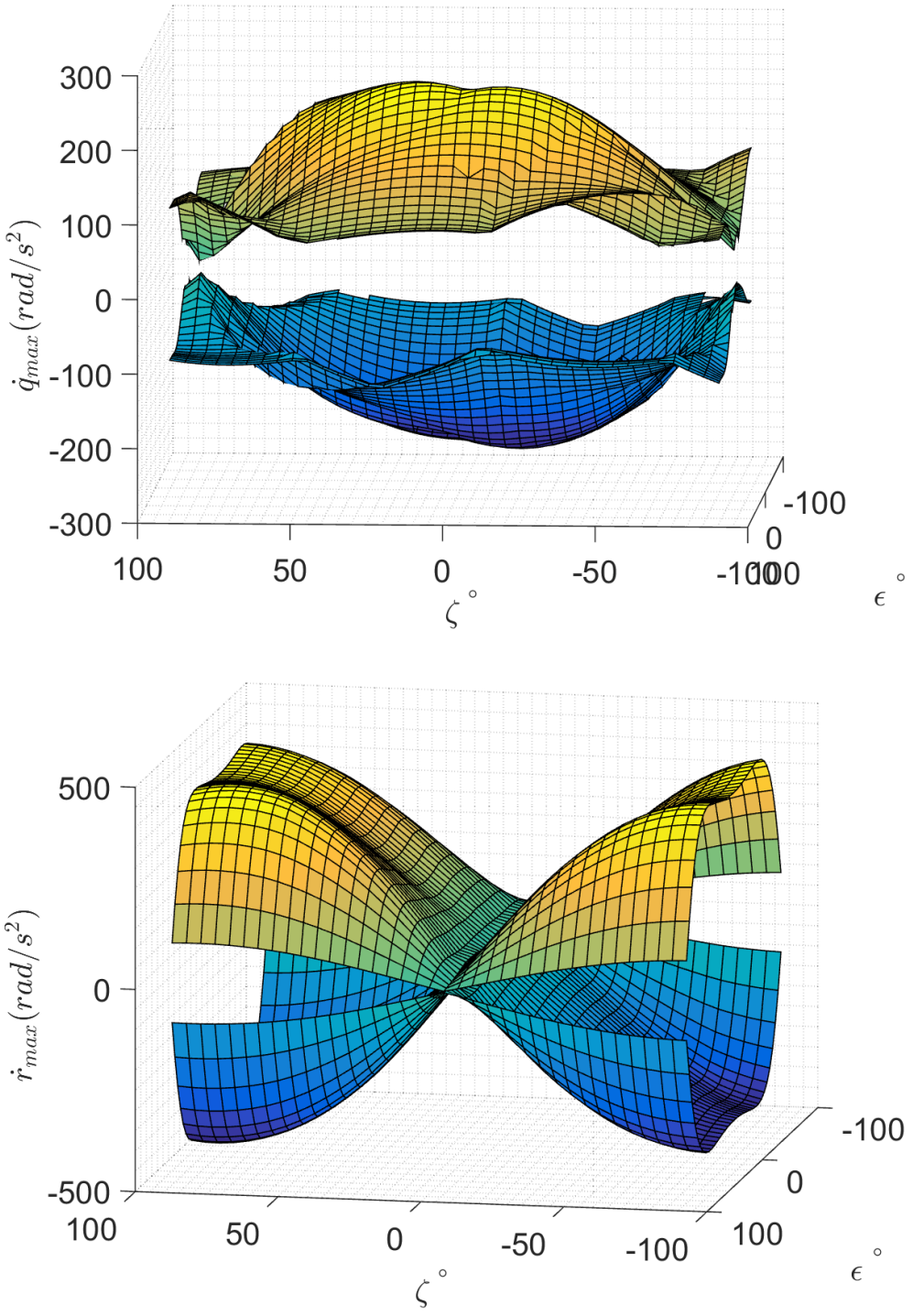

Figure 57: Composite LUT for *X6* failures of rotors *M1* through *M3*, pure motion not enforced

Table 25: Best design for *type* 3 optimization (all *sub-types* have identical solution): $\Delta\%$ comparison to control vehicle in positive and negative directions of all 6 axes along with fitness score, average number of generations

$\Delta\%$ +						$\Delta\%$ -						GA data	
p	q	r	x	y	z	p	q	r	x	y	z	$\Delta\%f$	N_g
17	18	35	0	0	0	17	18	35	0	0	0	3.5	40065

between longer arms producing larger moments and larger inertias is tipped in favor of smaller inertias when seeking the highest angular rates. As such, it is expected that the optimzer will select the smallest l possible to design the vehicle in this optimization. The results of this optimization align with those of [110]; all *sub-types* for this optimization converge on the shortest wheelbase vehicle possible for highest rates. This is limited by the blade-blade strikes as the rotors are in the same plane, as seen in Figure 58. Note that this is one run where *sub-type* should be irrelevant, since there is one absolute best design in this situation, where only l is free to change. See future work 5.2 for further discussion of overlapping blades.

Compared to the control 290 mm vehicle, this vehicle, sized to 254 mm, exhibits greater rates in all angular axes. Table 25 shows optimizer collective results from over 366,752 generations in 10 different runs.

The 254 mm optimized vehicle has 17-18% maximum higher rates in θ and ϕ axes, and 35% higher rates in ψ. This is true both in positive and negative directions, as expected due to the vehicle's symmetry. Linear accelerations in x_B and y_B of course remain impossible.

4.3.4 Optimization: types 5, 6, 7 for 6-DOF optimization

Type 5 is the first 6-DOF optimizer, where all six arm azimuths λ_i are design variables.

Many of the designs found here trade off $\dot{p}$ and $\dot{q}$ within $\pm$ 10%. The designs tend to have the rotors spaced more or less evenly with respect to λ around the vehicle. Of interest however is the design found by *sub-type* 7, shown in Table 26 and Figure 59. Perhaps since the CG moves and 5 arms become short, yaw rates are increased

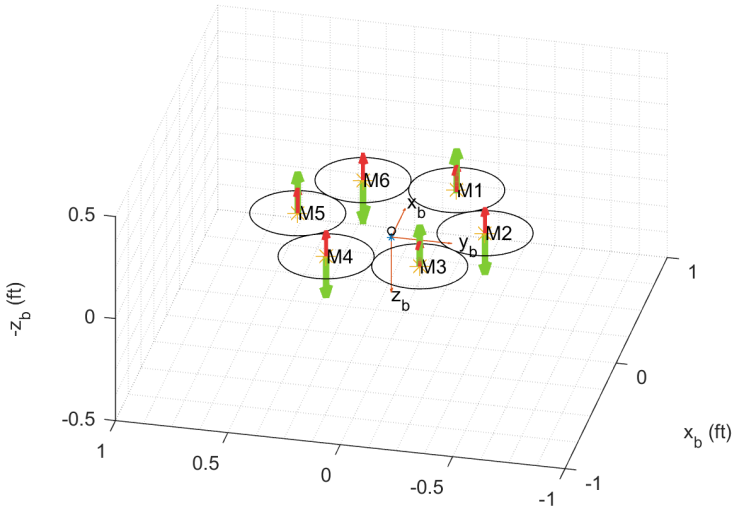

Figure 58: 1-DOF *X6* configuration optimization for rates, free $l(1)$

Table 26: Best design for *type* 5 optimization: $\Delta\%$ comparison to control vehicle in positive and negative directions of all 6 axes along with fitness score, average number of generations, and number of generations to find optimal design

$\Delta\%$ +						$\Delta\%$ -						GA data	
p	q	r	x	y	z	p	q	r	x	y	z	$\Delta\%f$	N_g
14	3	22	0	0	0	5	-8	21	0	0	0	12.5	85265

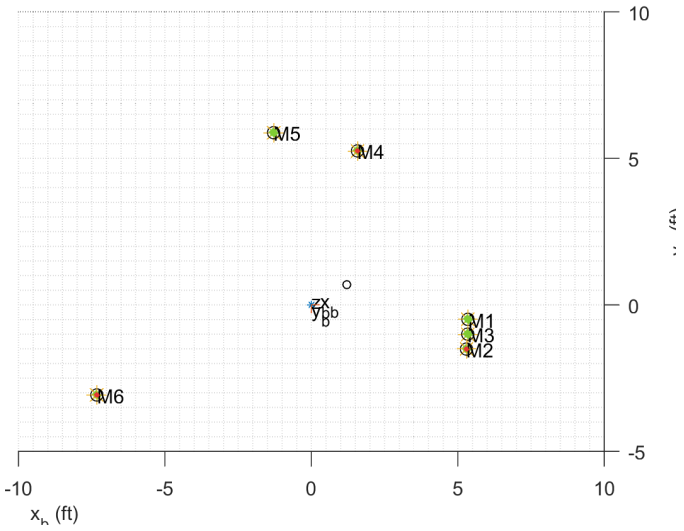

Figure 59: 6-DOF *X6* configuration optimization for rates, free $\lambda(6)$. Note extra l to decrease propeller strikes while optimizing.

Table 27: Best design for *type* 6, *sub-type* 7 optimization: $\Delta\%$ comparison to control vehicle in positive and negative directions of all 6 axes along with fitness score, average number of generations

$\Delta\%$ +						$\Delta\%$ -						GA data	
p	q	r	x	y	z	p	q	r	x	y	z	$\Delta\%f$	N_g
17	32	75	226	6	0	16	32	71	2205	3819	-12	2844	45390

by over 20%.

Type 6 allows the optimizer to choose six independent ϵ_i values.

Again, sub-type 7 finds an interesting design. With 12% loss of vertical acceleration compared to the control vehicle, gains in all other axes are seen. The vehicle is designed with ϵ = -33.9, 32.8, 14.8, 61.6, -60.1, -67.4° for M1 to M6, respectively. The design is shown in Figure 60.

Like *type* 6, *type* 7 allows the optimizer to choose six independent values for ζ_i.

Sub-type 2 creates an interesting vehicle shown in Figure 61, the improvements for which are shown in Table 28. Note the similarity of this vehicle to that created symmetrically in *type* 2 shown in Figure 55(b). The vehicle is designed with ζ = 82.3, -35.8, 5.6, 65.8, 44.8, -64.4° for M1 to M6, respectively.

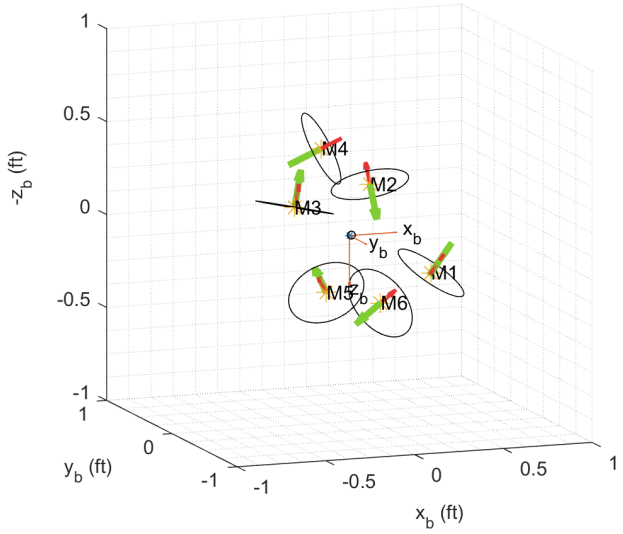

Figure 60: 6-DOF *X6* configuration optimization for rates, free $\epsilon(6)$

Table 28: Best design for *type* 7, *sub-type* 2 optimization: $\Delta\%$ comparison to control vehicle in positive and negative directions of all 6 axes along with fitness score, average number of generations

$\Delta\%$ +						$\Delta\%$ -						GA data	
p	q	r	x	y	z	p	q	r	x	y	z	$\Delta\% f$	N_g
-30	-51	55	2089	1892	0	-56	-49	170	1864	1508	-60	1115	35315

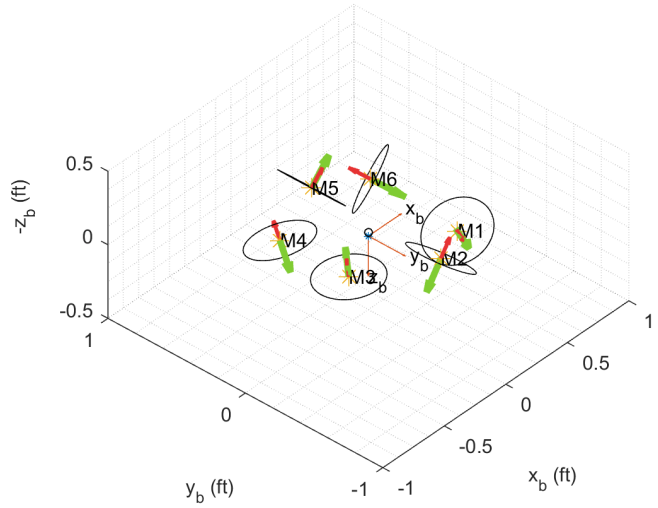

Figure 61: 6-DOF *X6* configuration optimization for rates, free $\zeta(6)$. Note qualitative similarity to vehicle in Figure 55(b)

CHAPTER V

CONCLUSIONS

Because of the ubiquity and vaset potential of electric multirotors, this thesis has looked into the sizing and design of the configuration of a generic multirotor's propulsion system. A framework for the sizing of the electric multirotor was presented. This sizing framework, termed multirotor sizing tool (MST) deals with selection of specific or a class of components which will allow a vehicle to accomplish a mission. To investigate this area, electric propulsion components are identified and modeled, with emphasis placed on the rotor. On top of this framework, a configuration optimizer was built. The configuration optimizer deals with the positioning and orientation of propulsion components on the vehicle. This allows for optimization of force and moment capability in certain axes, enabling the vehicle to perform certain tasks. MST and the configuration optimizer are used to study the effects of rotor layout on vehicle performance and to optimize configurations of several vehicles. Multirotor aerodynamics are briefly studied to increase the accuracy of these models. Wind tunnel data is provided for multirotor aerodynamic data. A multi-degree of freedom thrust stand is designed and built to study inter-rotor aerodynamic effects.

The thesis asks several research questions (RQs). These are reproduced here along with answers and other interesting data found in researching them.

RQ 1. How do we design the lightest vehicle system for mission-level requirements?

and

RQ 1a. How do we perform sizing optimization?

and

RQ 1b. How do we model components to predict performance?

and

RQ 1c. How much power does it take for cruise and what does the power bucket look like for multirotors? What about aerodynamic lift and drag data of multirotors? What is the ideal battery weight fraction for endurance?

Of interest here is to design the lightest and/or most efficient vehicle system which is capable of accomplishing a particular mission. In order to answer *RQs 1* and *RQ 1a*, *RQ 1b* needed to be answered. Electric propulsion components were parameterized and a classical aircraft sizing method was applied toward electric aerial vehicles. Parametrization of these components allows sizing to be accomplished with rubberized components removing the need to rely on a database of components in the early design phase. While there is a multitude of potential methods to sizing and optimization, a modified version of the classical approach to full-sized vehicles is applied to multirotors. This allows the designer to create a vehicle which will be capable of accomplishing the required mission. The framework is termed multirotor sizing tool (MST). and once created and validated against a set of vehicles, it is used to design several vehicles used for competitions and contract work for the UAVRF. MST is also used generate the well known required power vs. cruise speed plot for multirotors. To increase the accuracy here, aerodynamic data were found by testing multirotors in a wind tunnel. Some results were presented from these data. For example, decased antennae have less drag than cased ones, adding front-mounted cameras (or in general, flat plates) improve aerodynamics by shadowing the downstream components on small multirotors, and forward tilted rotors will be more efficient for multirotors in cruise. To answer the ideal battery weight fraction question, two methods are attempted. First, the MST optimizer just described is used to size a high-endurance multirotor. Second, a momentum theory approach is taken to calculate the theoretical value. Both converge on a battery weight fraction of 2/3.

RQ 2. For a multirotor, what linear and angular rates are possible in different

coplanar and non-coplanar configurations?

and

RQ 2a. What is the actuation authority of a DFC UAV?

and

RQ 2b. What are the effects of standard configurations x vs. +?

The vast majority of multirotors that have been designed and built share their propulsion system orientation design with other "standard" multirotors. These vehicles have their rotors oriented in a coplanar fashion with all rotor thrust vectors parallel and in the same direction, generally pointing along the $-z_B$ direction. By tilting the rotor planes such that rotors are not coplanar, it is possible to directly achieve rates in directions other than those possible in these standard multirotor designs. In literature, this technique may be called over-actuation or direct force control (DFC) if the controller is able to capitalize on the rotor geometry. To address *RQ 2* and *2a*, an optimizer framework is developed to analyze the forces and torques and hence linear and angular rate generation capability of generic vehicles. A dynamics framework capable of simulating generic vehicles, which are composed of the propulsion system components, is added to MST. These may be generically positioned, heterogeneous, and independently controlled. The framework is modular and several controllers are implemented to command the rotors in order to optimize for maximum rates in all six physical degrees of freedom. The framework is executed for UAVs of multiple configurations to study the effects of these configurations on the actuation authority of the vehicle. Standard configuration ($+$ vs X) effects and others are described with tradeoffs of each. For instance, a *+4* is generally worse than an *X4* in all cases. An *X4* with ϵ is found to have the added benefit of a quicker lateral disturbance response than both the standard *X4* and the *+4*. Also detailed are fault cases, counter- and co-rotating and semi-coaxial and coaxial setups for selected quad- to dodecarotor vehicles. In an attempt to validate the dynamics estimator, predicted

results are compared to data recorded by actual flown vehicles. There was a good corelation between predicted results and the data measured by the flight controller of a DFC *X6*.

RQ 2c. Is counter-rotating or co-rotating more efficient for coaxial setups? Pusher or puller? Tip to tip distance? Wake-wake interactions?

and

RQ 2d. What are other ways to aerodynamically increase actuation authority?

Because multirotors on this scale are relatively new in the field, there are only a number of studies into the aerodynamics of the rotors used to operate them. The results of this experiment are used to augment the dynamics in the rest of the document where wake-wake and wake-rotor interactions cannot be ignored. As such, a thrust stand has been designed, built, and used to investigate the effects these several configurations' effects on efficiency, namely those of co- vs. counter-rotating coaxial and semi-coaxial setups, pusher/puller mounted rotors, tip-tip clearance, wake interaction, and ground/ceiling effect. The thrust stand test also includes a look at ground effect, which is well studied in literature as well as ceiling effect, which is less often studied. It was found that in all cases tested, counter-rotating coaxial setups are more efficient than co-rotating configurations. Wake-wake interaction may be used to increase the hover efficiency of DFC vehicles, which suffer a geometric efficiency loss as rotors are tilted away from the coplanar configuration. An upgraded *X6* is then suggested where rotor wash is pointed at neighboring rotors which should increase hover efficiency as suggested by findings presented here. It is found that semi-coaxial configurations are more efficient than coaxial configurations. Hence, a novel vehicle (*Y6sC*) is also presented as an upgrade to the standard *Y6C* produced commonly in the field. Ceiling effect is found to increase rotor efficiency more than ground effect. Pusher rotor configurations are found to be more efficient, at least in hover. The

thesis also confirms results of another author who suggests stacking rotors and using reversible ESCs to increase actuation authority for multirotors and investigate *RQ 2d*. Such a configuration should be used to investigate additions to *RQ 3* in the future.

RQ 3. What is the best configuration for the X6 DFC vehicle?

and

RQ 3a. What is the best X6 to be single unknown fault tolerant?

This section deals with a closer look at the standard *X6* DFC vehicle, shown in the introduction. To investigate *RQ* 3, an optimizer is used to select the configuration of the *X6* DFC vehicle. The optimizer has ζ and ϵ as DOFs to design the vehicle, and an array of weights is used to indicate goals to the optimizer as to in which directions to optimize rates. Asymmetric (about the xz plane) vehicles are not considered except in $EXPT$ 3d. Depending on the importance of axes, *RQ* 3 really becomes *RQ 3. What is the best configuration for the X6 DFC vehicle for a set of weightings?*. Once this is decided, the question may be answered by using the optimizer. The same optimization technique is run on the standard *X6* with a failed rotor to answer *RQ 3a*. In this case, rotors M1-M3 are failed, as the vehicle is symmetric. Once this is done, the optimizer is run on the dataset to find the vehicle with the highest rates, weighing angular rates higher than linear ones. This is done to maintain the ability to have at least a partially trimmed hover. It is found that the best configuration for this vehicle is actually coplanar, if lateral linear rates are not required.

RQ 3b. Motor roll, arm dihedral for standard DFC X6 is equivalent tilting entire thrust vector x°?

and

RQ 3c. What is the maximum hover pitch and roll trim angle for an X6 DFC UAV?

and

RQ 3d. What are the rotor orientation configurations to provide the best linear and angular rates for a non-coplanar X6?

One metric to describe the authority of an *X6* DFC vehicle is the equivalence of reorienting the rotors with tilting the entire thrust vector of the vehicle. This provides some insight into the effectiveness of the added DFC authority. For this vehicle, the answer to *RQ 3b* is between 1.7 for small angles to 2.2 near the limit for ζ in the x_B axis. That is, every degree in tilt is equivalent to tilting the entire thrust vector by about two degrees in terms of linear rate authority. In the same axis, for ϵ, the ratio is 1.5 to 1.8. In the y_B direction, ζ ratio holds, while the ϵ ratio is slightly lower from 1.5 to 1.7.

Another performance metric is the answer to *RQ* 3*c*: the maximum hover trim pitch and roll angles of such a vehicle. The *X6* DFC UAV is then subjected to a set of test conditions to find the maximum roll and pitch values for hover as a function of ζ. The results depend on the overhead breathing room of the propulsion system during hover. At infinite thrust, the vehicle can hover at the angle of ζ in positive pitch. In negative pitch, since the vehicle is non-symmetric in that axis, performance is about 22% lower. In the roll direction, the performance is about 15% lower. A vehicle that hovers near 50% throttle has lower capability of course, hovering at a nonlinear ratio of ζ.

RQ 3*d* is approached by relaxing constraints on the DOFs for the optimizer built to answer *RQ* 2, allowing between 2-24 DOFs to try to find a more optimal vehicle than the standard, xz-symmetric design considered above. The case with 12-24 DOFs is deemed unecessary to answer the questions posed here. If only ϵ is free, a design with anhedral is chosen as the best for linear rates and hover efficiency recovery due to wake-wake interaction. If ζ is free with one DOF, the standard DFC configuration is better than the one where -ζ is used due to adverse yaw. With six DOF of ζ, the optimizer finds a design that qualitatively appears like the standard *X6* DFC vehicle.

Just like the answer to *RQ* 3, the configuration of the vehicle depends on the weights chosen, as there are nearly infinite designs that will satisfy the constrains placed on the optimizer. The genetic algorithm generates hundreds of thousands of these and is driven by these weights, which makes this question open ended and dependent on mission requirements.

5.1 Summary of contributions

Primary contributions of this thesis:

1. Framework and tool to validate electric multirotor performance that is validated on a set of multirotors in hover

   - input is a set of propulsion system parameters
   - output is a mission that's possible with the propulsion system

   The tool is capable of handling:

   - generic vehicle configurations including but not limited to multirotors, fixed wing, helicopter, hybrid vehicles, N_m heterogenous rotors
   - battery dynamics, including effects of discharge rate, temperature
   - environmental effects including altitude, temperature, wind

2. First framework and tool to optimize generic electric multirotor propulsion system for a particular mission using rubber components using classical approach to aircraft design

   - input is a set of mission parameters
   - output is a set of rubber propulsion system parameters capable of the required mission

3. Parametrization (rubberization) of propulsion components: motors, batteries, propellers, ESCs

4. Multirotor wind tunnel data and findings

    - multiple configurations for small multirotors: 122 to 450 mm, canopies, RTF configurations
    - C_{L_α}, C_{D_α}

5. Adjustable thrust stand design which can record thrust, independent P_e, and P_m with data for several configurations:

    - first review of semi-coaxial configuration
    - first review of co- vs. counter- rotating coaxial configuration
    - first review of puller vs. pusher configuration
    - first review of wake-wake interaction
    - coaxial

6. Framework to optimize generic rotor configurations which can handle:

    - N_m heterogenous rotors
    - positions and orientations may be generic, symmetric

7. Acceleration authority design space of multiple standard and non-coplanar configurations for ζ, ϵ for multiple vehicle types

    - quad to dodecarotors
    - co- and counter- rotating
    - pure to absolute maximum impure envelope
    - effect of configurations on rates

8. Novel multirotor design: *Y6sC* Figure 1 (j)

    - first description of semi-coaxial which is more efficient than coaxial configuration
    - rate advantages over *Y6C* in all axes
    - gains in two DOFs with no change in propulsion system: now $\ddot{x}, \ddot{y}$ are possible

9. For the "standard DFC" *X6* Figures 1 (i), 5

    - design optimization of rates using 1-24 DOF with different axis weights, dynamics coupling constrained and relaxed
    - design optimization for unknown single fault tolerance
    - mapping between ζ, ϵ and equivalent thrust vector tilt
    - hover trim attitude envelope
    - second novel design: efficiency enhancement if rotors are pointed at eachother to mimic configuration described in section 4.1.10.4 and shown in Figure 52

5.2 Recommendations

The capability to consider other fuel sources to the analysis algorithms should be studied. A hydrogen fuel cell model with the ability to consider hybrid systems as well (gas, gas/battery [146], Hydrogen fuel cell/battery) may be added with relative ease to the MST validator and optimizer. Each of these configurations offers unique benefits and allow for a more complete study of electric VTOL design. Several proposed designs have been made with gas and fuel cell technology, with the latter claiming to hover for around four hours using the propulsion system in section 3.4.2. For the modeling of propeller blades, a study of the same propellers with different materials

and how that affects thrust and torque coefficients would be of interest. Currently, the effects of blade stiffness on these data are estimated but not validated. Other optimization techniques should also be applied to the MST algorithms. For example, the GA algorithm used in the dynamics section of this thesis could be applied to the sizing effort, such as described in [147]. This has the ability to generalize the optimizer with respect to goals, instead of simply using loops to find the lightest vehicle. That is, in this way, multiple objectives may be satisfied based on a weighting supplied by the user.

For the dynamics section 4.1, it would be interesting to allow optimization and LUTs with 3D rotors, which may produce thrust and torque in two directions by reversing their rotation direction. As described in that section, a reversible ESC might be used to accomplish this, with either 3D propellers, or inverted stacked propellers, as described. In addition to the range of the rotors, heterogenous rotors and more generic placement might yield interesting results as well. Also, it should be possible to add a blade geometry optimization method (such as one presented by Carroll [148]) to the algorithm the way that it is structured.

For the thrust stand data, rotors of different sizes and in different conditions should be run to estimate the range of applicability of the results found in section 4.1.10. In addition to this, it would be of interest to run angled rotors with asymmetric angles and RPM, as the ones run in that section had identical angular velocity. The thrust stand in its current configuration allows for testing of semi to fully overlapping propellers. The former is not tested but it would be interesting to run these configurations at different percentages of overlap and seperations s_D. In addition to this, a circular set of clamps should be added such that the X6 DFC configuration may be tested, not just rotors directly at eachothera as they are tested now. This may change data slightly. Also, and independent thrust cell should be added such

that thrust values may be measured for each rotor individually, giving a clearer picture of what is actually happening in the configuration. These data may be useful for optimization of top and bottom rotors separately when designing the multirotor. In addition to the above, the work of Theys [14] is an interesting way to account for non-axial flow into the rotor disc, which should increase the accuracy of the BEMT model used by this thesis and should be investigated, as most of the conditions of the rotors described here have largely non-axial but more planar flow entering the rotor disc. It would also be interesting to include some of the data discussed by Pereira [149] dealing with shrouded rotors. Based on the findings of wake-wake interaction in section 4.1.10.4, it would be interesting to build a DFC vehicle with rotors pointed at eachother (such that the projection of the rotor axes of rotors that blow wake at eachother in the xy plane is parallel). This should increase the hover efficiency of such vehicles. It would also be interesting to build the *Y6sC* to compare predicted performance to this new vehicle type.

For the wind tunnel data described in section 3.3.1, a more complete array of experiments should include not just 0 to -90° of AOA, but also 0 to +90° (i.e., descent), and sideslip β from -180 to +180°. This would create a grid of aerodynamics coefficients covering every flight condition of the multirotor, useful for dynamics simulators such as flight trainers. It would also be interesting to test the tractor vs. pusher configuration in forward flight for multirotors, as the flow shadowing described above may play a part in non-hover efficiency conclusions.

APPENDIX A

SELECTED ALGORITHMS

A.1 3D circle-circle intersection

Suppose two circles lie in two planes. These circles are defined by a normal vector, a centroid, and a radius. n_1 is the normal vector to the plane in which circle 1 resides. The center of circle 1 is p_1 and its radius is r_1. If both circles are coplanar, i.e., $n_1 = n_2$, this check is trivial. Then there is an intersection iff:

$$|| \, p_1 - p_2 \, ||_2 \leq | \, r_1 + r_2 \, |$$

If the circles are not coplanar, the check is as follows. A new point $p0$ is defined between the centroids of the circles.

$$p_0 = (p_1 - p_2)/2$$

The point is used to find the intersection between the two planes in which the circles are contained. The plane check described by A.1.1 is used to find the intersection of the two planes defined by n_1, p_1 and n_2, p_2. This returns p_i and n_i, defining the line of intersection, if one exists.

The distance d_1 from p_1 and d_2 from p_2 to the line of intersection parameterized by p_i and n_i is found, and the following check is executed.

The distance of d_1 and the radius of the circle d_1 are 2-normed, as well as those for circle_2.

$$f_1 \; = || \, d_1 + d_2 \, ||_2$$

$$f_2 \; = || \, d_2 + d_2 \, ||_2$$

Then there exists an intersection iff:

$$(d_1 < r_1) \wedge (d_2 < r_2) \wedge (|| \, p_1 - p_2 \, ||_2 < (f_1 + f_2))$$

A.1.1 3D plane-plane intersection

This Lagrangian method is described by Krumm [150].

$$M = \begin{bmatrix} 2 & 0 & 0 & n_{1x} & n_{2x} \\ 0 & 2 & 0 & n_{1y} & n_{2y} \\ 0 & 0 & 2 & n_{1z} & n_{2z} \\ n_{1x} & n_{1y} & n_{1z} & 0 & 0 \\ n_{2x} & n_{2y} & n_{2z} & 0 & 0 \end{bmatrix} \tag{50}$$

$$\mathbf{M} \begin{bmatrix} p_x \\ p_y \\ p_z \\ \lambda \\ \mu \end{bmatrix} = \begin{bmatrix} 2p_{0x} \\ 2p_{0y} \\ 2p_{0z} \\ \mathbf{p}_1 \cdot \mathbf{n}_1 \\ \mathbf{p}_2 \cdot \mathbf{n}_2 \end{bmatrix} \tag{51}$$

Solving for p by inverting M and multiplying it by the right matrix leads to an intersection point which forms a line with $n1 \times n2$. Lagrange multipliers λ and μ and are not of particular interest here. The selection of P_0 is arbitrary but us chosen between the two points defining the planes $p1$ and $p2$.

APPENDIX B

ROTOR DYNAMICS AND WIND TUNNEL DATA

B.1 Large rotor dynamic data

Figure 62 shows the dynamic response of a T-motor U8-16 with a 30x10.5 propeller on 6S. PWM commands are given from 0 to 1000 μs which is full throttle. The maximum angular acceleration allowed by the Flame 60A ESC is 250 rad/s^2. This takes about 2 seconds to spin up from 0 to 100% throttle. During flight, the flight controller should not allow the rotor to stall as this may have detrimental effects on control. Figure 63 shows a stepped input instead of bang-bang inputs. These are particularly large rotors for hobby-grade multirotors.

B.2 Wind tunnel data

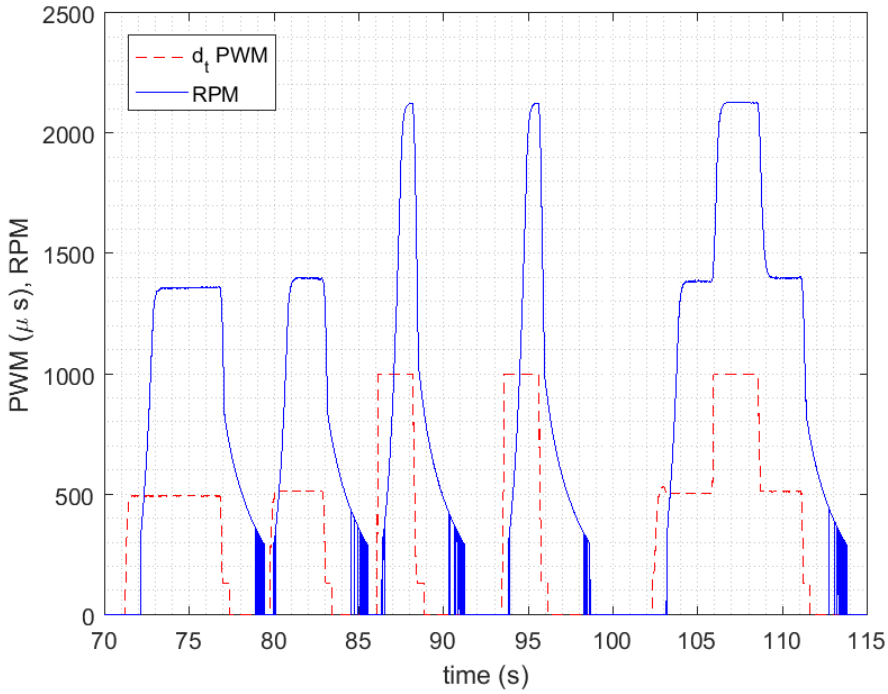

Figure 62: Dynamic response of U8-16 motor with T-motor 30x10.5 propeller, bang-bang inputs 0-50%, 50-100%, 0-100%, 100-0%, 50-0%

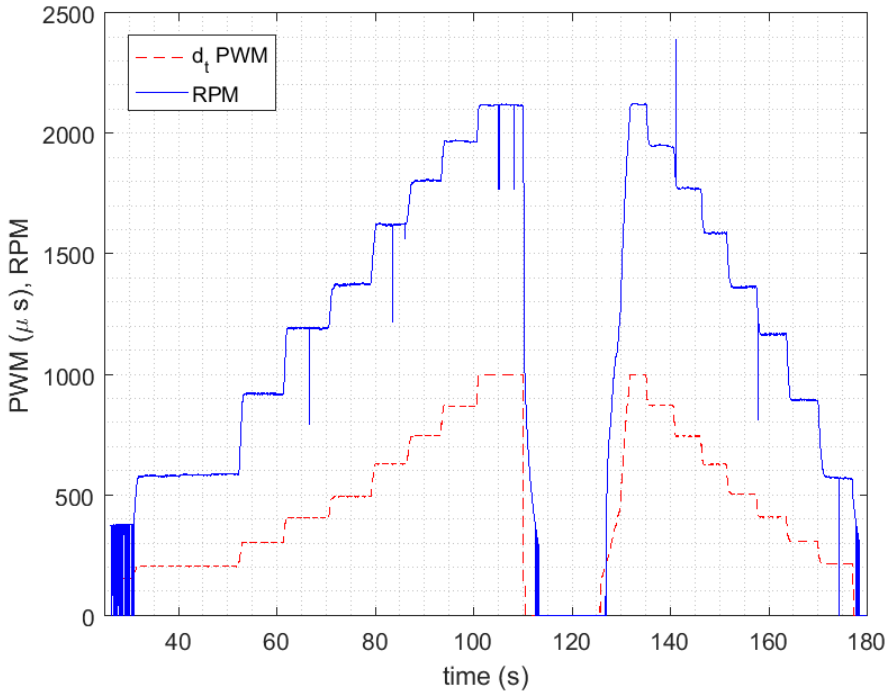

Figure 63: Dynamic response of U8-16 motor with T-motor 30x10.5 propeller with stepped inputs

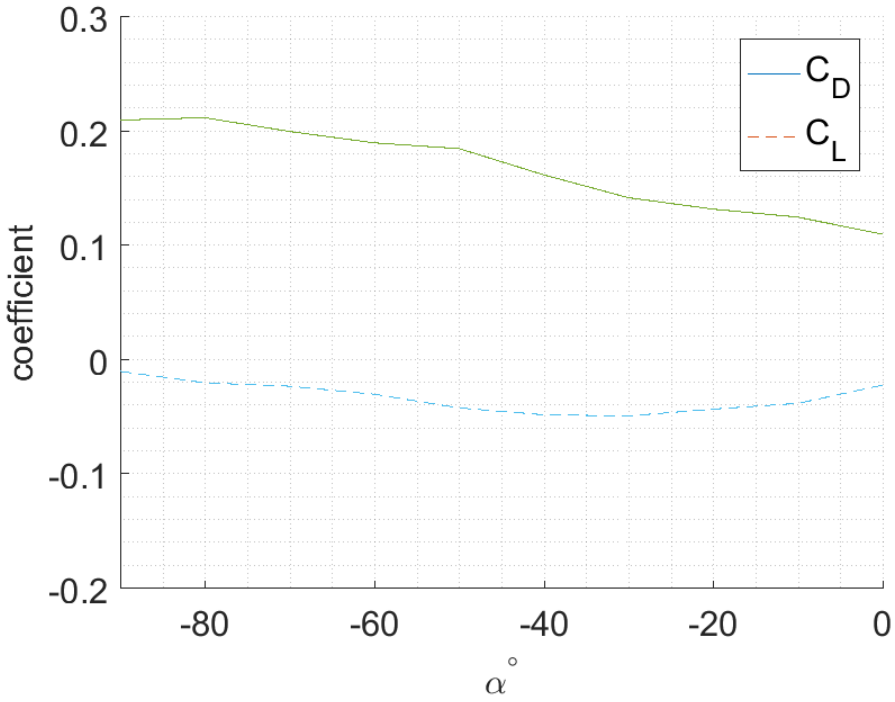

Figure 64: Drag and lift coefficients for generic 450 mm X frame, no propellers

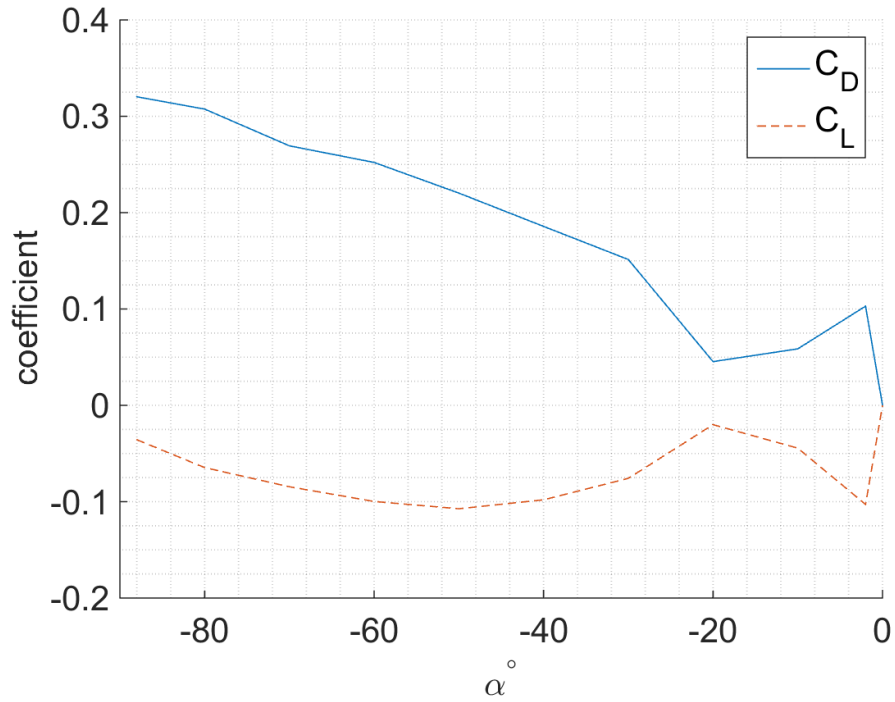

Figure 65: Drag and lift coefficients for RTF ZMR 250 mm X frame, no propellers

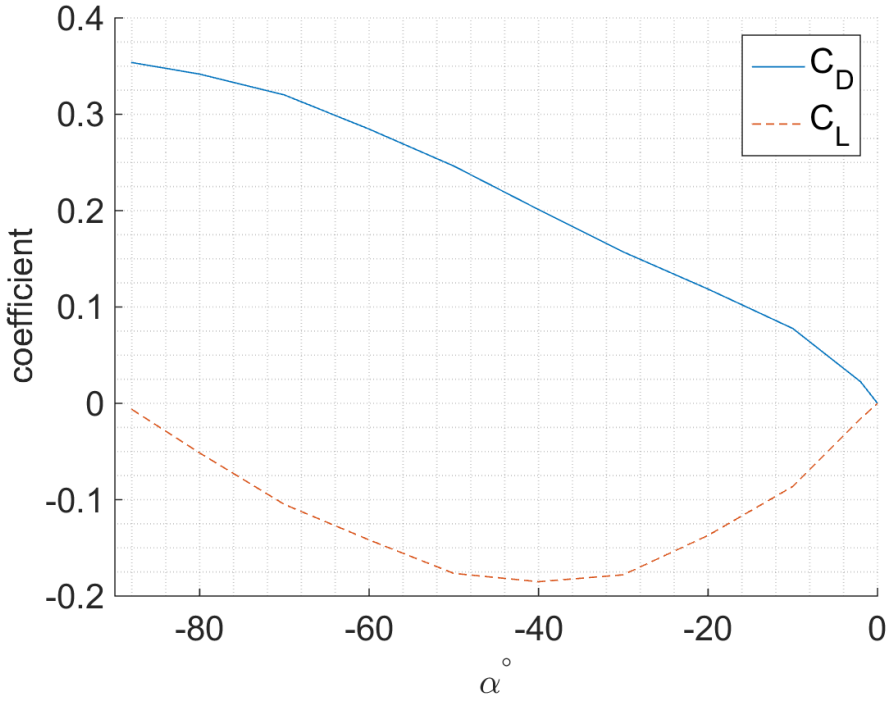

Figure 66: Drag and lift coefficients for bare ZMR 250 mm X frame, no propellers

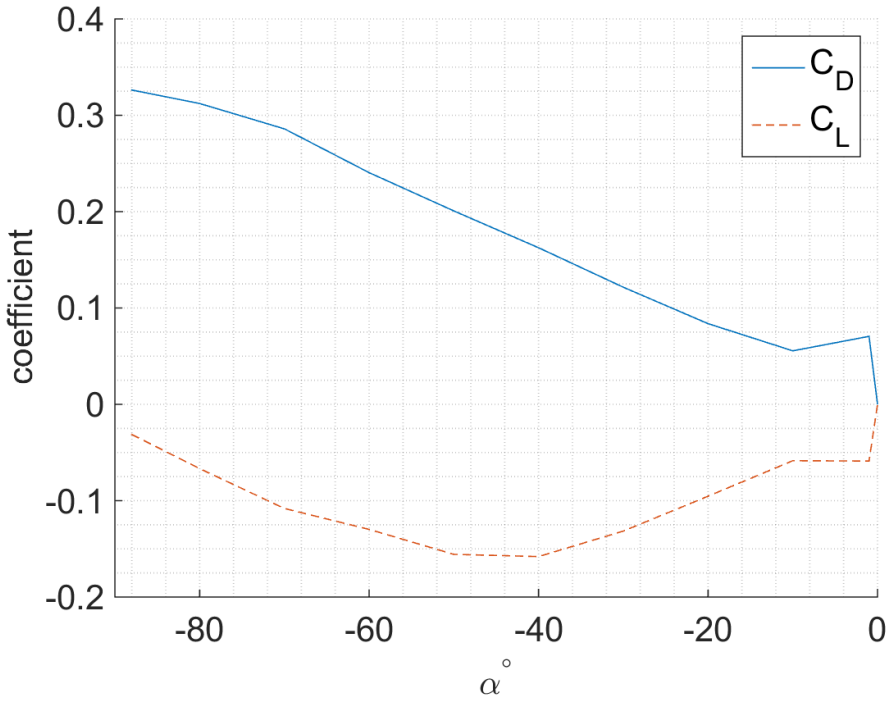

Figure 67: Drag and lift coefficients for TBS Vendetta 250 mm H frame [151]

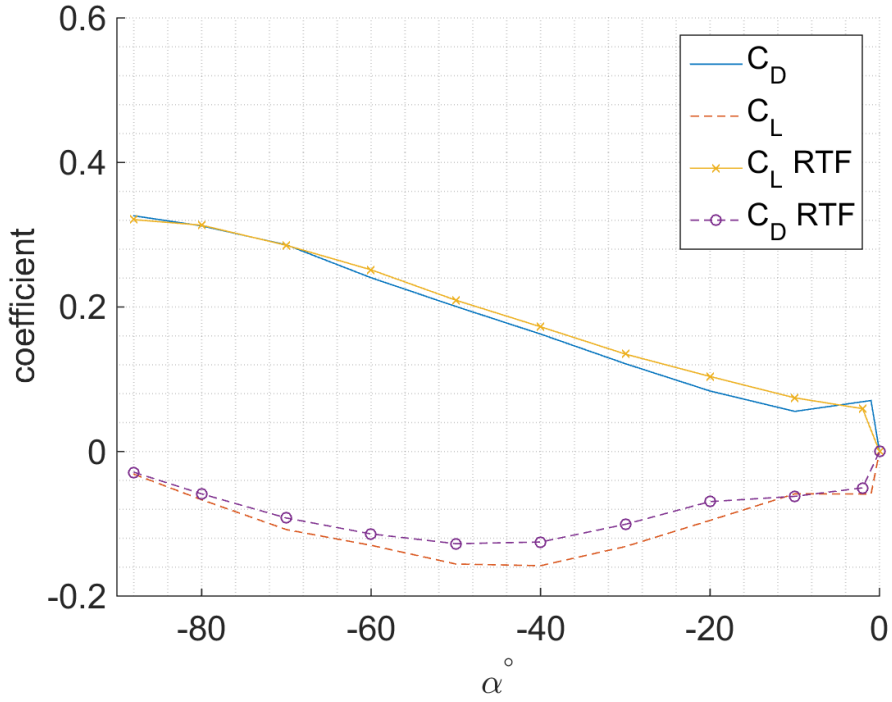

Figure 68: Drag and lift coefficients for bare vs RTF Vendetta 250 mm X frame, no propellers

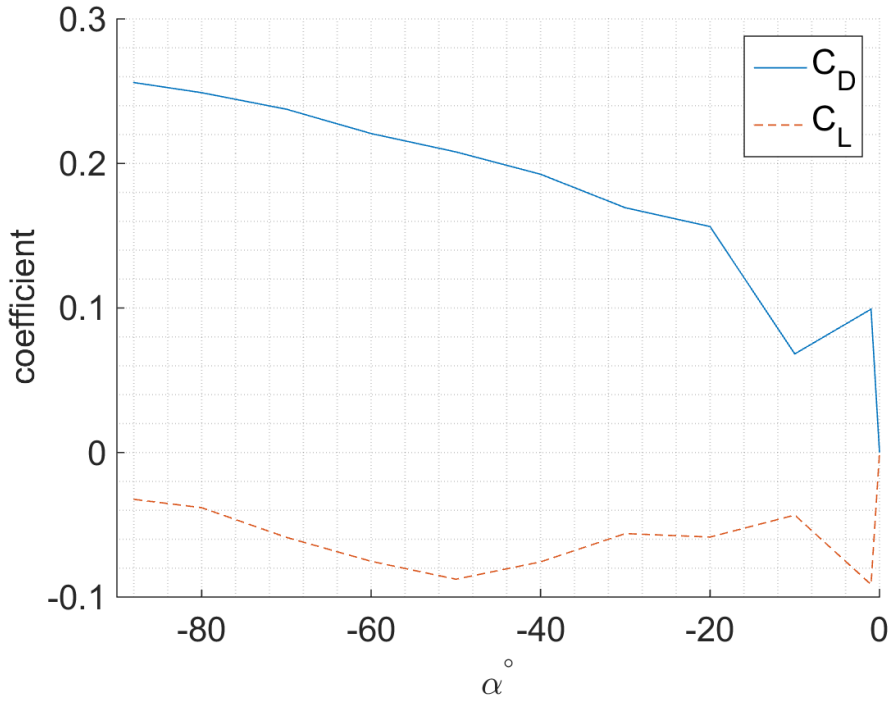

Figure 69: Drag and lift coefficients Shrike 250 mm X frame, no propellers

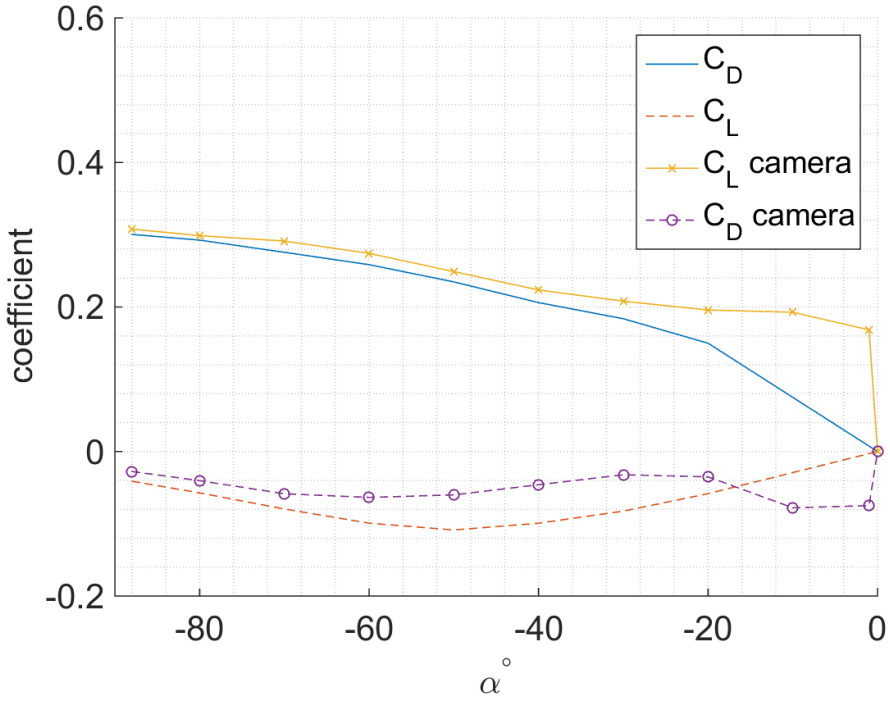

Figure 70: Drag and lift coefficients for Hoku 250 mm X frame with and without HD camera, no propellers

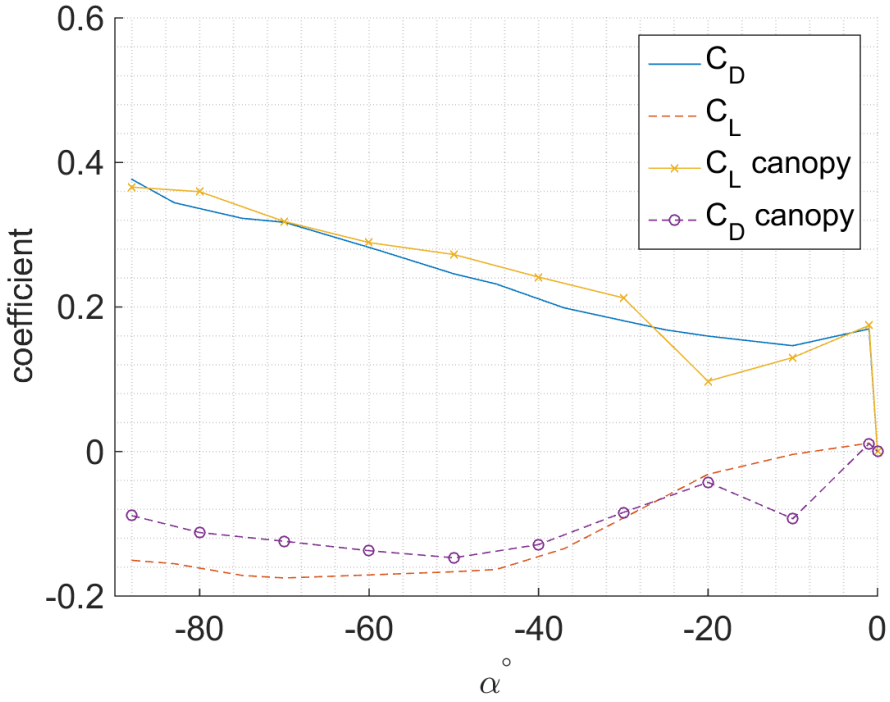

Figure 71: Drag and lift coefficients for Atom 122 mm X frame with and without canopy, no propellers

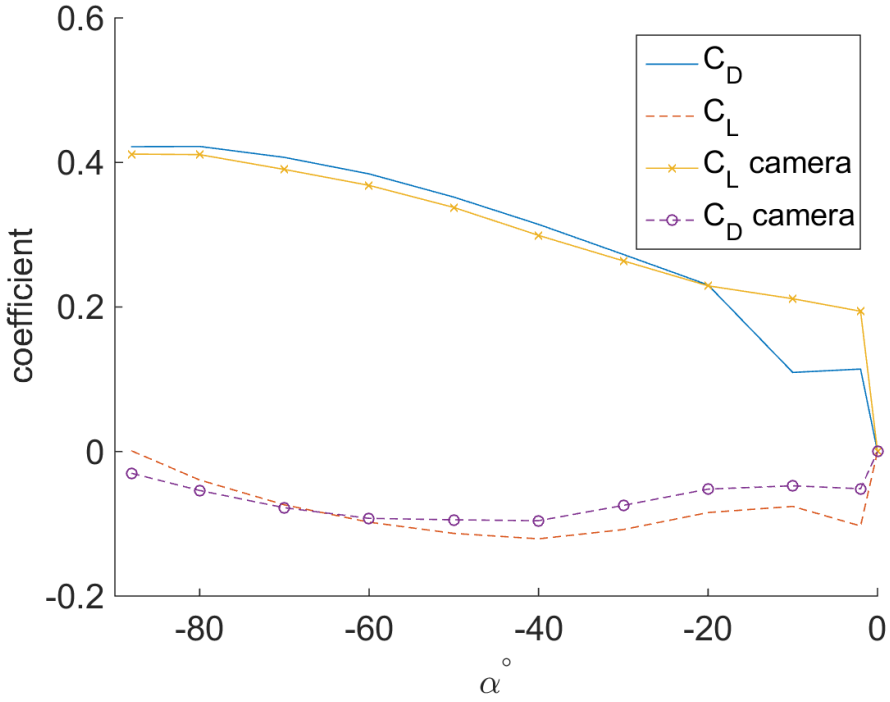

Figure 72: Drag and lift coefficients for Charpu 210 mm X frame with and without HD camera, no propellers

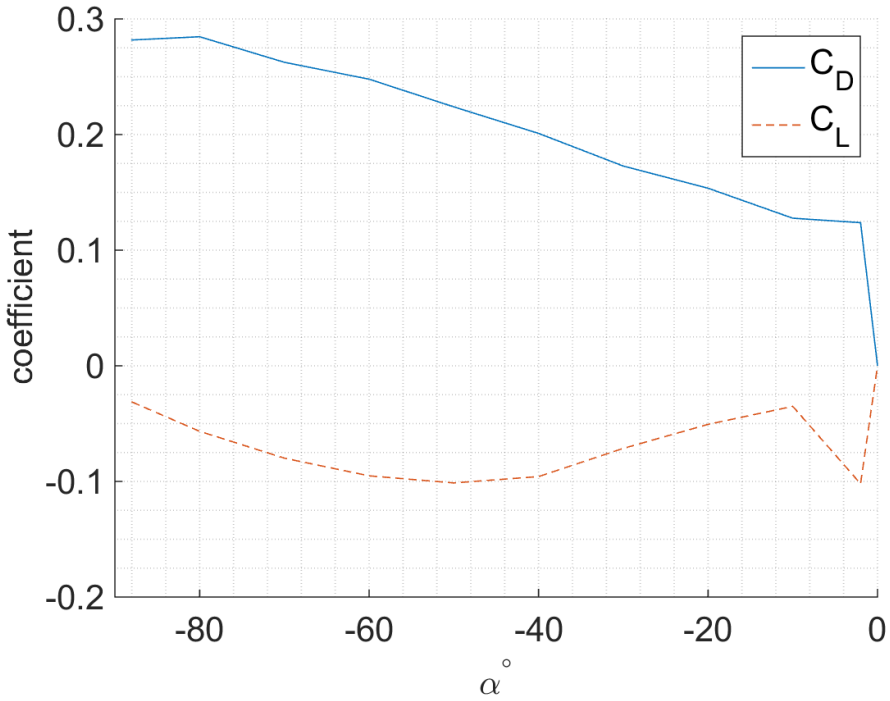

Figure 73: Drag and lift coefficients for Alien 250 mm X frame, no propellers

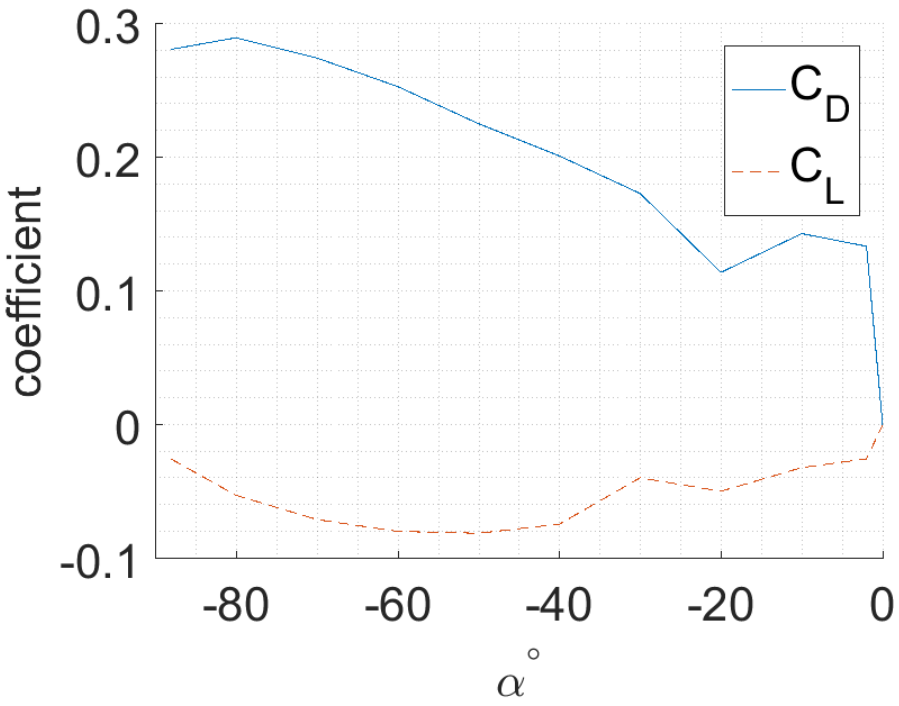

Figure 74: Drag and lift coefficients for Alien 250 mm X frame with HD camera, no propellers

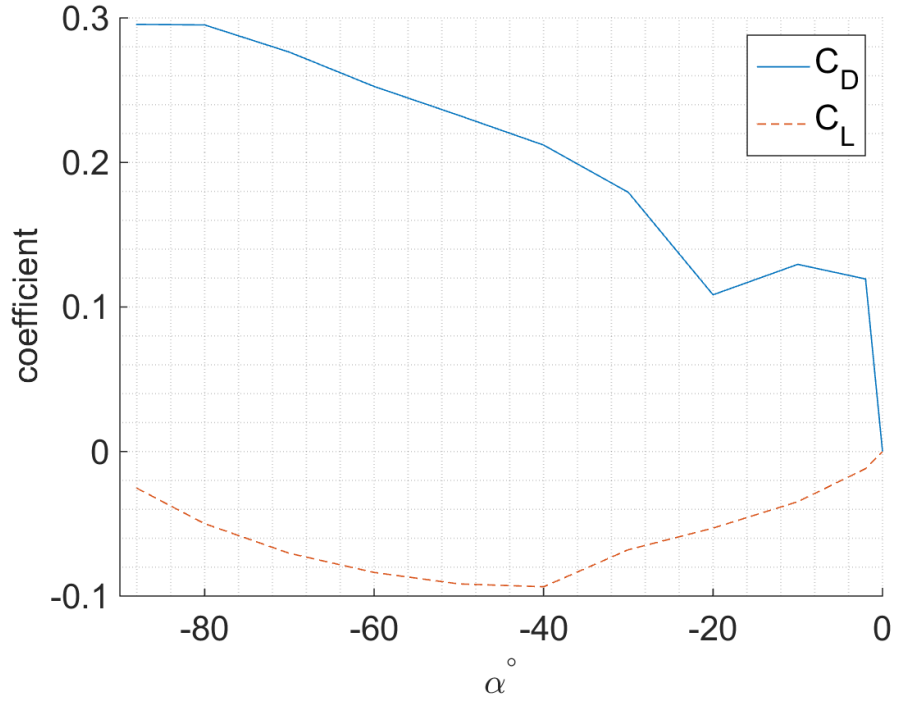

Figure 75: Drag and lift coefficients for Alien 250 mm X frame with 5.8 cased antenna, no propellers

APPENDIX C

DESIGN LOOKUP TABLES FOR ζ, ϵ

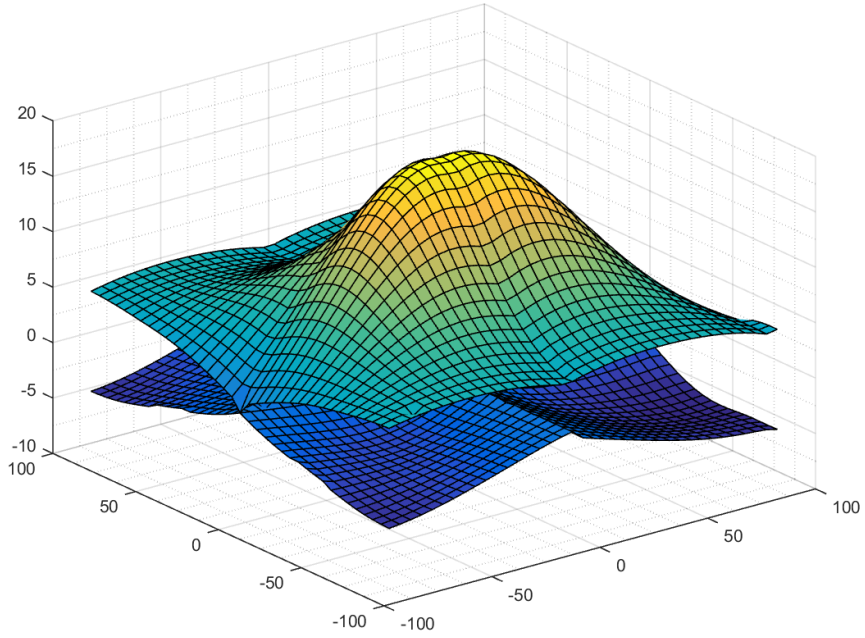

Figure 76: *+4* $\dot{p}$ design space, pure motion not enforced, M1 fault

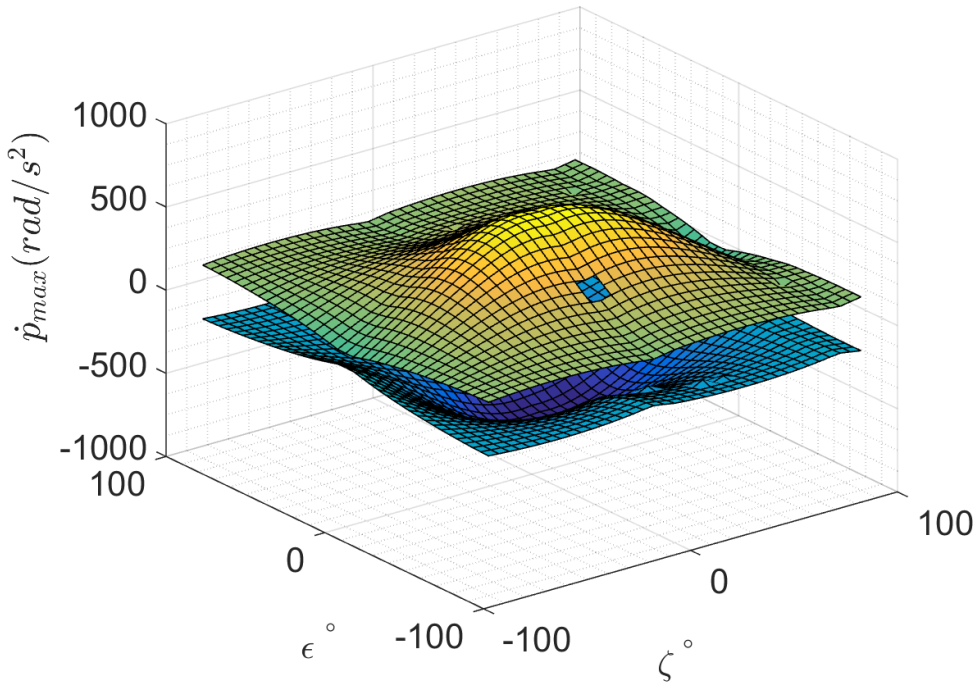

Figure 77: *+4* $\dot{p}$ design space, pure motion not enforced, no rotor faults

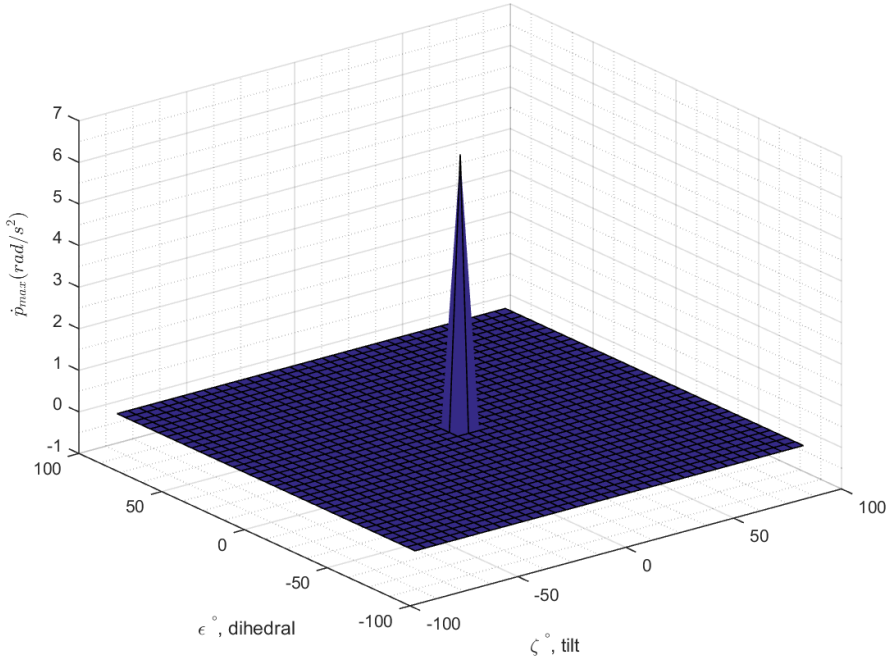

Figure 78: *+4* $\dot{p}$ design space, pure motion enforced, M1 fault

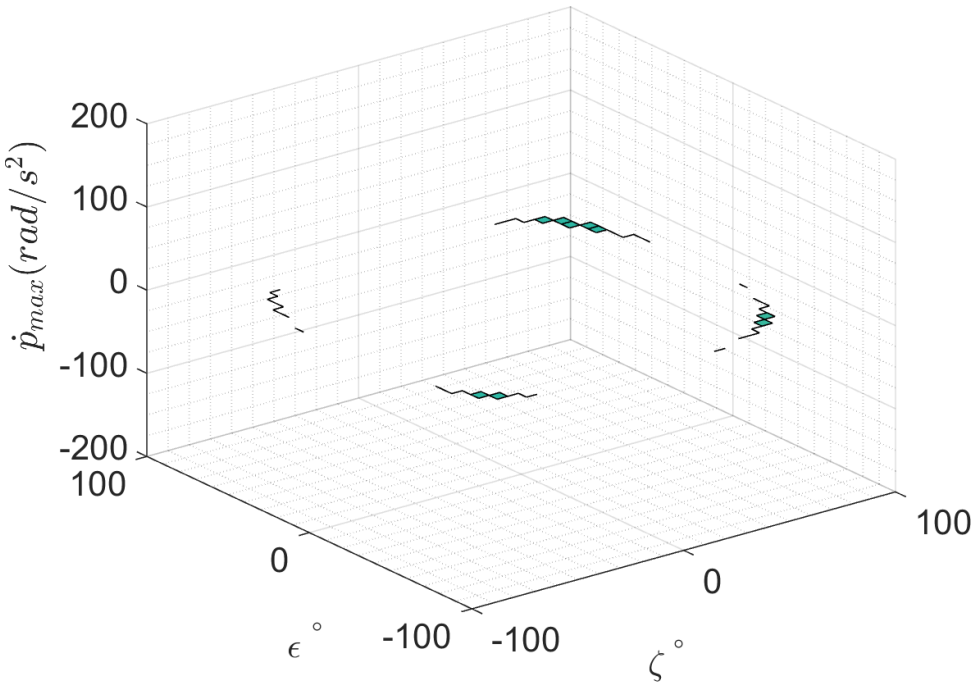

Figure 79: *+4* $\dot{p}$ design space, pure motion enforced, no rotor faults

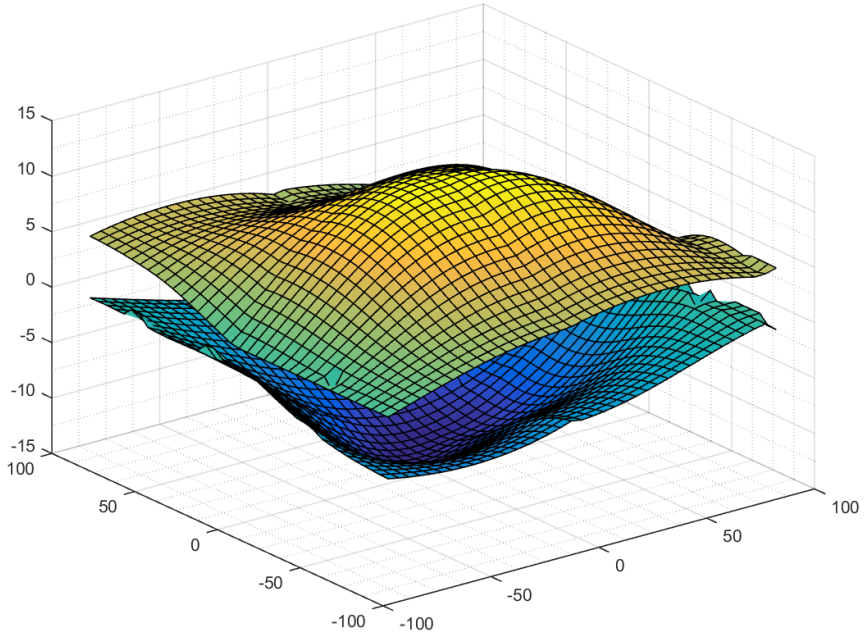

Figure 80: *+4* $\dot{q}$ design space, pure motion not enforced, M1 fault

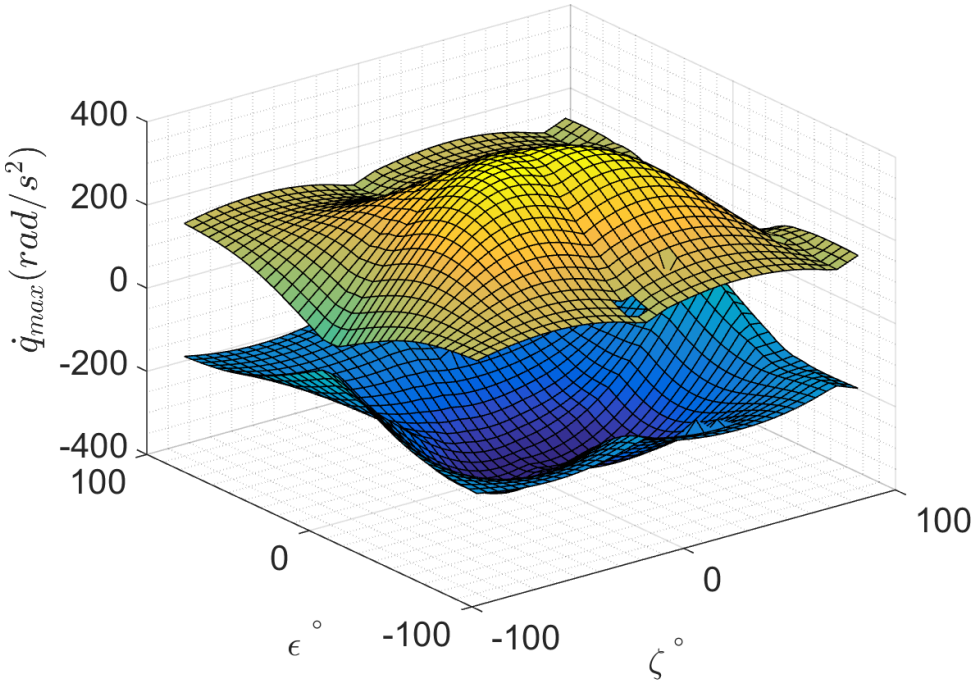

Figure 81: *+4* $\dot{q}$ design space, pure motion not enforced, no rotor faults

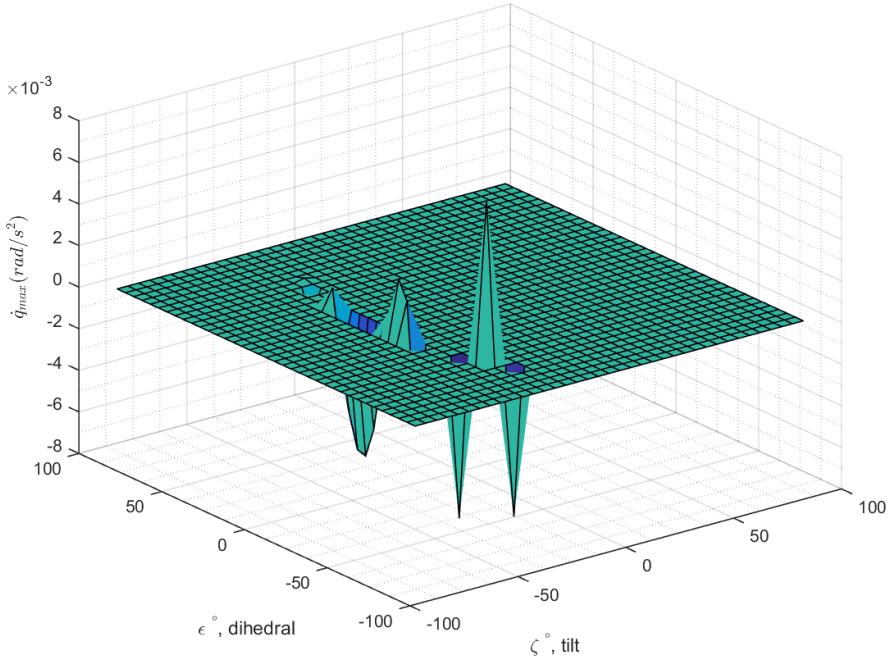

Figure 82: *+4* $\dot{q}$ design space, pure motion enforced, M1 fault

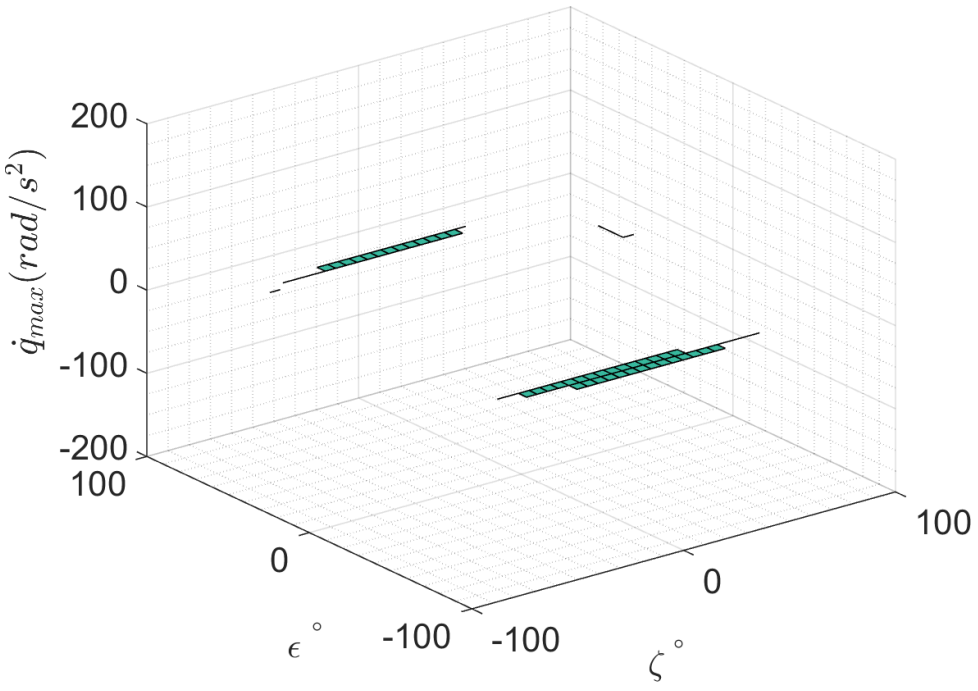

Figure 83: *+4* $\dot{q}$ design space, pure motion enforced, no rotor faults

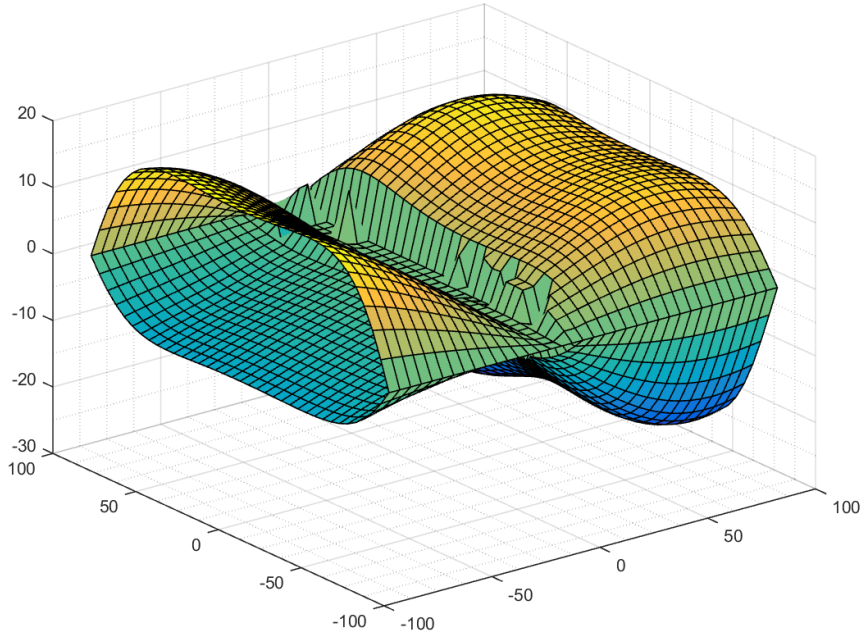

Figure 84: *+4* $\dot{r}$ design space, pure motion not enforced, M1 fault

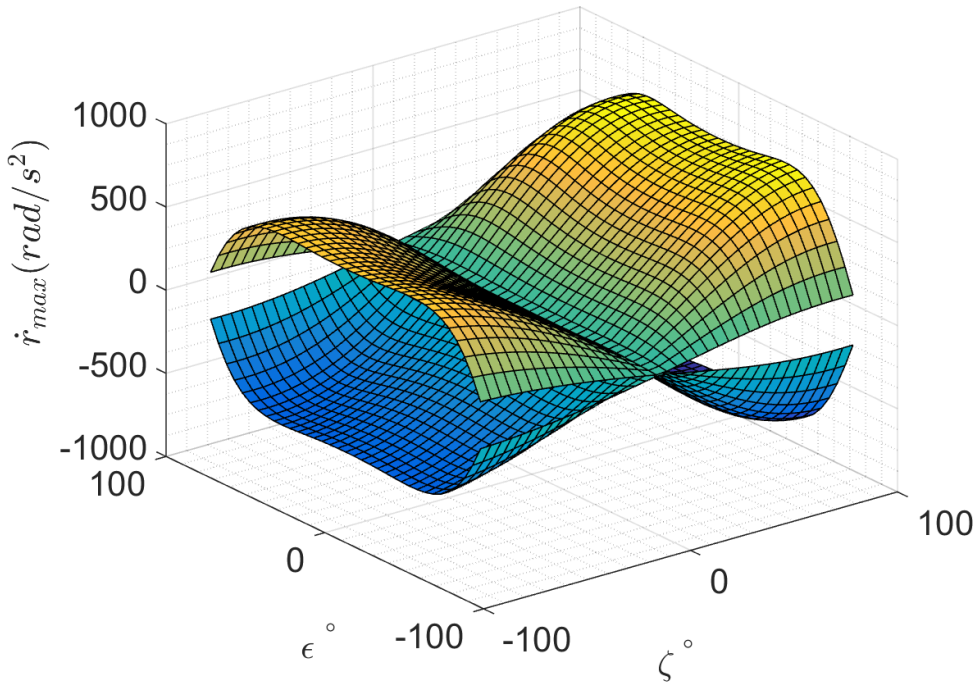

Figure 85: *+4* $\dot{r}$ design space, pure motion not enforced, no rotor faults

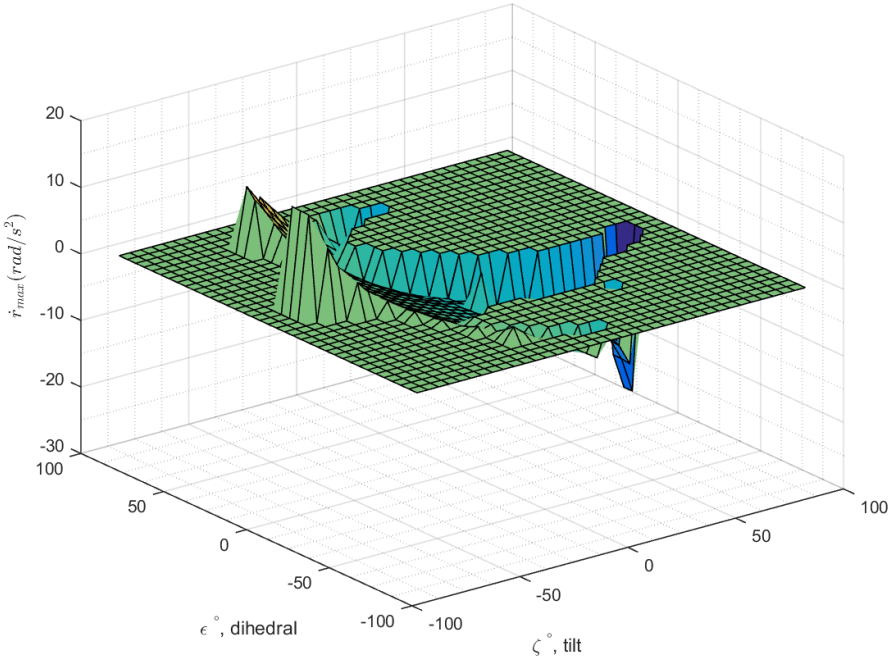

Figure 86: *+4* $\dot{r}$ design space, pure motion enforced, M1 fault

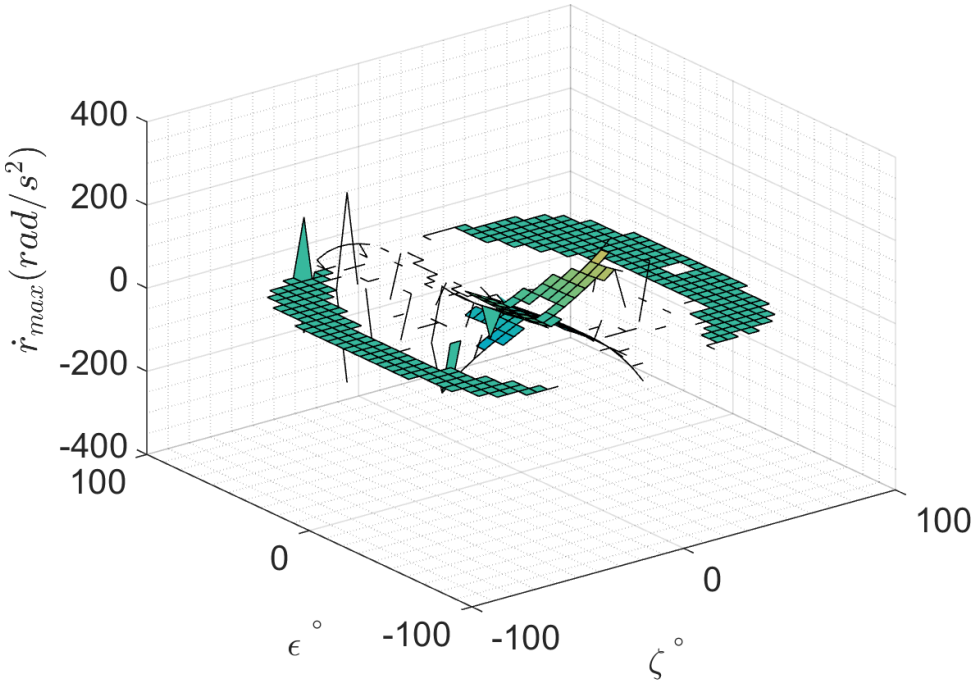

Figure 87: *+4* $\dot{r}$ design space, pure motion enforced, no rotor faults

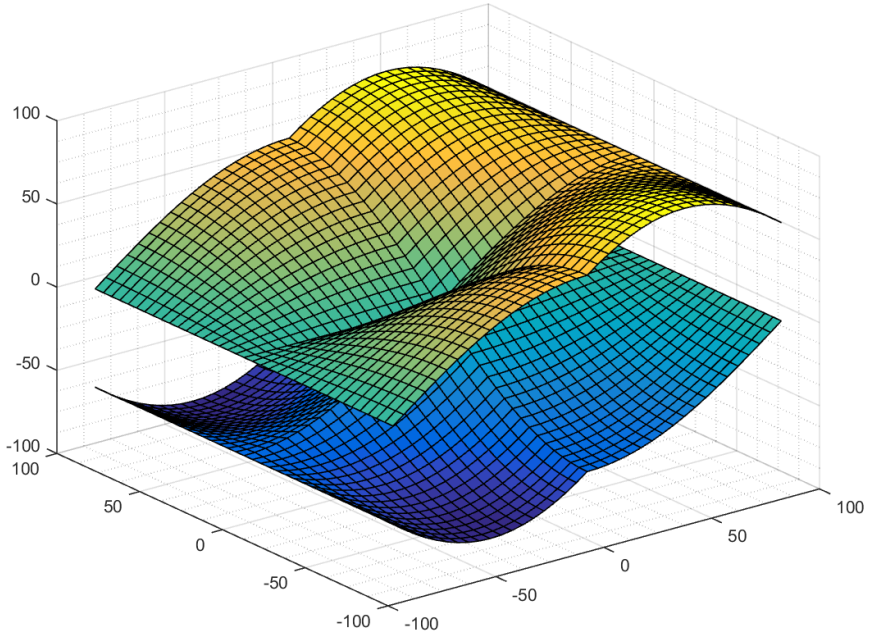

Figure 88: *+4* $\ddot{x}$ design space, pure motion not enforced, M1 fault

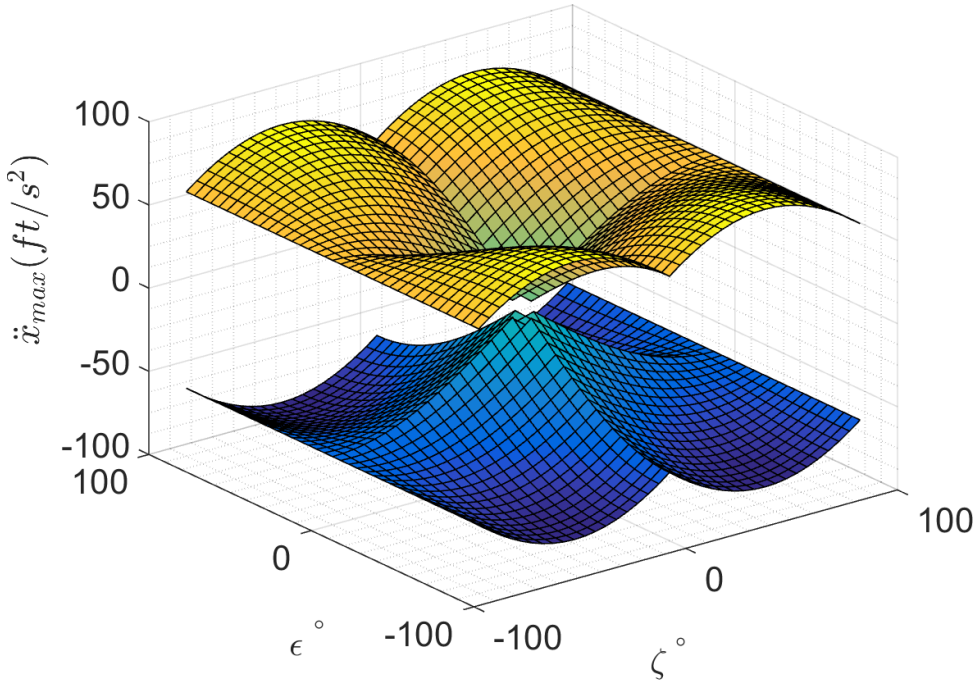

Figure 89: *+4* $\ddot{x}$ design space, pure motion not enforced, no rotor faults

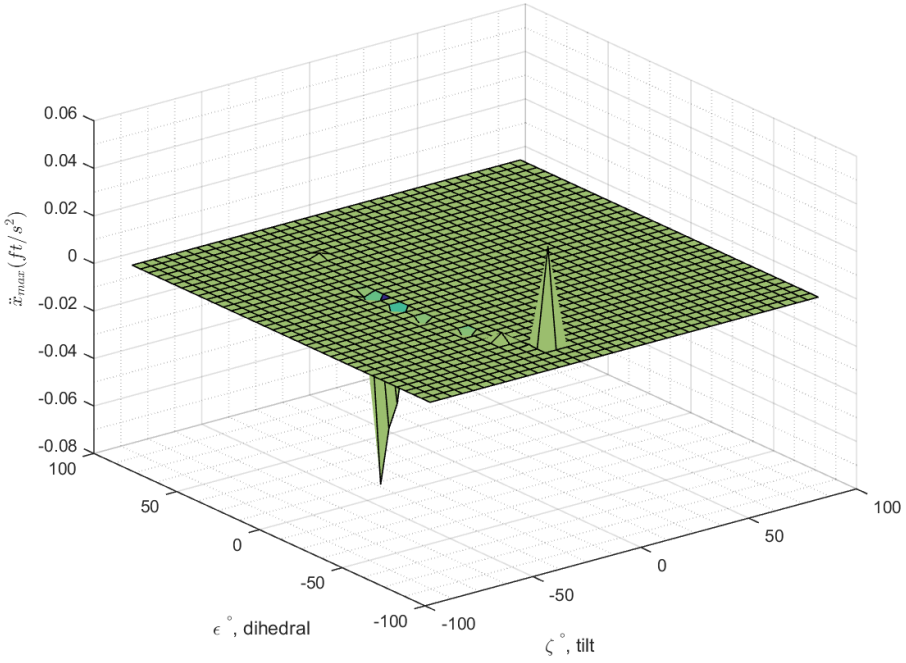

Figure 90: *+4* $\ddot{x}$ design space, pure motion enforced, M1 fault

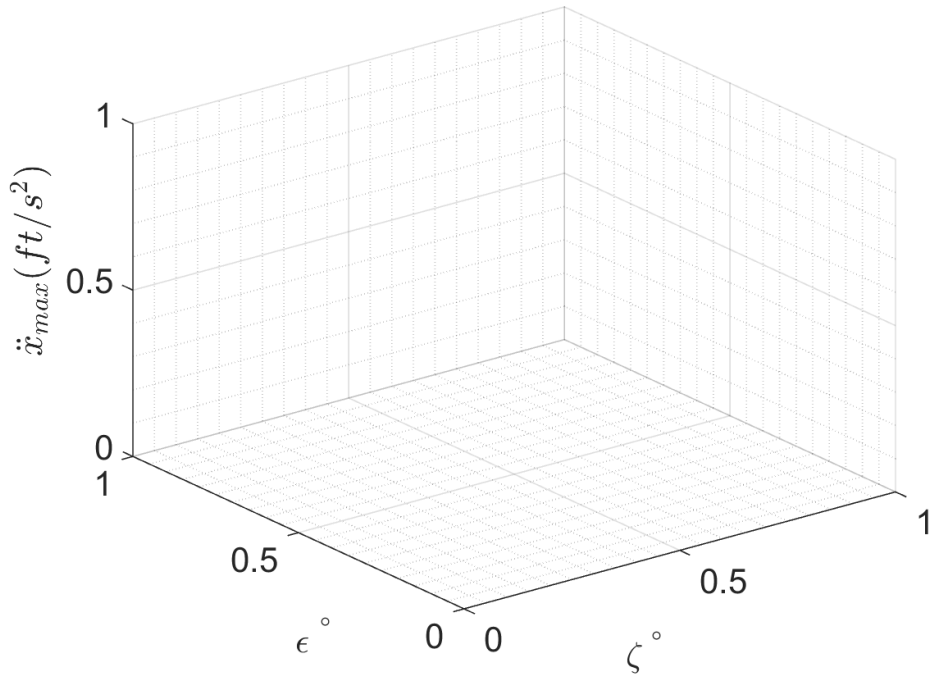

Figure 91: *+4* $\ddot{x}$ design space, pure motion enforced, no rotor faults

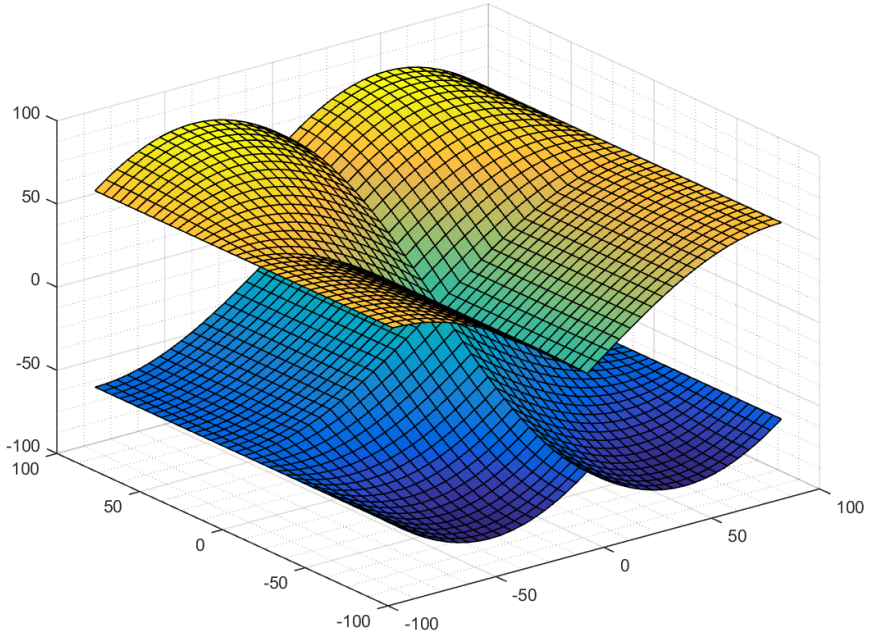

Figure 92: *+4 $\ddot{y}$* design space, pure motion not enforced, M1 fault

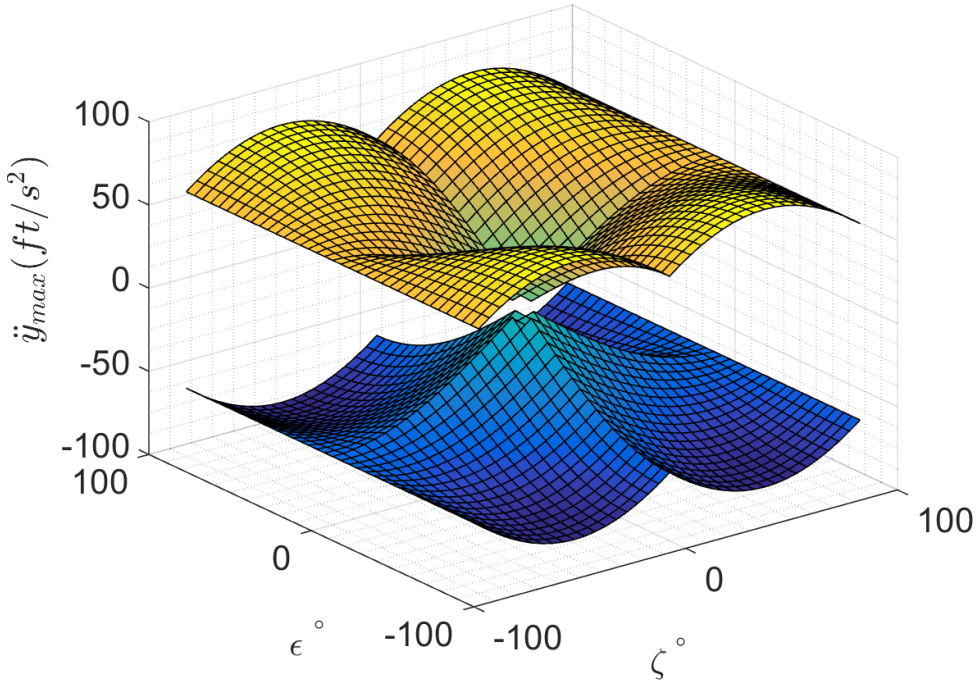

Figure 93: *+4 $\ddot{y}$* design space, pure motion not enforced, no rotor faults

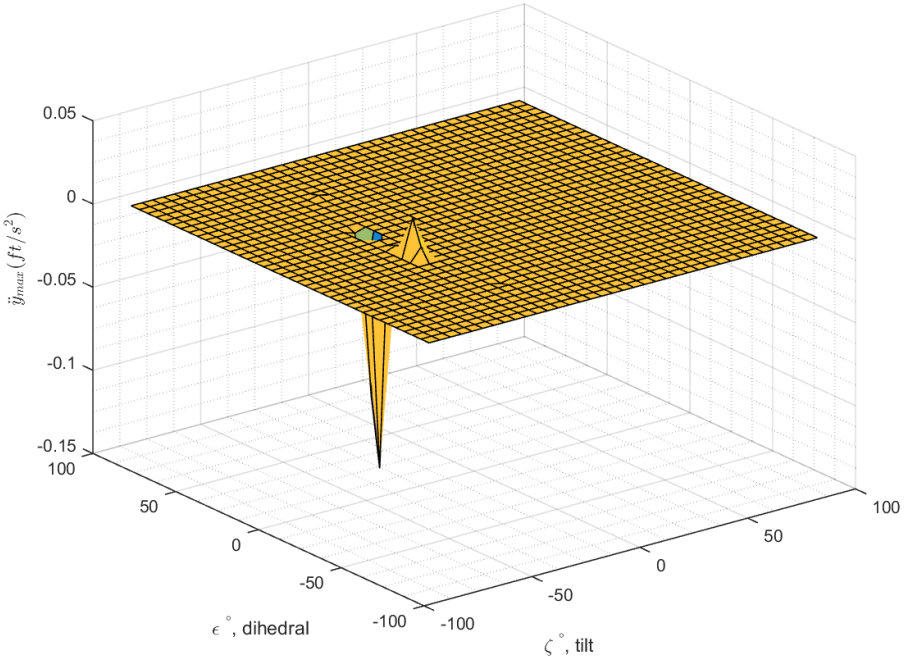

Figure 94: *+4 $\ddot{y}$* design space, pure motion enforced, M1 fault

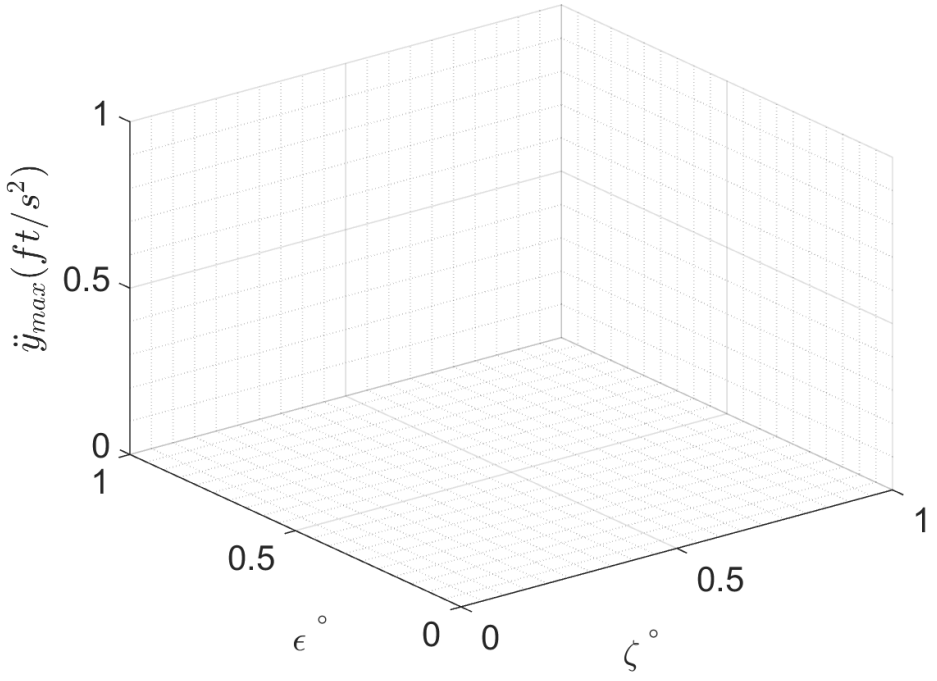

Figure 95: *+4 $\ddot{y}$* design space, pure motion enforced, no rotor faults

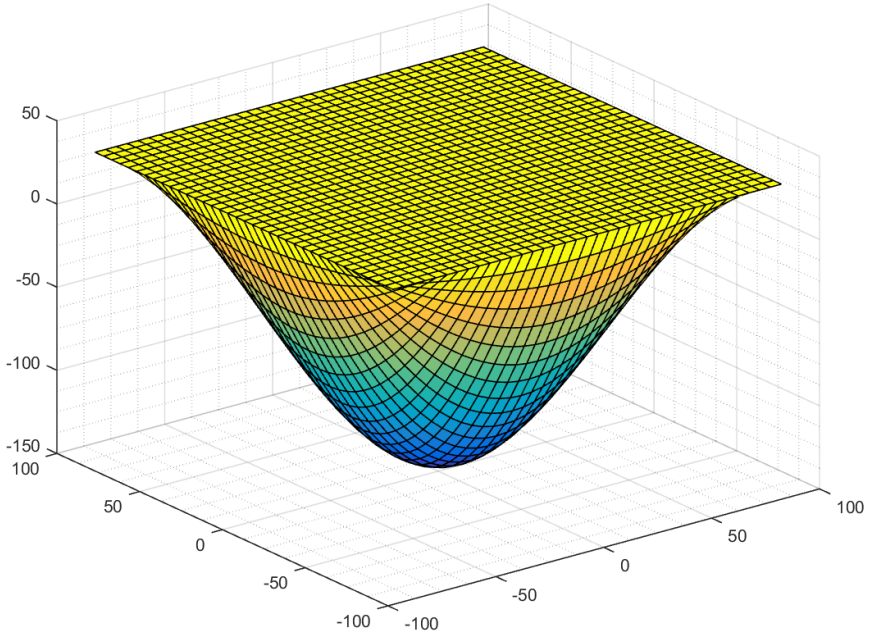

Figure 96: *+4* $\ddot{z}$ design space, pure motion not enforced, M1 fault

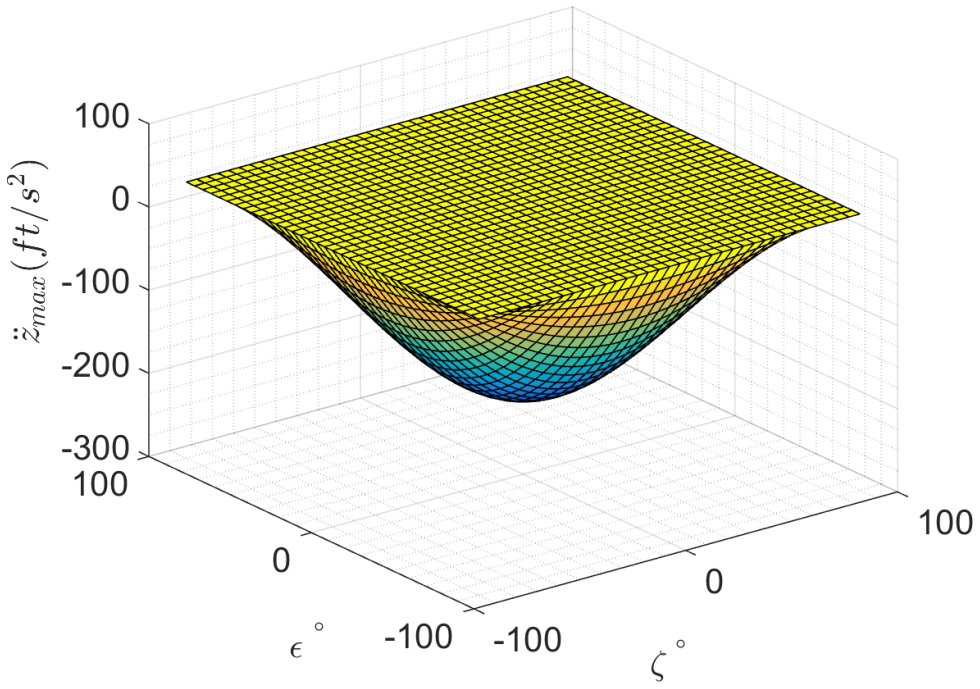

Figure 97: *+4* $\ddot{z}$ design space, pure motion not enforced, no rotor faults

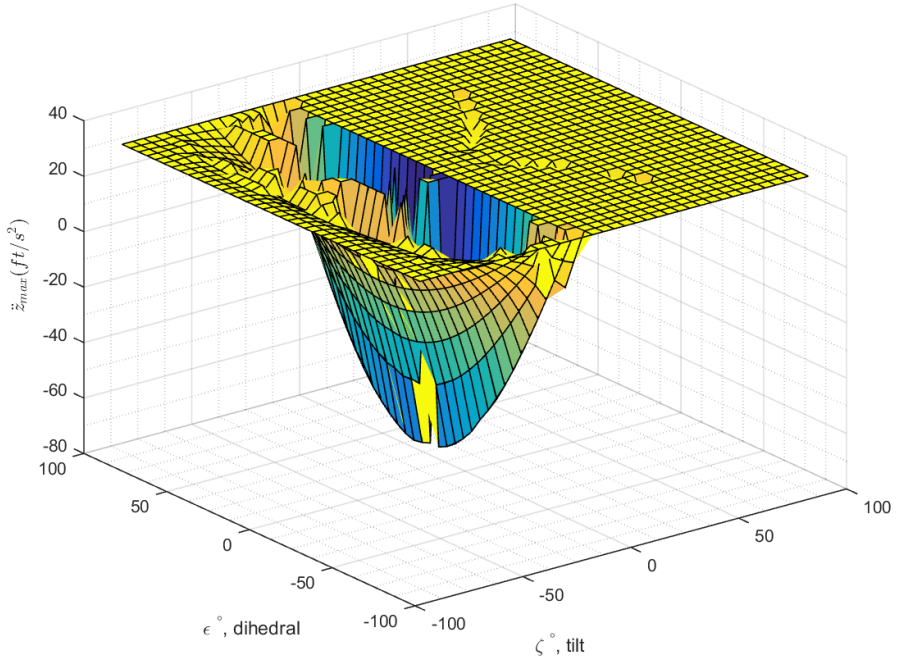

Figure 98: *+4* $\ddot{z}$ design space, pure motion enforced, M1 fault

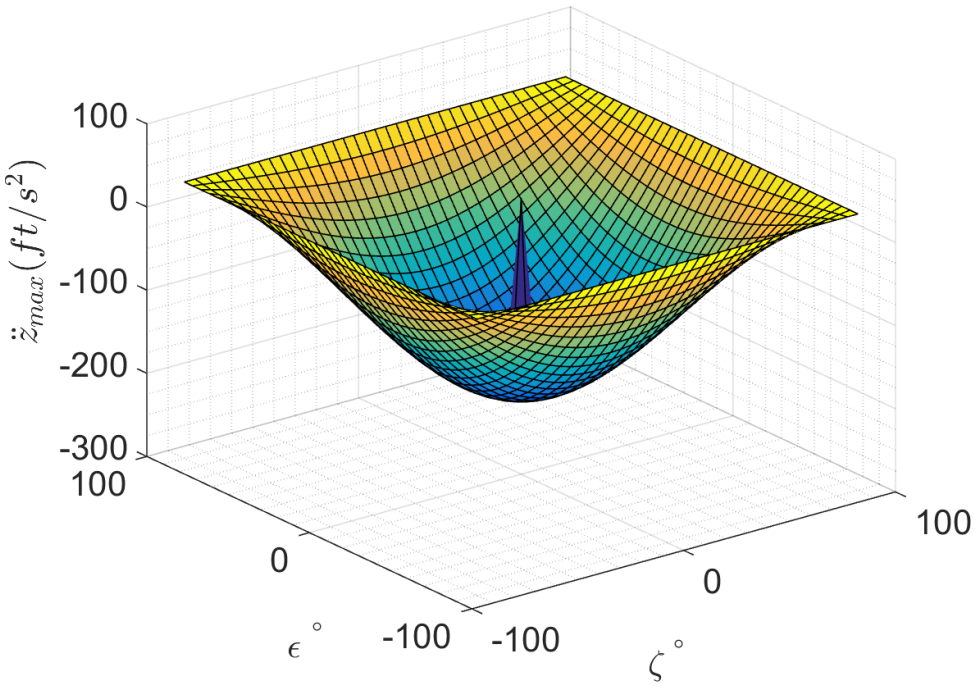

Figure 99: *+4* $\ddot{z}$ design space, pure motion enforced, no rotor faults

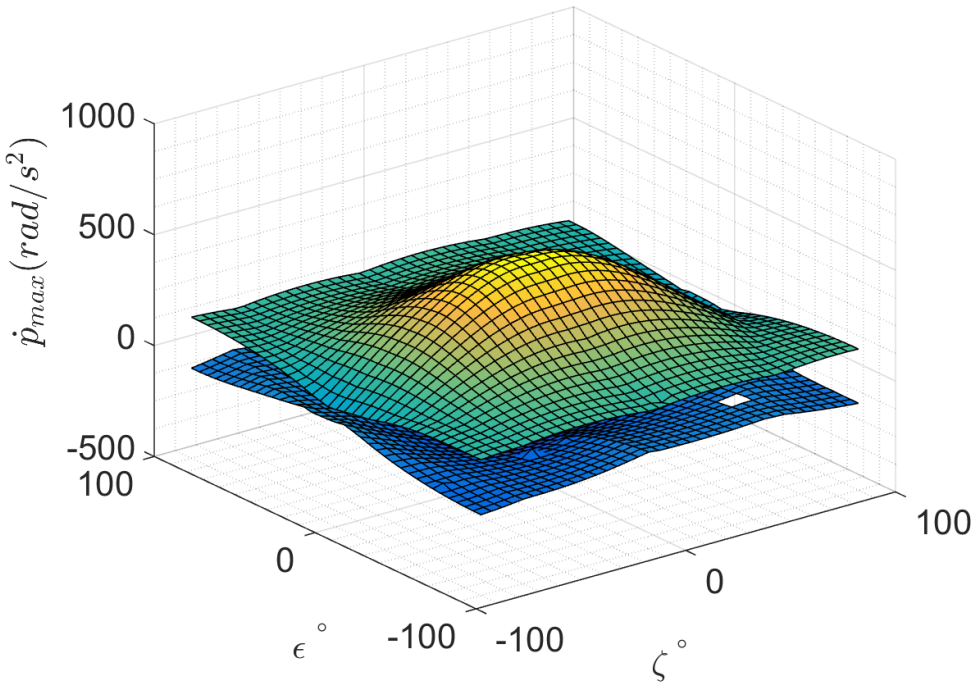

Figure 100: *+6 $\dot{p}$* design space, pure motion not enforced, M1 fault

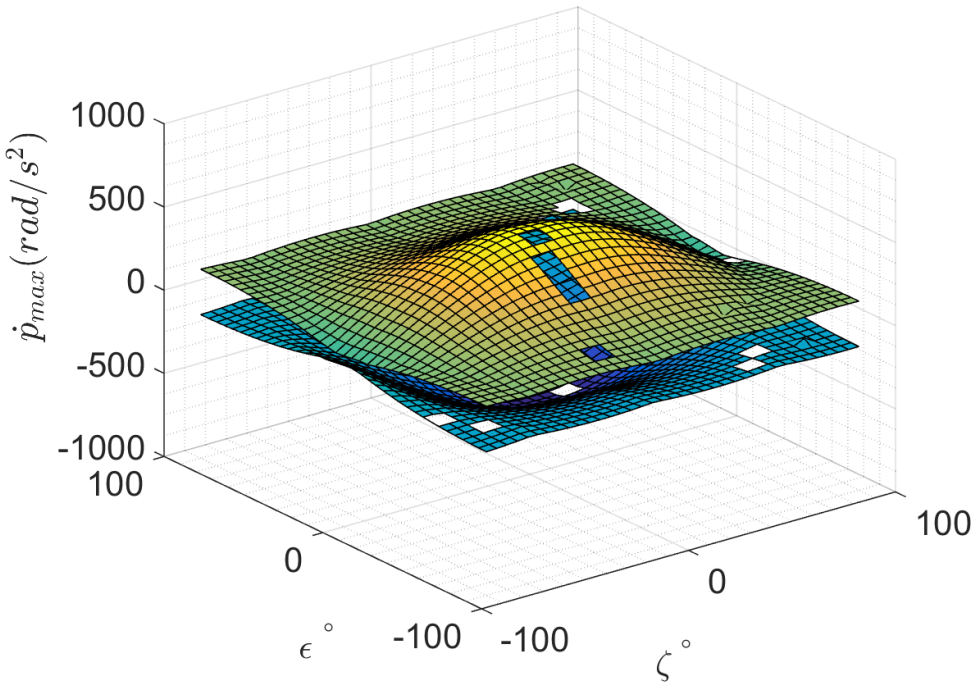

Figure 101: *+6 $\dot{p}$* design space, pure motion not enforced, no rotor faults

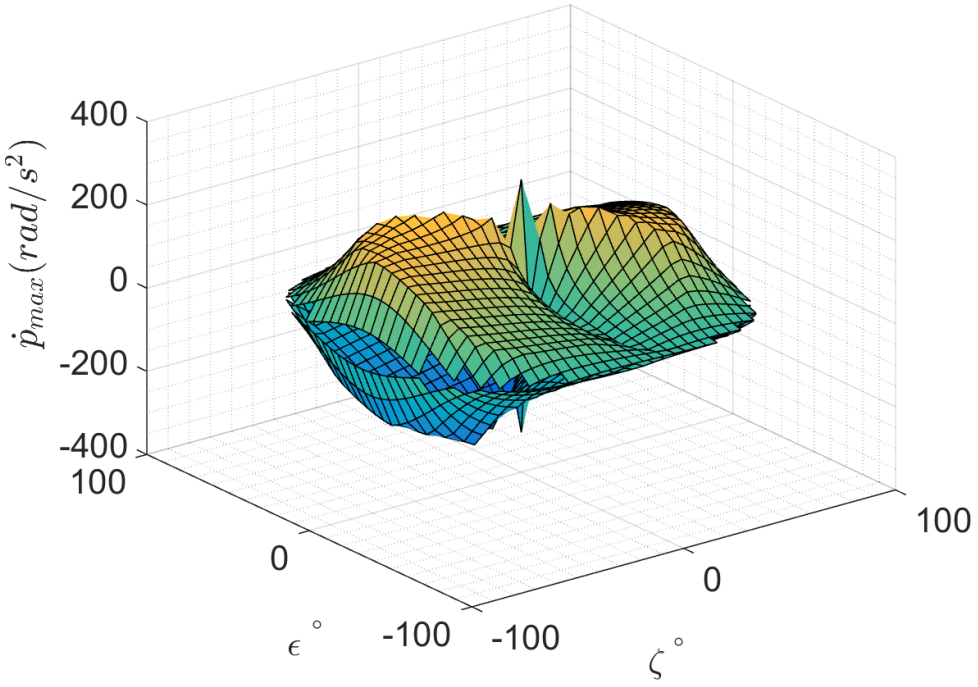

Figure 102: *+6 $\dot{p}$* design space, pure motion enforced, no rotor faults

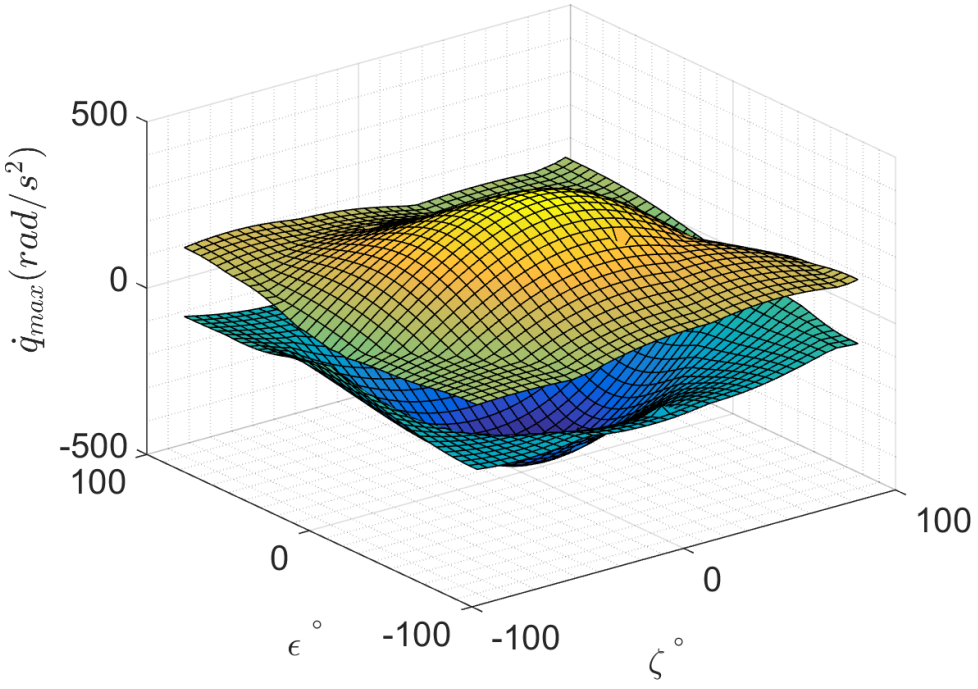

Figure 103: *+6 $\dot{q}$* design space, pure motion not enforced, M1 fault

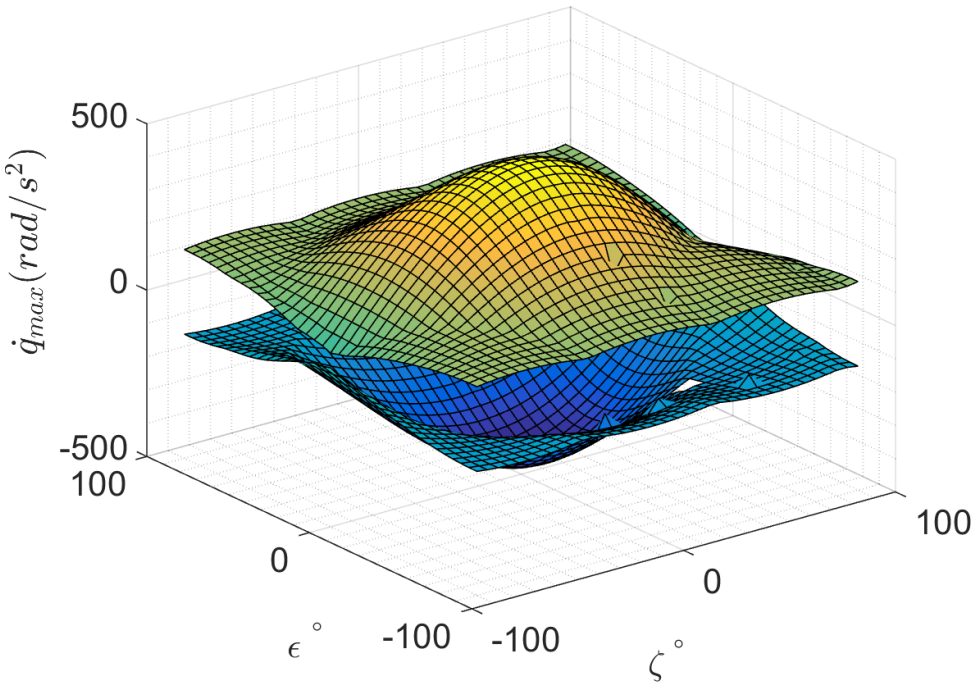

Figure 104: *+6 $\dot{q}$* design space, pure motion not enforced, no rotor faults

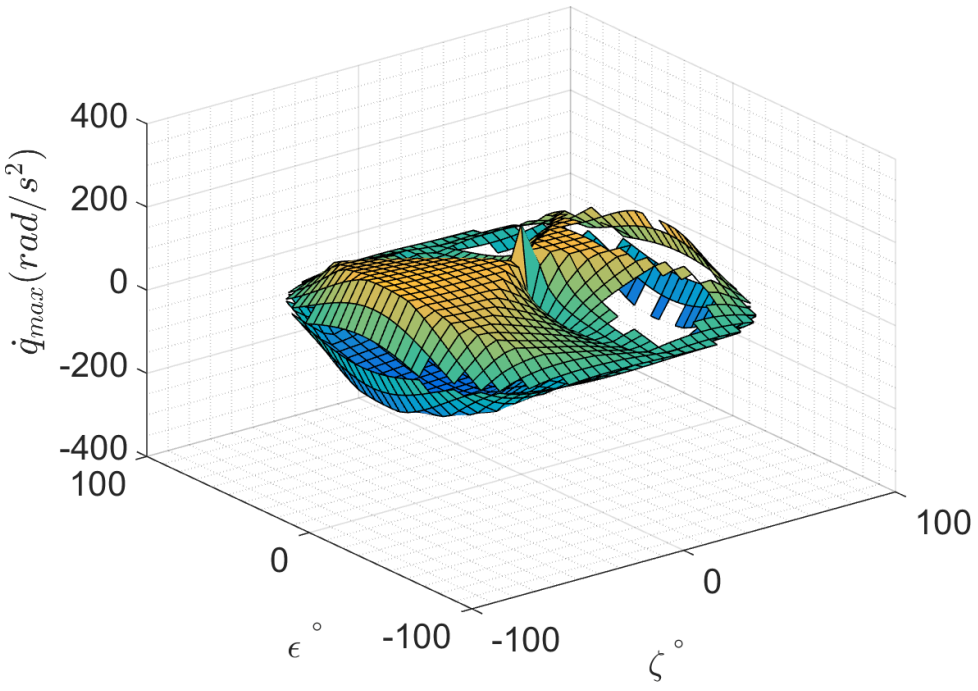

Figure 105: *+6 $\dot{q}$* design space, pure motion enforced, no rotor faults

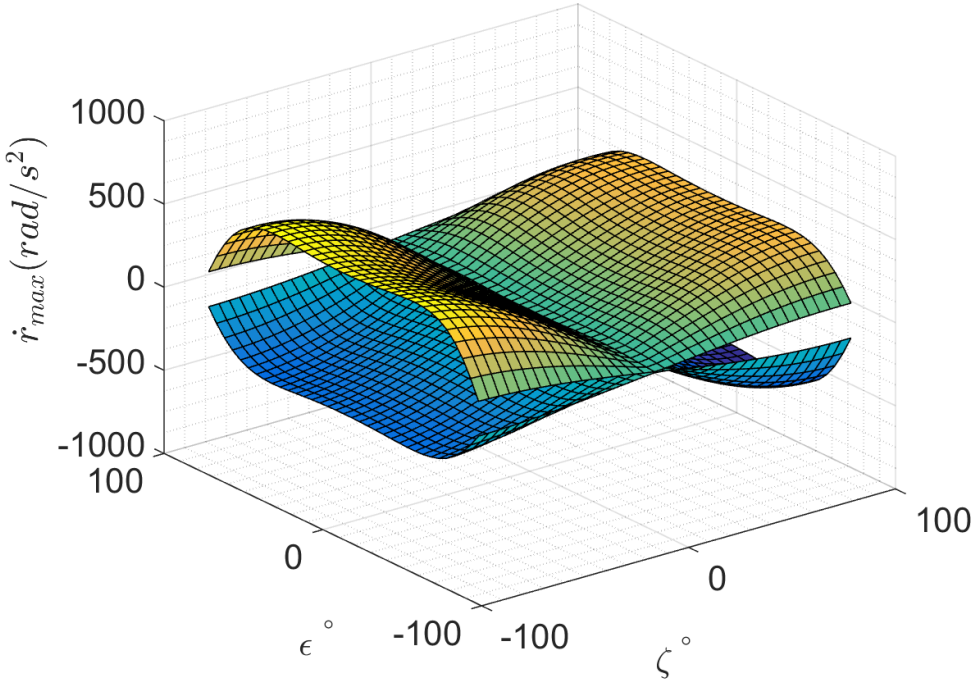

Figure 106: *+6 $\dot{r}$* design space, pure motion not enforced, M1 fault

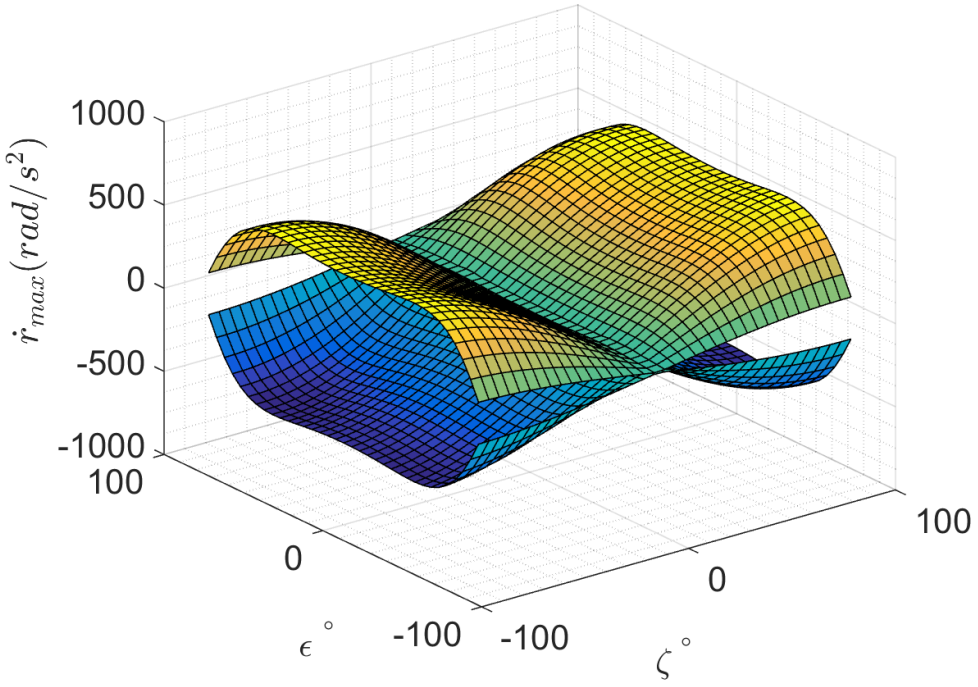

Figure 107: *+6 $\dot{r}$* design space, pure motion not enforced, no rotor faults

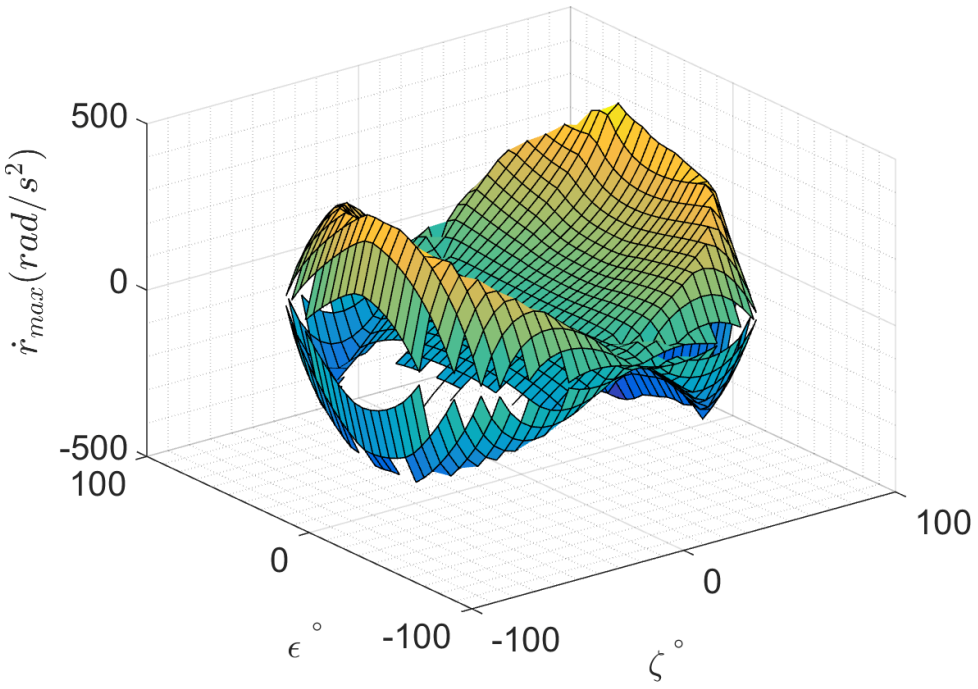

Figure 108: *+6* $\dot{r}$ design space, pure motion enforced, no rotor faults

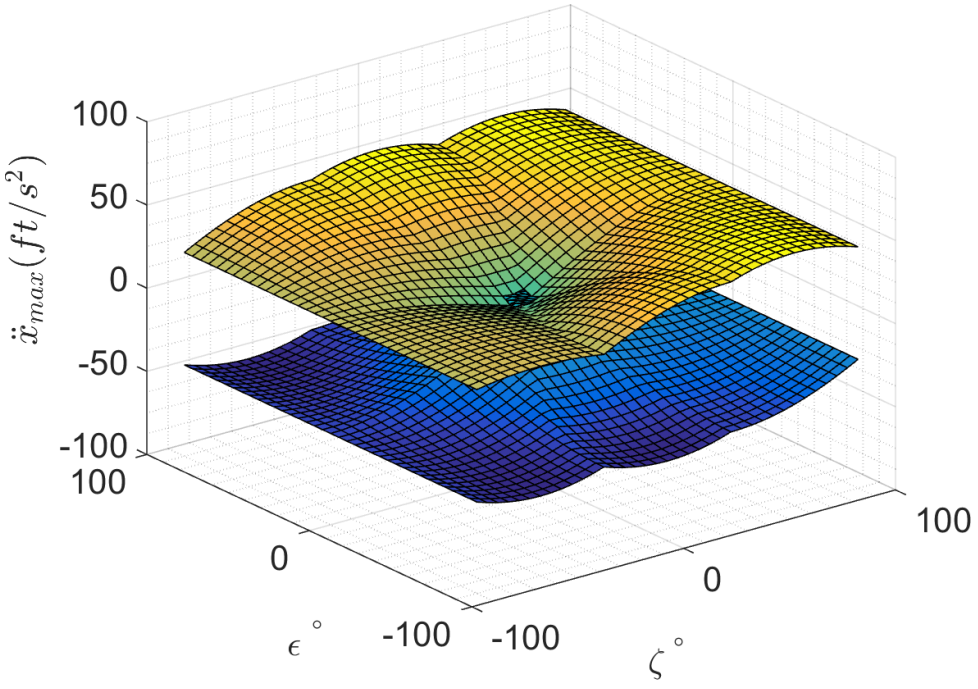

Figure 109: *+6* $\ddot{x}$ design space, pure motion not enforced, M1 fault

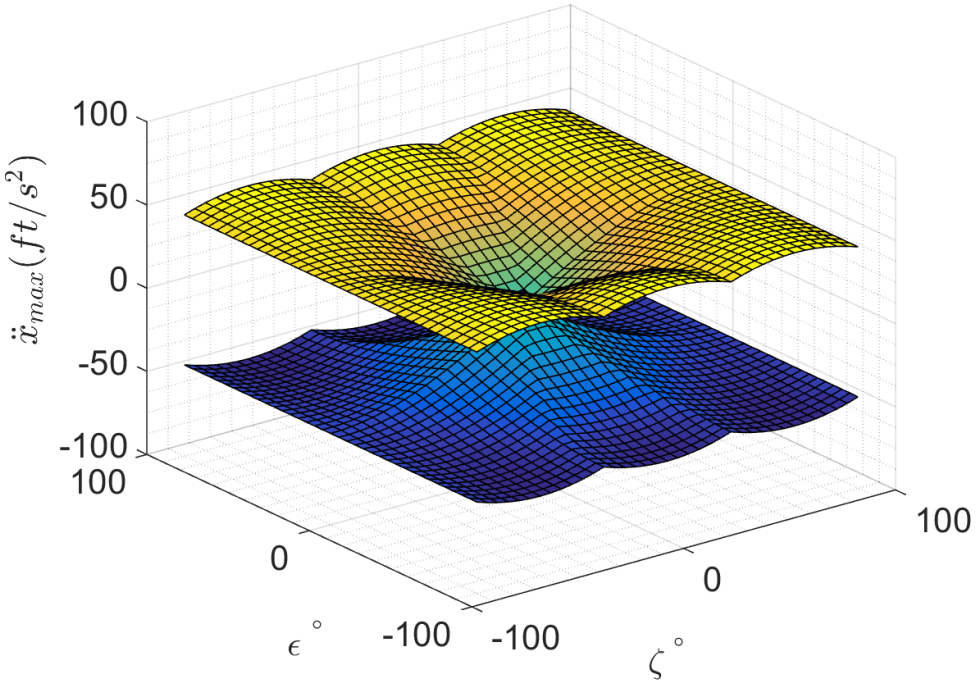

Figure 110: *+6* $\ddot{x}$ design space, pure motion not enforced, no rotor faults

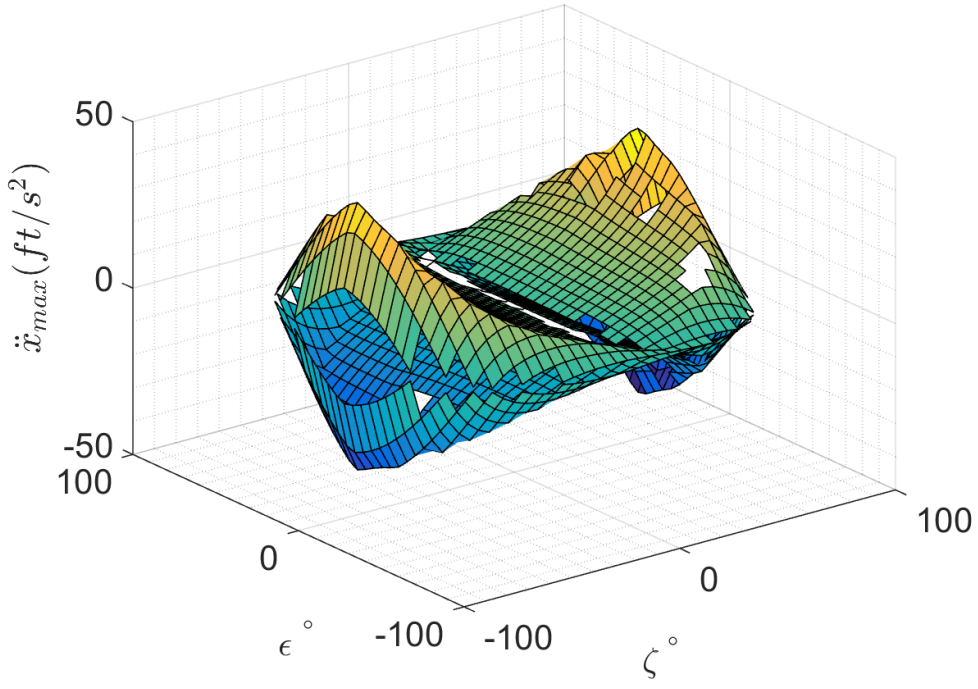

Figure 111: *+6* $\ddot{x}$ design space, pure motion enforced, no rotor faults

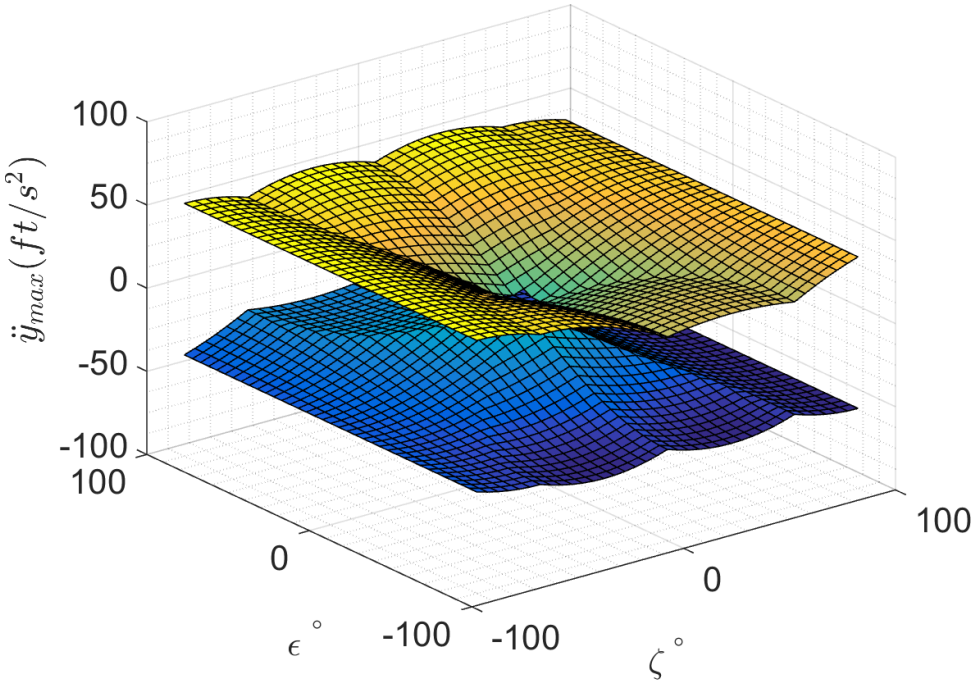

Figure 112: *+6 $\ddot{y}$* design space, pure motion not enforced, M1 fault

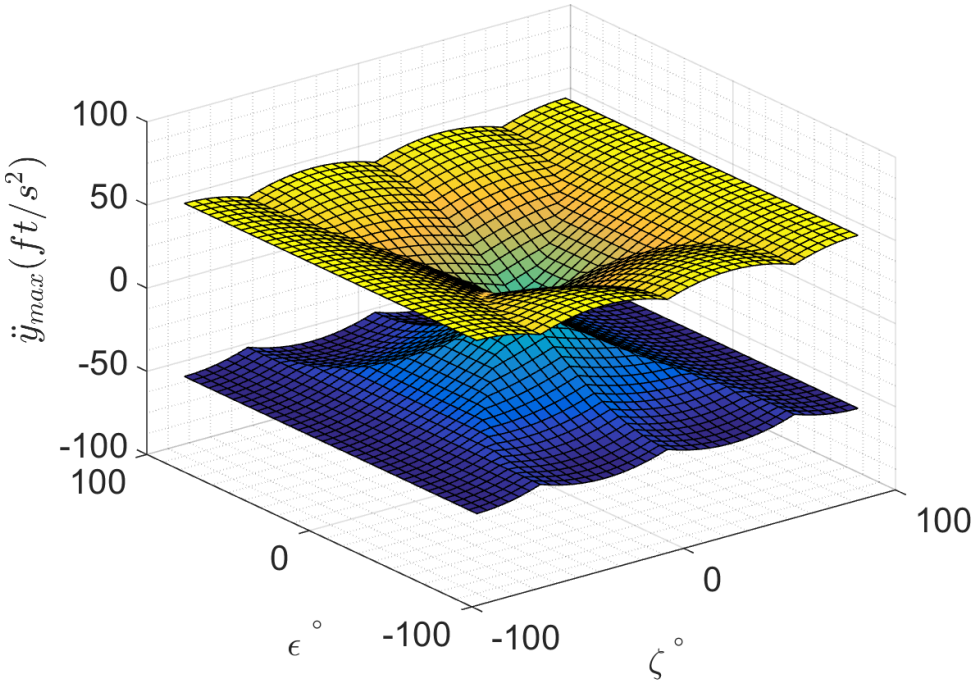

Figure 113: *+6 $\ddot{y}$* design space, pure motion not enforced, no rotor faults

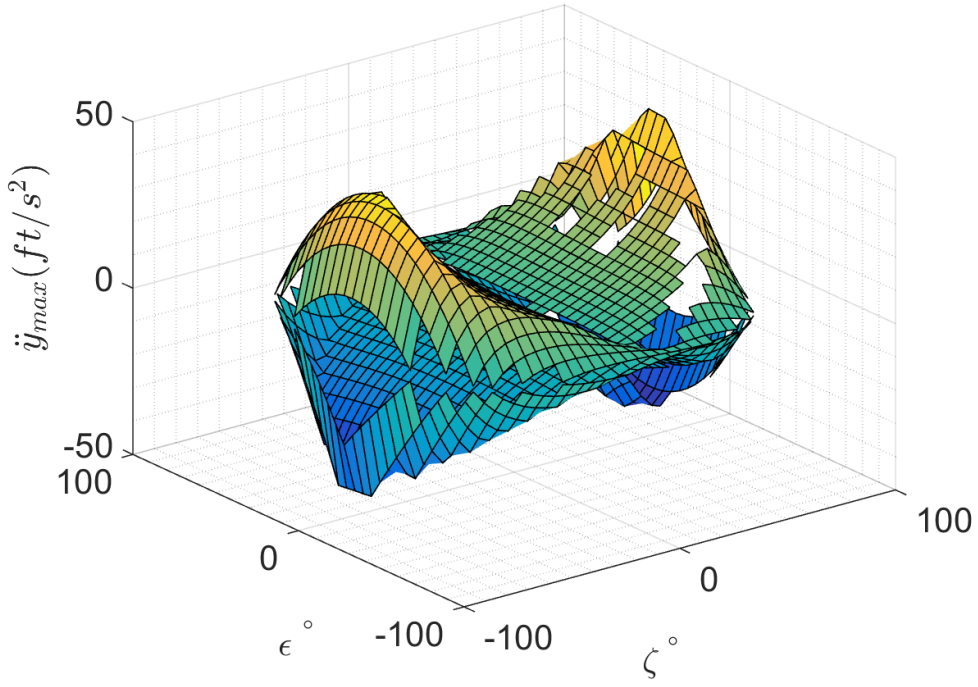

Figure 114: *+6* $\ddot{y}$ design space, pure motion enforced, no rotor faults

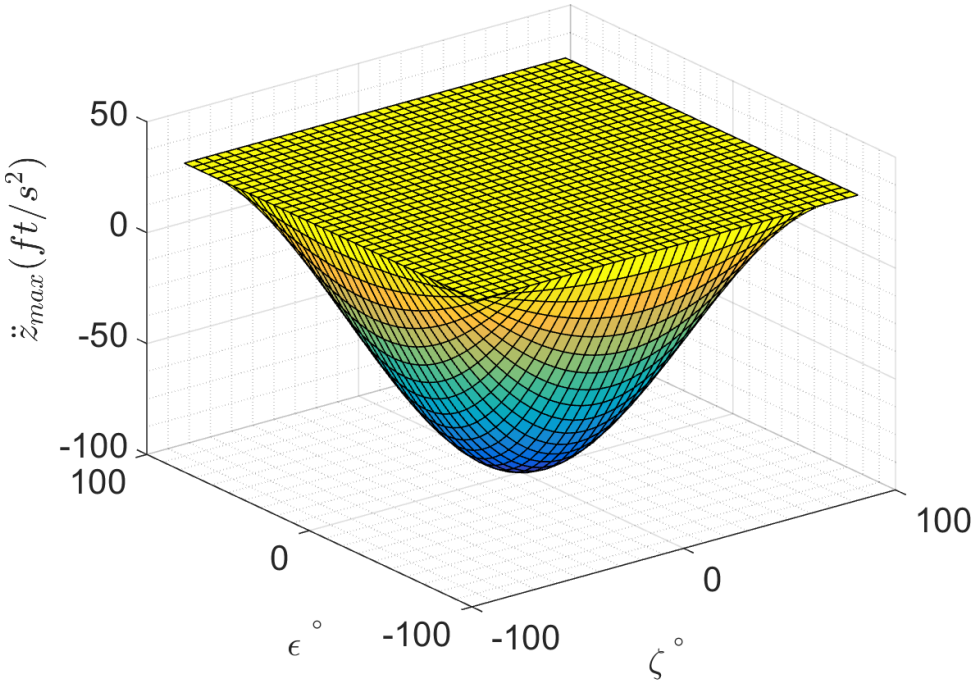

Figure 115: *+6* $\ddot{z}$ design space, pure motion not enforced, M1 fault

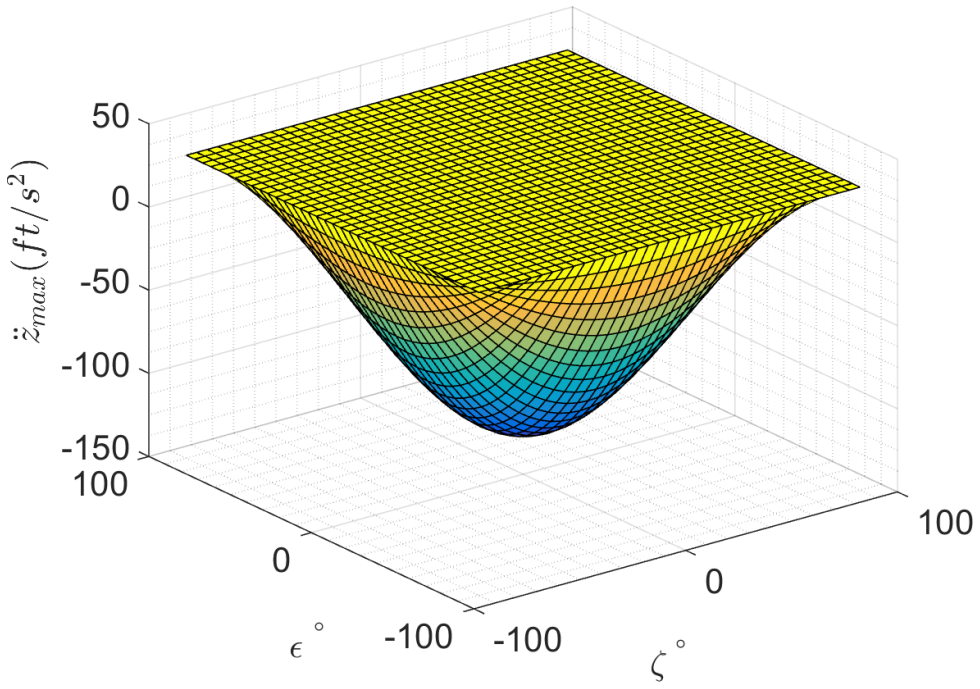

Figure 116: *+6* $\ddot{z}$ design space, pure motion not enforced, no rotor faults

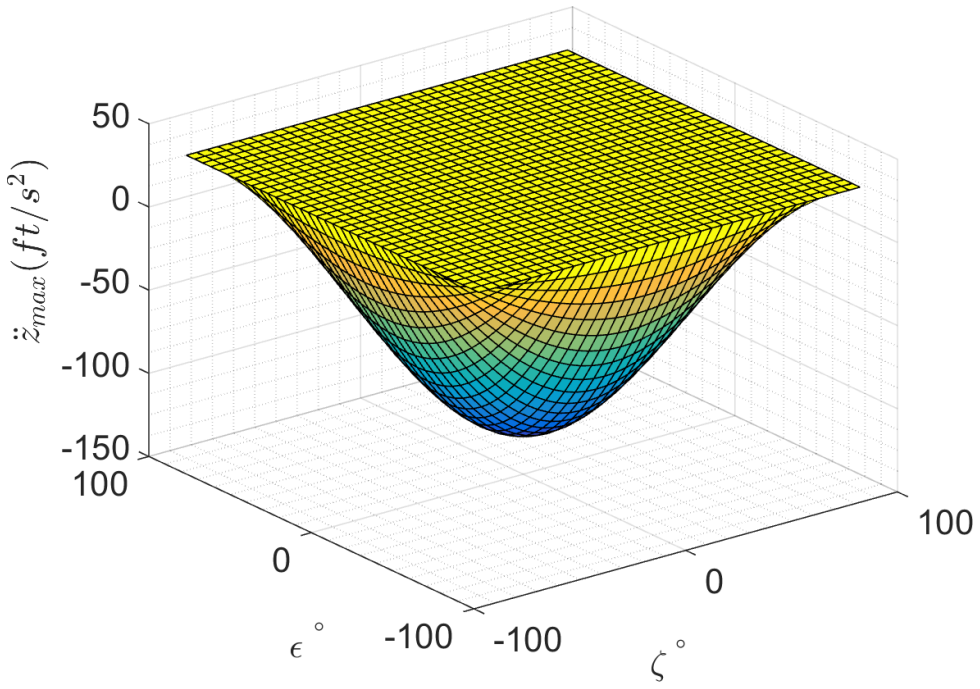

Figure 117: *+6* $\ddot{z}$ design space, pure motion enforced, no rotor faults

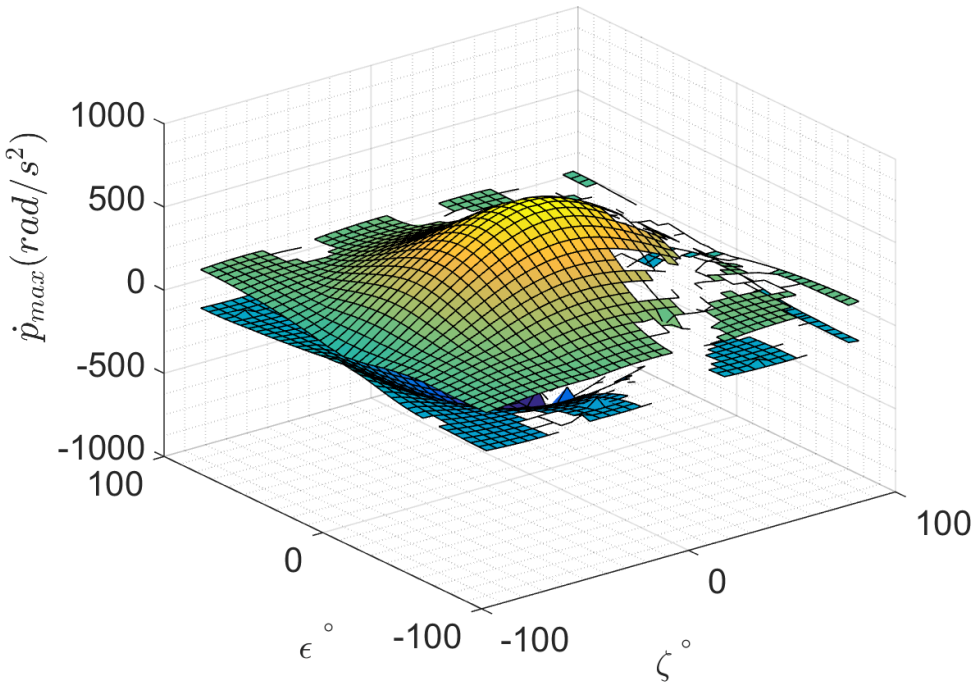

Figure 118: *X12C* $\dot{p}$ design space, pure motion not enforced, co-rotating, M1 fault

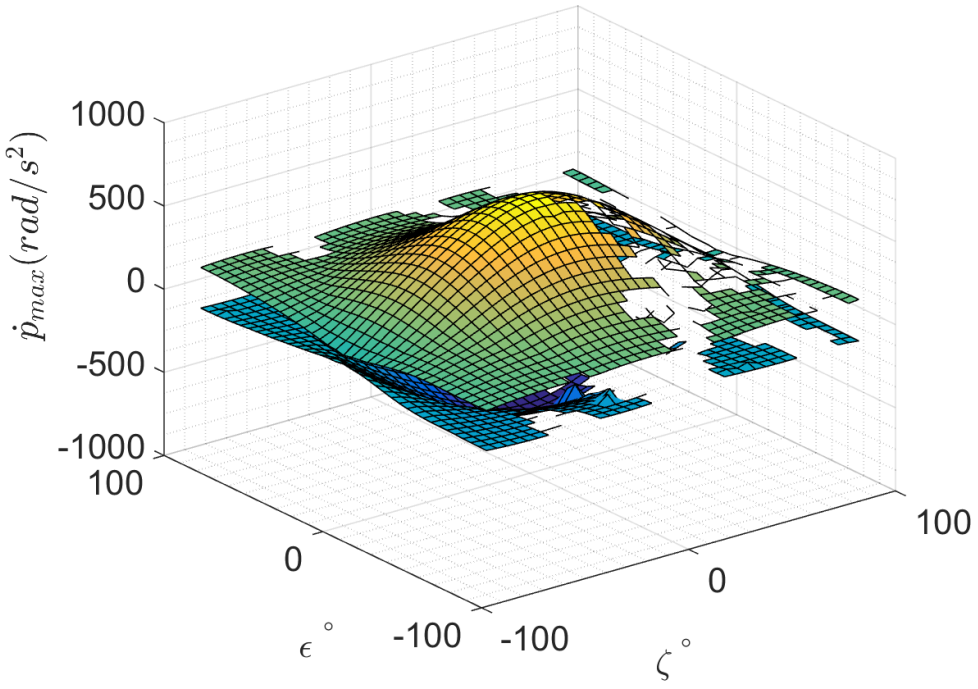

Figure 119: *X12C* $\dot{p}$ design space, pure motion not enforced, counter-rotating, M1 fault

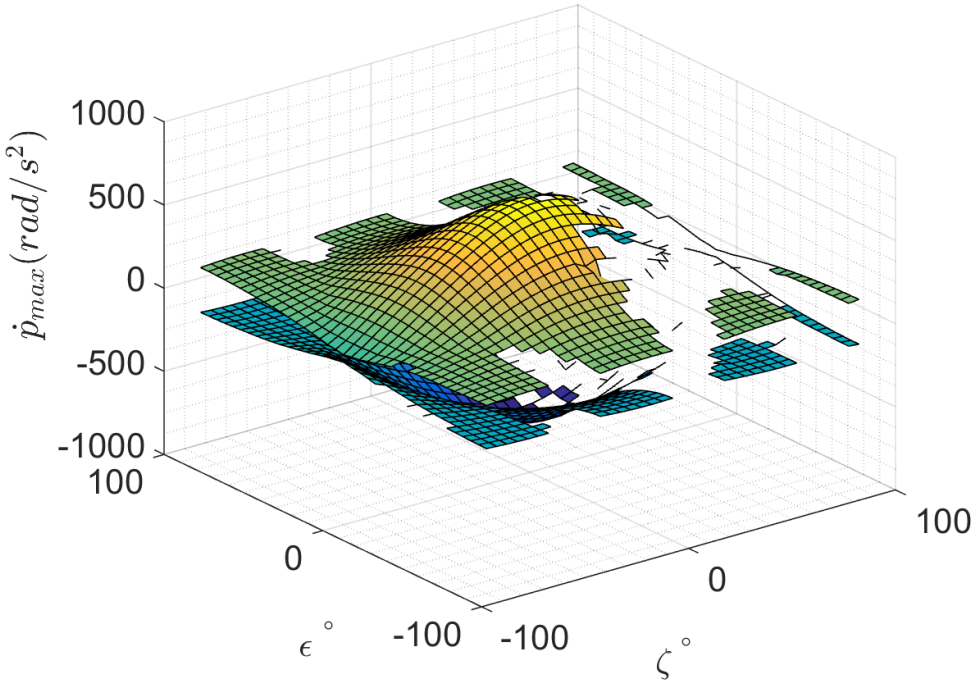

Figure 120: *X12C* $\dot{p}$ design space, pure motion not enforced, co-rotating, no rotor faults

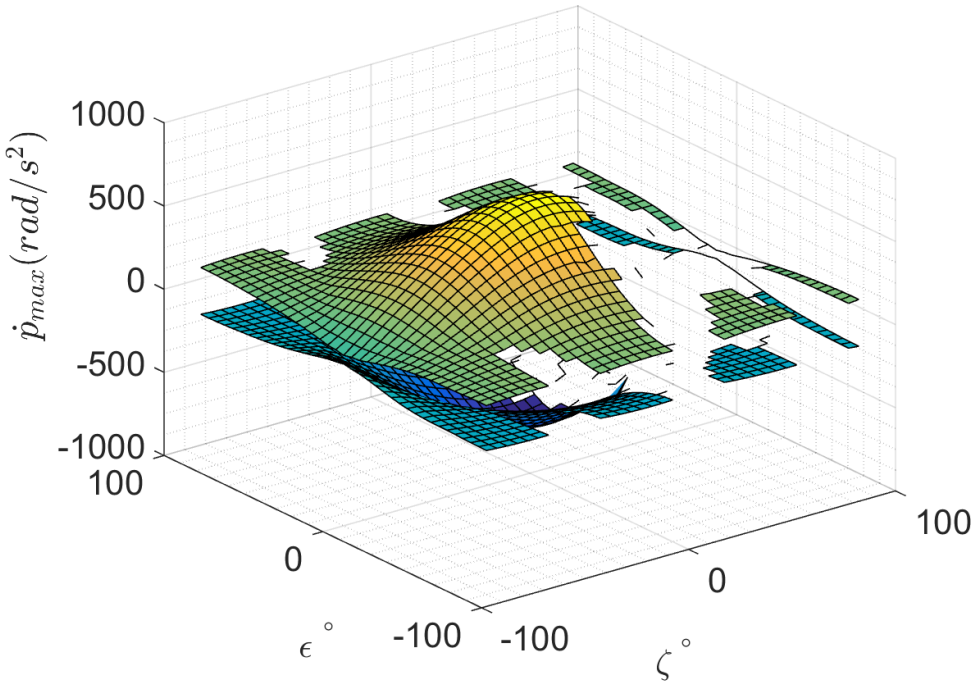

Figure 121: *X12C* $\dot{p}$ design space, pure motion not enforced, counter-rotating, no rotor faults

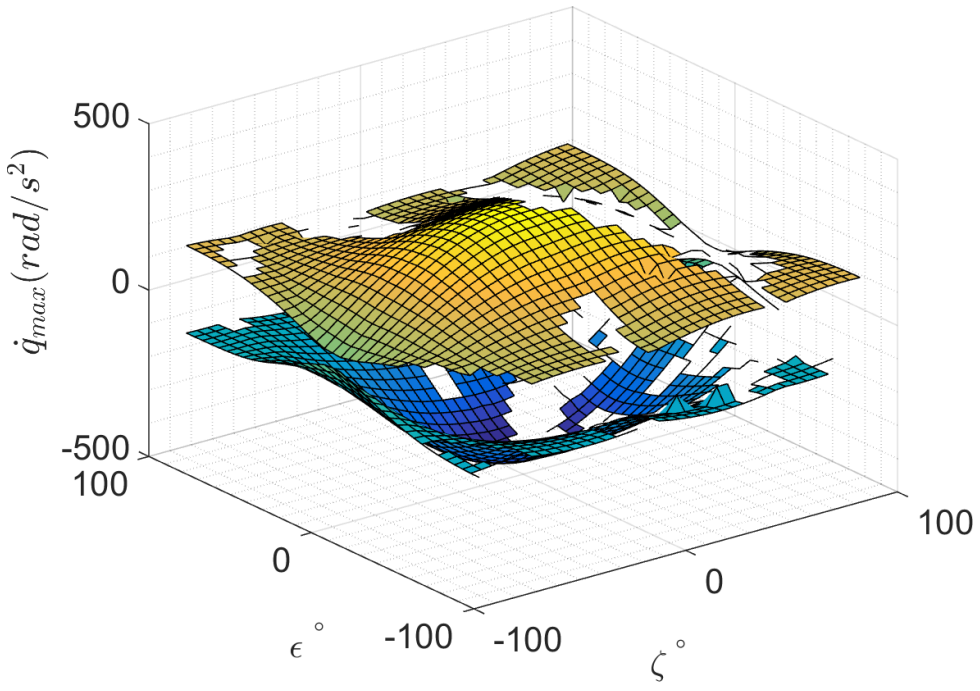

Figure 122: *X12C* $\dot{q}$ design space, pure motion not enforced, co-rotating, M1 fault

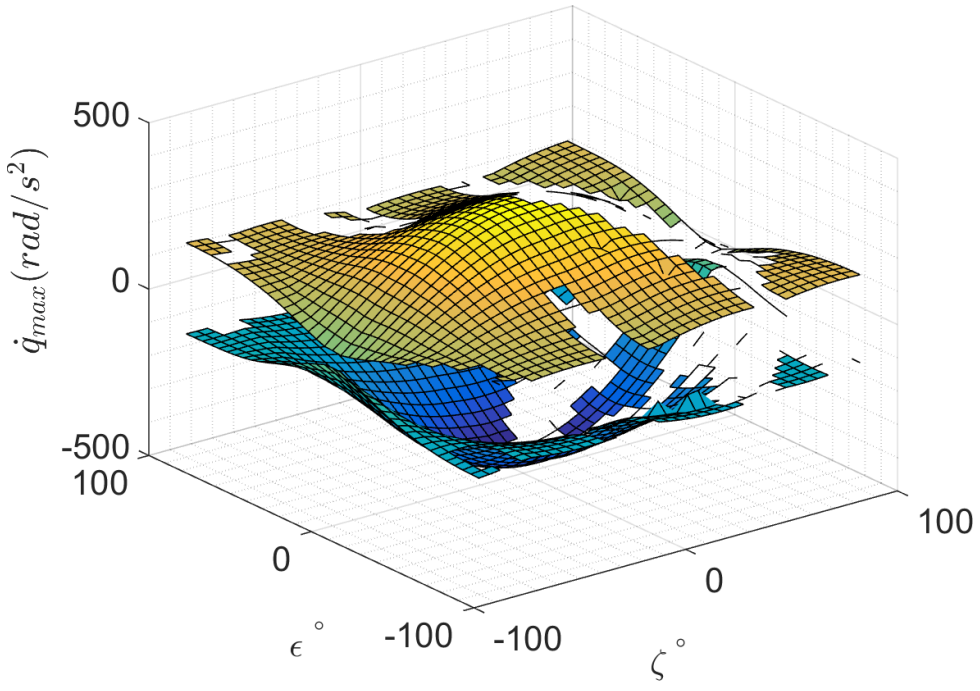

Figure 123: *X12C* $\dot{q}$ design space, pure motion not enforced, counter-rotating, M1 fault

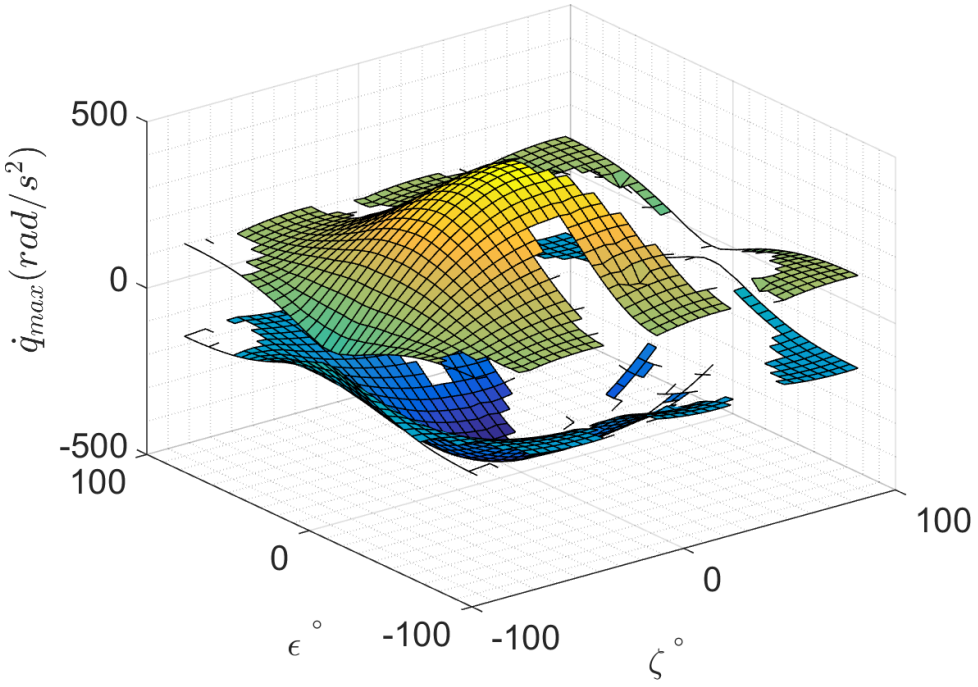

Figure 124: *X12C* $\dot{q}$ design space, pure motion not enforced, co-rotating, no rotor faults

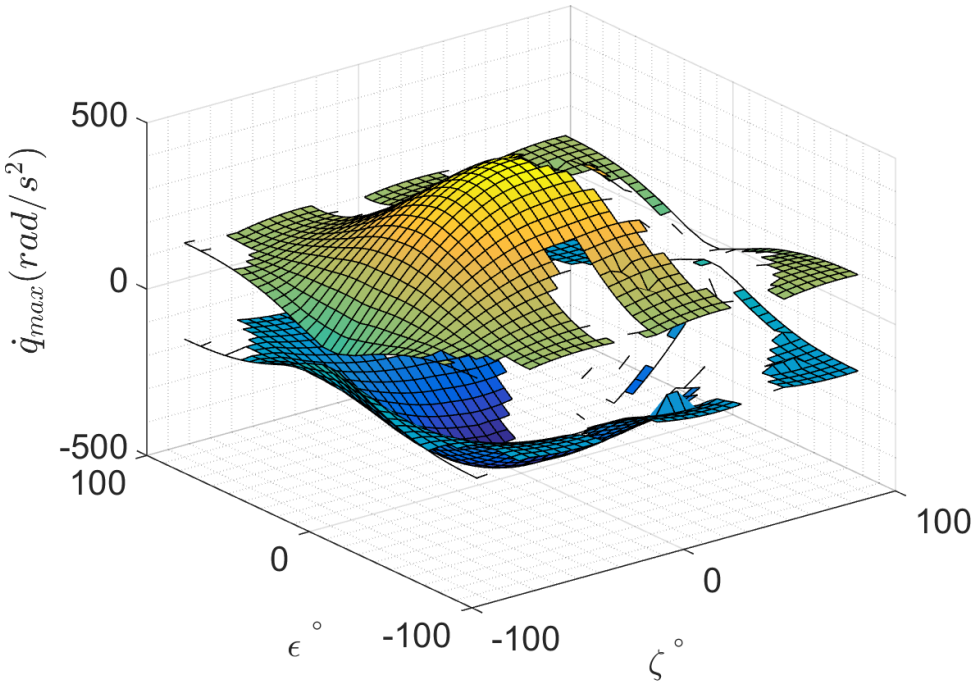

Figure 125: *X12C* $\dot{q}$ design space, pure motion not enforced, counter-rotating, no rotor faults

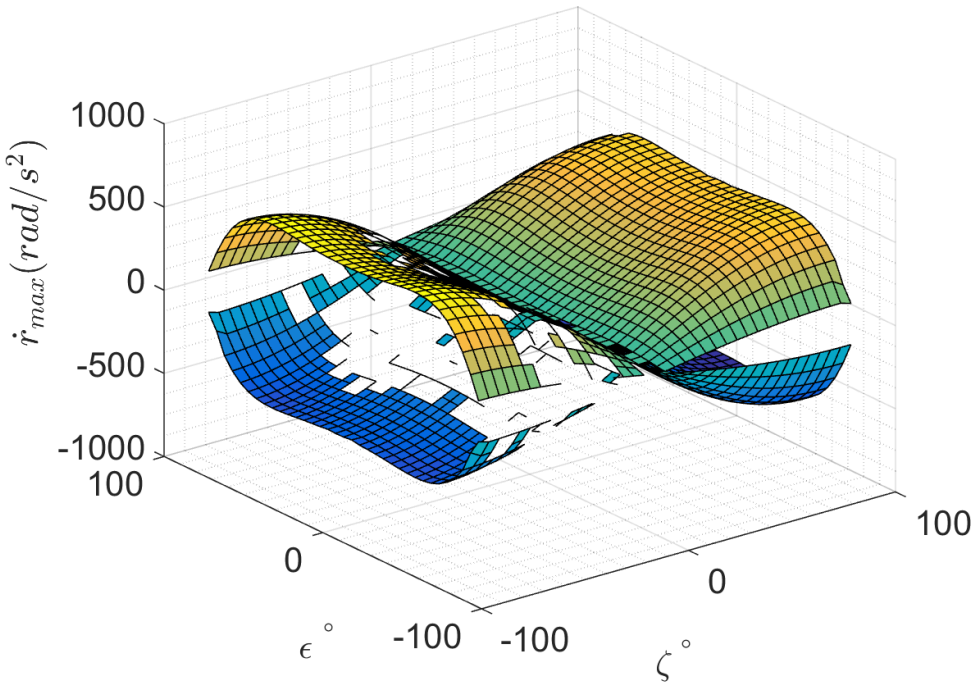

Figure 126: *X12C* $\dot{r}$ design space, pure motion not enforced, co-rotating, M1 fault

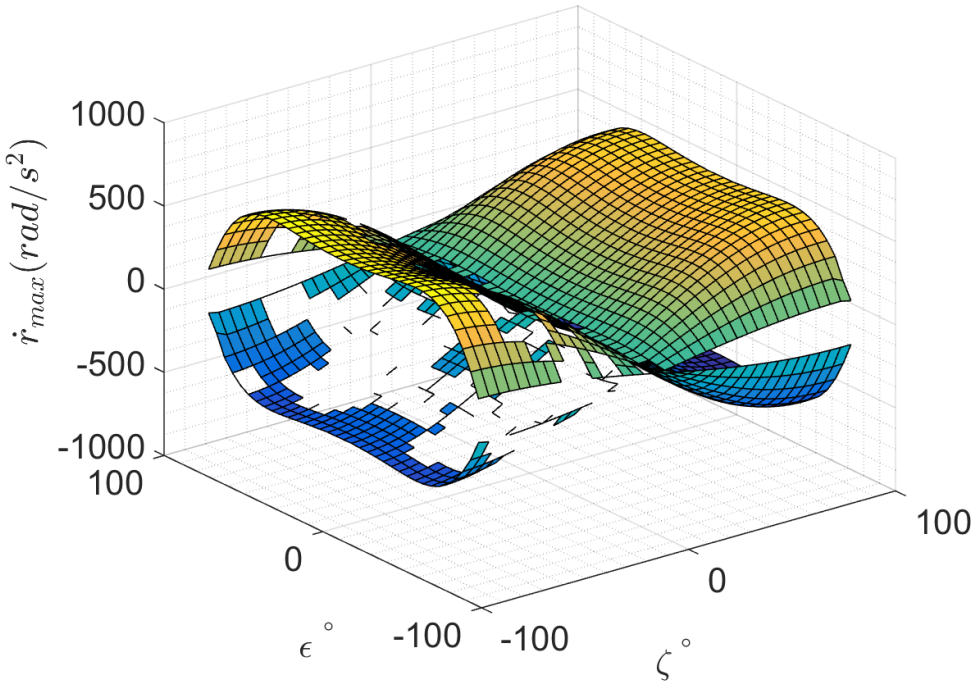

Figure 127: *X12C* $\dot{r}$ design space, pure motion not enforced, counter-rotating, M1 fault

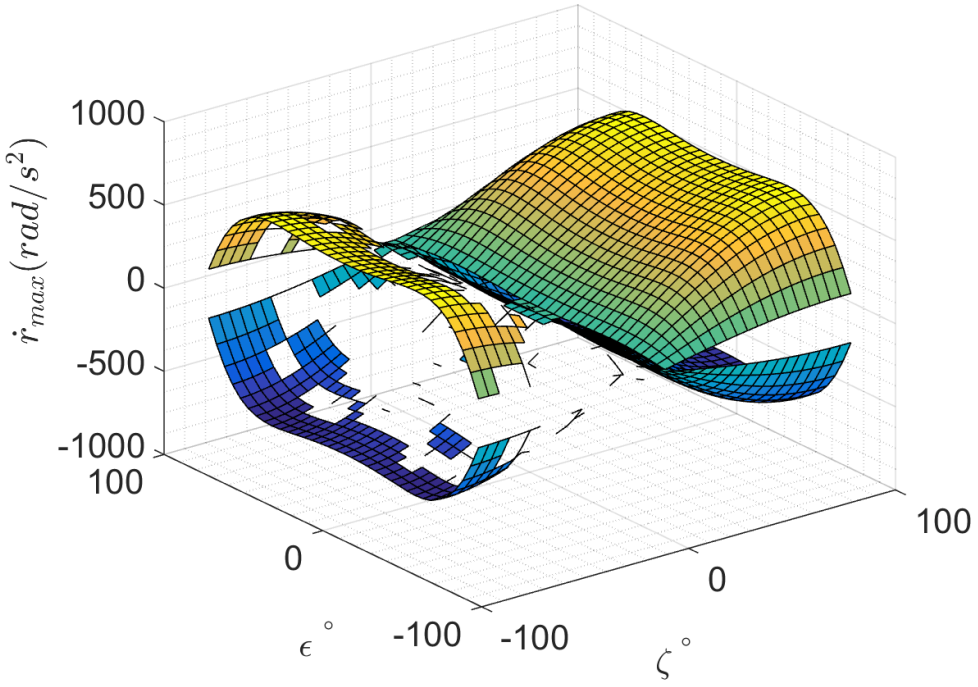

Figure 128: *X12C* $\dot{r}$ design space, pure motion not enforced, co-rotating, no rotor faults

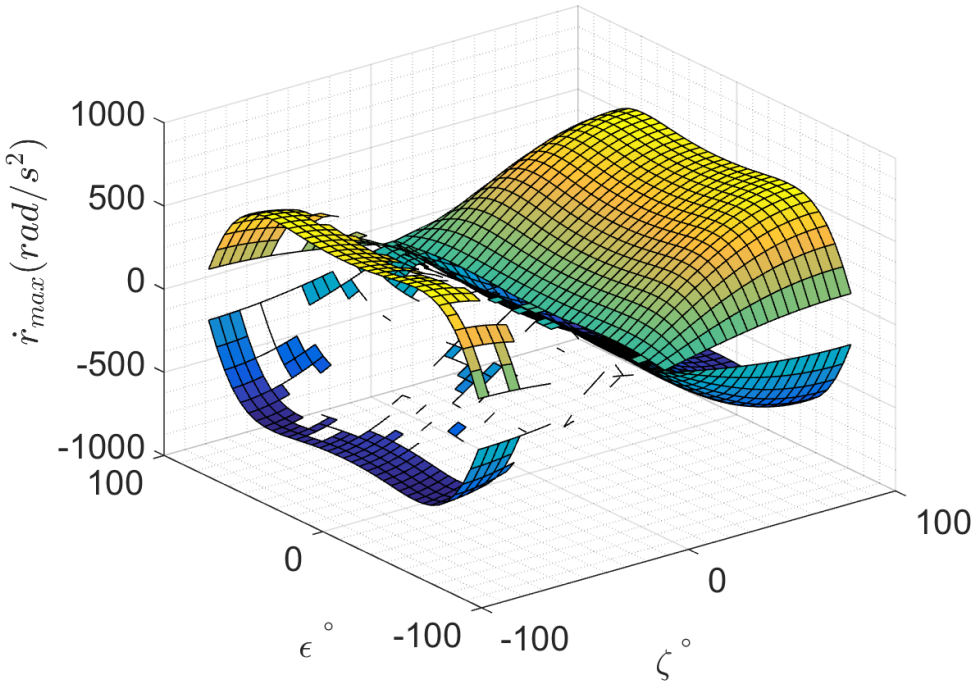

Figure 129: *X12C* $\dot{r}$ design space, pure motion not enforced, counter-rotating, no rotor faults

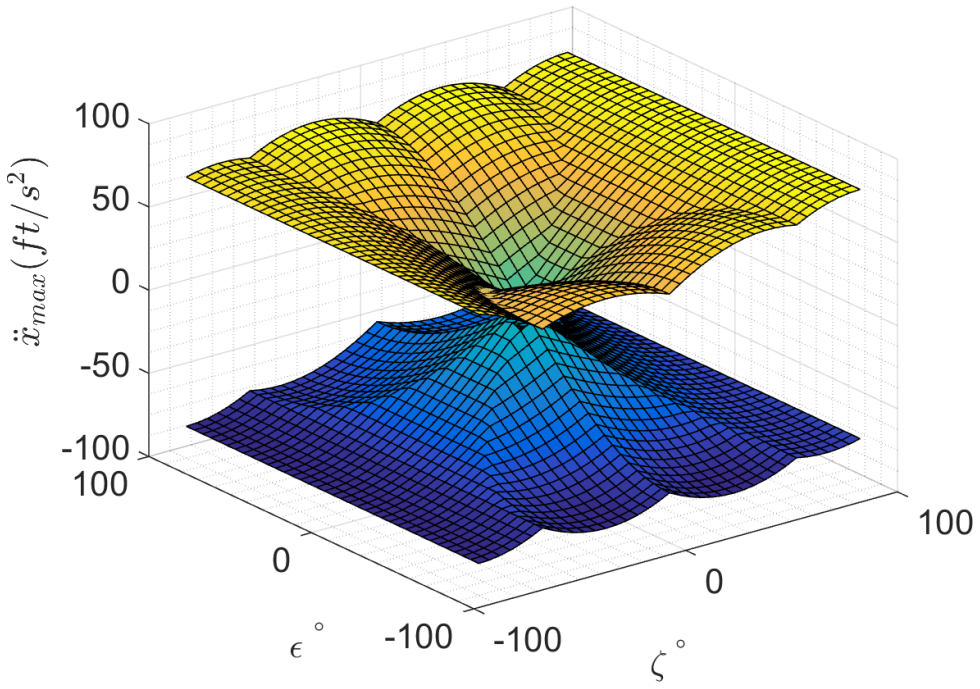

Figure 130: *X12C* $\ddot{x}$ design space, pure motion not enforced, co-rotating, M1 fault

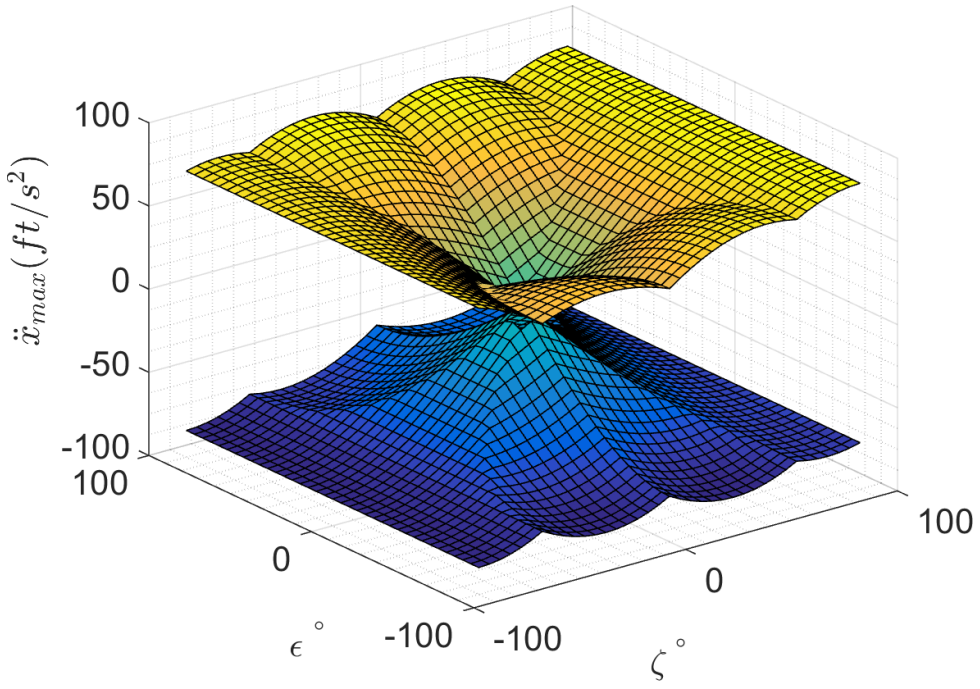

Figure 131: *X12C* $\ddot{x}$ design space, pure motion not enforced, counter-rotating, M1 fault

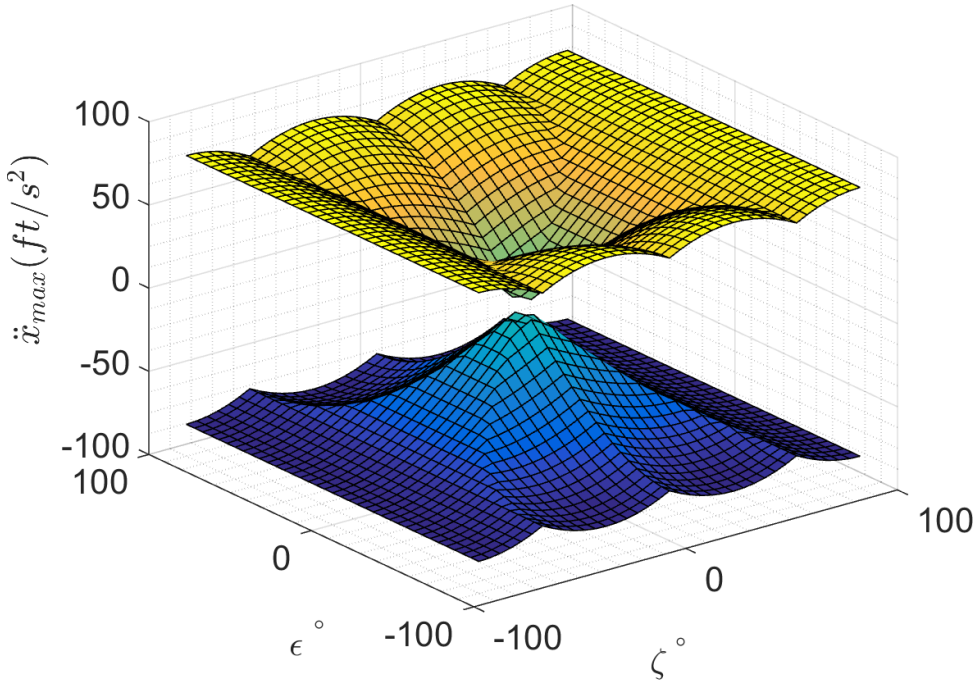

Figure 132: *X12C* $\ddot{x}$ design space, pure motion not enforced, co-rotating, no rotor faults

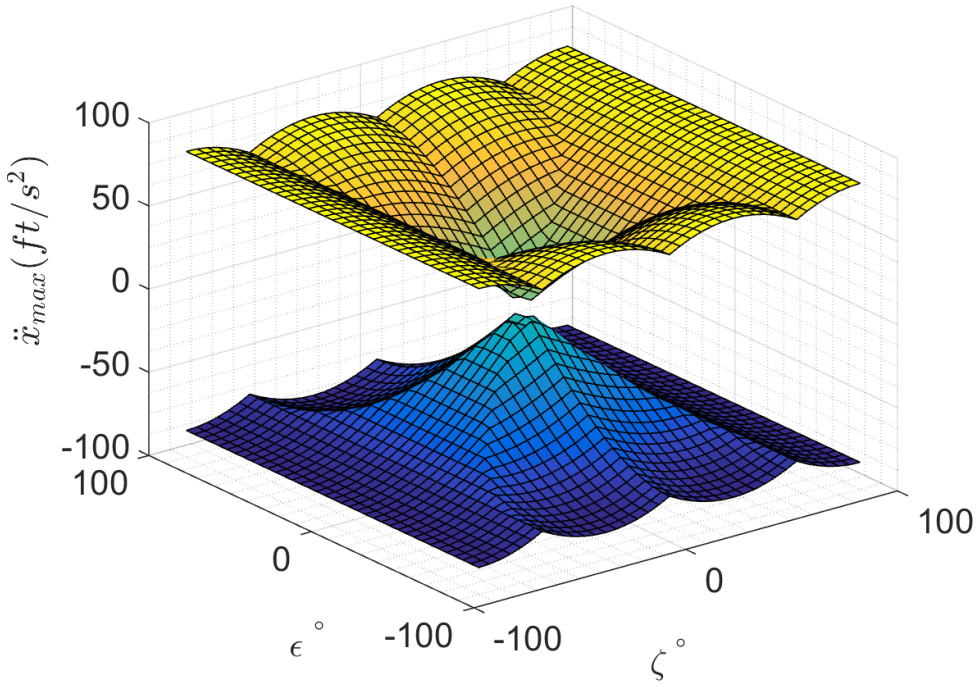

Figure 133: *X12C* $\ddot{x}$ design space, pure motion not enforced, counter-rotating, no rotor faults

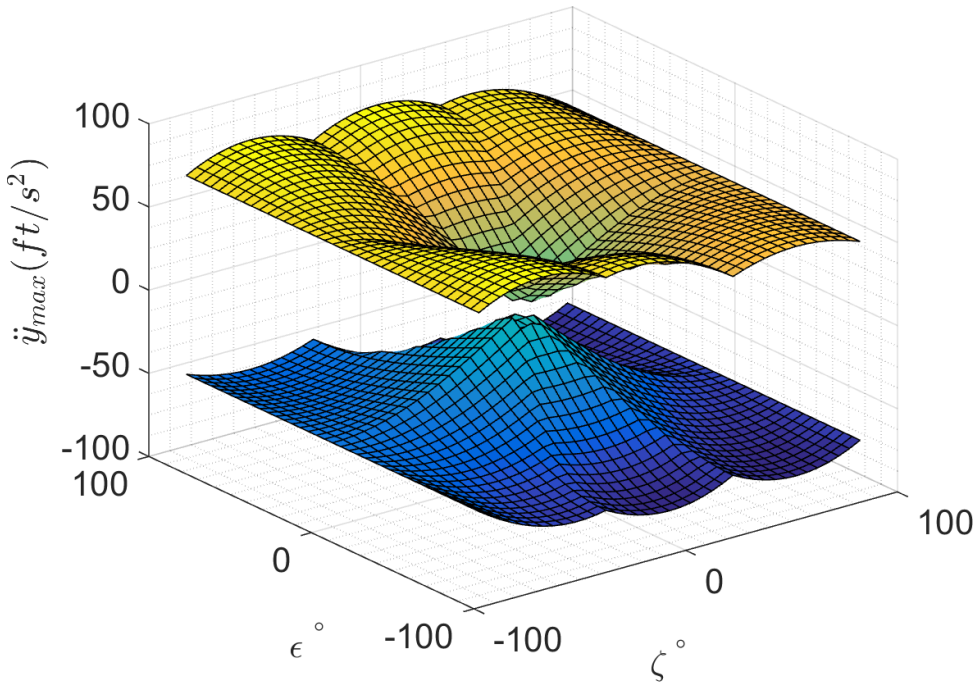

Figure 134: *X12C* $\ddot{y}$ design space, pure motion not enforced, co-rotating, M1 fault

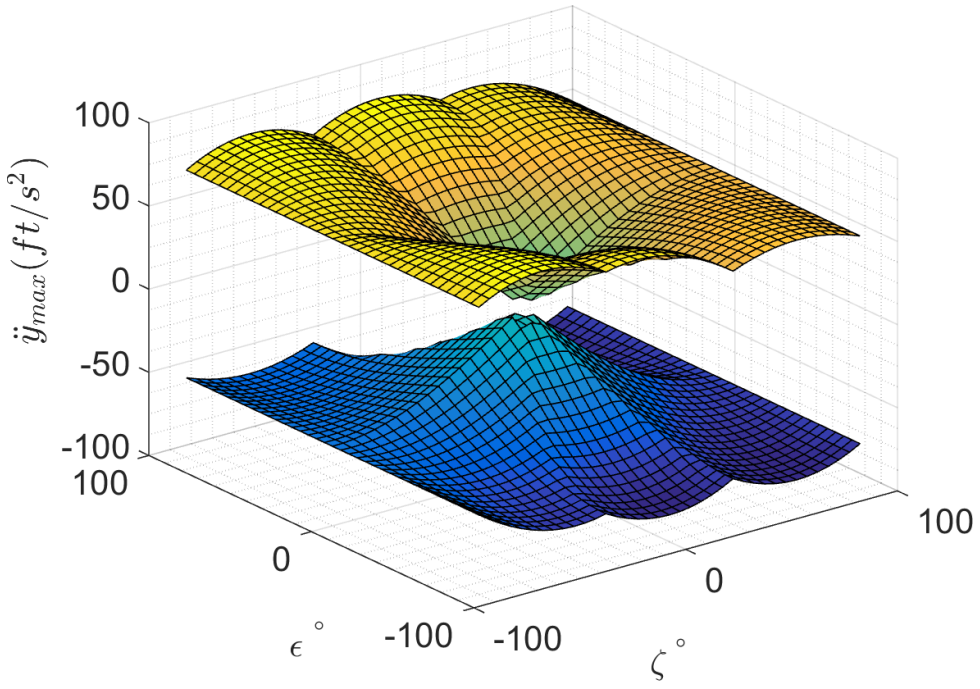

Figure 135: *X12C* $\ddot{y}$ design space, pure motion not enforced, counter-rotating, M1 fault

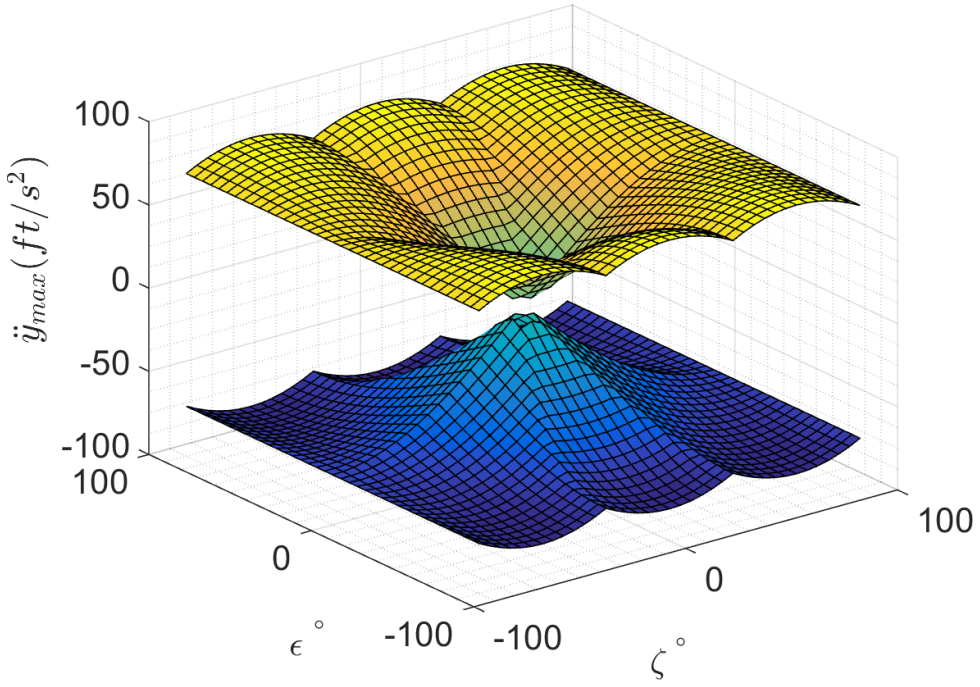

Figure 136: *X12C* $\ddot{y}$ design space, pure motion not enforced, co-rotating, no rotor faults

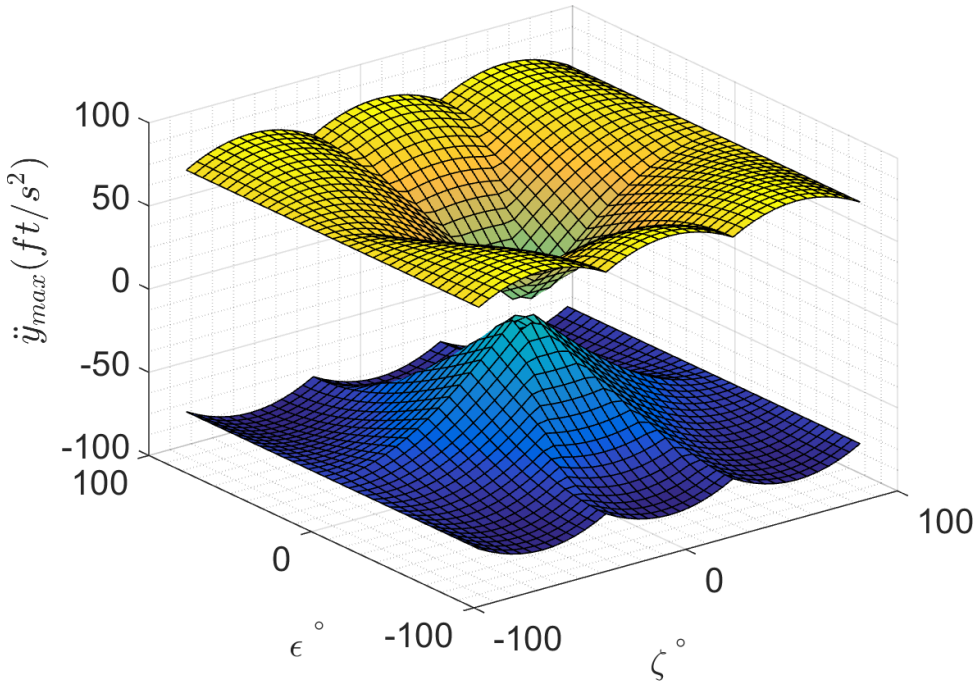

Figure 137: *X12C* $\ddot{y}$ design space, pure motion not enforced, counter-rotating, no rotor faults

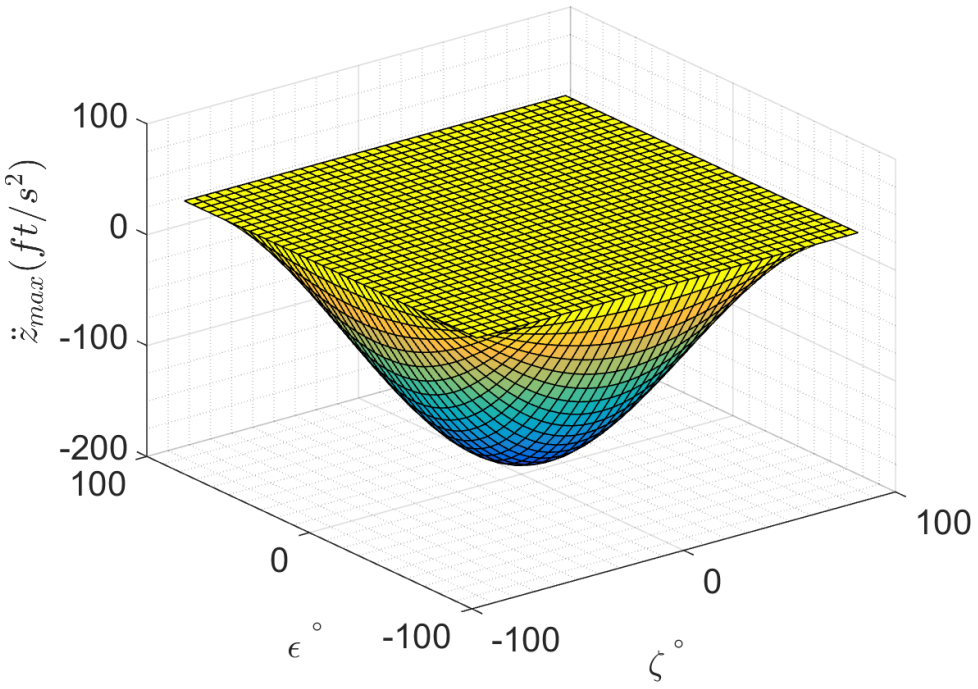

Figure 138: *X12C* $\ddot{z}$ design space, pure motion not enforced, co-rotating, M1 fault

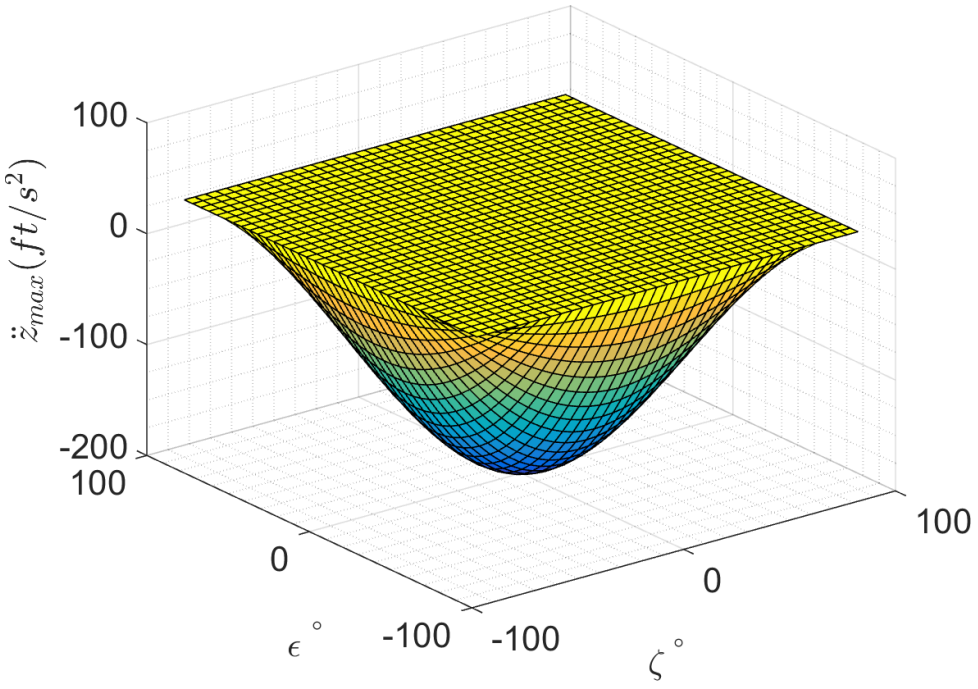

Figure 139: *X12C* $\ddot{z}$ design space, pure motion not enforced, counter-rotating, M1 fault

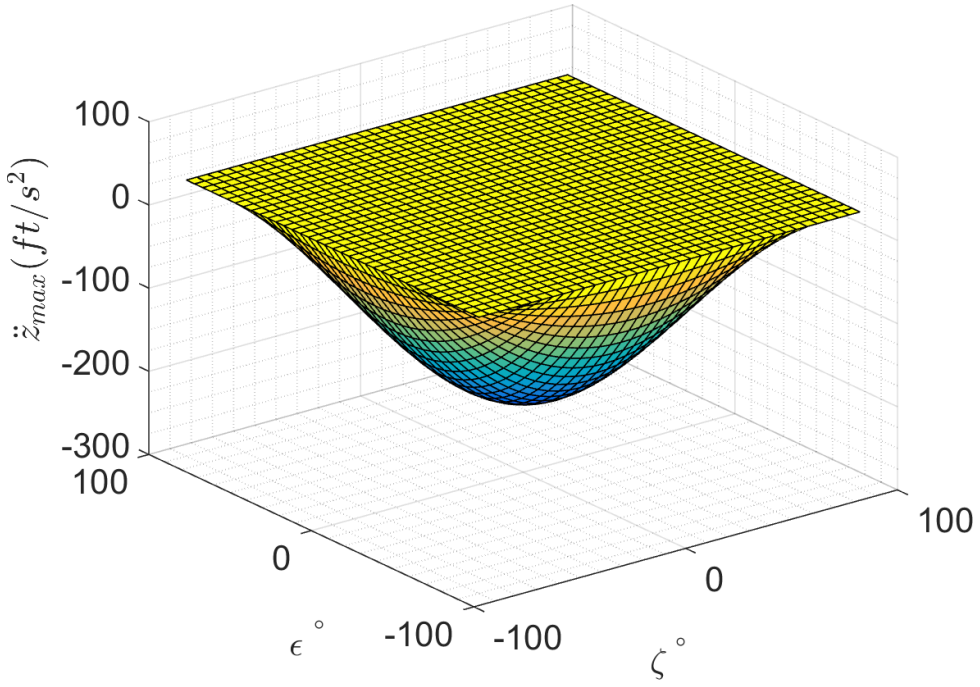

Figure 140: *X12C* $\ddot{z}$ design space, pure motion not enforced, co-rotating, no rotor faults

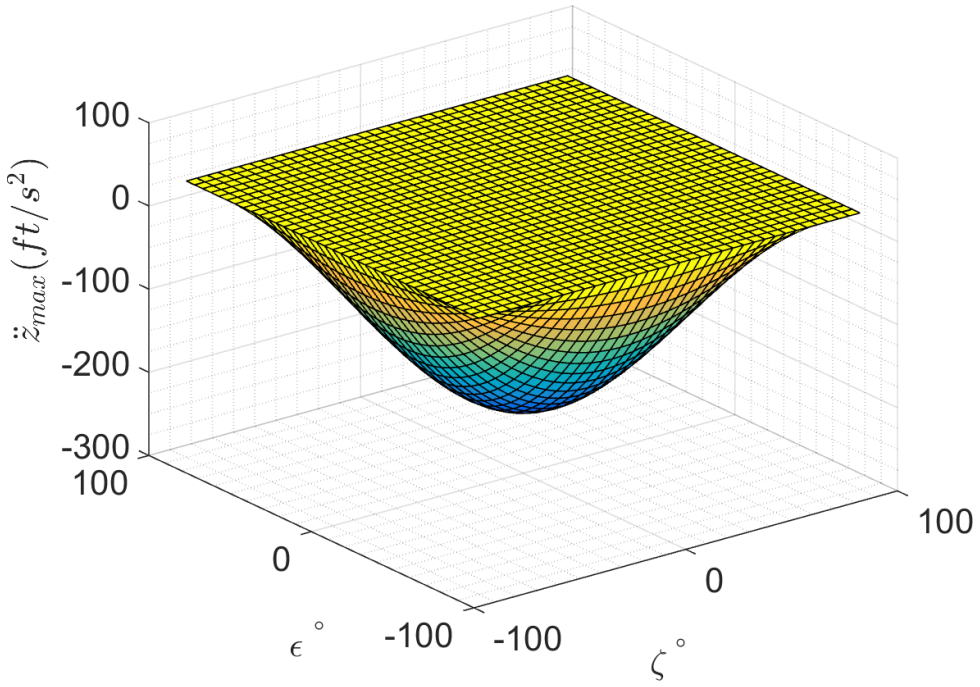

Figure 141: *X12C* $\ddot{z}$ design space, pure motion not enforced, counter-rotating, no rotor faults

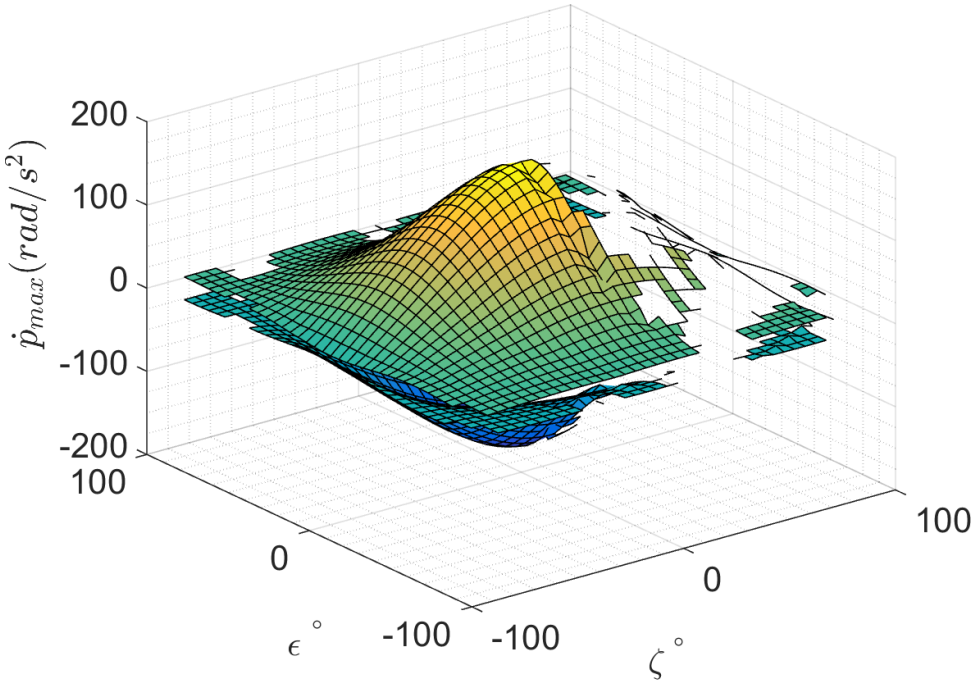

Figure 142: *X12 $\dot{p}$* design space, pure motion not enforced, M1 fault

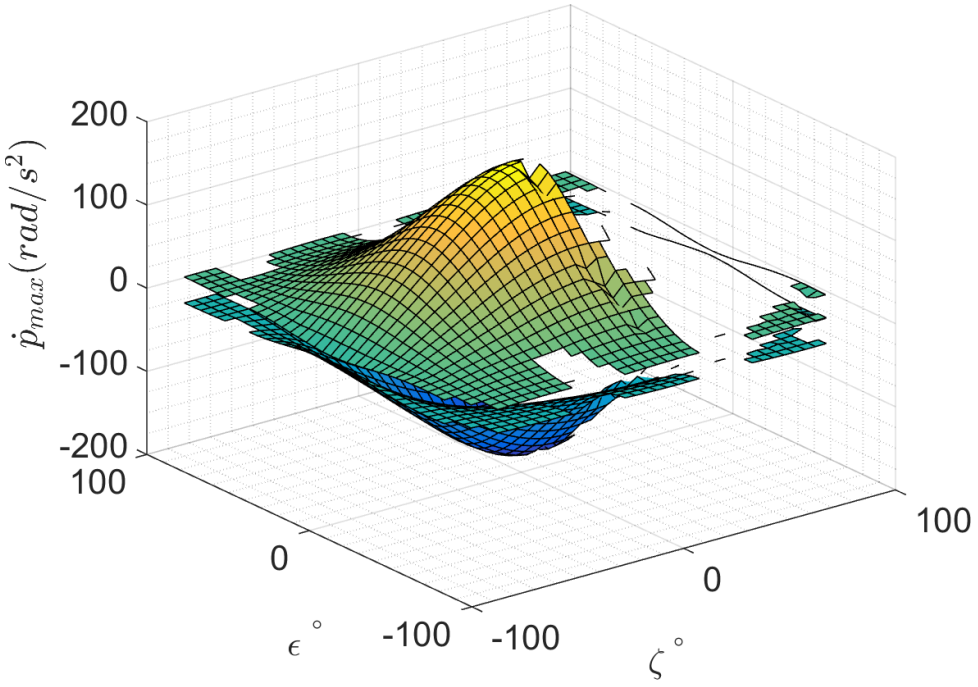

Figure 143: *X12 $\dot{p}$* design space, pure motion not enforced, no rotor faults

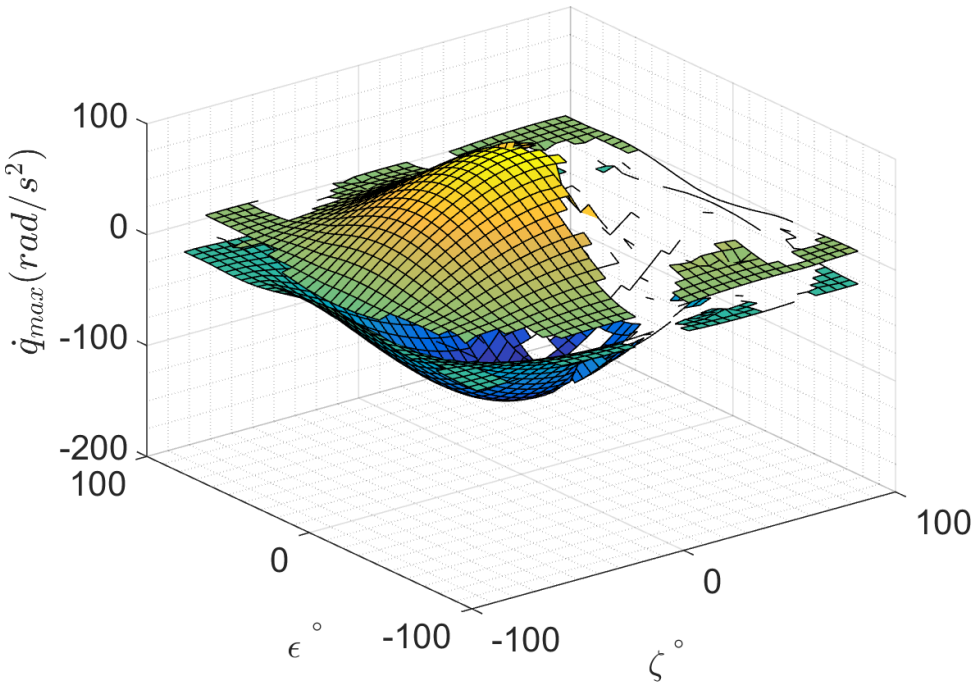

Figure 144: *X12* $\dot{q}$ design space, pure motion not enforced, M1 fault

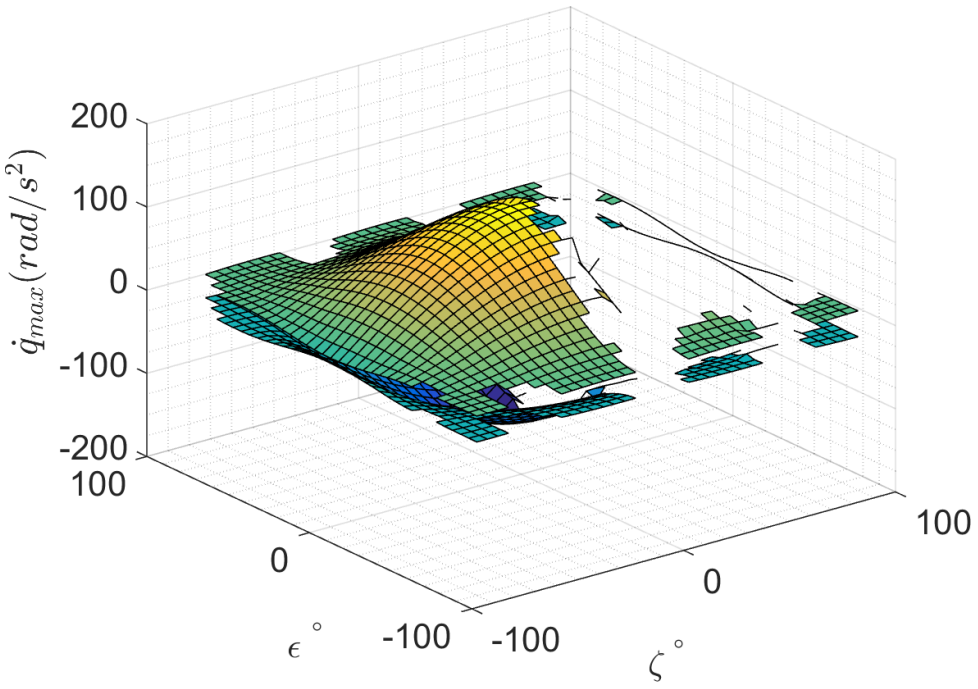

Figure 145: *X12* $\dot{q}$ design space, pure motion not enforced, no rotor faults

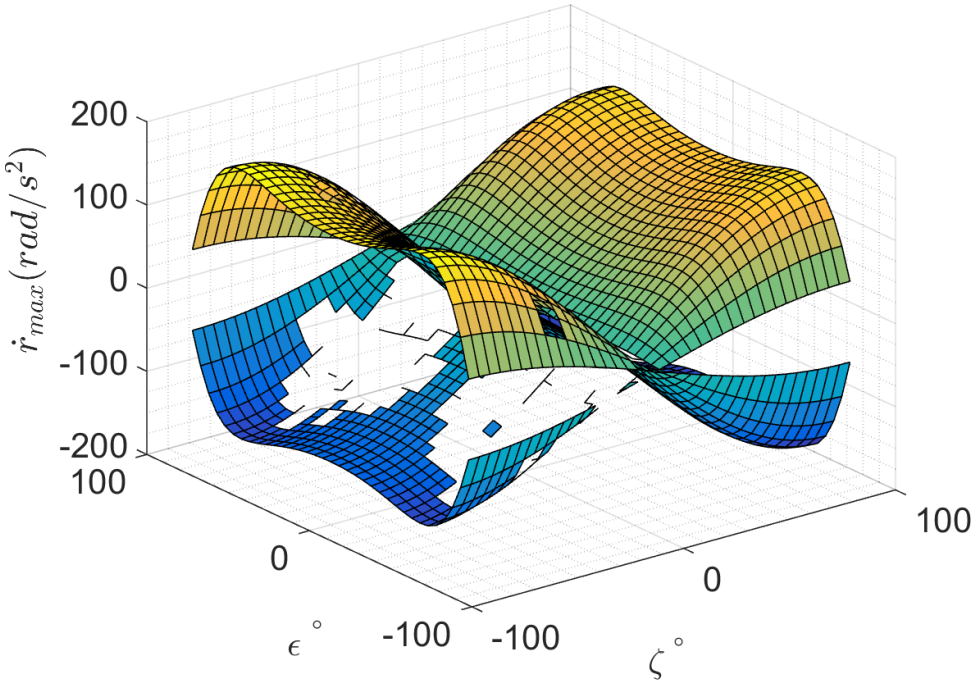

Figure 146: *X12* $\dot{r}$ design space, pure motion not enforced, M1 fault

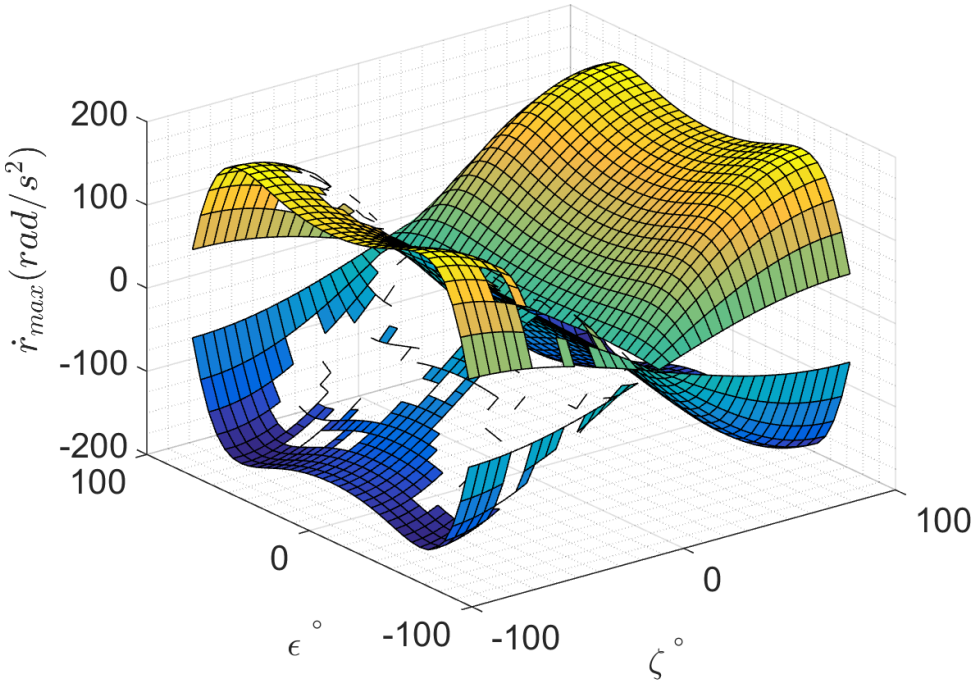

Figure 147: *X12* $\dot{r}$ design space, pure motion not enforced, no rotor faults

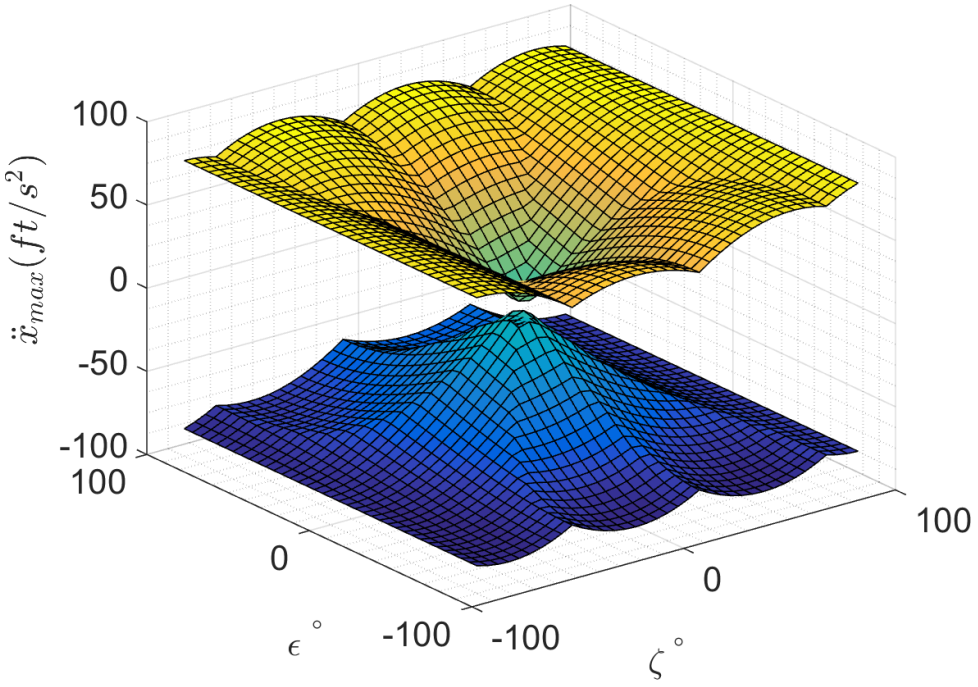

Figure 148: *X12* $\ddot{x}$ design space, pure motion not enforced, M1 fault

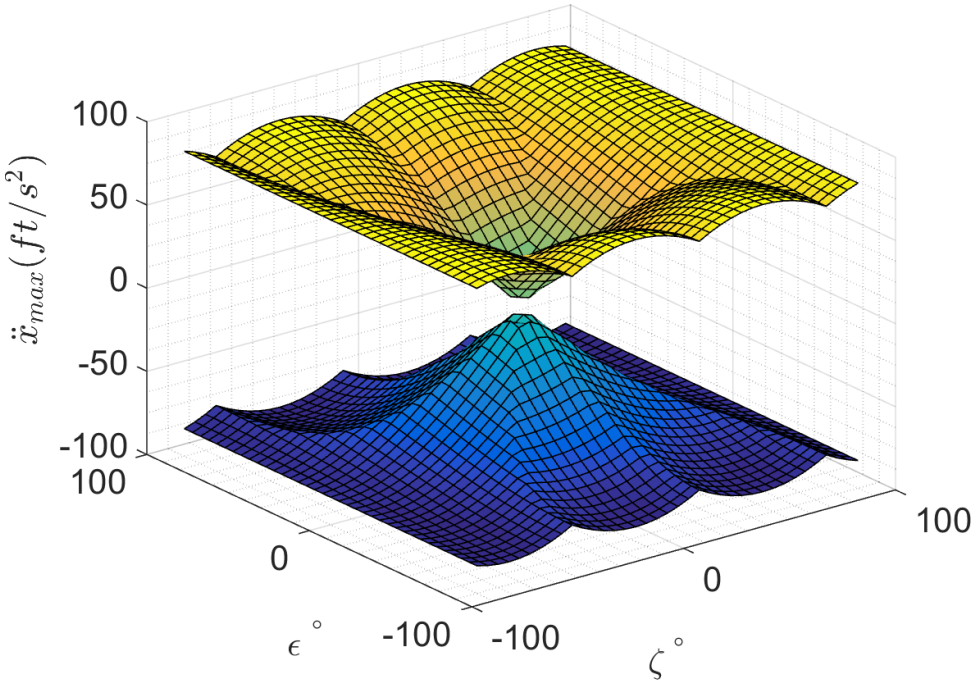

Figure 149: *X12* $\ddot{x}$ design space, pure motion not enforced, no rotor faults

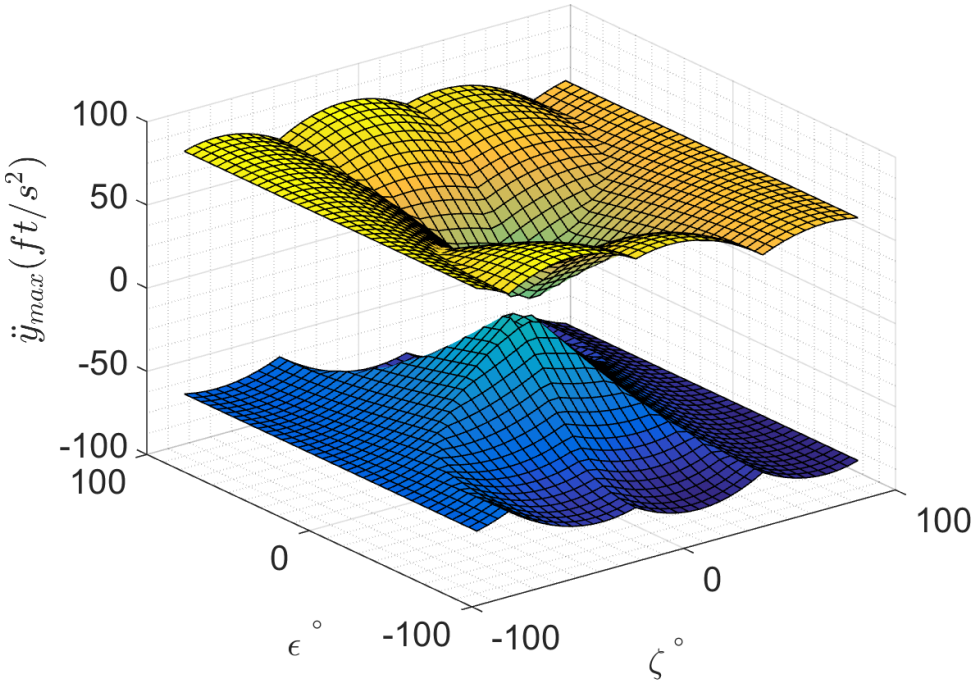

Figure 150: *X12 $\ddot{y}$* design space, pure motion not enforced, M1 fault

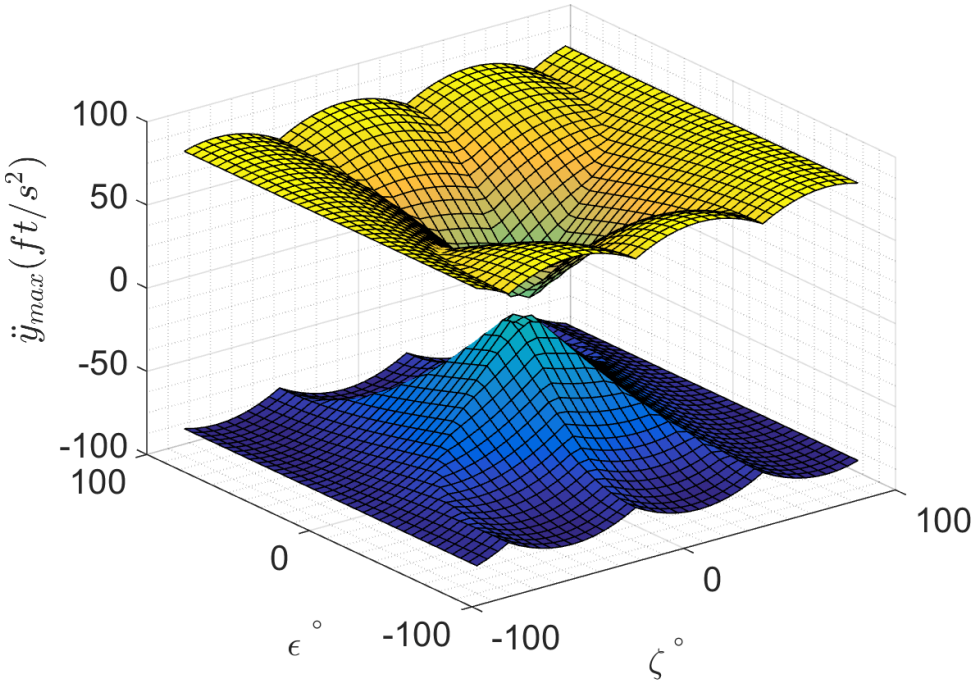

Figure 151: *X12 $\ddot{y}$* design space, pure motion not enforced, no rotor faults

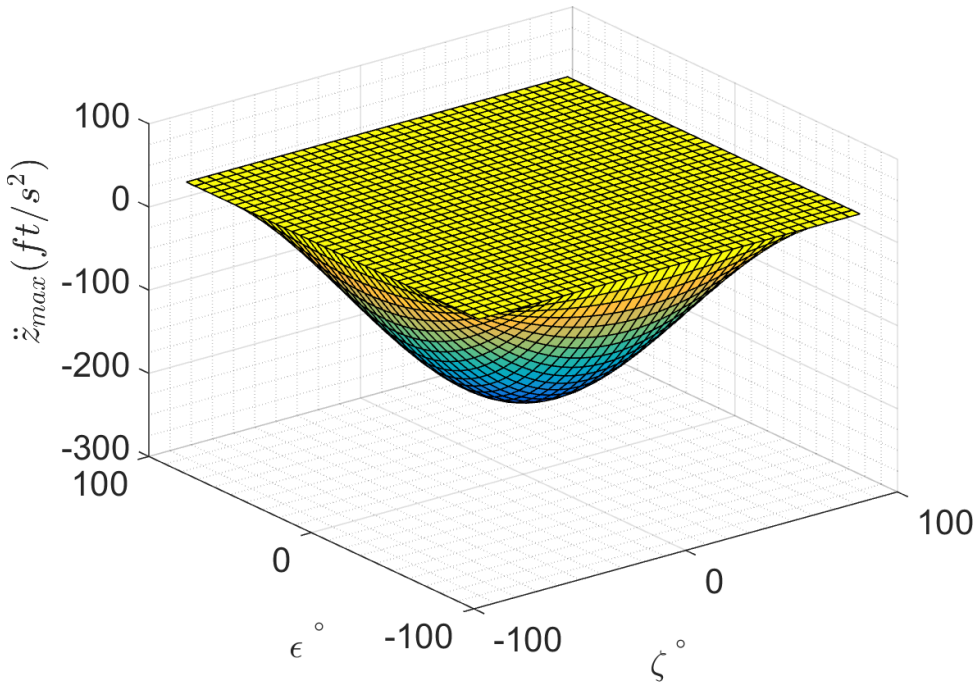

Figure 152: *X12* $\ddot{z}$ design space, pure motion not enforced, M1 fault

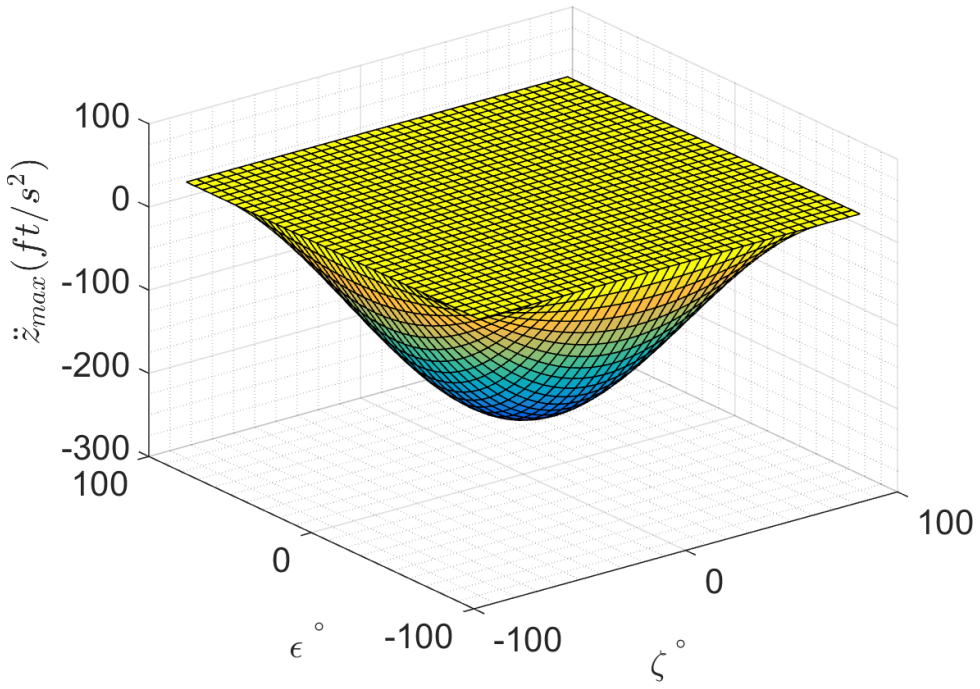

Figure 153: *X12* $\ddot{z}$ design space, pure motion not enforced, no rotor faults

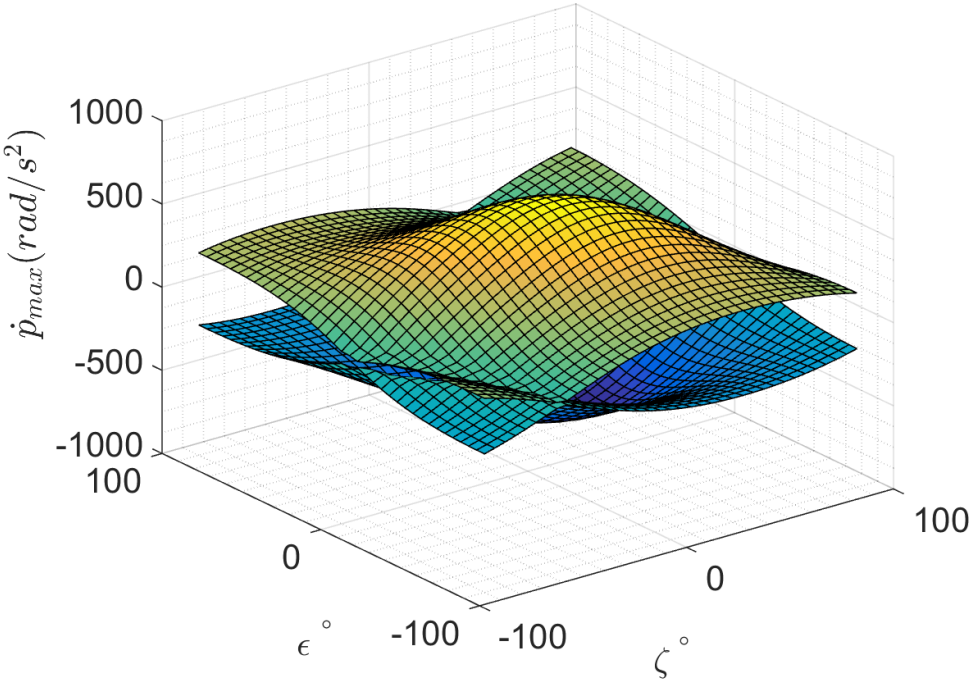

Figure 154: *X4* $\dot{p}$ design space, pure motion not enforced, no rotor faults

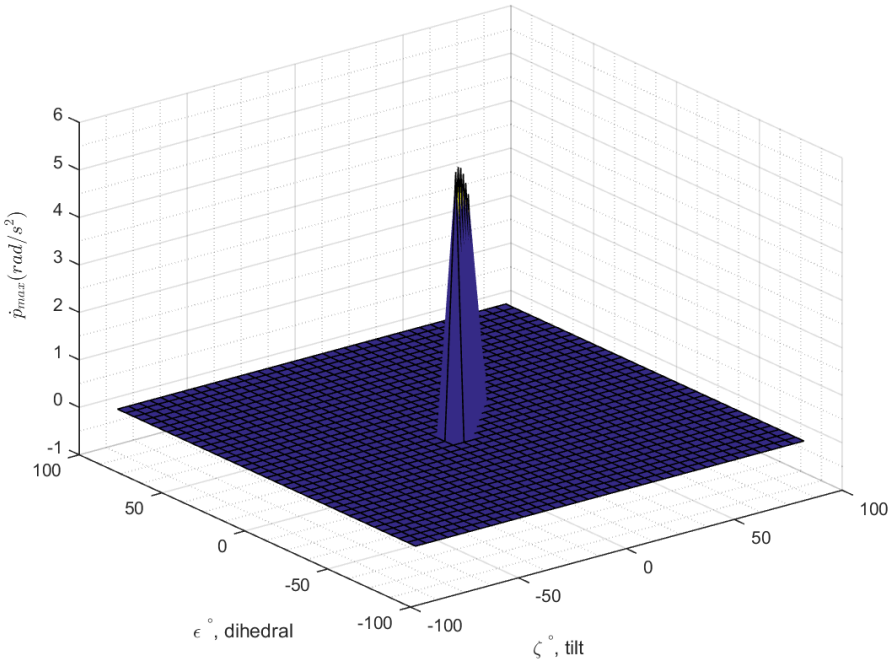

Figure 155: *X4* $\dot{p}$ design space, pure motion enforced, M1 fault

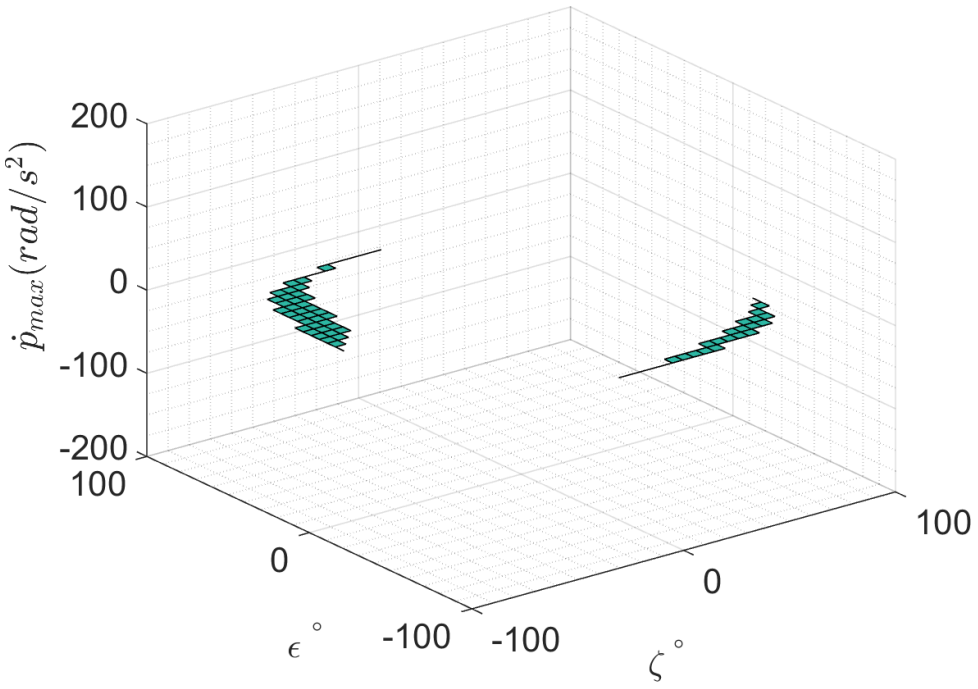

Figure 156: *X4* $\dot{p}$ design space, pure motion enforced, no rotor faults

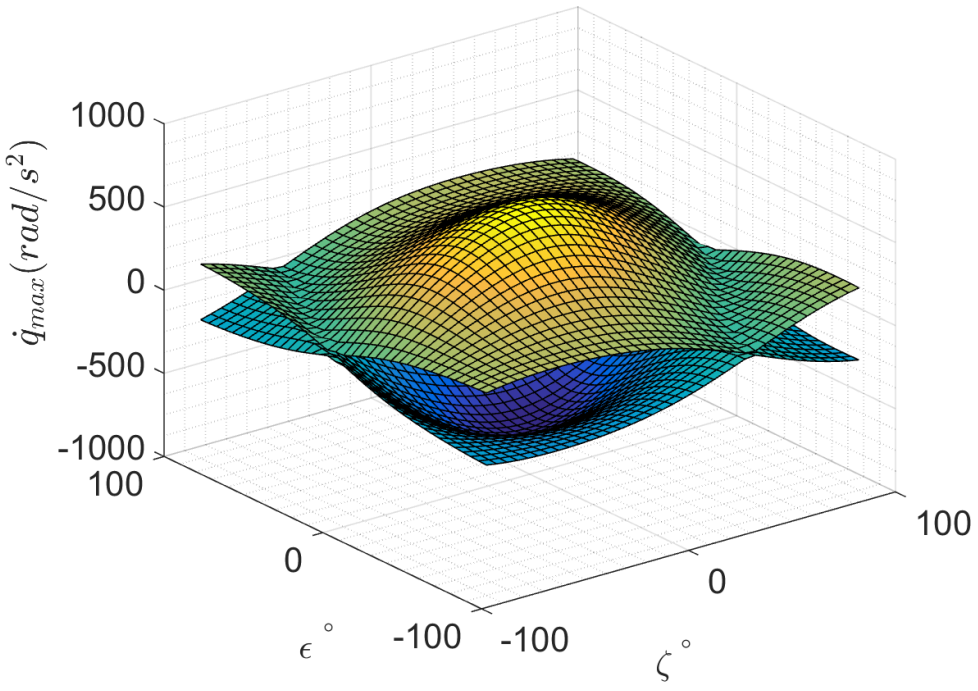

Figure 157: *X4* $\dot{q}$ design space, pure motion not enforced, no rotor faults

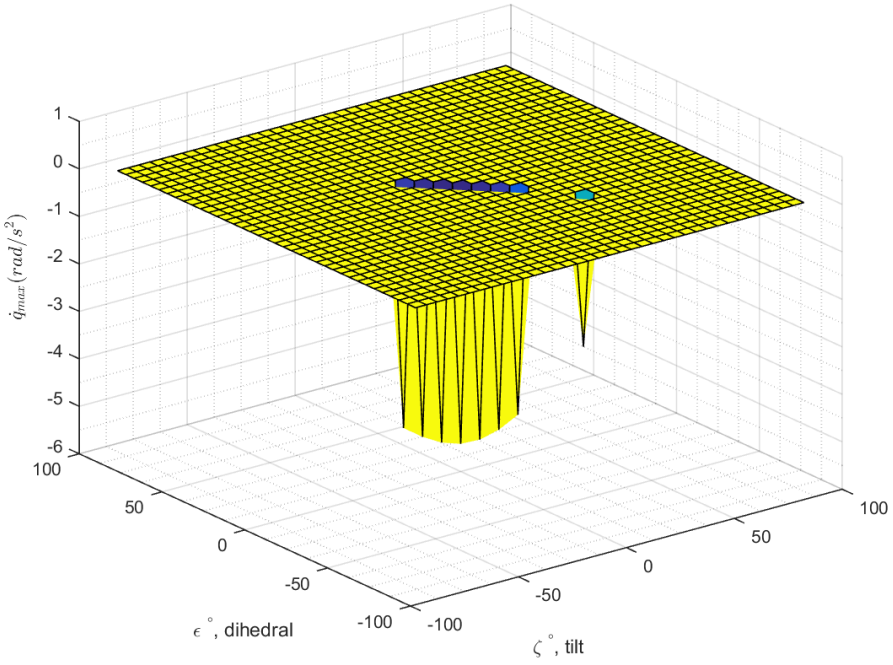

Figure 158: *X4* $\dot{q}$ design space, pure motion enforced, M1 fault

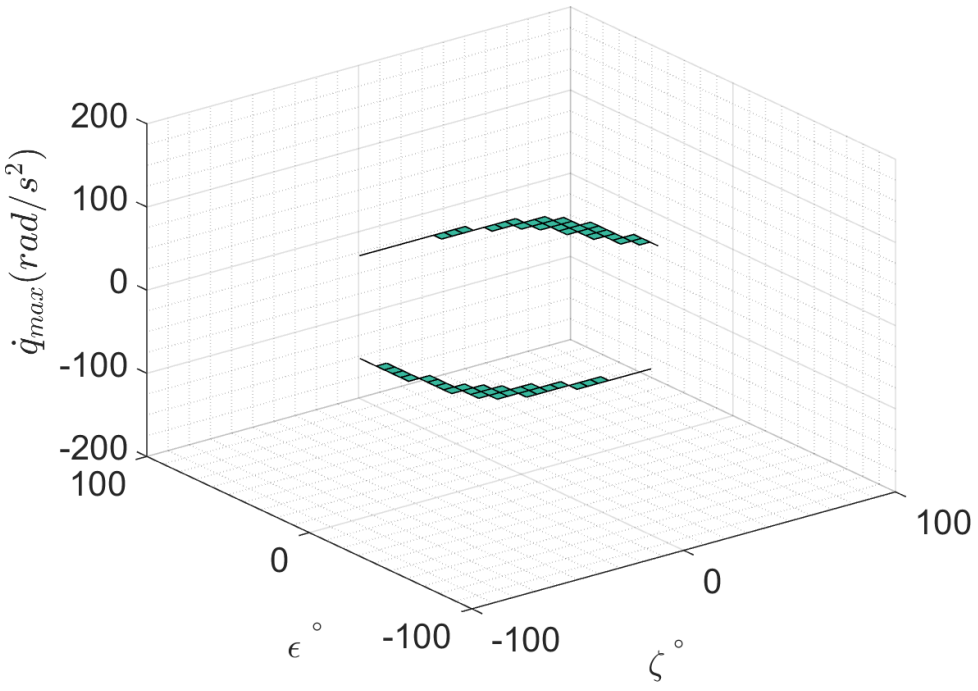

Figure 159: *X4* $\dot{q}$ design space, pure motion enforced, no rotor faults

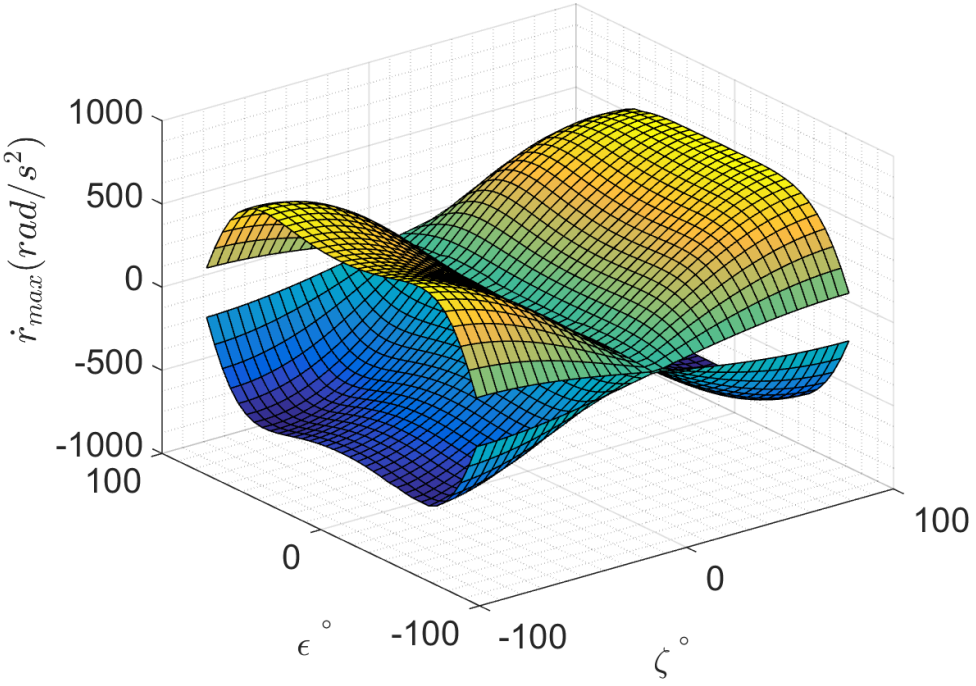

Figure 160: *X4* $\dot{r}$ design space, pure motion not enforced, no rotor faults

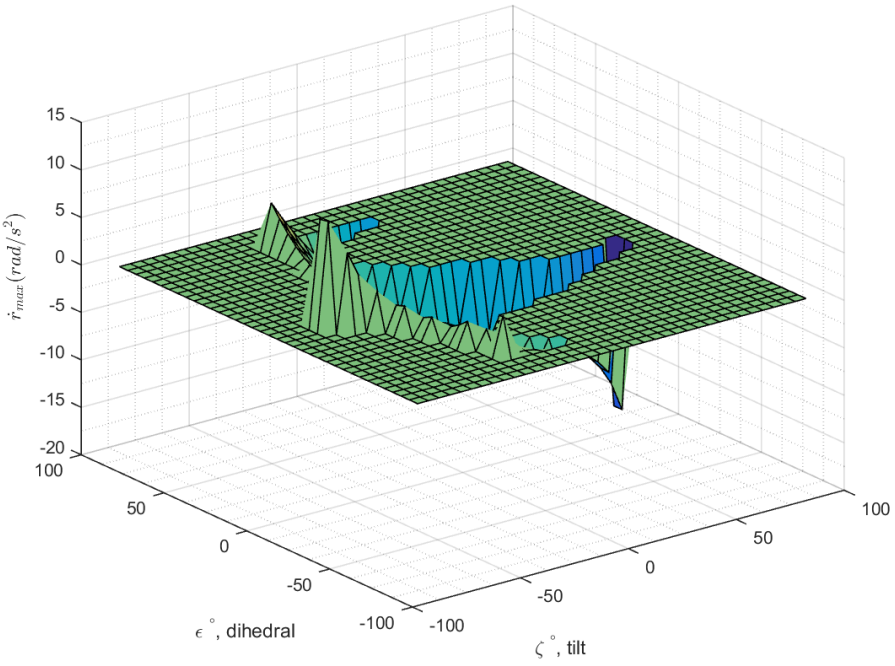

Figure 161: *X4* $\dot{r}$ design space, pure motion enforced, M1 fault

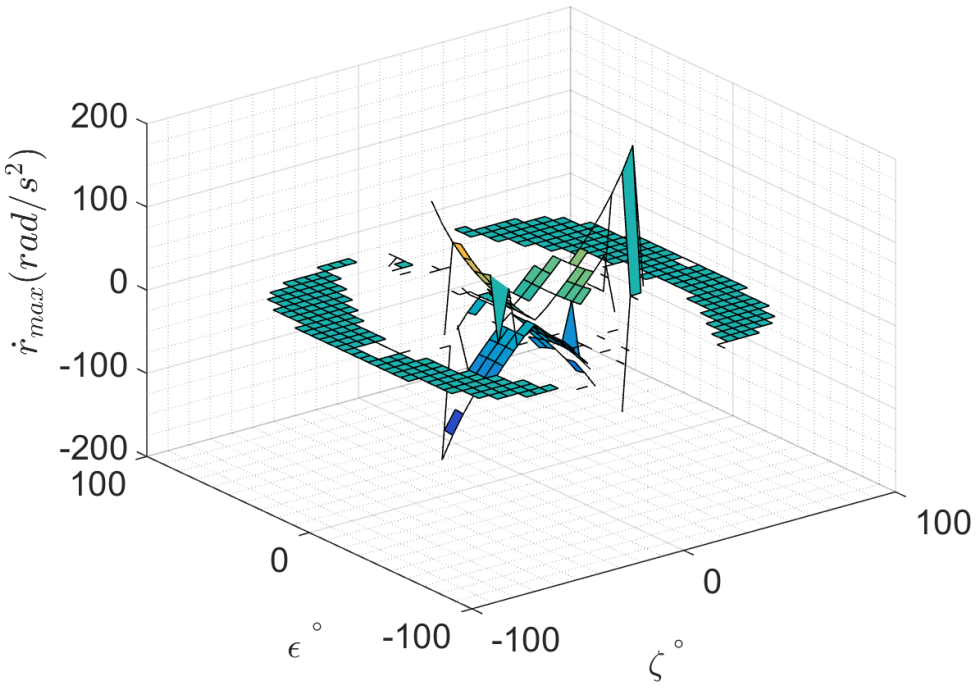

Figure 162: *X4* $\dot{r}$ design space, pure motion enforced, no rotor faults

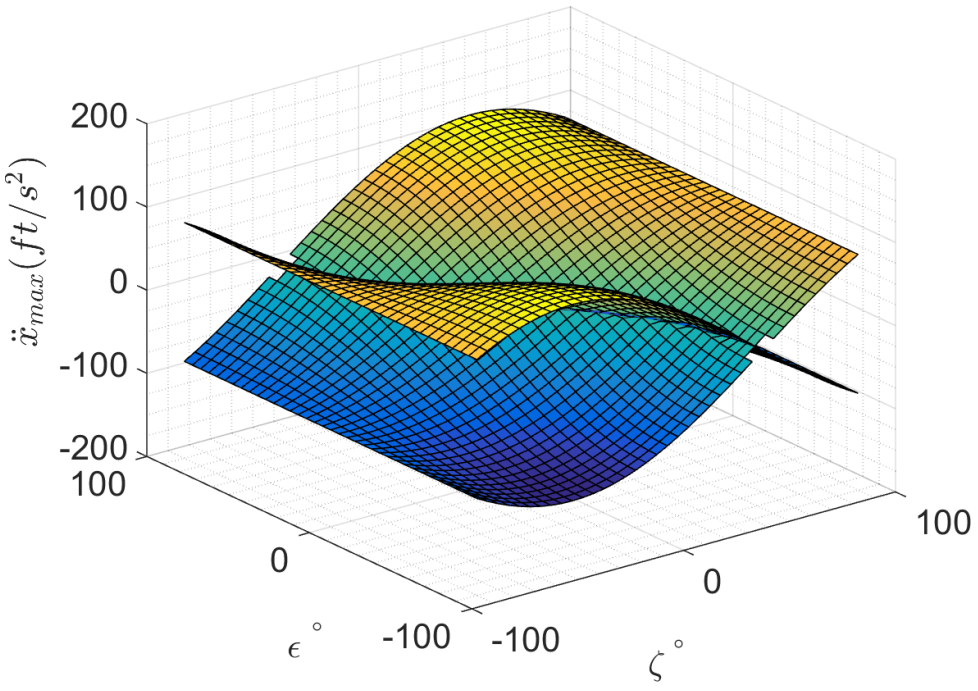

Figure 163: *X4* $\ddot{x}$ design space, pure motion not enforced, no rotor faults

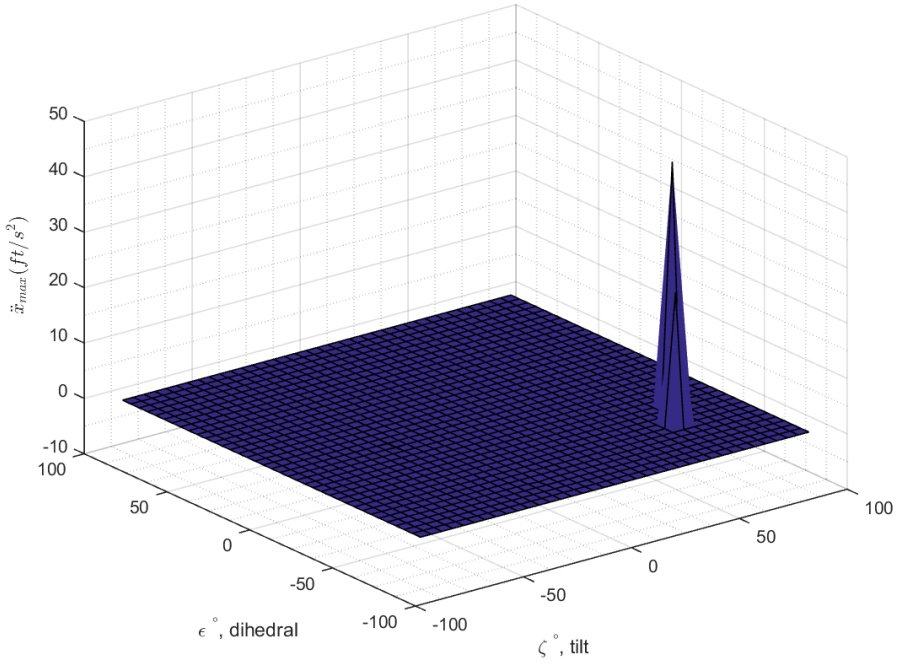

Figure 164: *X4* $\ddot{x}$ design space, pure motion enforced, M1 fault

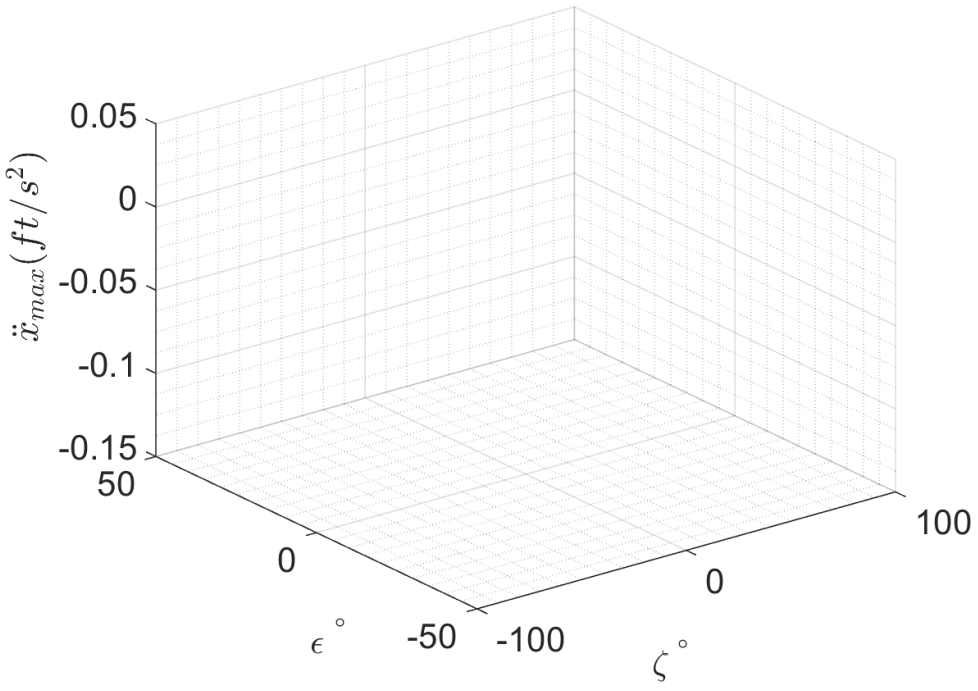

Figure 165: *X4* $\ddot{x}$ design space, pure motion enforced, no rotor faults

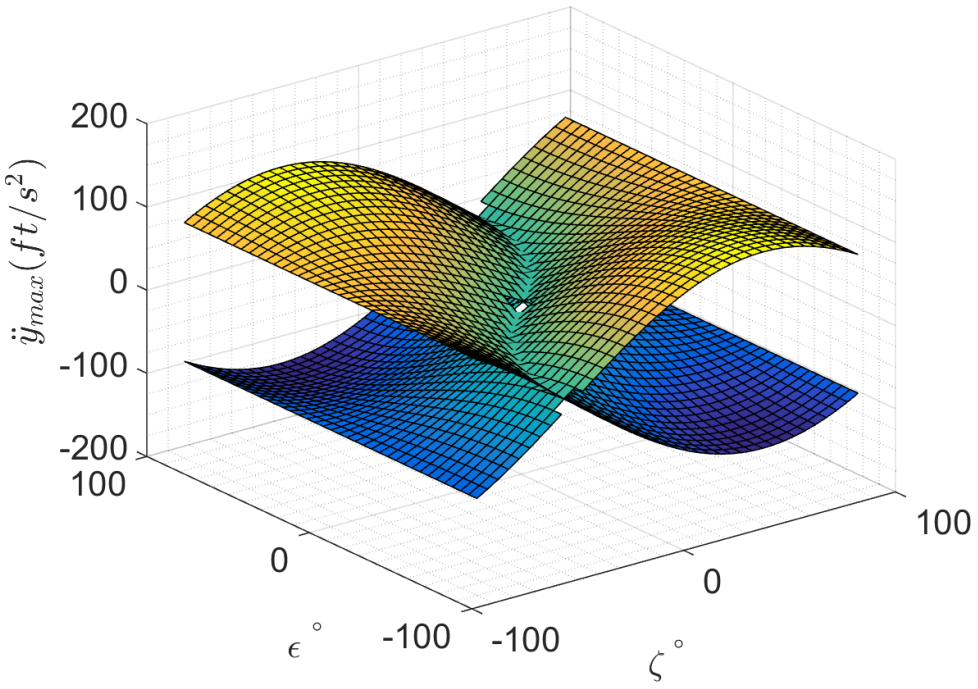

Figure 166: *X4* $\ddot{y}$ design space, pure motion not enforced, no rotor faults

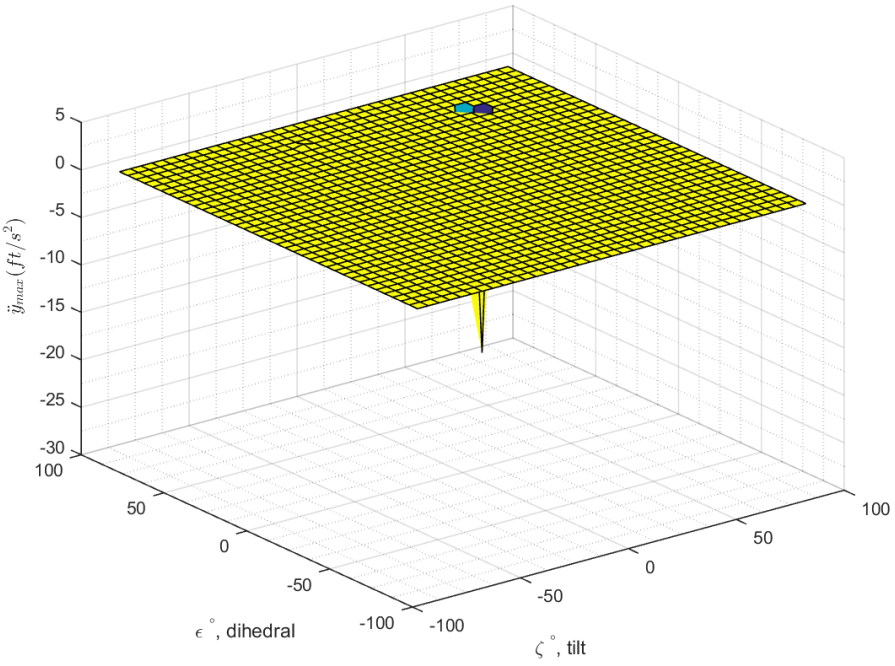

Figure 167: *X4* $\ddot{y}$ design space, pure motion enforced, M1 fault

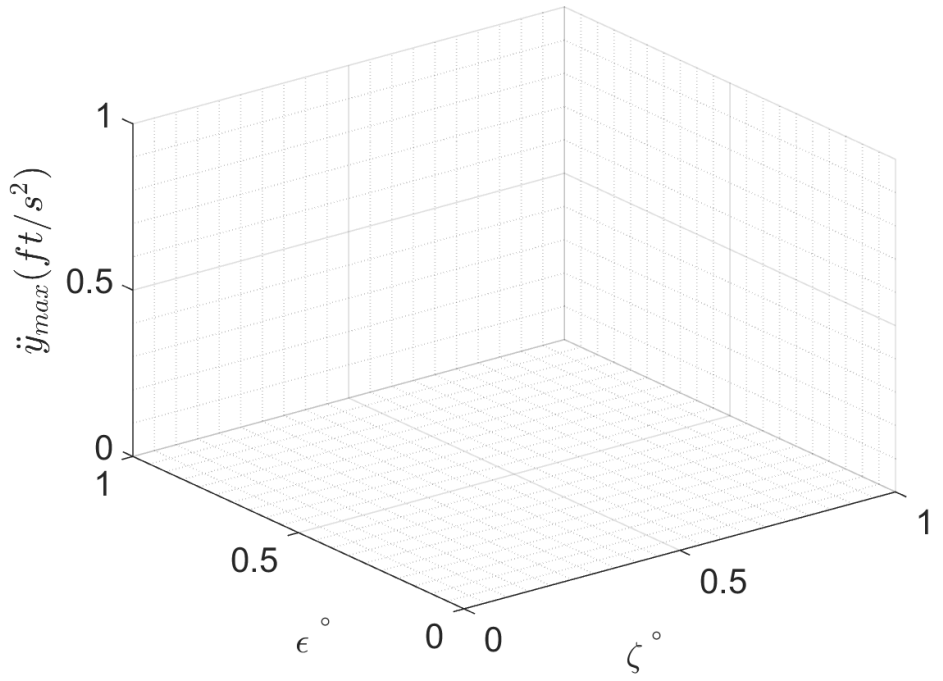

Figure 168: *X4* $\ddot{y}$ design space, pure motion enforced, no rotor faults

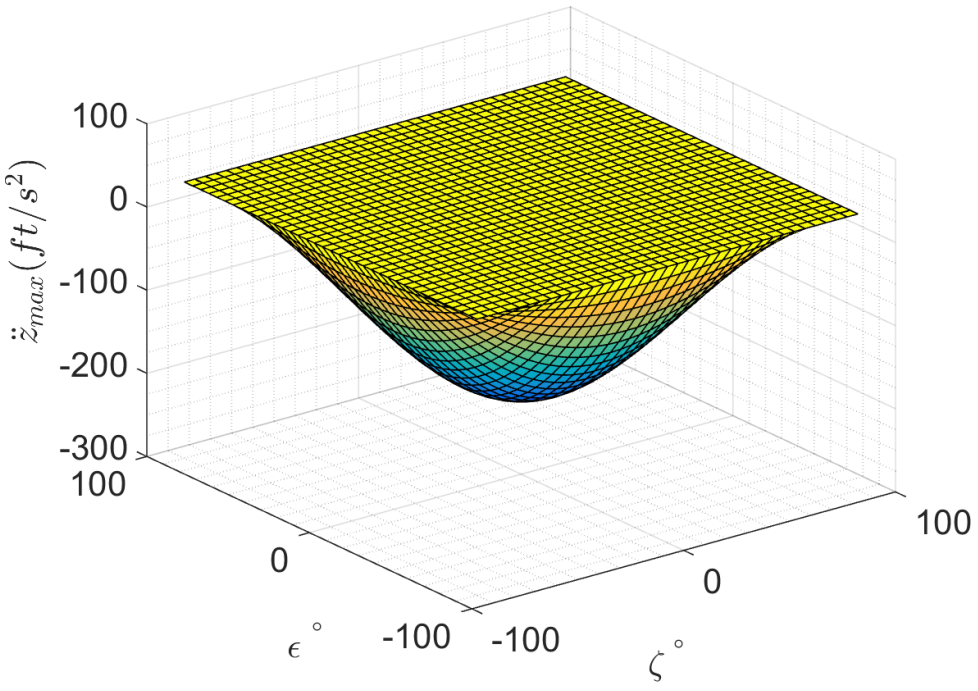

Figure 169: *X4* $\ddot{z}$ design space, pure motion not enforced, no rotor faults

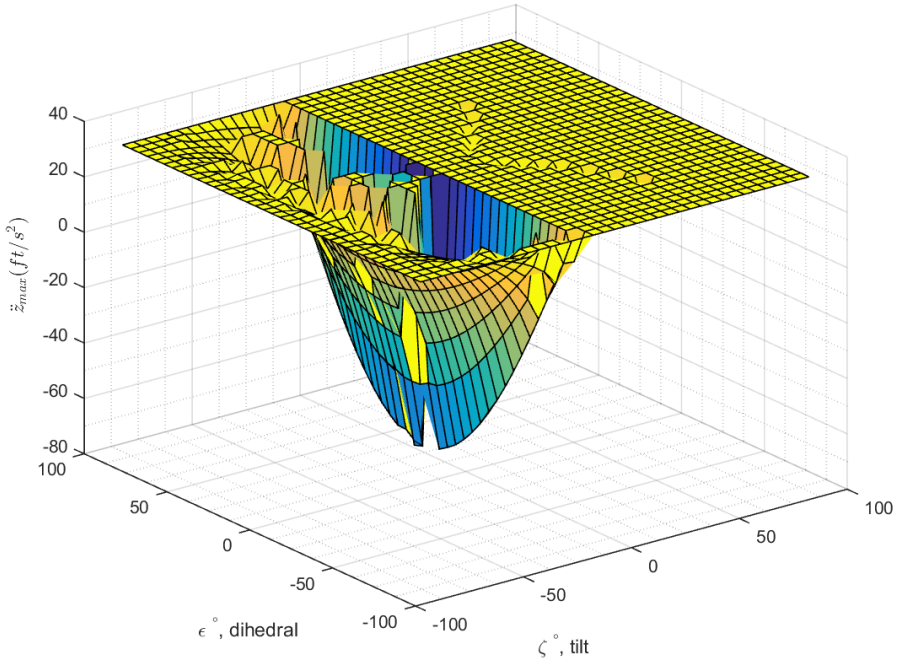

Figure 170: *X4* $\ddot{z}$ design space, pure motion enforced, M1 fault

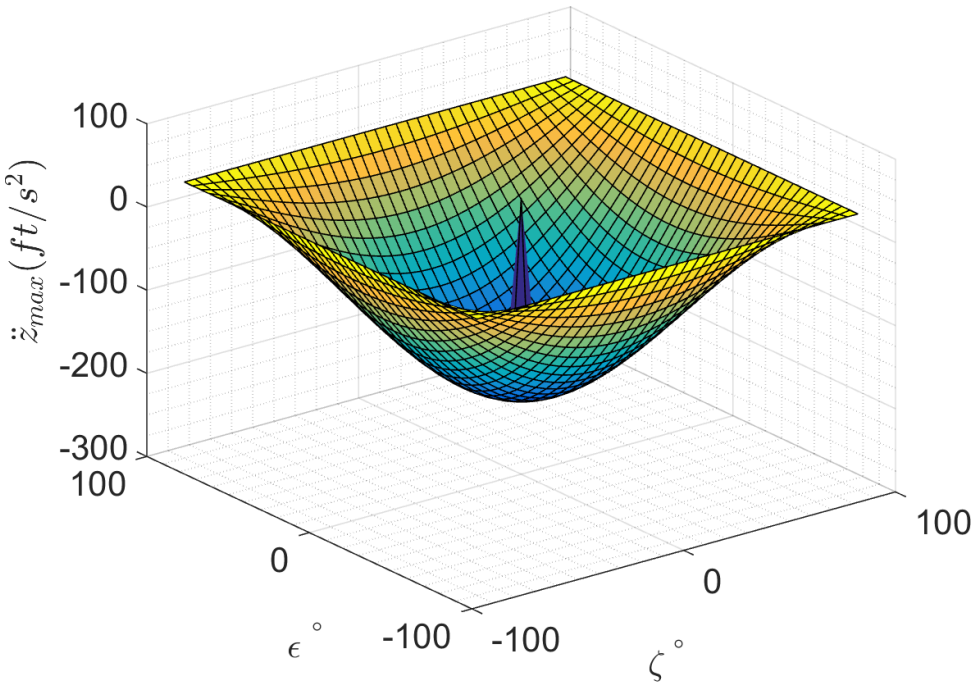

Figure 171: *X4* $\ddot{z}$ design space, pure motion enforced, no rotor faults

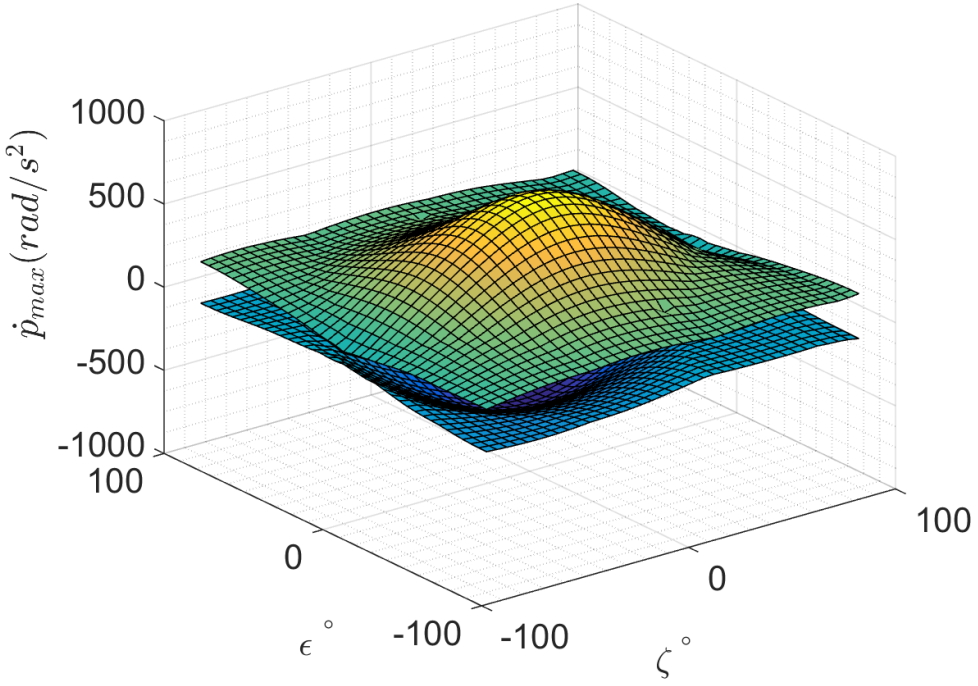

Figure 172: *X6* $\dot{p}$ design space, pure motion not enforced, M1 fault

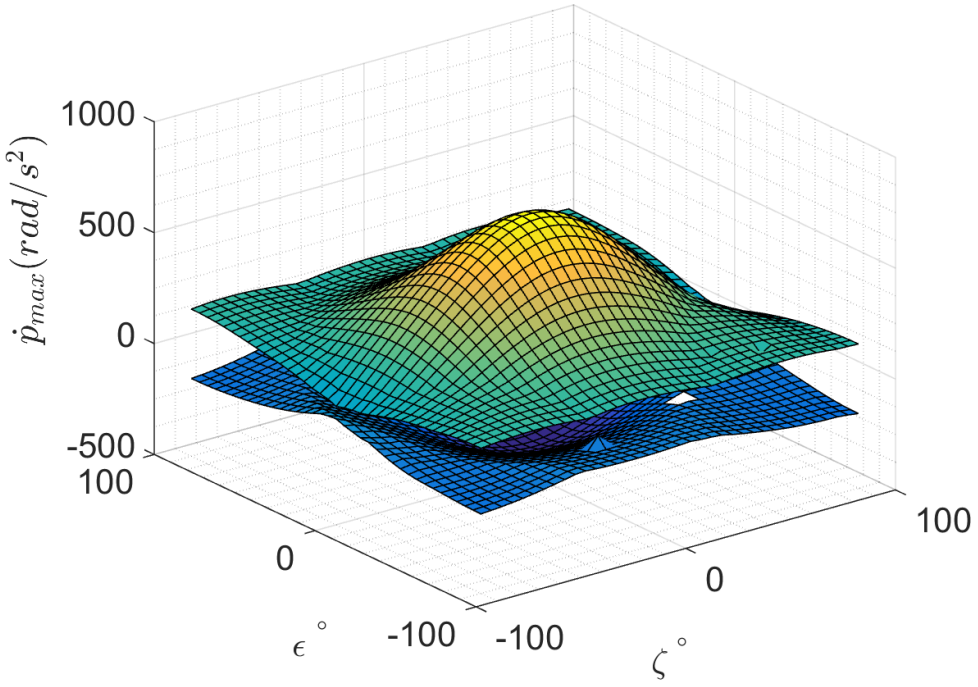

Figure 173: *X6* $\dot{p}$ design space, pure motion not enforced, M2 fault

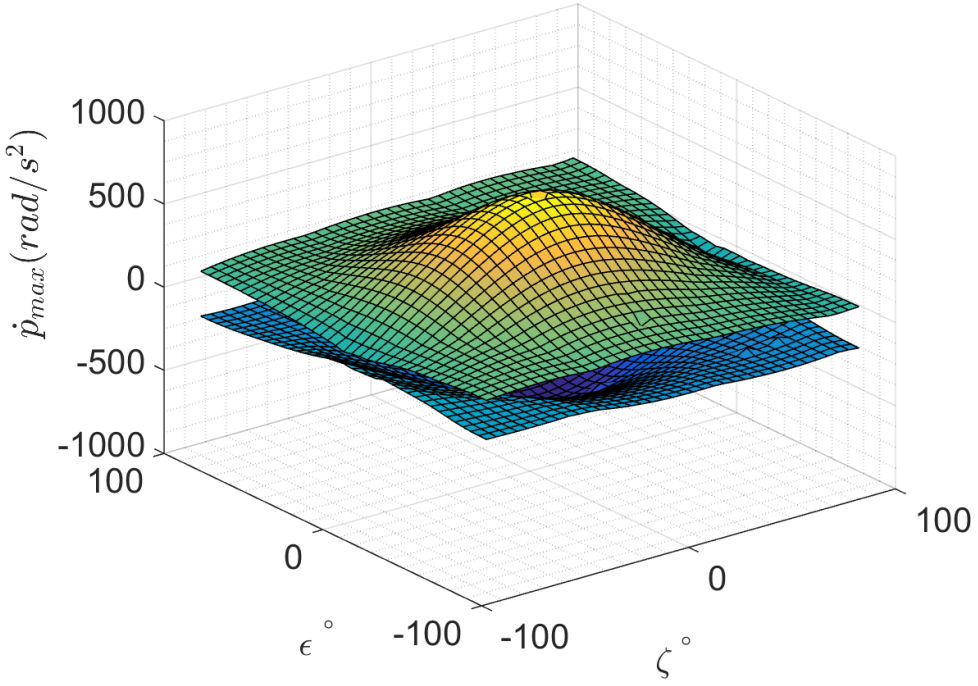

Figure 174: *X6* $\dot{p}$ design space, pure motion not enforced, M3 fault

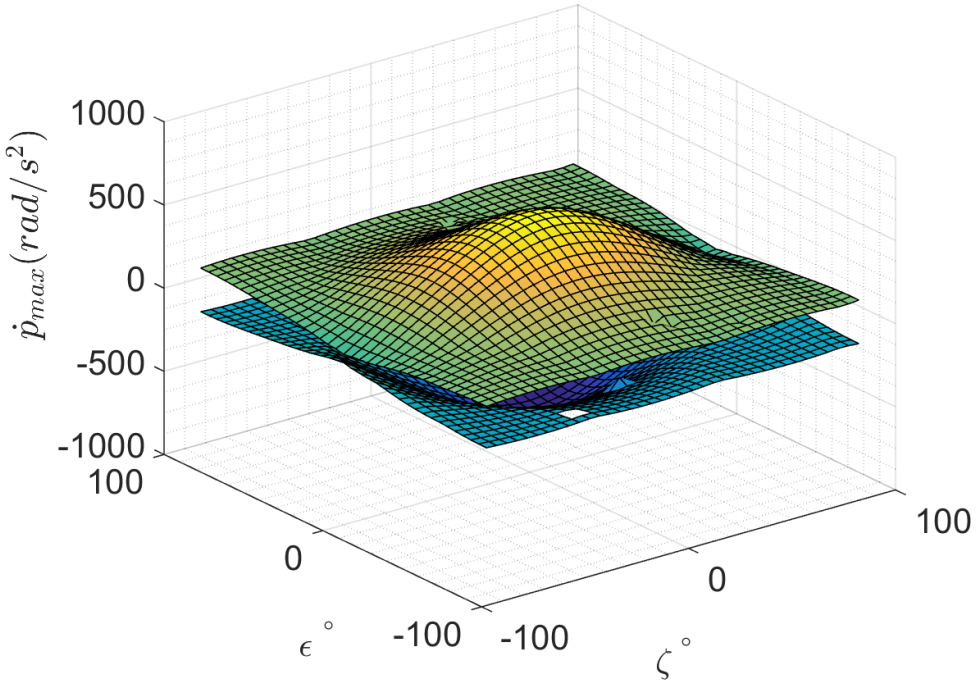

Figure 175: *X6* $\dot{p}$ design space, pure motion not enforced, no rotor faults

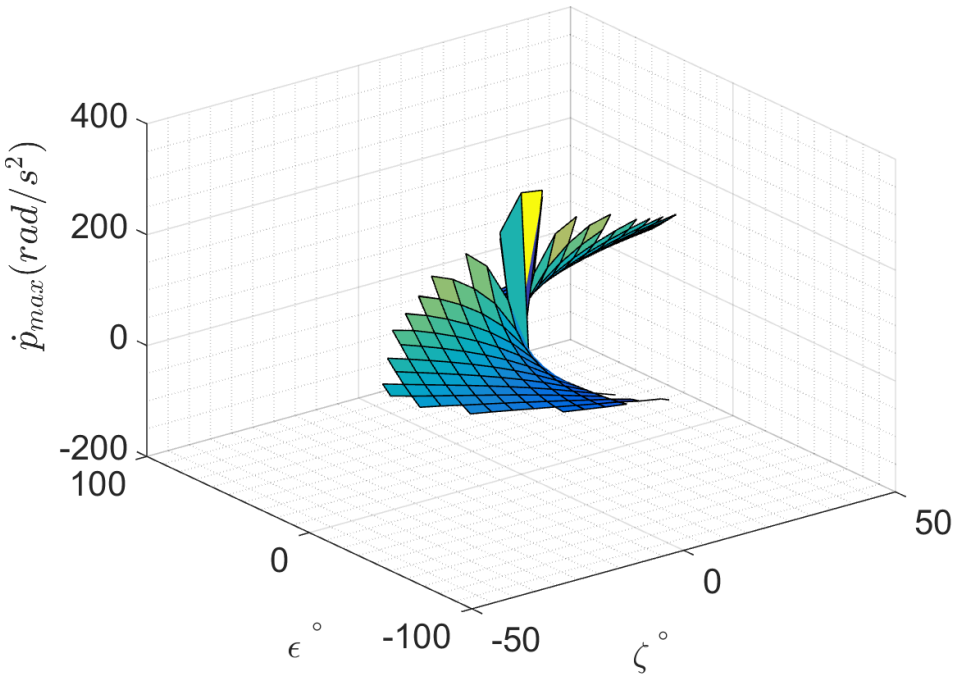

Figure 176: *X6* $\dot{p}$ design space, pure motion enforced, M1 fault

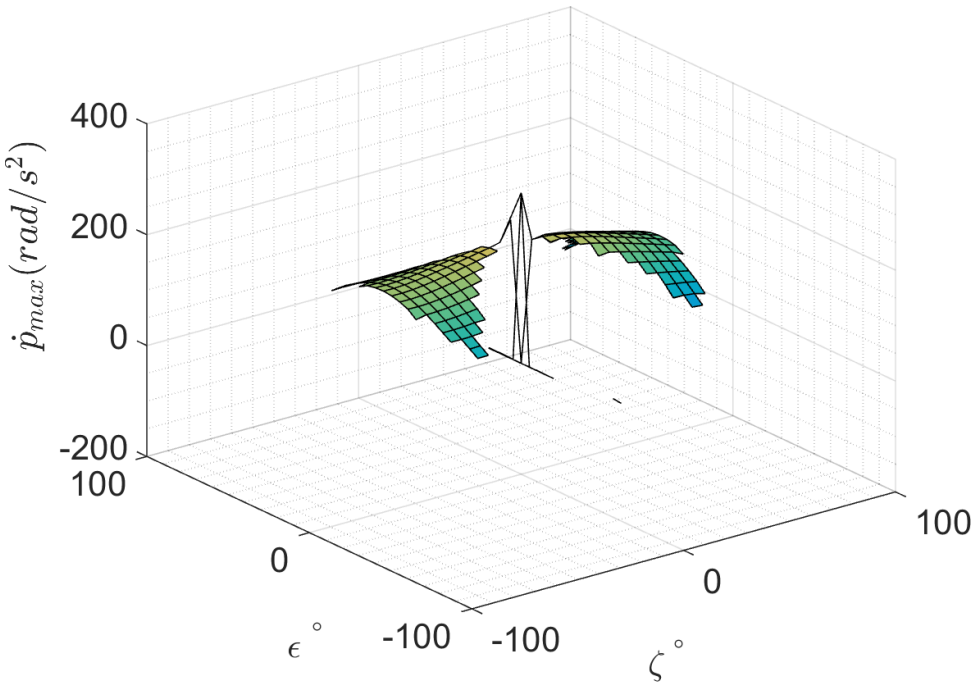

Figure 177: *X6* $\dot{p}$ design space, pure motion enforced, M2 fault

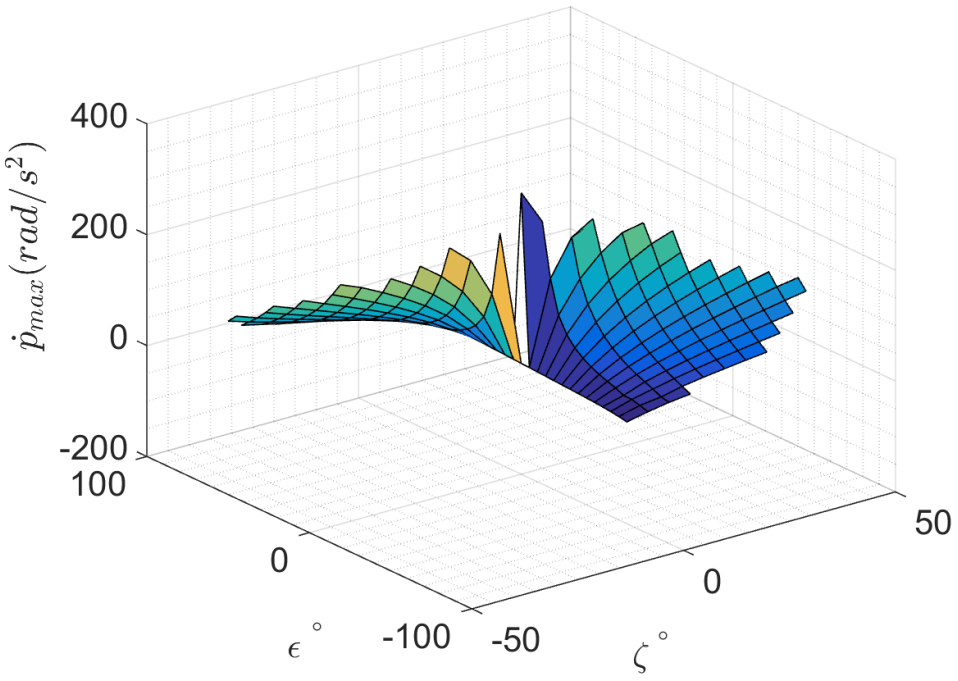

Figure 178: *X6 $\dot{p}$* design space, pure motion enforced, M3 fault

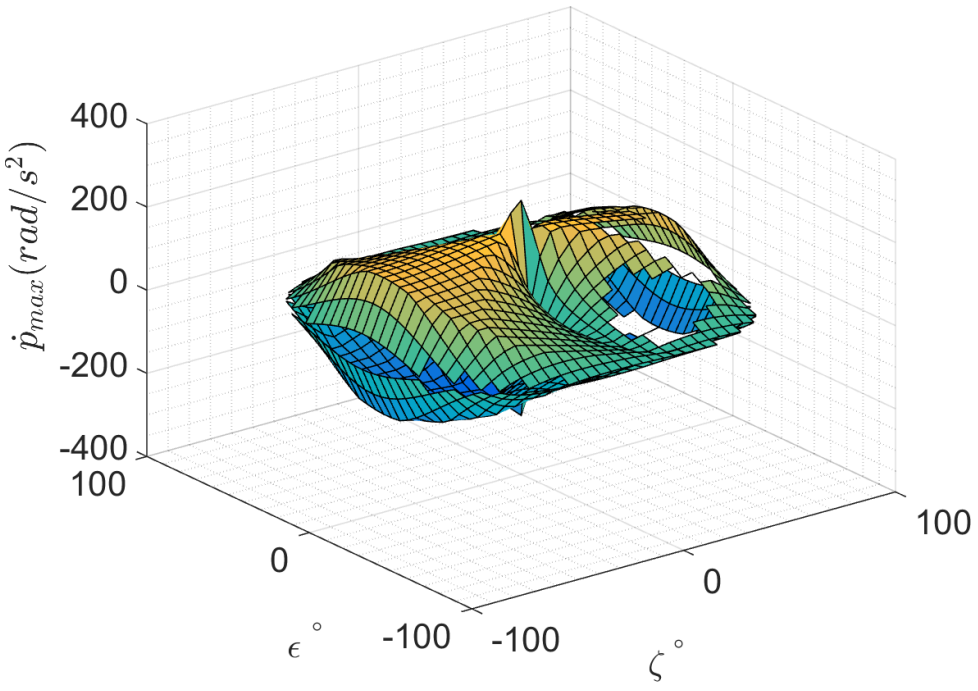

Figure 179: *X6 $\dot{p}$* design space, pure motion enforced, no rotor faults

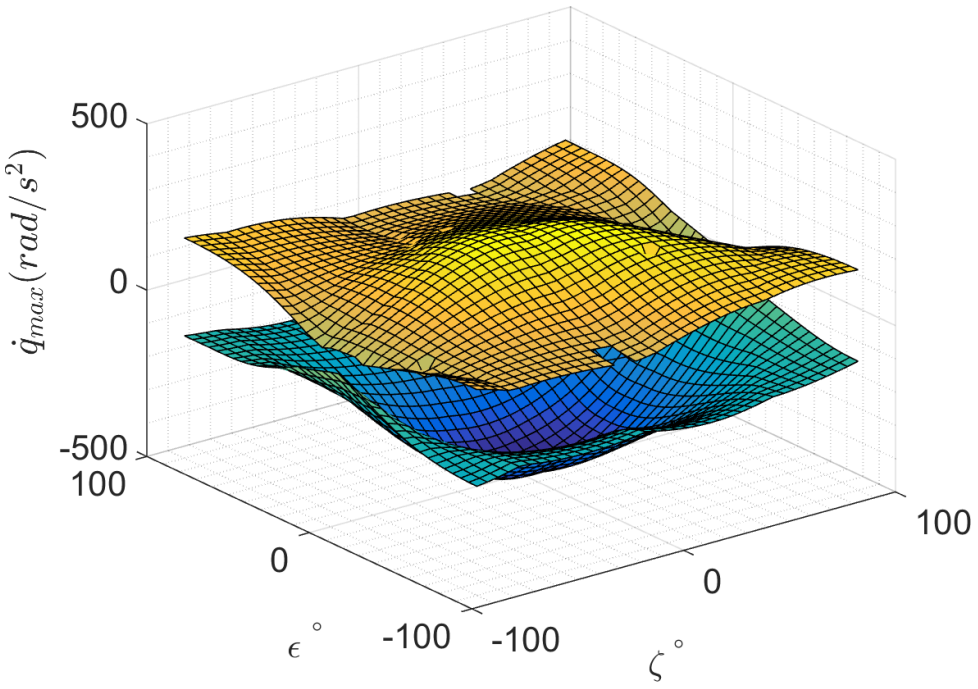

Figure 180: *X6* $\dot{q}$ design space, pure motion not enforced, M1 fault

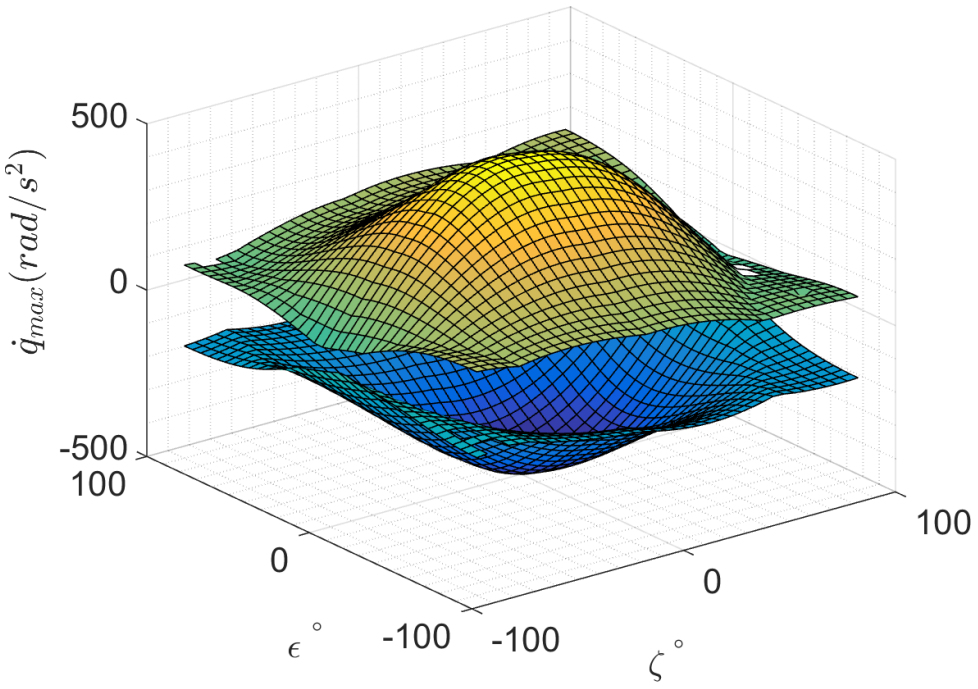

Figure 181: *X6* $\dot{q}$ design space, pure motion not enforced, M2 fault

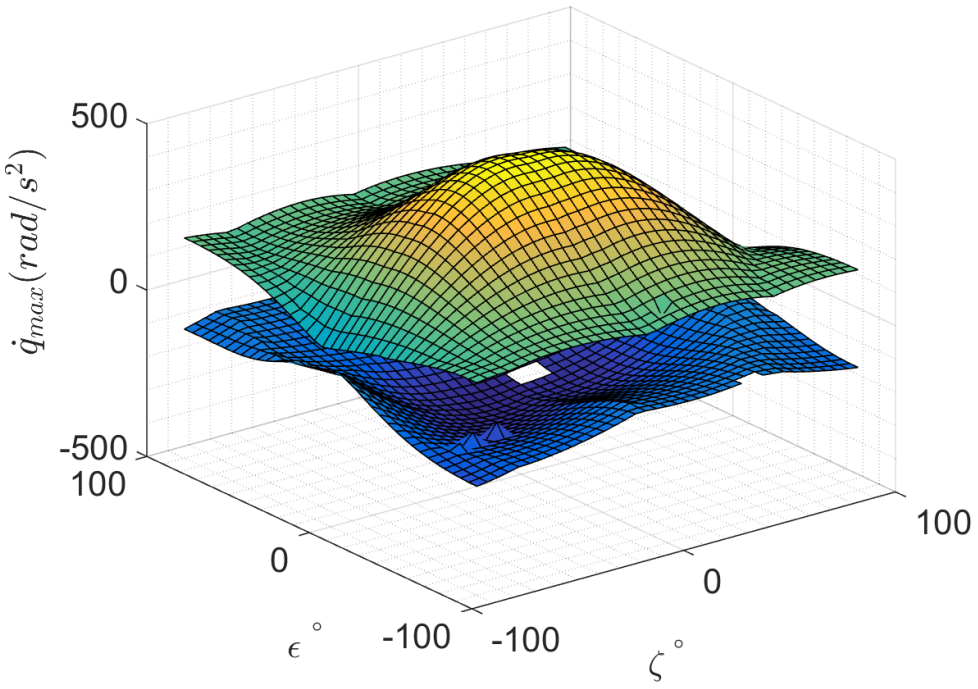

Figure 182: *X6* $\dot{q}$ design space, pure motion not enforced, M3 fault

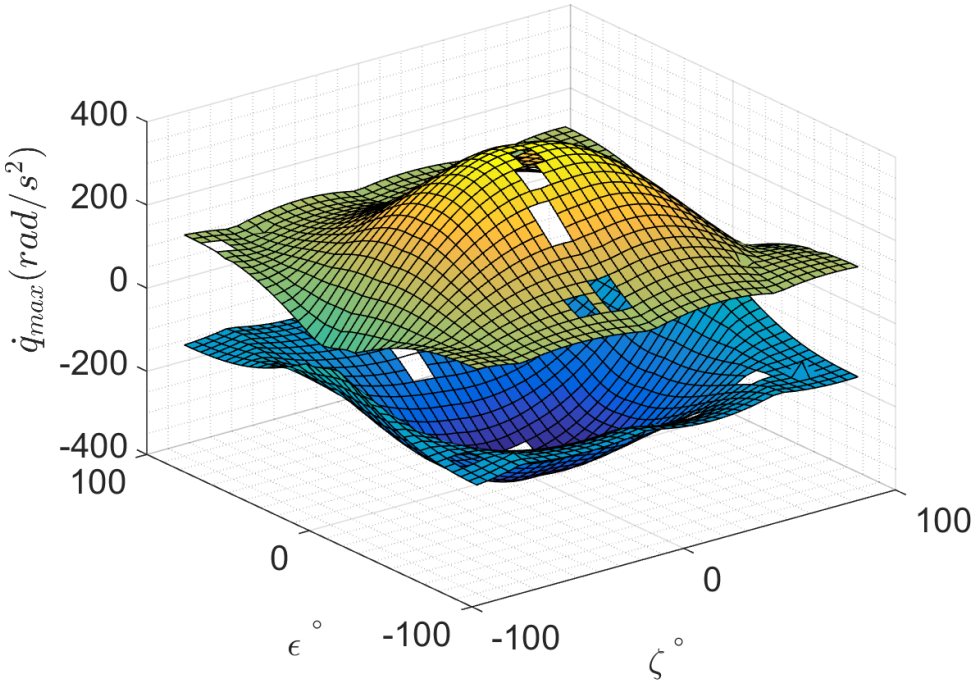

Figure 183: *X6* $\dot{q}$ design space, pure motion not enforced, no rotor faults

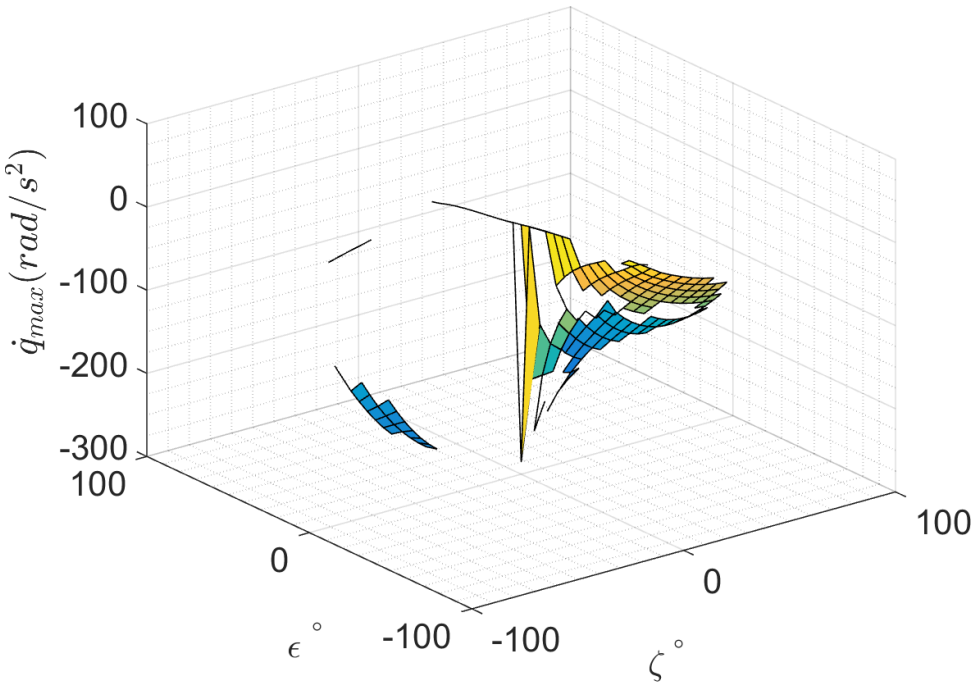

Figure 184: *X6* $\dot{q}$ design space, pure motion enforced, M1 fault

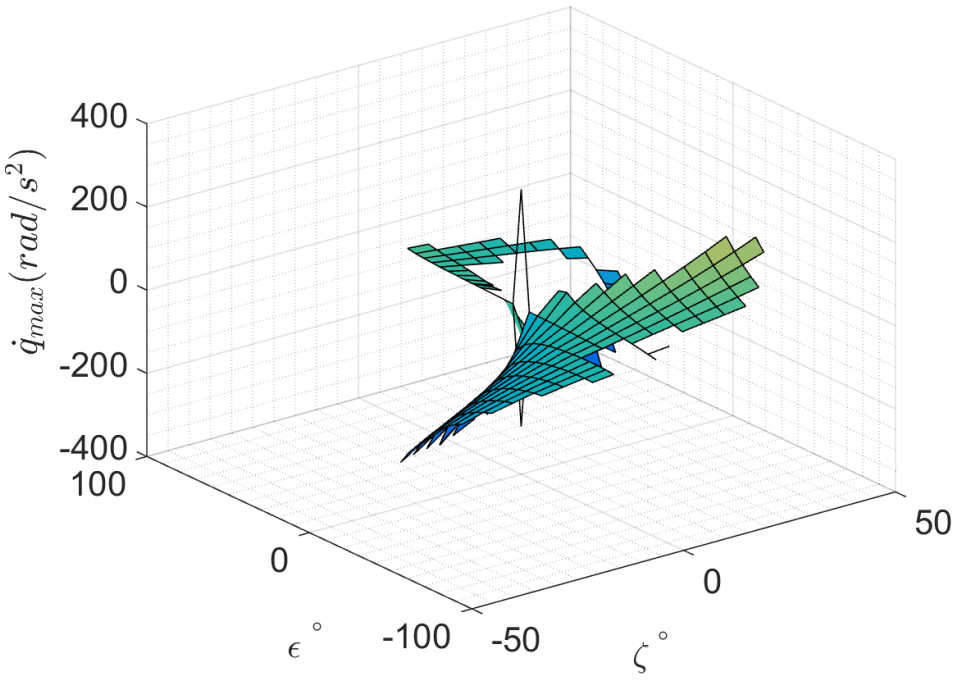

Figure 185: *X6* $\dot{q}$ design space, pure motion enforced, M2 fault

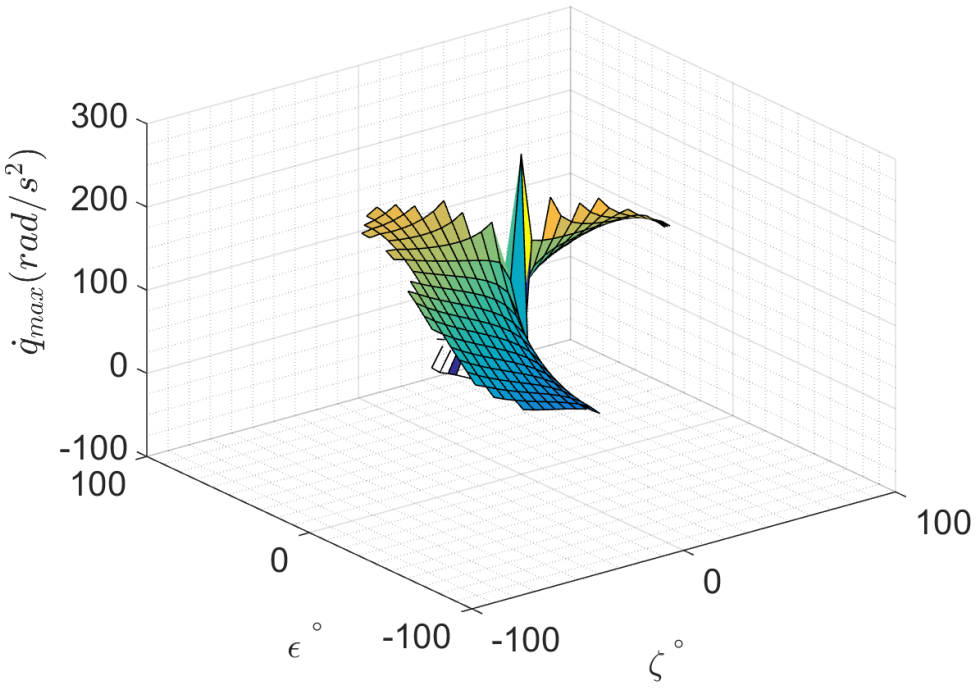

Figure 186: *X6* $\dot{q}$ design space, pure motion enforced, M3 fault

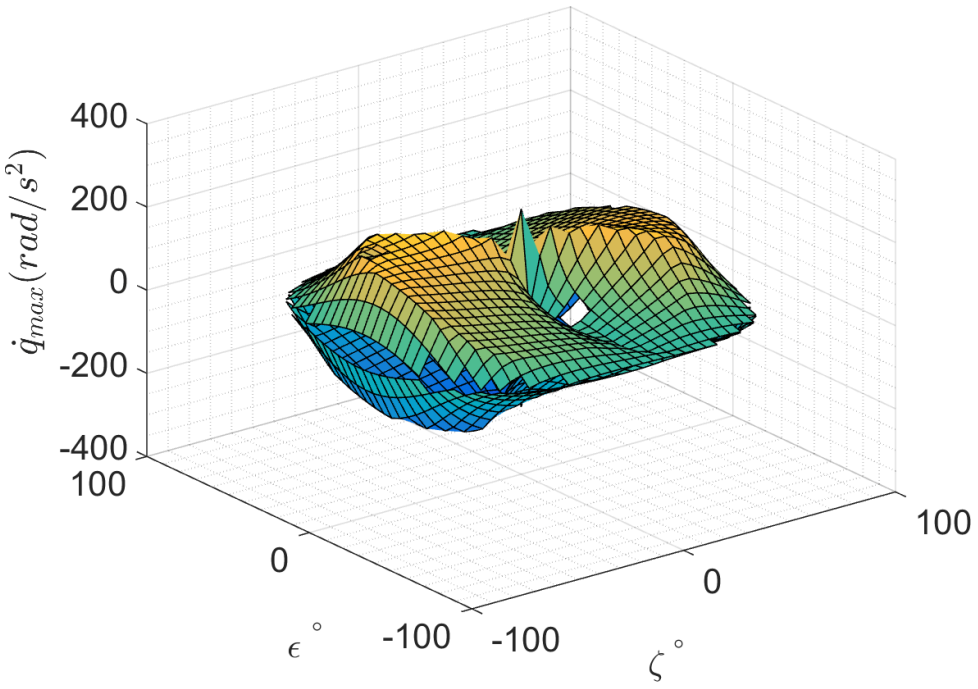

Figure 187: *X6* $\dot{q}$ design space, pure motion enforced, no rotor faults

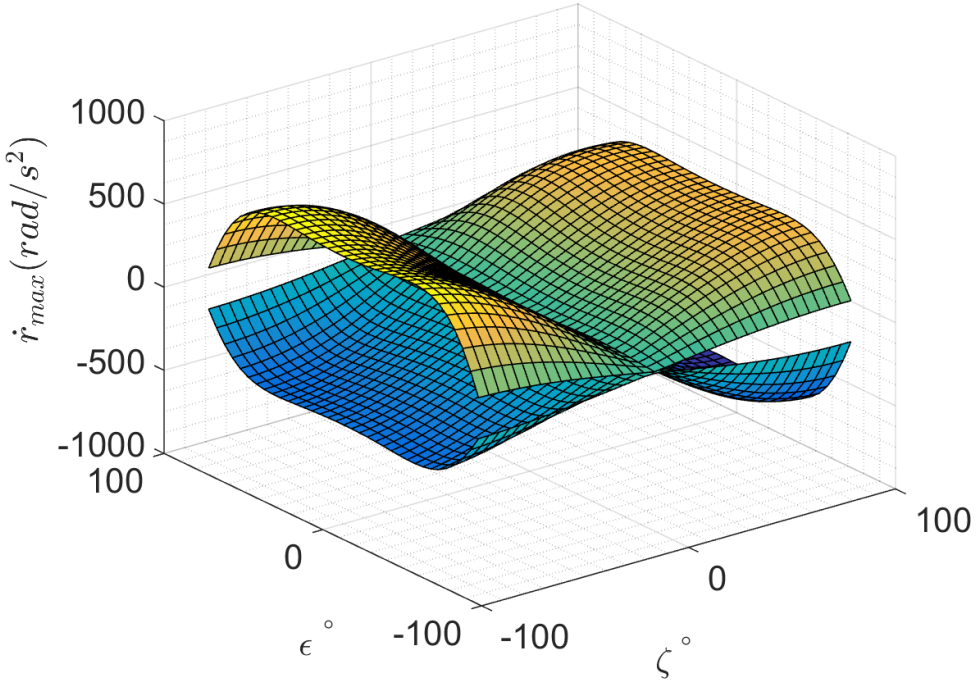

Figure 188: *X6* $\dot{r}$ design space, pure motion not enforced, M1 fault

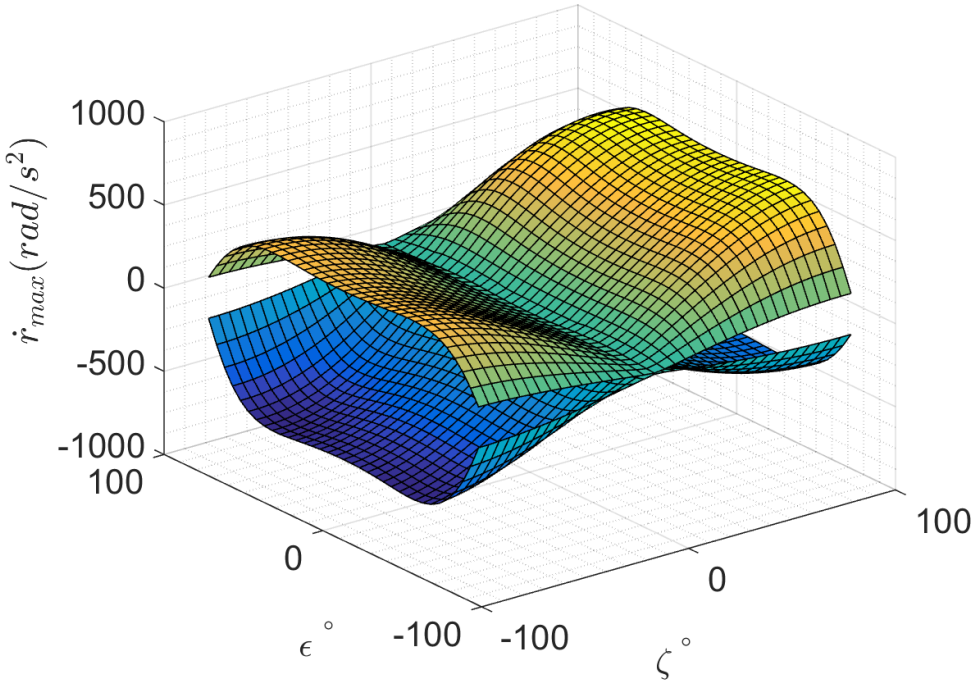

Figure 189: *X6* $\dot{r}$ design space, pure motion not enforced, M2 fault

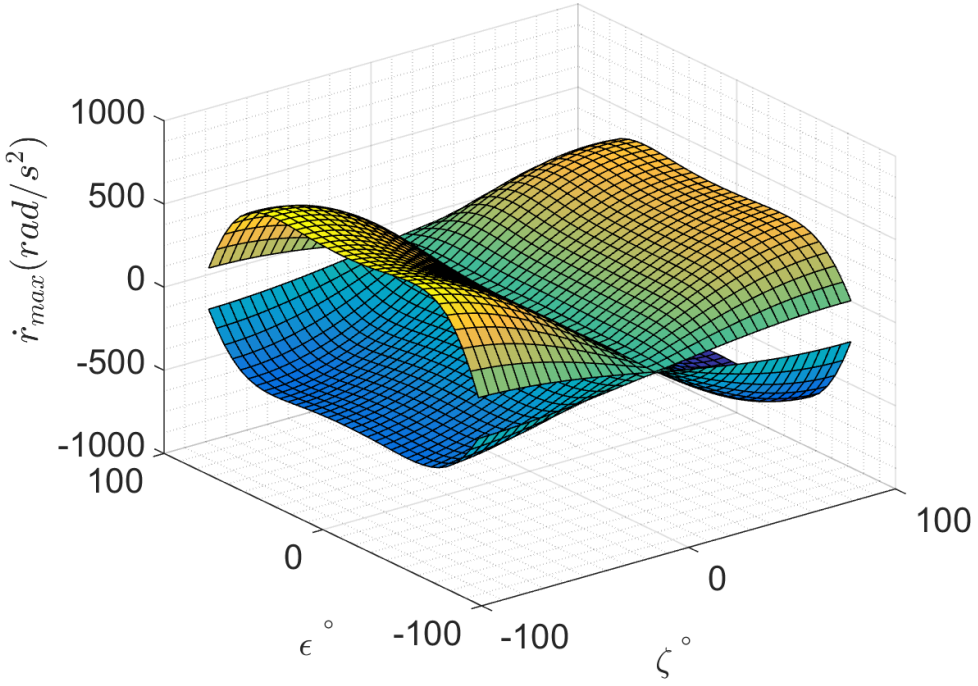

Figure 190: *X6* $\dot{r}$ design space, pure motion not enforced, M3 fault

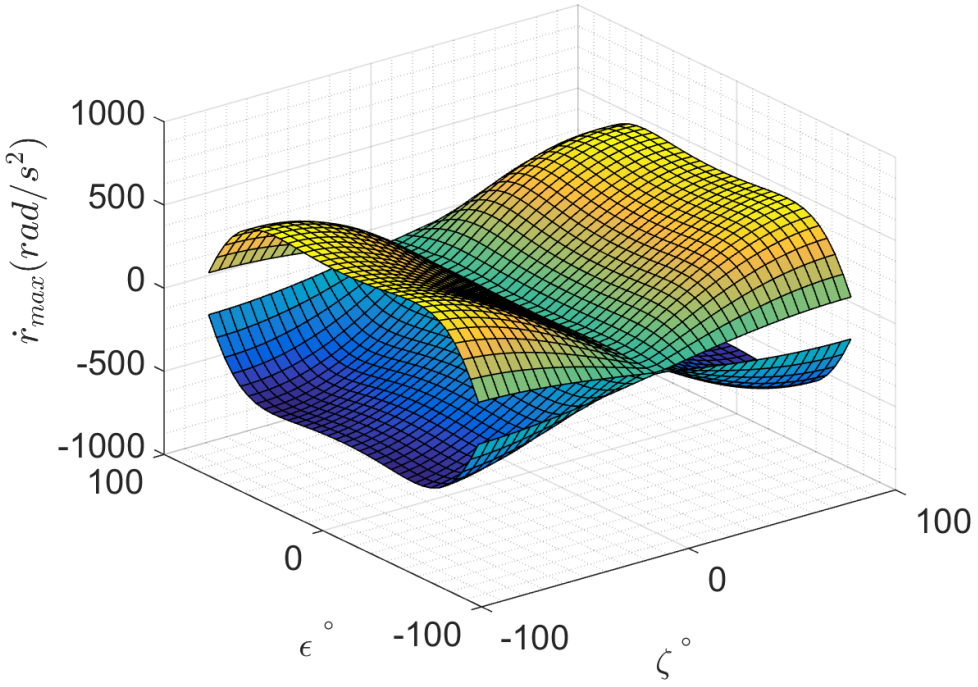

Figure 191: *X6* $\dot{r}$ design space, pure motion not enforced, no rotor faults

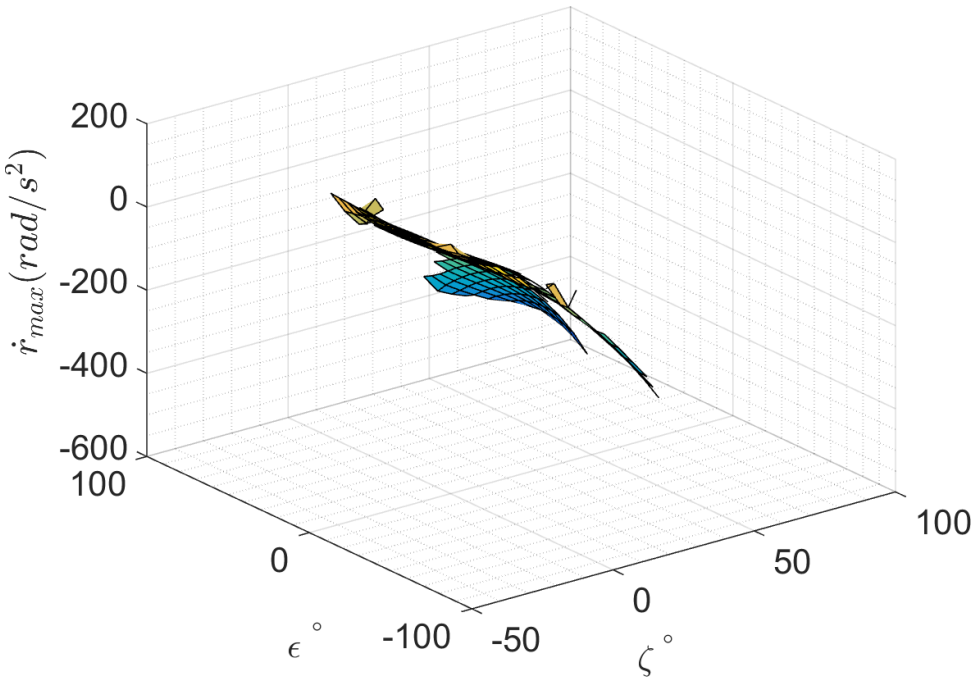

Figure 192: *X6* $\dot{r}$ design space, pure motion enforced, M1 fault

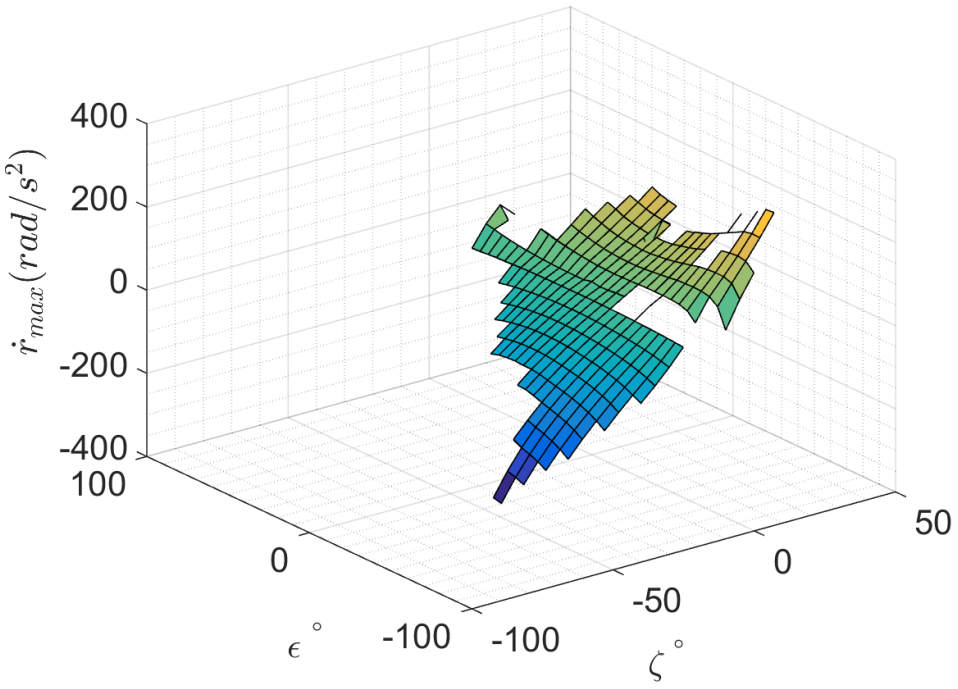

Figure 193: *X6* $\dot{r}$ design space, pure motion enforced, M2 fault

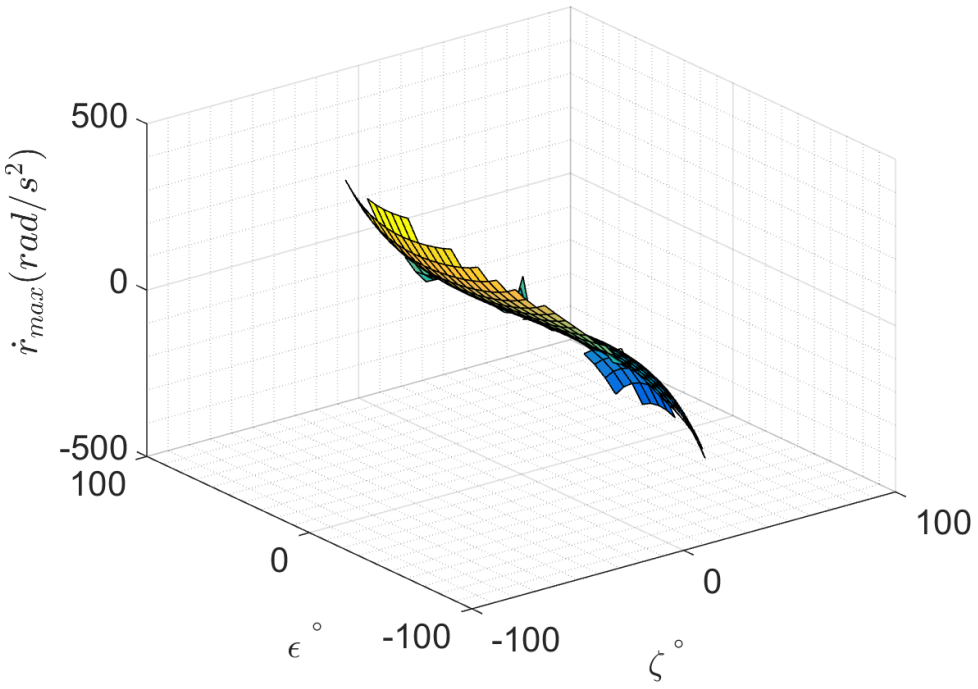

Figure 194: *X6* $\dot{r}$ design space, pure motion enforced, M3 fault

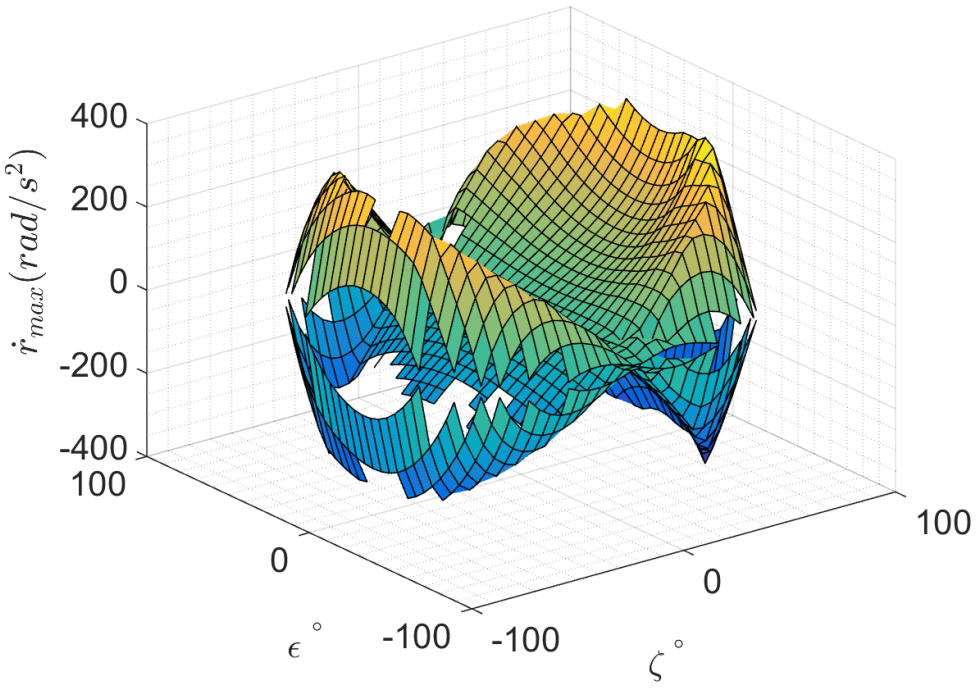

Figure 195: *X6* $\dot{r}$ design space, pure motion enforced, no rotor faults

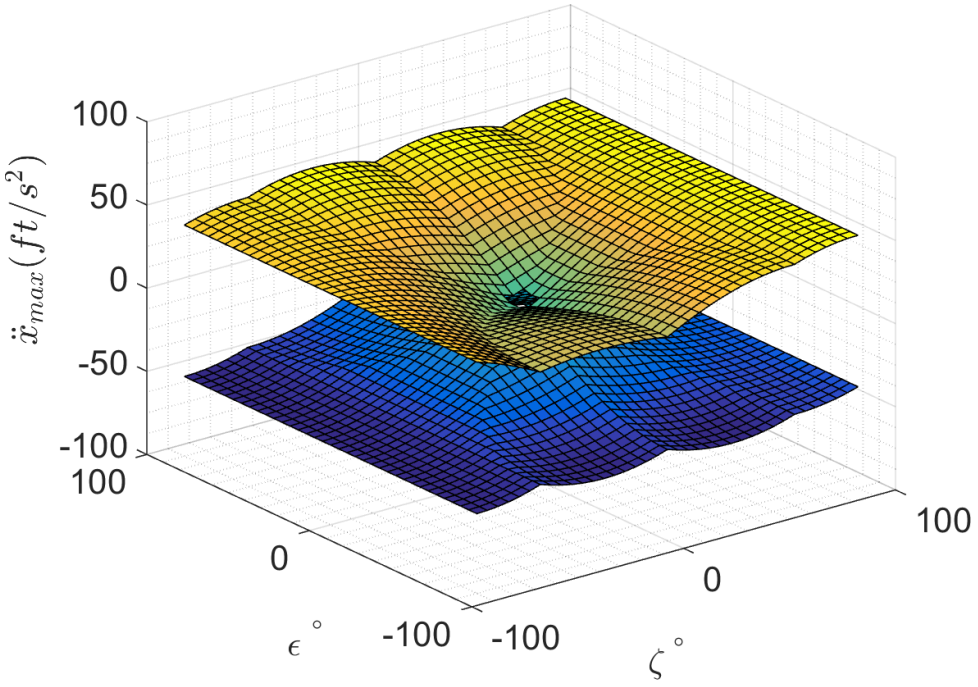

Figure 196: *X6* $\ddot{x}$ design space, pure motion not enforced, M1 fault

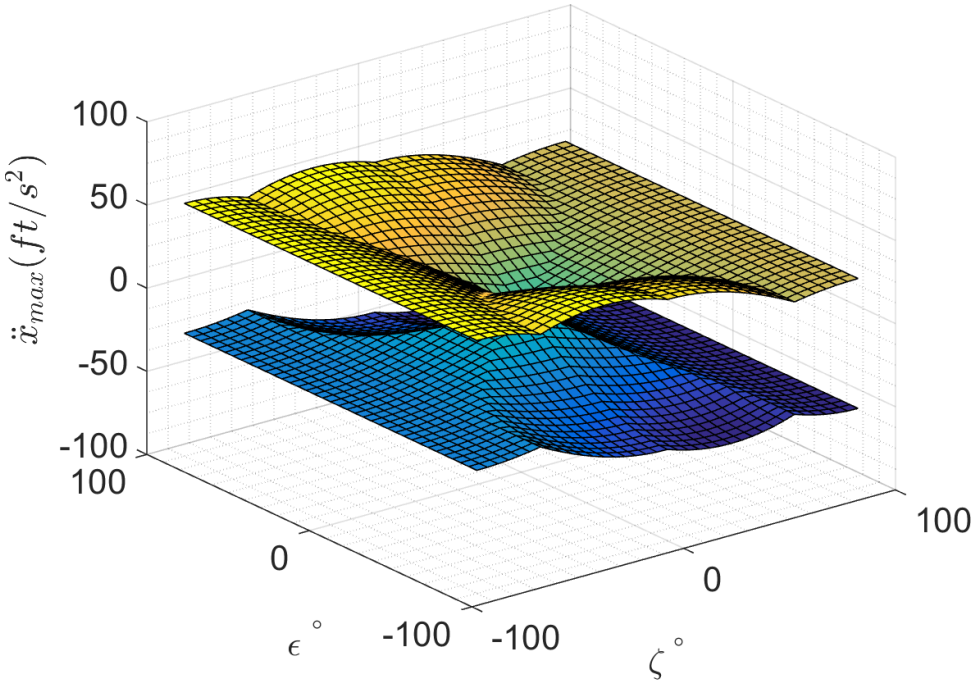

Figure 197: *X6* $\ddot{x}$ design space, pure motion not enforced, M2 fault

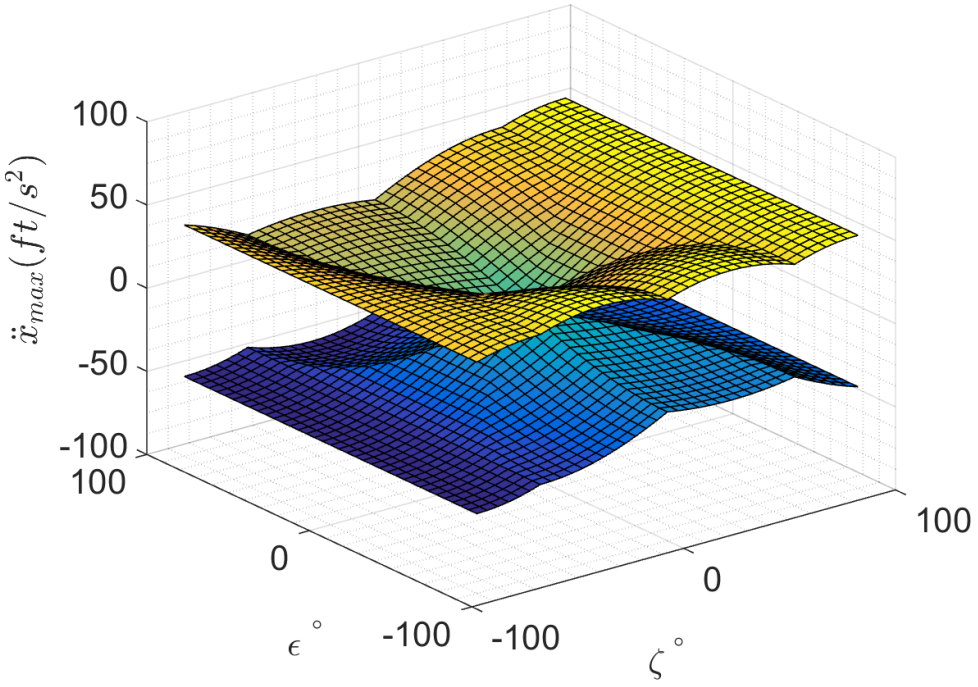

Figure 198: *X6* $\ddot{x}$ design space, pure motion not enforced, M3 fault

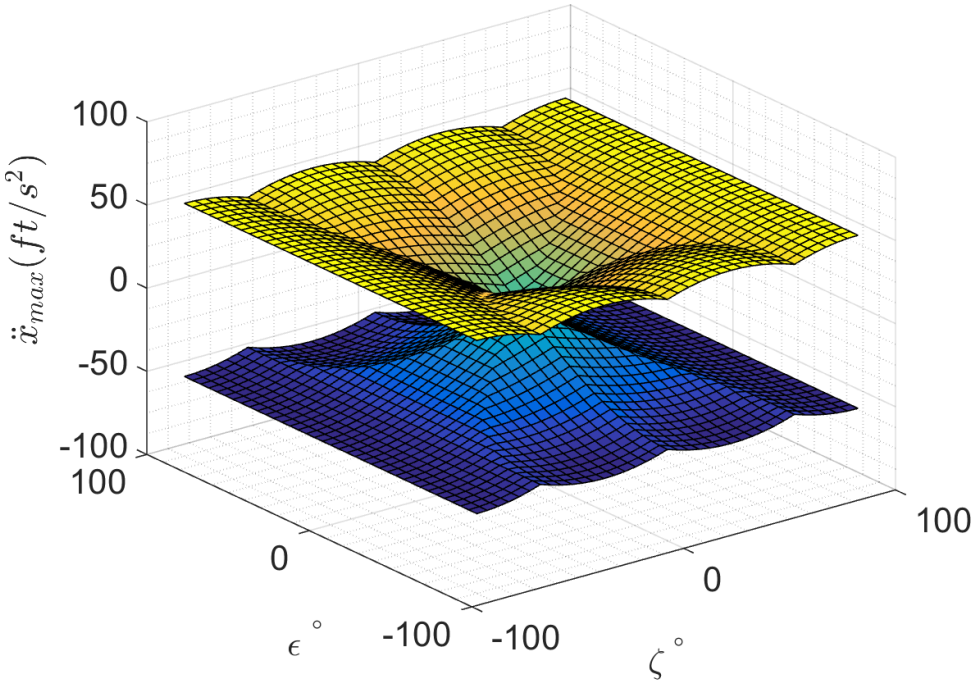

Figure 199: *X6* $\ddot{x}$ design space, pure motion not enforced, no rotor faults

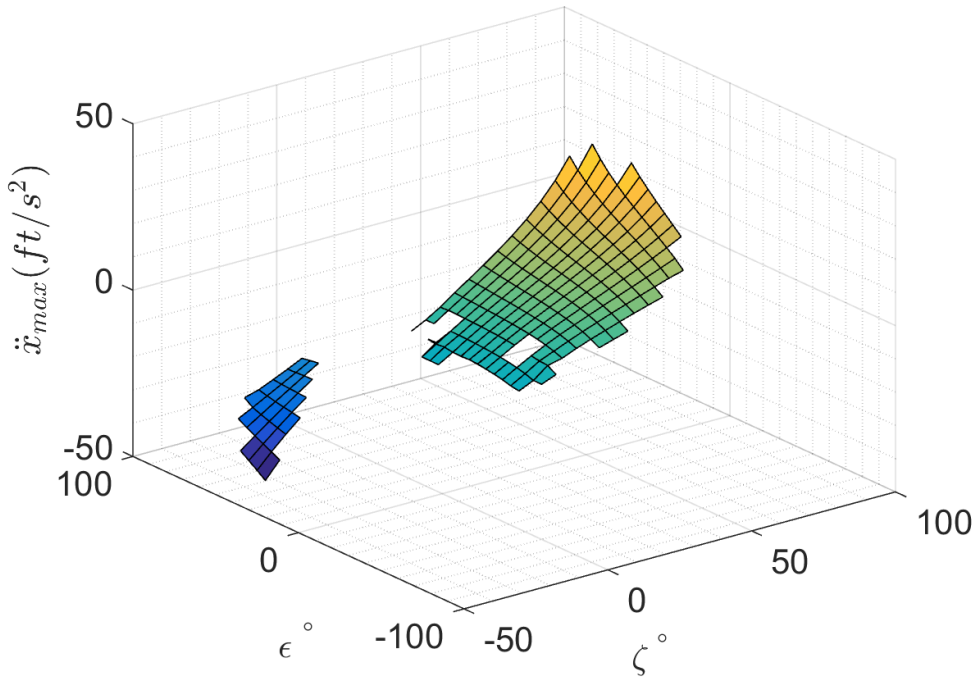

Figure 200: *X6* $\ddot{x}$ design space, pure motion enforced, M1 fault

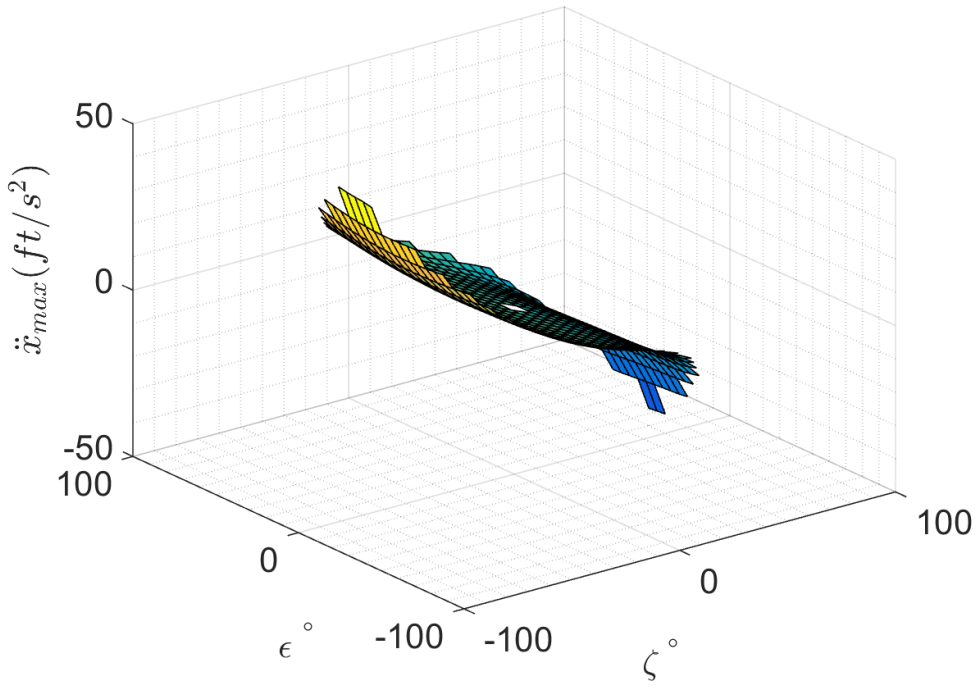

Figure 201: *X6* $\ddot{x}$ design space, pure motion enforced, M2 fault

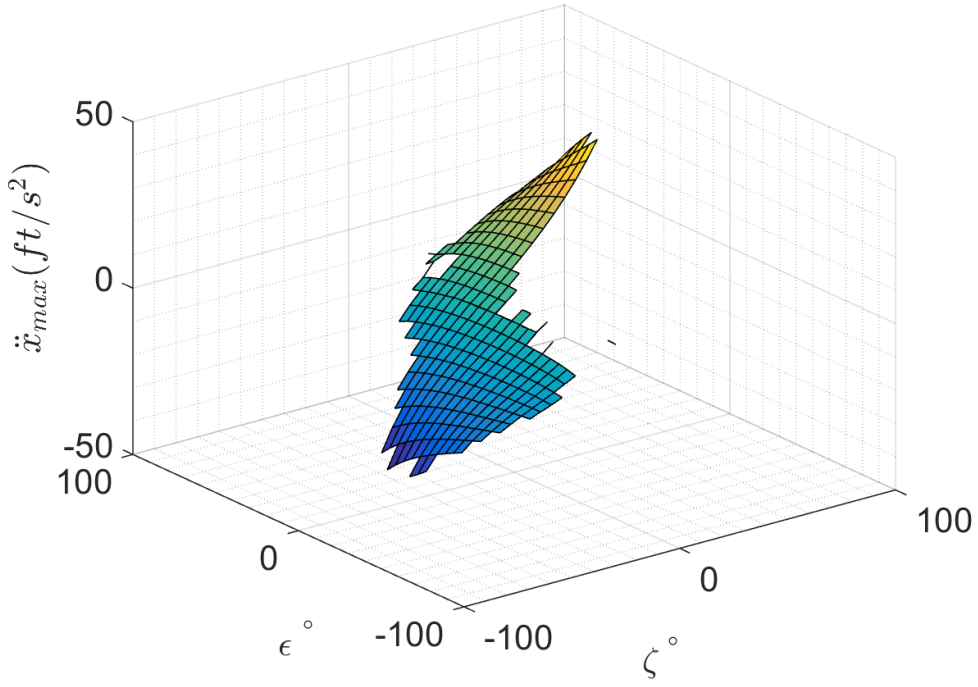

Figure 202: *X6* $\ddot{x}$ design space, pure motion enforced, M3 fault

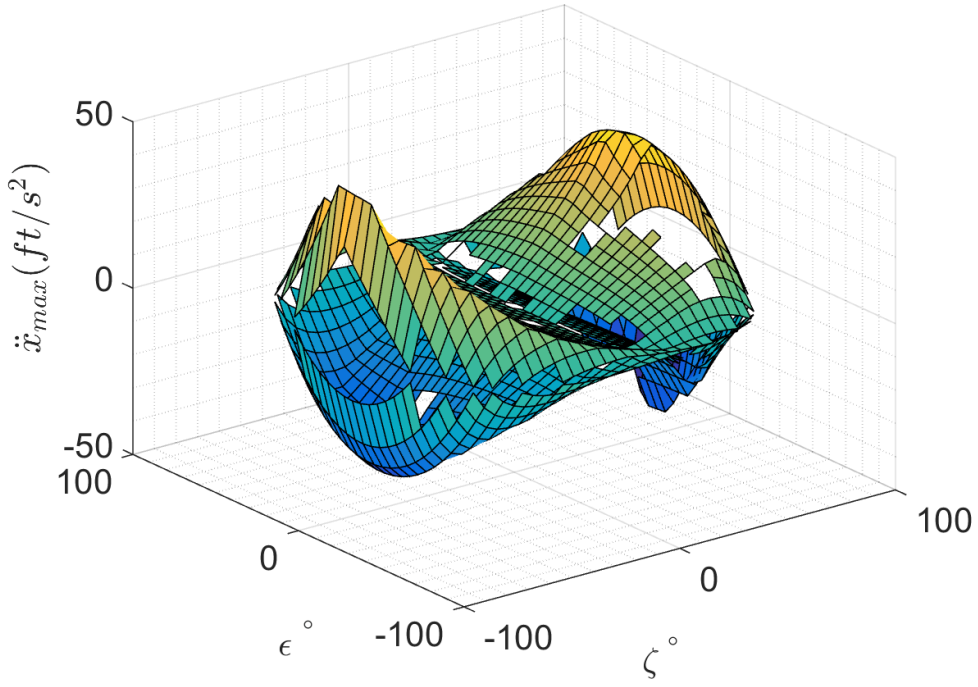

Figure 203: *X6* $\ddot{x}$ design space, pure motion enforced, no rotor faults

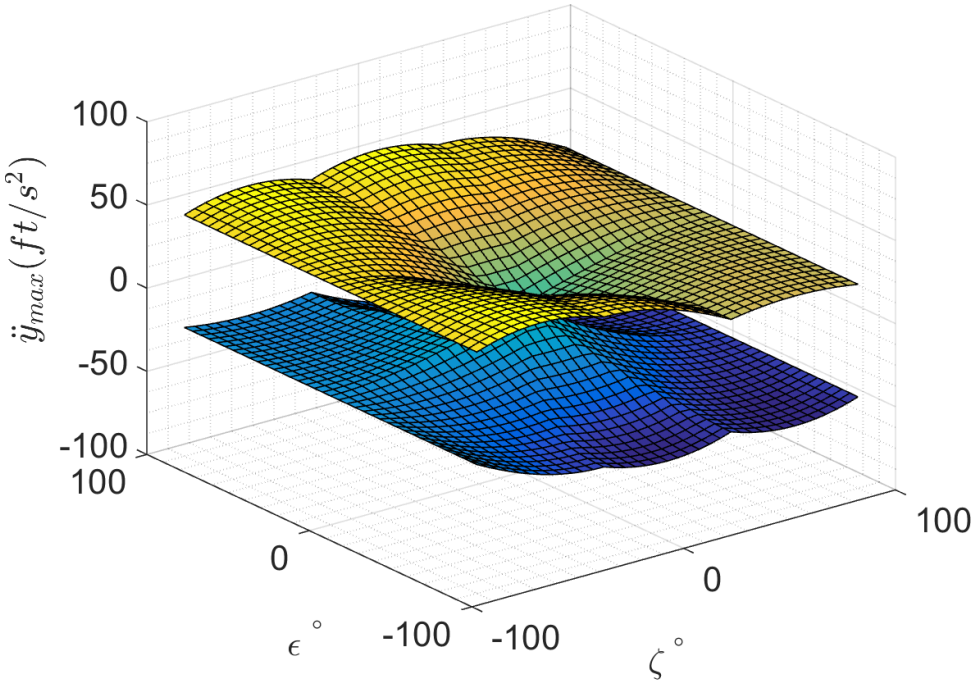

Figure 204: *X6* $\ddot{y}$ design space, pure motion not enforced, M1 fault

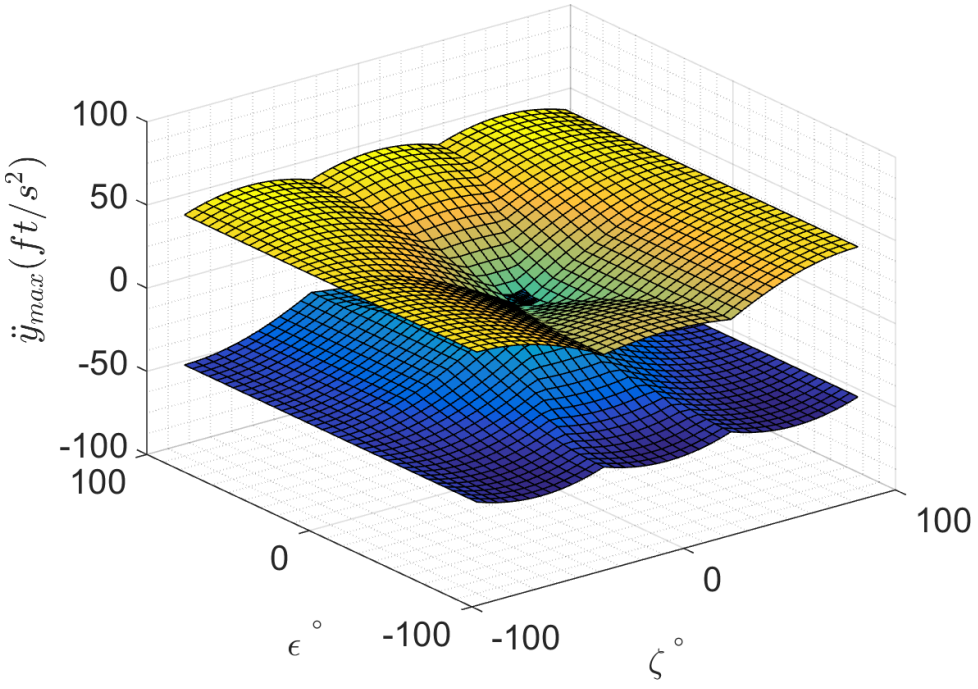

Figure 205: *X6* $\ddot{y}$ design space, pure motion not enforced, M2 fault

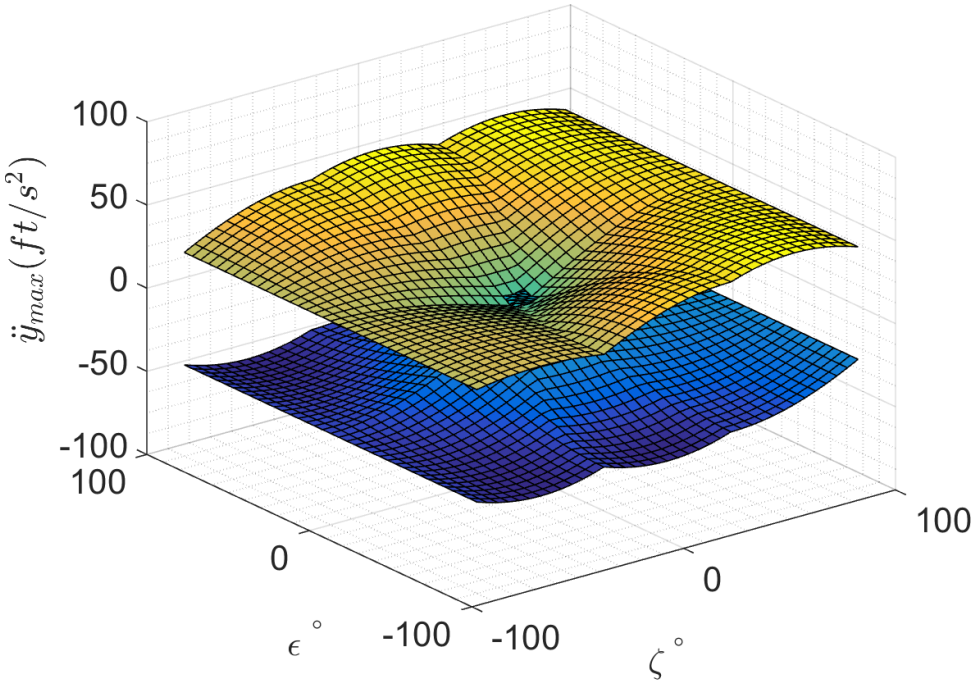

Figure 206: *X6 $\ddot{y}$* design space, pure motion not enforced, M3 fault

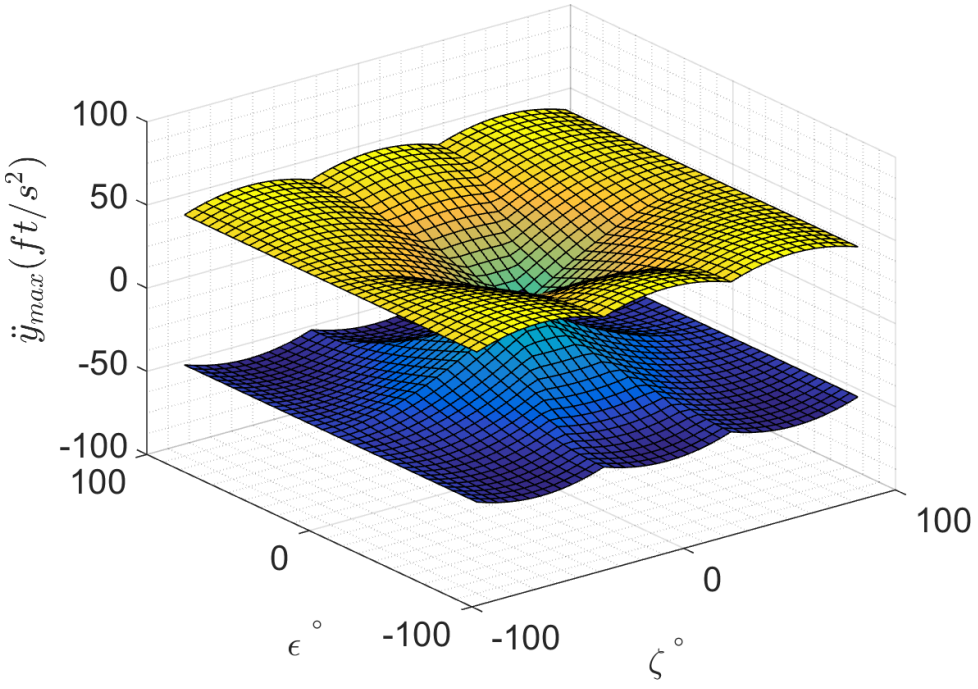

Figure 207: *X6 $\ddot{y}$* design space, pure motion not enforced, no rotor faults

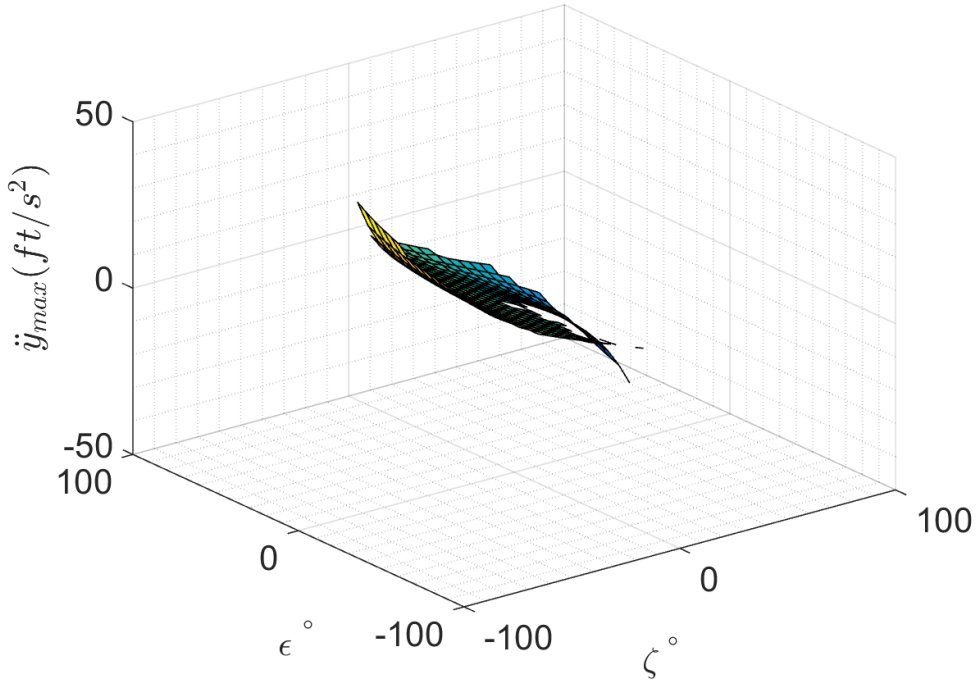

Figure 208: *X6* $\ddot{y}$ design space, pure motion enforced, M1 fault

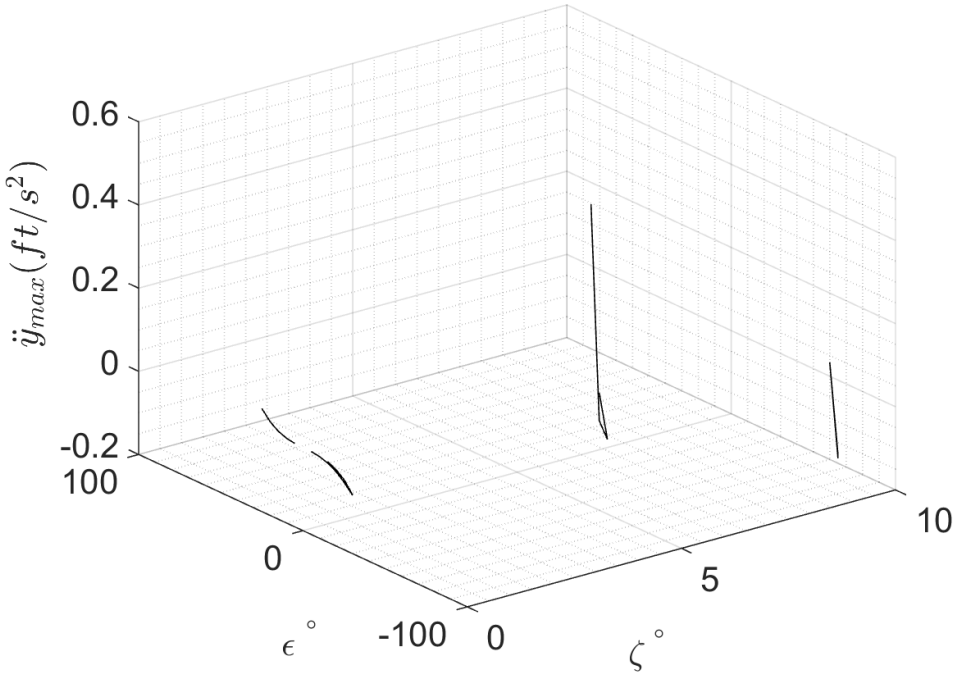

Figure 209: *X6* $\ddot{y}$ design space, pure motion enforced, M2 fault

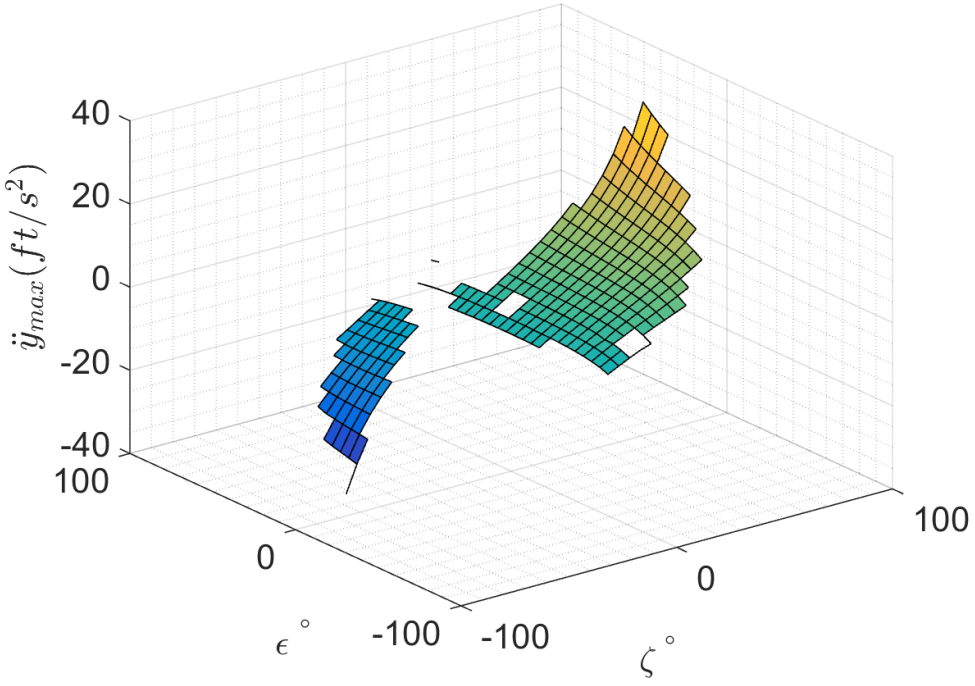

Figure 210: *X6 $\ddot{y}$* design space, pure motion enforced, M3 fault

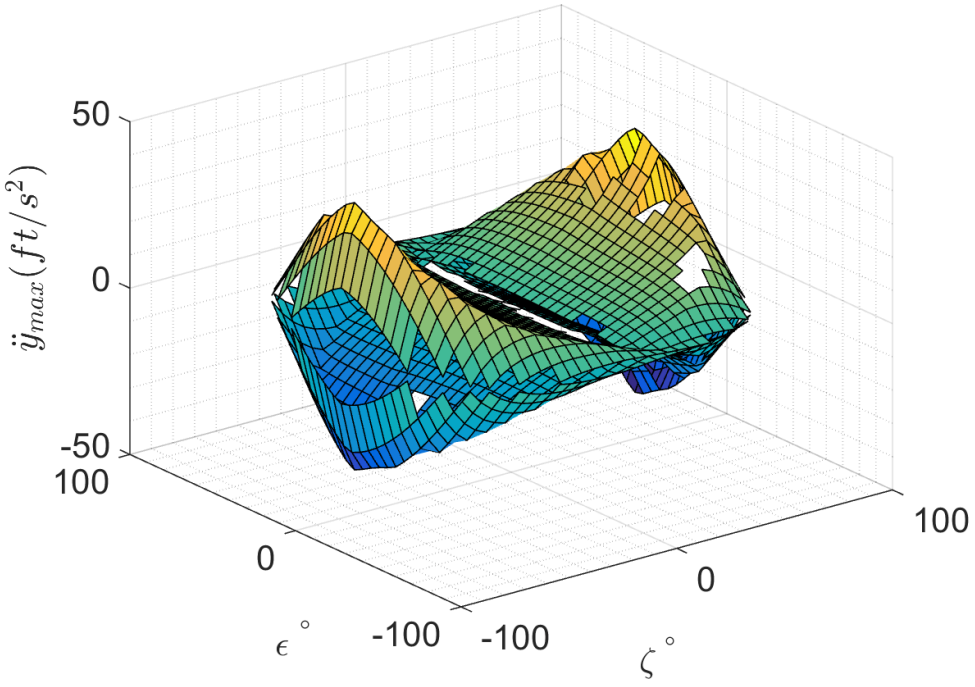

Figure 211: *X6 $\ddot{y}$* design space, pure motion enforced, no rotor faults

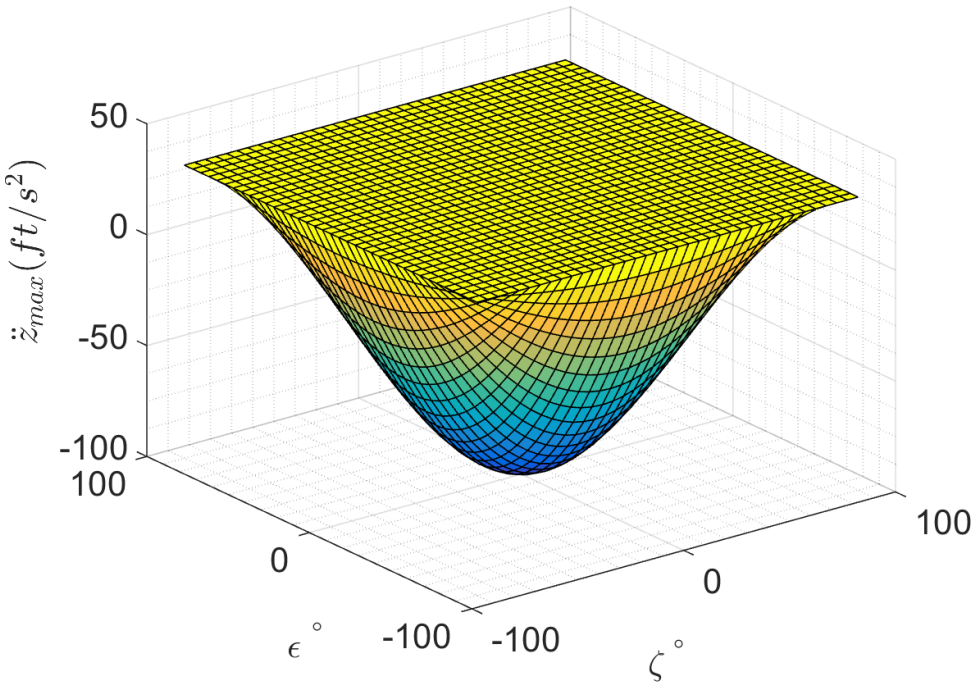

Figure 212: *X6* $\ddot{z}$ design space, pure motion not enforced, M1 fault

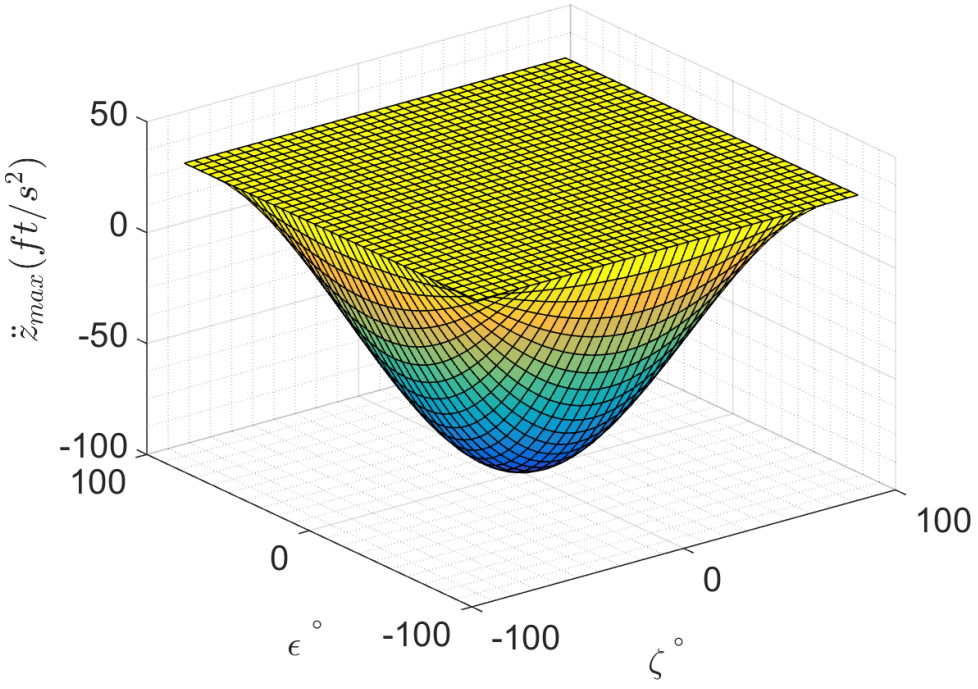

Figure 213: *X6* $\ddot{z}$ design space, pure motion not enforced, M2 fault

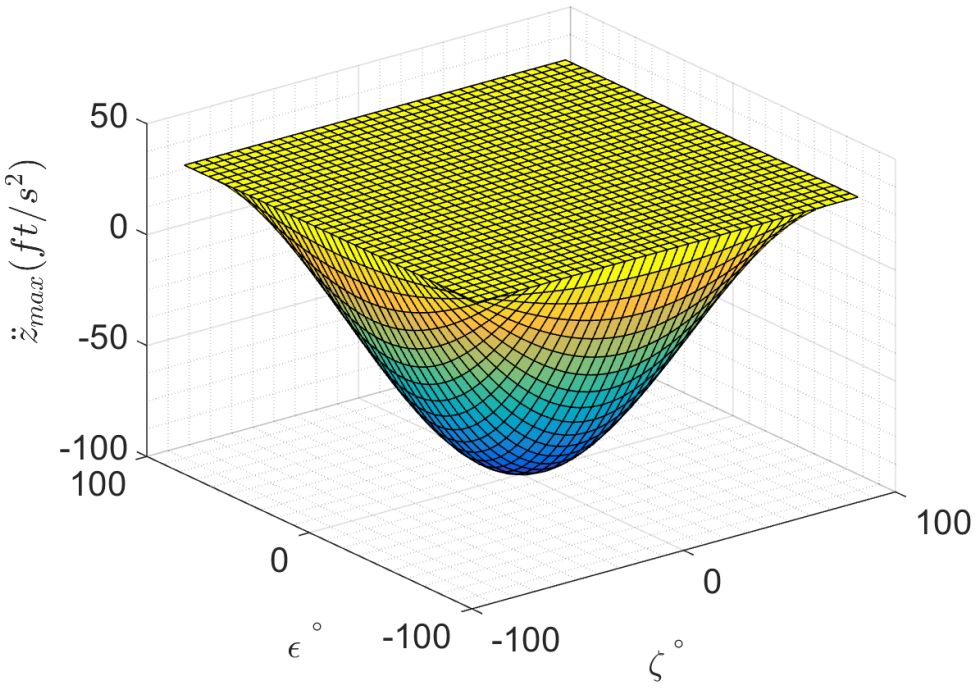

Figure 214: *X6* $\ddot{z}$ design space, pure motion not enforced, M3 fault

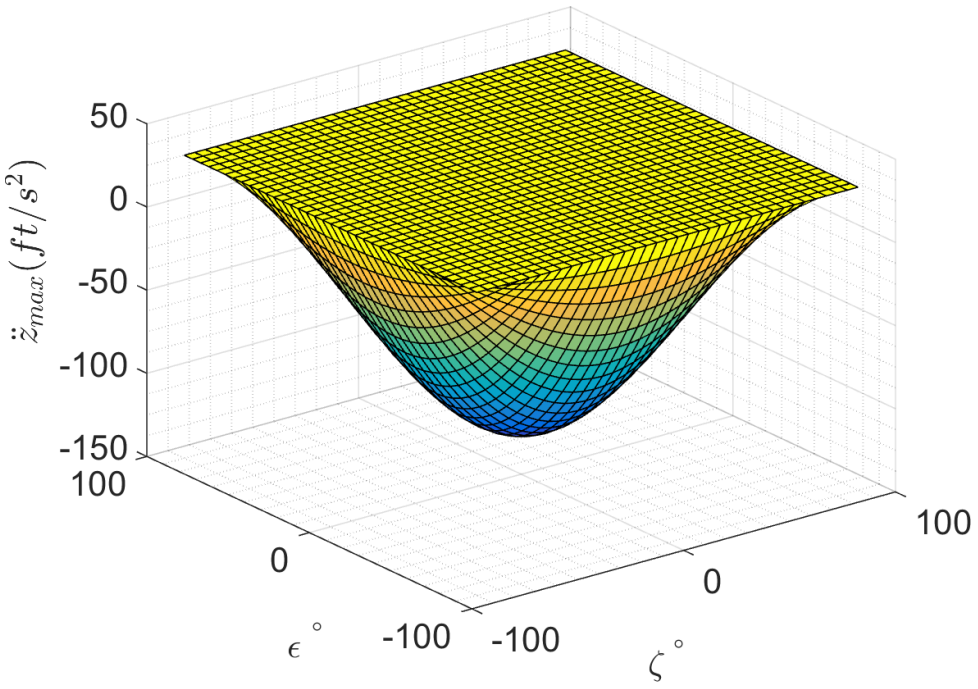

Figure 215: *X6* $\ddot{z}$ design space, pure motion not enforced, no rotor faults

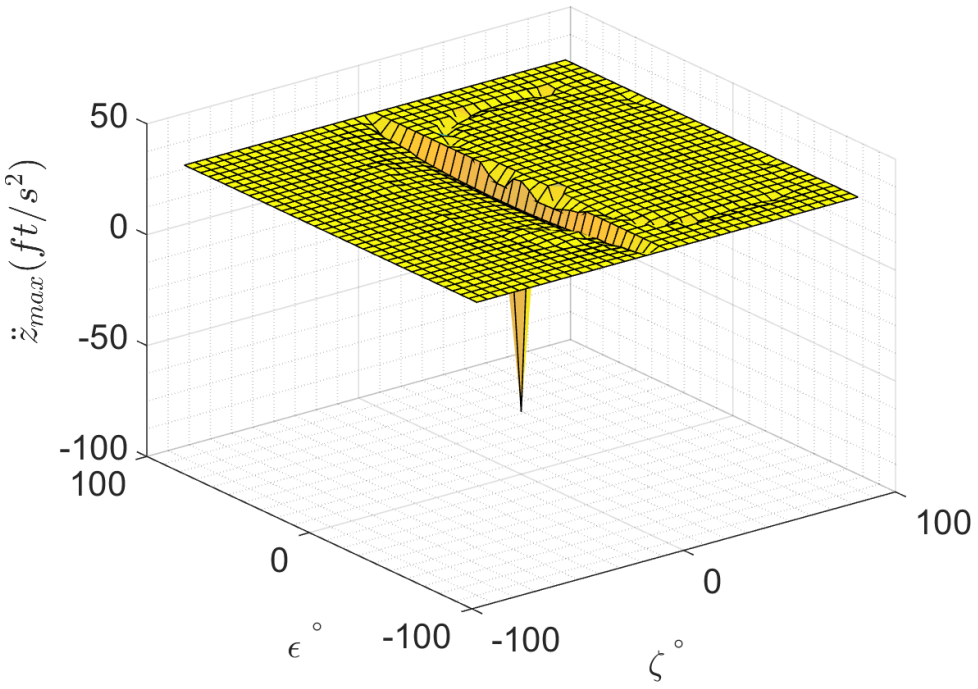

Figure 216: *X6* $\ddot{z}$ design space, pure motion enforced, M1 fault

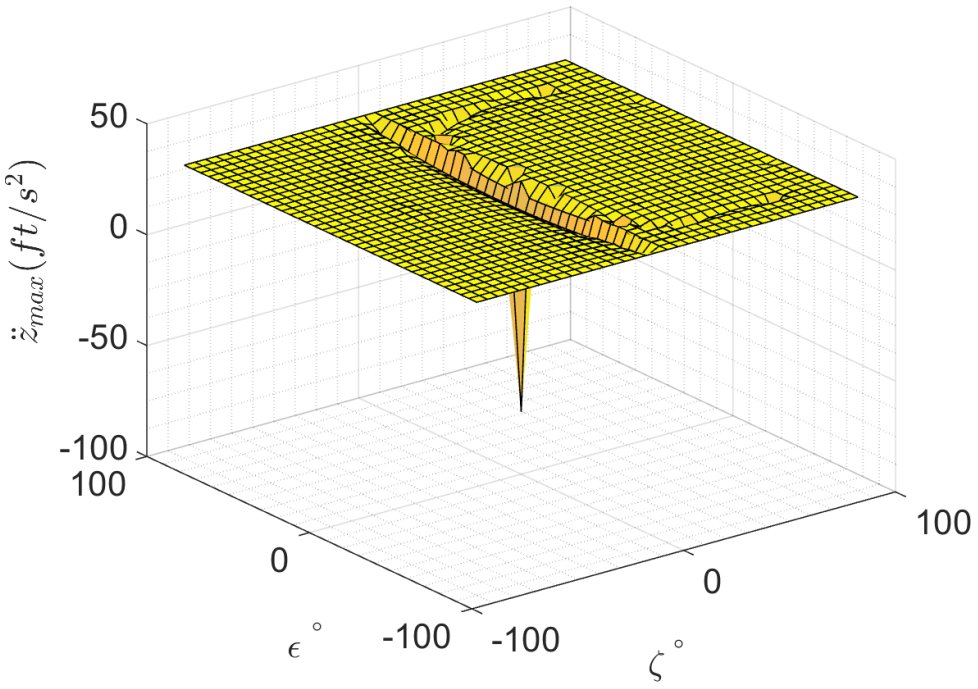

Figure 217: *X6* $\ddot{z}$ design space, pure motion enforced, M2 fault

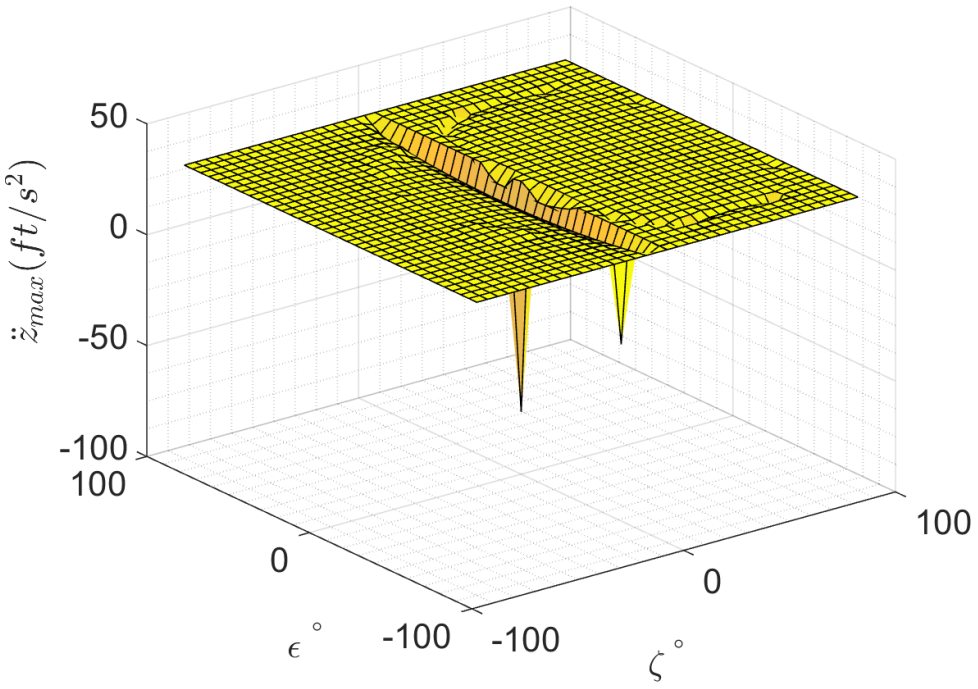

Figure 218: *X6* $\ddot{z}$ design space, pure motion enforced, M3 fault

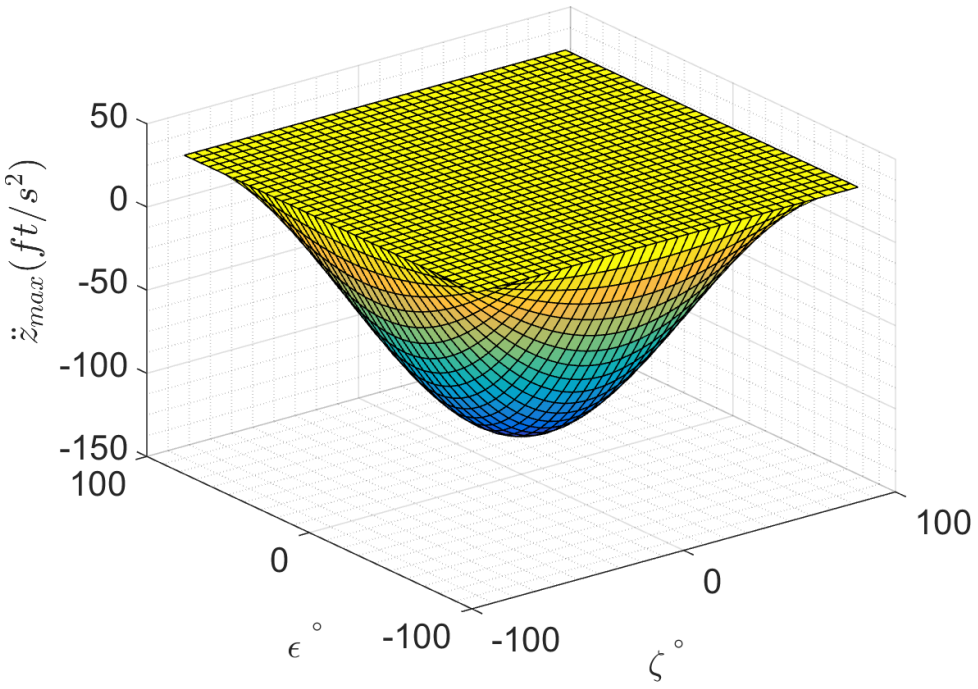

Figure 219: *X6* $\ddot{z}$ design space, pure motion enforced, no rotor faults

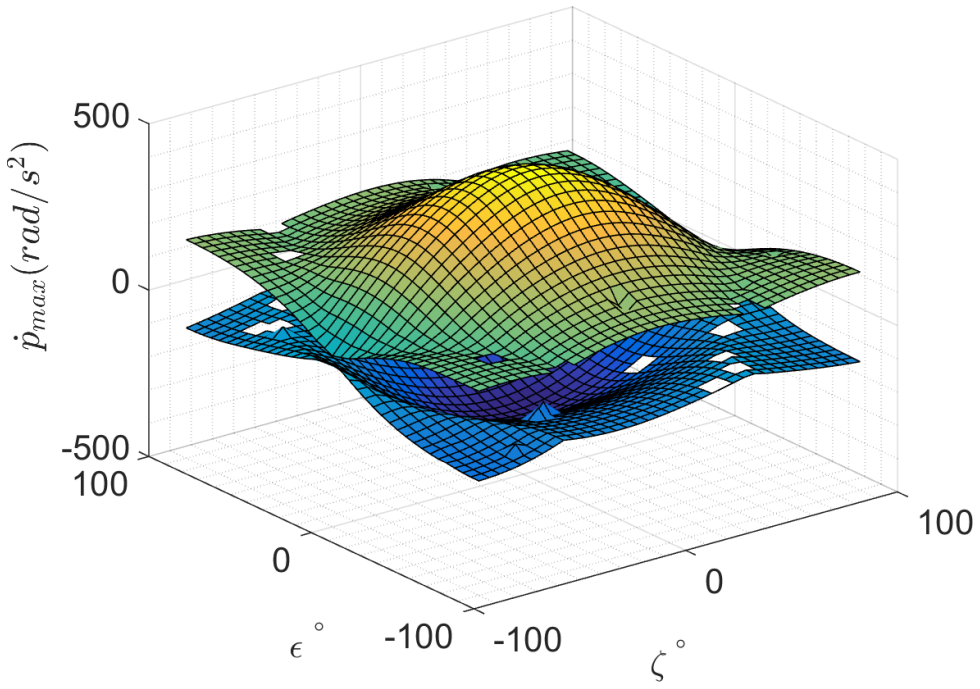

Figure 220: *X8C* $\dot{p}$ design space, pure motion not enforced, co-rotating, M1 fault

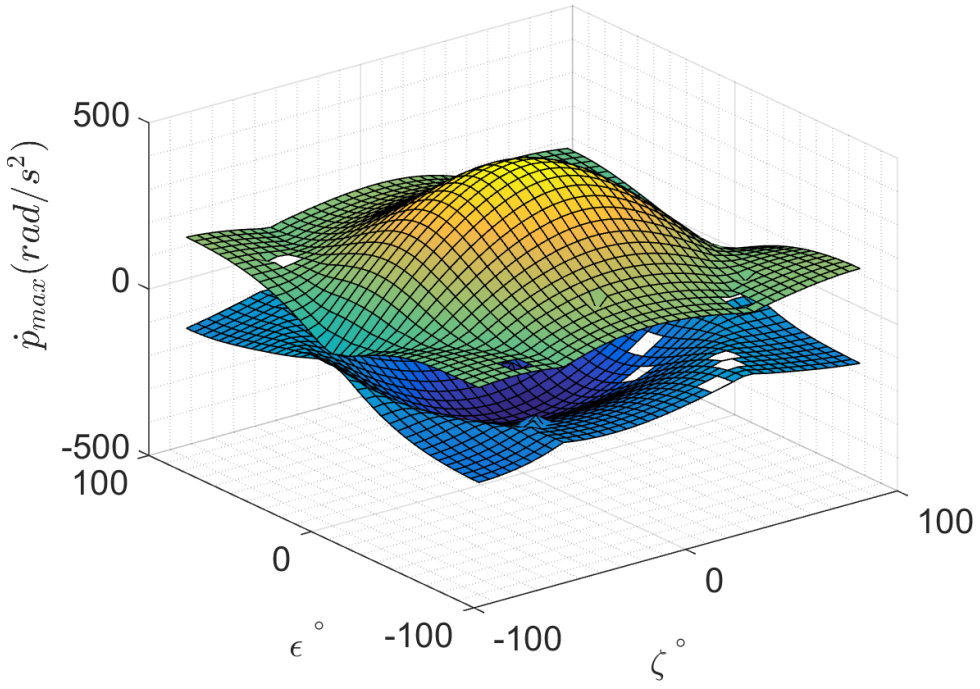

Figure 221: *X8C* $\dot{p}$ design space, pure motion not enforced, counter-rotating, M1 fault

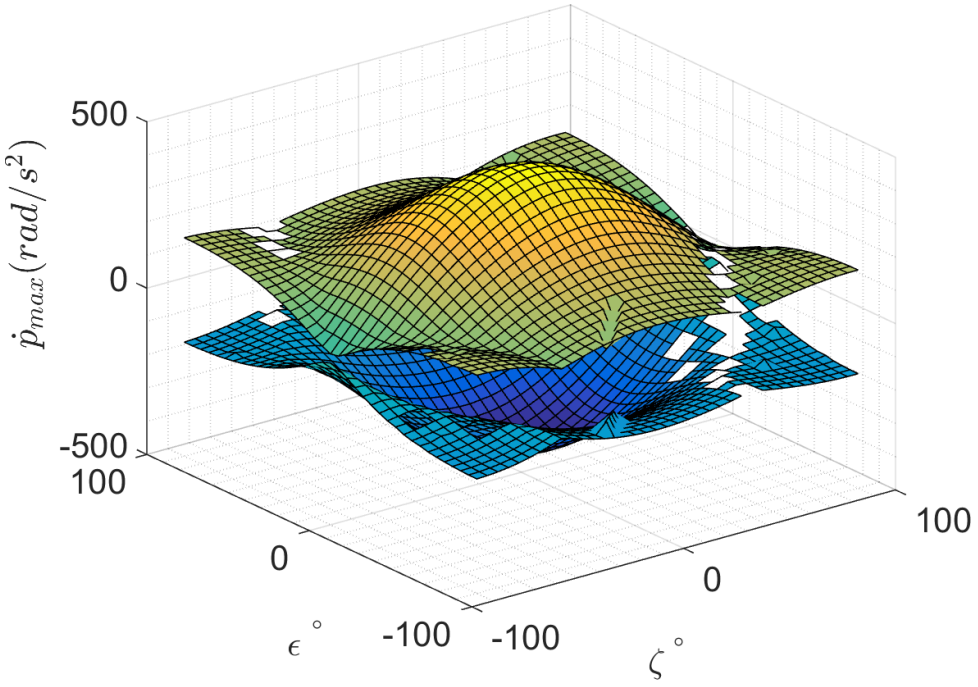

Figure 222: *X8C* $\dot{p}$ design space, pure motion not enforced, co-rotating, no rotor faults

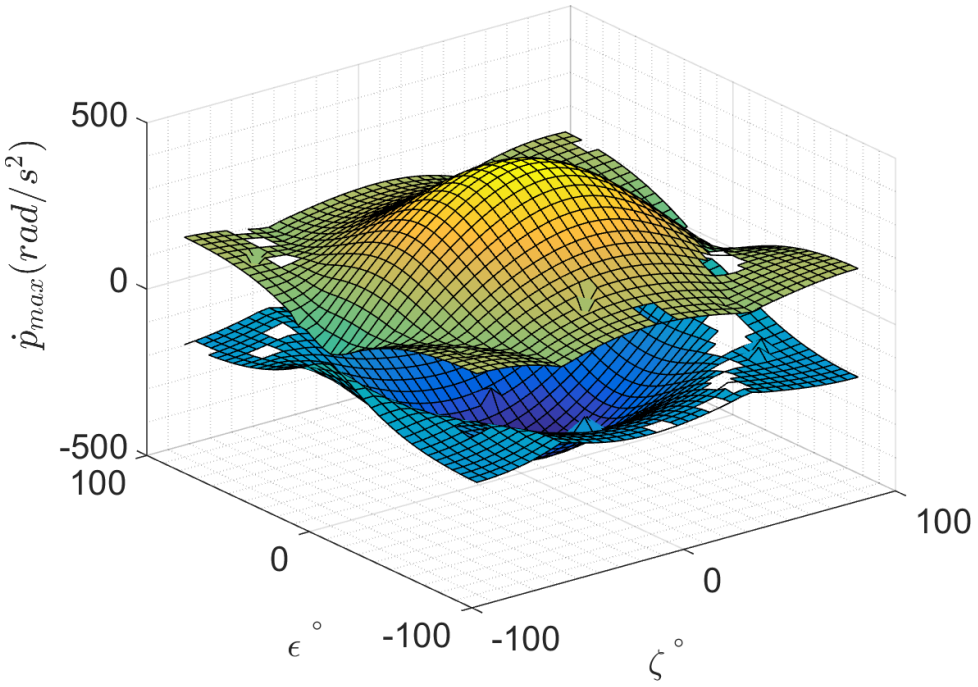

Figure 223: *X8C* $\dot{p}$ design space, pure motion not enforced, counter-rotating, no rotor faults

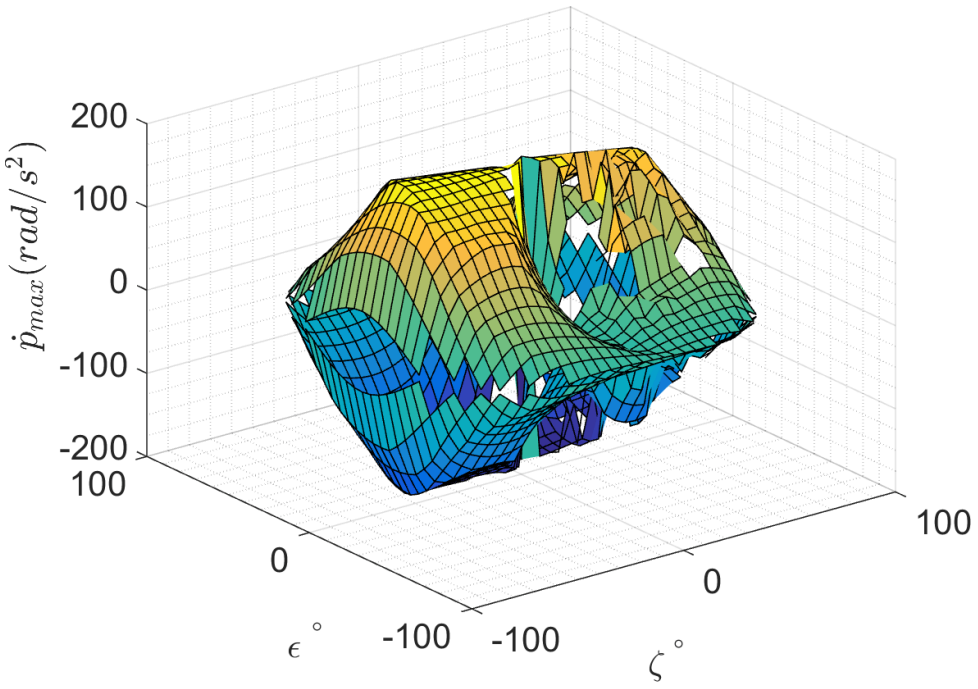

Figure 224: *X8C* $\dot{p}$ design space, pure motion enforced, counter-rotating, no rotor faults

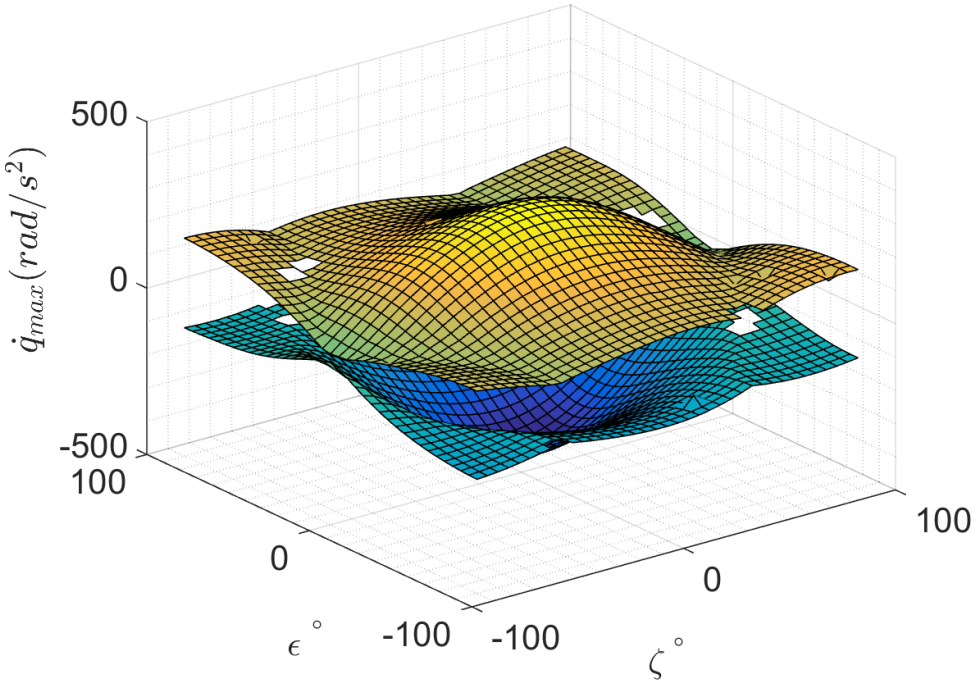

Figure 225: *X8C* $\dot{q}$ design space, pure motion not enforced, co-rotating, M1 fault

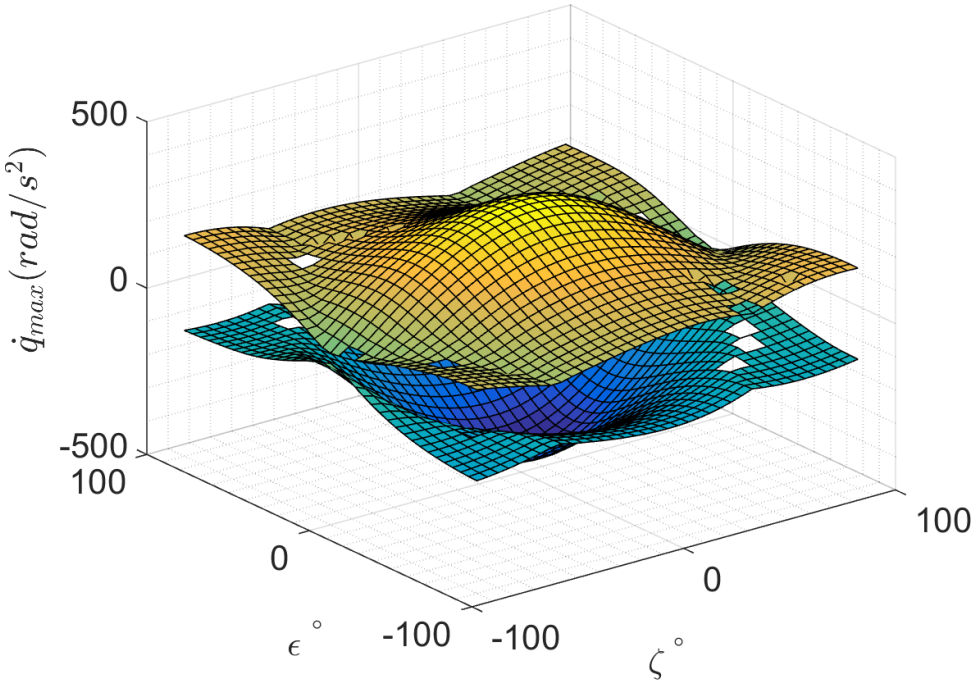

Figure 226: *X8C* $\dot{q}$ design space, pure motion not enforced, counter-rotating, M1 fault

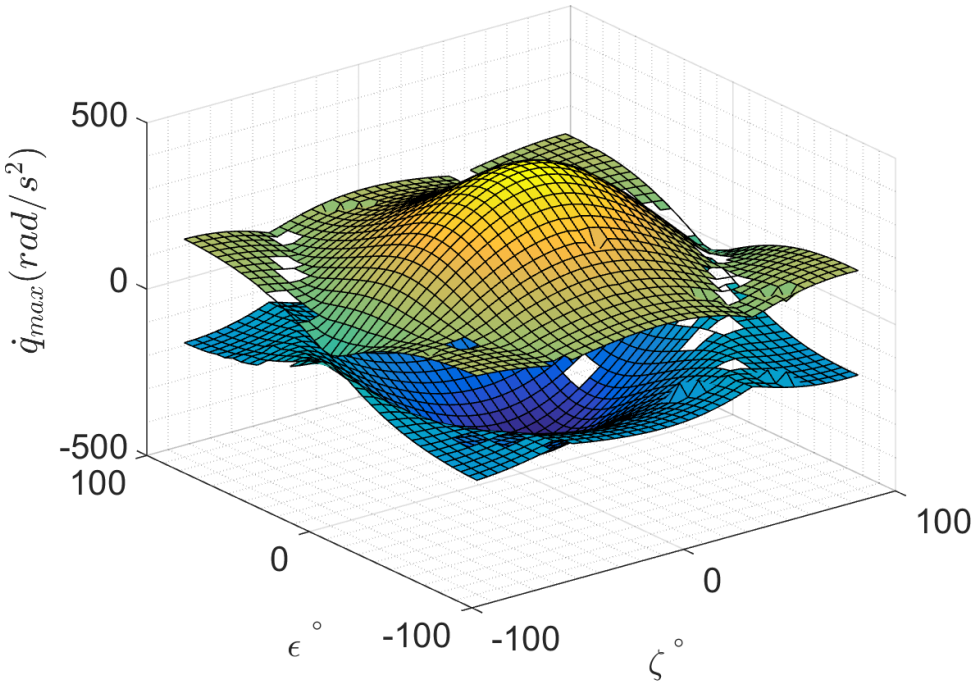

Figure 227: *X8C* $\dot{q}$ design space, pure motion not enforced, co-rotating, no rotor faults

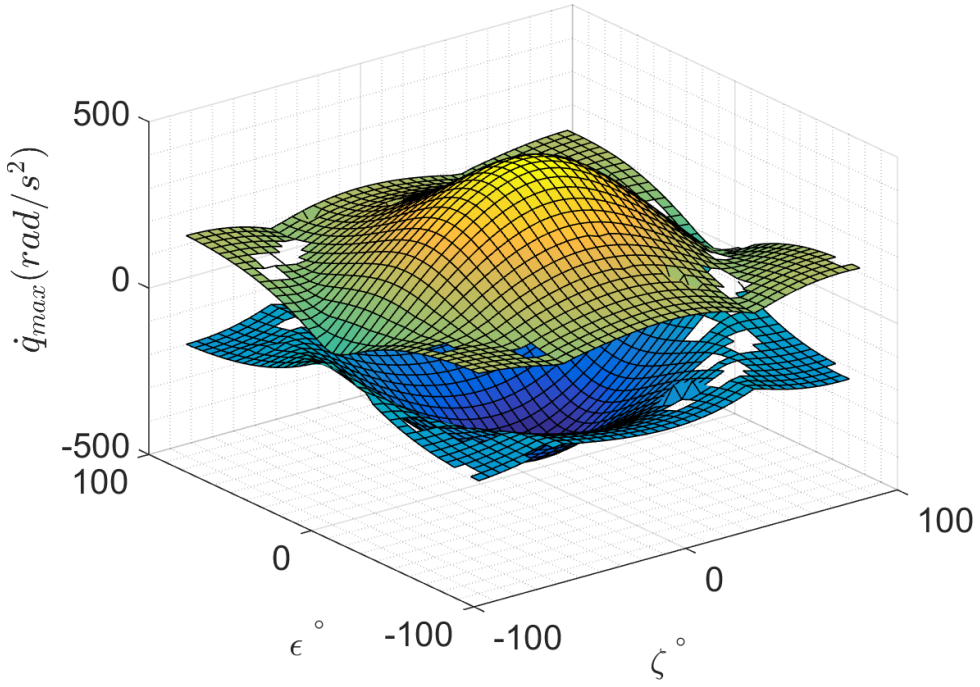

Figure 228: *X8C* $\dot{q}$ design space, pure motion not enforced, counter-rotating, no rotor faults

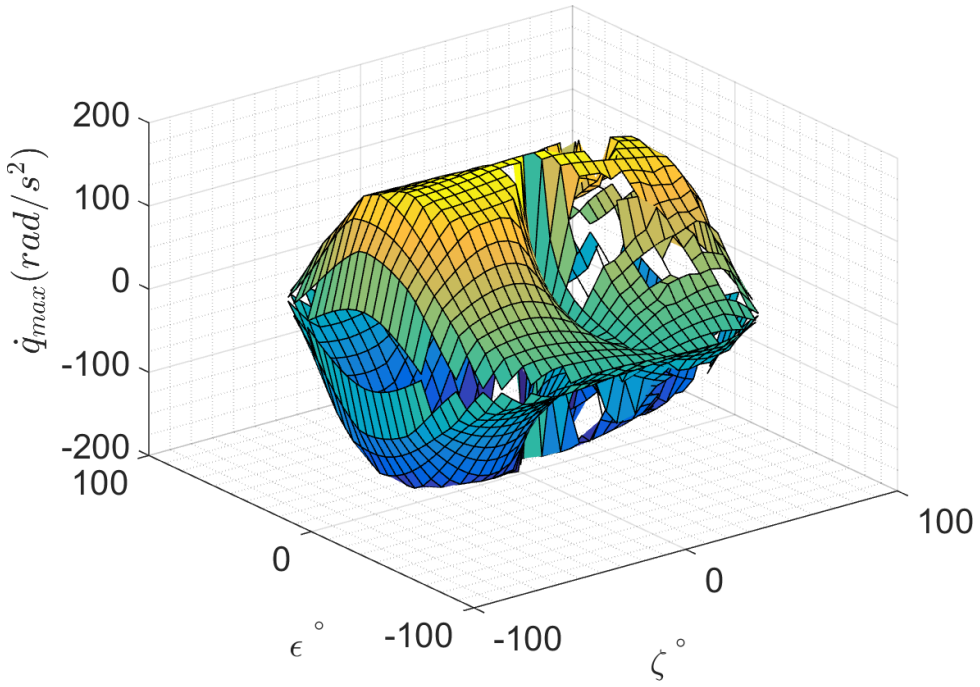

Figure 229: *X8C* $\dot{q}$ design space, pure motion enforced, counter-rotating, no rotor faults

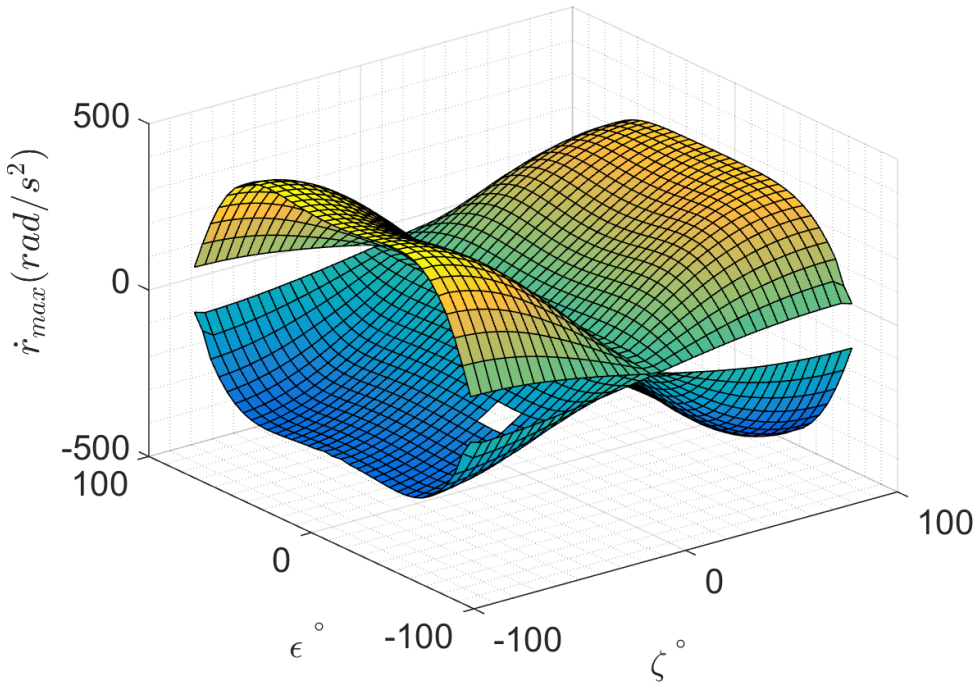

Figure 230: *X8C* $\dot{r}$ design space, pure motion not enforced, co-rotating, M1 fault

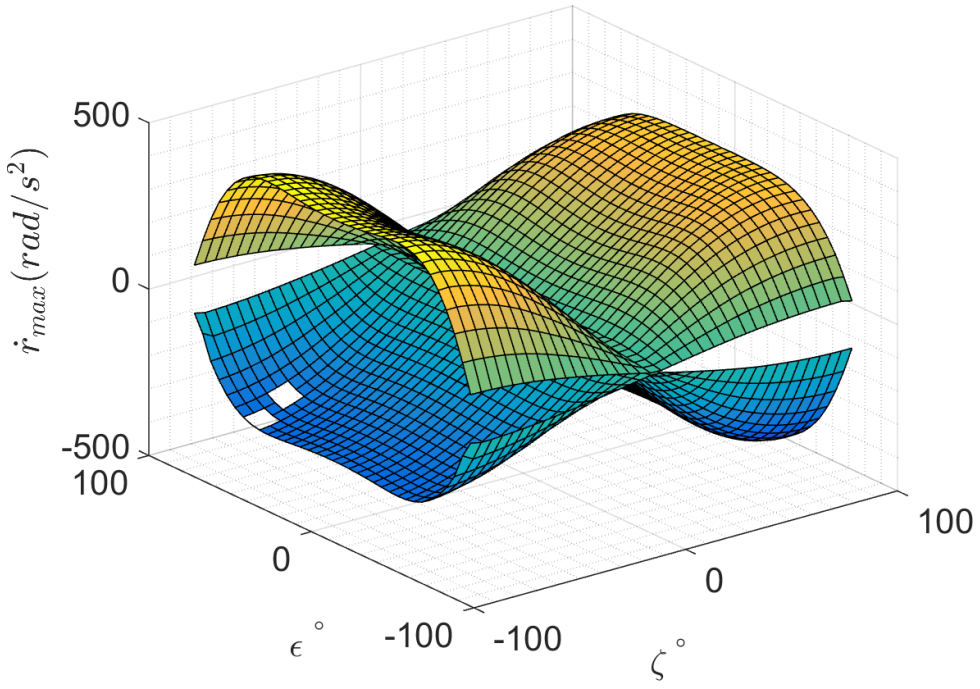

Figure 231: *X8C* $\dot{r}$ design space, pure motion not enforced, counter-rotating, M1 fault

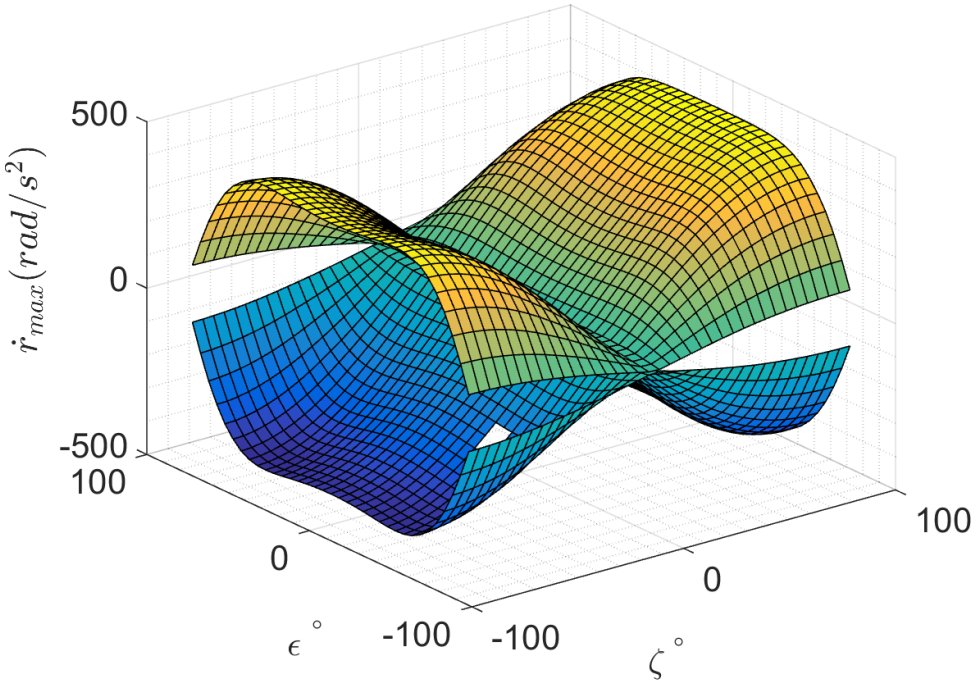

Figure 232: *X8C* $\dot{r}$ design space, pure motion not enforced, co-rotating, no rotor faults

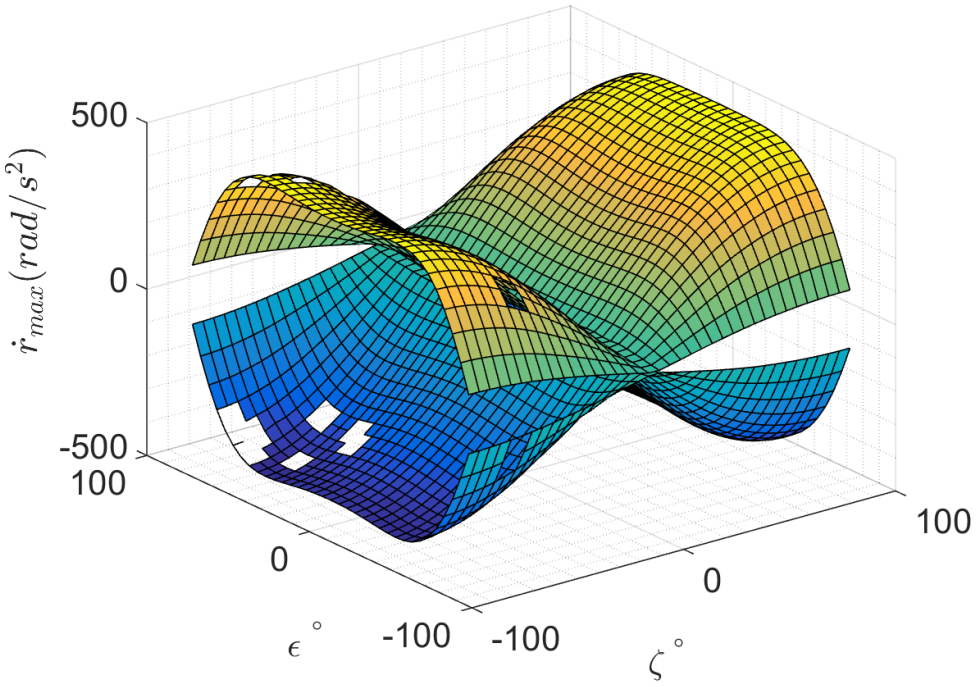

Figure 233: *X8C* $\dot{r}$ design space, pure motion not enforced, counter-rotating, no rotor faults

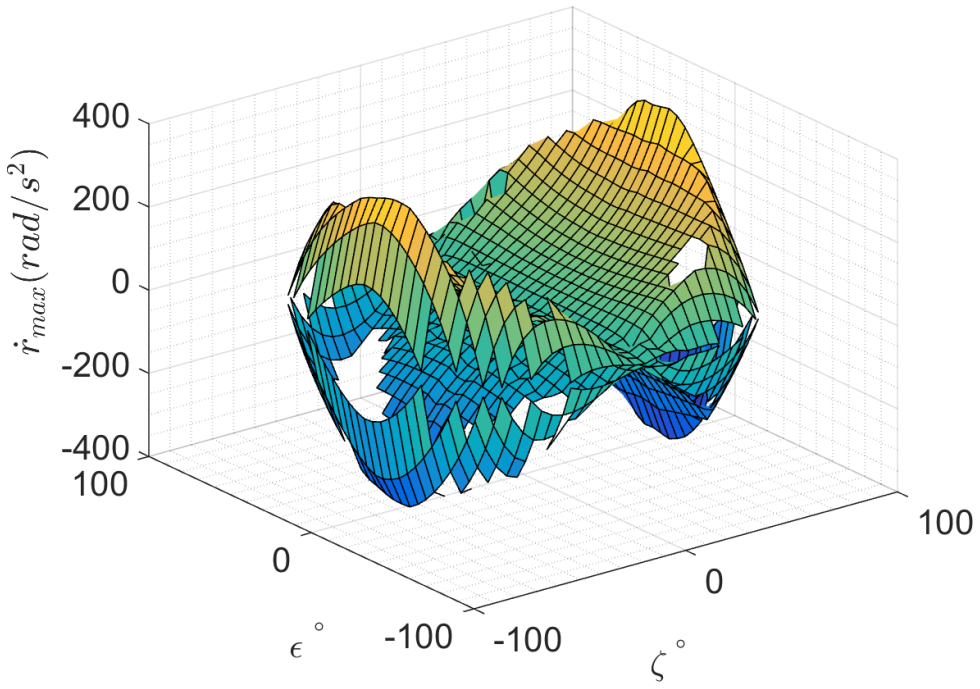

Figure 234: *X8C* $\dot{r}$ design space, pure motion enforced, counter-rotating, no rotor faults

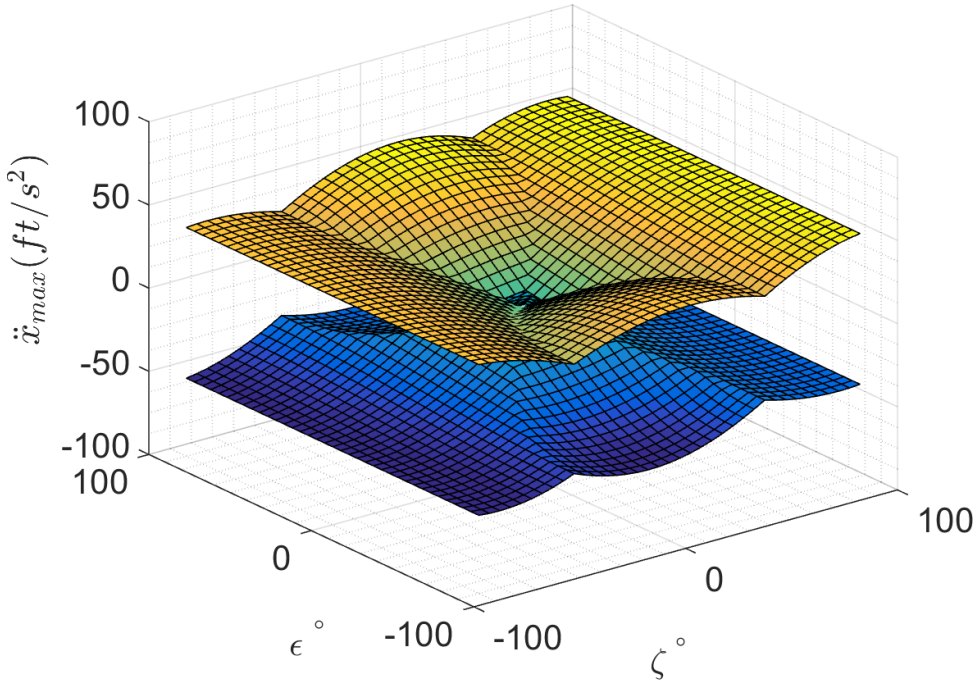

Figure 235: *X8C* $\ddot{x}$ design space, pure motion not enforced, co-rotating, M1 fault

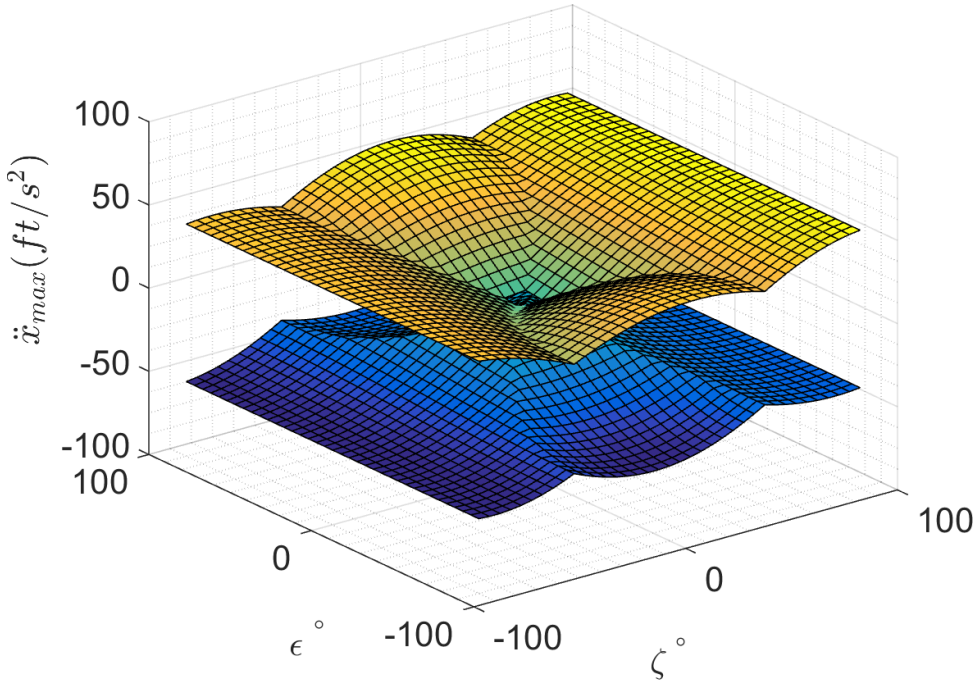

Figure 236: *X8C* $\ddot{x}$ design space, pure motion not enforced, counter-rotating, M1 fault

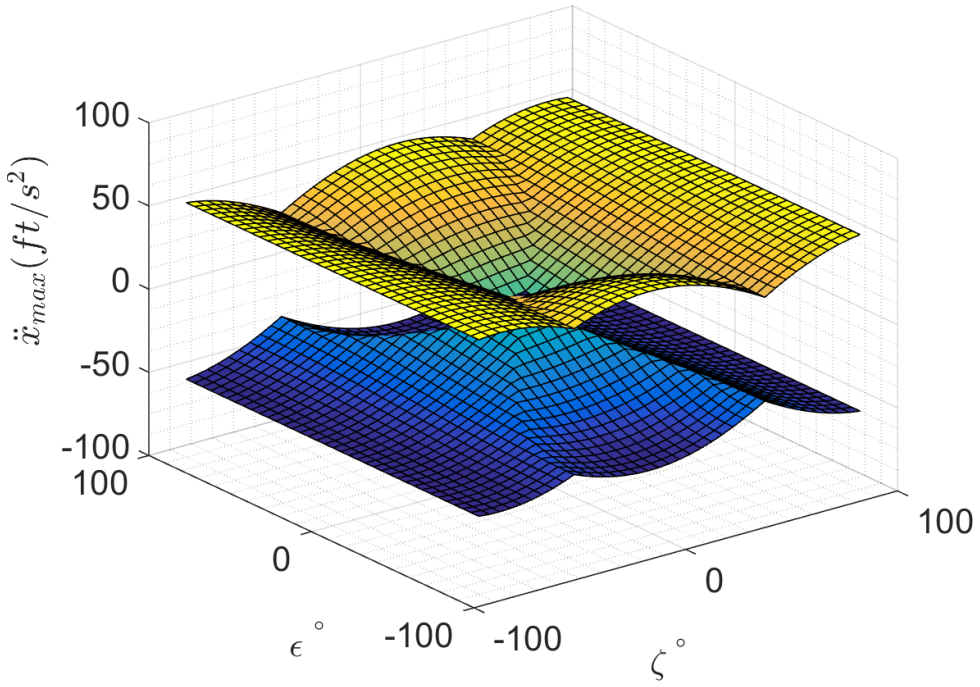

Figure 237: *X8C* $\ddot{x}$ design space, pure motion not enforced, co-rotating, no rotor faults

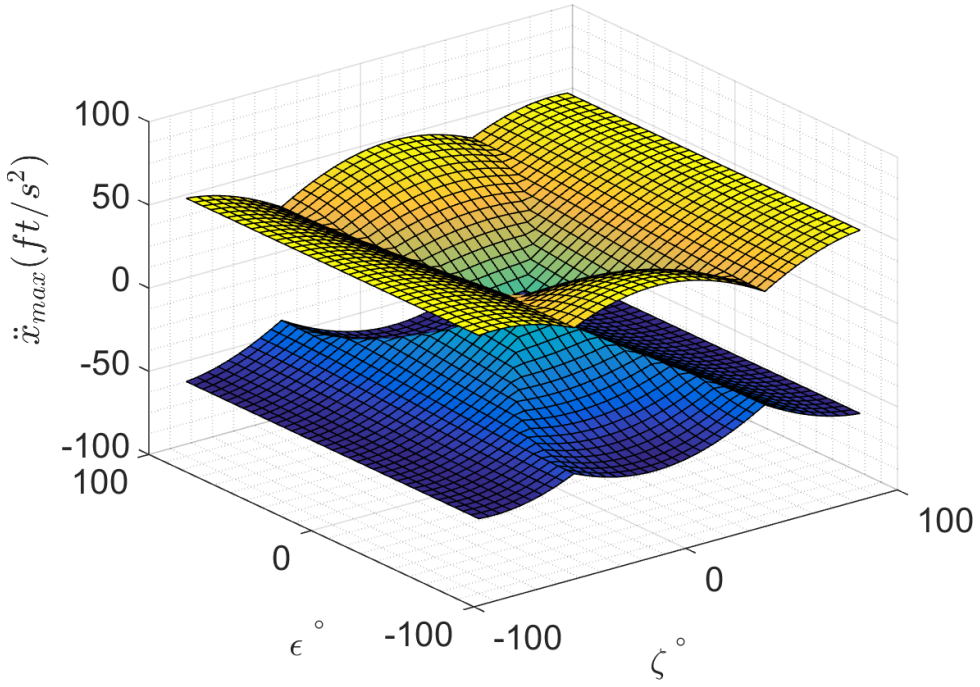

Figure 238: *X8C* $\ddot{x}$ design space, pure motion not enforced, counter-rotating, no rotor faults

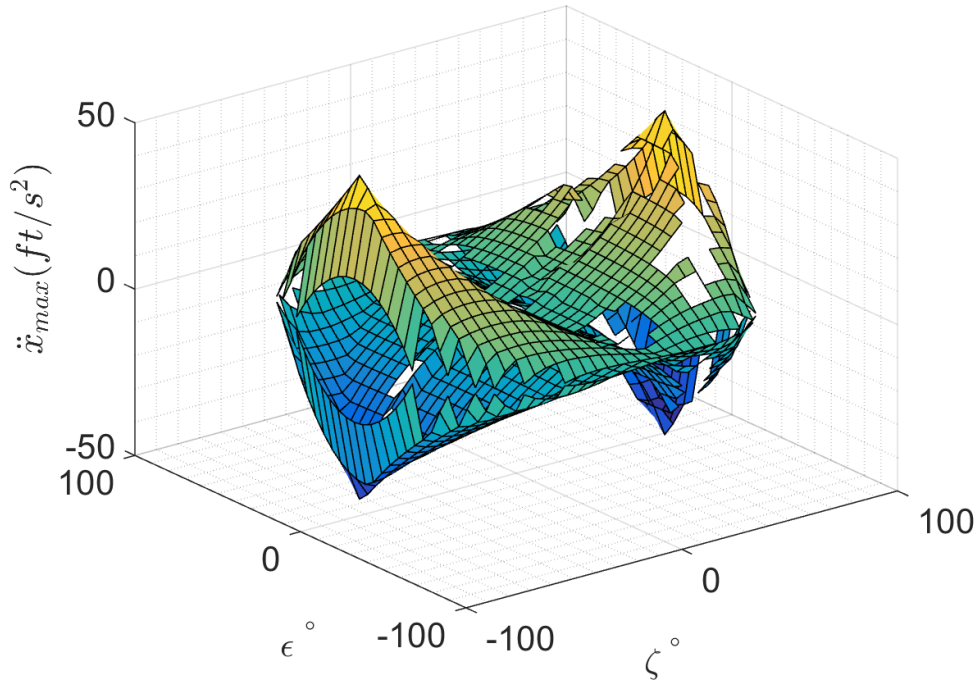

Figure 239: *X8C* $\ddot{x}$ design space, pure motion enforced, counter-rotating, no rotor faults

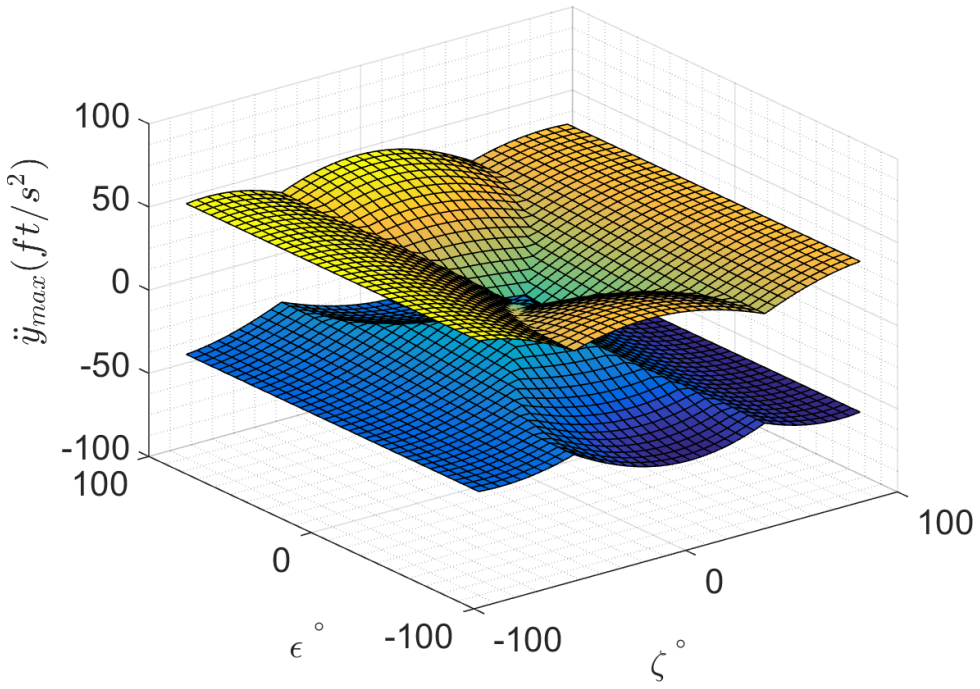

Figure 240: *X8C* $\ddot{y}$ design space, pure motion not enforced, co-rotating, M1 fault

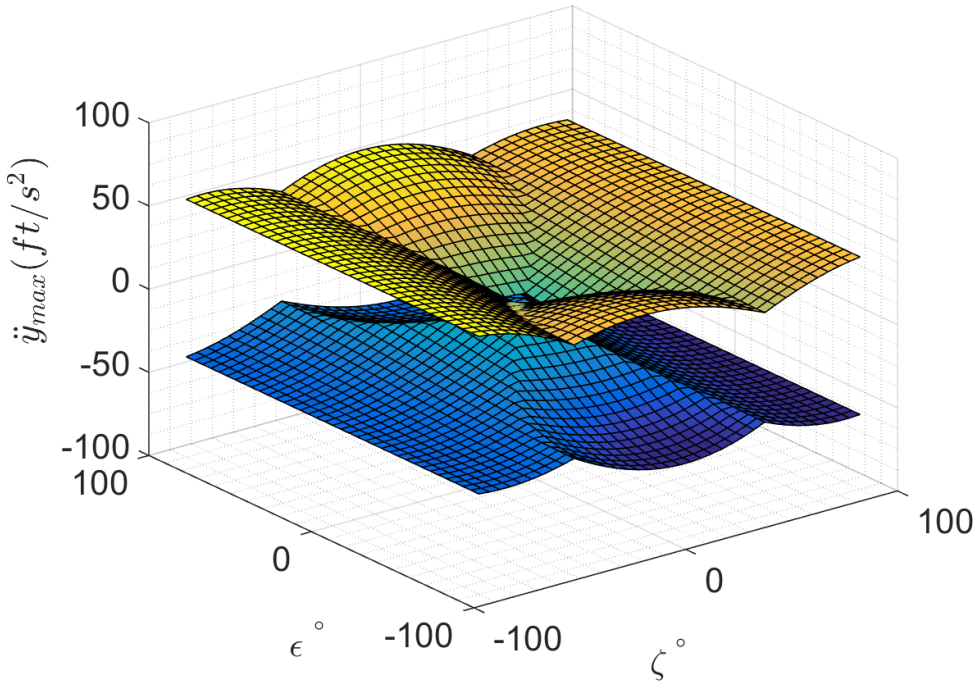

Figure 241: *X8C* $\ddot{y}$ design space, pure motion not enforced, counter-rotating, M1 fault

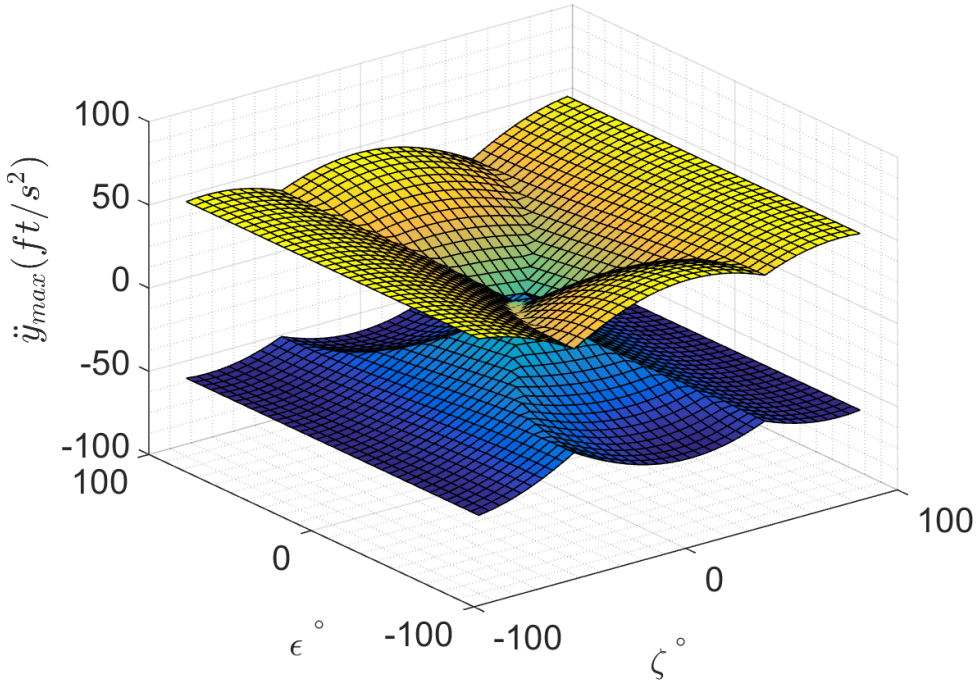

Figure 242: *X8C ÿ* design space, pure motion not enforced, co-rotating, no rotor faults

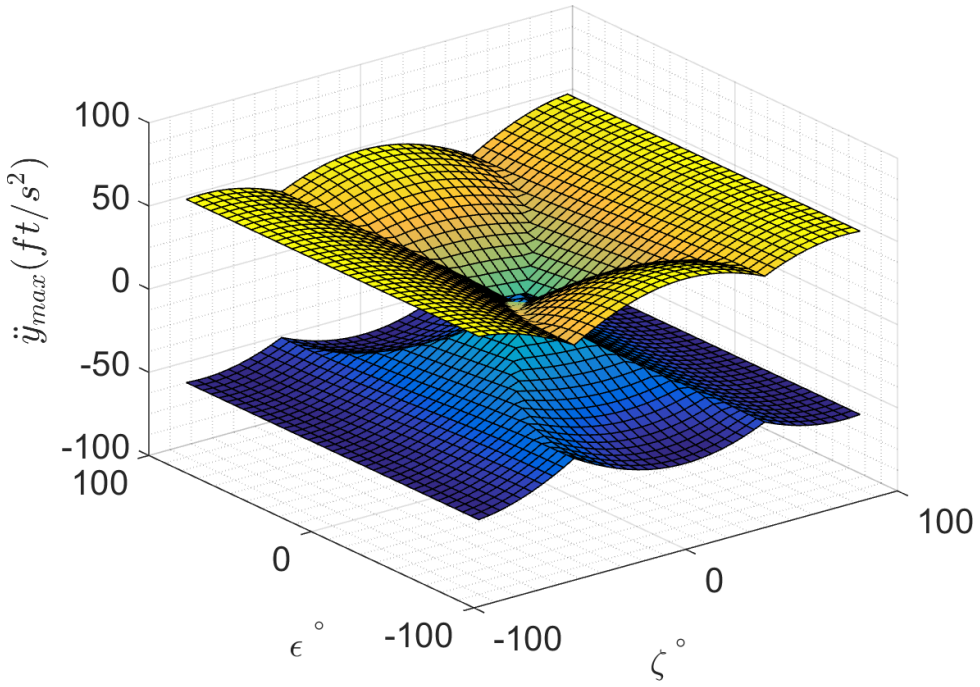

Figure 243: *X8C ÿ* design space, pure motion not enforced, counter-rotating, no rotor faults

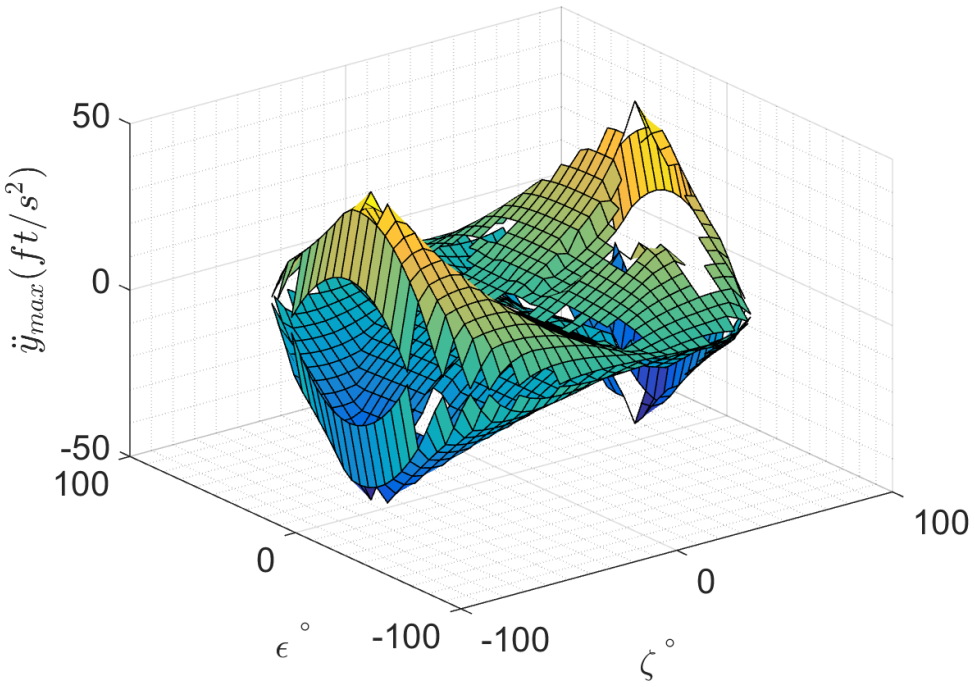

Figure 244: *X8C* $\ddot{y}$ design space, pure motion enforced, counter-rotating, no rotor faults

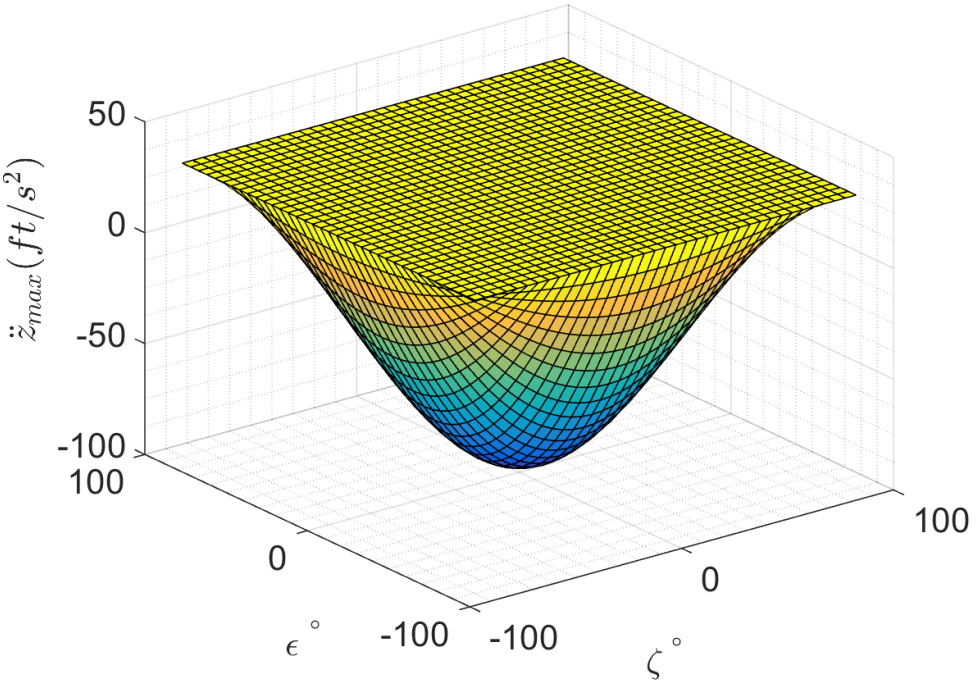

Figure 245: *X8C* $\ddot{z}$ design space, pure motion not enforced, co-rotating, M1 fault

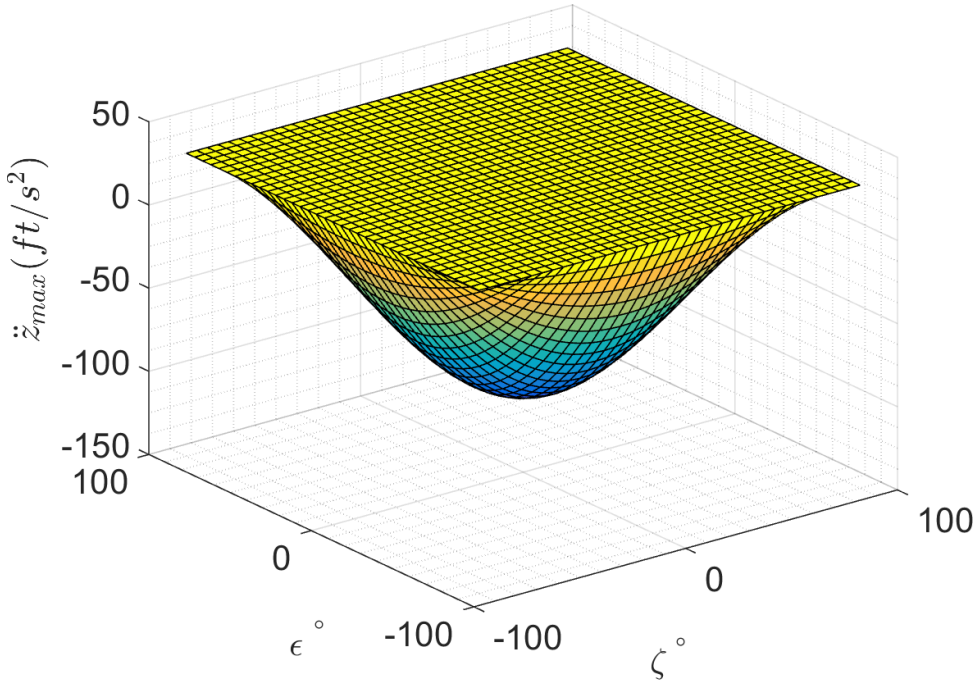

Figure 246: *X8C* $\ddot{z}$ design space, pure motion not enforced, counter-rotating, M1 fault

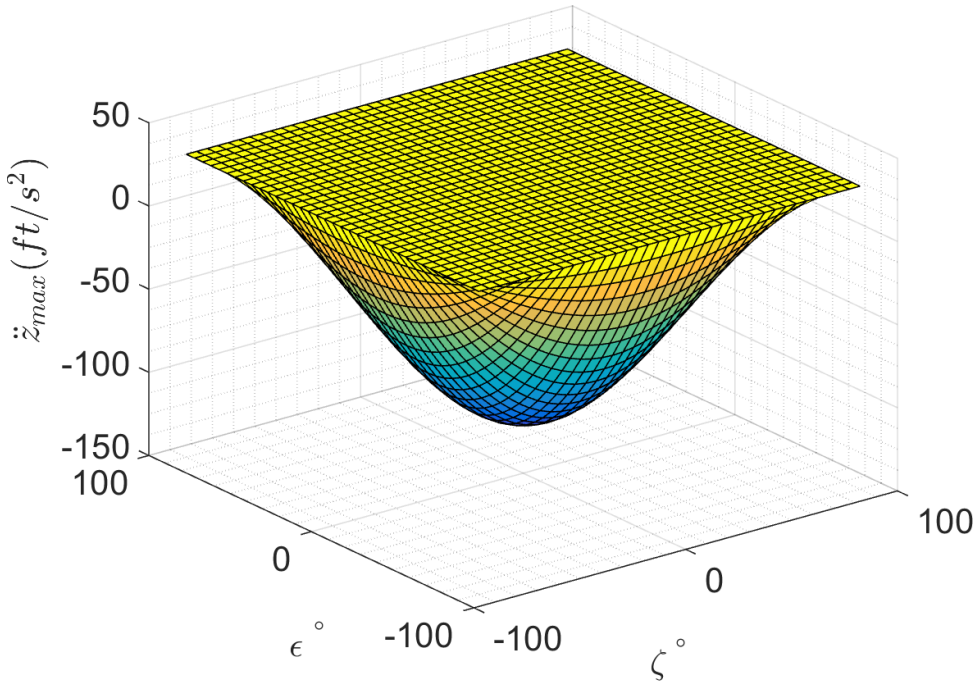

Figure 247: *X8C* $\ddot{z}$ design space, pure motion not enforced, co-rotating, no rotor faults

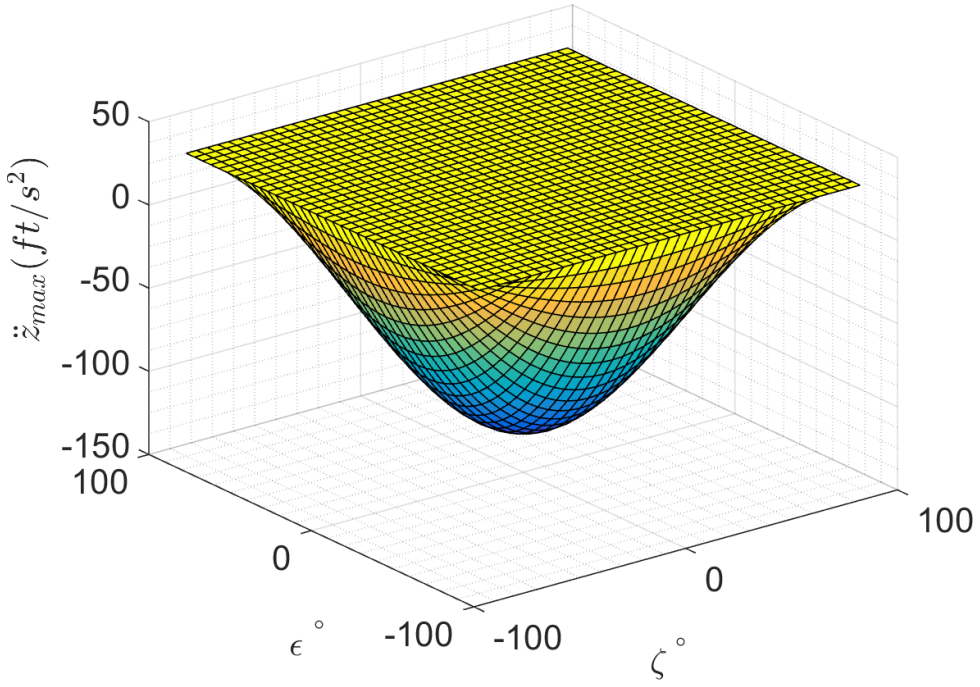

Figure 248: *X8C* $\ddot{z}$ design space, pure motion not enforced, counter-rotating, no rotor faults

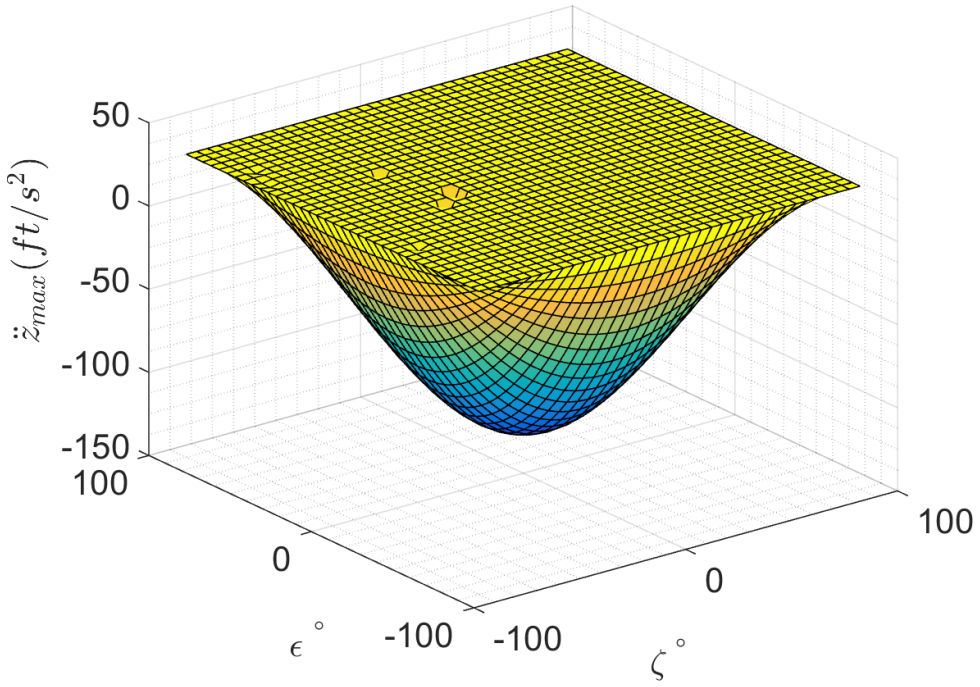

Figure 249: *X8C* $\ddot{z}$ design space, pure motion enforced, counter-rotating, no rotor faults

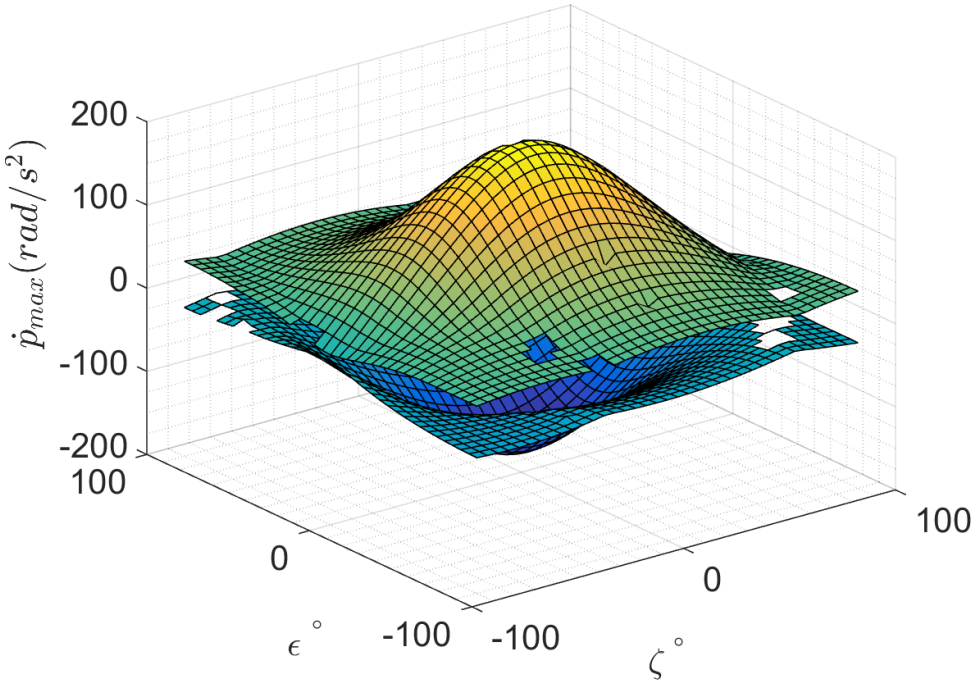

Figure 250: *X8* $\dot{p}$ design space, pure motion not enforced, M1 fault

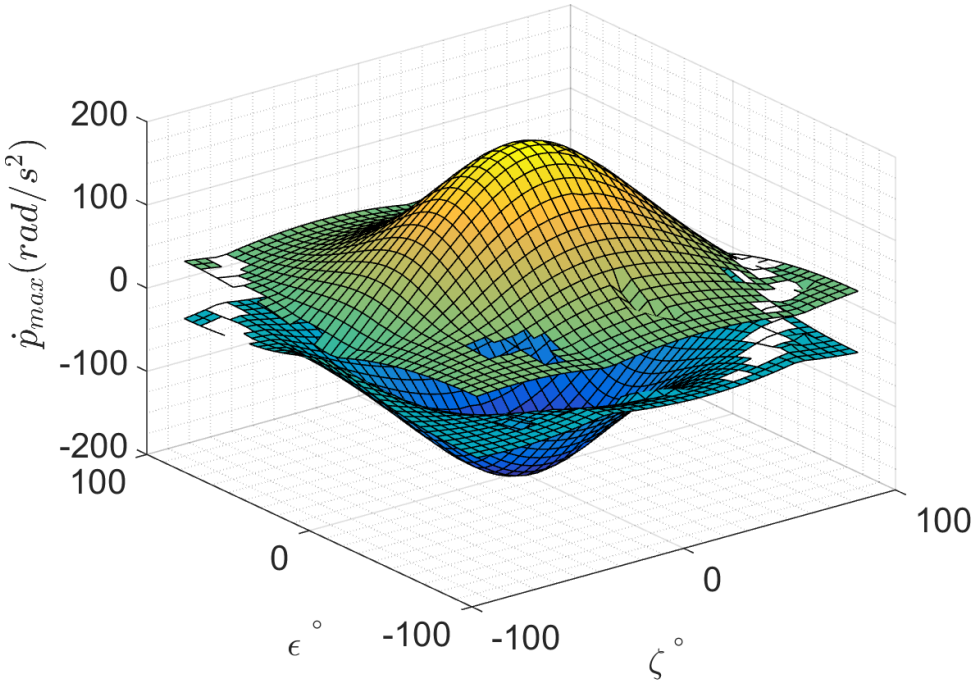

Figure 251: *X8* $\dot{p}$ design space, pure motion not enforced, no rotor faults

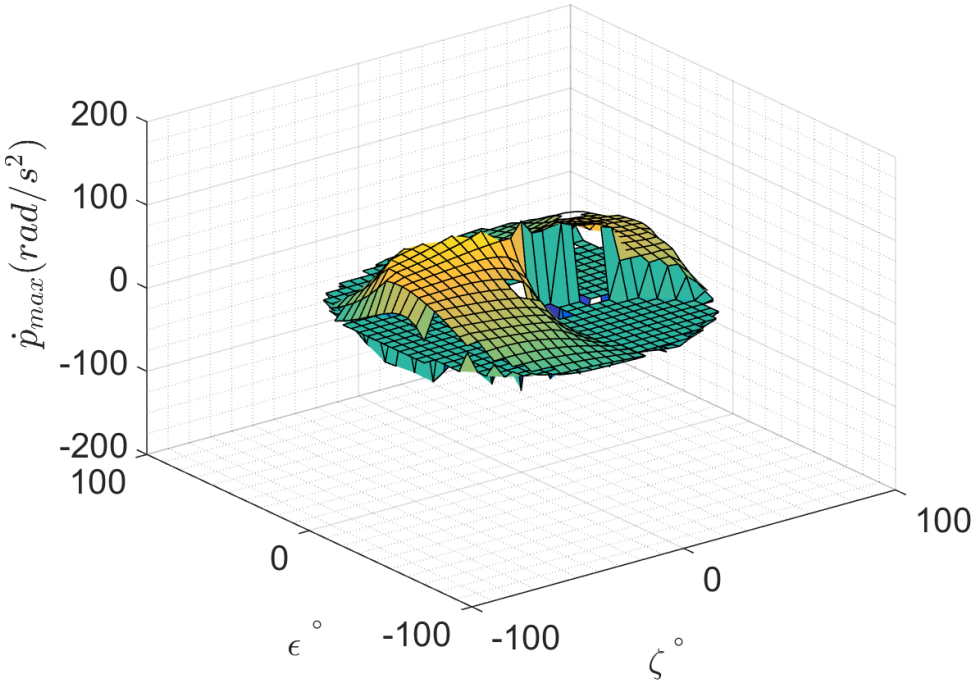

Figure 252: *X8* $\dot{p}$ design space, pure motion enforced, M1 fault

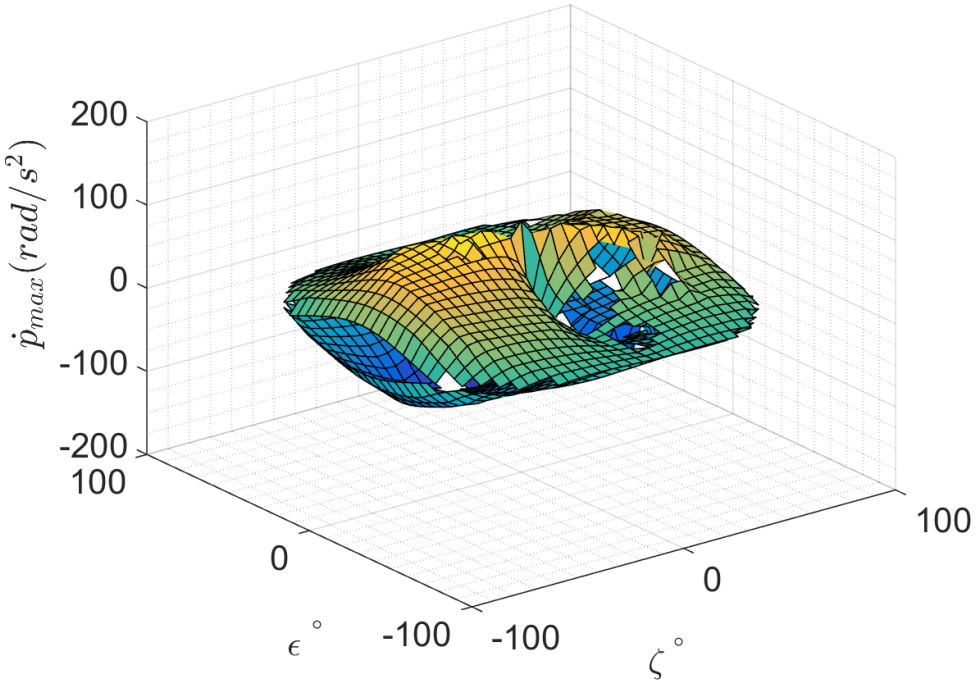

Figure 253: *X8* $\dot{p}$ design space, pure motion enforced, no rotor faults

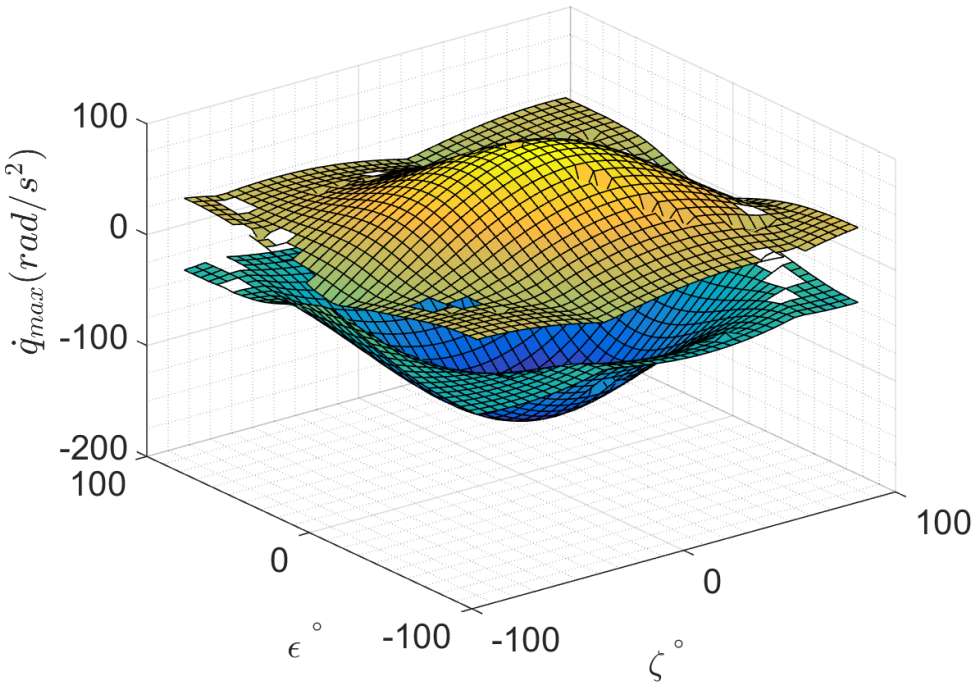

Figure 254: *X8* $\dot{q}$ design space, pure motion not enforced, M1 fault

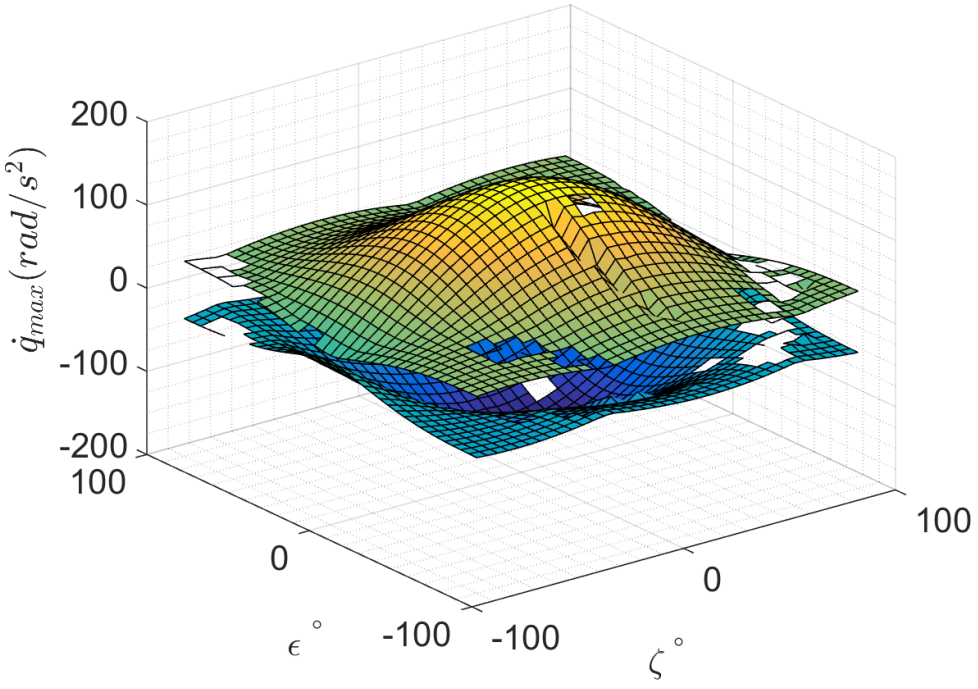

Figure 255: *X8* $\dot{q}$ design space, pure motion not enforced, no rotor faults

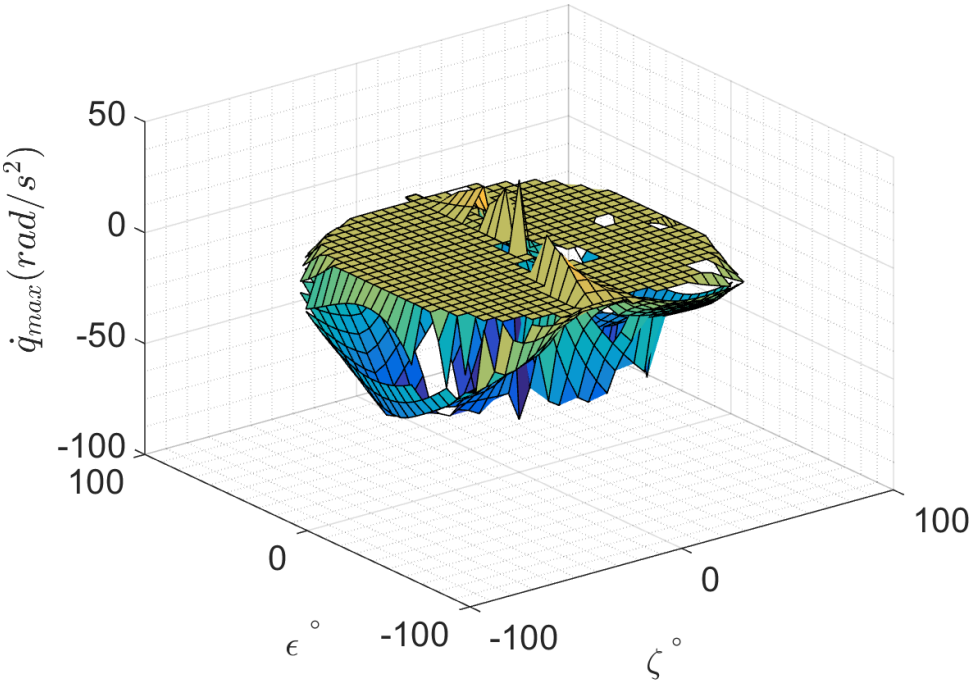

Figure 256: *X8* $\dot{q}$ design space, pure motion enforced, M1 fault

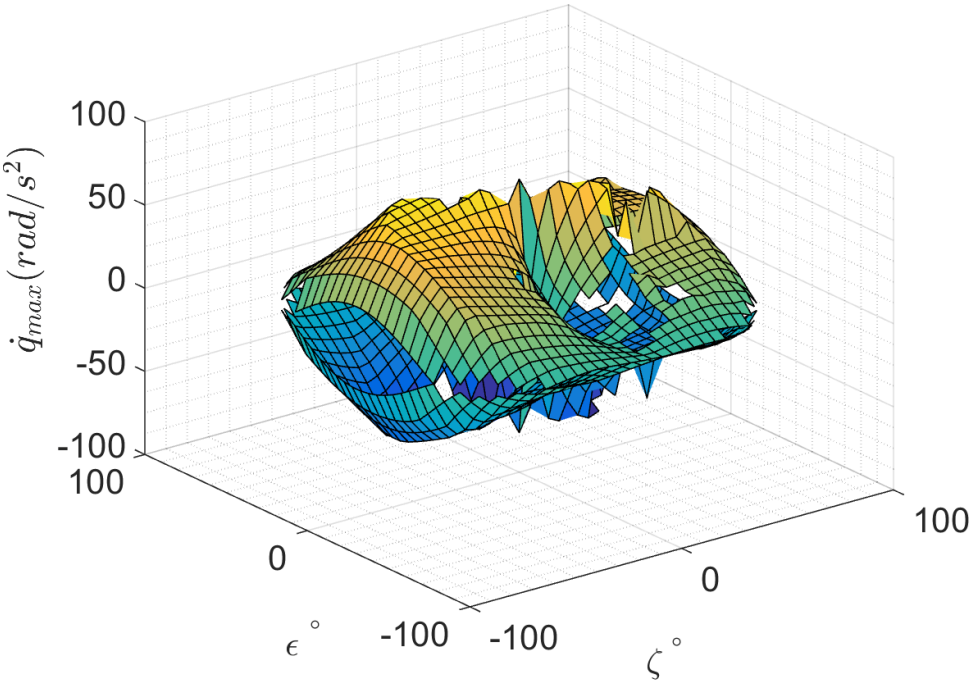

Figure 257: *X8* $\dot{q}$ design space, pure motion enforced, no rotor faults

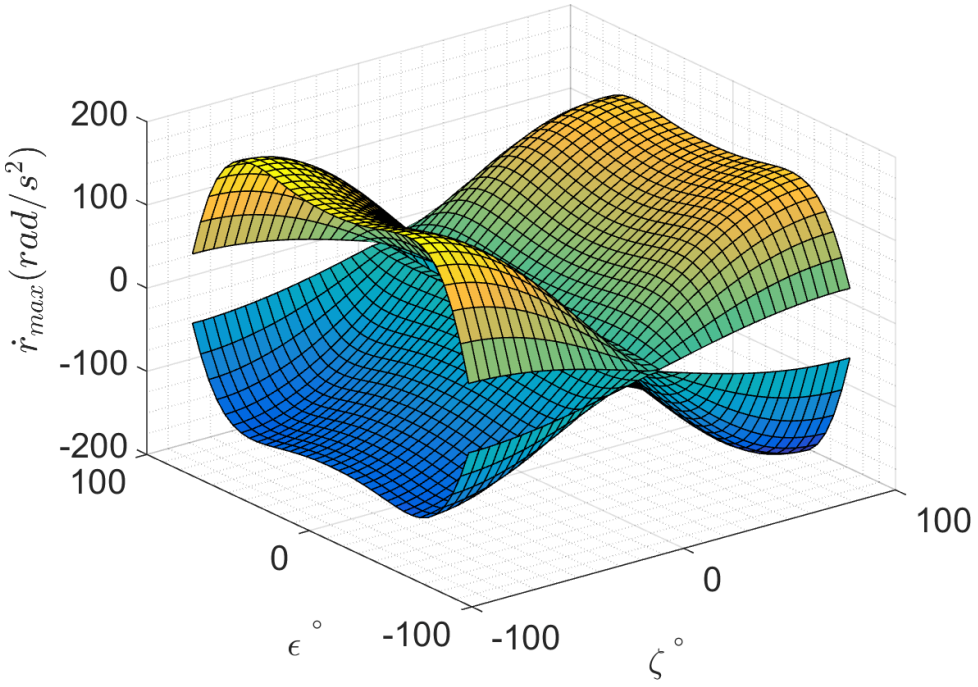

Figure 258: *X8* $\dot{r}$ design space, pure motion not enforced, M1 fault

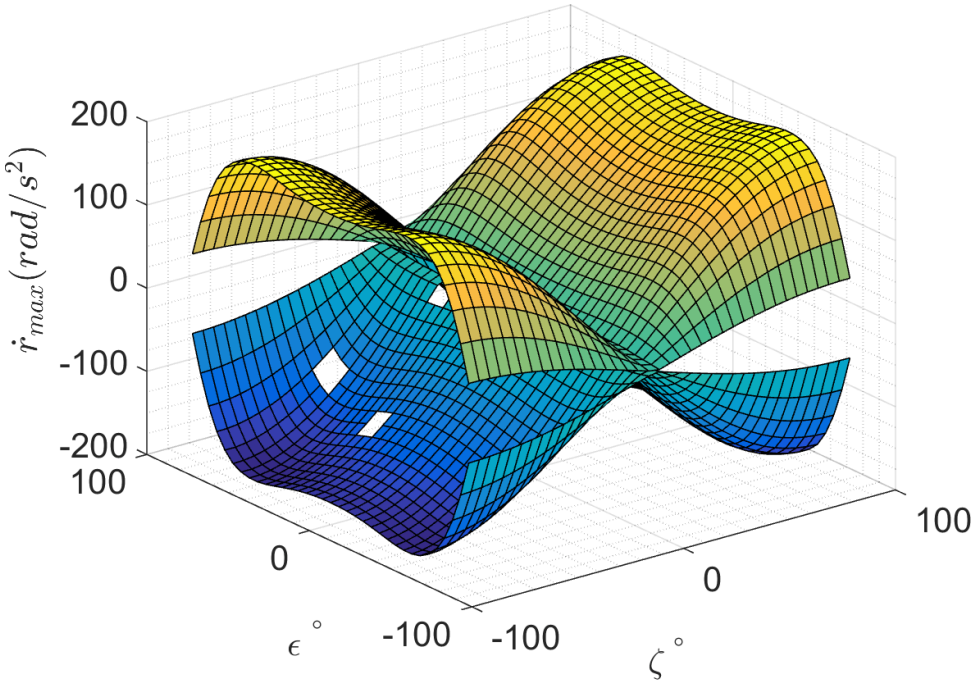

Figure 259: *X8* $\dot{r}$ design space, pure motion not enforced, no rotor faults

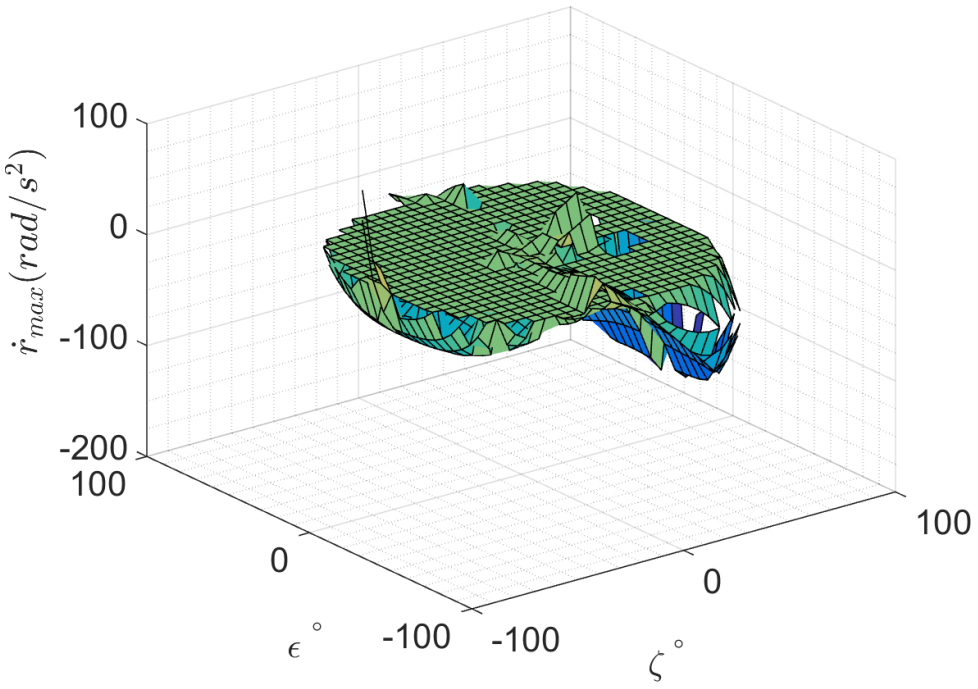

Figure 260: *X8* $\dot{r}$ design space, pure motion enforced, M1 fault

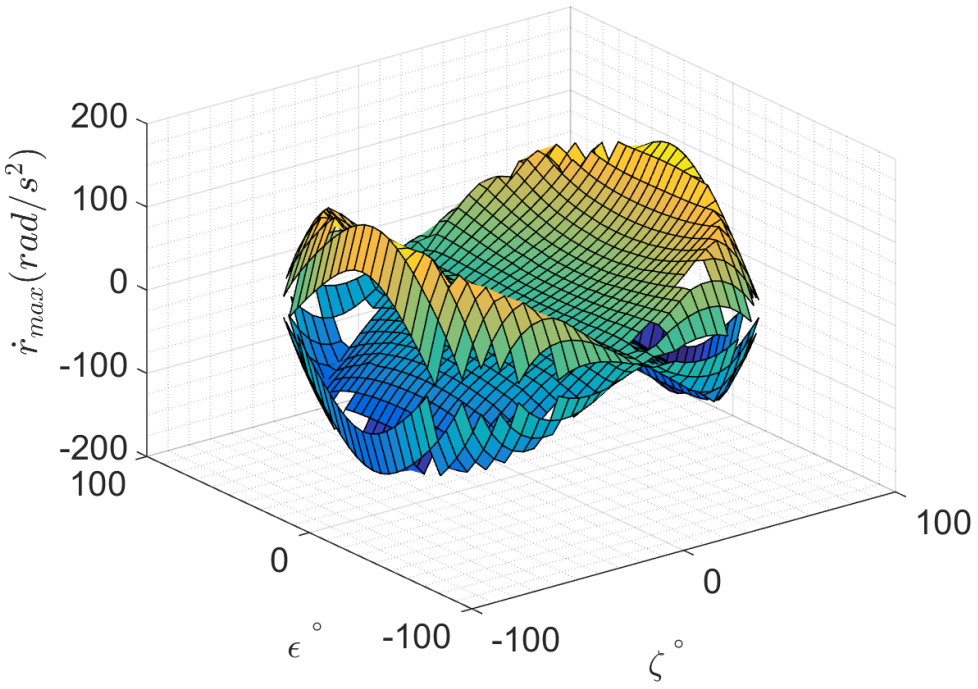

Figure 261: *X8* $\dot{r}$ design space, pure motion enforced, no rotor faults

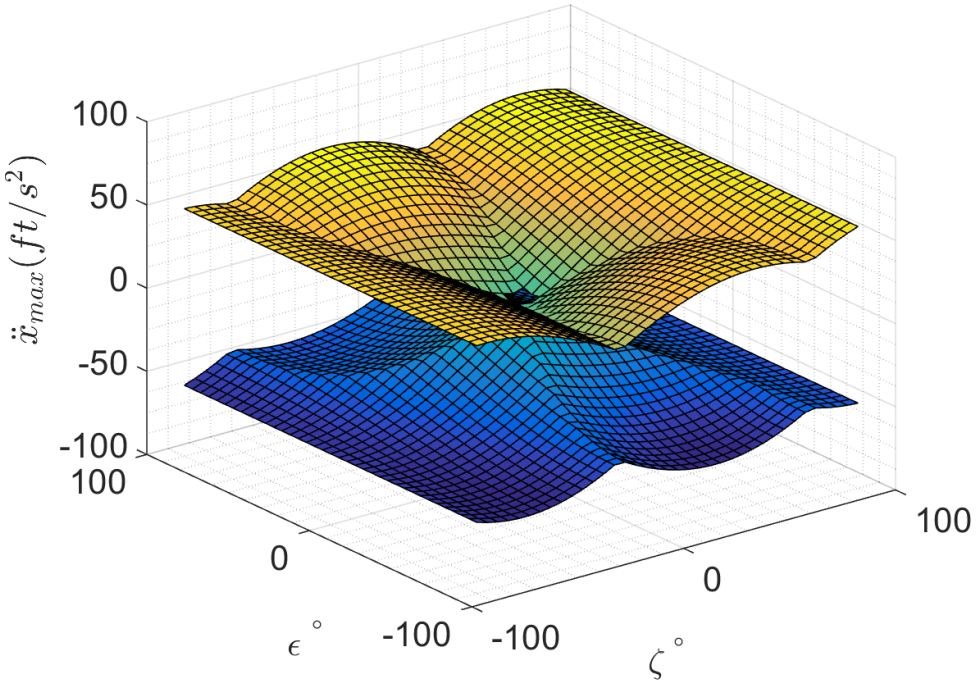

Figure 262: *X8* $\ddot{x}$ design space, pure motion not enforced, M1 fault

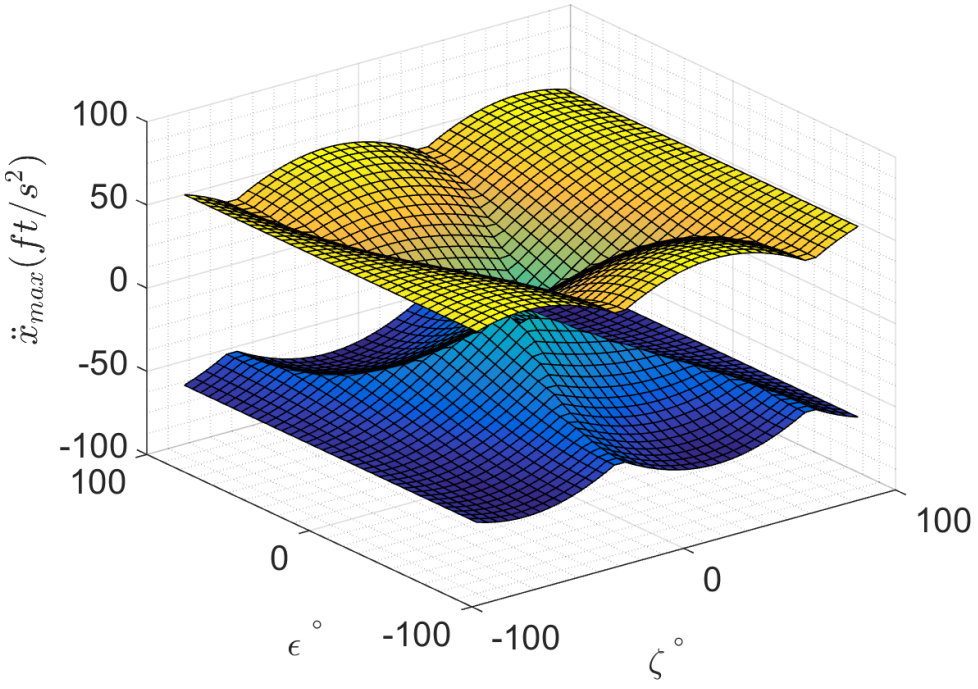

Figure 263: *X8* $\ddot{x}$ design space, pure motion not enforced, no rotor faults

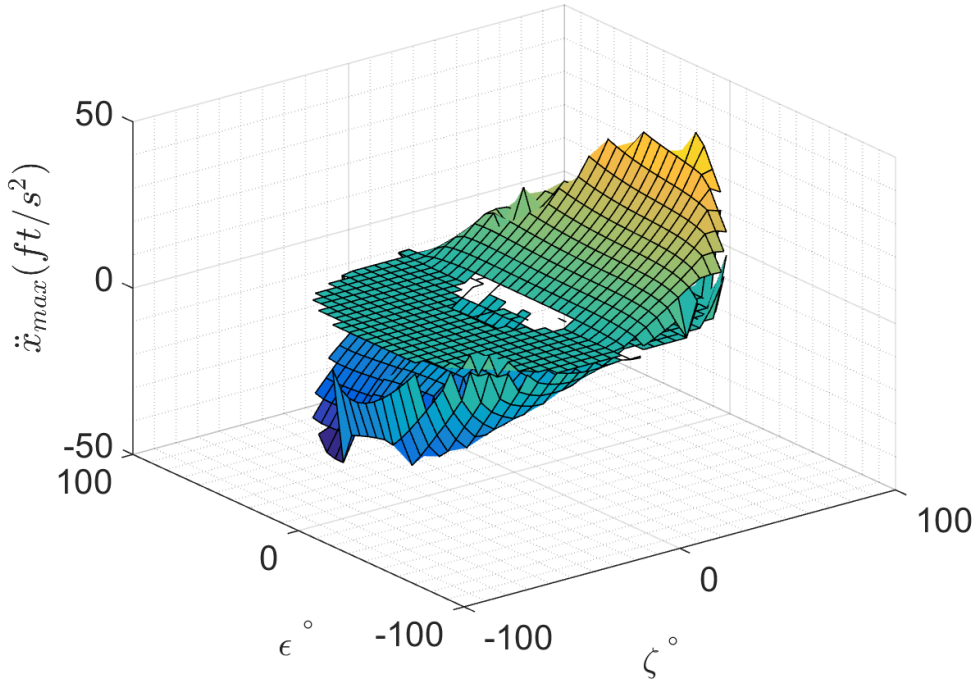

Figure 264: *X8* $\ddot{x}$ design space, pure motion enforced, M1 fault

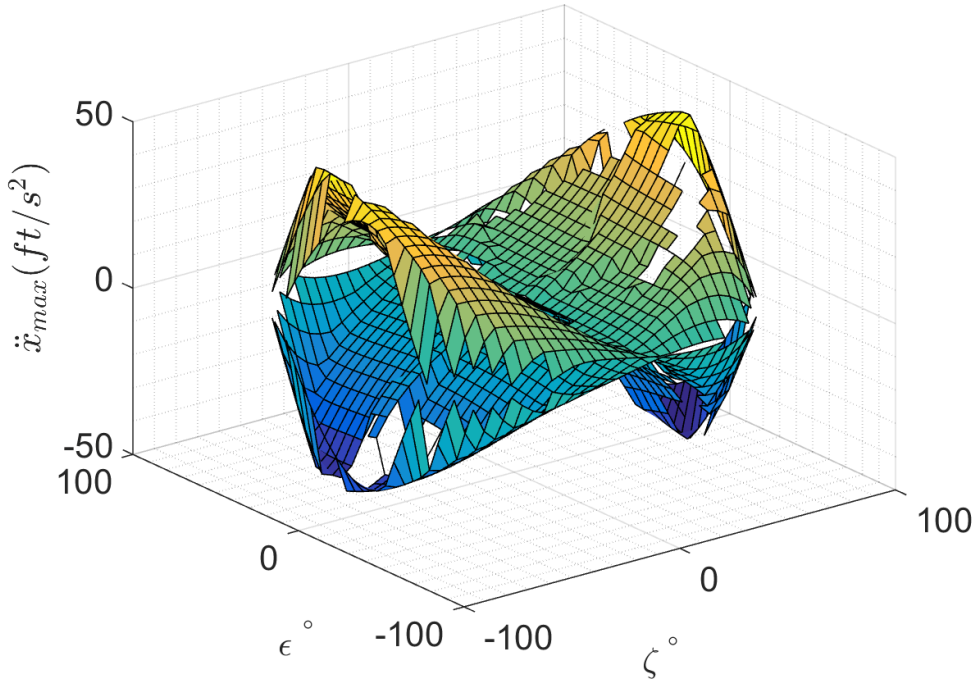

Figure 265: *X8* $\ddot{x}$ design space, pure motion enforced, no rotor faults

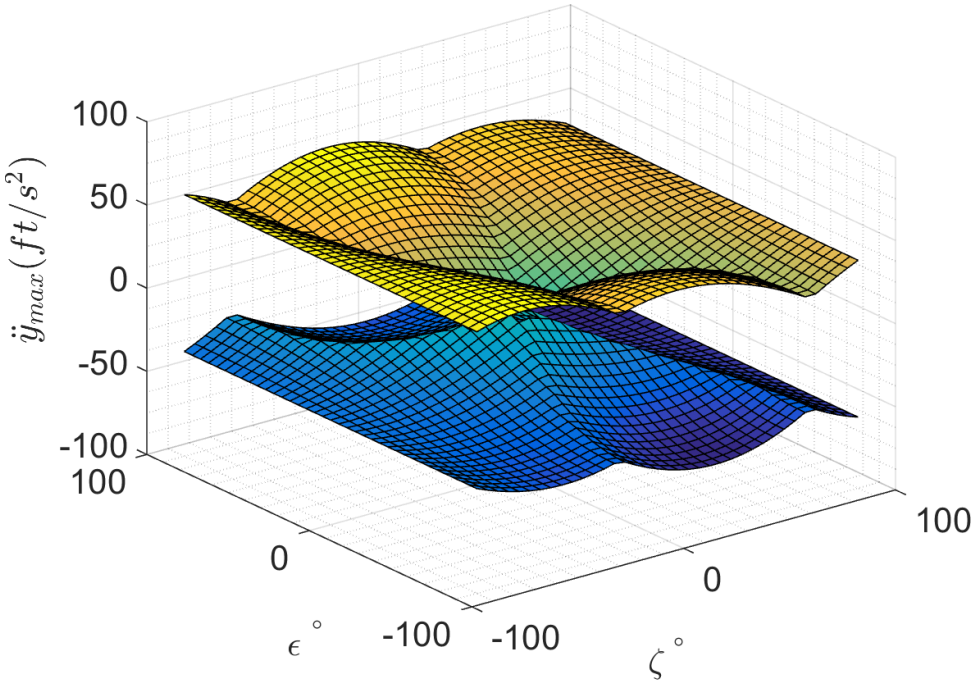

Figure 266: *X8 $\ddot{y}$* design space, pure motion not enforced, M1 fault

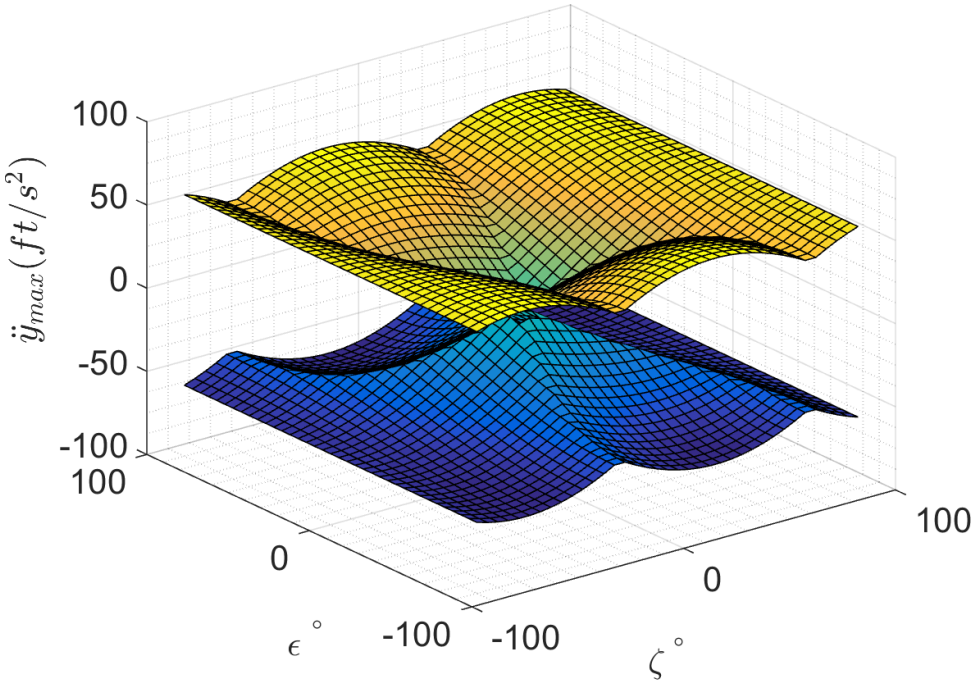

Figure 267: *X8 $\ddot{y}$* design space, pure motion not enforced, no rotor faults

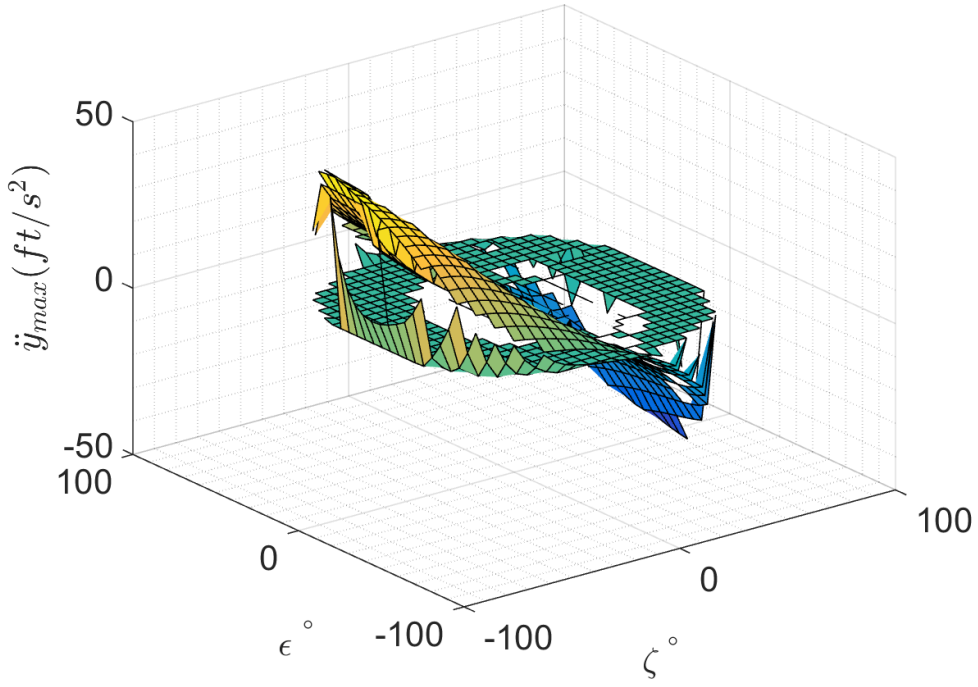

Figure 268: *X8* $\ddot{y}$ design space, pure motion enforced, M1 fault

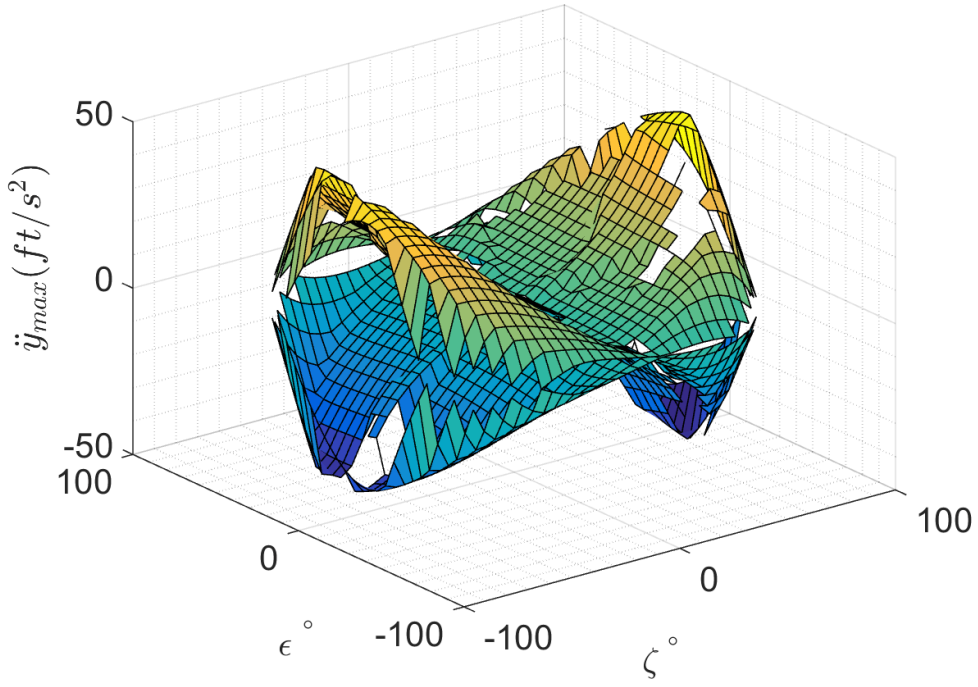

Figure 269: *X8* $\ddot{y}$ design space, pure motion enforced, no rotor faults

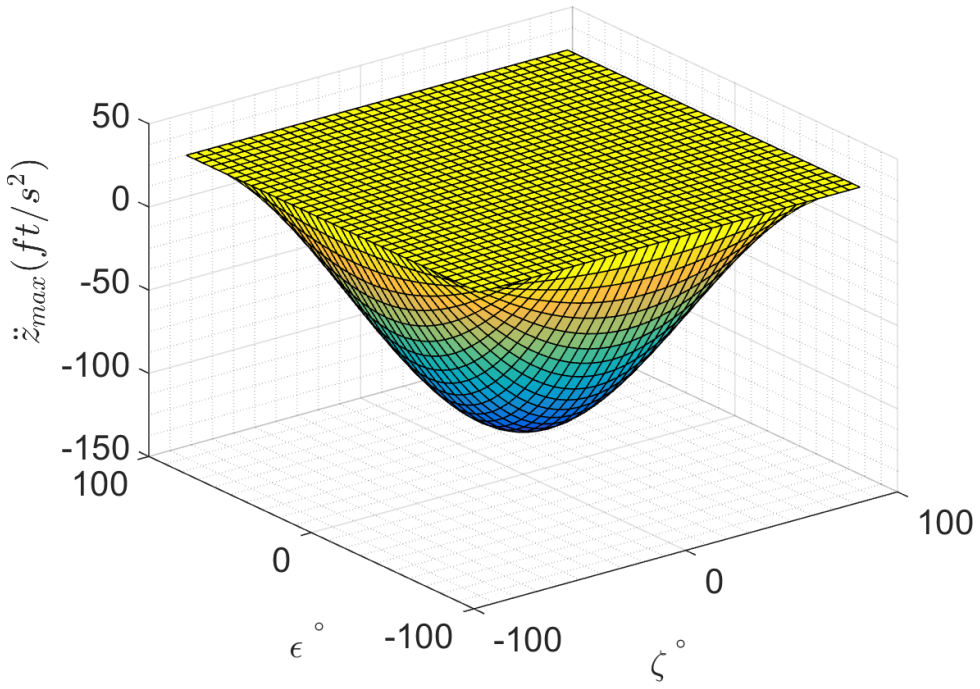

Figure 270: *X8* $\ddot{z}$ design space, pure motion not enforced, M1 fault

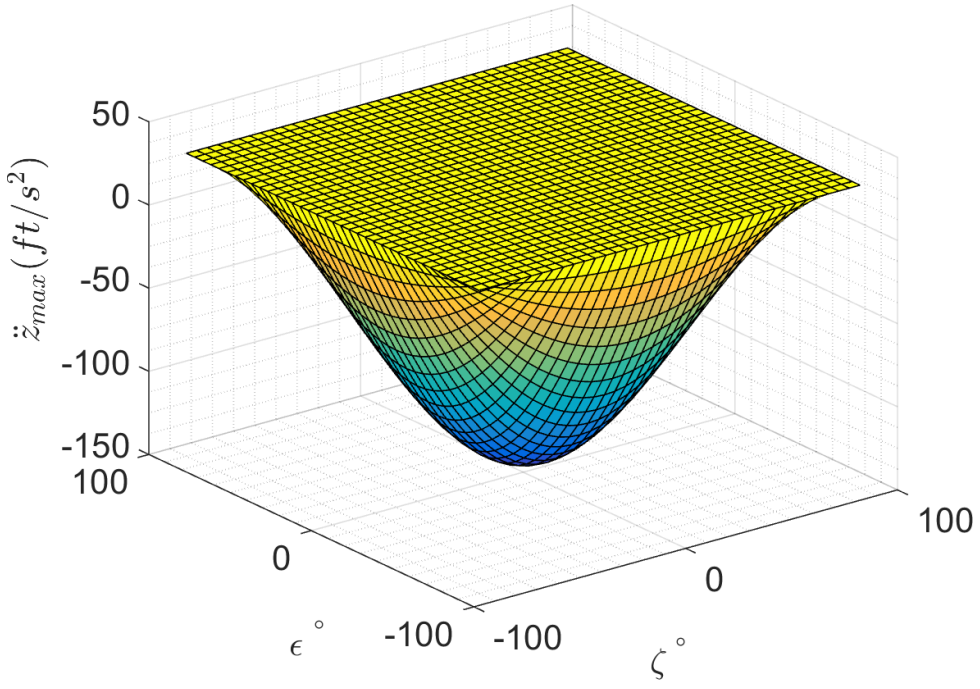

Figure 271: *X8* $\ddot{z}$ design space, pure motion not enforced, no rotor faults

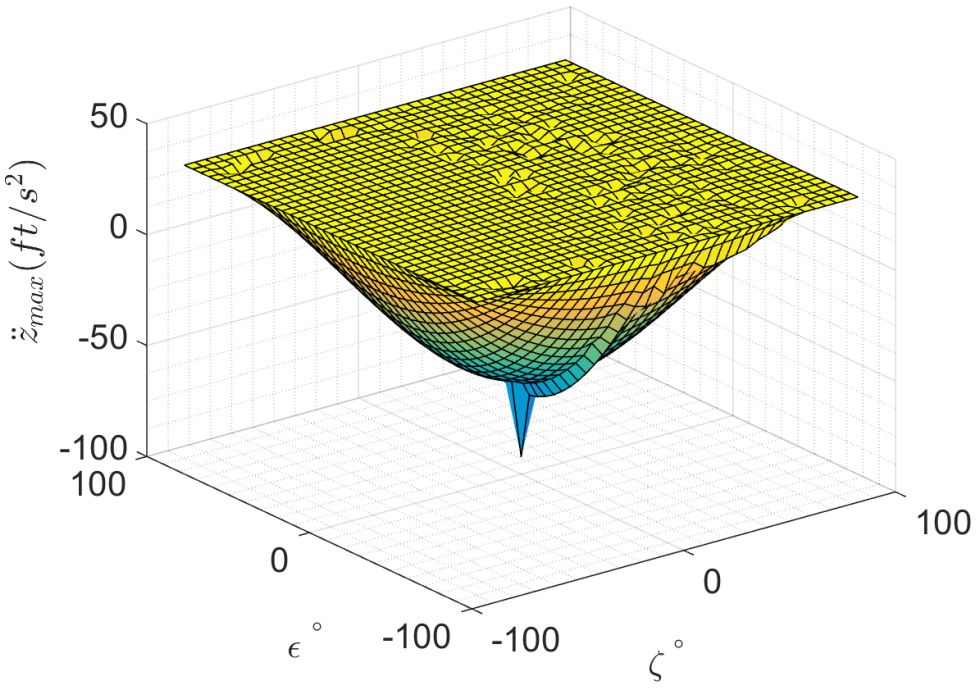

Figure 272: *X8* $\ddot{z}$ design space, pure motion enforced, M1 fault

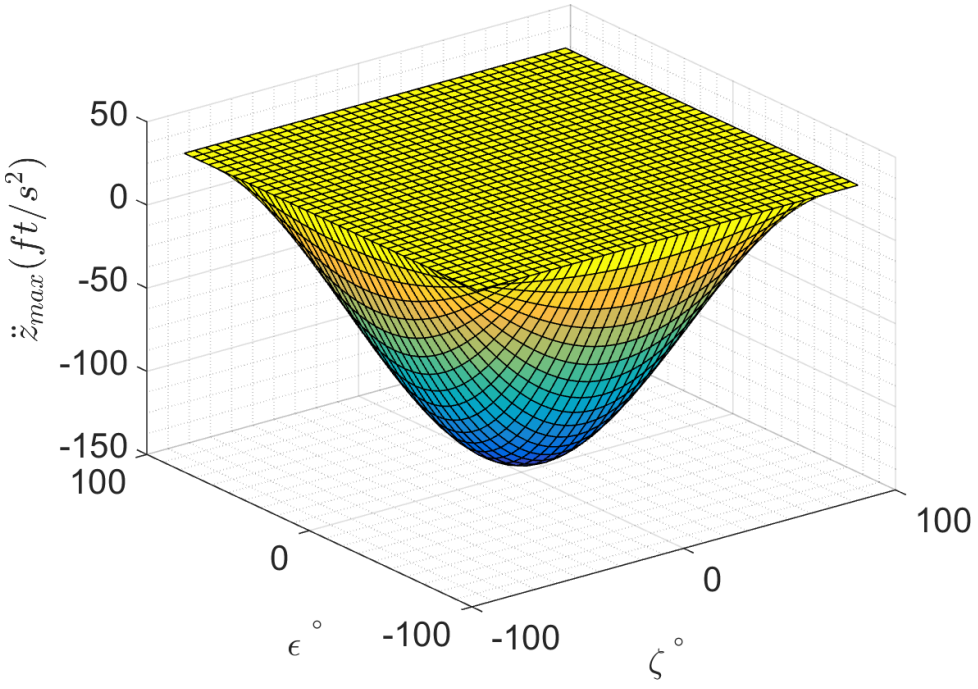

Figure 273: *X8* $\ddot{z}$ design space, pure motion enforced, no rotor faults

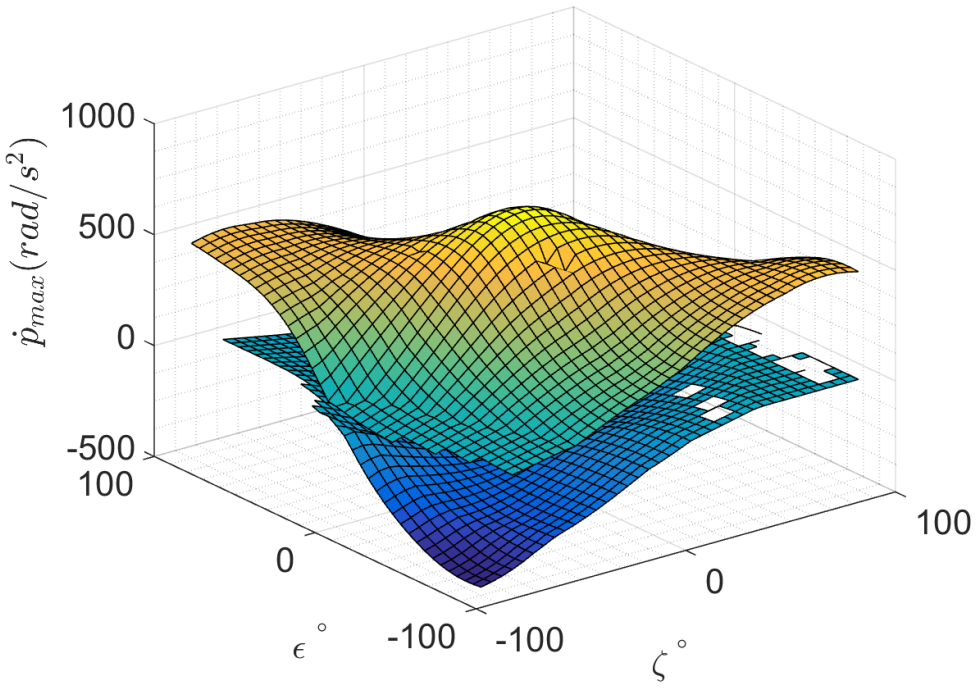

Figure 274: *Y6C* $\dot{p}$ design space, pure motion not enforced, co-rotating, M1 fault

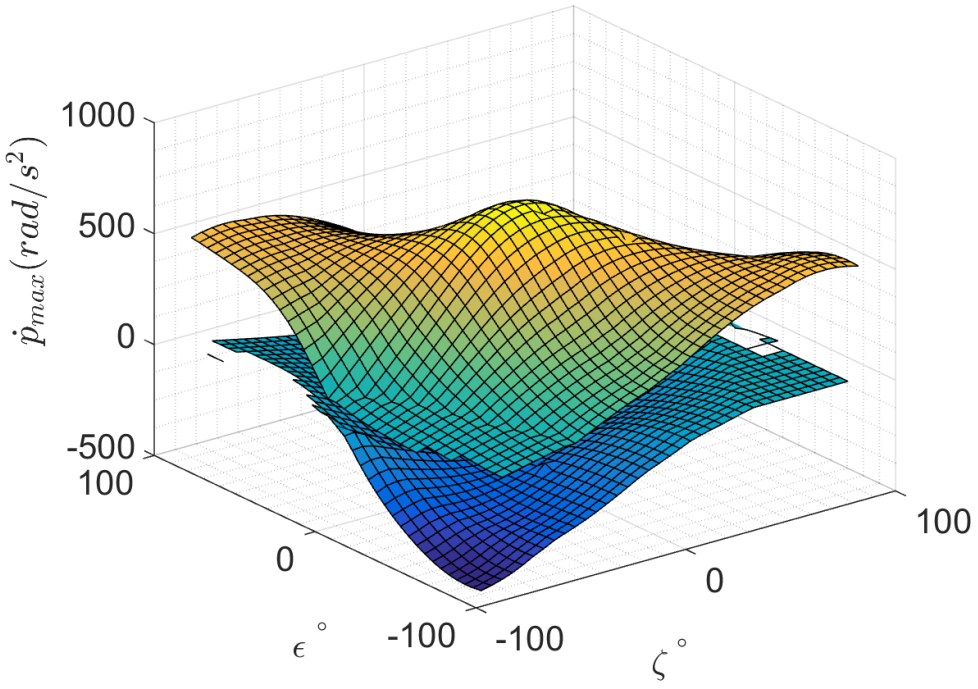

Figure 275: *Y6C* $\dot{p}$ design space, pure motion not enforced, counter-rotating, M1 fault

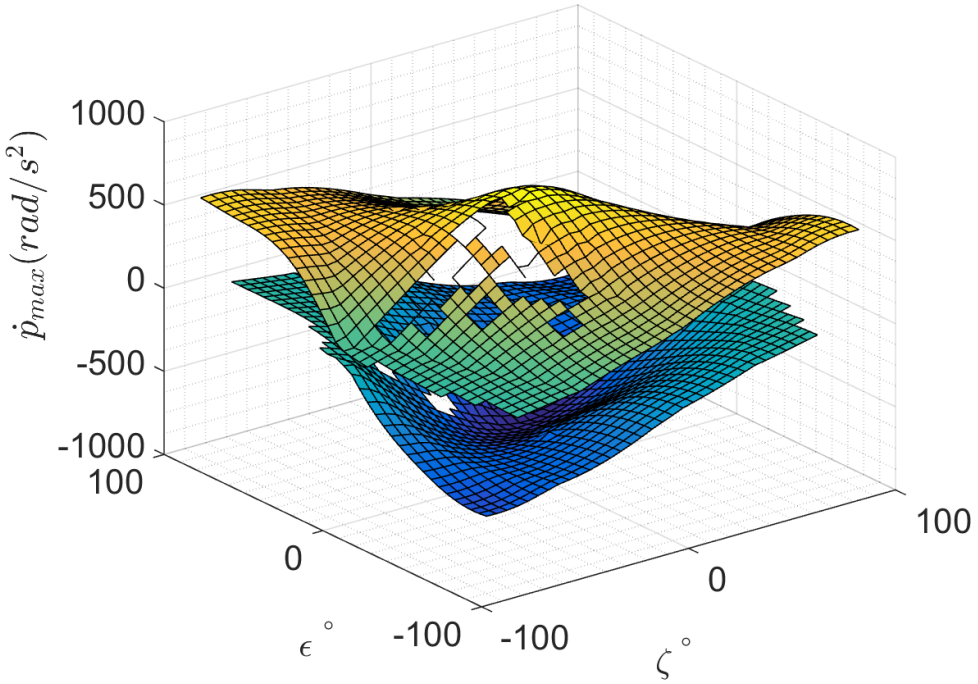

Figure 276: *Y6C* $\dot{p}$ design space, pure motion not enforced, co-rotating, no rotor faults

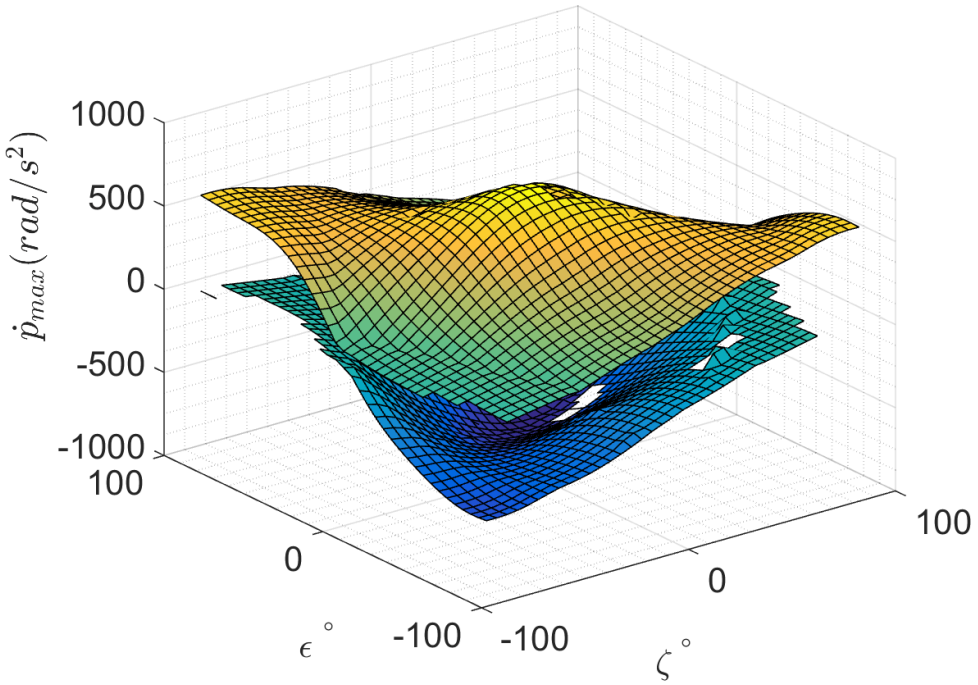

Figure 277: *Y6C* $\dot{p}$ design space, pure motion not enforced, counter-rotating, no rotor faults

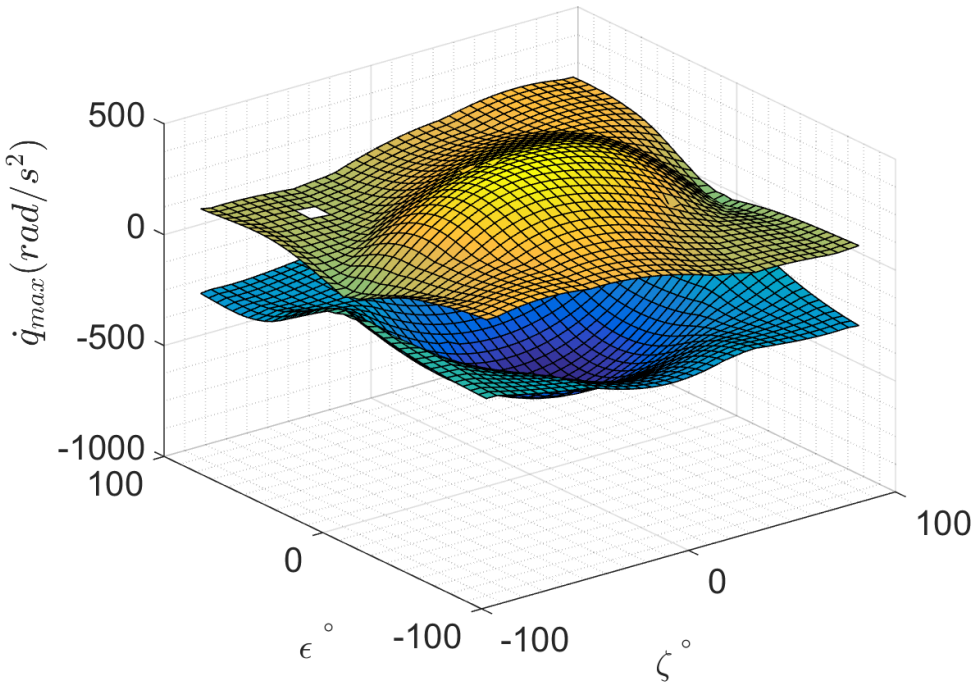

Figure 278: *Y6C* $\dot{q}$ design space, pure motion not enforced, co-rotating, M1 fault

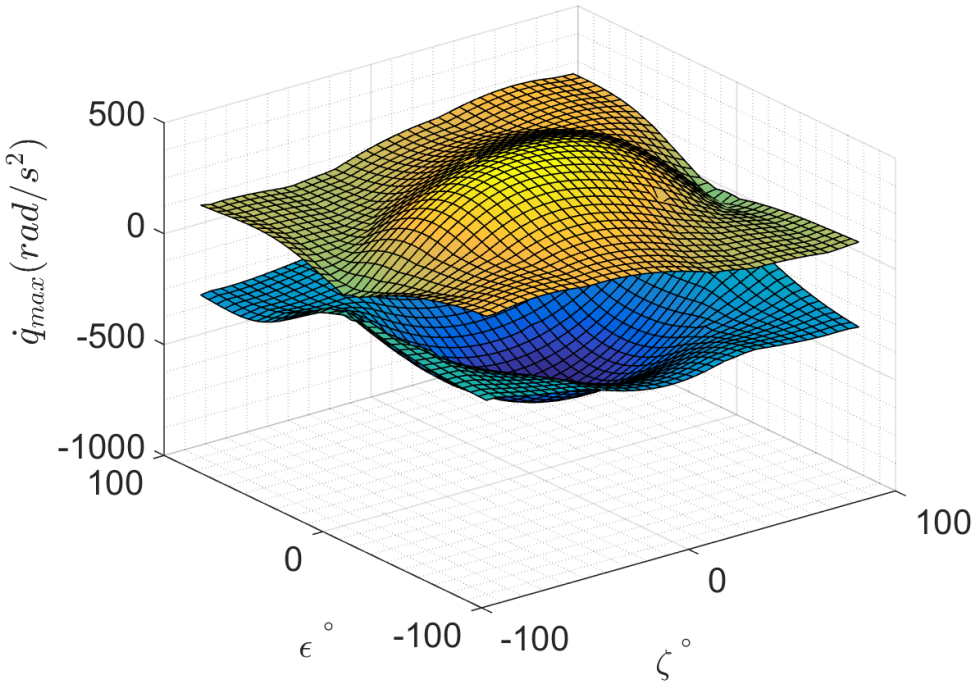

Figure 279: *Y6C* $\dot{q}$ design space, pure motion not enforced, counter-rotating, M1 fault

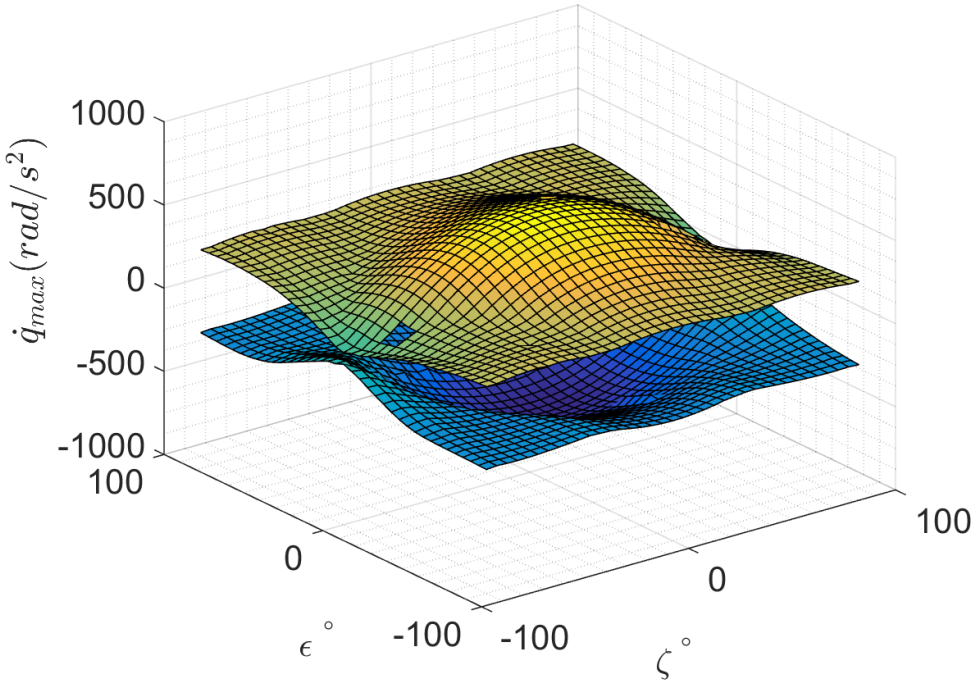

Figure 280: *Y6C* $\dot{q}$ design space, pure motion not enforced, co-rotating, no rotor faults

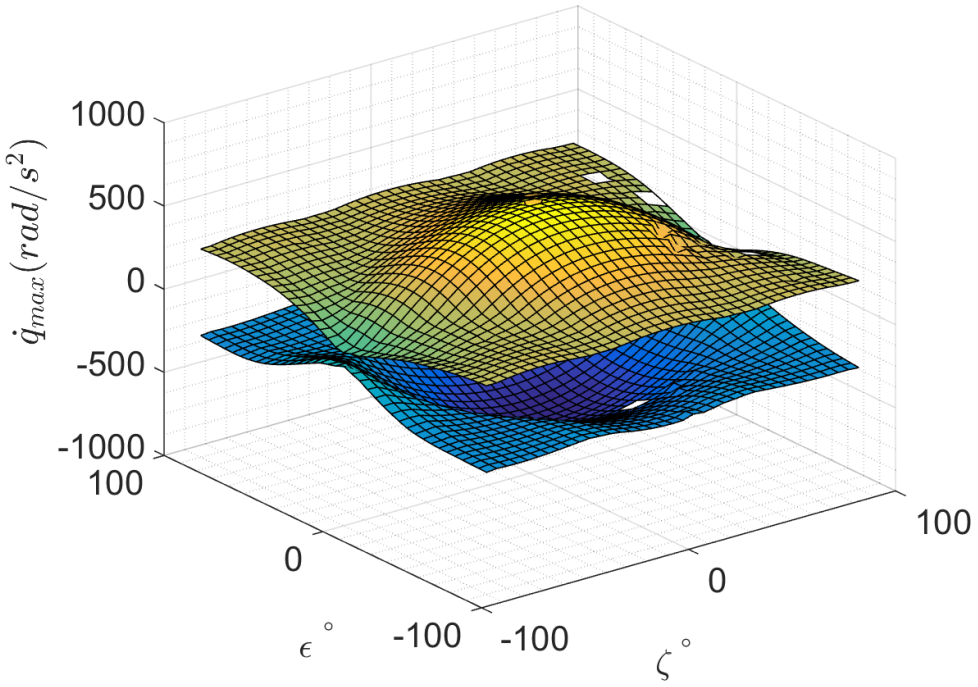

Figure 281: *Y6C* $\dot{q}$ design space, pure motion not enforced, counter-rotating, no rotor faults

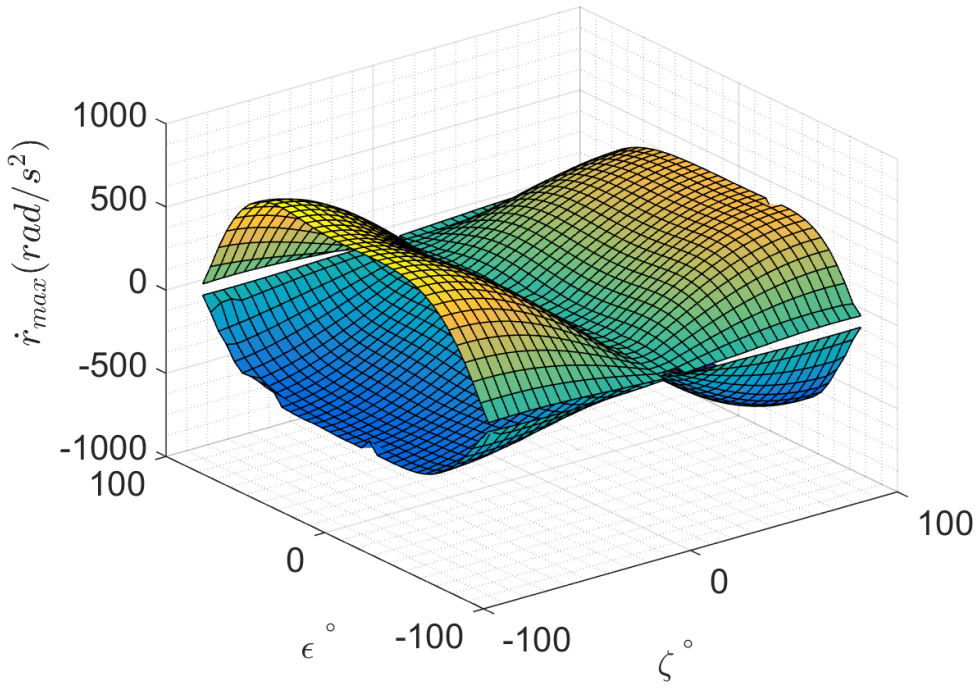

Figure 282: *Y6C* $\dot{r}$ design space, pure motion not enforced, co-rotating, M1 fault

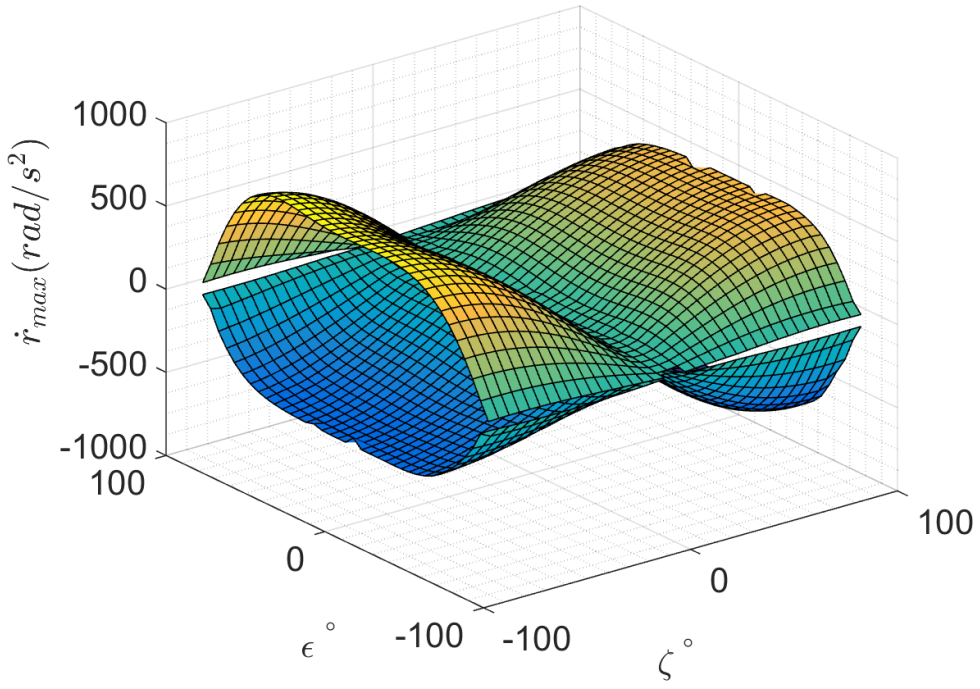

Figure 283: *Y6C* $\dot{r}$ design space, pure motion not enforced, counter-rotating, M1 fault

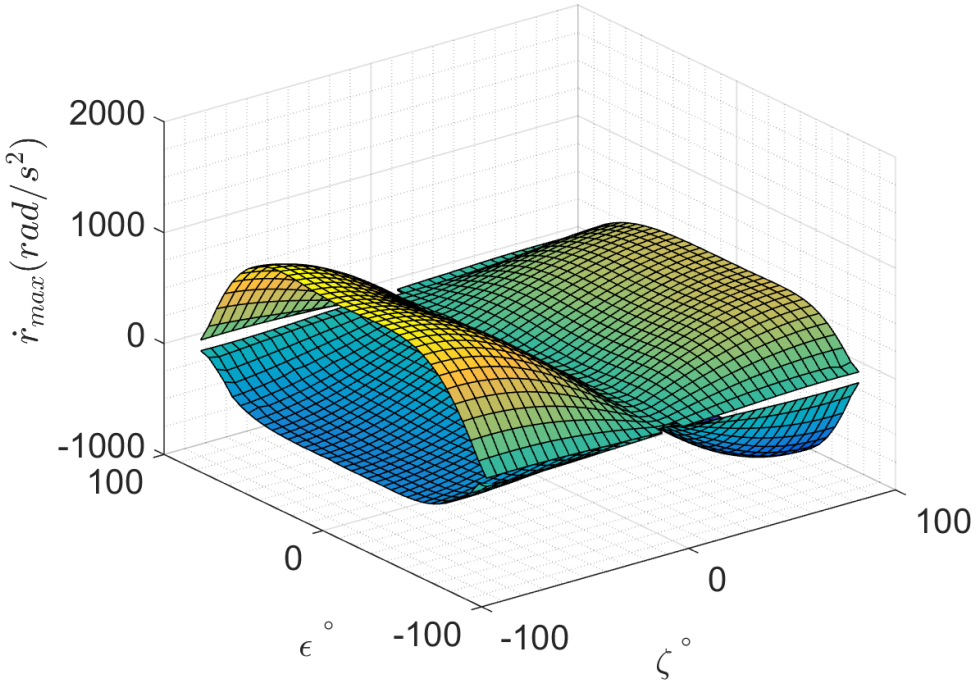

Figure 284: *Y6C* $\dot{r}$ design space, pure motion not enforced, co-rotating, no rotor faults

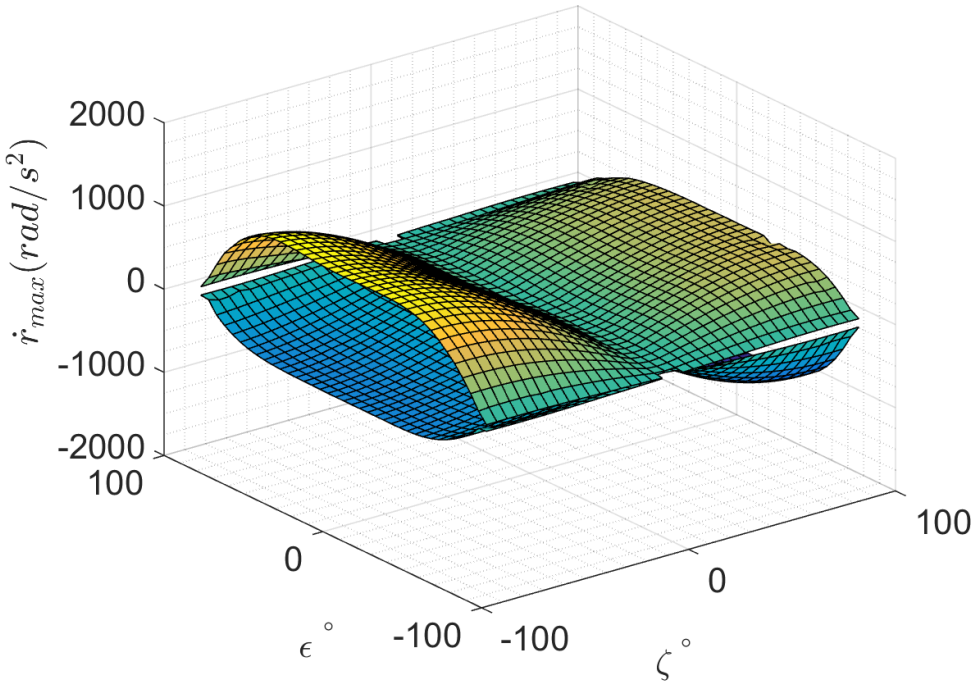

Figure 285: *Y6C* $\dot{r}$ design space, pure motion not enforced, counter-rotating, no rotor faults

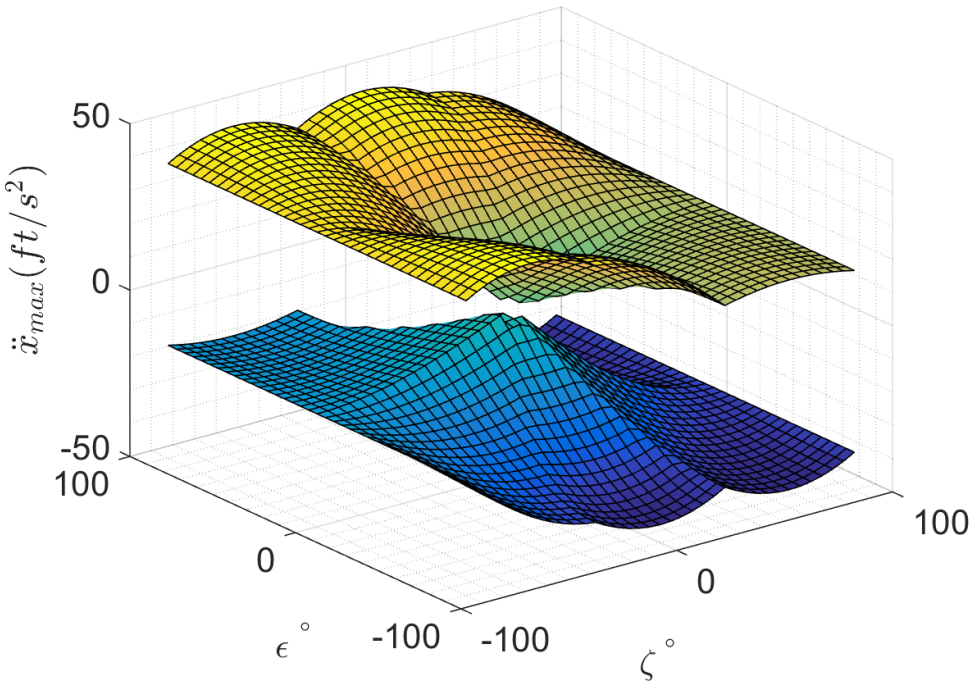

Figure 286: *Y6C* $\ddot{x}$ design space, pure motion not enforced, co-rotating, M1 fault

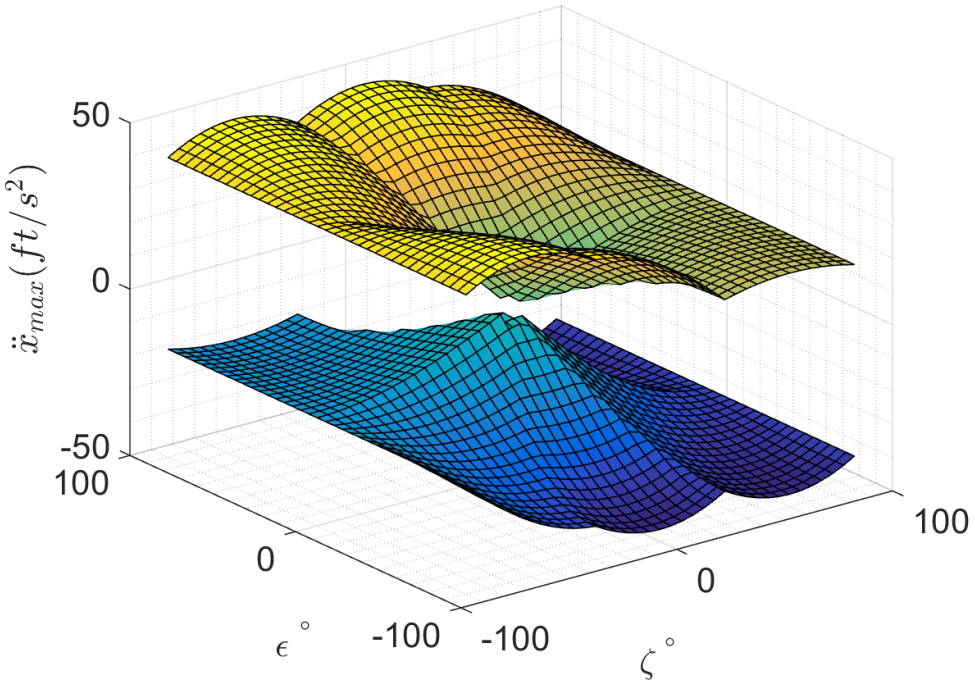

Figure 287: *Y6C* $\ddot{x}$ design space, pure motion not enforced, counter-rotating, M1 fault

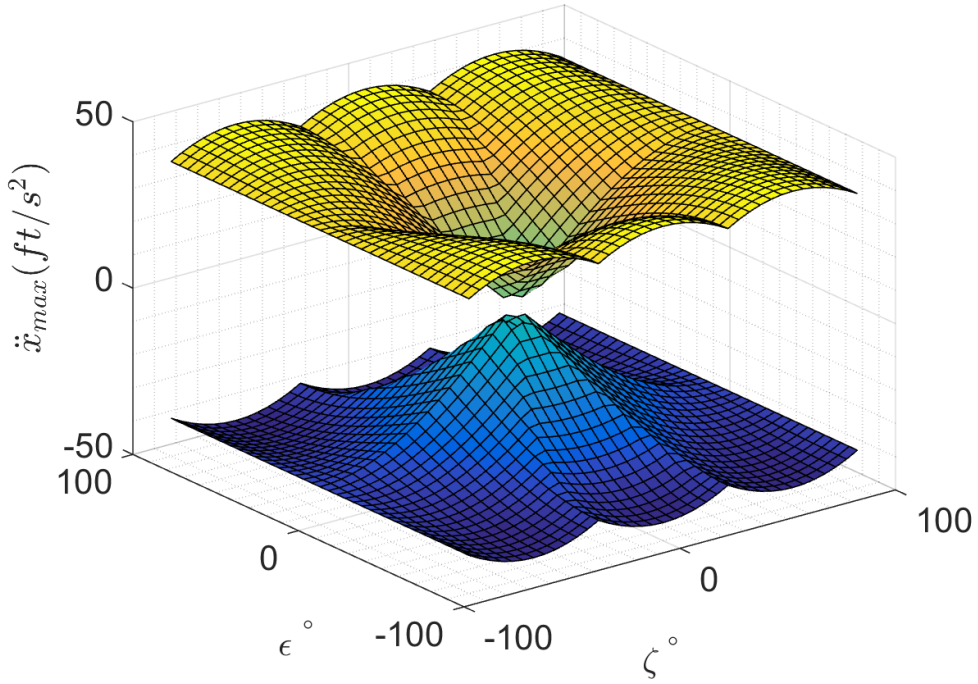

Figure 288: *Y6C* $\ddot{x}$ design space, pure motion not enforced, co-rotating, no rotor faults

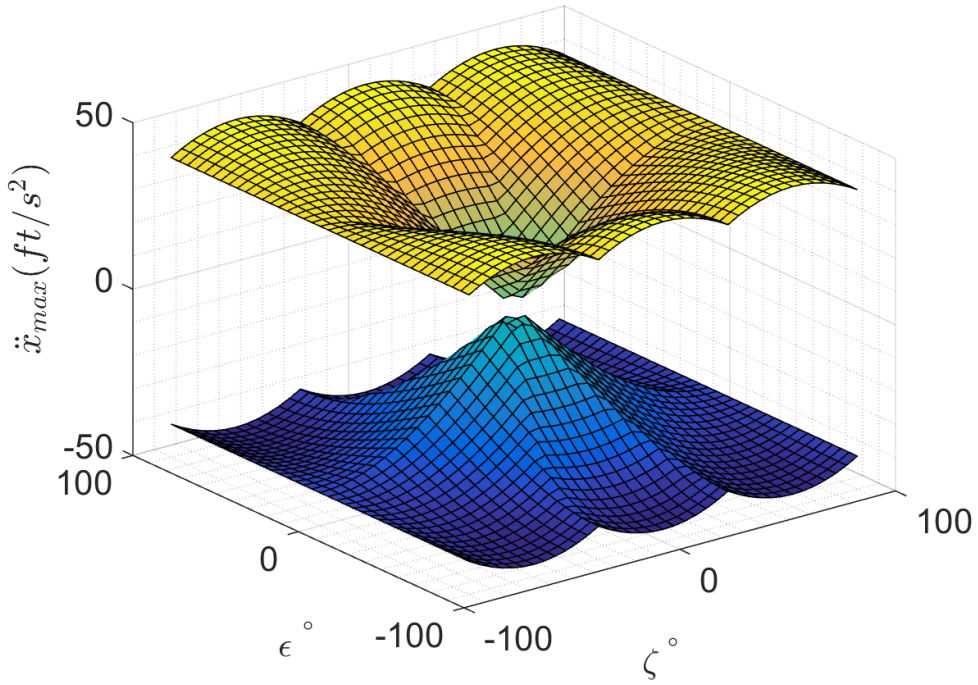

Figure 289: *Y6C* $\ddot{x}$ design space, pure motion not enforced, counter-rotating, no rotor faults

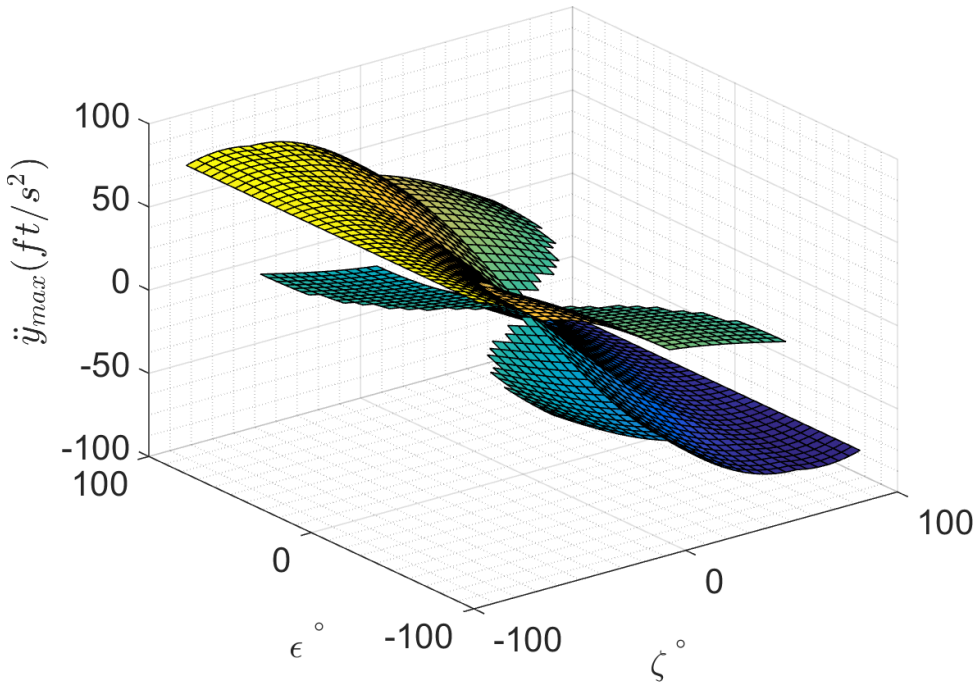

Figure 290: *Y6C* $\ddot{y}$ design space, pure motion not enforced, co-rotating, M1 fault

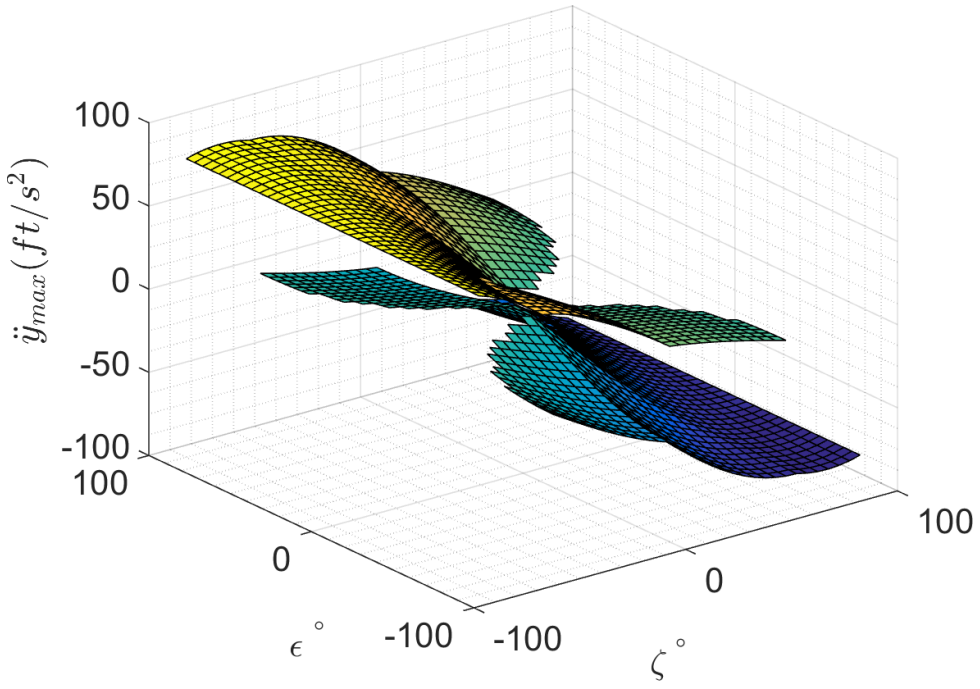

Figure 291: *Y6C* $\ddot{y}$ design space, pure motion not enforced, counter-rotating, M1 fault

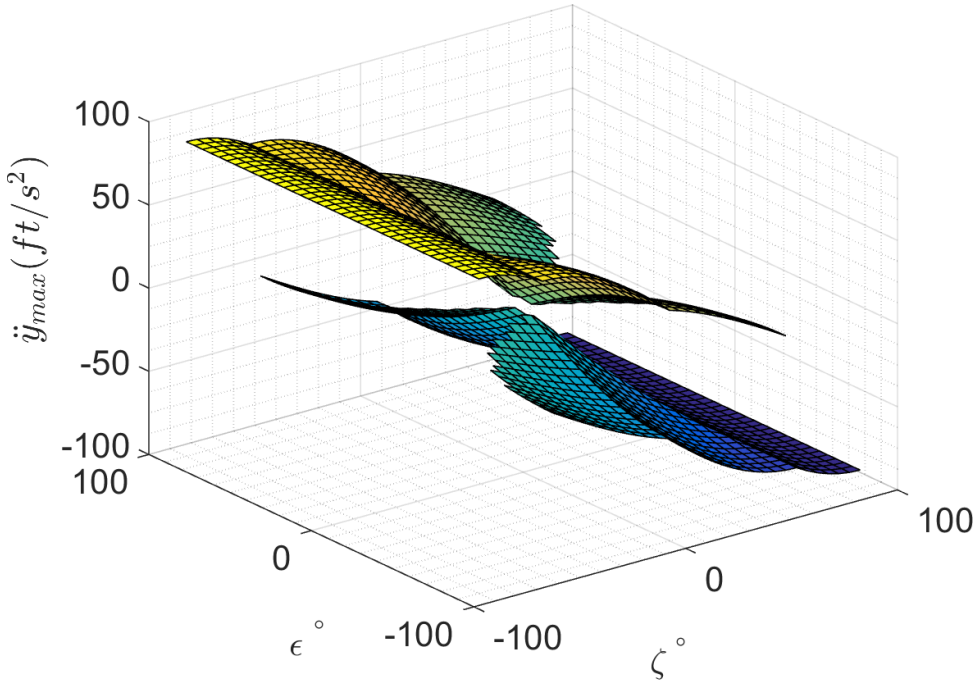

Figure 292: *Y6C* $\ddot{y}$ design space, pure motion not enforced, co-rotating, no rotor faults

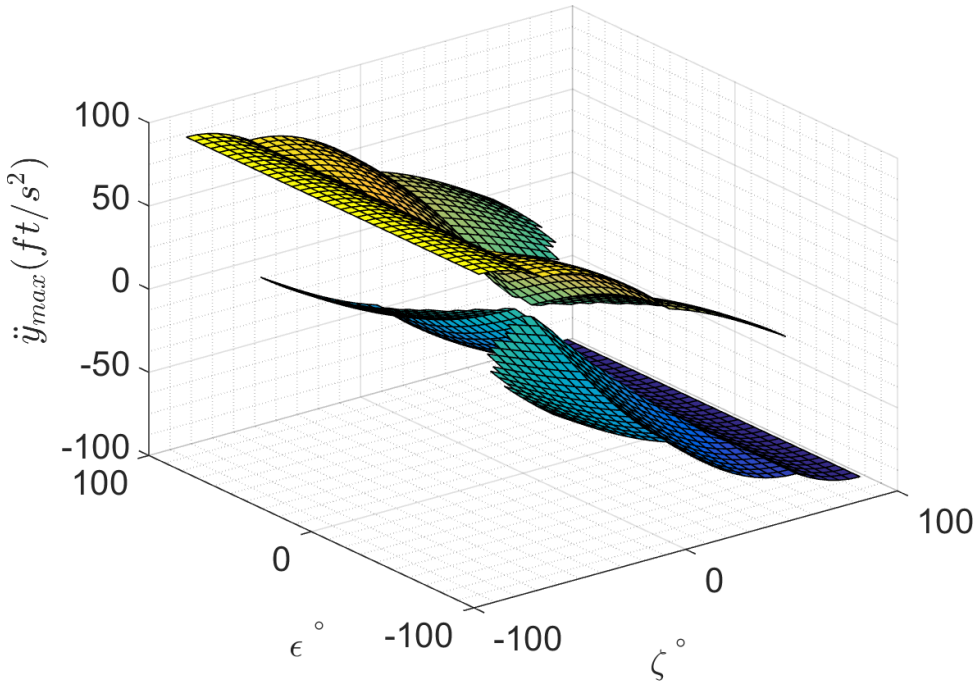

Figure 293: *Y6C* $\ddot{y}$ design space, pure motion not enforced, counter-rotating, no rotor faults

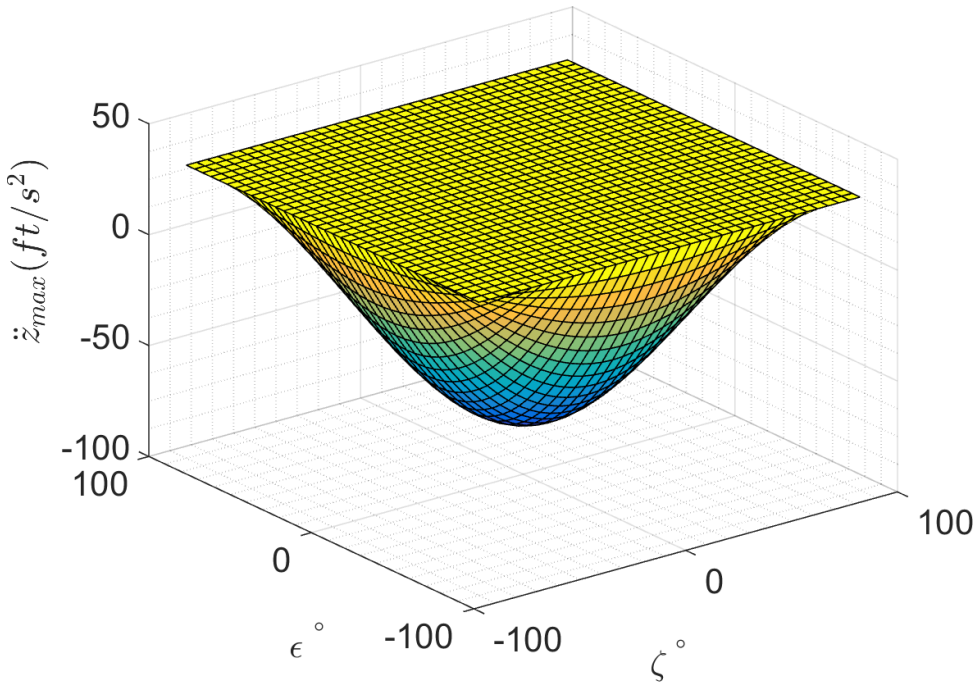

Figure 294: *Y6C* $\ddot{z}$ design space, pure motion not enforced, co-rotating, M1 fault

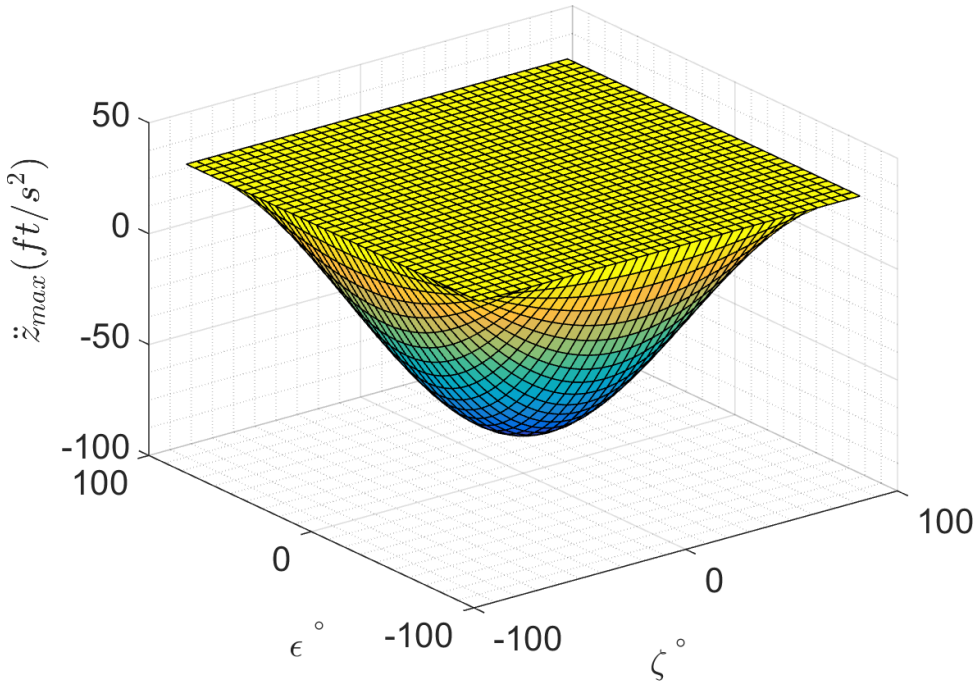

Figure 295: *Y6C* $\ddot{z}$ design space, pure motion not enforced, counter-rotating, M1 fault

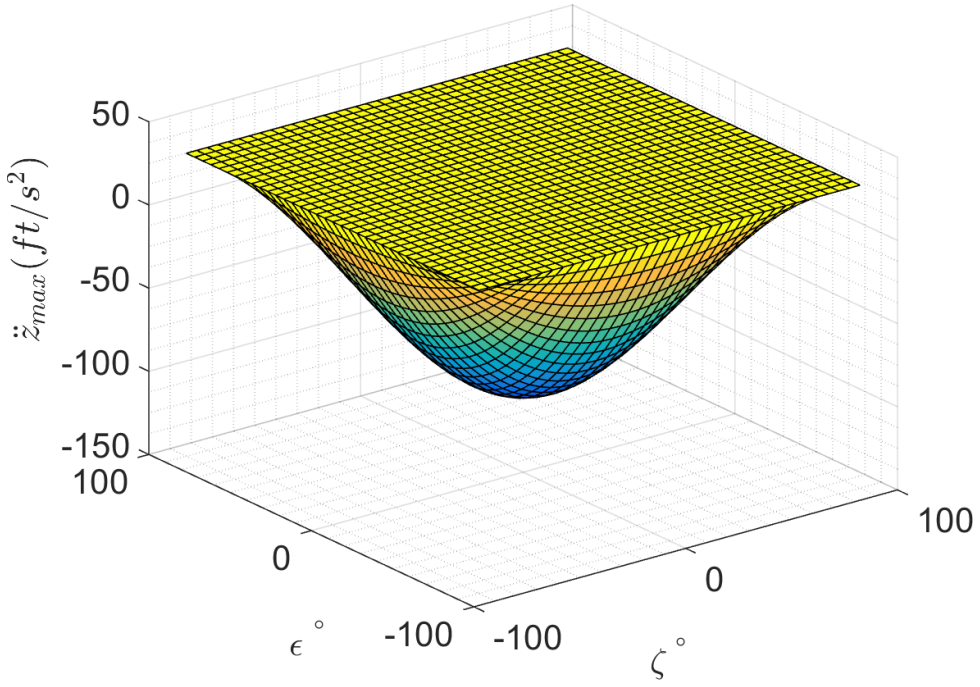

Figure 296: *Y6C* $\ddot{z}$ design space, pure motion not enforced, co-rotating, no rotor faults

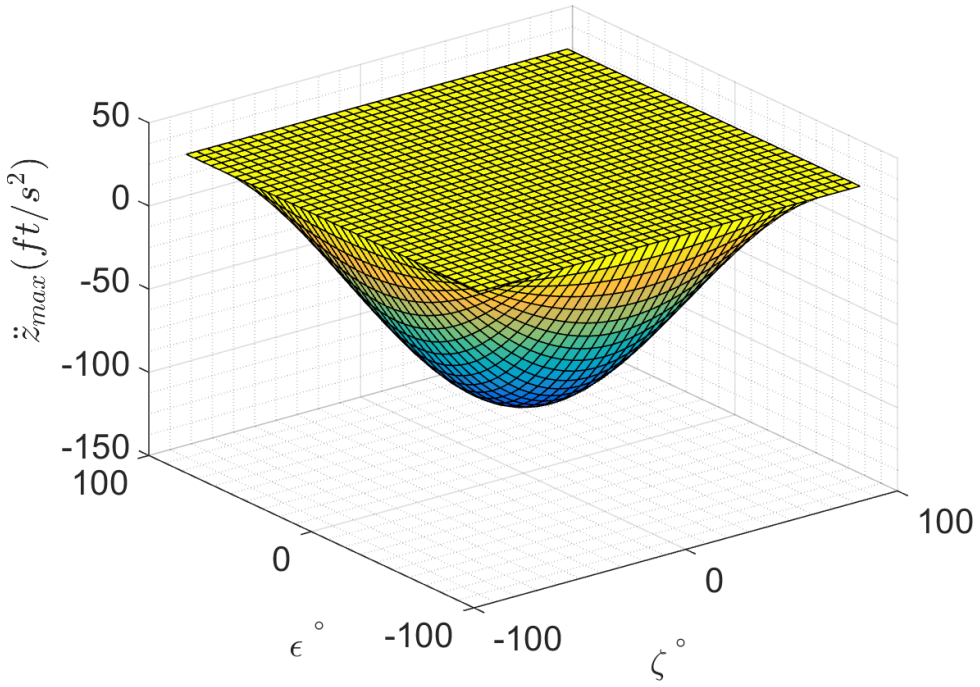

Figure 297: *Y6C* $\ddot{z}$ design space, pure motion not enforced, counter-rotating, no rotor faults

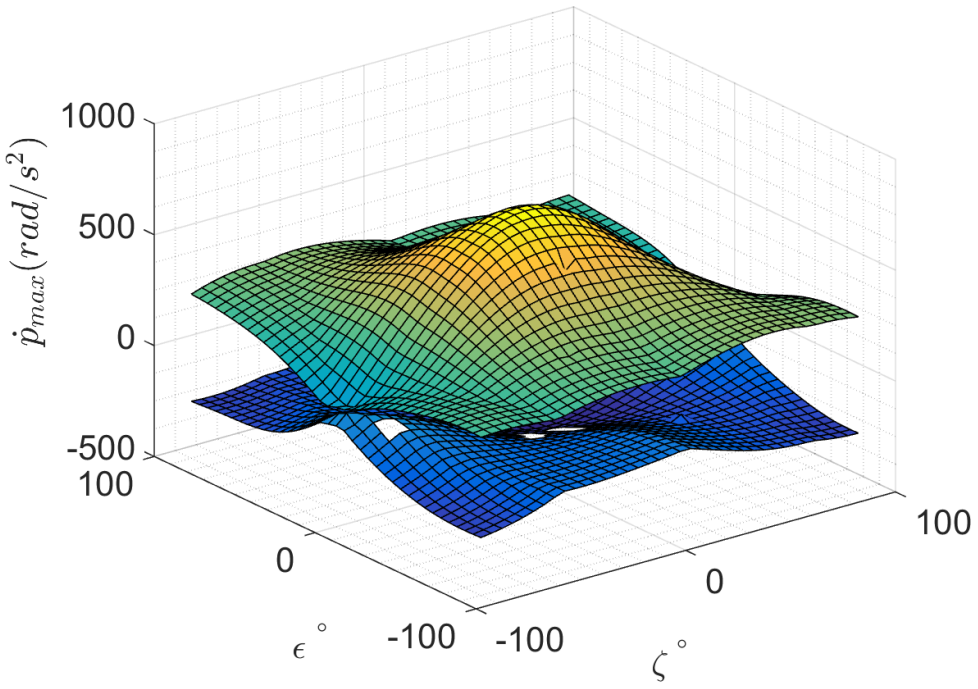

Figure 298: *Y6sC* $\dot{p}$ design space, pure motion not enforced, co-rotating, M1 fault

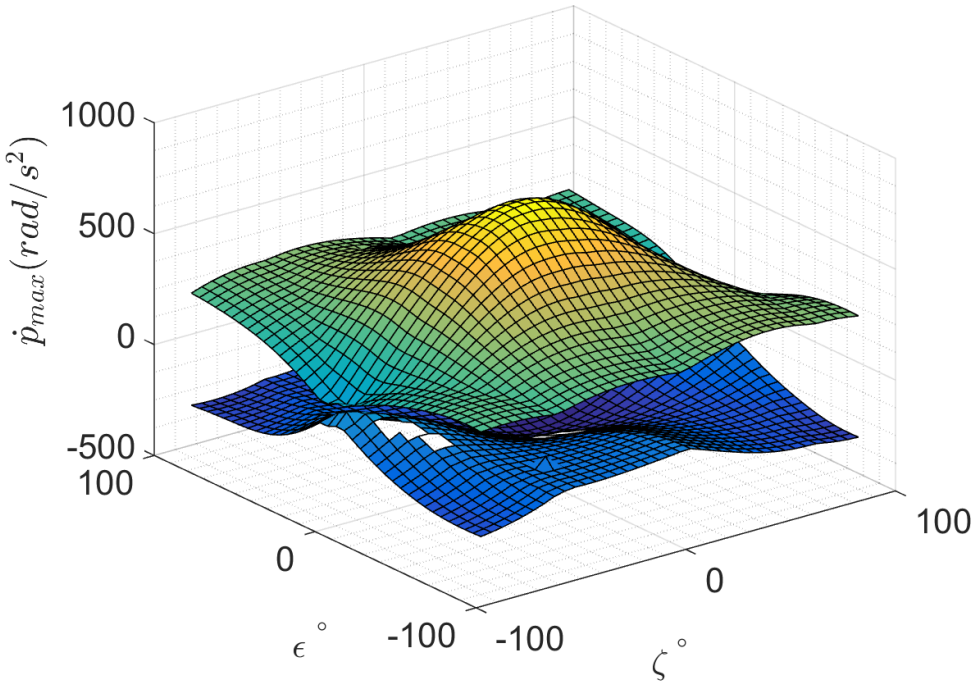

Figure 299: *Y6sC* $\dot{p}$ design space, pure motion not enforced, counter-rotating, M1 fault

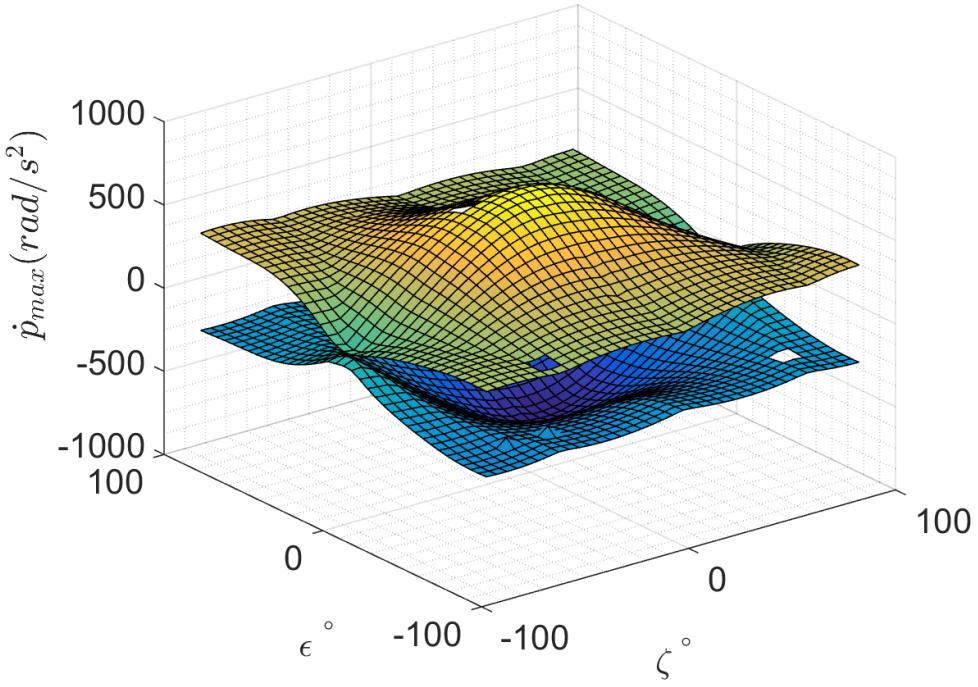

Figure 300: *Y6sC* $\dot{p}$ design space, pure motion not enforced, co-rotating, no rotor faults

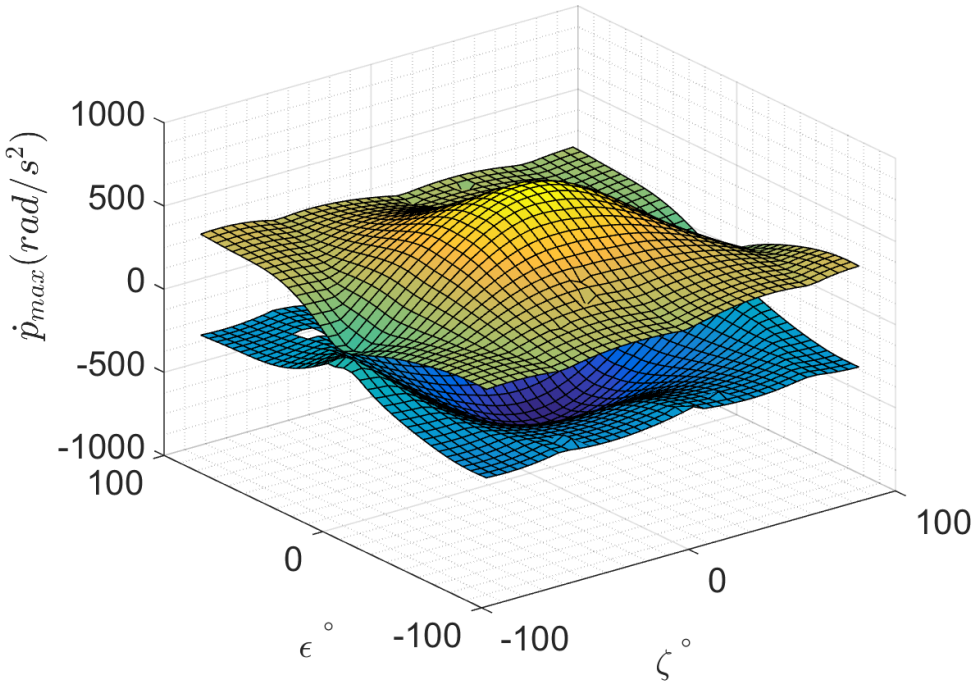

Figure 301: *Y6sC* $\dot{p}$ design space, pure motion not enforced, counter-rotating, no rotor faults

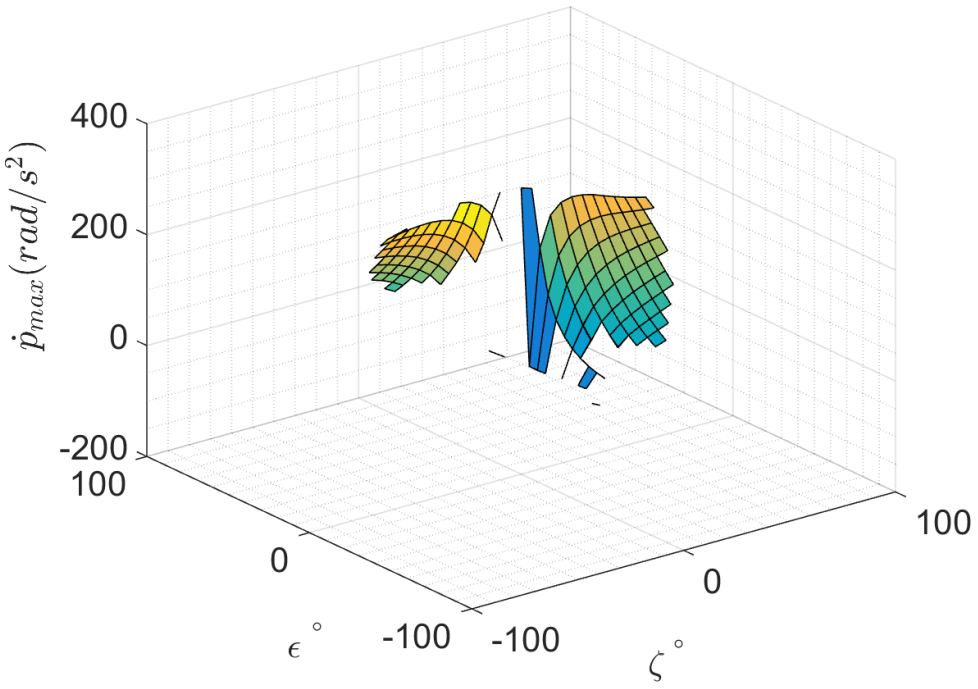

Figure 302: *Y6sC* $\dot{p}$ design space, pure motion enforced, co-rotating, M1 fault

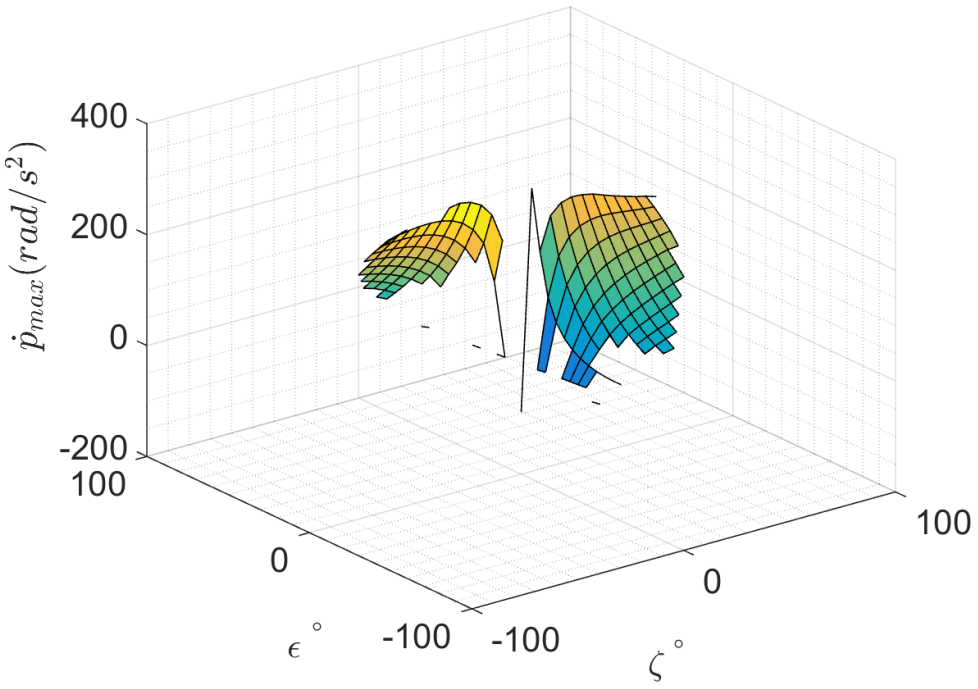

Figure 303: *Y6sC* $\dot{p}$ design space, pure motion enforced, counter-rotating, M1 fault

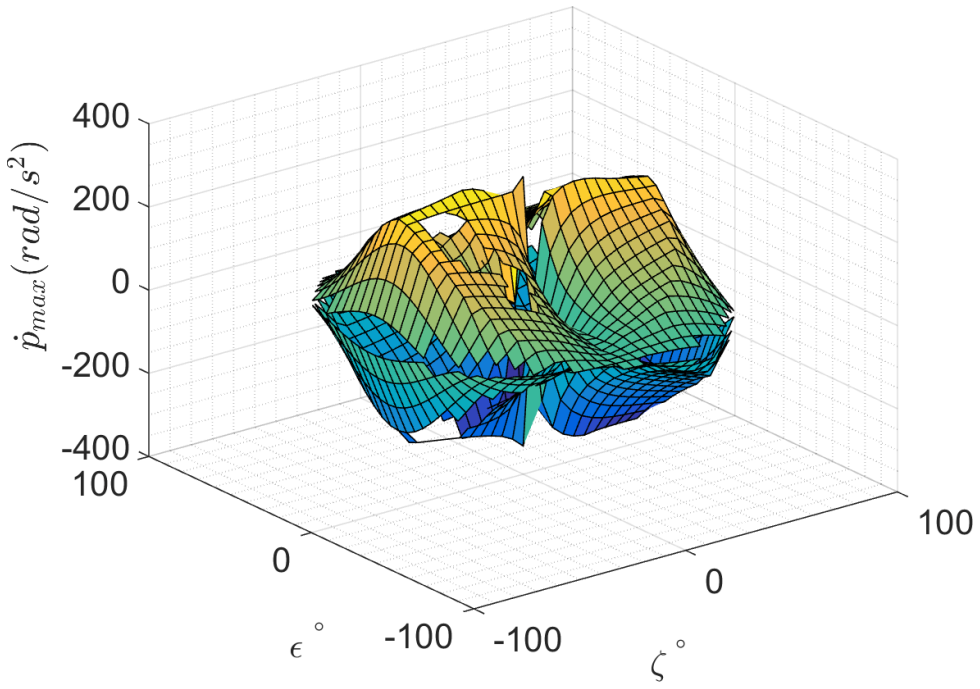

Figure 304: *Y6sC* $\dot{p}$ design space, pure motion enforced, co-rotating, no rotor faults

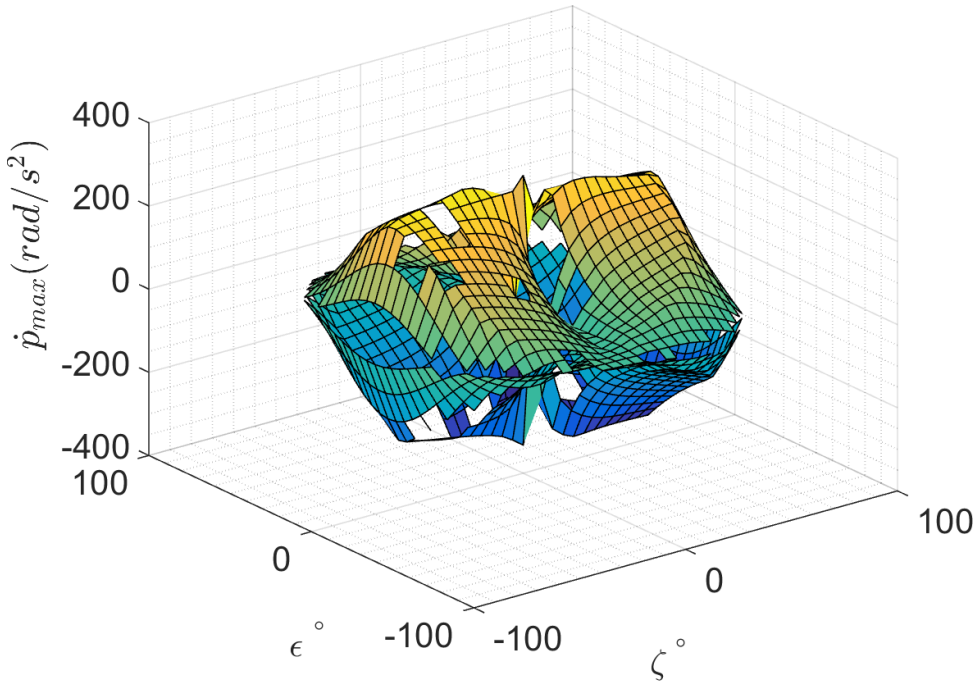

Figure 305: *Y6sC* $\dot{p}$ design space, pure motion enforced, counter-rotating, no rotor faults

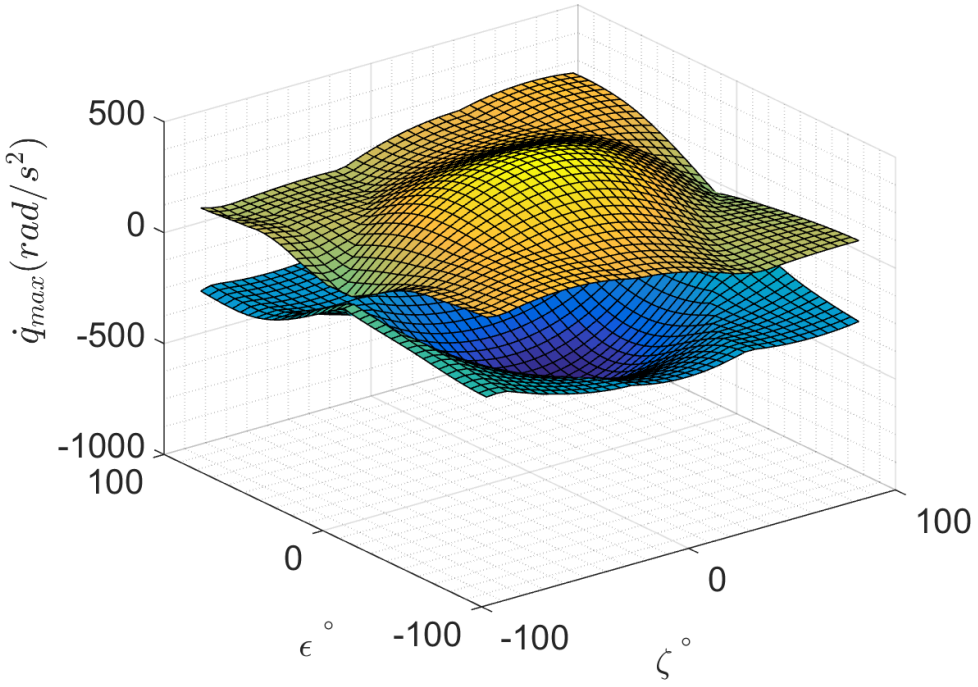

Figure 306: *Y6sC* $\dot{q}$ design space, pure motion not enforced, co-rotating, M1 fault

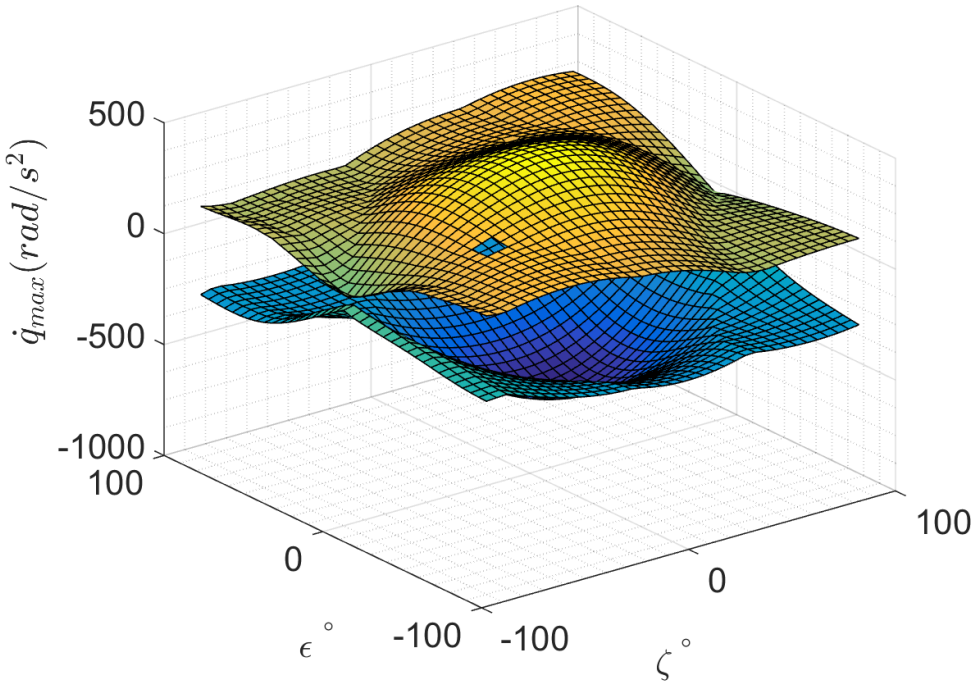

Figure 307: *Y6sC* $\dot{q}$ design space, pure motion not enforced, counter-rotating, M1 fault

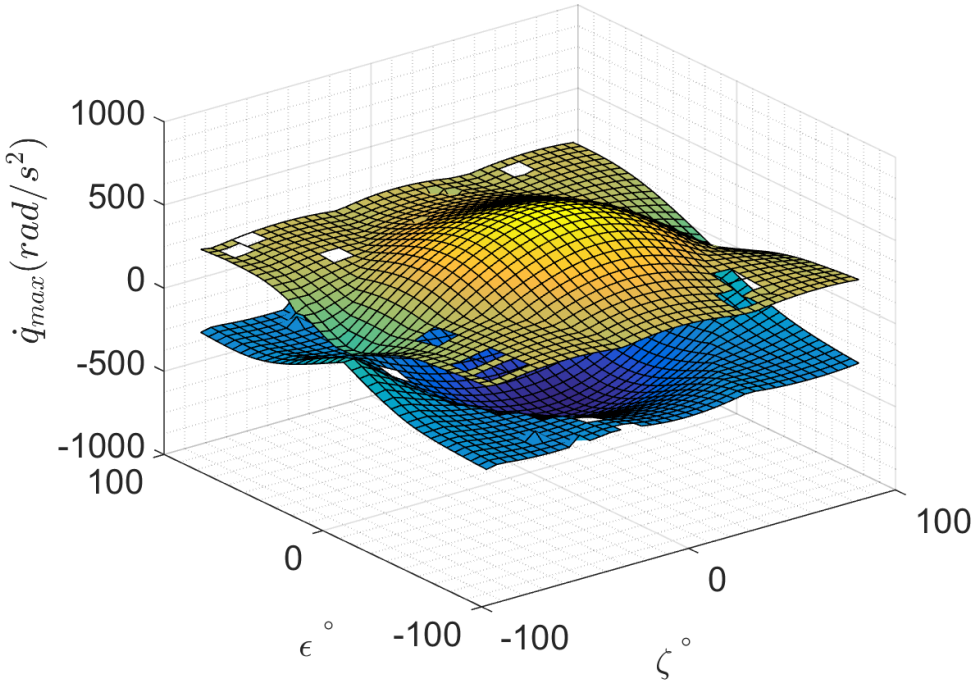

Figure 308: *Y6sC* $\dot{q}$ design space, pure motion not enforced, co-rotating, no rotor faults

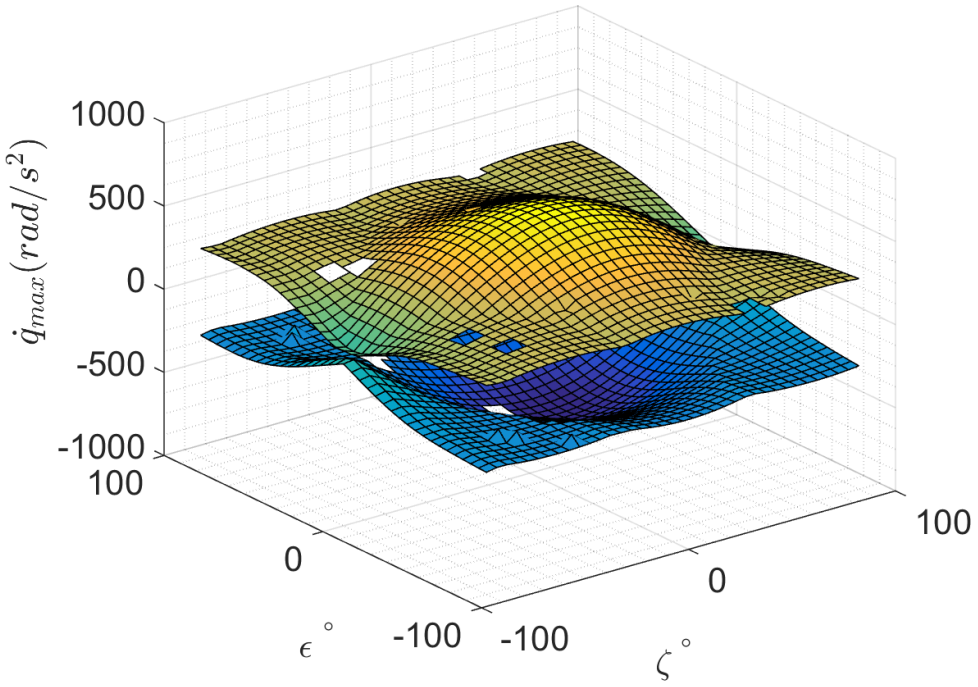

Figure 309: *Y6sC* $\dot{q}$ design space, pure motion not enforced, counter-rotating, no rotor faults

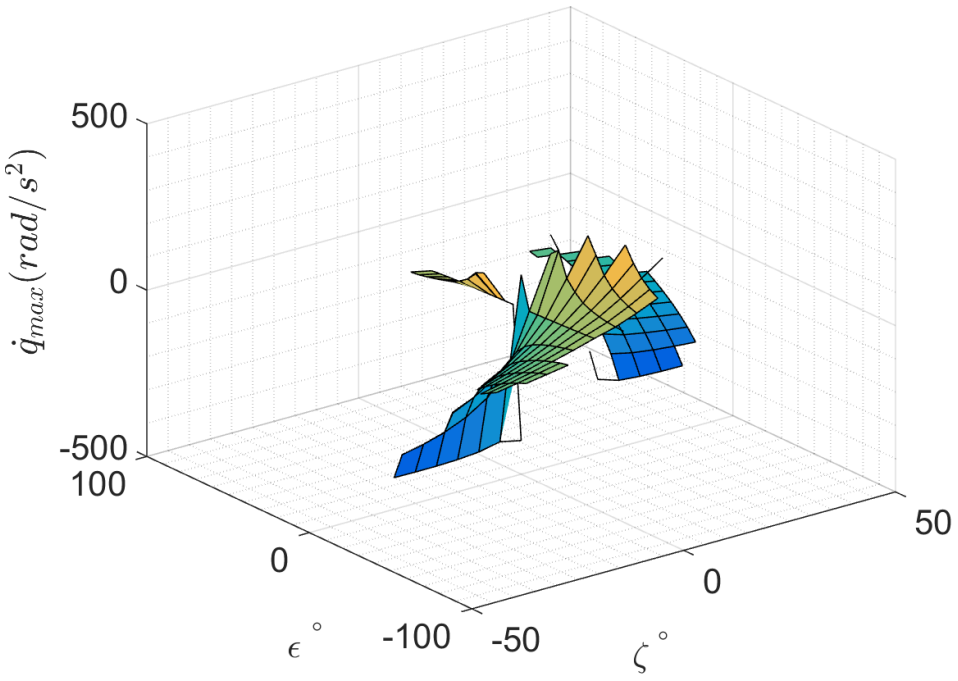

Figure 310: *Y6sC* $\dot{q}$ design space, pure motion enforced, co-rotating, M1 fault

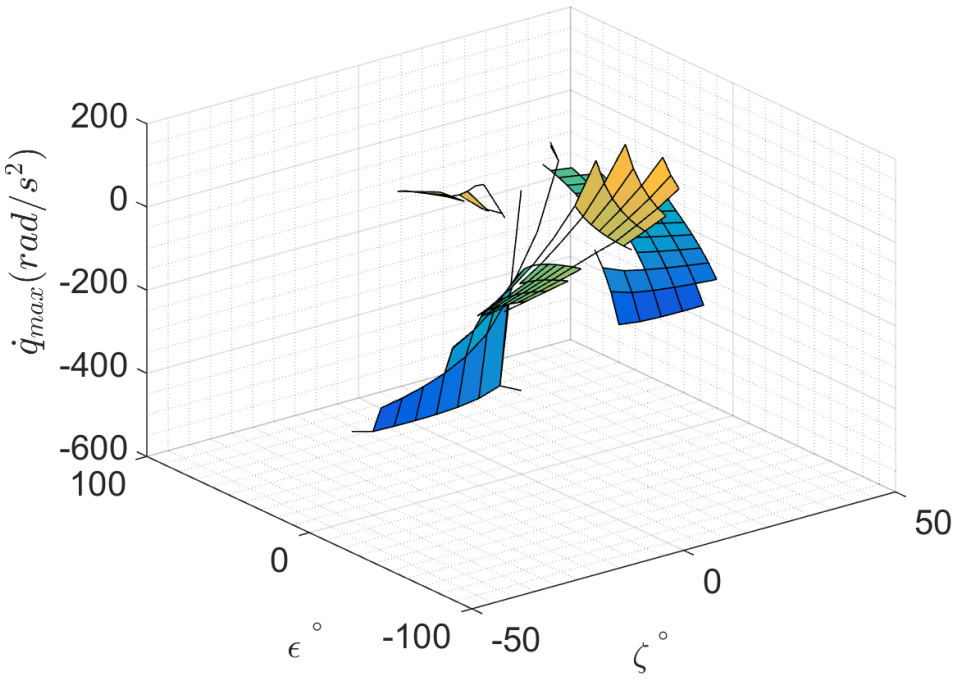

Figure 311: *Y6sC* $\dot{q}$ design space, pure motion enforced, counter-rotating, M1 fault

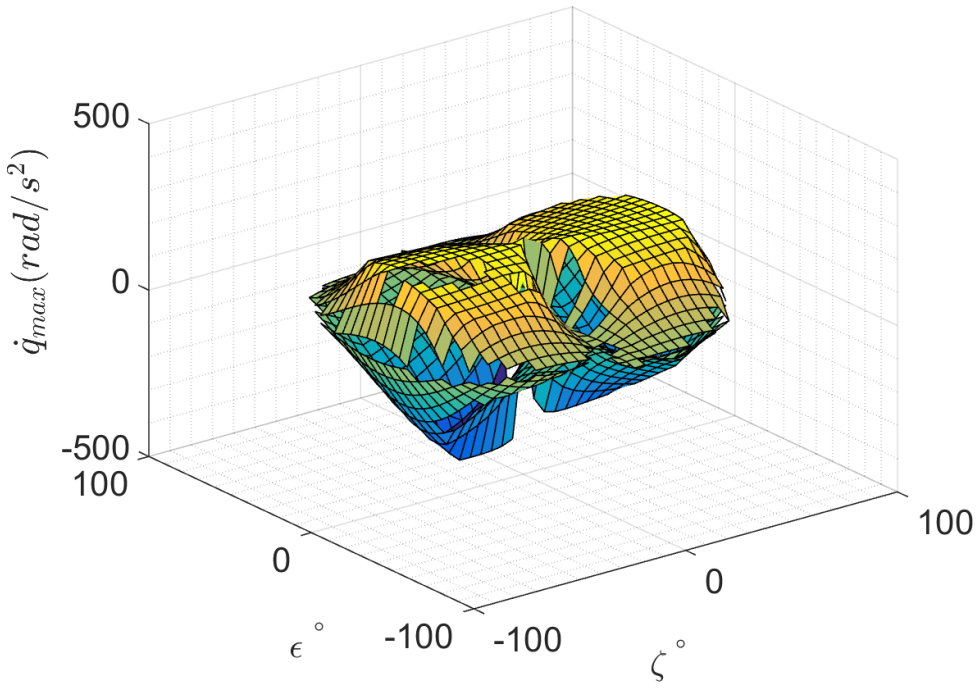

Figure 312: *Y6sC* $\dot{q}$ design space, pure motion enforced, co-rotating, no rotor faults

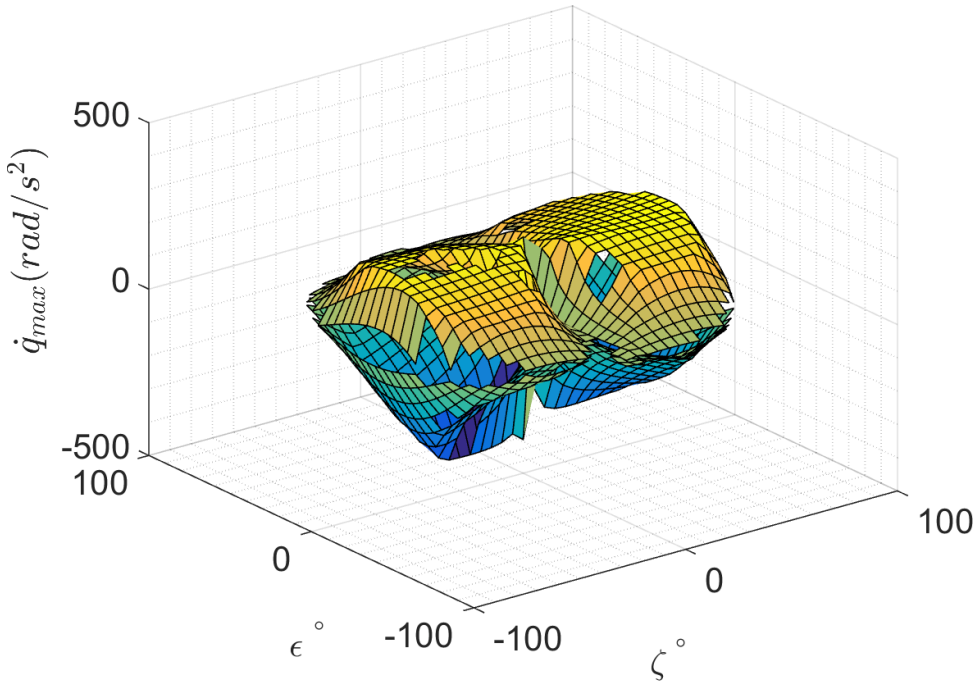

Figure 313: *Y6sC* $\dot{q}$ design space, pure motion enforced, counter-rotating, no rotor faults

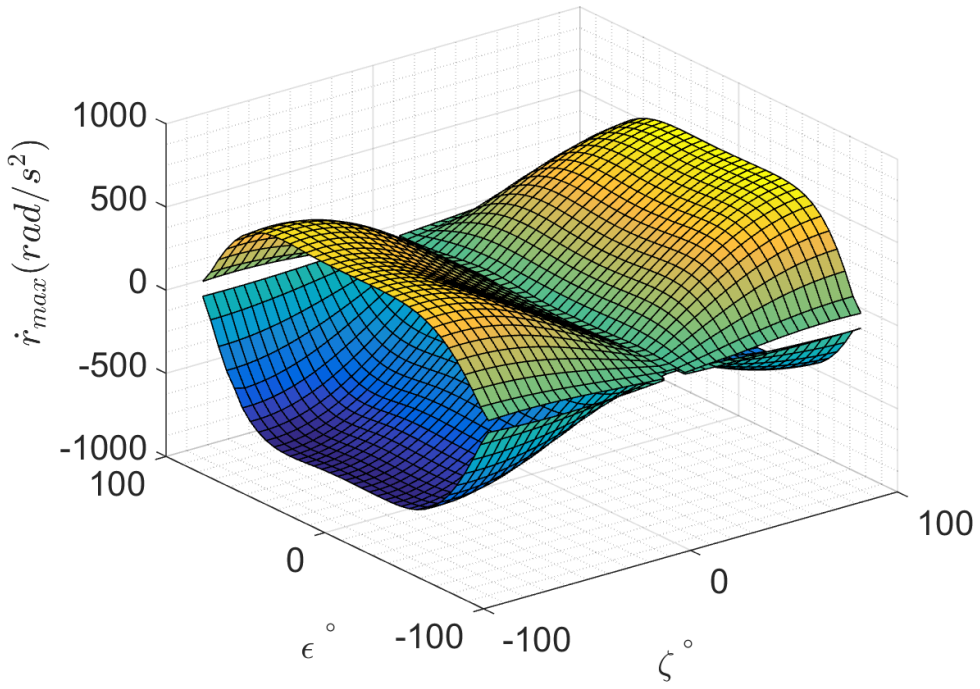

Figure 314: *Y6sC* $\dot{r}$ design space, pure motion not enforced, co-rotating, M1 fault

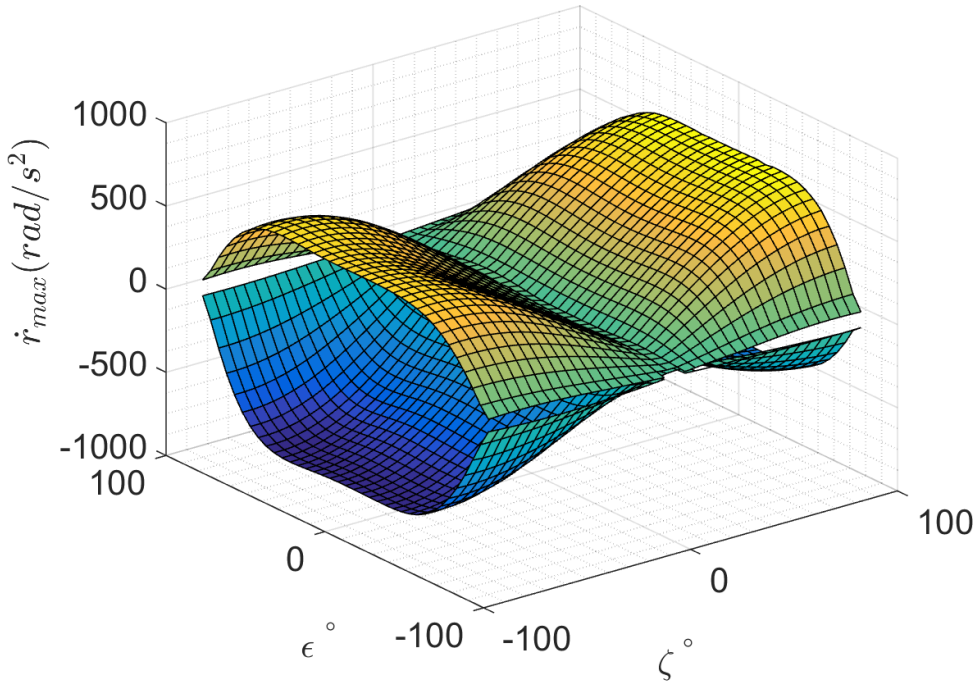

Figure 315: *Y6sC* $\dot{r}$ design space, pure motion not enforced, counter-rotating, M1 fault

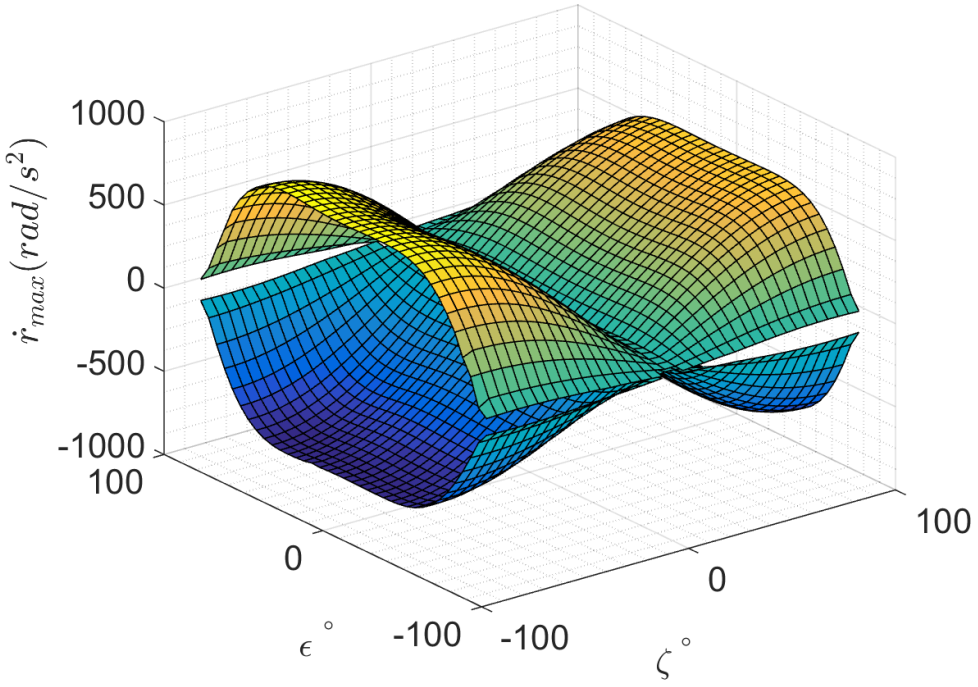

Figure 316: *Y6sC* $\dot{r}$ design space, pure motion not enforced, co-rotating, no rotor faults

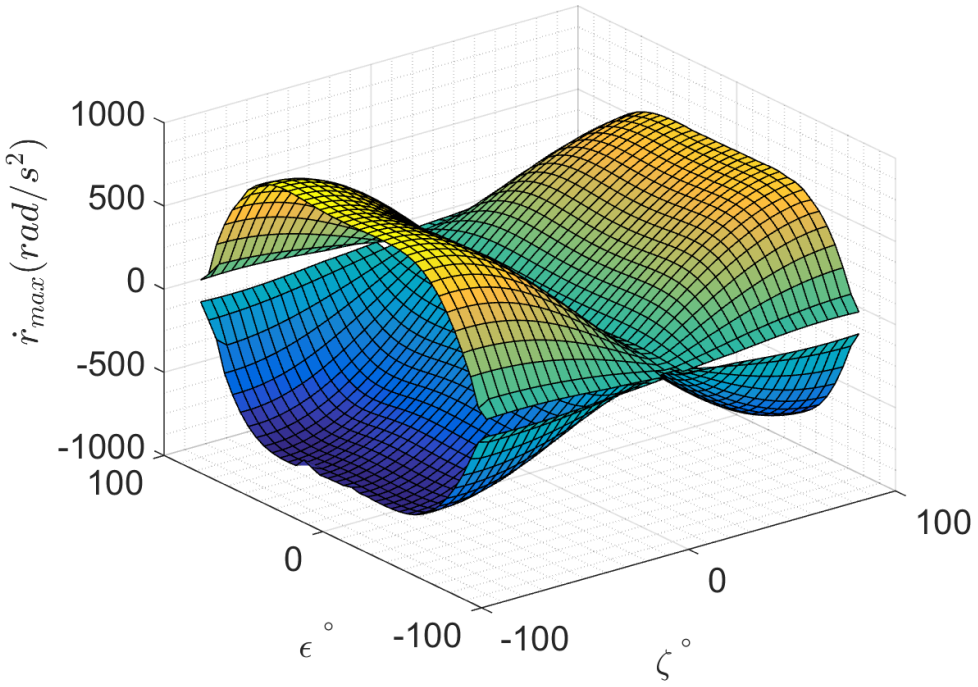

Figure 317: *Y6sC* $\dot{r}$ design space, pure motion not enforced, counter-rotating, no rotor faults

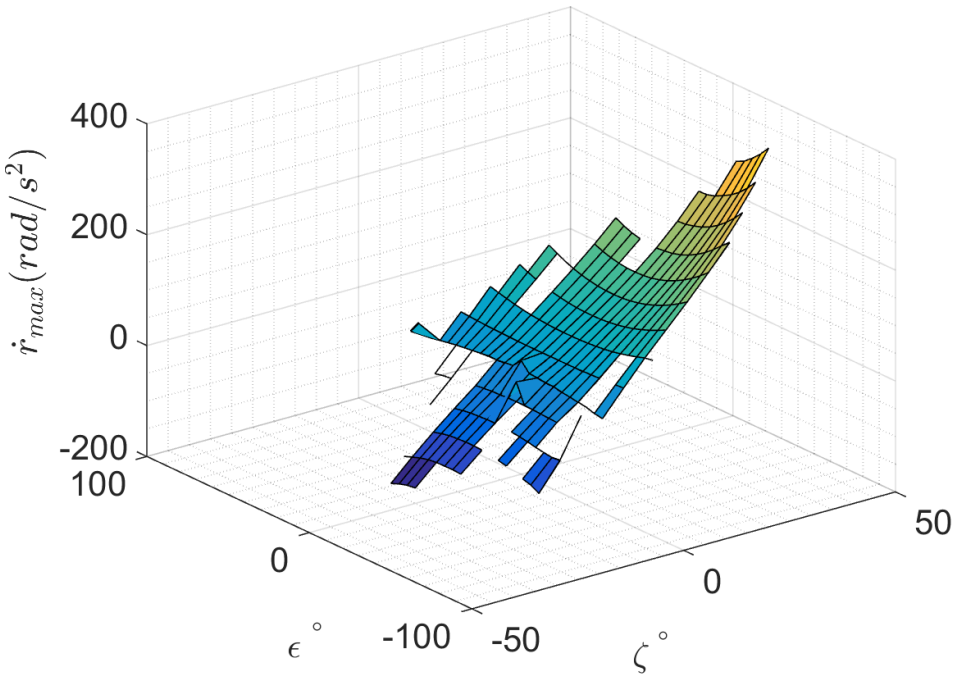

Figure 318: *Y6sC* $\dot{r}$ design space, pure motion enforced, co-rotating, M1 fault

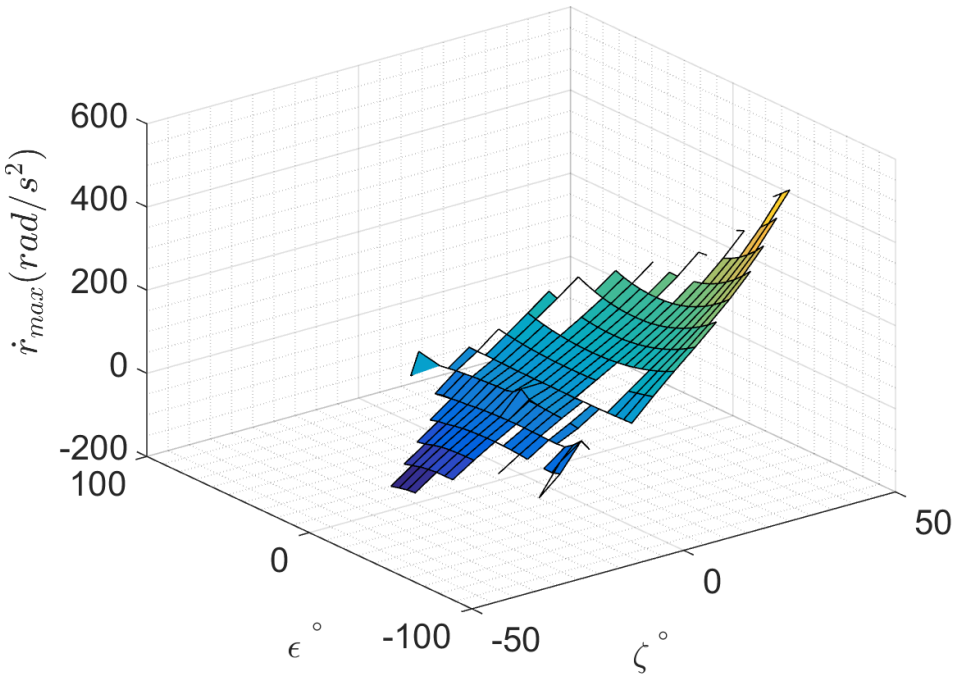

Figure 319: *Y6sC* $\dot{r}$ design space, pure motion enforced, counter-rotating, M1 fault

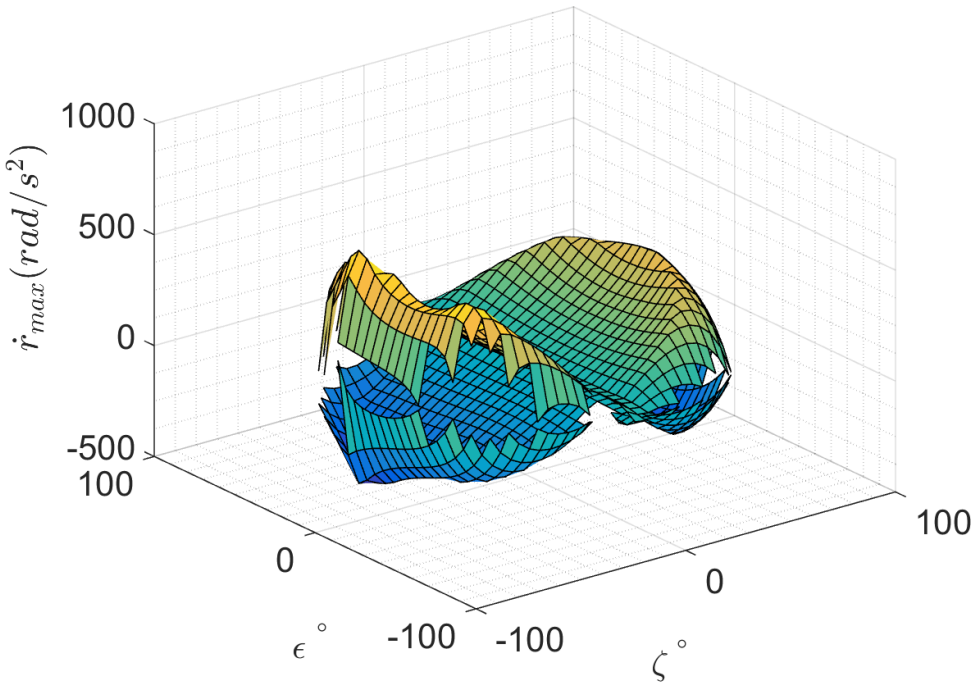

Figure 320: *Y6sC* $\dot{r}$ design space, pure motion enforced, co-rotating, no rotor faults

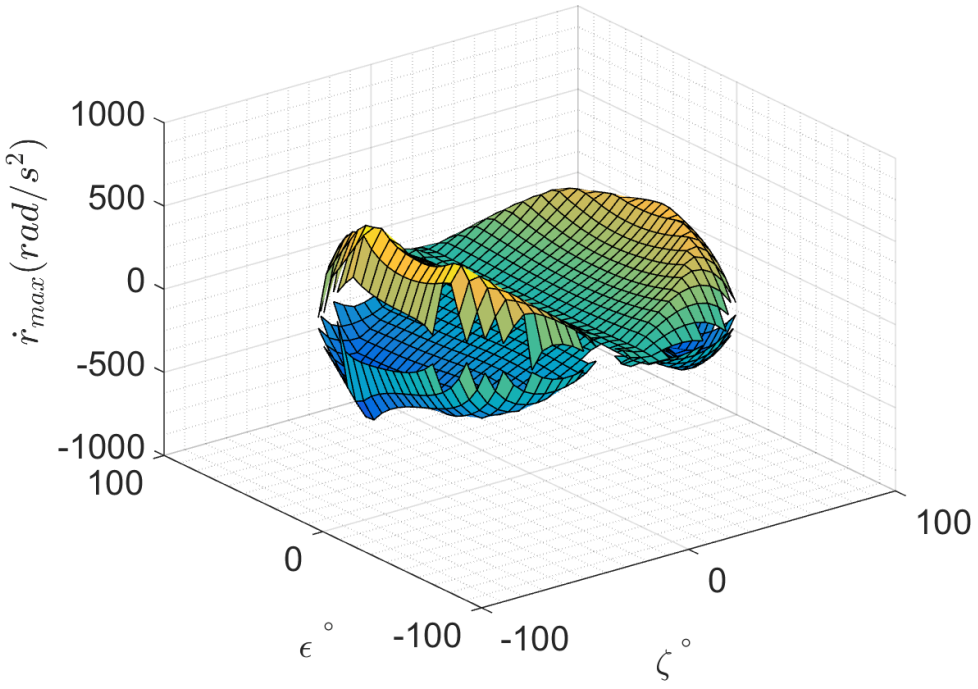

Figure 321: *Y6sC* $\dot{r}$ design space, pure motion enforced, counter-rotating, no rotor faults

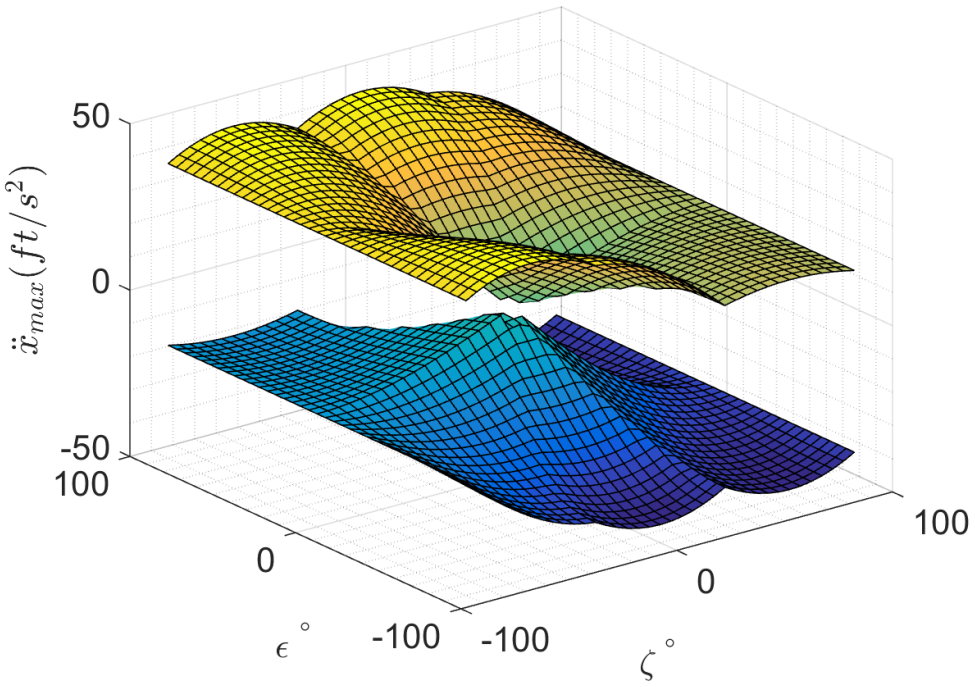

Figure 322: *Y6sC* $\ddot{x}$ design space, pure motion not enforced, co-rotating, M1 fault

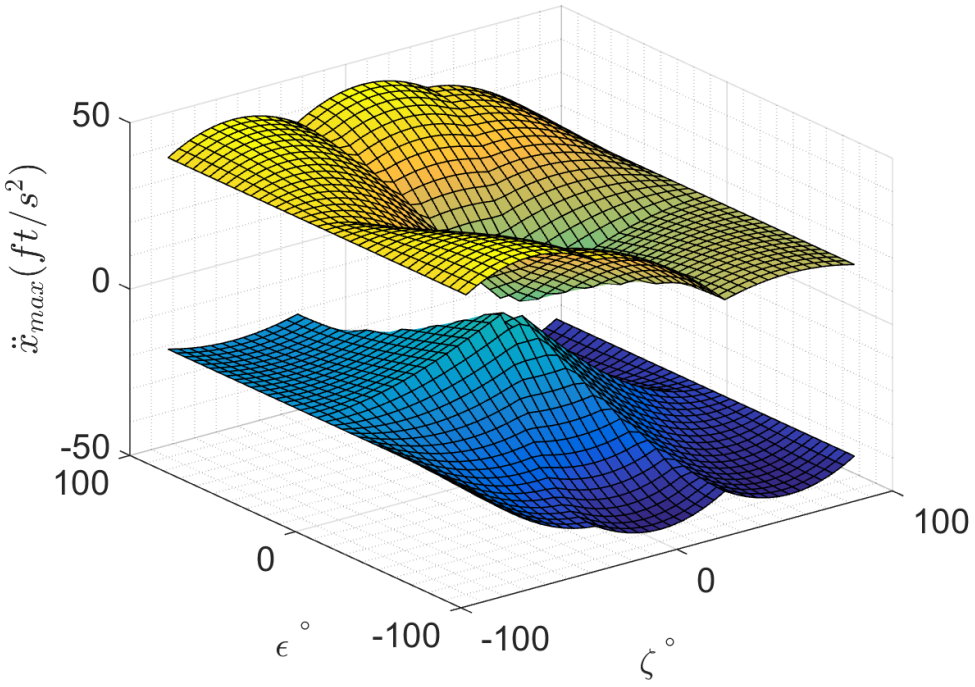

Figure 323: *Y6sC* $\ddot{x}$ design space, pure motion not enforced, counter-rotating, M1 fault

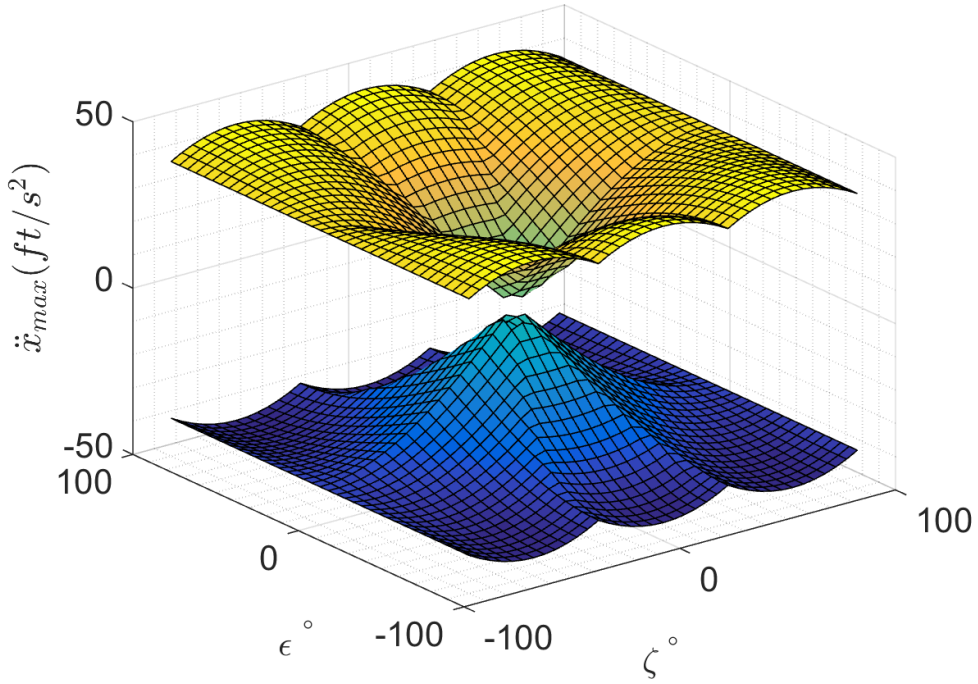

Figure 324: *Y6sC* $\ddot{x}$ design space, pure motion not enforced, co-rotating, no rotor faults

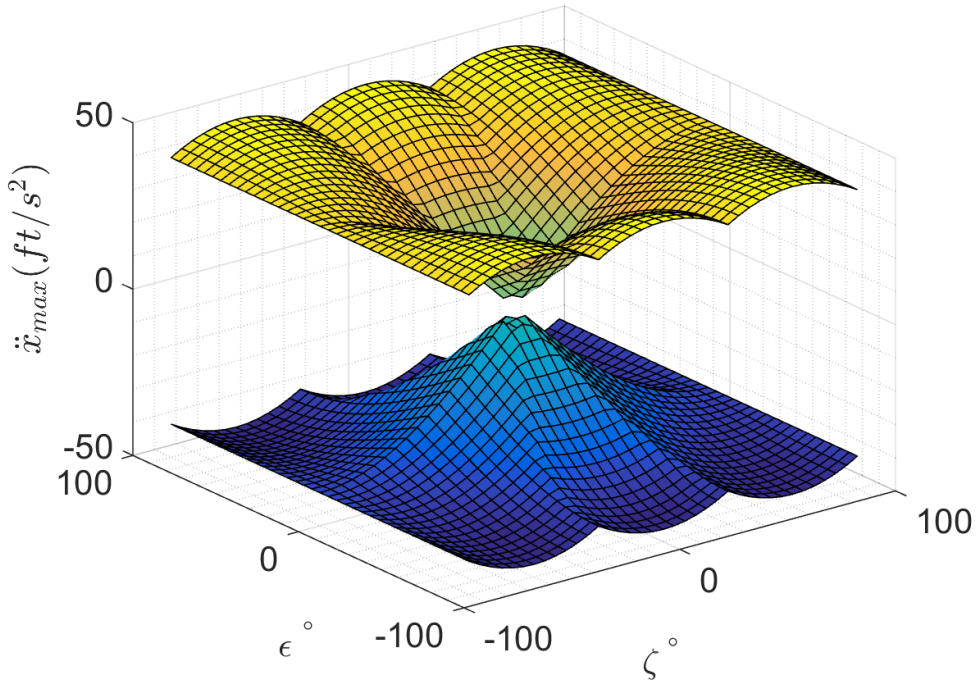

Figure 325: *Y6sC* $\ddot{x}$ design space, pure motion not enforced, counter-rotating, no rotor faults

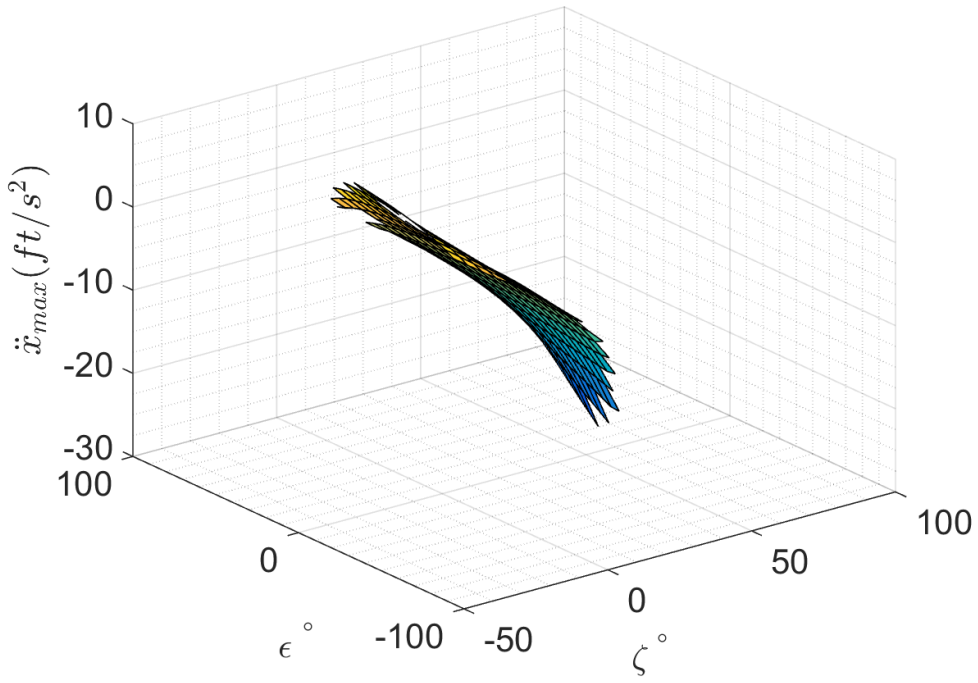

Figure 326: *Y6sC* $\ddot{x}$ design space, pure motion enforced, co-rotating, M1 fault

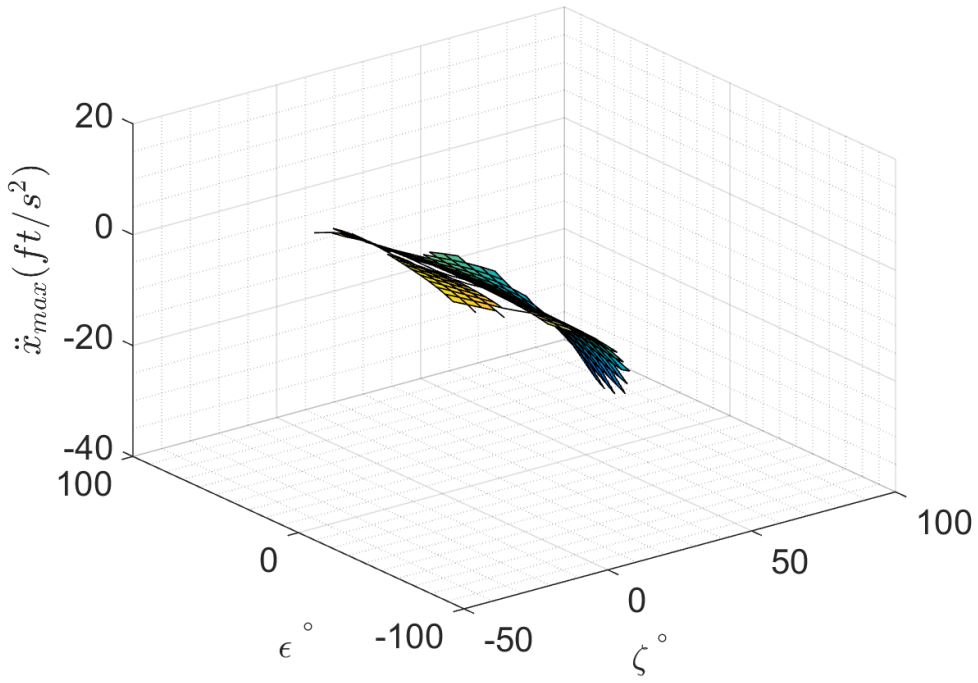

Figure 327: *Y6sC* $\ddot{x}$ design space, pure motion enforced, counter-rotating, M1 fault

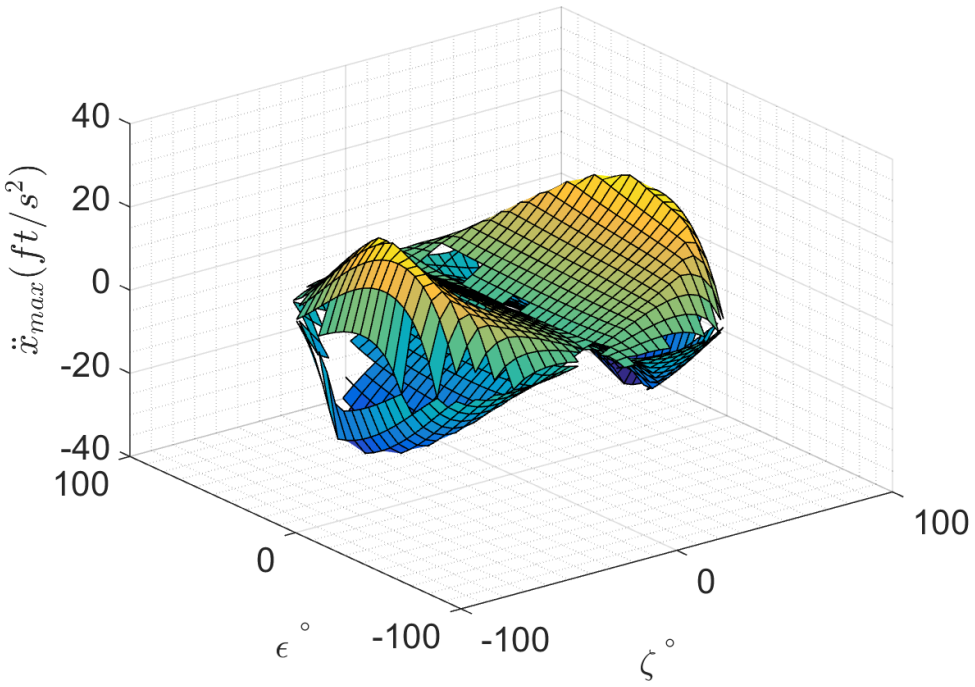

Figure 328: *Y6sC* $\ddot{x}$ design space, pure motion enforced, co-rotating, no rotor faults

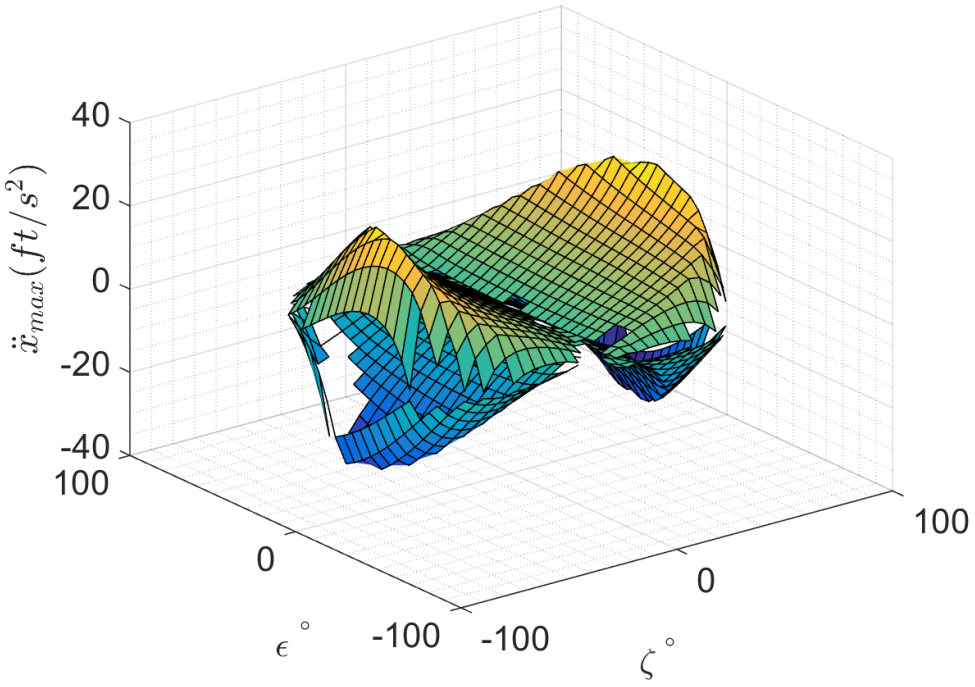

Figure 329: *Y6sC* $\ddot{x}$ design space, pure motion enforced, counter-rotating, no rotor faults

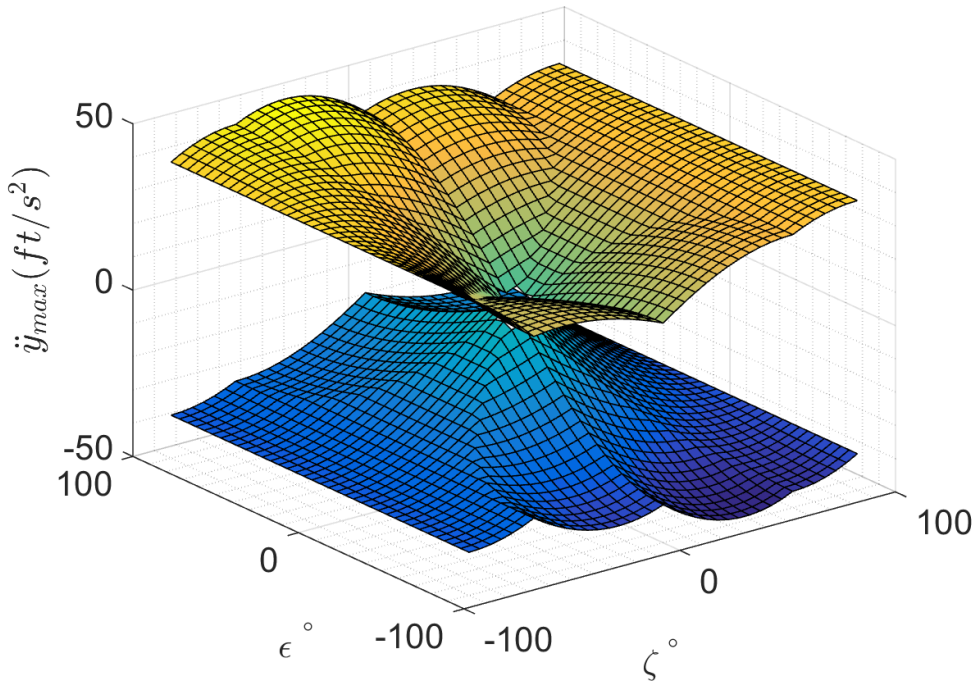

Figure 330: *Y6sC* $\ddot{y}$ design space, pure motion not enforced, co-rotating, M1 fault

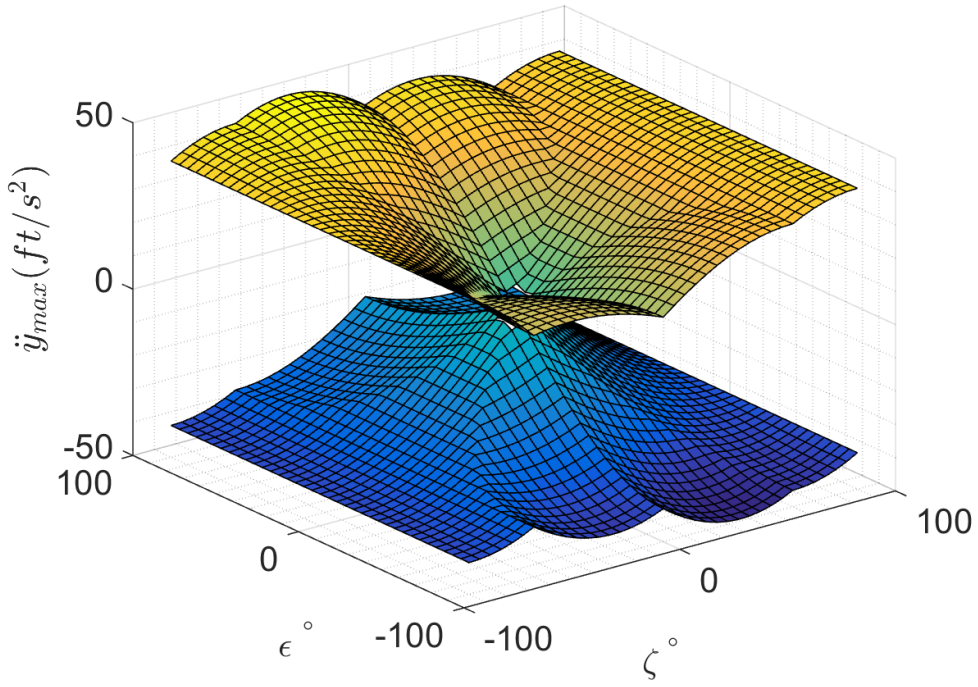

Figure 331: *Y6sC* $\ddot{y}$ design space, pure motion not enforced, counter-rotating, M1 fault

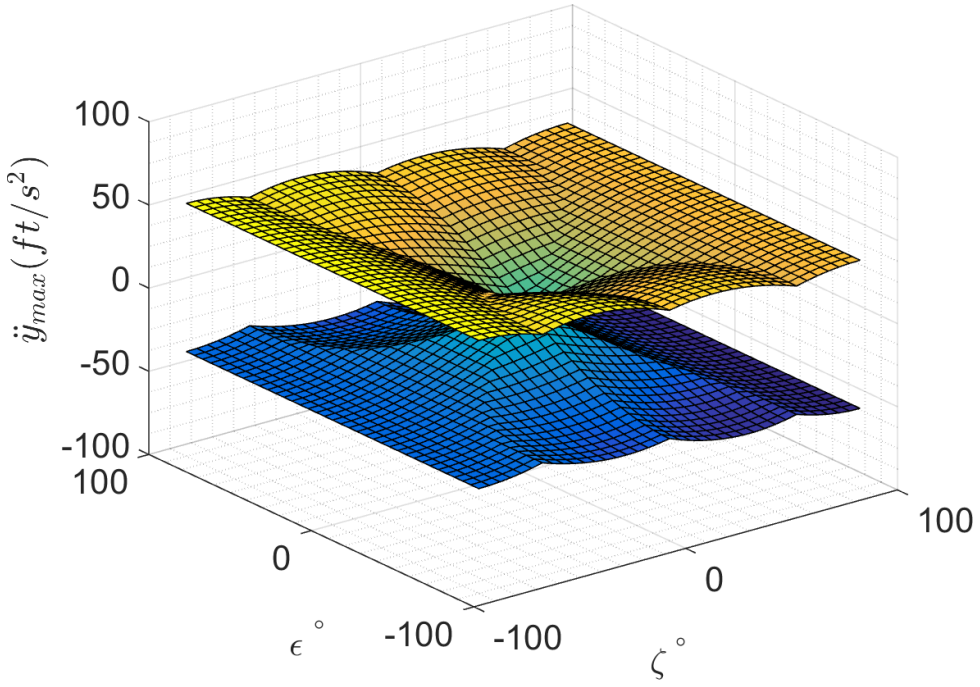

Figure 332: *Y6sC* $\ddot{y}$ design space, pure motion not enforced, co-rotating, no rotor faults

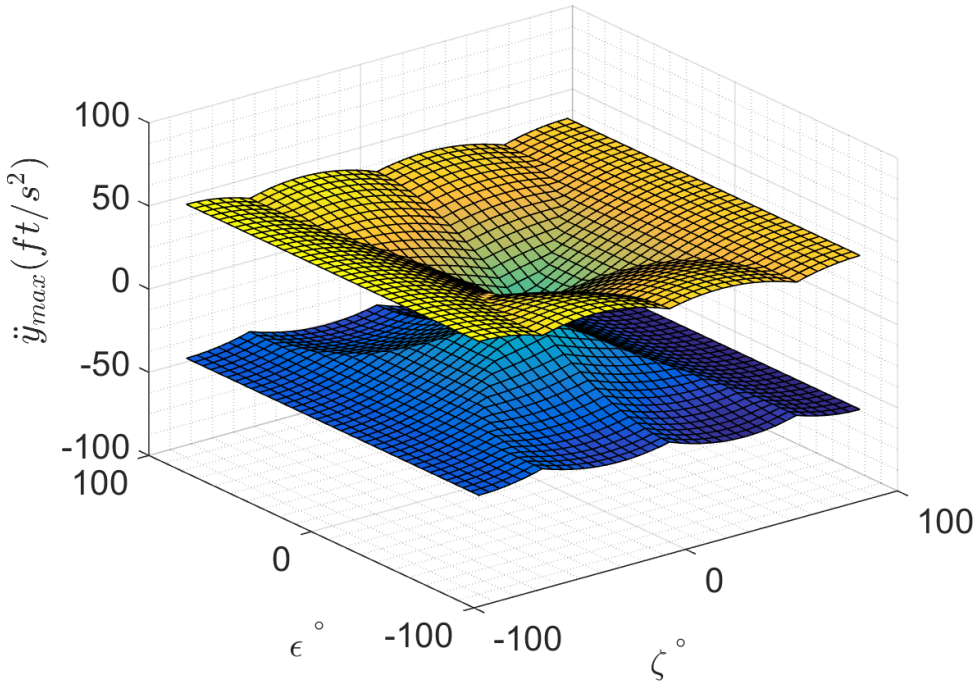

Figure 333: *Y6sC* $\ddot{y}$ design space, pure motion not enforced, counter-rotating, no rotor faults

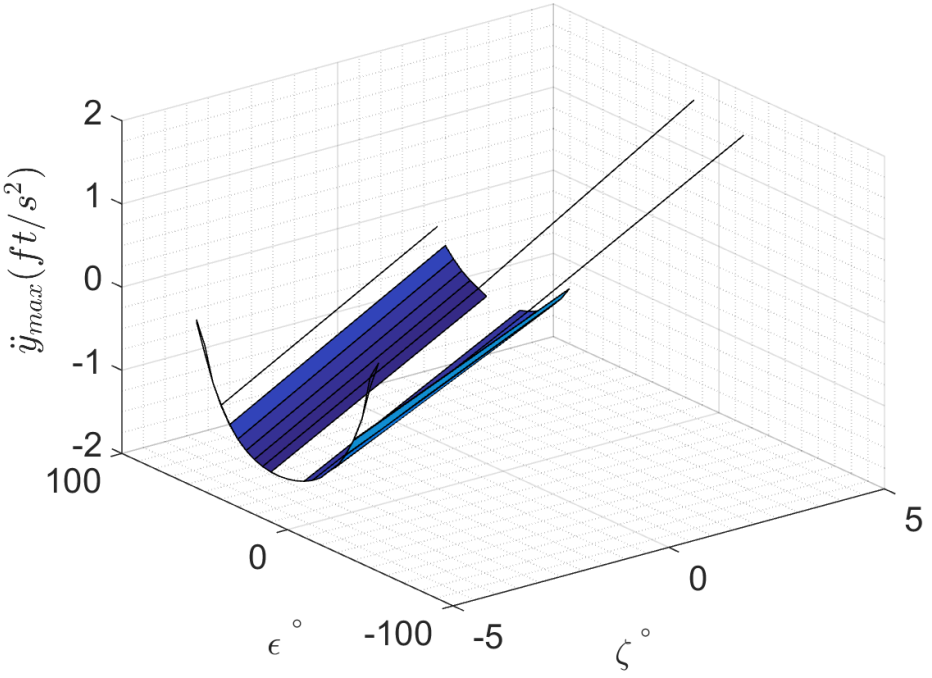

Figure 334: *Y6sC* $\ddot{y}$ design space, pure motion enforced, co-rotating, M1 fault

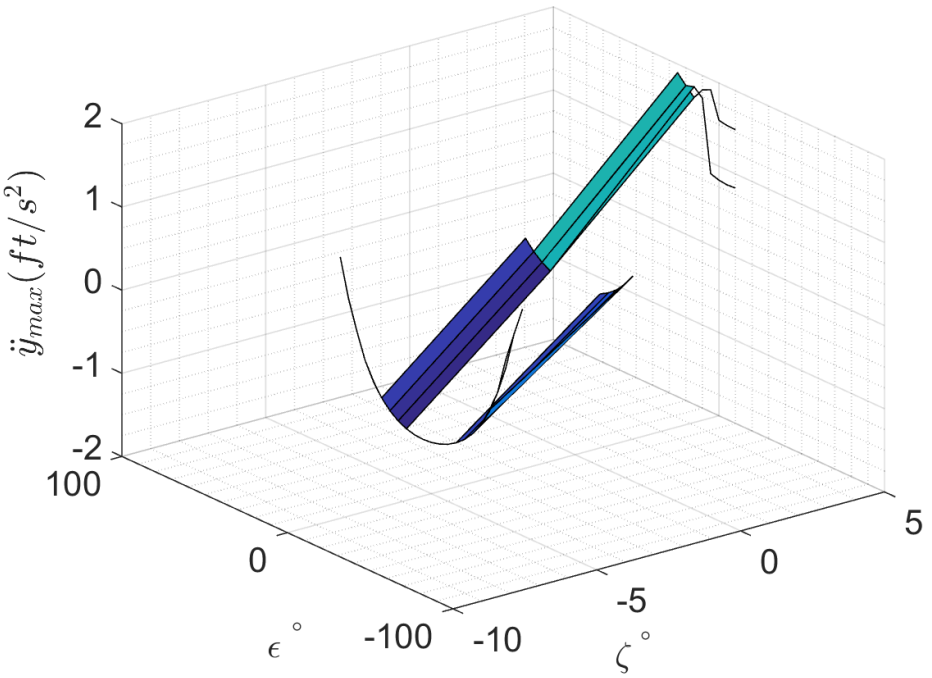

Figure 335: *Y6sC* $\ddot{y}$ design space, pure motion enforced, counter-rotating, M1 fault

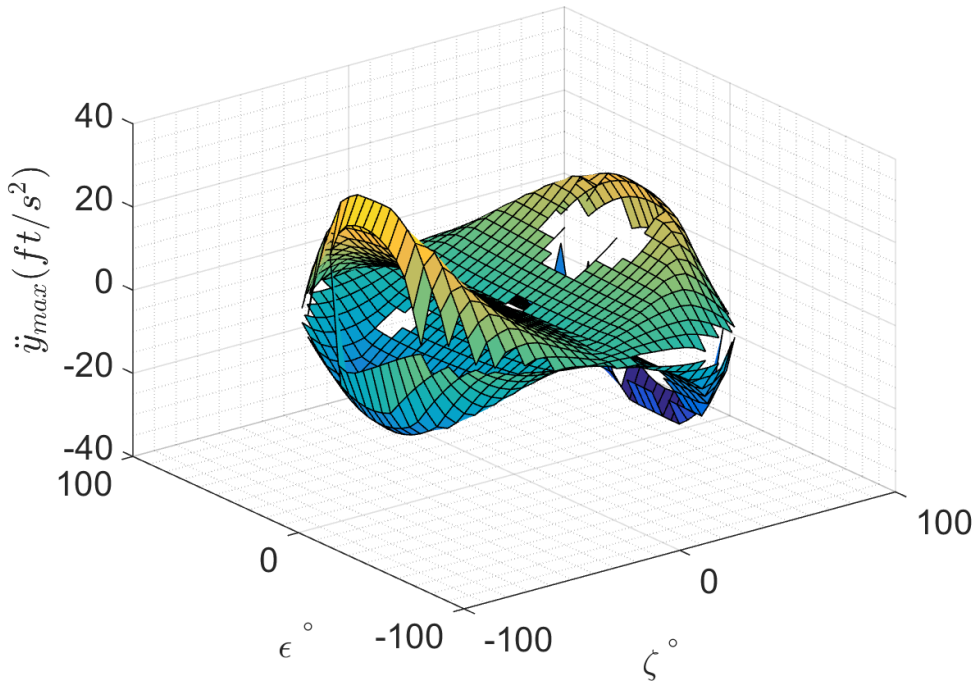

Figure 336: *Y6sC* $\ddot{y}$ design space, pure motion enforced, co-rotating, no rotor faults

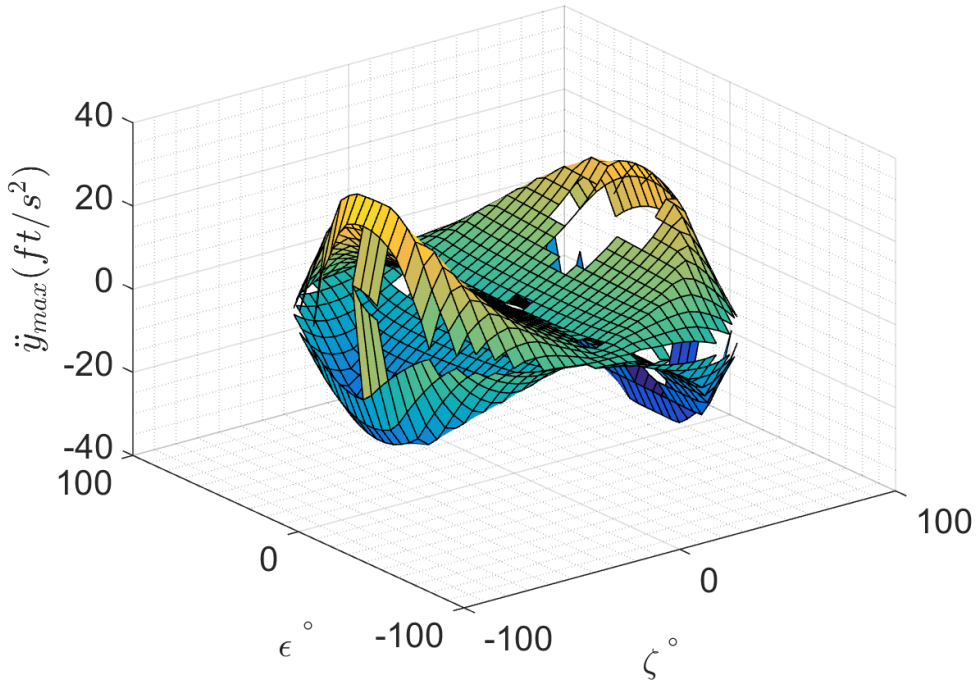

Figure 337: *Y6sC* $\ddot{y}$ design space, pure motion enforced, counter-rotating, no rotor faults

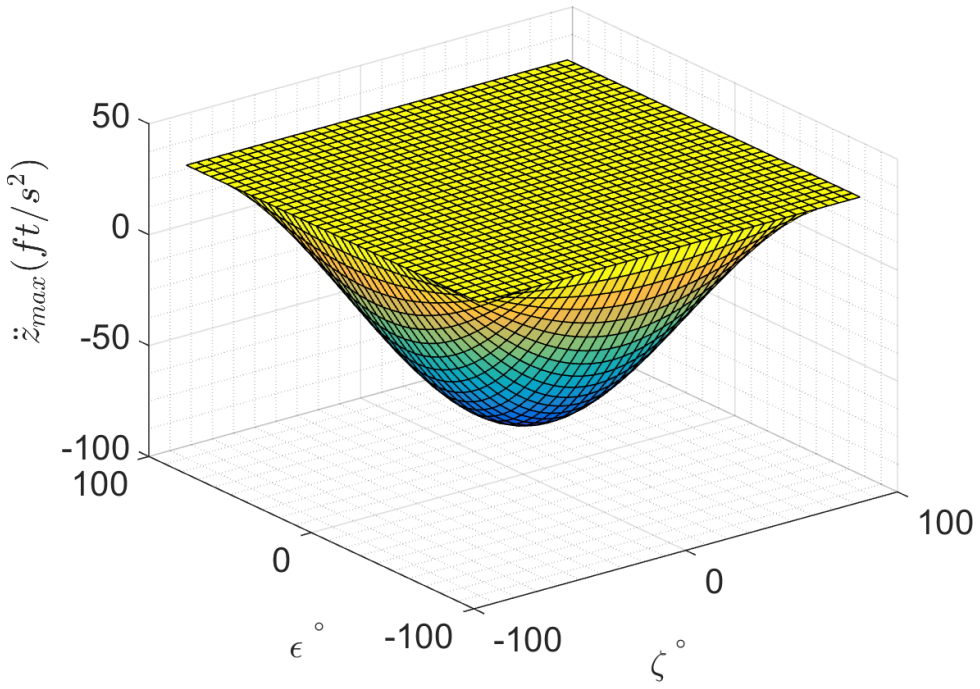

Figure 338: *Y6sC* $\ddot{z}$ design space, pure motion not enforced, co-rotating, M1 fault

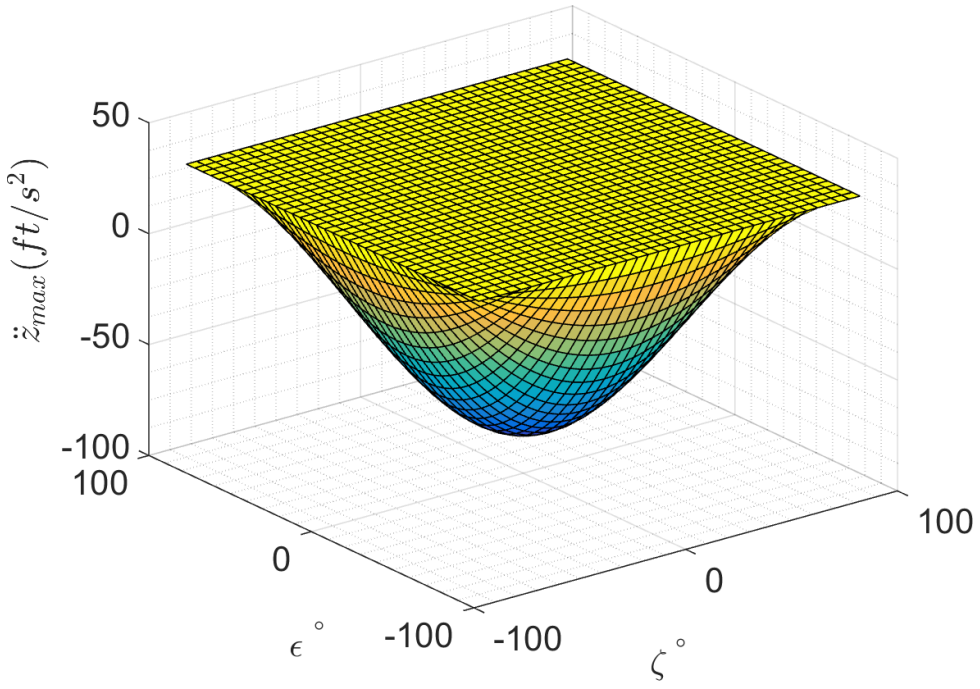

Figure 339: *Y6sC* $\ddot{z}$ design space, pure motion not enforced, counter-rotating, M1 fault

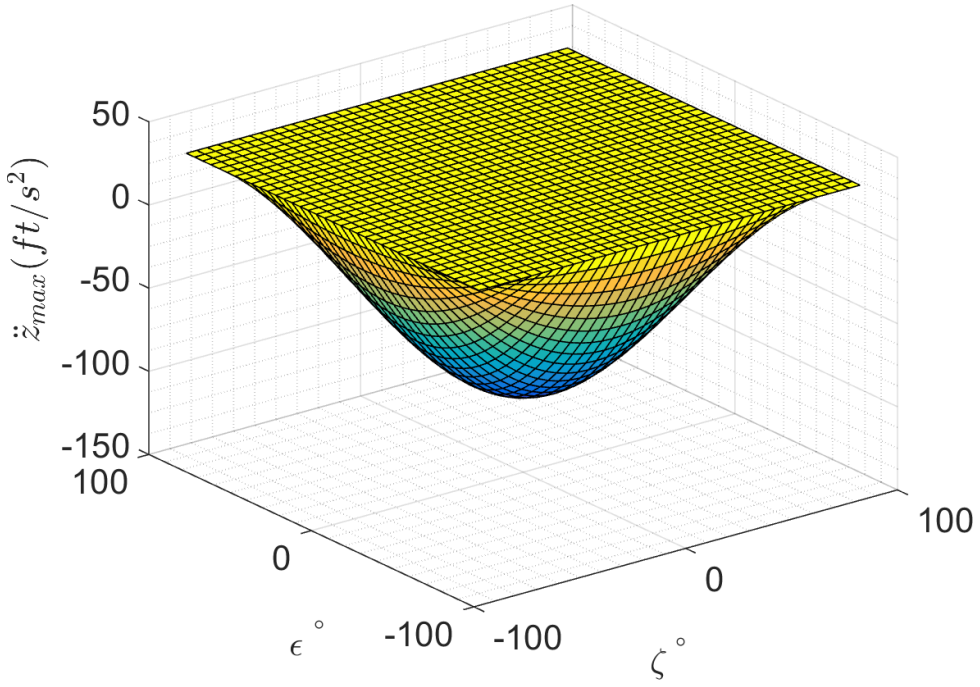

Figure 340: *Y6sC* $\ddot{z}$ design space, pure motion not enforced, co-rotating, no rotor faults

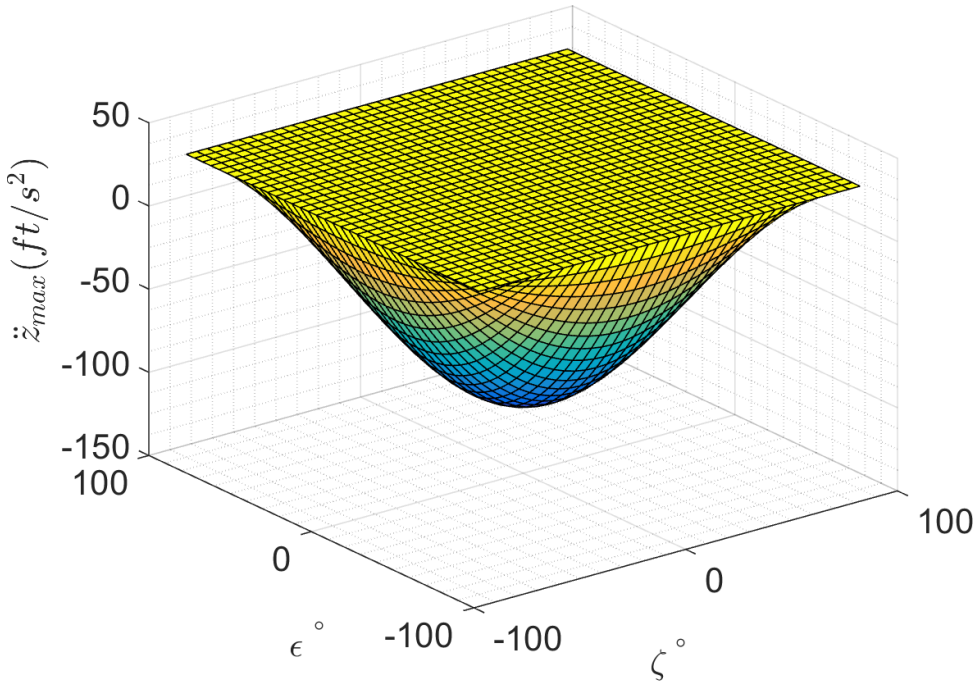

Figure 341: *Y6sC* $\ddot{z}$ design space, pure motion not enforced, counter-rotating, no rotor faults

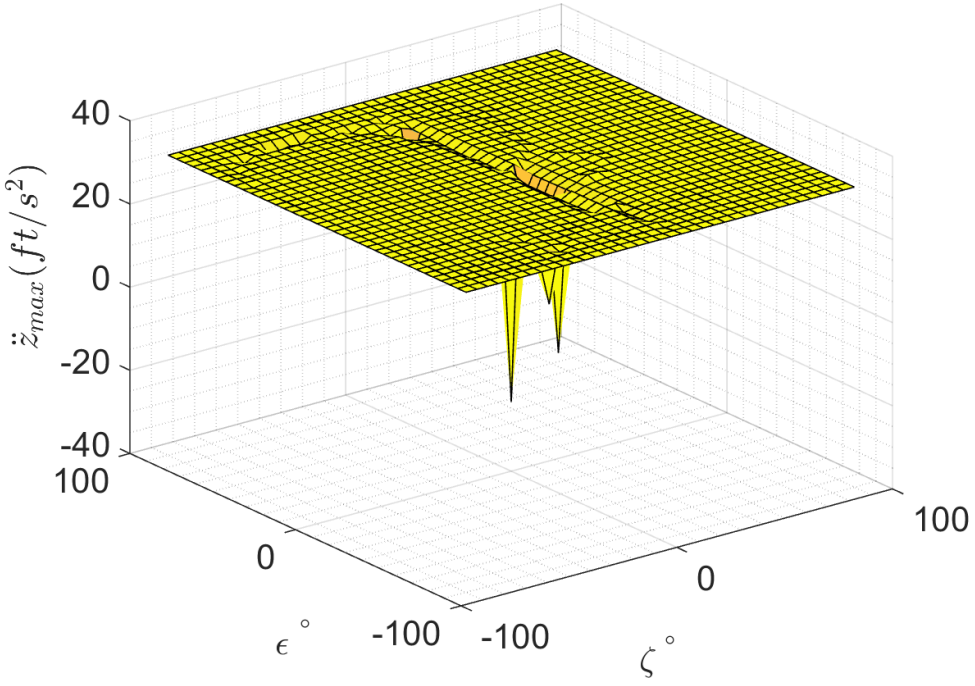

Figure 342: *Y6sC* $\ddot{z}$ design space, pure motion enforced, co-rotating, M1 fault

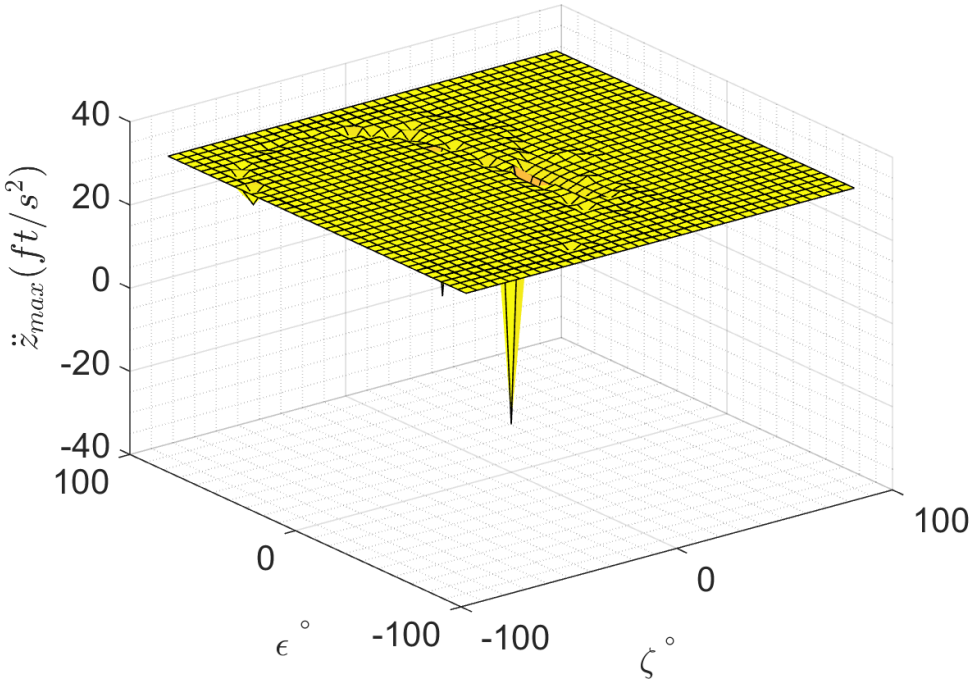

Figure 343: *Y6sC* $\ddot{z}$ design space, pure motion enforced, counter-rotating, M1 fault

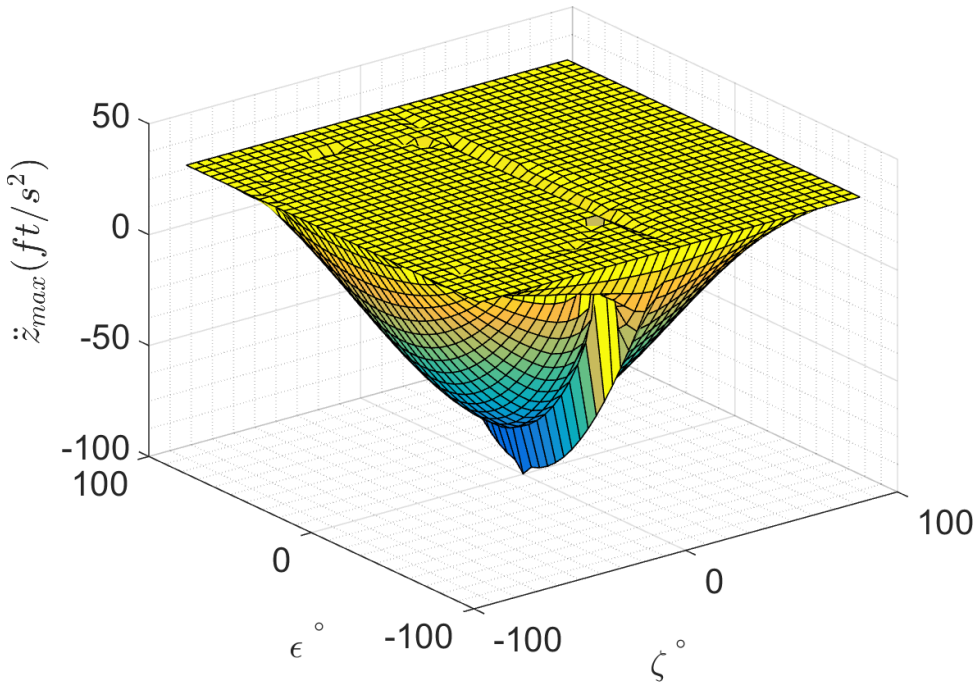

Figure 344: *Y6sC* $\ddot{z}$ design space, pure motion enforced, co-rotating, no rotor faults

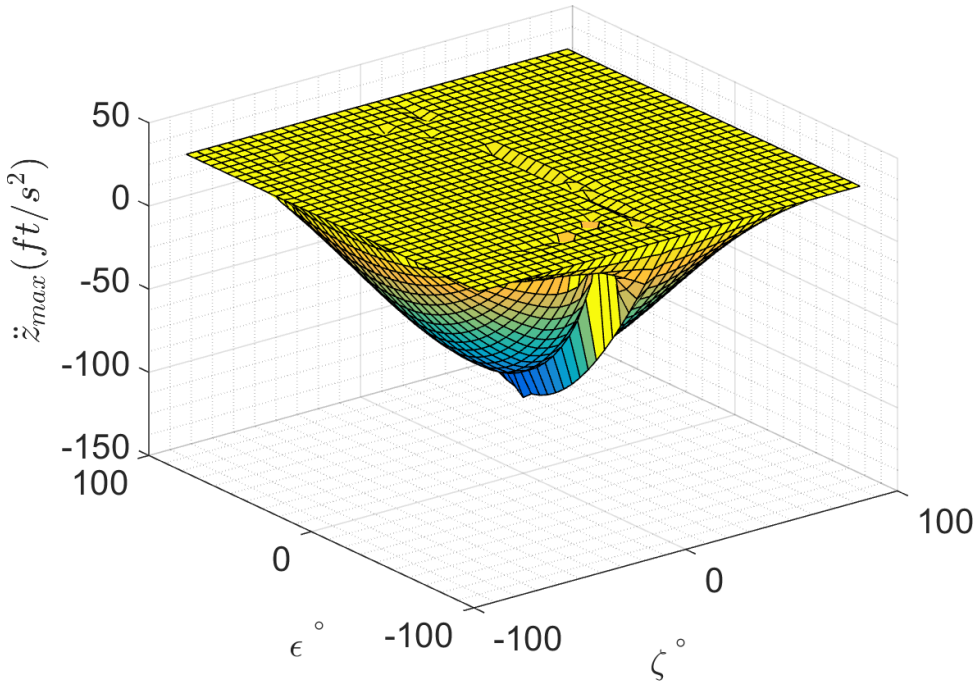

Figure 345: *Y6sC* $\ddot{z}$ design space, pure motion enforced, counter-rotating, no rotor faults

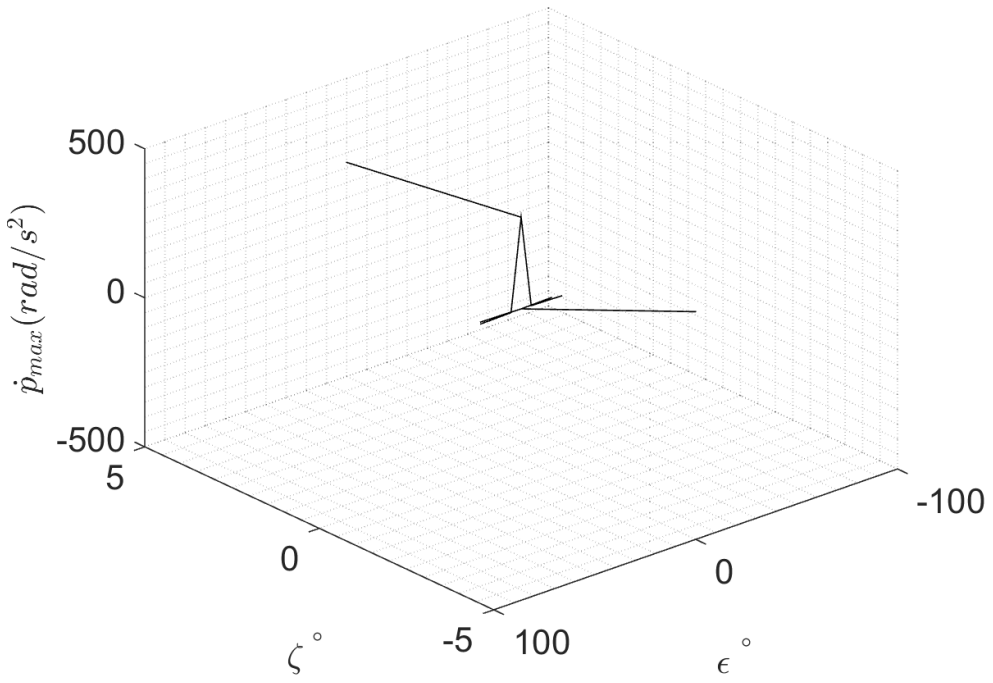

Figure 346: Composite LUT for *X6* failures of rotors *M1* through *M3*, pure motion enforced

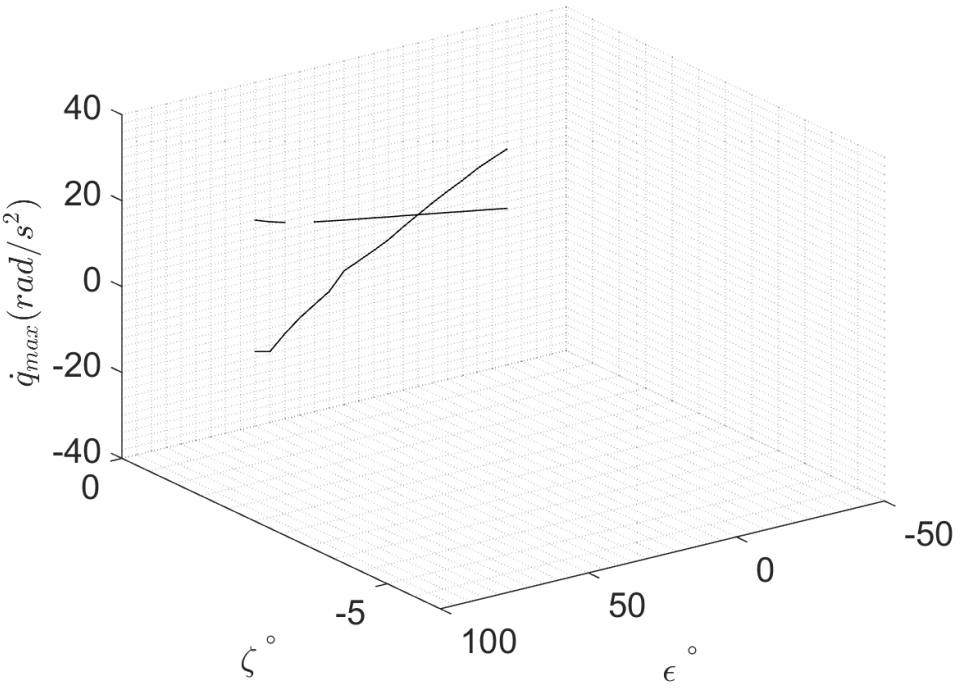

Figure 347: Composite LUT for *X6* failures of rotors *M1* through *M3* , pure motion enforced

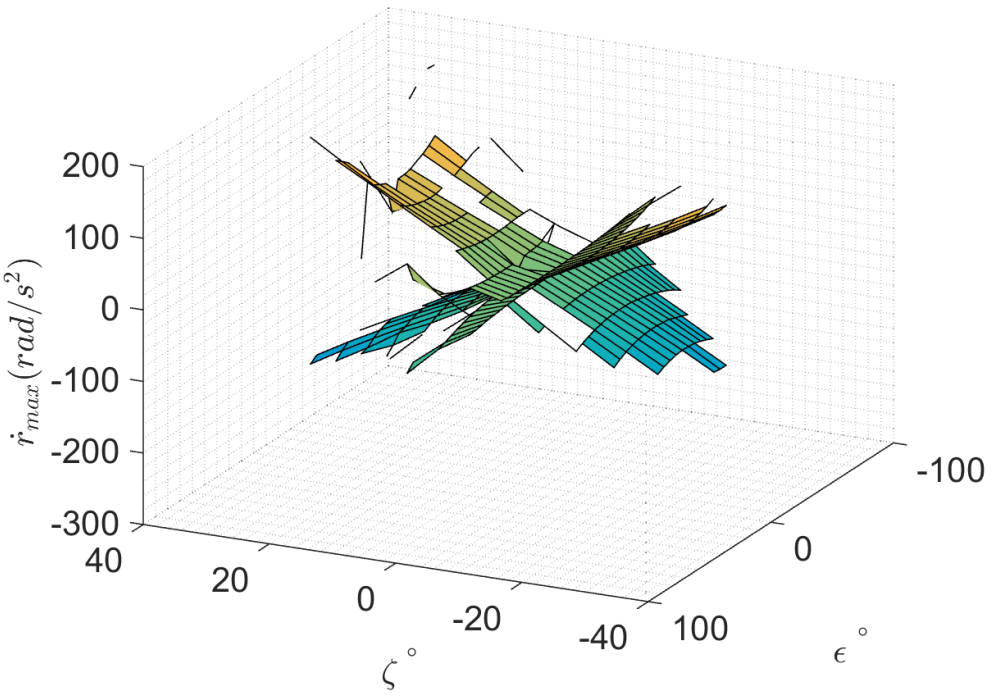

Figure 348: Composite LUT for *X6* failures of rotors *M1* through *M3* , pure motion enforced

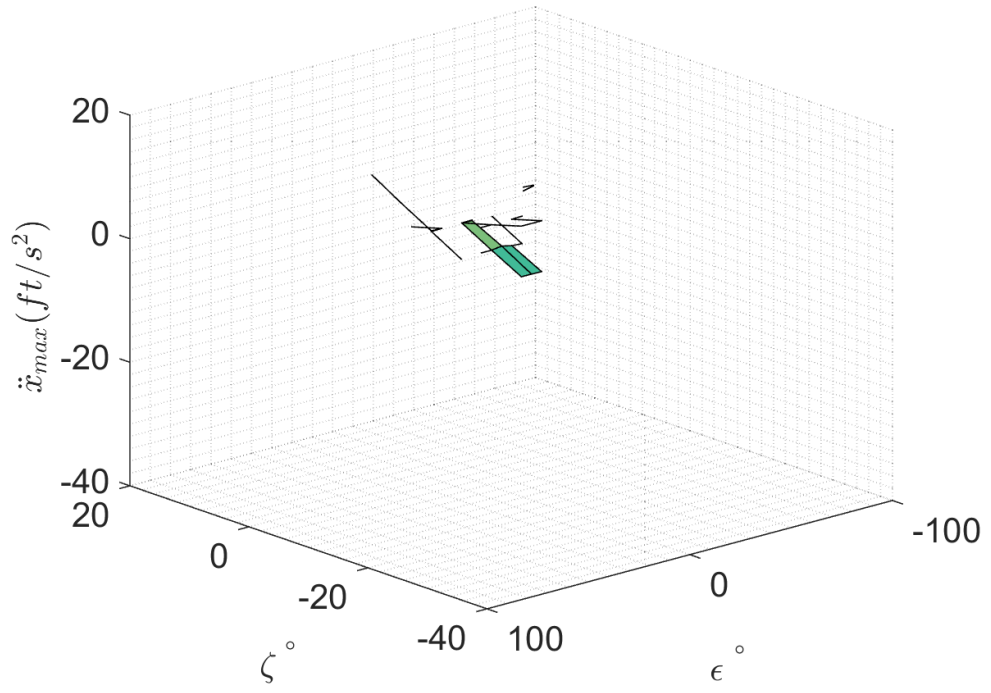

Figure 349: Composite LUT for *X6* failures of rotors *M1* through *M3* , pure motion enforced

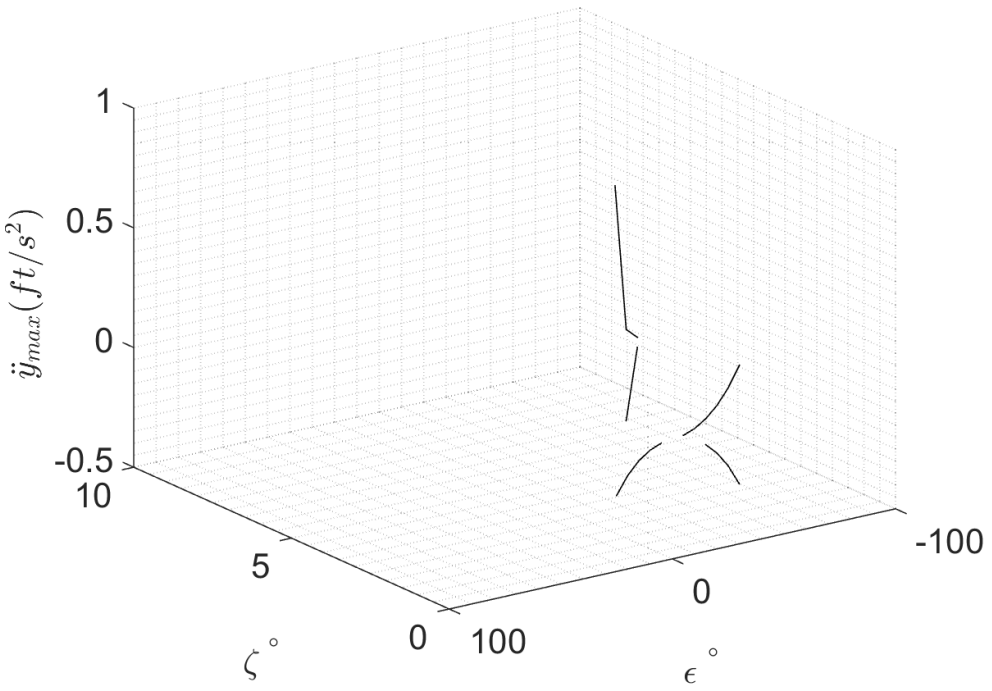

Figure 350: Composite LUT for *X6* failures of rotors *M1* through *M3* , pure motion enforced

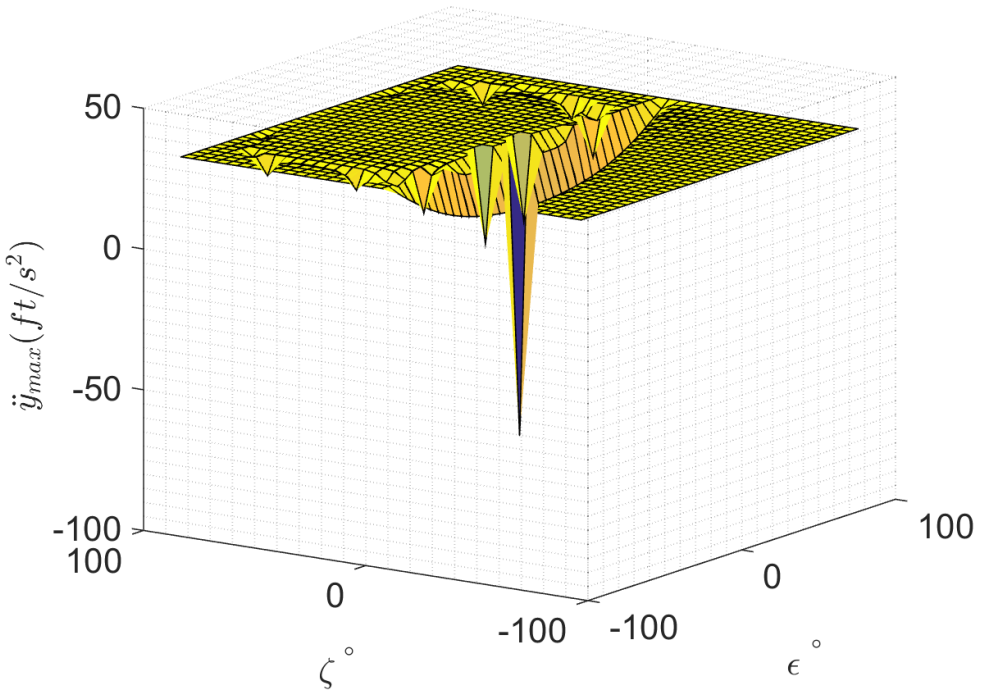

Figure 351: Composite LUT for *X6* failures of rotors *M1* through *M3* , pure motion enforced

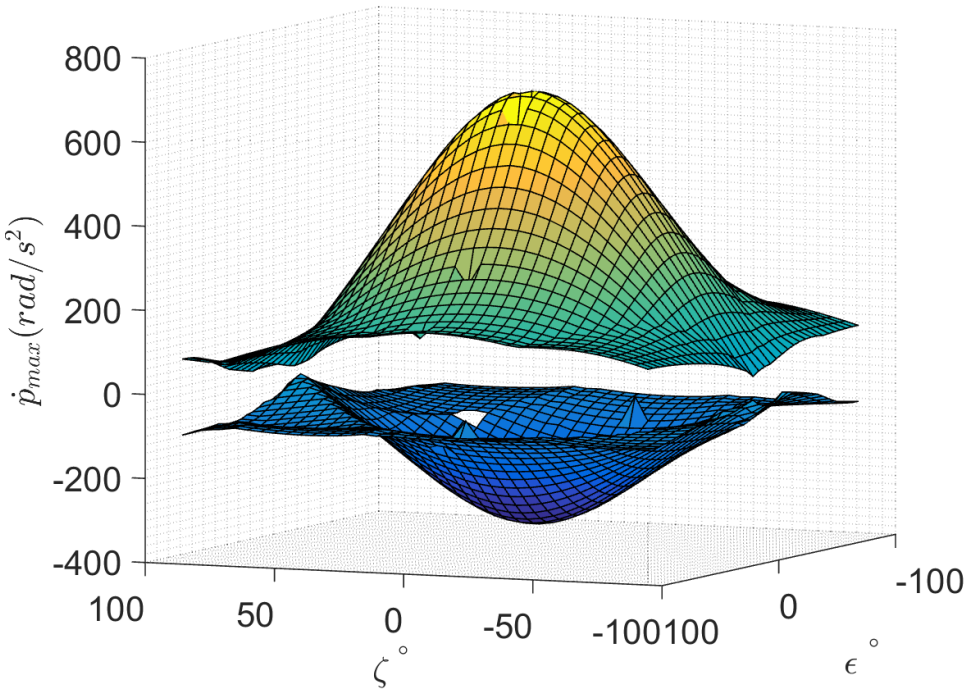

Figure 352: Composite LUT for *X6* failures of rotors *M1* through *M3*, pure motion not enforced

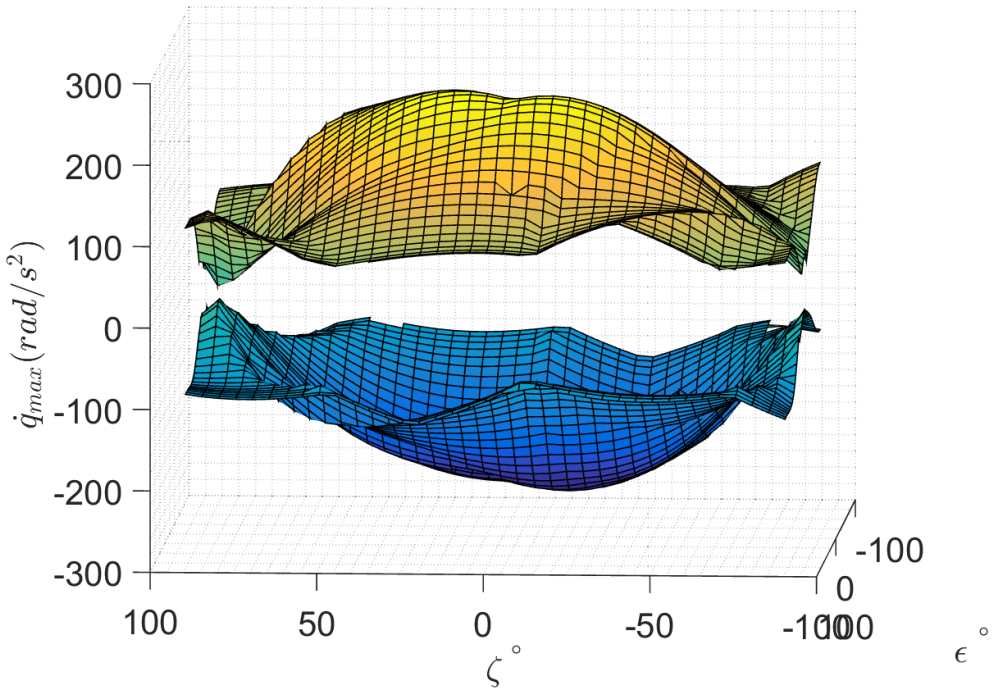

Figure 353: Composite LUT for *X6* failures of rotors *M1* through *M3* , pure motion not enforced

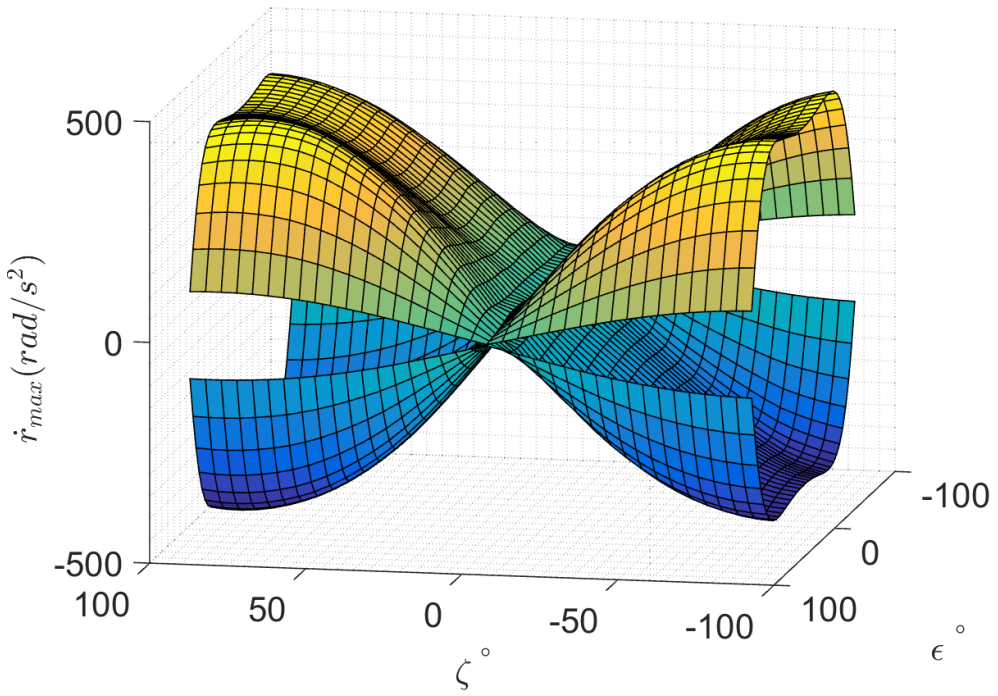

Figure 354: Composite LUT for *X6* failures of rotors *M1* through *M3* , pure motion not enforced

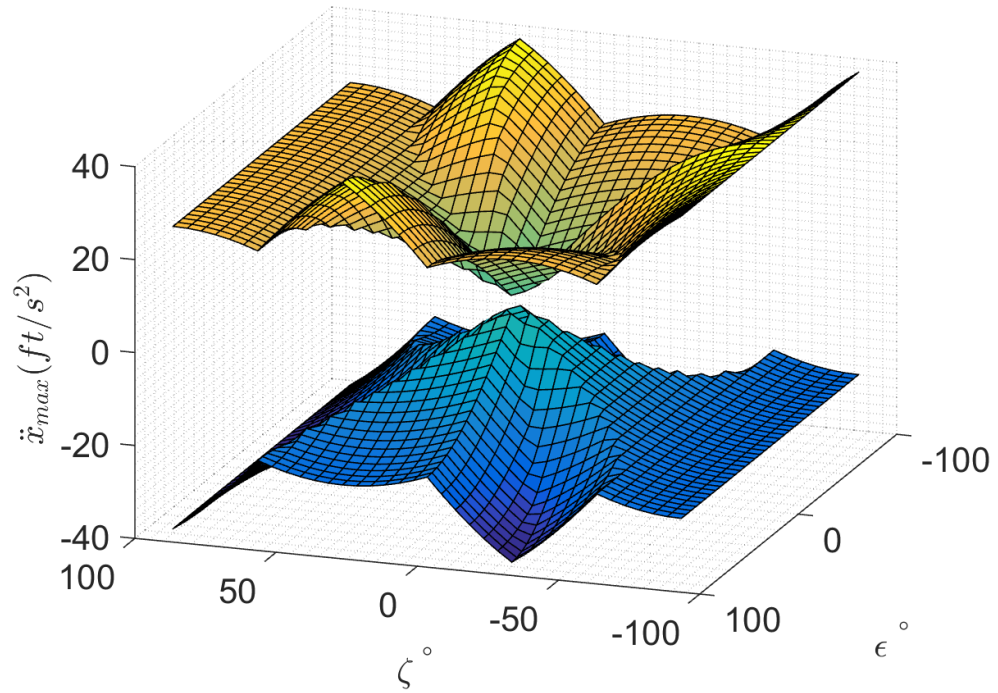

Figure 355: Composite LUT for *X6* failures of rotors *M1* through *M3* , pure motion not enforced

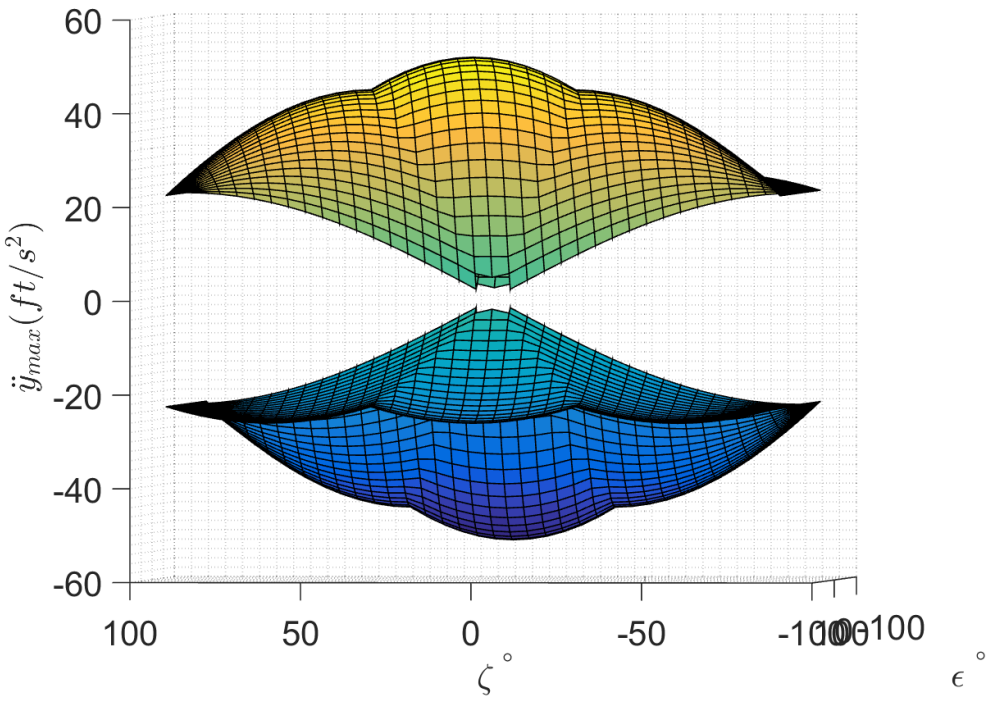

Figure 356: Composite LUT for *X6* failures of rotors *M1* through *M3* , pure motion not enforced

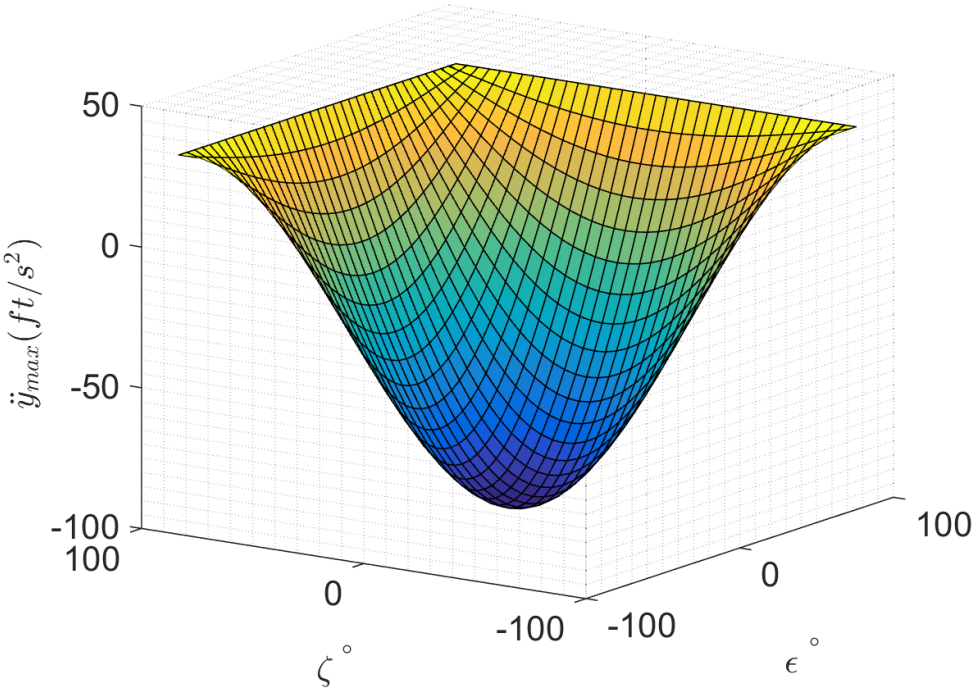

Figure 357: Composite LUT for *X6* failures of rotors *M1* through *M3* , pure motion not enforced

REFERENCES

[1] Achtelik, Michael, et al. "Design of a Multi Rotor MAV with regard to Efficiency, Dynamics and Redundancy." AIAA Guidance, Navigation, and Control Conference. 2012.

[2] Harrington, A. M., "Optimal propulsion system design for a micro quad rotor," M.S. Thesis, Department of Aerospace Engineering, University of Maryland, College Park, MD, 2011.

[3] Leishman, J.G., *Principles of Helicopter Aerodynamics*, Cambridge University Press, New York, 2006.

[4] Tarascon, J.M., "Issues and challenges facing rechargeable lithium batteries," Nature Publishing Group, 2001.

[5] Moore, Mark D., Goodrich, K., Viken, J., Smith, J., Fredericks, B., Trani, T., Barraclough, J., German, B., Patterson, M., . "High Speed Mobility through On-Demand Aviation," 2013 Aviation Technology, Integration, and Operations Conference , (2013).

[6] A123 Systems, http://www.a123systems.com/technology/life, accessed 12/12/2016.

[7] Vetter, J., et. al., "Ageing mechanisms in lithium-ion batteries ." *Journal of Power Sources*, Volume 147, Issues 1172, 9 September 2005, Pages 26917281.

[8] Froude, R. E., "On the Part Played in Propulsion by Differences of Fluid Pressure," *Transactions of the Institute of Naval Architects*, Vol. 30, 1889, pp. 390-405.

[9] Rankine, W. J. M., "On the Mechanical Principles of the Action of Propellers," *Transactions of the Institute of Naval Architects*, Vol. 6, 1865, pp. 13-39.

[10] McCormick, Jr., B. W., *Aerodynamics of V/STOL Flight*, Dover, Mineola, New York, 1999.

[11] Drzewiecki, S., *Theorie generale de l'helice*, Gauthier-Villars et cie., Paris, 1920.

[12] Glauert, H., *Aerodynamic Theory* , Vol. IV, Div. L, chap. Airplane Propellers, Julius Springer, Berlin, 1935, pp. 169-269.

[13] Prouty, Raymond W. *Helicopter performance, stability, and control*. 1995.

[14] B. Theys, G. Dimitriadis, P. Hendrick, and J. De Schutter. "Experimental and Numerical Study of Micro-Aerial-Vehicle Propeller Performance in Oblique Flow", Journal of Aircraft, Vol. 54, No. 3 (2017), pp. 1076-1084.

[15] Stepaniak, M. J., Van Graas, F.,Uijt De Haag, M., "Design of an Electric Propulsion System for a Quadrotor Unmanned Aerial Vehicle", Journal of Aircraft, 2009 Vol. 46, No. 3, 1050-1058. DOI: 10.2514/1.38409.

[16] Scorpion Calc v3.37, http://www.scorpionsystem.com/downloads/, accessed 01/13/2015.

[17] Ampatis, C., Papadopoulos, E. "Parametric Design and Optimization of Multi-Rotor Aerial Vehicles." In Applications of Mathematics and Informatics in Science and Engineering, pp. 1-25. Springer International Publishing, 2014.

[18] Gur, O., Rosen, A., 10-12 September 2008, "Optimizing Electric Propulsion Systems for UAVs," AIAA 2008-5916. 12th AIAA/ISSMO Multidisciplinary Analysis and Optimization Conference Victoria, British Columbia Canada.

[19] P.R. Bates, D.P. Schrage, "The Configuration and Conceptual Design for Rotary Wing Aircraft", Proceedings of the AIAA/AHS/ASEE Aircraft Design Systems and Operations Meeting, St. Louis, Missouri, USA, September 14-16, 1987, pp. 10

[20] Schrage, D.P., 2013, Lecture Notes on Rotorcraft Systems Design, Vehicle Synthesis for Advanced VTOL Aircraft, School of Aerospace Engineering, Georgia Institute of Technology.

[21] Khalid, A. "Development And Implementation Of Rotorcraft Preliminary Design Methodology Using Multidisciplinary Design Optimization," Ph.D. Dissertation, Department of Aerospace Engineering, Georgia Institute of Technology, Atlanta, GA, 2006.

[22] Wood, K., Aerospace Vehicle Design, vol. I. Johnson Publishing Company, Third Ed., 1968.

[23] Ibrahim, K. , "Selecting Wing Loading and Thrust to Weight Ratio for Military Jet Trainers," 20th AIAA Applied Aerodynamics Conference, 2002.

[24] Mattingly, J. D., Heiser, W. H., and Daley, D. H., Aircraft Engine Design, AIAA Education Series, Second ed., 2002.

[25] Howe, D., Aircraft Conceptual Design Synthesis, Professional Engineering Publishing, 2000.

[26] Arjomandi, M.and Liseytsev, N., "A Simplified Method for Estimating the Take-off Weight for Short-haul Transports," Journal of Aircraft Design, Vol. 3, pp. 49-56.

[27] Anderson, J. D., Aircraft Performance and Design. McGraw-Hill, 1999.

[28] Torenbeek, E., Synthesis of Subsonic Airplane Design: An Introduction to the Preliminary Design of Subsonic General Aviation and Transport Aircraft, With Emphasis on Layout, Aerodynamic Design, Propulsion and Performance, Delft Univeristy Press, 1976.

[29] Crisler, W. P.and Brandt, S. A., "Teaching the Nine Technologies of Conceptual Aircraft Design," in 1998 World Aviation Conference, Anaheim, CA, Sept. 28-30, no. AIAA-1998-5531, AIAA and SAE, 1998.

[30] Johnson, W. (2010). NDARCNASA Design and Analysis of Rotorcraft. Validation and Demonstration. In American Helicopter Society Aeromechanics Specialists17 Conference.

[31] Nam, T. "A Generalized Sizing Method for Revolutionary Concepts Under Probablistic Design Constraints," Ph.D. Thesis, Department of Aerospace Engineering, Georgia Institute of Technology, Atlanta, GA, 2007.

[32] Nam, T.,Soban, D. S., and Mavris, D. N. , "Generalized Aircraft Sizing Method and Application to Electric Aircraft," in The 3rd International Energy Conversion Engineering Conference, San Francisco, California, Aug. 15 - 18 , 2005.

[33] Pate, D. J., Patterson, M. D., German, B. J. (2012). Optimizing families of reconfigurable aircraft for multiple missions. Journal of Aircraft, 49(6), 1988-2000.

[34] Aliaga-Aguilar, H., Cuerno-Rejado, C. (2017). Development and validation of software for rapid performance estimation of small RPAS. Advances in Engineering Software, 110, 1-13.

[35] Quan, Q. (2017). Introduction to multicopter design and control. Springer.

[36] Latorre, A. M., "Propulsion system optimization for an unmanned lightweight quadrotor," M.S. Thesis, Department of Aerospace Engineering, Universitat Politcnica de Catalunya, Catalonia, Spain, 2011.

[37] Daskilewicz, M. J., German, B. J., Takahashi, T., "Effects of disciplinary uncertainty on multi-objective optimization in aircraft conceptual design." Structural and Multidisciplinary Optimization 44.6 (2011): 831-846.

[38] Lundström, D., Amadori, K., Krus, P., "Automation of Design and Prototyping of Micro Aerial Vehicle", AIAA-2009-629, 47th AIAA Aerospace Sciences Meeting, Orlando, FL, USA, Jan. 2009.

[39] Bouabdallah, S., Siegwart, R., "Design and Control of a Miniature Quadrotor," *Advances in Unmanned Aerial Vehicles*, Springer Netherlands, 2007.

[40] Magnussen, yvind, Morten Ottestad, and Geir Hovland. "Multicopter design optimization and validation." Modeling, Identification and Control 36.2 (2015): 67.

[41] Cinar, G., Emeneth, M., and Mavris, D., "A Methodology for Sizing and Analysis of Electric Propulsion Subsystems for Unmanned Aerial Vehicles," Proceedings of the AIAA Aerospace Sciences Meeting, January 2016.

[42] Chakraborty, I., Trawick, D., and Mavris, D., "A Requiremen ts-driven Methodology for Integrating Subsystem Archi-tecture Sizing and Analysis into the Conceptual Aircraft Design Phase," 14th AIAA Aviation Technology, Integration, and Operations Conference, AIAA., Atlanta, GA, 2014

[43] Winslow, Justin M., Vikram Hrishikeshavan, and Inderjit Chopra. "Design Methodology for Small Scale Unmanned Quadrotors." 55th AIAA Aerospace Sciences Meeting. 2017.

[44] Traub, Lance W. "Optimal Battery Weight Fraction for Maximum Aircraft Range and Endurance." Journal of Aircraft (2016).

[45] Avanzini, G., Giulietti, F. (2013). Maximum range for battery-powered aircraft. Journal of Aircraft.

[46] Traub, L. W. (2016). Calculation of Constant Power Lithium Battery Discharge Curves. Batteries, 2(2), 17. Chicago

[47] Gatti, M., Giulietti, F., Turci, M. (2015). Maximum endurance for battery-powered rotary-wing aircraft. Aerospace Science and Technology, 45, 174-179.

[48] Avanzini, G., de Angelis, E. L., Giulietti, F. (2016). Optimal performance and sizing of a battery-powered aircraft. Aerospace Science and Technology, 59, 132-144.

[49] Wang, B., Hou, Z., Liu, Z., Chen, Q., Zhu, X. (2016). Preliminary Design of a Small Unmanned Battery Powered Tailsitter. International Journal of Aerospace Engineering, 2016.

[50] Abdilla, A., Richards, A., Burrow, S. (2015, September). Power and endurance modelling of battery-powered rotorcraft. In Intelligent Robots and Systems (IROS), 2015 IEEE/RSJ International Conference on (pp. 675-680). IEEE.

[51] Riboldi, C. E. D., Gualdoni, F. (2016). An integrated approach to the preliminary weight sizing of small electric aircraft. Aerospace Science and Technology, 58, 134-149.

[52] Donateo, T., Ficarella, A., Spedicato, L., Arista, A., Ferraro, M. (2017). A new approach to calculating endurance in electric flight and comparing fuel cells and batteries. Applied Energy, 187, 807-819.

[53] McCrink, M. H., Gregory, J. W. (2017). Range and Endurance Estimation for Low-Re Electric UAS. In 55th AIAA Aerospace Sciences Meeting (p. 1214).

[54] Abdilla, Analiza, Arthur Richards, and Stephen Burrow. "Endurance optimisation of battery-powered rotorcraft." Conference Towards Autonomous Robotic Systems. Springer, Cham, 2015.

[55] Chang, Tan, and Hu Yu. "Improving electric powered UAVs17 endurance by incorporating battery dumping concept." Procedia Engineering 99 (2015): 168-179.

[56] Mulgaonkar, Yash, and Vijay Kumar. "Autonomous charging to enable long-endurance missions for small aerial robots." Proceedings of SPIE-DSS (2014): 90831S.

[57] Toksoz, Tuna, et al. "Automated battery swap and recharge to enable persistent UAV missions." AIAA Infotech@ Aerospace Conference. 2011.

[58] Roberts, James F., Jean-Christophe Zufferey, and Dario Floreano. "Energy management for indoor hovering robots." Intelligent Robots and Systems, 2008. IROS 2008. IEEE/RSJ International Conference on. IEEE, 2008.

[59] Nugent, Thomas, et al. "12-hour hover: Flight demonstration of a laserpowered quadrocopter." White Paper (2011).

[60] Driessens, Scott, and Paul EI Pounds. "Towards a more efficient quadrotor configuration." Intelligent Robots and Systems (IROS), 2013 IEEE/RSJ International Conference on. IEEE, 2013.

[61] Benito, J.A., et. al., "Design considerations of a small UAV platform carrying medium payloads." *Design of Circuits and Integrated Circuits (DCIS)*, 2014.

[62] eCalc, http://www.ecalc.ch/, accessed 3/20/2016.

[63] Multirotor Sizing Tool FLight TIme Calculator, http://controls.ae.gatech.edu/dbershad/EMSTAirTimeCalculator.html, accessed 5/30/2016.

[64] Bershadsky, D., Haviland, S., and Johnson, E.N., "Electric Multirotor Propulsion System Sizing for Performance Prediction and Design Optimization," Proceedings of the AIAA Design Processes and Tools Forum, January 2016.

[65] Russell, C. R., Jung, J., Willink, G., Glasner, B. (2016). Wind Tunnel and Hover Performance Test Results for Multicopter UAS Vehicles.

[66] F. Augugliaro, A. Mirjan, F. Gramazio, M. Kohler, and R. DAndrea, Building tensile structures with flying machines,17 in IEEE/RSJ International Conference on Intelligent Robots and Systems (IROS), pp. 3487173492, Nov 2013.

[67] D. Mellinger, Q. Lindsey, M. Shomin, and V. Kumar, Design, modeling, estimation and control for aerial grasping and manipulation,17 in IEEE/RSJ International Conference on Intelligent Robots and Systems (IROS), pp. 2668172673, Sept 2011.

[68] M. Fumagalli, R. Naldi, A. Macchelli, F. Forte, A. Keemink, S. Stramigioli, R. Carloni, and L. Marconi, Developing an aerial manipulator prototype: Physical interaction with the environment,17 IEEE Robotics Automation Magazine, vol. 21, pp. 411750, Sept 2014.

[69] G. Gioioso, M. Ryll, D. Prattichizzo, H. H. Bulthoff, and A. Franchi, Turning a near-hovering controlled quadrotor into a 3D force effector,17 in 2014 IEEE Int. Conf. on Robotics and Automation, Hong Kong, China, May. 2014, pp. 6278176284.

[70] B. Yuksel, C. Secchi, H. H. Bulthoff, and A. Franchi, A nonlinear force observer for quadrotors and application to physical interactive tasks,17 in 2014 IEEE/ASME Int. Conf. on Advanced Intelligent Mechatronics, Besancon, France, Jul. 2014, pp. 43317440.

[71] Cleandrone, http://www.cleandrone.com/, accessed 06/19/2017.

[72] G. Jiang and R. Voyles, "A nonparallel hexrotor UAV with faster response to disturbances for precision position keeping," 2014 IEEE International Symposium on Safety, Security, and Rescue Robotics (2014), Hokkaido, 2014, pp. 1-5.

[73] G. Jiang, R. Voyles, K. Sebesta and H. Greiner, "Mock-up of the exhaust shaft inspection by dexterous hexrotor at the DOE WIPP site," 2015 IEEE International Symposium on Safety, Security, and Rescue Robotics (SSRR), West Lafayette, IN, 2015, pp. 1-2.

[74] B. Crowther, A. Lanzon, M. Maya-Gonzalez, and D. Langkamp, Kinematic analysis and control design for a nonplanar multirotor vehicle,17 Journal of Guidance, Control, and Dynamics, vol. 34, no. 4, pp. 1157171171, 2011.

[75] G. Jiang and R. Voyles, Hexrotor uav platform enabling dextrous interaction with structures-flight test,17 in IEEE International Symposium on Safety, Security, and Rescue Robotics (SSRR), pp. 1176, Oct 2013.

[76] E. Kaufman, K. Caldwell, D. Lee, and T. Lee, Design and development of a free-floating hexrotor uav for 6-dof maneuvers,17 in IEEE Aerospace Conference, pp. 11710, March 2014.

[77] S. Rajappa, M. Ryll, H. H. Bulthoff, and A. Franchi, Modeling, control and design optimization for a fully-actuated hexarotor aerial vehicle with tilted propellers,17 in IEEE International Conference on Robotics and Automation (ICRA), May 2015.

[78] A. Nikou, G. C. Gavridis, and K. J. Kyriakopoulos, Mechanical design, modelling and control of a novel aerial manipulator,17 in IEEE International Conference on Robotics and Automation (ICRA), pp. 4698174703, May 2015.

[79] D. Brescianini and R. D'Andrea, "Design, modeling and control of an omni-directional aerial vehicle," 2016 IEEE International Conference on Robotics and Automation (ICRA), Stockholm, 2016, pp. 3261-3266.

[80] S. Park, J. Her, J. Kim and D. Lee, "Design, modeling and control of omni-directional aerial robot," 2016 IEEE/RSJ International Conference on Intelligent Robots and Systems (IROS), Daejeon, 2016, pp. 1570-1575. doi: 10.1109/IROS.2016.7759254

[81] K. Kiso, T. Ibuki, M. Yasuda and M. Sampei, "Structural optimization of hexrotors based on dynamic manipulability and the maximum translational acceleration," 2015 IEEE Conference on Control Applications (CCA), Sydney, NSW, 2015, pp. 774-779.

[82] H. Mehmood, T. Nakamura and E. N. Johnson, "A maneuverability analysis of a novel hexarotor UAV concept," 2016 International Conference on Unmanned Aircraft Systems (ICUAS), Arlington, VA, 2016, pp. 437-446.

[83] M. Ryll, D. Bicego and A. Franchi, "Modeling and control of FAST-Hex: A fully-actuated by synchronized-tilting hexarotor," 2016 IEEE/RSJ International Conference on Intelligent Robots and Systems (IROS), Daejeon, 2016, pp. 1689-1694.

[84] M. Ryll, H. Bulthoff, and P. Giordano, Modeling and control of a quadrotor uav with tilting propellers,17 in IEEE International Conference on Robotics and Automation (ICRA), pp. 4606174613, May 2012.

[85] C. Papachristos, K. Alexis, and A. Tzes, Efficient force exertion for aerial robotic manipulation: Exploiting the thrust-vectoring authority of a tri-tiltrotor uav,17 in IEEE International Conference on Robotics and Automation (ICRA), pp. 4500174505, May 2014.

[86] Langkamp, D. 17 Roberts, G. 17 Scillitoe, A. 17 Lunnon, I. 17 Llopis-Pascual, A. 17 Zamecnik, J. 17 Proctor, S. 17 Rodriguez-Frias, M. 17 Turner, M. 17 Lanzon, A. 17 Crowther, W. An engineering development of a novel hexrotor vehicle for 3D applications. In International Micro Air Vehicle conference and competitions, 2011

[87] Y. Long and D. Cappelleri, Omnicopter: A novel overactuated micro aerial vehicle,17 in Advances in Mechanisms, Robotics and Design Education and Research, vol. 14 of Mechanisms and Machine Science, pp. 21517226, Springer International Publishing, 2013.

[88] Mellinger, Daniel, Nathan Michael, and Vijay Kumar. "Trajectory generation and control for precise aggressive maneuvers with quadrotors." The International Journal of Robotics Research 31.5 (2012): 664-674.

[89] Franchi, Antonio, et al. "Full-Pose Geometric Tracking Control on SE (3) for Laterally Bounded Fully-Actuated Aerial Vehicles." arXiv preprint arXiv:1605.06645 (2016).

[90] J. I. Giribet, R. S. Sanchez-Pena and A. S. Ghersin, "Analysis and design of a tilted rotor hexacopter for fault tolerance," in IEEE Transactions on Aerospace and Electronic Systems, vol. 52, no. 4, pp. 1555-1567, August 2016.

[91] Michieletto, Giulia, Markus Ryll, and Antonio Franchi. "Control of statically hoverable multi-rotor aerial vehicles and application to rotor-failure robustness for hexarotors." 2017 IEEE International Conference on Robotics and Automation. 2017.

[92] G. P. Falconi and F. Holzapfel, Adaptive fault tolerant control allocation for a hexacopter system,17 in 2016 American Control Conference, Boston, MA, May 2016, pp. 6760176766.

[93] J. Lee, H. S. Choi, and H. Shim, Fault tolerant control of hexacopter for actuator faults using time delay control method,17 International Journal of Aeronautical and Space Sciences, vol. 17, no. 1, pp. 5417 63, 2016.

[94] M. W. Mueller and R. DAndrea, Relaxed hover solutions for multicopters: Application to algorithmic redundancy and novel vehicles,17 The International Journal of Robotics Research, vol. 35, no. 8, pp. 87317889, 2016.

[95] Markusic, Thomas, Jonathon Jones, and M. Cox. "Thrust stand for electric propulsion performance evaluation." 40th AIAA/ASME/SAE/ASEE Joint Propulsion Conference and Exhibit. 2004.

[96] Rand, Omri, and Vladimir Khromov. "Aerodynamic optimization of coaxial rotor in hover and axial flight." 27th international Congress of the Aeronautical Sciences. 2010.

[97] Leishman, J. Gordon, and Shreyas Ananthan. "Aerodynamic optimization of a coaxial proprotor." Annual Forum Proceedings-American Helicopter Society. Vol. 62. No. 1. American Helicopter Society, INC, 2006.

[98] H. Otsuka and K. Nagatani, "Thrust loss saving design of overlapping rotor arrangement on small multirotor unmanned aerial vehicles," 2016 IEEE International Conference on Robotics and Automation (ICRA), Stockholm, 2016, pp. 3242-3248.

[99] Aleksandrov, D., and I. Penkov. "Optimal gap distance between rotors of mini quadrotor helicopter." Proceedings of the 8th DAAAM Baltic Conference, Tallinn, Estonia. 2012.

[100] McDonald, R. A., "Electric Propulsion Modeling for Conceptual Aircraft Design," 52nd Aerospace Science Meeting, AIAA SciTech, National Harbor, Maryland, Jan. 2014.

[101] http://www.adl.gatech.edu/expaero/lowturb.html, accessed 6/25/2017.

[102] Stevens, Brian L., Frank L. Lewis, and Eric N. Johnson. Aircraft control and simulation: dynamics, controls design, and autonomous systems. John Wiley and Sons, 2015.

[103] Johnson, Eric, and Sumit Mishra. "Flight Simulation for the Development of an Experimental UAV." AIAA Modeling and Simulation Technologies Conference and Exhibit. 2002.

[104] https://www.kickstarter.com/projects/1719668770/cyphy-lvl-1-drone-reinvented-for-performance-and-c, accessed 6/25/2017.

[105] Jiang, Guangying, "Dexterous Hexrotor UAV Platform" (2013). *Electronic Theses and Dissertations.* Paper 321.

[106] 3DR, http://3drobotics.com/x8/, accessed 02/19/2015.

[107] Altus Intelligence, https://altusintelligence.com/, accessed 05/25/2017.

[108] S. Bouabdallah and R. Siegwart, "Backstepping and Sliding-mode Techniques Applied to an Indoor Micro Quadrotor," Proceedings of the 2005 IEEE International Conference on Robotics and Automation, 2005, pp. 2247-2252.

[109] Godston, J., and C. Reynolds. "Future prop-fans-Tractor or pusher." 21st Joint Propulsion Conference. 1985.

[110] Kushleyev, A., Mellinger, D., Powers, C., Kumar, V., "Towards a swarm of agile micro quadrotors", Journal of Autonomous Robots, 2013, p. 287-300, DOI:10.1007/s10514-013-9349-9.

[111] Powers, Caitlin, et al. "Influence of aerodynamics and proximity effects in quadrotor flight." Experimental robotics. Springer International Publishing, 2013.

[112] Rossow, Vernon J. "Effect of ground and/or ceiling planes on thrust of rotors in hover." (1985).

[113] Haviland, S., Bershadsky, D., Magree, D., and Johnson, E.N., "Development of a 500 gram Vision-based Autonomous Quadrotor Vehicle Capable of Indoor Navigation," Proceedings of the AHS International 71st Annual Forum and Technology Display, May 2015.

[114] Sheldahl, R E, and P C Klimas. 1981. "Aerodynamic Characteristics of Seven Symmetrical Airfoil Sections through 180-Degree Angle of Attack for Use in Aerodynamic Analysis of Vertical Axis Wind Turbines". United States. doi:10.2172/6548367.

[115] Electrofly, http://electrofly.free.fr/download.php?lng=en, accessed 03/10/2015.

[116] Hobbyking, http://www.hobbyking.com/hobbyking/store/index.asp, accessed 02/07/2015.

[117] Brandt, J., Selig, M., "Propeller Performance Data at Low Reynolds Numbers", 49th AIAA Aerospace Sciences Meeting, 2011, AIAA 2011-1255. http://www.ae.illinois.edu/m-selig/props/propDB.html. accessed 01/30/2015.

[118] Magree, D., Bershadsky, D., Haviland, S., et. al., "Georgia Tech Team Entry for the 2012 AUVSI International Aerial Robotics Competition," Fourth Symposium on Indoor Flight Issues, August 2012.

[119] http://www.uavrf.gatech.edu/, accessed 01/22/2015.

[120] http://thequadshot.com/w/index.php?title=Quadshot_Technical_Specifications, accessed 02/19/2015.

[121] http://www.tech-sov.com/news_13.htm, accessed 02/22/2015.

[122] http://www.bladehelis.com/Products/Default.aspx?ProdID=BLH7600, accessed 02/18/2015.

[123] http://kmelrobotics.com/, accessed 02/19/2015.

[124] http://diydrones.com/group/arducopterusergroup/forum/topics/new-vehicle-design-tool?xg_source=activity, accessed 09/17/2015.

[125] http://rc.runryder.com/helicopter/t669735p1/, accessed 02/19/2015.

[126] https://www.dji.com/product/inspire-1, accessed 06/06/2015.

[127] http://www.asctec.de/en/uav-uas-drone-products/asctec-hummingbird/, accessed 07/22/2015.

[128] https://store.3drobotics.com/products/iris, accessed 02/19/2015.

[129] http://www.dji.com/product/phantom, accessed 07/22/2015.

[130] http://www.dji.com/matrice600, accessed 06/19/2017.

[131] http://www.rcgroups.com/forums/showthread.php?t=1880665, accessed 01/22/2015.

[132] http://diydrones.com/profiles/blogs/my-97minute-06second-record-quadcopter-flight, accessed 01/22/2015.

[133] Mulgaonkar, Y, et. al, "Power and weight considerations in small, agile quadrotors," Proc. SPIE 9083, Micro- and Nanotechnology Sensors, Systems, and Applications VI, 90831Q 2014.

[134] Panasonic, http://industrial.panasonic.com/lecs/www-data/pdf2/ACA4000/ACA4000CE417.pdf, accessed 11/01/2015.

[135] Floreano, Dario, and Robert J. Wood. "Science, technology and the future of small autonomous drones." Nature 521.7553 (2015): 460-466.

[136] G. P. Falcon17, J. Angelov and F. Holzapfel, "Hexacopter outdoor flight test results using adaptive control allocation subject to an unknown complete loss of one propeller," 2016 3rd Conference on Control and Fault-Tolerant Systems (SysTol), Barcelona, 2016, pp. 373-380. doi: 10.1109/SYSTOL.2016.7739779

[137] Powell, M. J. D. "A Fast Algorithm for Nonlinearly Constrained Optimization Calculations." Numerical Analysis, ed. G. A. Watson, Lecture Notes in Mathematics, Springer-Verlag, Vol. 630, 1978.

[138] Powell, M. J. D. "The Convergence of Variable Metric Methods For Nonlinearly Constrained Optimization Calculations." Nonlinear Programming 3 (O. L. Mangasarian, R. R. Meyer, and S. M. Robinson, eds.), Academic Press, 1978.

[139] Han, S. P. "A Globally Convergent Method for Nonlinear Programming." Journal of Optimization Theory and Applications, Vol. 22, 1977, pp. 297.

[140] Gill, P. E., W. Murray, and M. H. Wright. Practical Optimization, London, Academic Press, 1981.

[141] Condor High Performance Cluster documentation, http://research.cs.wisc.edu, accessed 6/1/2017.

[142] Mini quad test bench, http://www.miniquadtestbench.com/motor-explorer.html, accessed 5/2/2017.

[143] Previati, Giorgio, et al. "A new test rig for measuring the inertia properties of vehicles and their subsystems." Proceedings of IMECE. 2004.

[144] Mehmood, Hamza, and Eric N. Johnson. "A Daisy-Chain Control Design for a Multirotor UAV with Direct Force Capabilities." AIAA Guidance, Navigation, and Control Conference. 2017.

[145] M. W. Mueller and R. DAndrea, Stability and control of a quadrocopter despite the complete loss of one, two, or three propellers,17 in 2014 IEEE Int. Conf. on Robotics and Automation, Hong Kong, China, May 2014, pp. 451752.

[146] Schoemann, Joachim. Hybrid-electric propulsion systems for small unmanned aircraft. Dr. Hut, 2014.

[147] Roth, B. A., German, B. J., Mavris, D.N., "Adaptive selection of engine technology solution sets from a large combinatorial space." (2001).

[148] Carroll, T. George, I.E., Bramesfeld, G., "Design Optimization of Small Rotors in Quad-Rotor Configuration", AIAA SciTech, San Diego, CA, Jan. 2016.

[149] Pereira, Jason L. Hover and wind-tunnel testing of shrouded rotors for improved micro air vehicle design. University of Maryland, College Park, 2008.

[150] Krumm, J., "Intersection of Two Planes," https://www.microsoft.com/en-us/research/wp-content/uploads/2016/02/note.doc, accessed 1/20/2017.

[151] http://www.team-blacksheep.com/products/prod:vendetta, accessed 6/25/2017.

[152] Pesaran, A.A., Vlahinos, A., Burch, S.D., "Thermal Performance of EV and HEV Battery Modules and Packs," Proceedings of the 14th International Electric Vehicle Symposium, Orlando, Florida, December 151717, 1997.

[153] Battery University, http://batteryuniversity.com/learn/article/discharging_at_high_and_low_t accessed 11/01/2015.

[154] Bohorquez, F., Pines, D., Samuel, P.D., "Small Rotor Design Optimization Using Blade Element Momentum Theory and Hover Tests", Journal of Aircraft, 2010 Vol. 47, No. 1, 268-283. DOI: 10.2514/1.45301

[155] Etkin, Bernard, and Lloyd Duff Reid. Dynamics of flight: stability and control. Vol. 3. New York: Wiley, 1996.

[156] C. D. Heise, G. P. Falconi, and F. Holzapfel, Hexacopter Outdoor Flight Test Results of an Extended State Observer based Controller . 2014 IEEE ICARES, 2014.

[157] A. Nemati and M. Kumar, Modeling and Control of a Single Axis Tilting Quadcopter. 2014 American Control Conference, 4-6 June, 2014, Portland, Oregon, USA

[158] Yip, Long P. "Wind-tunnel investigation of a full-scale canard-configured general aviation airplane." (1985).

[159] Larminie, J., Lowry, J., Electric Vehicle Technology Explained, John Wiley and Sons, 2nd ed., June 2012.

[160] Delany, Noel K., and Norman E. Sorensen. "Low-speed drag of cylinders of various shapes." 1953.

[161] Shur, M., et al. "Detached-eddy simulation of an airfoil at high angle of attack." Engineering turbulence modelling and experiments 4 (1999): 669-678.

[162] Logan, M. J., Chu, J., Motter, M., Carter, D. L., Ol, M., and Zeune, C., "Small UAV Research and Evolution in Long Endurance Electric Powered Vehicles," AIAA Infotech at Aerospace Conference and Exhibit, 2007.

[163] https://downanddirtydrones.com/portfolio/, accessed 6/25/2017.

[164] http://fortune.com/2017/07/14/fastest-drone-guinness-world-record/, accessed 7/15/2017.

[165] https://www.rcgroups.com/forums/showthread.php?1055847-stability-changes-under-power/page2, accessed 6/25/2017.

VITA

Dmitry Bershadsky was born in Ukraine in 1982. He started his undergraduate study at Cornell University, Ithaca, NY in 2001 and received a Bachelor of Science in in Mechanical and Aerospace Engineering in 2004. He then received his Master of Engineering in Biomechanics from the same university in 2005. For the next five years, he worked at Lockheed Martin Systems Integration in Owego, NY on avionics and algorithm development. In January 2011, he joined the graduate study program in the School of Aerospace Engineering at Georgia Institute of Technology as part of the Unmanned Aerial Vehicle Research Facility. He received a Master of Science in Aerospace Engineering from Georgia Institute of Technology in 2013 and is continuing in the Ph.D. program.